Setif 1 University - Ferhat ABBAS

A Dissertation Submitted in Partial Fulfillment
of the Requirements for the Degree of

DOCTORATE

Field: Physics
Specialization: Physics of the Globe
At the Faculty of Sciences – Department of Physics
University Ferhat Abbes Setif 1 (Algeria)

High-Resolution Aftershock-Based Imaging of Active Faults, Source Parameters and Earthquake Driving Mechanisms: A Contribution to Seismic Hazard Assessment in Northeastern Algeria

Tikhamarine El-Mahdi

Presented and publicly defended on: 18 / 02 / 2025

The examination committee:

Mansouri Abdelaziz	Chair of the Jury	Professor, Ferhat Abbas University Setif 1
Abacha Issam	Supervisor	Research Director, CRAAG Setif
Boulahia Oualid	Co-supervisor	Research Master, CRAAG Setif
Chabou Moulley Charaf	Examiner	Professor, Ferhat Abbas University Setif 1
Beldjoudi Hamoud	Examiner	Research Director, CRAAG Algiers
Semmane Fethi	Examiner	Research Director, CRAAG Algiers
Bendjama Hichem	Guest	Research Master, CRAAG Constantine

Abstract

Seismology has experienced significant advancements since its establishment in the mid-20th century, driven by the increasing need to comprehend and mitigate the impacts of earthquakes. Earthquakes, often sudden and violent, have long been a source of fear and terror due to their devastating effects on both infrastructure and human lives. As the understanding of plate tectonics and seismic activity evolved, modern seismology emerged as a powerful tool to investigate the underlying causes of these natural phenomena. The present thesis, titled "High-Resolution Aftershock-Based Imaging of Active Faults, Source Parameters, and Earthquake Driving Mechanisms: A Contribution to Seismic Hazard Assessment in Northeastern Algeria" builds upon these developments. The main aim is to contribute valuable insights to the assessment of seismic hazards in the northeastern region of Algeria. The thesis is structured around three core components. First, it focuses on high-resolution aftershock-based imaging, providing detailed depictions of fault systems to improve the understanding of fault geometries and potential earthquake nucleation zones. Utilizing advanced techniques such as double-difference relocation and hierarchical clustering of earthquake multiplet, this work identifies previously unmapped fault segments. Second, it involves the analysis of earthquake source parameters, including seismic moment, fault geometry, stress drop, and source radius. These parameters provide crucial insights into earthquake mechanics and the characteristics of faults in the study area. Third, the research investigates earthquake driving mechanisms, including tectonic loading, stress transfer, fluid intrusion, and aseismic slip, to unravel the complex factors contributing to earthquake occurrence in this tectonically active region. Our research began with a detailed analysis of the Beni-Ilmane sequence 2010, serving as a foundation for generalizing our methodology to seismic sequences that occurred between 2007 and 2022 across northeastern Algeria. By analyzing seismic sequences from 2007 to 2022, this research compiles a comprehensive database of active faults, seismic parameters, and earthquake mechanisms. The Findings serves as a critical resource for evaluating seismic hazard and developing risk mitigation strategies. This work highlights the importance of integrating seismic data, fault imaging, and earthquake modeling to enhance the resilience of infrastructures in northeastern Algeria against future seismic events.

Key words: High precision relocation. Aftershocks-based imaging. Focal mechanism analysis. Moment tensor analysis. Earthquake mutiplet. Repeating earthquakes. Driving mechanisms. Earthquake source parameters. Active faults. Northeastern Algeria. Beni-Ilmane. Seismic hazards.

<u>الملخـص</u>

شهد علم الزلازل تطورات كبيرة منذ نشأته في منتصف القرن العشرين، مدفوعًا بالحاجة المتزايدة لفهم وتخفيف آثار الزلازل. كانت الزلازل، التي غالبًا ما تكون مفاجئة وعنيفة، مصدرًا للرعب والاهتمام نظرًا لتأثيراتها المدمرة على البنية التحتية والحياة البشرية. مع تطور فهم الصفائح التكتونية والنشاط الزلزالي، برز علم الزلازل الحديث كأداة قوية للتحقيق في الأسباب الكامنة وراء هذه الظواهر الطبيعية. تبنى الأطروحة الحالية، بعنوان "التصوير عالي الدقة للفوالق النشطة من خلال الهزات الارتدادية، خصائص المصدر الزلزالي، وآليات حدوث الزلازل: مساهمة في تقييم المخاطر الزلزالية في شمال شرق الجزائر"، على هذه التطورات. الهدف الرئيسي هو تقديم رؤى قيمة للمساهمة في تقليل المخاطر الزلزالية في منطقة شمال شرق الجزائر. تُبنى الأطروحة حول ثلاثة ركائز أساسية. أولاً، تركز على التصوير عالي الدقة للفوالق النشطة اعتمادا على توزع الهزات الارتدادية، حيث تقدم تصورات دقيقة لأنظمة الفوالق لتحسين فهم هندسة الفوالق ومناطق نشوء الزلازل المحتملة. باستخدام تقنيات متقدمة مثل إعادة تحديد المواقع باستخدام طريقة الفرق المزدوج وتصنيف مجموعات الزلازل المتعددة بطريقة هرمية، تُحدد هذه الدراسة قطاعات فوالق غير معروفة سابقًا. ثانيًا، تتناول الأطروحة تحليل خصائص المصدر الزلزالي، بما في ذلك العزم الزلزالي، وفرق الإجهاد، ونصف قطر المصدر. تقدم هذه المعلومات رؤى أساسية حول ميكانيكا الزلازل وخصائص الفوالق في منطقة الدراسة. ثالثًا، تدرس الأطروحة الآليات المحركة للزلازل، بما في ذلك التحميل التكتوني، وانتقال الإجهاد، وتأثير السوائل، والانزلاق الزلزالي، لفهم العوامل المعقدة التي تساهم في حدوث الزلازل في هذه المنطقة النشطة تكتونيًا. بدأت دراستنا بتحليل مفصل لسلسلة زلازل بني يلمان 2010، والذي شكل الأساس لتعميم منهجيتنا على التسلسلات الزلزالية التي حدثت بين عامي 2007 و2022 عبر شمال شرق الجزائر. من خلال تحليل التسلسلات الزلزالية من 2007 إلى 2022، تجمع هذه الدراسة قاعدة بيانات شاملة للفوالق النشطة، وخصائصها الزلزالية، وآليات حدوث الزلازل. تُعد نتائج هذه الاطروحة هذه موردًا هامًا لتقييم المخاطر الزلزالية وتطوير استراتيجيات التخفيف من المخاطر. كما وتسلط هذه الدراسة الضوء على أهمية دمج البيانات الزلزالية وتصوير الفوالق ونمذجة الزلازل لتعزيز جاهزية البنى التحتية في شمال شرق الجزائر أمام الأحداث الزلزالية التي قد تحدث.

<u>كلمات مفتاحيـة</u>

إعادة تحديد المواقع بدقة عالية. تصوير الفوالق بالستعمال الهزات الارتدادية. تحليل الآليات البؤرية. تحليل العزم الزلزالي. زلازل متعددة. الزلازل المتكررة. الآليات المحرضة للزلازل. خصائص المصدر الزلزالي. الفوالق النشطة. شمال شرق الجزائر. بني يلمان. المخاطر الزلزالية.

Résumé

La sismologie a connu des avancées significatives depuis sa création au milieu du XXe siècle, en réponse à un besoin croissant de comprendre et d'atténuer les effets des tremblements de terre. Ces derniers, souvent soudains et violents, suscitent à la fois crainte et terreur en raison de leurs conséquences dévastatrices sur les infrastructures et les vies humaines. Avec l'évolution des connaissances sur la tectonique des plaques et l'activité sismique, la sismologie moderne est devenue un outil puissant pour explorer les causes profondes de ces phénomènes naturels. La présente thèse, intitulée « Imagerie haute résolution des failles actives à partir des répliques, paramètres de source et mécanismes déclencheurs des séismes : une contribution à l'évaluation de l'aléa sismique dans le nord-est de l'Algérie. », s'appuie sur ces avancées. L'objectif principal est d'apporter des contributions importantes pour l'évaluation de l'aléa sismiques dans la région nord-est de l'Algérie. La thèse est structurée autour de trois composantes principales. Tout d'abord, elle se concentre sur l'imagerie haute résolution basée sur les répliques, fournissant des représentations détaillées des systèmes de failles pour améliorer la compréhension de la géométrie des failles et des zones potentielles de nucléation des séismes. Grâce à des techniques avancées telles que la relocalisation par double différence et le regroupement hiérarchique des multiplets sismiques, ce travail identifie des segments de failles non cartographiés précédemment. Ensuite, elle analyse les paramètres des sources sismiques, tels que le moment sismique, la géométrie des failles, la chute de contrainte et le rayon de la source. Ces paramètres fournissent des informations cruciales sur la mécanique des tremblements de terre et les caractéristiques des failles dans la zone étudiée. Enfin, cette recherche explore les mécanismes forçants des tremblements de terre, notamment le chargement tectonique, le transfert de contraintes, l'intrusion de fluides et le glissement asismique, afin de comprendre les facteurs complexes qui contribuent à l'occurrence des séismes dans cette région tectoniquement active. Notre recherche a débuté par une analyse détaillée de la séquence de Beni-Ilmane 2010, servant de base pour généraliser notre méthodologie aux séquences sismiques ayant eu lieu entre 2007 et 2022 dans le nord-est de l'Algérie. En analysant les séquences sismiques de 2007 à 2022, cette recherche compile une base de données exhaustive sur les failles actives, les paramètres sismiques et les mécanismes de déclenchement des tremblements de terre. Cette base de données constitue une ressource essentielle pour évaluer l'aléa sismique et élaborer des stratégies de réduction des risques. Ce travail souligne l'importance d'intégrer les données sismiques, l'imagerie des failles et la modélisation des séismes afin de renforcer la résilience des infrastructures du nord-est de l'Algérie face aux futurs événements sismiques.

Mots-clés : Relocalisation de haute précision. Imagerie des failles à partir les répliques. Analyse des mécanismes focaux. Analyse du tenseur de moment. Multiplets sismiques. Séismes récurrents. Mécanismes forçant. Paramètres de la source sismique. Failles actives. Nord-est de l'Algérie. Beni-Ilmane. Aléa sismique.

Acknowledgment

First and foremost, I thank Allah, the All-Knowing, who taught by the pen, taught man what he did not know. I praise Him with abundant, pure, and blessed praise for the apparent and hidden blessings He has bestowed upon us.

Secondly, I would like to sincerely thank my parents, who did not tire or falter, and spared no effort to see their son reach the highest academic degrees. I thank them for their love, for their care, for their continuous material and moral support, and for their sincere prayers, the effects of which I have seen and continue to see in my life. May Allah reward you both with the best that He rewards parents for their children.

My deepest thanks to my brother, sisters, and all my family for their unwavering support and encouragement.

I extend my deepest thanks to the examination committee, consisting of the esteemed professors: *Mansouri Abdelaziz* as the chair of the jury, *Hammoud Beldjoudi*, *Fethi Semmane*, and *Moulley Charaf Chabou* as examiners, and *Hichem Bendjema* as a guest. I thank you for honoring me by accepting to evaluate my dissertation.

The journey of preparing for my Ph.D. has been a challenging and exhausting one from the very beginning, but the difficulty was matched by its joy. After completing my MASTER's degree, which was in the field of hydrocarbon exploration through geophysical methods, I began in the same year my scientific research journey, which was in the field of seismology. Despite the proximity of the two fields, due to their shared physical principles related to the propagation of seismic waves in the Earth's interior, the transition was not as easy as I had anticipated. However, the field of scientific research was worth that sacrifice. It is a field far from monotony, routine, and repetition, and one that is full of rapid and astonishing developments that contribute to our understanding of the planet we live on.

After five years of research in this field, I find myself now capable of understanding seismic phenomena, processing their signals, analyzing them, and even interpreting them. My scientific knowledge has developed to the point where I can now participate in scientific research, write papers, and publish them in peer-reviewed international scientific journals. After Allah's grace, none of this would have been possible without the work environment I was in, an environment that pushes you daily to learn new things, to develop your skills and scientific competence. Behind this motivational environment is a team of disciplined and dedicated researchers. A research team that complements each other, enjoys their work, and is passionate about it. My relationship with this team went beyond that of a professor with their students or a colleague with their colleague; what binds me to this team is a bond of brotherhood.
By this team, I mean the researchers and workers at the Research Center for Astronomy, Astrophysics, and Geophysics (CRAAG) at the Experimental Station in Setif. Following the Hadith of the Prophet, peace be upon him, "*He who does not thank people, does not thank Allah,*" I find it my duty to thank these people, whom I had the honor of knowing, with gratitude befitting their stature and their deeds:

My brother and supervisor, *Issam Abacha*, the esteemed professor and exceptional researcher, you are a role model in perseverance and discipline. Your hard work, ambition, and passion for research have always been a source of motivation for me in difficult times. I thank you for standing by my side from the very first step until today. I thank you for your support and for taking a lot of your time to help me despite your many obligations. I will never forget your efforts and sacrifices and everything you have done for me during this exciting scientific journey. May Allah reward you with all good and keep all harm away from you.

My brother and co-supervisor, *Oualid Boulahia*, the sharp researcher and skilled programmer, you have been a model to emulate with your precision and diligence in your work. Your guidance saved me a lot of time and effort. I learned a lot from your spirit of scientific critique. I thank you for your advice and for standing with me during the tough times I went through. I thank you for your encouragement, your support, your sacrifice, and all the effort you put in to complete this work. May Allah reward you with all good and keep all harm away from you.

My brother and friend, *Hichem Bendjema*, the passionate researcher with a deep thirst for learning. Your vast knowledge in various fields and recent scientific research made our discussions incredibly enjoyable. I learned so much from you in many scientific areas. I admire your perseverance in research and your dedication to spending long hours searching for a single piece of information. I thank you for the immense effort you put into editing and refining my paper. May Allah reward you with all good and keep all harm away from you.

My brothers *Khaled Roubeche* and *Sofiane Taki-Eddine Rahmani*, working with both of you has been both productive and motivating at the same time. I thank you both for your assistance, and hope you a prosper scientific career.

My brother, *Zohir Radi*, I admire your spirit of perseverance and hard work. Thank you for your support.

My brother, *Meziane Mohand*, Director of the Experimental Seismic Station in Setif, thank you for providing me with suitable working conditions.

I also extend my deepest thanks to all the staff of the Research Center for Astronomy, Astrophysics, and Geophysics, as well as all professors of the Department of Physics at the Faculty of Sciences – University Ferhat Abbas 1.

Thank you all.

Tikhamarine El-Mahdi
Setif: 12ᵗʰ September 2024

TABLE OF CONTENTS

Chapter I
Faults Kinematics and Earthquakes Nucleation

Table of Contents

Chapter II
New Seismotectonic Model for Beni-Ilmane Region

Table of Contents

Chapter III
Dynamic Source Parameters' Analysis

Table of Contents

Table of Contents

List of Figures

List of Figures

List of Figures

List of Figures

List of Tables

General Introduction

Seismology has undergone significant evolution since its establishment as a formal scientific discipline in the mid-20th century. Throughout history, humankind's encounters with earthquakes have consistently evoked profound fear and shock. The idea that the solid foundation beneath our feet, the basis we rely upon for stability, is abruptly and violently shaken is truly terrifying. Earthquakes' devastating effects on buildings may take years to recover from, and the loss of human lives are irreparable. This unsettling phenomenon has captivated human curiosity since ancient times, prompting thoughtful inquiries into its underlying causes and mechanisms. From the earliest civilizations to the present day, the quest to comprehend and mitigate the impact of earthquakes remains a crucial pursuit in safeguarding lives and infrastructure worldwide. Although the field of seismology is relatively young, our understanding of earthquake dynamics has rapidly advanced, underpinned by a foundational understanding of plate tectonics as the primary driver of seismic activity. Modern seismology benefits from sophisticated monitoring techniques, improved data processing, and increasingly comprehensive datasets.

The present thesis, titled "High-Resolution Aftershock-Based Imaging of Active Faults, Source Parameters and Earthquake Driving Mechanisms: A Contribution to Seismic Hazard Assessment in Northeastern Algeria," is built on three main pillars that work together to achieve a central goal. These three pillars are:

- High-Resolution Aftershock-Based Imaging of Active Faults.
- Analysis of Earthquake Source Parameters.
- Examination of Earthquake Driving Mechanisms.

The primary objective of this work is to provide a valuable contribution to seismic hazard assessment in the northeastern region of Algeria.

General Introduction

High-resolution imaging of active faults

High-resolution imaging of active fault structures is crucial for advancing our understanding of fault systems and assessing seismic hazards. Detailed imaging enables us to map fault geometries, interactions, and potential earthquake generation zones. This precision is particularly important in identifying zones of potential earthquake nucleation, monitoring the propagation of seismic ruptures, and assessing the likelihood of fault reactivation, all of which contribute to improving seismic hazard assessments and early warning systems .

Several techniques exist to image active fault structures, each offering distinct advantages. Reflection and refraction seismology, commonly used for large faults or fault zones with strong seismic reflectors, relies on seismic wave reflections and refractions to produce images of subsurface structures (Improta & Bruno 2007; Kaiser *et al.* 2009; Ishiyama *et al.* 2016). This method is particularly effective in areas where sedimentary layers obscure fault zones, providing a detailed view of fault geometries at depth. Another method, seismic tomography, utilizes travel-time data from natural or induced seismic events to images the Earth's subsurface. Seismic tomography is highly effective in revealing variations in material properties across fault zones, which may indicate zones of weakness or fluid saturation (Qian & Liu 2020). Additionally, geodetic methods such as GPS and InSAR (Interferometric Synthetic Aperture Radar) provide crucial data on ground deformations caused by fault movements, offering indirect information about underlying fault structures and slip distributions.

Aftershock-based high-resolution imaging has emerged as a leading approach for resolving fine details of active fault structures. Aftershocks, which are smaller seismic events following a major earthquake, offer critical information about fault geometry and stress redistribution following the mainshock. The spatial and temporal patterns of aftershocks can illuminate the areas of a fault that slipped during the mainshock and those that remain locked. This makes aftershock-based imaging a valuable tool for understanding complex fault systems, as it often reveals previously unmapped fault

segments. Imaging fault based on precise hypocenter location has been used by several researchers (e.g Ding *et al.* (2023)) .

One of the significant advantages of aftershock-based imaging is its capacity to capture the immediate post-seismic response of a fault system. After a major earthquake, stress redistribution across the fault system often results in aftershocks occurring in areas not involved in the mainshock rupture. These aftershocks help outline the full extent of the fault system, highlighting stress concentration areas and revealing previously unidentified fault branches. Techniques such as double-difference earthquake relocation have significantly improved the precision of aftershock location, providing more accurate depictions of fault geometries by minimizing errors associated with unknown velocity structures .

In regions characterized by complex fault systems, such as those with multiple interacting faults or a combination of thrust and strike-slip fault regimes, aftershock-based imaging provides a detailed view of fault segment connectivity. This information is essential for understanding the full seismic hazard posed by a fault system, as it highlights the potential for cascading fault failures where rupture on one fault can trigger slip on adjacent faults.

Earthquake Source Parameeters

Analyzing earthquake source parameters is essential for understanding seismic events and improving seismic hazard assessments. These parameters include the earthquake's location, fault geometry (strike, dip, rake), seismic moment, corner frequency, source radius, stress drop and others. Each parameter contributes to a detailed picture of the earthquake's mechanics and the characteristics of the fault that produced it, (Ide *et al.* 2003; Abercrombie & Rice 2005; Viegas *et al.* 2010).

The location of an earthquake is a fundamental parameter that determines the epicenter and depth of the event. Accurate location data are crucial for assessing the

spatial distribution of seismic activity and its potential impact on populated areas. This information helps correlate seismic events with geological structures, providing insights into the tectonic setting and potential hazards associated with the earthquake.

Fault geometry, which encompasses the strike, dip, and rake of the fault, provides detailed information about the orientation and movement along the fault plane. The strike is the direction of the fault trace on the Earth's surface, while the dip represents the angle of inclination of the fault plane relative to the horizontal. The rake describes the direction of slip on the fault. Understanding these parameters is critical for determining the type of faulting (e.g., normal, reverse, or strike-slip) and for modeling seismic wave propagation. Accurate fault geometry also aids in assessing how the fault interacts with surrounding geological structures.

Seismic moment is a measure of the earthquake's size and is directly related to the amount of energy released during the event. It quantifies the product of the fault's slip and the fault area, providing a critical parameter for understanding the earthquake's potential to cause ground shaking.

Corner frequency is another key parameter that relates to the size of the earthquake source. It represents the frequency at which the earthquake's spectrum shifts from a low-frequency to a high-frequency range. By analyzing the seismic spectrum, researchers can estimate the source radius, which indicates the size of the fault rupture. Understanding corner frequency and source radius helps characterize the dimensions of the fault that slipped during the earthquake and provides insights into the rupture's time.

Stress drop measures the reduction in stress on the fault during the earthquake and reflects the fault's strength and the dynamics of the rupture. A high stress drop indicates significant stress reduction during the event, while a low stress drop suggests a more gradual stress release. Stress drop is important for evaluating the fault's potential for future seismic activity and understanding the overall seismic hazard.

General Introduction

Several methods are used to assess these earthquake source parameters. Moment tensor inversion is a widely used technique that analyzes seismic waveforms recorded at multiple stations to decompose the seismic moment into its components. This method provides detailed information about the fault's orientation and slip distribution, offering a comprehensive view of the earthquake source. The individual spectra method involves analyzing the frequency content of seismic waves from individual events to estimate parameters such as seismic moment, corner frequency, and source radius. This approach fits theoretical spectra to observed data, providing valuable estimates, particularly for smaller earthquakes or events with limited data. The Empirical Green's Function (EGF) approach is another technique used to estimate source parameters. It involves using smaller, well-characterized earthquakes as "green's functions" to infer the source properties of larger events. Through deviding the spectra of larger events by those of smaller earthquakes, researchers can derive the source parameters of the mainshock. The EGF approach is useful for obtaining high-resolution estimates of earthquake source characteristics.

Overall, the analysis of earthquake source parameters is crucial for advancing our understanding of seismic events and assessing seismic hazards. By accurately characterizing fault geometry, seismic moment, and other key parameters, researchers can develop better models of earthquake behavior, improve predictions of ground shaking, and enhance infrastructure resilience. This comprehensive understanding of earthquake sources is essential for effective hazard assessment and for advancing our knowledge of fault systems and their dynamics.

Earthquake Driving Mechanisms

Investigating earthquake driving mechanisms is in its turn important for understanding the fundamental processes that lead to seismic events and for improving hazard assessment. At the core of most seismic activity is tectonic loading, a process wherein the Earth's tectonic plates interact, accumulate stress, and eventually release it

through earthquakes. This mechanism forms the primary driver of seismicity, but the complexity of the Earth's lithosphere indicates that additional factors such as stress transfer, fluid intrusion, and aseismic slip can also significantly influence earthquake behavior (Ross *et al.* 2017; De Barros *et al.* 2020).

Tectonic loading is the principal force behind most earthquakes. The Earth's lithosphere is divided into several tectonic plates that are constantly moving due to mantle convection. As these plates interact at their boundaries—whether convergent, divergent, or transform—stress accumulates along faults and within the surrounding rock masses. When the stress exceeds the strength of the fault or rock, it is released as an earthquake. This basic understanding of tectonic loading provides the foundation for earthquake mechanics and helps in predicting where and when earthquakes are likely to occur based on plate boundaries and known fault lines.

Stress transfer plays a significant role in earthquake sequences and can influence the occurrence of subsequent seismic events. When a major earthquake occurs, it alters the stress field in the surrounding area, redistributing stress along nearby faults. This process can either increase the likelihood of additional earthquakes by pushing nearby faults closer to their failure point or, conversely, relieve stress on some faults, thereby reducing their likelihood of slipping. This phenomenon has been observed in various earthquake sequences, where aftershocks follow the mainshock due to the redistribution of stress. Understanding stress transfer is vital for assessing the seismic hazard in a region, as it helps predict how a large earthquake can trigger subsequent events.

In addition to tectonic loading and stress transfer, other factors such as fluid intrusion and aseismic slip can also play crucial roles in earthquake dynamics. Fluid intrusion into fault zones can significantly affect fault behavior by altering the stress conditions and lubricating the fault plane. Fluids, such as water or hydrocarbons, can reduce the effective normal stress on a fault, making it easier for the fault to slip. This mechanism is particularly relevant in regions with significant fluid reservoirs or where anthropogenic activities such as hydraulic fracturing or fluid injection are conducted. The

presence of fluids can lead to induced seismicity, where earthquakes are triggered by human activities that alter the stress field.

Aseismic slip, or the gradual slip of a fault without the release of significant seismic waves, is another important factor in earthquake dynamics. Aseismic slip can occur in the form of slow slip events or creep, which might not be immediately detectable as earthquakes but can significantly influence the stress distribution along a fault. These slow-slip phenomena can accumulate over time, eventually leading to a larger, more noticeable seismic event.

In some seismic sequences, the interplay of tectonic loading, stress transfer, fluid intrusion, and aseismic slip can manifest through an intricate, imbricated forcing mechanism where all these drivers interact simultaneously. Such complex sequences occur when a primary tectonic event triggers a cascade of secondary processes, integrating various mechanisms into a cohesive sequence of seismic activity. For instance, a major earthquake driven by tectonic forces might initially release significant stress along a fault, leading to immediate aftershocks. Concurrently, the redistribution of stress could activate nearby faults, which may be influenced by fluid migration or aseismic slip, adding further complexity to the seismic sequence. This multifaceted interaction highlights how diverse driving factors can converge, creating a complex seismic response that encompasses multiple triggering mechanisms.

Contribution to seismic hazard assessment in Northeastern Algeria

Analyzing the active faults, source parameters, and driving mechanisms of recent seismic sequences in northeastern Algeria from 2007 to 2022 provides invaluable insights for seismic hazard assessment in the region. This comprehensive analysis involves a detailed examination of fault structures, including their geometries, orientations, and interactions, as well as the source parameters of individual earthquakes, such as seismic moment, corner frequency, source radius, and stress drop. Additionally, investigating the driving mechanisms behind these seismic events—whether primarily tectonic loading,

stress transfer, fluid intrusion, or aseismic slip—offers a nuanced understanding of the factors contributing to earthquake occurrence and behavior.

By systematically reviewing recent seismic sequences and compiling the results into a structured database, including tables and figures, we can achieve a clearer picture of the seismic hazard landscape in northeastern Algeria. This database serves as a critical resource for assessing the current state of fault systems and their associated seismic risks. For example, detailed tables summarizing fault parameters and source characteristics allow for easy comparison and identification of patterns. Figures illustrating the spatial distribution of active faults and their associated earthquakes provide a visual representation of seismic hazards and highlight areas of heightened risk.

Furthermore, this database facilitates the identification of key driving mechanisms for the observed seismic activity. By categorizing events based on their primary driving forces—whether tectonic, fluid-induced, or related to stress redistribution—researchers and policymakers can better understand the underlying processes influencing earthquake behavior in the region. This knowledge is essential for developing targeted mitigation strategies that address the specific risks associated with different types of driving mechanisms. For instance, in areas where fluid intrusion is a significant factor, measures to monitor and manage subsurface fluid pressures can be prioritized.

Overall, an overview analysis and database compilation of recent seismic sequences in northeastern Algeria represent a valuable contribution to seismic hazard assessment efforts. By providing detailed, organized information on fault systems, earthquake source parameters, and driving mechanisms, this work enhances our ability to assess and manage seismic risks in the region.

To present the aforementioned topics in a well-structured and academic manner, I have divided my thesis into five chapters as follows:

Chapter I: titled " *Faults kinematics and earthquakes nucleation* ". In this chapter we explored the fundamental seismological and geological concepts that are necessary for

understanding fault mechanics and earthquake generation. A detailed review of fault dynamics, fluid behavior in fault zones, and the physics underlying earthquake generation sets the stage for the following chapters, where these concepts are applied to the Beni-Ilmane region particularly and the northeastern Algeria globally. This introduction serves as a framework for the detailed seismic analysis that follows

Chapter II: titled " *New Seismotectonic Model for Beni-Ilmane Region* ". The main objective of this chapter is to uncover the intricate seismotectonic model activated during the 2010 Beni-Ilmane seismic sequence. To achieve this, we conducted a thorough analysis that included the estimation of a new minimum 1D velocity model for the BI region, high-precision earthquake relocation, comprehensive focal mechanism analysis, and the investigation of the spatio-temporal evolution of earthquake multiplets. Finally, we proposed a plausible scenario illustrating the role of the strike-slip fault in shaping the thrust belt in the region.

Chaptter III: titled **" *Dynamic Source Parameters' Analysis* "**. We began this chapter with a theoretical overview of earthquake source parameters. Following this, we applied the theory to the Beni-Ilmane 2010 seismic sequence, using two different approaches to estimate these parameters: the individual spectra approach and the Empirical Green's Function (EGF) approach. Our analysis focused on 41 key seismic events within the sequence. One of the main findings of this chapter is the confirmation that self-similarity is preserved in the BI region, contrary to previous studies. Additionally, we conducted several comparative studies and derived various scaling relationships between the different source parameters.

Chapter IV: titled "*Mechanisms Driving the BI-2010 Sequence: An Analysis*". In this chapter, we analyzed the driving mechanisms behind the BI-2010 sequence, emphasizing the significance of tectonic loading based on stress inversion results. Our findings demonstrated consistency between the local stress orientation and the direction of the African-Eurasian plate motion, underscoring tectonic forces as a key factor. While previous studies have investigated stress transfer, we argued that it alone is insufficient

to account for the observed seismicity in the BI-2010 sequence. Despite the earlier evidence of fluid involvement, we presented three additional lines of evidence—multiplet analysis, moment tensor decomposition, and the temporal variation of stress drop—that further confirmed the role of fluids in driving the seismicity. Additionally, for the first time, we highlighted the contribution of aseismic slip, as indicated by seismicity migration analysis and the detection of repeating earthquakes. In conclusion, we posited that the BI-2010 sequence resulted from a nuanced interplay of tectonic loading, stress transfer, fluid dynamics, and aseismic slip transients.

Chapter V: titled " *Geometric and Physical Characterization of Active Faults in Northeastern Algeria*". In this chapter we examined Algeria's seismic hazard landscape, focusing on key seismotectonic features and recent earthquake activity, particularly in northeastern Algeria, provided a detailed understanding of regional seismic risks. The chapter analyzes specific seismic zones, including the Hodna Mountain Range, Lesser Kabylia Block, Mila-Constantine Basin, and Central Tellian Atlas. Finally, we compiled geometric and physical parameters of the main earthquake and their seismogenic source faults to provide a valuable contrbution for a better seismic hazard assessments.

At this stage, we should highlight that this thesis has been elaborated under an internal CRAAG project titled: "*Imagerie Haute Résolution des Failles Actives Dans L'est Algérien. Réévaluation de L'aléa Sismique*" of reference ES-04-2020. Additionally, it is a basic document for the new project ES-01-2024, see **Appendix E** and **Appendix F**.

Finally, we hope and assume that this thesis provides a meaningful contribution to seismic hazard assessment and risk mitigation in northeastern Algeria. By analyzing the physical and geometrical characteristics of various faults, both those already activated and those with potential to be, this work enhances our understanding of fault behavior in the region. The insights gained from fault mechanics, dynamic source parameters, driving mechanisms and their implication onto seismotectonics, offer valuable data to improve seismic risk models and preparedness efforts in this seismically active area.

Chapter I

Faults kinematics
and
earthquakes nucleation

Content

I.1 Introduction

Seismology, as it is understood today—particularly with its reliance on plate tectonics as a primary driving force—is a relatively young science, having fully emerged in the mid-20th century. Despite its youth, it has rapidly evolved, with concepts, models, and laws continually being updated in tandem with advancements in monitoring techniques, data processing methods, and the increasing density and precision of scientific data. Throughout the years I spent working on this thesis, I encountered various seismic and geological terms that have multiple interpretations depending on the field of expertise—whether among physicists, statisticians, geologists, or geophysicists. Discrepancies in terminology also exist within subfields, often requiring continual refinement and clarification as new discoveries arise. These observations motivated the inclusion of this chapter, where we aim to summarize and clarify the seismic and geological concepts encountered in our research while also offering perspectives on some ongoing debates within the scientific community.

In order to achieve this, we present, in this chapter, a clear and comprehensive explanation of two pivotal topics: (1) the nature and mechanisms of fault movement and (2) the physics underlying earthquake generation. Faults are integral to geology, playing crucial roles in both natural processes and human activities. Not only are they key to understanding earthquake genesis, thus being vital for seismic hazard assessment and earthquake studies, but they also significantly influence fluid dynamics within aquifers, a topic explored in depth by Bense *et al.* (2013). Understanding how faults affect fluid flow is essential for effective groundwater management and resource assessment. Faults are also critical in the extraction of hydrocarbons and geothermal energy. Studies by Gabrielsen *et al.* (1990) and Loveless *et al.* (2014) highlight the impact of faults on fluid behavior in subsurface reservoirs, knowledge that is crucial for optimizing extraction techniques, assessing reservoir sustainability, and mitigating environmental risks associated with resource exploitation. On the other hand, understanding the fundamental physics behind earthquake generation allows researchers to investigate the mechanisms

driving seismic activity. These include tectonic plate movements, fault interactions, stress accumulation, high-pressure fluid migration, and volcanic activity-induced earthquakes.

Textbooks on general seismology often dedicate entire sections to earthquake mechanisms, with foundational works by Aki & Richards (1980), Lay & Wallace (1995), and Udías *et al.* (2014) offering comprehensive overviews. Furthermore, specialized texts such as Scholz 2019 delve deeply into the intricacies of earthquake mechanisms. The book "Source Mechanisms of Earthquakes: Theory and Practice" by Udías *et al.* (2014) stands out for its exhaustive treatment of the subject, integrating both theoretical and practical aspects. This chapter aims to present the main topics related to fault kinematics and earthquake nucleation. Furthermore, it provides a theoretical foundation for the subsequent chapters.

I.2 What Is a Fault?

A fault is a geological discontinuity or fracture surface within the Earth's crust along which there has been displacement of rock on either side relative to each other. This displacement can occur in various directions and magnitudes, resulting in changes in the configuration and relationships of adjacent rock units. Fault representations on seismic or geological maps or cross-section typically appear as singular lines with uniform width. While in reality, observed fault traces are not continuous straight lines but have bends, bifurcations, offsets and other complexities. The non-continuous nature of observed faults has led to the consideration that their nature might be fractal (Udías *et al.* 2014). In essence, this means that faults display similar patterns of irregularity and complexity at different scales, much like fractals, which are geometric shapes that exhibit self-similarity across different magnifications. In the context of faults, this suggests that the same fault features, such as bends, branches, and fractures, can be observed at both large and small scales within the fault system (**Fig. I.1**). When modeling fault geometry and architecture, geo-scientists may consider either a complex or simplistic fault model, depending on the level of detail and accuracy needed for specific purposes. For example, when analyzing earthquake focal mechanisms, a simple planar fault model is preferred. Conversely, when

considering the structure, mechanics, and fluid flow properties of fault zones, a more complex representation of a fault is typically favored.
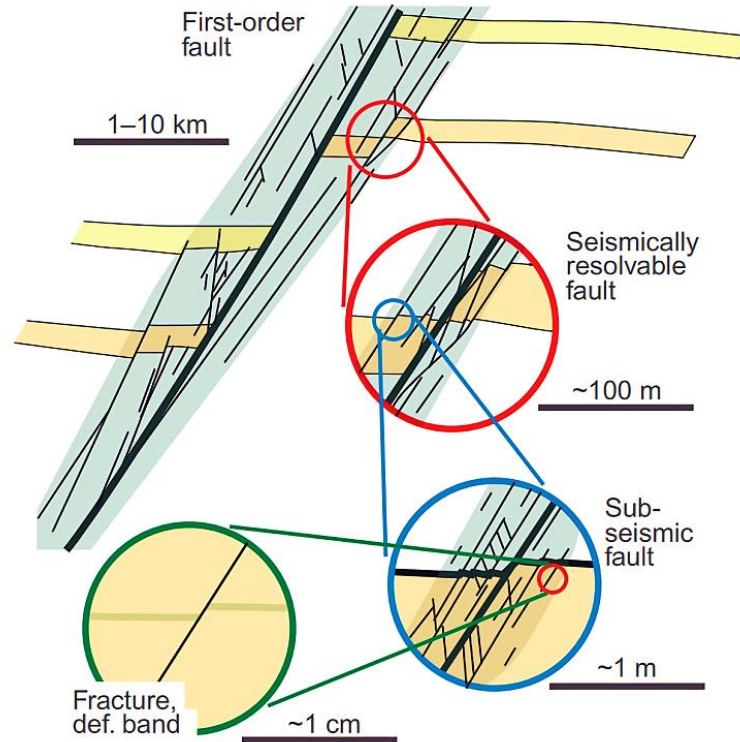
Fig. I.1: Schematic representation of fault fractal nature, showing how a major first-order fault with displacement of several kilometers' branches into smaller-scale structures, down to individual fractures or deformation bands. Adapted from (Fossen 2020)

I.2.1 Complex Fault Model

In this model faults are viewed as zones of deformed rock with a complex internal structure. As illustrated in **Fig. I.2**, these zones are mainly composed of: (1) a single or multiple core zones generally filled with gouge, where most of the fault displacement is accommodated, (2) a fractured damage zone surrounded by (3) a host rock; the host rock is also knowing as protolith (non-deformed rock). No scalar relationship is implied between these components, nor must all of the components be present in any given fault zone.
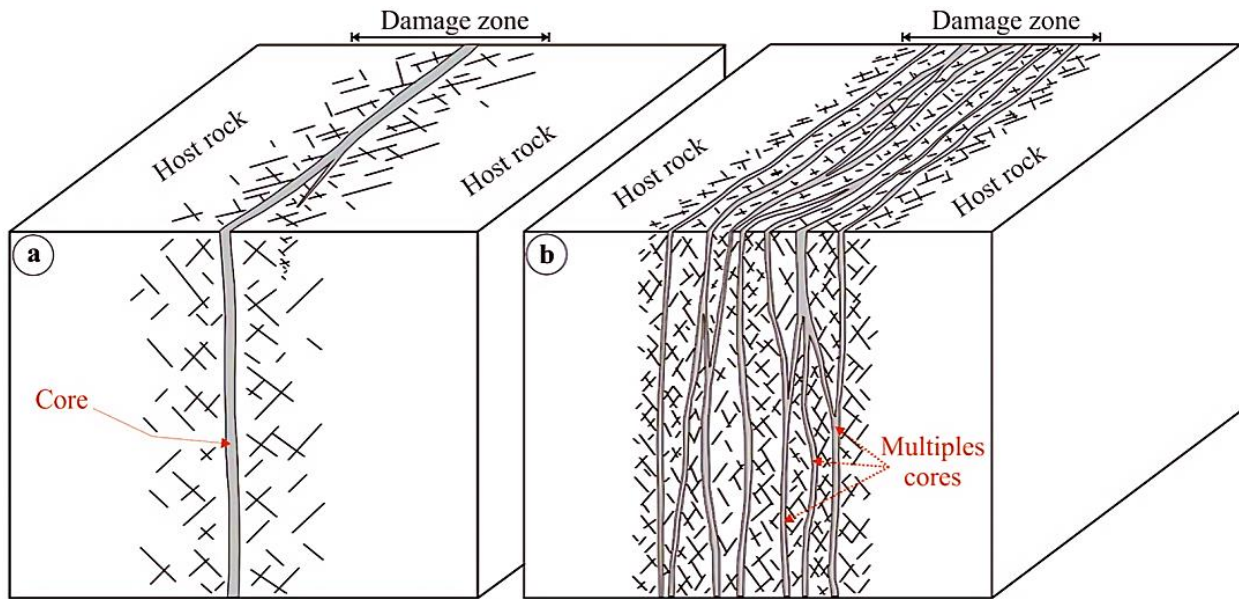
Fig. I.2: Typical fault zone structures. **(a)** Shows a single high-strain core surrounded by a fractured damage zone and **(b)** shows high-strain multiple cores model. (After Faulkner *et al.* 2010).

The fault core is the central region where the majority of displacement and deformation occur. It can consist of various components, including one or several slip surfaces, different types of fault rocks (such as fault gouge, breccia, and clay smear), fractures (like veins, extension, and shear fractures), as well as diagenetic structures like cement and mineralization. Additionally, it may contain lenses of both deformed and undeformed rocks that are trapped between slip surfaces (Wibberley *et al.* 2008). As depicted in **Fig. I.3a,** away from the fault core, the intensity of deformation decreases as one moves into the surrounding damage zone and host rock. The fault damage zone encompasses a broader area surrounding the fault core and may include features such as smaller faults, fault-related folds, deformation bands, and fractures. The damage zone of a single fault is spatially classified into wall damage zone (cross-fault and along-fault damage zones) and tip damage zone, depending on its location around the fault (Torabi *et al.* 2019).
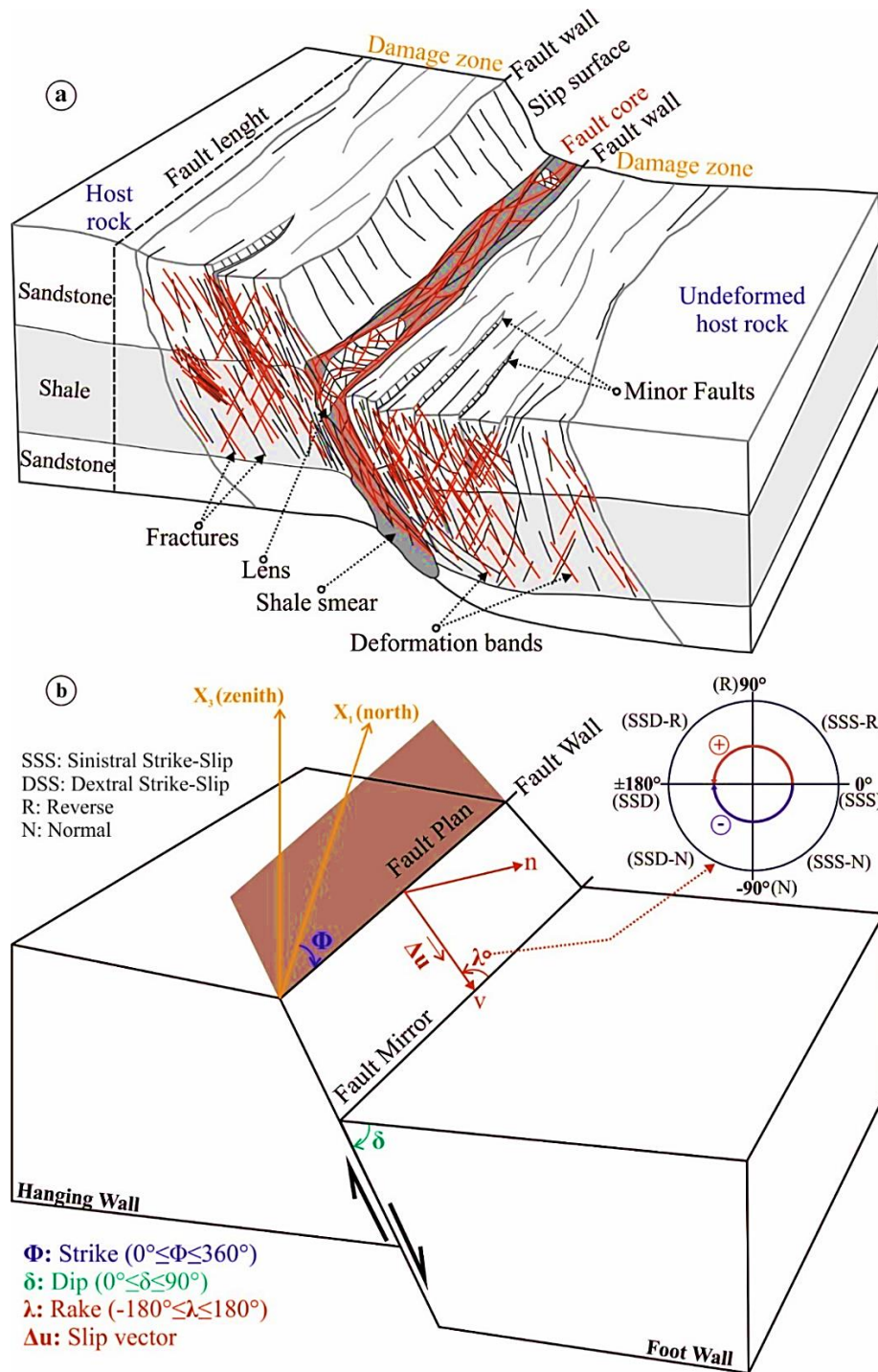
Fig. I.3: Complex and simple fault model. **(a)** An illustration of a complex fault model (normal fault) with its characteristics. The boundaries of the fault core and damage zone, along with their internal structures, are depicted. (After Torabi et al., (2019)). **(b)** Simplistic fault model. The fault's orientation can be described by the angles φ (azimuth), δ (dip), and λ (rake or slip angle), or alternatively by the unit vectors n (normal to the fault plane) and v (in the slip direction). The fault slip is represented by Δu, and the fault surface by S.

As mentioned earlier this complex fault representation is of utmost importance, and it is widely considered in hydro-geological studies (Bense *et al.* 2013; Roche *et al.* 2018; Dogan 2023). The composition and distribution of structures within the fault core and damage zone play a crucial role in determining the hydrogeological characteristics of a fault zone, especially its permeability. The works of Caine *et al.* (1996) are a corner-stone in this analysis. They outlined a framework for understanding, comparing, and correlating the fluid flow properties of fault zones in various geologic settings. Fault core and damage zone are distinct units within a fault zone, both structurally and hydrogeologically. The fault core and damage zone represent different regions with unique material properties and deformation conditions resulting from faulting processes. The behavior of a fault zone in terms of fluid flow can vary depending on the relative proportions of fault core and damage zone structures. Specifically, whether a fault zone will function as a conduit for fluid movement, act as a barrier limiting fluid flow, or exhibit characteristics of both conduit and barrier systems, is influenced by the interplay between these two components. Additionally, the inherent variability in grain scale and fracture permeability within the fault core and the damage zone, respectively, further contribute to the hydrogeological behavior of the whole fault zone. Based on the proportions of these two components, Caine *et al.* (1996) suggested a four end-member conceptual scheme for fault-related fluid flow. These end-members are as follow:

Localized-barrier: in this case the damage zone is absent to poorly developed, and the lower permeability of the well-developed fault core causes the fault zone to act as a barrier to across-fault fluid flow.

Localized-conduit: in this case, the damage zone is absent to poorly developed, while the fault core which is also poorly-developed is characterized by high permeability, prompting the fault zone to act as a localized conduit for a long-fault fluid flow.

Distributed-conduit: it is the case where the damage zone is well-developed with enhanced permeability, and the fault core is poorly developed and characterized by high

permeability. In such case the fault zone has higher permeability, facilitating fluid movement along the fault and the fractures.

Combined conduit-barrier: in this case both fault core and damage zone are well-developed. The fault core has low permeability, while the damage zone is characterized by high permeability (highly fractured). This causes the fault zone to act as a combined conduit-barrier system, a barrier for across-fault fluid flow, and a conduit for along-fault fluid flow.

In **Fig. I.4** we present the conceptual scheme modified from Caine et al. (1996).
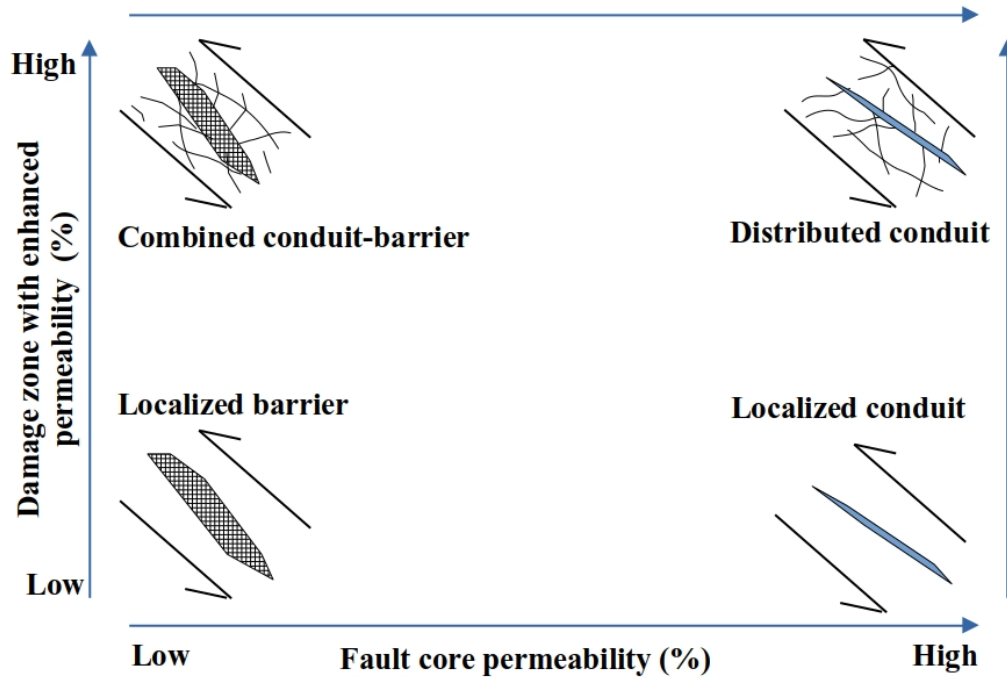
Fig. I.4: Conceptual scheme for fault architecture and fault-related fluid flow. (Modified from Caine et al. (1996))

I.2.2 Simplistic Fault Model

In this model fault are viewed as 2D planes. Simplistic fault models serve as conceptual tools for understanding fundamental faulting processes and their implications for geological structures and tectonic activity. They provide a basic framework upon which more detailed analyses can be built. In some analyses, such as

earthquake focal mechanism studies, a simple planar fault model may provide sufficient insights without the need for more complex representations. This is because focal mechanism solutions are often based on assumptions of uniform slip along a fault plane. The concept of a fault plane serves as a practical simplification of the complex three-dimensional geometries inherent in fault surfaces. While actual fault surfaces can exhibit non-planar features such as bends, branches, and irregularities, representing them as theoretical flat planes facilitates visualization, interpretation, and analysis in seismology, structural geology, and tectonics. Despite its simplicity, the fault plane concept remains a valuable tool for describing fault-related structures, understanding fault kinematics, and interpreting geological deformation.

The fault size is determined by its area, denoted as S. For a rectangular fault, the area (S) is calculated as the product of its length (L) and width (W), expressed by the formula $S = L * W$. Similarly, for a circular fault, the area (S) is computed using the formula $S = \pi * r^2$, where r represents the radius. These two geometric approximations are commonly utilized to estimate fault dimensions due to their frequent use in earthquake source analysis and geological studies.

In **Fig. I.3b** we present the planar model of the fault with its main parameters. The fault plane is defined by its normal vector $\vec{n}$. The direction of motion is determined by the slip vector $\overrightarrow{\Delta u}$. This slip vector indicates the movement of the hanging-wall block (upper side of the fault) relative to the foot-wall block (lower side of the fault). Since the slip vector lies within the fault plane, it is perpendicular to the normal vector. Generally speaking, this relative displacement (slip) can be written as $\overrightarrow{\Delta u}\ (x_i, \tau)$, this quantity can exhibit variations in both magnitude and direction across the fault plane, with position specified by the vector x_i, and changing over time τ at each position x_i. If we consider the displacement amplitude, and a unity vector $\vec{v}$ in the slip direction, we can write

$$\overrightarrow{\Delta u} = \Delta u \cdot \vec{v} \tag{I.1}$$

The time dependence is usually separated from the amplitude and direction, so $\overrightarrow{\Delta u}$ can be expressed by:

$$\overrightarrow{\Delta u} = \Delta u \cdot \vec{v} = \Delta u(x_i) \cdot v_i(x_i) \cdot T(\tau) \tag{I.2}$$

where the time dependence T is taken to be the same for all points on the fault plane. We can also consider the slip rate (velocity) as

$$\overrightarrow{\dot{\Delta u}} = \dot{\Delta u}(x_i) \cdot v_i(x_i) \cdot S(\tau) \tag{I.3}$$

Where $S(\tau) = \dot{T}(\tau)$, is knowing as the source time function.

The fault plane's orientation is defined by two angles. The azimuth angle ϕ represents the angle between the fault's trace which is the intersection of the fault plane with the horizontal plane, and the geographical north, where $0° \le \phi \le 360°$. The dip angle δ signifies the angle between the fault plane and the horizontal plane ($0° \le \delta \le 90°$). Additionally, a third angle, λ, known as the rake or slip angle, specifies the direction of motion on the fault plane. It is determined by the angle between the slip direction and the horizontal, measured on the fault plane ($-180° \le \lambda \le 180°$). In the upper right panel of **Fig. I.3b**, we present a diagram illustrating the relationship between rake and the corresponding fault type: Pure Reverse Fault (R, where the rake angle λ is $+90°$); Pure Normal Fault (N, where λ is $-90°$); Dextral Strike-Slip Fault (DSS, where λ is $\pm180°$); Sinistral Strike-Slip Fault (SSS, where λ is $0°$), as well as various cases of oblique faulting that involve combinations of these primary fault types. (x_1, x_2, x_3), is a local coordinate system, where x1 axis aligns with the geographical north, the x3 axis points upward, while the x2 axis is orthogonal to both.

I.3 Focal Mechanism and Fault Motion

A focal mechanism, also known as a fault-plane solution or moment tensor solution, is a graphical representation of the three-dimensional orientation of the forces acting at the hypocenter of an earthquake. It provides information about the type of faulting (e.g., normal, reverse, or strike-slip), the orientation of the fault plane, and the direction of fault movement. Focal mechanisms are essential tools in seismology for understanding earthquake dynamics, fault behavior, and stress patterns in the Earth's crust. Seismic waves exhibit varying amplitudes and polarities in different directions

relative to a seismic station, depending on the source's position. This characteristic is effectively utilized through different methods:

1) The classical approach involves solely analyzing polarities, particularly with first motion P-wave polarities.

2) A more advanced technique involves considering amplitudes or amplitude ratios in conjunction with polarity data from P waves.

3) The most sophisticated methods entail analyzing the moment tensor solution through partial or full waveform inversion.

I.3.1 First Motion Polarities

This method relies on the P-wave first motion polarities. The fundamental concept revolves around the variation in polarity (direction) of the initial P-wave arrival among seismic stations positioned at different angles from an earthquake's epicenter. The initial motion can be either compressional, indicating movement toward the station for nearby fault material, or dilatational, signifying movement away from the station. Consequently, when a P-wave reaches a seismometer from beneath, the vertical component of the seismogram depicts either an upward or downward initial motion, corresponding respectively to compression or dilation. **Fig. I.5** shows an illustrative example of this concept from of a strike-slip vertical fault. The initial movements delineate four quadrants—two marked by compression and two by dilation. This division occurs along both the fault plane and a plane perpendicular to it. In these directions, the transition from dilation to compression results in minimal or zero initial movements on seismograms. These perpendicular planes, known as nodal planes, serve to segregate the compression and dilation quadrants. Determining these planes enables understanding of the fault's geometry. However, a challenge arises: the initial movements resulting from slip on the actual fault plane and on the perpendicular auxiliary plane appear identical. Thus, relying solely on initial movements cannot definitively ascertain the actual fault plane. Nevertheless, additional information from geological knowledge, aftershocks'

distribution, or from the directivity effect of the source time function, can help to decide which plane is most probably the fault plane.
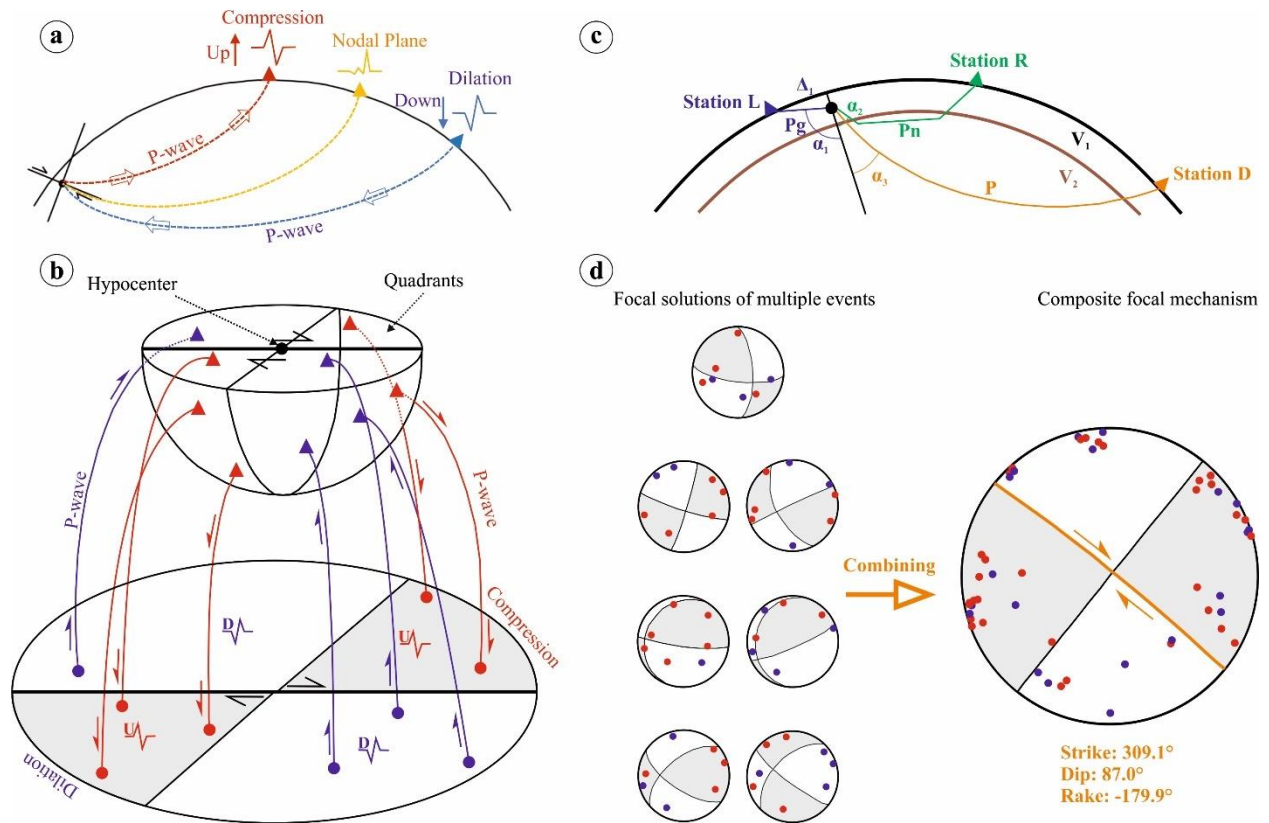
Fig. I.5: Focal mechanism notions. **(a)** Use of first motion of seismic wave at several seismographs (open boxes) to determine mode of earthquake faulting. One seismogram shows a compression (first wave goes up, reading from left to right), indicating that the first motion was away from the source. Another shows a dilation (first wave goes down), indicating that the first motion was toward the source. A third is indetermined, suggesting that it is on the boundary between compression and dilation. **(b)** The projection of the surface stations onto points on the surface of the focal sphere by ray back-tracing. **(c)** Take-off angle for different rays (local, regional and distant). $v1$ and $v2$ are the P velocities in respective layers (Modified from Havskov & Ottemoller (2010)). **(d)** The composite focal mechanism solution for the 2006 El Lalaam earthquake was determined by (Boulahia *et al.* 2021) through the integration of data from multiple seismic events, as originally compiled by (Abbes *et al.* 2019).

To calculate a focal mechanism solution using this method, the surface observation points on Earth (i,e stations) are projected onto points on the surface of the focal sphere by retracing the paths of the rays back to the focal point (a process known as ray back-tracing) **Fig. I.5b**. Two input parameters are needed 1) the station azimuth, 2) the take-off

angle (the angle at which the seismic ray leaves the source, measured from the downward normal). If we consider the distance classification of earthquake (local, regional, and distant), we find that the take-off angle is estimated differently. For local distances where direct waves (P_g) are expected to reach the sensor first (station L in **Fig. I.5c**), $\tan(180 - \alpha1) = \Delta1 /h$ (h is hypocentral depth and $\Delta1$ is the epicentral distance to station L) and it is seen that the take-off angle is sensitive to the hypocentral depth. Conversely, for regional distances at which refracted waves (P_n) hit the sensor first (station R in **Fig. I.5c**), the take-off angle is determined through Snell's law, $\sin(\alpha_2) = V_1 /V_2$, where V_1 and V_2 are the P wave velocity at the first and the second layer respectively. Under the approximation of a constant layer-velocity, this means that the take-off angle for all the refracted phases, will be constant, irrespective of distance. When it comes to distant events (station D in **Fig. I.5c**) the take-off angle is estimated using the travel-time curve as $\sin(\alpha_3) = (V_h/r_h)* (dt/d\Delta)$. where rh=R-h, with R the Earth's radius and V_h is the velocity at the focal depth. $dt/d\Delta$ is the derivative of the travel time curve (Jeffreys & Bullen 1958).

In a case of small events or small seismic network (i,e limited data), the available polarities often fail to provide sufficient information to confidently determine a fault plane solution. Consequently, inferring the faulting mechanism responsible for the earthquake becomes highly uncertain. To address this challenge, seismologists commonly employ a method known as *composite focal mechanism* analysis. This method hinges on the assumption that the underlying stress conditions give rise to events with comparable fault plane solutions. By combining data from multiple events, a composite focal mechanism solution can be derived, offering an averaged representation of these presumably similar solutions (**Fig. I.5d**). The advantage of this approach lies in its ability to leverage the collective information from various events, each with distinct azimuths and angles of incidence. This diversity of observations ensures a more comprehensive coverage across the focal sphere, resulting in a more robust and well-constrained focal mechanism solution.

I.3.2 More Constraints Through Temporal or Spectral Amplitude Information

It is frequently observed that the recorded amplitude at stations with approximately the same epicentral distance varies according to the station's azimuth. This amplitude variation contains valuable information about the source mechanism, making it desirable for use in determining the focal mechanism (Havskov & Ottemöller., 2010), see **Fig. I.6.** The Figure exhibits three stations located at a comparable distances, due to their different azimuths, there is a distinct variation in the relative amplitudes of P and S waves.
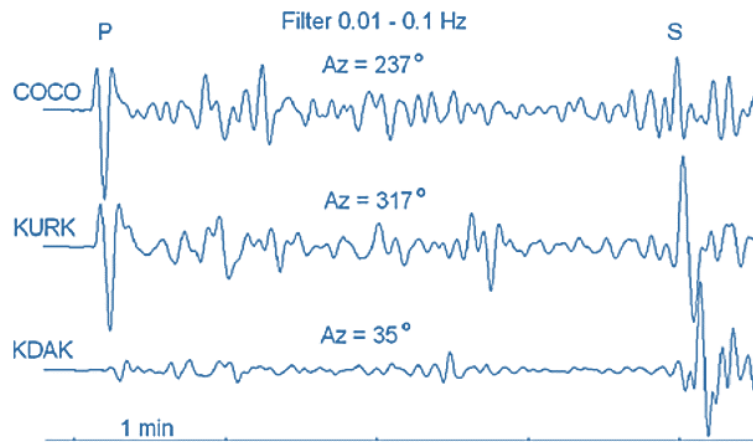
Fig. I.6: Azimuth's effect on amplitude. Broadband seismograms of the vertical component display P and S waves from a deep earthquake near Japan. The three stations, positioned at similar distances (54–58°), have different azimuths (Az), as shown in the figure. The earthquake's origin time is 13:38 on September 28, 2007, with a hypocentral depth of 260 km and a magnitude of mb=6.7. After Havskov & Ottemöller. (2010).

Practically, the displacement at frequencies below the corner frequency, where we can assume no time function dependance can be described by:

$$u_r = M_0 \cdot F(\Phi, \delta, \lambda, x, x_0) \cdot P \cdot I \tag{I.4}$$

Where M_0 is the seismic moment, F is a non-linear function of the source parameters and the position of the event x_0 and the station x. P is the path effect including geometrical

spreading (G), and inelastic attenuation (A). I is the instrument effect. By incorporating the displacement amplitude information alongside with the polarities, a best fit of the source parameters in **equation (I.4)** can be found through forward modeling and grid search.

Given the uncertainty associated with determining absolute amplitudes, relying on amplitude ratios is more dependable. This approach minimizes the influence of factors such as moment, geometrical spreading, wave directivity, and instrument effect, leaving only the impact of the free surface and potential differences in attenuation between the two amplitudes (typically P and S waves) to be accounted for. The displacement amplitude ratio is given by:

$$u_2/u_1 = F_r(\Phi, \delta, \lambda, x, x_0) \cdot A_r \cdot FR \tag{I.5}$$

Where, F_r is the ratio of the F's functions, A_r and FR, represent the attenuation and the free surface effect respectively. It is assumed that the two amplitudes are of the same type, e.g. Pg and Sg for the assumptions to hold (Havskov & Ottemöller. 2010). If Sv and Sh phases are used, then seismogram axes rotation should be performed (ZNE to ZRT), where Sv and Sh information are read on the radial (R) and the transverse (T) components respectively.

Another approach to utilizing amplitudes involves employing spectral amplitudes. Analyzing P-wave amplitude spectra provides a reliable method for estimating amplitude. Assuming a circular model of the source (Brune 1970), see **Chapter III**. The displacement spectra can be written as:

$$D_C(f) = \frac{\Omega_0}{(1 + (\frac{f}{f_0})^2)} = \frac{M_0 \cdot 0.6 \cdot 2}{4\pi\rho v^3 (1 + (\frac{f}{f_0})^2)} \cdot G \tag{I.6}$$

where Ω_0 is the source spectral level (instrument and attenuation corrected), f, the frequency, f_0 the corner frequency, ρ the density and v the P-wave velocity. The factor $0.6 \cdot 2$ accounts for the free surface effect and source radiation in an average sense. Replacing the source factor 0.6 with the source radiation function from **equation (I.4)**, assuming the free surface factor 2.0 to be included in G and assuming $f < f_0$, **equation (I.6)** can be written:

$$D_C(f) = \frac{M_0 \cdot F(\Phi, \delta, \lambda, x, x_0)}{4\pi\rho v^3(1 + (\frac{f}{f_0})^2)} \cdot G \qquad (I.7)$$

The current observations consist of spectral levels that have been corrected for both instrument response and attenuation. These corrected levels can be readily determined automatically using an optimization process. Therefore, by applying a grid search the fault's geometric parameters (strike, dip, and rake) can be estimated.

I.3.3 Moment Tensor

a) Important Notions

The moment tensor (MT) is a mathematical representation used to describe the nature and orientation of a seismic source, such as earthquakes, explosions, or mines' collapses. It quantifies the set of forces and their orientations based on the source's radiation pattern, which is the distribution of seismic wave energy as it propagates from the source. Typically, fault plane solutions are often depicted as force couples, see **Fig. I.7**. Two fundamental types of couples are depicted. The first type involves a pair of forces offset in a direction perpendicular to the force. The couple M_{xy} comprises two forces of magnitude **F**, separated by a distance **d** along the y-axis, and acting in opposite (±x) directions. The magnitude of M_{xy} is given by $\boldsymbol{F} \cdot \boldsymbol{d}$, commonly measured in *dyn.cm* or *N.m* in seismology. The second type, known as a vector dipole, features forces offset in the direction of the force itself. The couple M_{xx} includes two forces of magnitude **F**, acting in the ±x directions, and separated by **d** along the x-axis. This couple also has a magnitude of $\boldsymbol{F} \cdot \boldsymbol{d}$. The primary distinction between these two types is that the vector dipole exerts no rotation.
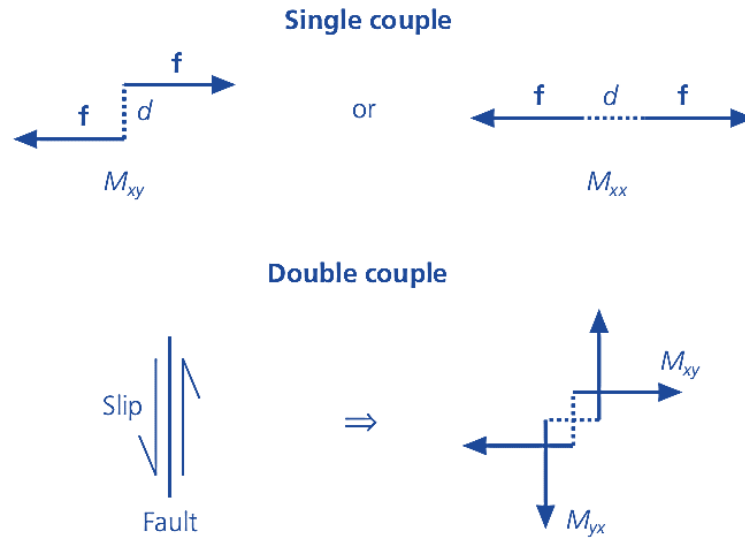
Fig. I.7: Equivalent body force descriptions of a single force, a single couple, and a double couple. The force couple can take two forms. One, shown for M_{xy} has two forces **f** offset by distance d such that a torque is exerted. The other, shown for M_{xy}, is a force dipole which exerts no torque. Slip on a fault can be described by the superposition of both couples like M_{xy} and M_{yx}. Modified after Stein & Wysession (2009).

Additionally, **Fig. I.7** demonstrates the relationship between an earthquake's fault geometry and the double-couple of equivalent body forces. In this example, the earthquake involves left-lateral strike-slip motion in the ±y directions on a fault in the y–z plane. The corresponding equivalent body forces, M_{xy} and M_{yx}, together form the double-couple source. While the M_{yx} couple is intuitive since the forces align with the slip direction, the M_{xy} couple is also necessary to prevent a net torque on the fault. Because these equivalent body forces constitute a double couple, the resulting seismic waves would be identical if the slip were instead right-lateral on a fault in the x–z plane. This means that, for a point double-couple source, seismic waves are indistinguishable regardless of which plane is the fault plane and which is the perpendicular auxiliary plane.

In seismic modeling, several approximations are employed to simplify the complex rupture process of an earthquake. Initially, the rupture process involves a complicated slip function that varies both spatially and temporally, with the scalar

seismic moment representing the integral of this intricate slip process. To deduce source parameters, this complex rupture is approximated as a constant slip D occurring on a geometrically simple fault. This simplification allows the moment to be expressed as the product of the rigidity, average slip, and fault area. Furthermore, the faulting process is approximated as a double couple of equivalent body forces, characterized by the moment $\boldsymbol{F} \cdot \boldsymbol{d}$. These approximations make the complex nature of seismic ruptures more tractable for analysis and modeling, enabling more practical and computationally feasible representations of earthquake sources, see **Fig I.8**.
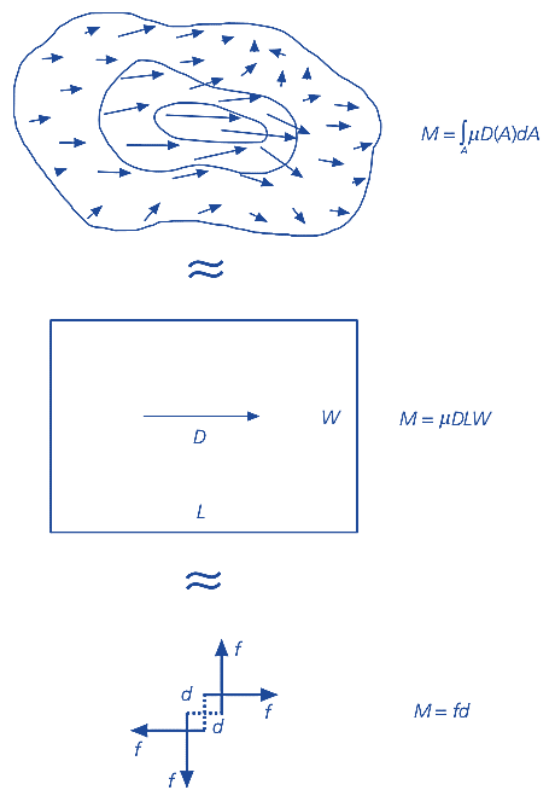
Fig. I.8: Schematic approximations in modeling the seismic rupture process are illustrated. At the top, the rupture process is depicted as involving a complex slip function that varies across space and time, with the scalar seismic moment representing the integral of this slip. In the middle, to infer source parameters, this complex rupture is simplified to assume a uniform slip D on a geometrically simple fault, allowing the moment to be calculated as the product of rigidity, average slip, and fault area. At the bottom, the faulting is further simplified by representing it as a double couple of equivalent body forces with moment $\boldsymbol{F} \cdot \boldsymbol{d}$. After Stien & Wysession. (2009)

However, seismic sources are often more intricate than a single, or even double couple. In actuality, the radiation from most seismic sources can be elucidated as a composite of nine force couples. expressed as a 3-by-3 matrix (i.e., as three shear force couples and three linear vector dipole forces). In a Cartesian coordinate system (i.e., x-axis: +east/-west, y-axis: +north/-south, z-axis: +up/ down), the dipole forces are contained along the diagonal M_{xx}, M_{yy}, and M_{zz} of the tensor. The off-diagonal elements M_{xy}, M_{xz}, and M_{yz} contain the shear force couples. Hence, the moment tensor is giving by:

$$M = \begin{Bmatrix} M_{xx} & M_{xy} & M_{xz} \\ M_{yx} & M_{yy} & M_{yz} \\ M_{zx} & M_{zy} & M_{zz} \end{Bmatrix} \tag{I.8}$$

Its components represent the nine force couples, with the scalar moment M_0 of the moment tensor being

$$M_0 = \sqrt{\sum_{ij} M_{ij}^2} / \sqrt{2} \tag{I.9}$$

The symmetry of the MT implies that $M_{xy} = M_{yx}$, $M_{xz} = M_{zx}$, and $M_{yz} = M_{zy}$, resulting in only six out of the nine unique tensor elements, which can also be represented in vector form. $\vec{M}(M_{xx}, M_{xy}, M_{xz}, M_{yy}, M_{yz}, M_{zz})$, see **Fig. I.9**
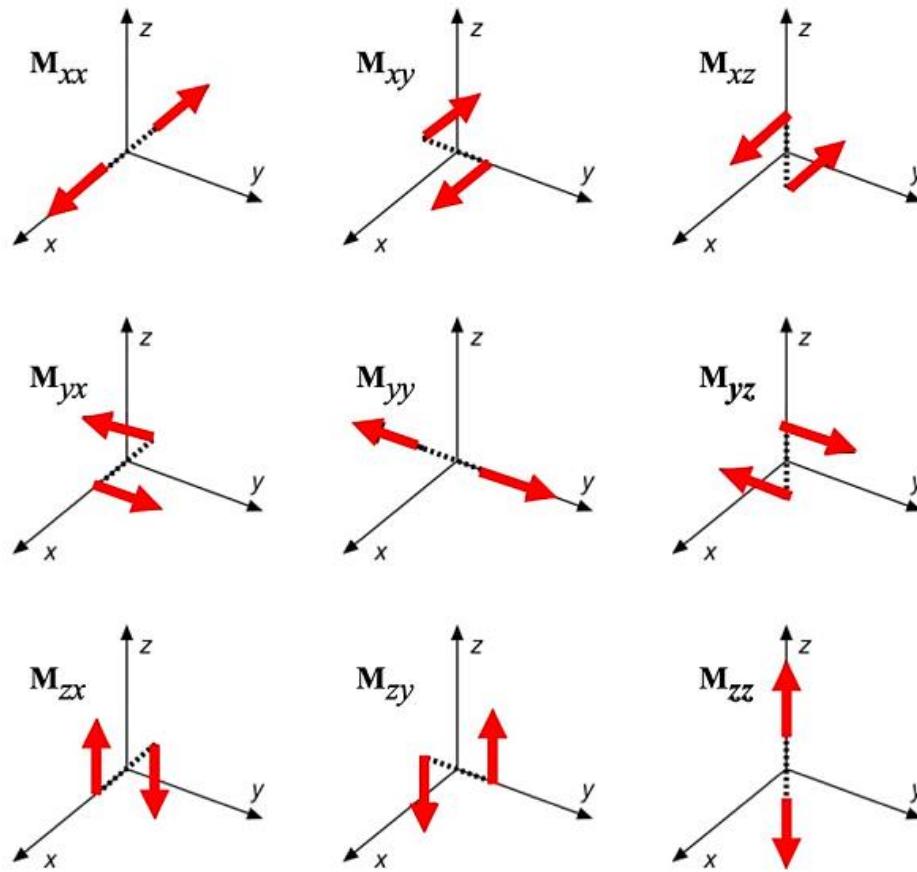
Fig. I.9: The nine force couples that make up the seismic moment tensor are shown. Each couple consists of two opposing forces separated by a distance d (indicated by the dashed line), ensuring that the net force remains zero.

The moment tensor characterizes a broad class of seismic sources. To understand the various source types depicted by the moment tensor, we can examine their eigenvalues. As anticipated, the most general form of the moment tensor has distinct eigenvalues that do not sum to zero ($\sigma_1 \neq \sigma_2 \neq \sigma_3$ and $\sigma_1 + \sigma_2 + \sigma_3 \neq 0$). This source encompasses volume changes and can be decomposed into its isotropic and deviatoric components. The **isotropic** component represents changes in volume, often associated with explosive or implosive events. The **deviatoric** component reflects the shear deformations without any volume change.

Tectonic earthquake sources are typically considered to be shear fractures or nearly so. However, it is important to note that some volume change in shear faulting cannot be entirely ruled out. Methods for determining the moment tensor components from seismic wave observations, without imposing any constraints on the eigenvalues, might yield solutions that include some volume change and a deviatoric part that doesn't align with a pure double couple. In such case we can decompose the moment tensor as **M=M$_{iso}$ + M$_{dev}$.** The deviatoric part can be decomposed into three double couples (Jost & Herrmann 1989) major and minor double couples (Kanamori & Given 1981), double couples sharing the same T axis, or a combination of a double couple and a compensated linear vector dipole (CLVD) component (Knopoff & Randall 1970). The latter decomposition into DC and CLVD components (**M$_{dev}$=M$_{DC}$+M$_{CLVD}$**) has proven valuable for physical interpretations and gained widespread acceptance among the seismological community. This decomposition has been further developed and applied by Sipkin 1986, Vavryčuk 2015 and others.

The CLVD is viewed as a non-double couple component of the seismic source. These are sets of three force dipoles where one dipole has a magnitude that is twice as large in magnitude but opposite in direction compared to the other two dipoles, ensuring overall compensation. In most studies related to tectonic earthquakes, the isotropic part M$_{iso}$ is typically assumed to be zero. For a deviatoric seismic source, the deviation from a pure double couple (DC) is quantified by the percentage of compensated linear vector dipole (CLVD) present.

The presence of non-double couple (DC) components in seismic observations often stems from errors in measurement and inaccuracies in accounting for propagation effects, rather than characteristics of the seismic source itself. Distinguishing between effects originating from the source and those arising from wave propagation is inherently challenging due to limited knowledge of the medium through which waves travel. Perfect separation of these effects is not always achievable (Udías *et al.* 2014).
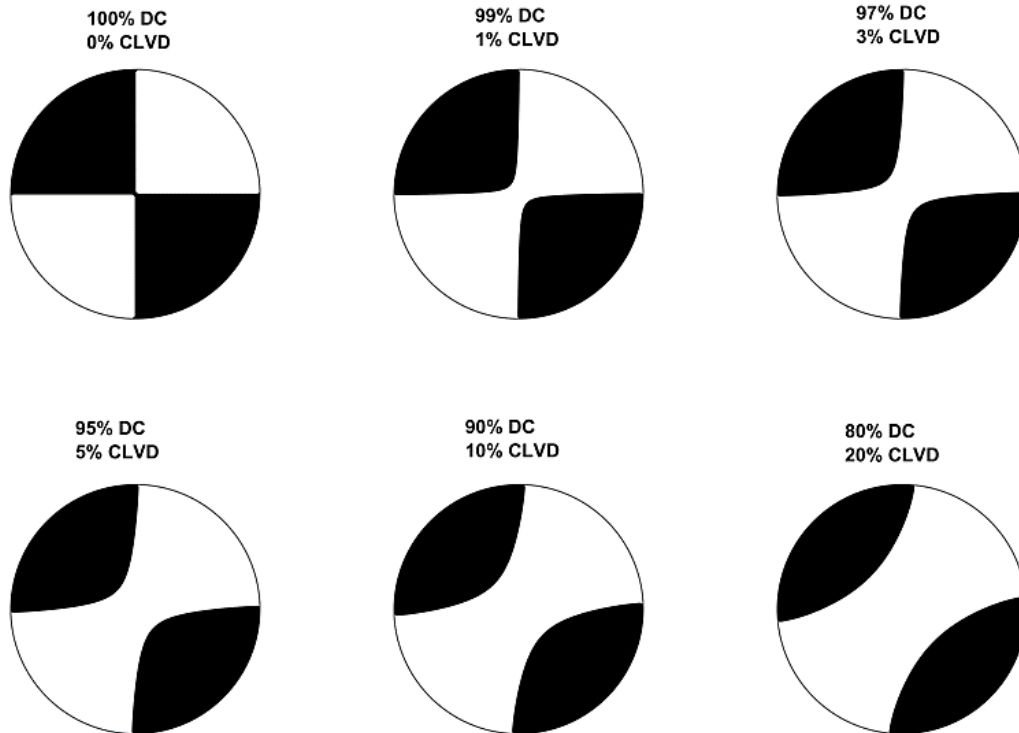
Fig. I.10: An example illustrating the impact of the CLVD percentage on the pure double couple (DC) source representation; an increase in CLVD results in a greater deviation from the pure DC.

The inclusion of a compensated linear vector dipole (CLVD) component in the moment tensor alters the distribution of compressions and dilations in P-wave quadrants. As the percentage of CLVD increases, this distribution diverges significantly from that of a pure double couple source, see **Fig. I.10**. Typically, observed values of CLVD's percentage are less than approximately 15%. Higher values often indicate issues in moment tensor determination from observed data or incorrect assumptions about wave propagation models. However, in certain instances, higher CLVD's percentage values may indeed, signify real deviations of the seismic source from a pure DC type. Deep earthquakes are frequently considered as potential sources exhibiting such non-DC characteristics (Frohlich 2006), It can also originate from various sources such as the collapse of a cavity in mines (Rudajev & Šílený 1985; Šílený & Milev 2008), shear faulting on a non-planar (curved or irregular) fault (Sipkin 1986), tensile faulting induced by fluid injection in geothermal or volcanic regions (Ross et al. 1996) where the slip vector causes

fault opening (Vavryčuk 2001), or from seismic anisotropy within the focal area (Kawasaki & Tanimoto 1981; Vavryčuk 2005).

b) MT Inversion

Moment tensor inversion, is an advanced technique in seismology used to discern the source characteristics of earthquakes. By analyzing the seismic waves recorded at various stations, scientists can reconstruct the intricate pattern of fault slip associated with the earthquake's rupture. Typically, the objective of moment tensor inversion is to establish a series of equations in the following format (Havskov & Ottemöller. 2010):

$$\text{Obs\_data} = P \cdot I \cdot H(\text{known parameters}) \cdot M \qquad (I.10)$$

With Obs_data represents the observed seismogram, the *known parameters* include the locations of stations and hypocenters, as well as the crustal model incorporating attenuation. Here, **M** represents the moment tensor. If we consider only the six independent moment tensor elements, a simplification can be expressed as:

$$Obs\_data = P.I.H(known\ parameters) * m = G * m \qquad (I.11)$$

m here is a vector composed of the six independent element of the moment tensor, while G = P.I.H. The Obs_data can be: 1) temporal amplitudes, 2) spectral amplitudes, 3) P/S-phases part of the waveform, 4) surface wave part of the waveform, 5) the full waveform. It is noted that the observed data types from 1) to 4), use only a part of the information embedded in the seismogram. Full waveform inversion is widely regarded as the best methods for moment tensor inversion due to its comprehensive use of seismic data. It leverages the entire seismic waveform, including amplitude, phase, and waveform shape, to achieve a detailed and accurate representation of the seismic source.

The fault geometry and slip direction are included in the moment tensor, while the matrix H reflects the effects of the Earth's structure. Green's functions are of utmost importance when performing moment tensor inversion, these functions represent the medium response to an excitation by a delta source time function. The response of the medium would be in the form a synthetic seismogram which will be stored in the matrix

H. The element G_{ij} represents the theoretical seismogram due to the moment tensor element m_j at station i, and the observed seismograms u_i are expressed as a linear combination of the Green's functions and the vector of moment tensor elements m_1 to m_6, as represented bellow.

$$\begin{Bmatrix} u_1 \\ u_2 \\ u_3 \\ u_4 \\ . \\ . \\ u_n \end{Bmatrix} = \begin{Bmatrix} G_{11} & G_{12} & G_{13} & G_{14} & G_{15} & G_{16} \\ G_{21} & G_{22} & G_{23} & G_{24} & G_{25} & G_{26} \\ G_{31} & G_{32} & G_{33} & G_{34} & G_{35} & G_{36} \\ G_{41} & G_{42} & G_{43} & G_{44} & G_{45} & G_{46} \\ . & . & . & . & . & . \\ . & . & . & . & . & . \\ G_{n1} & G_{n2} & G_{n3} & G_{n4} & G_{n5} & G_{n6} \end{Bmatrix} \cdot \begin{Bmatrix} m_1 \\ m_2 \\ m_3 \\ m_4 \\ m_5 \\ m_6 \end{Bmatrix} \qquad (\text{I}.12)$$

The data vector **u** comprises **n** observed seismograms u_i from multiple seismic stations and components, sequentially arranged, typically maintaining a consistent number of samples for each seismogram. Thus, the dimension equals the total number of samples across all seismograms. The kernel matrix **G** includes the corresponding Green's functions (six columns) for the specified distances and assumed source depth. Consequently, the number of Green's functions will be 6n, and the total number of rows in **G** equals the total number of samples.

Typically, the problem is overdetermined (as G is not a square matrix), and the inversion for **m** should be in a least squares sense. This approach determines **m** by minimizing the misfit between observed and computed seismograms. While at least six seismograms are necessary to invert for **m**, additional data often results in an overdetermined problem. The inversion is performed for a single depth, Nevertheless, variance can be computed across a range of fixed depths. Although theoretically straightforward, waveform data inversion for the moment tensor demands high-quality data from multiple stations with good azimuthal coverage and the capability to compute synthetic seismograms.

Computing synthetic seismograms is simpler for larger magnitude earthquakes since the synthetics are less sensitive to the model's physical properties for longer period waves. Thus, moment tensor computation is routinely performed for earthquakes above

magnitude 4 at local and regional distances, and above magnitude 5.5 at global distances. However, for smaller earthquakes, higher frequency inclusions necessitate better models, often unavailable. With accurate models, it might be possible to invert waveforms for moment tensors of earthquakes down to magnitude 3.

I.4 Stress Tensor and Faulting Mechanisms

In addition to the geological investigations, focal mechanism inversion is a crucial method for determining the orientation of current stress fields from earthquake data. By inverting focal mechanisms, seismologists can deduce the stress tensor in a specific region, thereby gaining insights into the tectonic forces at work. The stress tensor, a key concept in seismology, quantifies the internal forces within the Earth's crust and directly governs faulting and tectonic deformation. The stress tensor comprises nine components (as shown in **Fig. I.11**), but since it is symmetrical $\sigma_{ij} = \sigma_{ji}$, it can be diagonalized, reducing it to six independent components. The components where the indices are identical $(\sigma_{11}, \sigma_{22}, \sigma_{33})$ represent normal stresses (tensile or compressive), while those with differing indices $(\sigma_{12}, \sigma_{13}, \sigma_{23})$ correspond to shear stresses. The stress tensor's decomposition reveals three orthogonal principal directions, each associated with an eigenvalue σ_1, σ_2, and σ_3 known as the principal stresses, knowing that σ_1 is the maximum stress, σ_3 is the minimum stress and σ_2 is the intermediate stress. A direction qualifies as a principal direction when the stress on the corresponding plane is purely normal, meaning it lacks any shear stress (illustrated in **Fig. I.11**). If $\sigma_1 = \sigma_2$, then any vector in the plane normal to z-axis or x_3 is an eigenvector. If $\sigma_1 = \sigma_2 = \sigma_3 = P$, then any vector in the space is an eigenvector, and the stress tensor is known as a pressure (fluid at rest) or isotropic stress tensor (**Fig. I.11**).
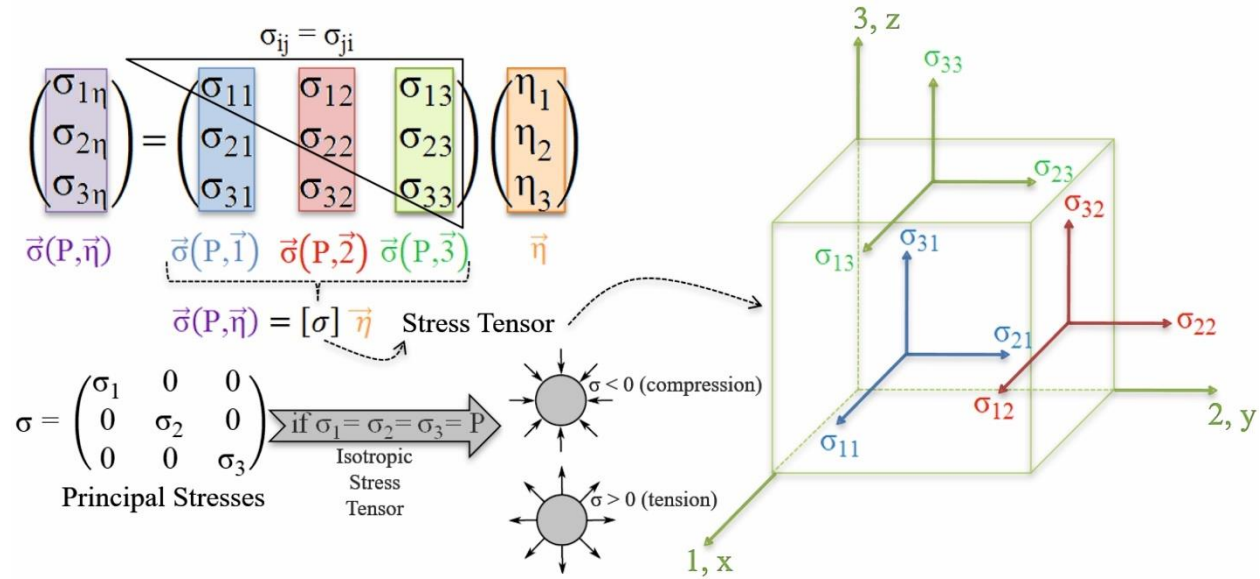
Fig. I.11: Stress tensor with the cases of principal stresses and the isotropic stress tensor

Assuming the vertical stress in the Earth's crust, Sv=g·ρ·z (where g is gravitational acceleration, ρ is rock density, and z is depth), acts as a principal stress, the two horizontal stresses, Sh_{min} and SH_{max}, represent the minimum and maximum horizontal principal stresses, respectively. This reduced stress tensor is fully characterized by four key parameters: the orientation of SH_{max} and the magnitudes of Sv, SH_{max}, and Sh_{min}. In a normal faulting stress regime, Sv exceeds the horizontal stresses, making Sv=σ_1. In a strike-slip faulting regime, Sv is the intermediate principal stress, $S_V=\sigma_2$. In a thrust faulting regime, Sv is the smallest principal stress, SV= σ_3 (see **Fig. 12a**). Additionally, knowing the direction of the maximum horizontal compressive stress (σ_1 or SHmax), we can anticipate the range of faulting that may result. In **Fig. I.12b (left)**, the three primary fault types resulting from a NW-SE SHmax orientation are simplified, whereas **Fig. I.12b (right)** presents a more complex scenario involving a Riedel ellipse, illustrating all potential faulting scenarios.
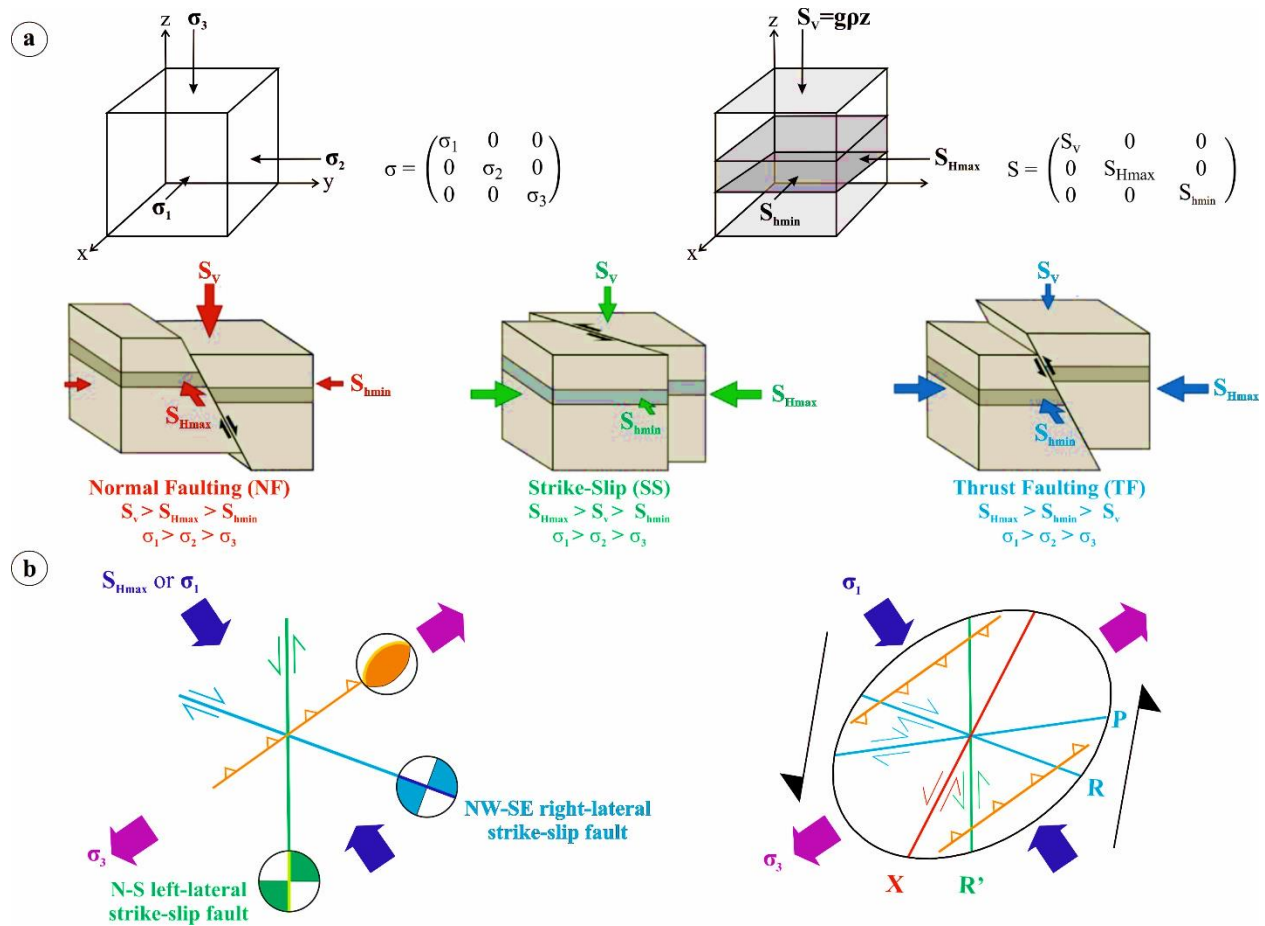
Fig. I.12: (a) Schematic representation of tectonic regimes based on principal stress axes, adapted from (Heidbach *et al.* 2018).**(b)** Potential faulting scenarios corresponding to the orientation of maximum horizontal stress: primary faults shown in the left panel and complex fault patterns within a Riedel ellipse in the right panel.

I.5 Do Earthquakes Always Initiate New Ruptures?

Earthquakes are traditionally understood to initiate new ruptures in previously unbroken rock, as the accumulated tectonic stress overcome the rock resistance, creating a sudden release of energy. This process typically involves the formation of a new fault or the propagation of a fracture through an unbroken rock mass. However, earthquakes can also occur along pre-existing faults, where the rock has already been fractured. This fracturing model is based on the rock friction, see **Fig. I.13**. In these cases, the

accumulated tectonic stress overcomes the frictional resistance along the fault plane, causing a slip and releasing the stored elastic energy. These reactivations of existing faults can be influenced by factors such as changes in stress conditions due to natural tectonic processes, fluid injections from human activities, or even the stress alterations from nearby seismic events.

It is important to note that within a fractured medium, earthquakes typically occur along preexisting faults rather than initiating new ruptures. This is because preexisting faults represent zones of weakness.
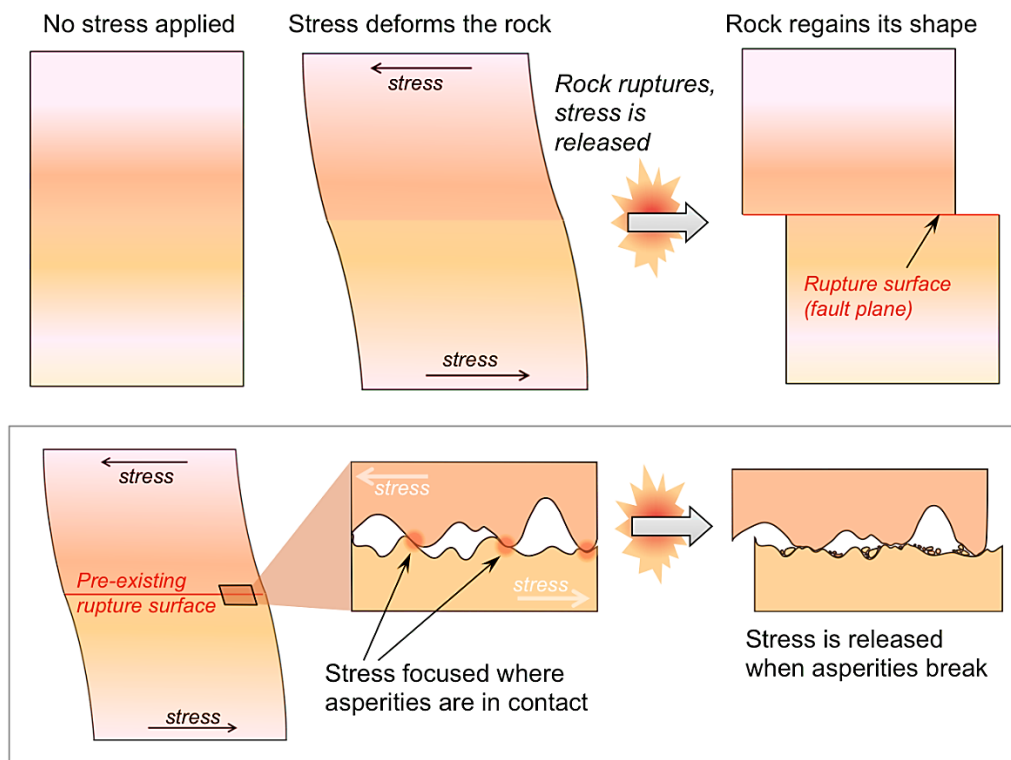
Fig. I.13: Elastic deformation and rupture. Top: When stress is applied to a rock, it deforms by stretching. If the stress exceeds the rock's strength, the rock ruptures, creating a fault. Bottom: On an existing fault, asperities prevent rocks on either side from sliding. As stress builds, it deforms the rock until the asperities break, releasing the accumulated stress. (Modified after Earle *et al.* 2019).

I.6 Seismic Fracture Dynamics

I.6.1 Fracture Expansion Modes

A crucial aspect of fracture mechanics is understanding how fractures propagate. When stress is progressively applied to a real material, deformation ultimately becomes concentrated in a narrow, localized zone. This leads to fracture, resulting in the creation of new crack surfaces as inter-atomic bonds within the localized zone break down (Ohnaka 2010).

As the fracture front advances, the material behind it becomes fractured. The stress behind the fracture front either drops to zero, indicating a total stress drop, or retains a residual value depending on the friction conditions between the fault's two sides. The relationship between the slip direction at the fracture front and the direction of rupture propagation defines three fracture modes. When the relative displacement is perpendicular to the fracture plane, causing the crack to open, it is referred to as tensile fracture (*mode I*). When the relative displacement is parallel to the fracture plane, it is termed shear fracture. Shear fracture includes two fundamental modes: sliding mode or in-plane shear mode (*mode II*), where the relative displacement (or slip) is perpendicular to the crack edge, and tearing mode or anti-plane shear mode (*mode III*), where the relative displacement (or slip) is parallel to the crack edge, see **Fig. I.14.**
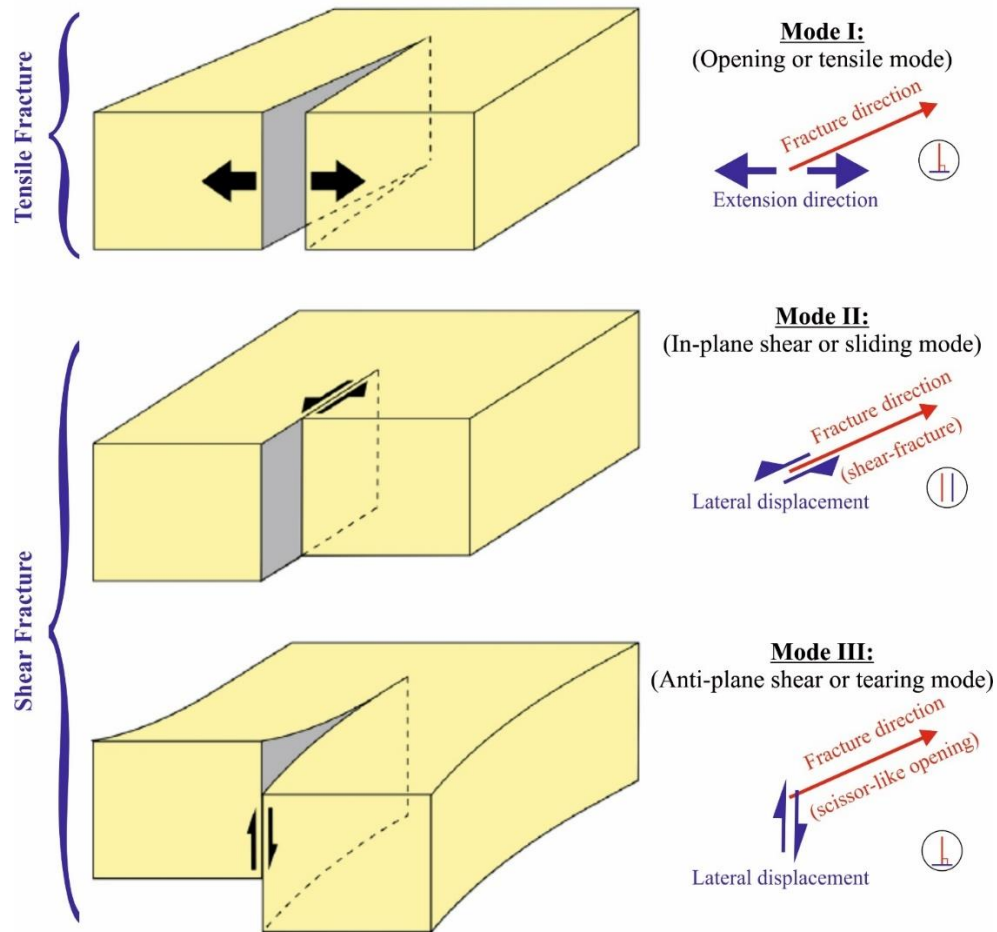
Fig. I.14: The three crack propagation modes modified after (Brandes & Tanner 2020)

I.6.2 The Cohesive Zone

The cohesive zone is a concept used in fracture mechanics to describe the process of material separation or fracture. It provides a detailed understanding of the fracture process by incorporating a zone where stresses and displacements develop before a complete separation occurs. In a homogeneous and isotropic material containing a single crack, the material is assumed to be linearly elastic outside the crack. According to the theory of linear elasticity, the stresses σ_{ij} outside the crack, particularly near its tip, can be accurately approximated by the following formula (Irwin 1957):

$$\sigma_{ij} = \frac{K f_{ij}(\theta)}{\sqrt{2\pi r}} \tag{I.13}$$

where r is the distance from the crack-tip, θ is the angle measured from the plane ahead of the crack, K is the stress intensity factor, and $f_{ij}(\theta)$ is a dimensionless function of θ. In this elastic crack model, σ_{ij} approaches infinity as r approaches zero outside the crack. Inside the crack, σ_{ij} remains zero or reaches a finite level of residual friction stress. In other words, the stresses drop abruptly to zero or to a residual stress level at the crack tip, without a transitional zone where stresses decrease gradually. This stress singularity suggests that the model is not physically realistic, as no real material can sustain infinitely high stress. To remedy this singularity, Barenblatt 1962, suggested that the stresses directly ahead of the fracture front should be moderated by cohesive forces, which maintain the integrity of the material during the breaking process. These forces are distributed near the rupture front and can be regarded as an inherent material property. The area where these forces are active is known as the cohesive zone, and its dimension d must be small relative to the overall size of the fracture, see **Fig. I.15**. Consider a simple model of a cohesive zone with length d, where the cohesive stresses are constant and equal to σ_c, a compressive stress that resists the opening of the cohesive zone. Typically, the cohesive stress σ_c is greater than the applied stress σ_0. Beyond the cohesive zone, at a distance d from the tip, the tensile stresses drop to zero. Barenblatt 1962, demonstrated that for stresses to remain finite ahead of the crack tip, the stress intensity caused by the cohesive forces beyond the crack must precisely counterbalance the stress concentration generated by the external load on the crack.
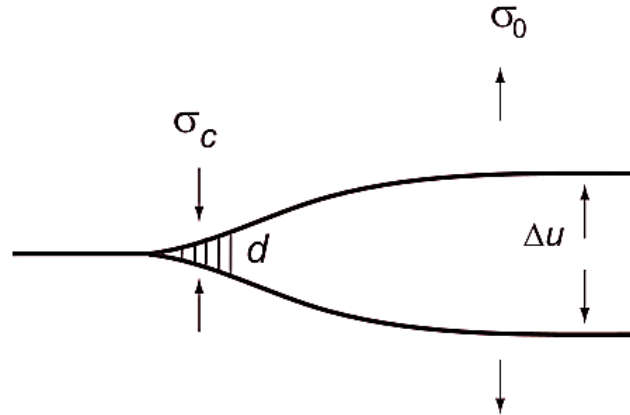
Fig. I.15: Cohesive zone model for a Mode I crack. The fault is subjected to a tensile stress σ, causing it to open with a crack opening displacement Δu. The cohesive zone, which has a length d, experiences a cohesive stress σ_c.

I.6.3 Frictional Laws

When we observe two objects in contact, it may appear that they are in complete contact over the entire area, known as the apparent area of contact (Aa). However, in reality, they only touch at specific points. The total of these actual contact points constitutes the real area of contact (Ar). Consequently, friction between two materials occurs along the real area of contact. For all materials in contact, $Ar < Aa$. This observation also applies to rocks. The evolution of earthquake friction laws has been a significant area of research in seismology, aiming to understand and predict the complex behavior of faults during earthquakes. Understanding earthquake frictional laws is crucial for advancing our knowledge of seismic phenomena and improving our ability to predict and mitigate the impacts of earthquakes. These laws describe the behavior of friction on fault surfaces, where tectonic stresses accumulate until they are released in the form of earthquakes.

a) Stick-Slip Friction Model (Static/Dynamic Model)

Earthquakes have long been recognized as resulting from a stick–slip frictional instability. Burridge & Knopoff (1967) were among the first to develop models

incorporating friction to describe dynamic rupture behavior. Their model consisted of interconnected blocks linked by horizontal springs, sliding on a frictional surface that impedes block motion. This frictional interaction causes the blocks to move in a *stick-and-slip* manner. Stick-slip results from a familiar phenomenon: it is harder to start an object sliding against friction than to keep it going once it is sliding. It consists in a process where a fault remains locked (stick) due to friction until the stress overcomes the static friction, leading to a sudden slip (earthquake). In a shear fault, the frictional stress operates parallel to the fault surface, maintaining cohesion between the two sides through static friction stress σ_s, with:

$$\sigma_s = \mu_s \sigma_n \qquad (I.14)$$

Where μ_s represents the coefficient of static friction and σ_n denotes the normal stress. When the applied stress surpasses the static friction threshold ($\sigma > \sigma_s$), movement initiates along the fault surfaces. This movement encounters resistance from the kinematic/dynamic friction stress σ_k.

$$\sigma_k = \mu_k \sigma_n \qquad (I.15)$$

Where μ_k represents the coefficient of kinematic or dynamic friction. In a basic scenario, when sliding initiates along the fault, the friction stress instantaneously transitions from σ_s to σ_k at time $t = t_0$, and the displacement between the fault sides increases from zero to Δu, see **Fig. I.16a**. The effective or dynamic stress drop that drives this motion is:

$$\Delta \sigma_d = \sigma_s - \sigma_k \qquad (I.16)$$

b) Slip-Weakening Friction Model

Physically, an instantaneous drop in friction as depicted by the stick-slip model is not feasible. There is a finite region near the crack tip where stress gradually decreases from σ_s to σ_k. As proposed by Palmer & Rice (1973), behind the rupture front, there is a slip-weakening zone where friction decreases as slip increases. This reduction in friction is influenced by the distribution of slip *Δu* between the two sides of the fault. For an

antiplane fault (Mode III), a simplified slip-weakening model can be described as follows (Ida 1973):

The elastic medium is subjected to a uniform initial stress σ_0. Rupture begins when the stress near the fracture edge increases to the peak or static friction value σ_s, see **Fig. I.16b**. Ahead of the rupture front, the stress σ_0 is less than the static friction stress. At the rupture front itself, the stress is exactly equal to the static friction and then decreases over a distance d, the width of the slip-weakening zone, until it reaches the dynamic or kinematic friction σ_k. As shown in the figure, when the slip Δu increases, the friction $\sigma_c(\Delta u)$ decreases until a critical value $\Delta u = Dc$ is reached, at which point $\sigma_c = \sigma_k$. This critical value Dc is commonly referred to as the critical slip-weakening distance.
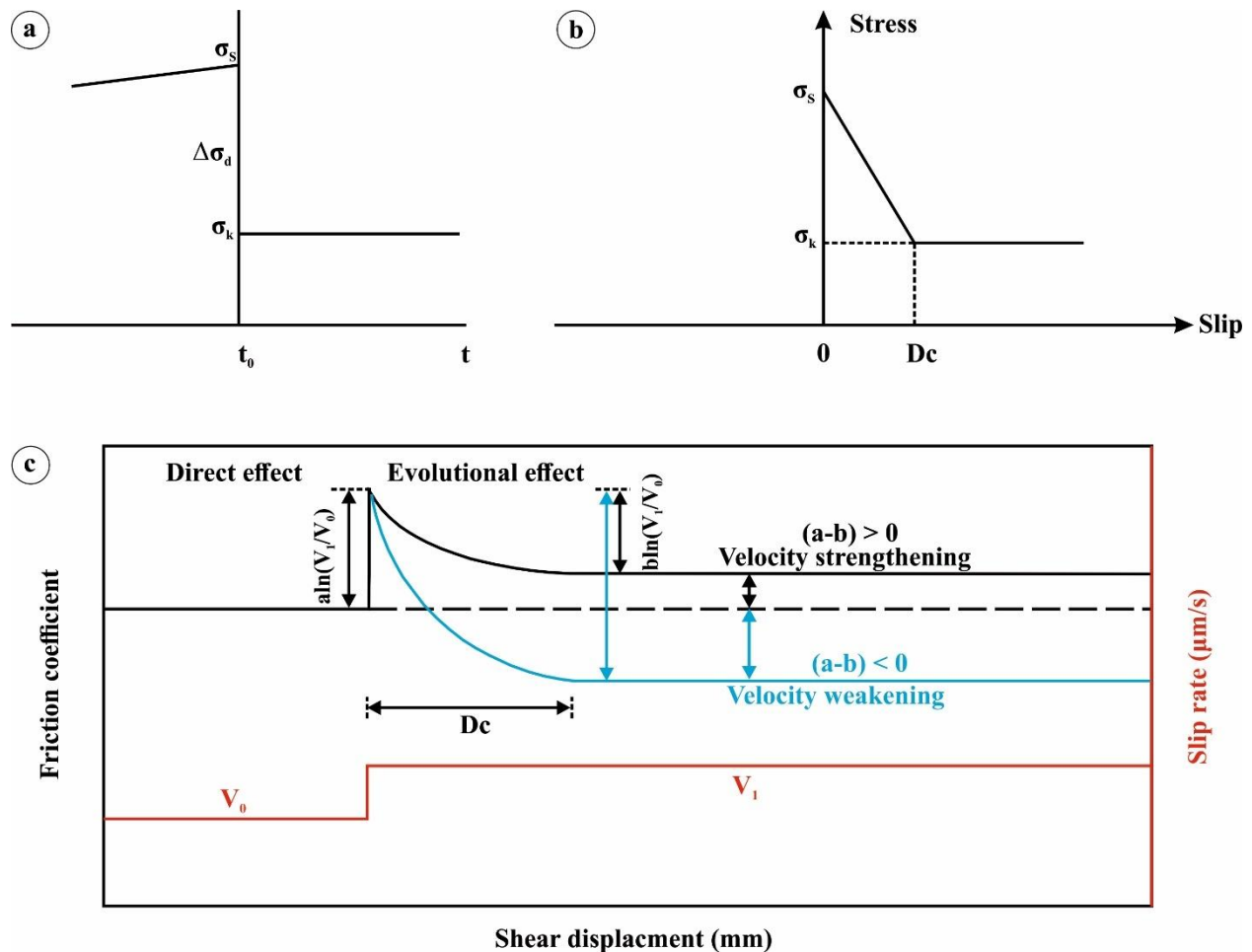
Fig. I.16: Friction models. **(a)** Stick-slip frictio model. Instantaneous stress drop from static friction σ_s to kinematic friction σ_k. **(b)** Slip-weakening friction model. Dependence of the

stress drop on the slip $\varDelta u$. Dc is the critical slip. **(c)** The schematic diagram for idealized rate and state friction law exhibiting velocity-strengthening and velocity weakening behaviors. Due to the slip rate change, the friction coefficient will reach a peak value and continue to evolve to its steady state. The positive value of (a–b) means the velocity strengthening behavior while a negative value of (a–b) is the velocity weakening behavior.

c) Rate-And-State Friction Model

The rate-and-state friction law is a phenomenological model that describes how the frictional resistance between two sliding surfaces depends on the sliding velocity (rate) and the history of contact (state). introduced to capture experimental observations of both steady state velocity dependence and transient slip and time dependence of friction. The shear stress σ depends on both rate and state logarithmically as follow:

$$\sigma = \sigma_n \left[\mu_0 + aLog\left(\frac{V}{V_0}\right) + bLog\left(\frac{\theta V_0}{L}\right) \right]$$ (I.17)

σ_n is normal stress, constants a and b determining the rate and state dependence, L is the characteristic sliding distance, and reference friction coefficient and reference slip velocity, μ_0 and V_0, respectively.

The evolution of θ is giving by:

$$\frac{d\theta}{dt} = 1 - \frac{\theta V}{L}\Big|_n$$ (I.18)

θ has dimensions of time and is often interpreted as the history of surface asperity contacts. An interface is sheared at a constant slip rate V0, and reaches steady state. The slip rate is then suddenly increased to V1 > V0, and the friction evolves to a new value over a length scale L. There is a transient increase in the friction, with a magnitude of a. The change in the steady state friction is $(a - b)$. If $(a - b) < 0$ the friction decreases as the sliding velocity increases, which is called *velocity weakening*, the fault may experience dynamic instability, meeting the conditions for earthquake nucleation. However, if $(a - b) > 0$, the friction increases with an increasing sliding velocity, called *velocity strengthening,* slip is accommodated by stable sliding, see **Fig. I.16c**.

I.7 Nucleation and Arrest Process Of Earthquake Rupture

I.7.1 Nucleation Process

The previously discussed friction models outline the shift from static friction at the fault's edge to kinematic friction within the fault. A pivotal concept in this context is the cohesive zone, as described by Kostrov & Das (1988), which plays a key role in initiating rupture. For a rupture to commence, a small initial stress perturbation or asperity on the fault interface is essential. This asperity undergoes aseismic slip, transferring stress to the adjacent material. It must be large enough to release sufficient strain energy to trigger the rupture, as noted by Yamashita & Ohnaka (1991). According to the slip-weakening model applied to the breakdown zone, slip begins when the stress reaches its peak or static friction level. At this juncture, slip starts, and friction decreases in line with the slip-weakening model. Although the initial stress drop is minor, it transfers stress to the surrounding area, facilitating further fault propagation. Initially, this process is stable and progresses slowly until the friction at a specific point on the fault diminishes to the kinematic value, σ_k, see **Fig. I.16b**. This stable slip in a localized area, termed the nucleation zone Lc, precedes unstable seismic slip and represents the nucleation process. As the nucleation zone expands, the friction at its center eventually drops to σ_k, leading to an accelerating progression of the breakdown zone until the slip reaches the critical value Dc. Beyond this point, dynamic instability occurs, and seismic waves are generated (Ohnaka 2013). At this stage, the fault surfaces slide against each other, with only kinematic (or dynamic) friction σ_k opposing the motion. The nucleation zone is defined as the region where the rupture progresses stably and quasistatically, extending from the initial failure point to where unstable rupture begins. Ohnaka 2000 relates an earthquake's moment to both the critical slip-weakening distance Dc and the nucleation zone size Lc, with $M_0 \propto Dc^3$ and $M_0 \propto Lc^3$. This indicates that larger earthquakes necessitate a larger nucleation zone and greater critical slip. Thus, the initial conditions for small and large earthquakes differ significantly.

I.7.2 Arrest Process

Once an earthquake rupture start it will last for a finite period of time, then it will stop. The general reason for this arrest is the heterogeneous properties of the medium and the fault plane. For a propagating rupture to stop, the conditions that gave rise to it should no longer exist. In other words, there must be places on the fault where the friction and geometrical conditions are different from those that allowed it to propagate. Seismologist provided two plausible interpretations to explain the arrest process of a rupture: 1) When an earthquake rupture propagates along a fault, it is driven by the stress concentration at the rupture front. The stress concentration is the localized increase in stress around the tip of the propagating fracture. For the rupture to continue, this stress concentration must be sufficient to overcome the fracture strength of the material along the fault. If there is a significant, abrupt increase in the fracture strength of the material — such as encountering a stronger rock type or a highly cemented section of the fault — the stress concentration produced by the propagating rupture may no longer be adequate to break the material. This abrupt increase in strength acts as a barrier to the rupture. 2) A rupture in an earthquake can also stop when it encounters an area with very low stress. It is an area along the fault that has significantly lower stress compared to surrounding areas. For the fracture to continue propagating, there must be enough energy released at the rupture front to drive the movement. When the rupture encounters such zone, the available energy is insufficient to sustain the fracture's forward movement.

I.7.3 Fault Plane Complexities, Barriers and Asperities

A fault plane is inherently complex and cannot be considered homogeneous due to its intricate structure and varying properties. This complexity arises from the heterogeneous nature of geological materials. Two models were proposed to explain these observed complexities, which are barriers and asperities. In the barrier model, fault plane complexity arises from permanent features that cause variations in strength and influence nucleation, arrest, and wave radiation. These permanent features act as barriers that disrupt fault slip and impact seismic activity. Conversely, in the asperity model,

complexity stems from initial stress conditions in the fault zone, which are a result of previous seismic or aseismic activity. This form of complexities is continually evolving, with features being constantly created and destroyed. Thus, while the barrier model focuses on static, enduring elements on the fault plane, the asperity model emphasizes the transient and ever-changing stress conditions within the fault zone.

a) Barriers model

The barrier model of complex fracture suggests that barriers on the fault surface interact with rupture propagation. While fracture occurs under uniform stress conditions, the material's rupture resistance, static friction, or strength varies. Barriers are unbroken patches on a fault surface that remain intact after an earthquake (Das & Aki 1977). Initially, the entire fault surface is under stress, which is released during the earthquake. If this stress release is uneven across the fault, some patches release stress while others remain stressed and unbroken, forming barriers, see **Fig. I.17a**. These barriers, characterized by their strength and dimensions, can be categorized as weak or strong. Generally, the interaction between the barrier and rupture front is based on the relative values of the tectonic stress (σ_0) and barrier strength (σ_b). If tectonic stress is higher ($\sigma_0 > \sigma_b$), the barrier breaks, allowing fracture continuation but with slower propagation velocity. If tectonic stress is lower ($\sigma_0 < \sigma_b$), the crack front may stop at the barrier or jump across it, leaving it intact. The barrier might later break due to increased dynamic stress. Once the rupture process terminates over the fault plane, stress is released in fractured zones and accumulates in unbroken barriers. These intact yet highly stressed barriers may break later in the form of aftershocks.

b) Asperities Model

Asperities are regions between two fault blocks characterized by high frictional strength, causing the fault to lock at these points. These are strong patches on the fault surface that remain stressed, while the surrounding areas have already released their

stress (Lay & Kanamori 1981), see **Fig. I.17b**. Large fault surfaces can contain multiple asperities, where stress levels are higher than the average stress on the fault. When the shear stress on the fault surface surpasses the stress of these asperities, localized slip occurs, leading to increased stress on stronger asperities. This model was first proposed by (Kanamori & Stewart 1978), after they observed a highly complex P waveform during their study of the 1976 Guatemala earthquake. They attributed this complexity to a source comprising 10 subevents, spaced 14 to 40 km apart along a 250 km fault length, which ruptured over approximately 2 minutes. They proposed that the heterogeneity in the fracture process was due to the sequential breaking of zones with greater strength, known as asperities. This suggests that, prior to the earthquake, the fault exhibited a heterogeneous stress distribution, with high-strength asperities surrounded by regions of lower stress.
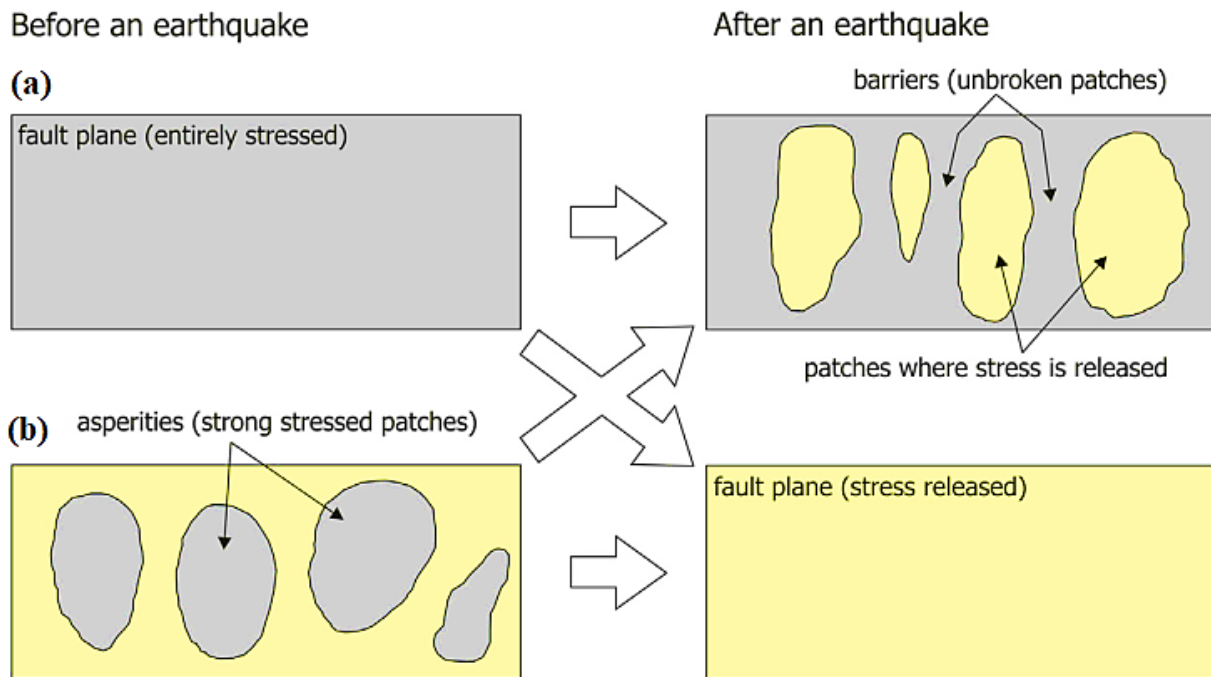
Fig. I.17: Barrier and asperity model. Barriers are unbroken patches on a fault surface that remain intact after an earthquake. (B) Asperities are regions between two fault blocks with high frictional strength, causing the fault to lock at these locations. After Brandes & Tanner (2020).

c) Barrier-Asperity Duality

In the asperity model, stable asperities on the fault surface repeatedly break during major earthquakes. Conversely, the barrier model involves fractures occurring between strong, stable barriers that do not break. Due to the occurrence of both foreshocks and aftershocks, strong patches on a fault surface behave as barriers and others as asperities (Aki 1984).

The barrier model accounts for aftershocks, as unbroken barriers eventually fail, while the asperity model explains foreshocks, where smaller quakes occur in the zone surrounding an asperity. Given that both foreshocks and aftershocks are observed, a combined approach of the two models provides a more comprehensive explanation. In this integrated view, foreshocks or small tremors before a major quake introduce heterogeneity on the fault surface, leaving the high-strength asperities to be broken by the main event. After the main shock, residual stress concentrations, or barriers, on the fault surface can later fail, leading to aftershocks. Thus, it is concluded that the fault surface's stress or strength distribution must be heterogeneous both before and after earthquakes to account for the occurrence of both foreshocks and aftershocks (Udías *et al.* 2014).

I.8 Earthquakes Interactions

C. Richter stated in his book *Elemntary Seismology*: "An earthquake within a sequence is never an isolated event". Indeed, earthquakes mostly occur in an interactive way. They typically manifest in sequences with distinct characteristics. The most recognized sequences include three different patterns: 1) Foreshock-Mainshock-Aftershock, 2) Mainshock-Aftershock, and 3) Swarms. The foreshock-mainshock-aftershock sequence involves smaller initial tremors (foreshocks) preceding a larger mainshock, which is then followed by a series of aftershocks. In the mainshock-aftershock sequence, a significant earthquake (mainshock) occurs without any notable preceding foreshocks, followed by aftershocks. Swarms, on the other hand, consist of numerous earthquakes of similar magnitudes occurring over a short period without a single

dominant mainshock, see **Fig. I.18**. Understanding these patterns is crucial for gaining insights into earthquake processes.
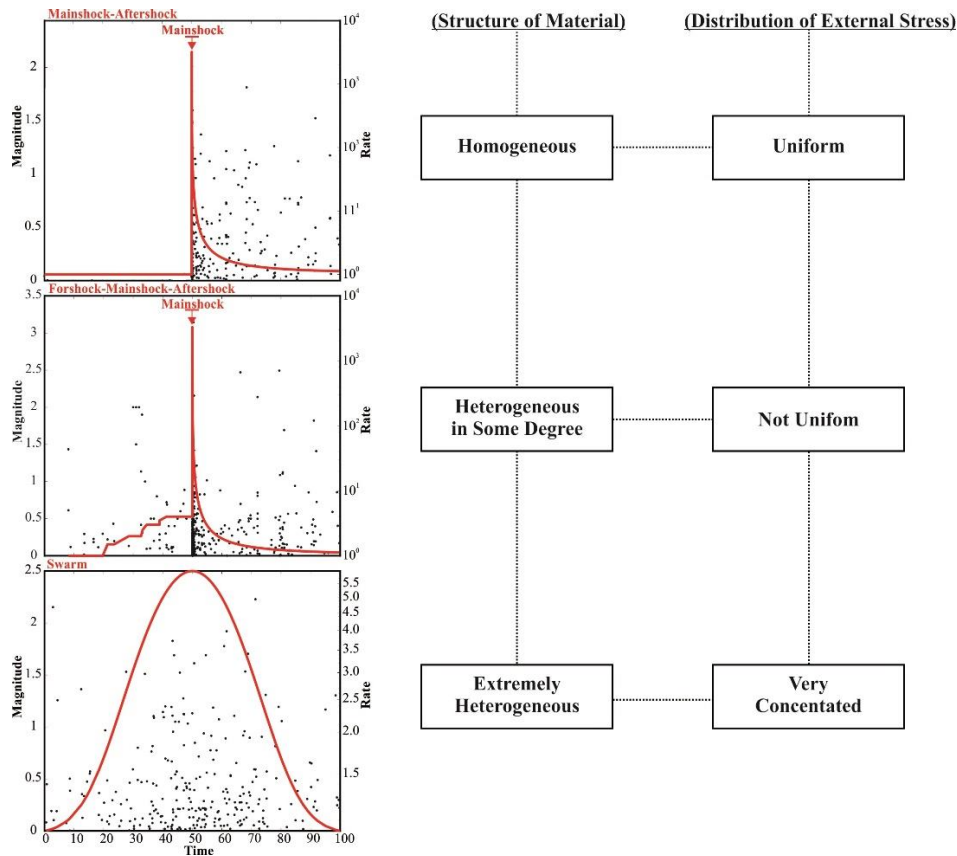
Fig. I.18: Schematic diagram depicting different types of earthquake sequences: (a) a mainshock (MS) accompanied by foreshocks and aftershocks; (b) a mainshock–aftershock sequence; (c) an earthquake swarm. After Scholz 2019.

I.8.1 Foreshocks

Foreshocks are smaller seismic events that occur prior to the mainshock, typically in close proximity to its hypocenter, suggesting they may be part of the nucleation process leading to the larger earthquake (Das & Scholz 1981). It is important to note that earthquakes occurring before the mainshock but situated far from the hypocenter are likely not causally linked to it and should not be classified as foreshocks. In contrast to aftershocks, which follow a mainshock in a more predictable manner, the occurrence of foreshocks is highly variable; a mainshock may be preceded by either a

single foreshock or multiple foreshocks. The Denali earthquake was preceded 10 days by a single large foreshock, whereas the L'Aquila earthquake was preceded by a swarm of foreshocks lasting four months (Scholz 2019). On the other hand, no foreshock has been observed before several sequences.

There is no established correlation between the largest foreshock size or the total number of foreshocks and the magnitude of the subsequent mainshock. However, when multiple foreshock sequences are analyzed collectively, a discernible pattern emerges (Jones & Molnar 1979), indicating that the frequency of foreshocks follows a specific distribution, known as inverse Omori law:

$$n(t) = \frac{K_f}{(t_c - t)^{p'}} \tag{I.19}$$

where t_c is the time of the mainshock and $p' \approx 1$.

The occurrence of foreshocks, quantified by the parameter K_f, varies significantly across different tectonic environments. It is most common in shallow subduction zones and oceanic transform faults, while it is least frequent in intraplate regions (McGuire *et al.* 2005; Bouchon *et al.* 2013). Approximately 80% of earthquakes in shallow subduction zones and along oceanic transform faults are preceded by at least one foreshock, whereas foreshocks are much rarer for intraplate earthquakes (Scholz 2019). Ellsworth & Beroza (1995) proposed two models to explain foreshocks nucleation: the pre-slip patch model and the cascade model. The pre-slip patch model suggests that a nucleation zone experiences very slow slip in preparation for a future earthquake. Conversely, the cascade model describes a sequence of interacting events leading to increasingly larger occurrences. Although this information is not predictive due to significant variability in magnitude and timing, it enhances our understanding of the processes occurring before major seismic events.

I.8.2 Aftershocks

Aftershocks are the most prevalent type of earthquake sequence, with their occurrence being a near-universal phenomenon following any substantial shallow

tectonic earthquake. Moreover, aftershocks exhibit the most well-defined and consistent characteristics among all earthquake sequence types. A particularly notable feature of aftershock sequences is their temporal decay pattern, which closely aligns with the Omori law. The Omori law, describes the temporal evolution of aftershock activity following a mainshock. It states that the rate of aftershock occurrence is inversely proportional to the time elapsed since the mainshock. This relationship is mathematically expressed as:

$$n(t) = \frac{K}{(c + t)^p} \tag{I.20}$$

where $n(t)$ is the number of aftershocks per unit time at time t after the mainshock, K and c are constants, and p is the Omori exponent, typically ranging between 0.7 and 1.5. The Omori law provides a robust framework for understanding and predicting the temporal decay of aftershock sequences, underscoring the well-defined nature of this type of earthquake sequence compared to others, such as foreshocks or swarms. Following Bath's law, it is often stated that the largest aftershock in the sequence is typically at least 1.2 magnitude units smaller than the mainshock. Conversely, Utsu 1972 found that the largest aftershock was typically about one magnitude unit less than the mainshock.

Despite its significance, the physical processes that lead to the generation of aftershocks are still not well understood. A commonly proposed explanation suggests that aftershocks occur due to the redistribution of strain energy caused by the mainshock. However, this explanation falls short in many cases, particularly for aftershocks that occur within the mainshock's slip area, where the strain energy has already been released. Indeed, a large earthquake is typically followed by numerous aftershocks. These aftershocks can occur both within the rupture area of the mainshock (the zone where the primary slip and energy release happened) and in the surrounding regions. The redistribution of stress caused by the mainshock's rupture is generally understood to explain the occurrence of aftershocks around the rupture area. This redistribution involves the transfer of stress to adjacent faults or areas of the crust, which can then trigger further seismic activity. However, this widely accepted explanation is not always

applicable. For example, the exact physical mechanisms that generate aftershocks within the rupture area itself, where much of the strain energy has already been released, remain a topic of ongoing scientific debate and investigation.

Another intriguing aspect of aftershocks is the significant variation in the number of aftershock events generated by each mainshock. While it is accepted that the number of aftershocks increase with the increasing magnitude according to the following expression (Utsu 1971)

$$N_{aft} = K10^{b(M_m - M_{th})} \tag{I.21}$$

where M_m is the magnitude of the mainshock, M_{th} is the lower threshold of measuring aftershocks, and K is a usually considered a constant. Nevertheless, it has been observed that different tectonic environments with varying stress conditions, fault structures, and rock properties, can influence aftershock productivity. For instance, An M5 earthquake within highly fractured or heterogeneous fault zone might produce more aftershocks compared to an M6 earthquake within more homogeneous fault zone. Or even in similar tectonic settings, an earthquake of lower magnitude can exhibit higher aftershock productivity compared to an earthquake with higher magnitude. This suggests that another forcing mechanism is influencing the high productivity of the lower magnitude earthquake. High-pore pressure fluids are commonly the primary suspected forcing mechanism driving aftershocks. This is because fluids are usually abundant within the Earth's crust, particularly in fault zones. Miller 2020 conducted a thorough investigation to answer an important, yet a poorly addressed problematic in seismology, *why some earthquakes generate thousands of aftershocks while other earthquakes generate few?* The main conclusion of his research highlighted that a scarcity of aftershocks often indicates the lack of high-pressure fluid sources at depth. Conversely, abundant and long-lasting aftershock sequences typically signal the presence of high-pressure fluid reservoirs that sustain these events. These reservoirs can maintain elevated pore pressures over extended periods, thereby promoting ongoing seismic activity. The mechanisms with

which fluids prompt faults to failure is straightforward. Knowing that the effective shear stress acting on a fault is giving by:

$$\sigma' = \sigma - P \qquad\qquad (I.22)$$

where: σ' is the effective stress, σ is the total normal stress, and P is the pore fluid pressure.
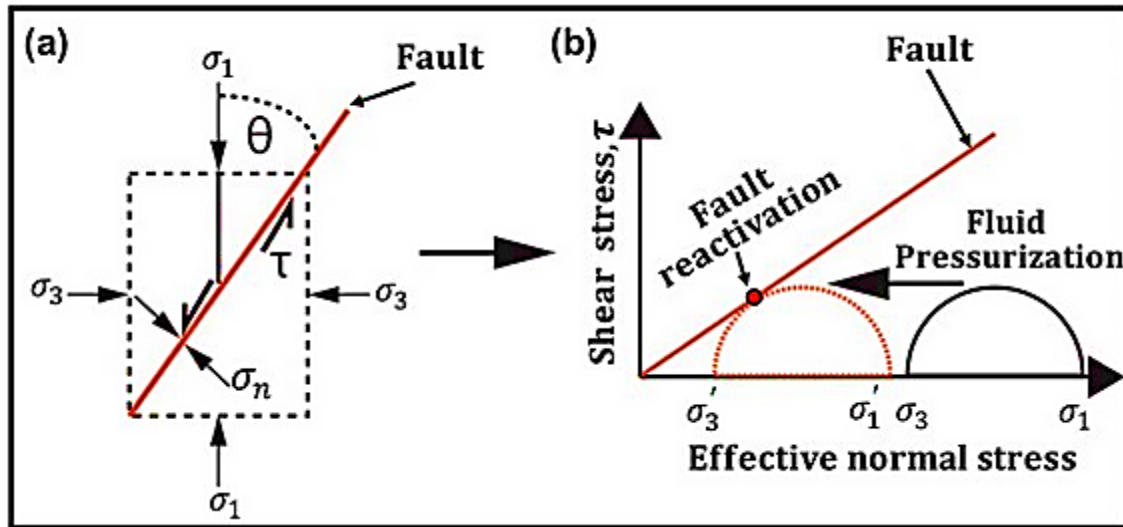
Fig. I.19: Fault plane stress analysis: **(a)** Resolution of normal and shear stresses along a fault plane with a specific orientation, based on remote principal stresses (Modified from Cappa & Rutqvist (2011)). Here, σ1 and σ3 represent the maximum and minimum principal stresses acting on the fault plane in the vertical and horizontal directions, respectively; σn is the normal stress perpendicular to the plane, τ is the shear stress parallel to the fault plane, and θ is the angle between σ1 and the fault plane. **(b)** Slip failure mechanism induced by fluid pressurization (Modified from Gan & Elsworth (2014)). An increase in pore pressure lowers the total normal stresses to their effective normal stresses, shifting the Mohr circle (black semi-circle) to the left (red semi-circle) until it touches the failure envelope, thereby meeting the conditions for shear failure (indicated by a small red solid circle on the Mohr-Coulomb failure criterion line). After Akande *et al.* 2021.

When fluids infiltrate a fault zone, they increase the pore pressure (P). This increase in pore pressure reduces the effective stress (σ') acting normal to the fault plane. Since the shear stress required to cause fault slip is a function of the effective normal stress, a

reduction in effective normal stress lowers the frictional resistance on the fault, potentially inducing slip. This can be well explained through the Mohr-cercle illustrated in **Fig. I.19**. The figure shows a fault plane within a stress field. The normal stress (σ_n) and shear stress (τ) acting on the fault plane are shown, along with the principal stresses σ_1 (maximum) and σ_3 (minimum). The figure exhibits the slip failure mechanism by fluid pressurization. An increase in pore pressure reduces the total normal stresses to their respective effective normal stresses and pushes the Mohr circle (black semi-circle) to the left (red semi-circle) to touch the failure envelope, and thus satisfying the conditions for shear failure.

I.8.3 Swarms

Earthquake swarms consist of a series of tremors that gradually start and cease, within a small area, with none of the individual quakes being significantly larger than the others. Sykes 1970 conducted a comprehensive global survey and found that swarms frequently occur in volcanic regions, although this is not a universal rule. Others (Nur 1974; Kisslinger 1975) found that fluid injections constitute favorable conditions for earthquake swarms to be triggered. This mechanism involves the increase of pore pressure due to fluid diffusion (natural and/or anthropogenic), leading to earthquakes in areas with a significant stress gradient. This gradient prevents any single event in the sequence from becoming very large, as the fluid flow controls the strain relief, thus averting a dominant large quake.

I.9 Clusters of Earthquakes with Similar Waveform

Seismograms (also known as earthquakes waveform) are graphical records produced by seismographs that capture the vibrations of the earth generated by various seismic sources such as earthquakes, volcanic activity, and artificial explosions. They represent the variation of the shaking amplitude as a function of time. These records are essential for seismologists to analyze the characteristics of seismic waves, allowing them to infer information about the Earth's interior structure, seismic source mechanisms, and

tectonic processes. An earthquake seismogram, $U(t)$, is the convolution of the radiation from the earthquake source, $S(t)$, with the combined propagation effects along the path including site effect, $P(t)$, and finally the instrument response, $I(t)$.

$$U(t) = S(t) * P(t) * I(t) \qquad (I.23)$$

Each wiggle in a recorded seismogram is an information carrier. The change in amplitude and/or frequency indicates the arrival of different seismic phases. Each earthquake has its own characteristic source and its own traveled path depending on the source-receiver distance, hence the take-off angle (the angle at which the rays leave the source). Therefore, Seismogram can be viewed as the fingerprint of an earthquake. Each seismogram is unique and contains detailed information about the earthquake's characteristics, much like a fingerprint uniquely identifies an individual. However, observations have revealed that some earthquakes come with highly similar waveforms. These similar waveforms, often referred to as "earthquake multiplet" or "repeating earthquakes". While each seismogram generally provides a unique signature of an earthquake's characteristics, these special events can produce nearly identical seismograms. These phenomena have been widely exploited by researchers to investigate various important topics, including fault geometry and fault zone characterization, estimation of slip rate and aseismic slip, inferring earthquake recurrence intervals (assessing predictability), and revealing insights into fluid migration along existing faults

I.9.1 Earthquake Multiplet

Under certain conditions, seismologists may detect seismic events that share prominent features in amplitude and frequency, and sometimes exhibit highly similar characteristics. Such similar seismic events are classified as doublets when there are two events, and as multiplets when more than two events display these features. Multiplets are of particular interest because they provide valuable insights into the underlying tectonic processes and the behavior of seismic sources. The concept of multiplets was first defined and analyzed by Fréchet 1985 and Poupinet *et al.* (1996). Seismic multiplets are

generally characterized by their spatial proximity rather than temporal proximity. The identification of multiplet groups primarily relies on waveform similarity, which can be quantified using time-domain cross-correlation or frequency-domain coherency measurements, see **Chapter II** for more details. Although there is no universally accepted minimum threshold for waveform similarity to define multiplet groups, this threshold typically ranges from 0.7 to 0.95.

The similarity in waveforms among these events suggests that they originate from the same source and follow the same propagation path, indicating a shared Green's function. Theoretically, this resemblance in waveforms implies similar focal mechanisms. However, the question of whether these events originated from the same fault remains unanswered, as several models of multiplet generation have been proposed.

1) Common Fault Patch: In this model, multiplet events radiate from the exact same fault patch. For this model to hold, the events in a multiplet group should have overlapping source areas, meaning their source regions should intersect. However, the minimum area of intersection is not well defined.

2) Separated Fault Patches Along the Same Fault Plane: This model posits that each event in a multiplet group originates from distinct rupture patches along the same fault plane.

3) Sub-Parallel Faults: According to this model, events within a multiplet group can be generated from several parallel faults. Bourouis 2004 highlighted these three models. Nevertheless, I believe that within a complex fault system, events from the same multiplet may also originate from intersecting faults that have approximately the same azimuthal orientation (e.g., N-S or NNE-SSW). **Fig. I.20** exhibit the different possible models for multiplet.
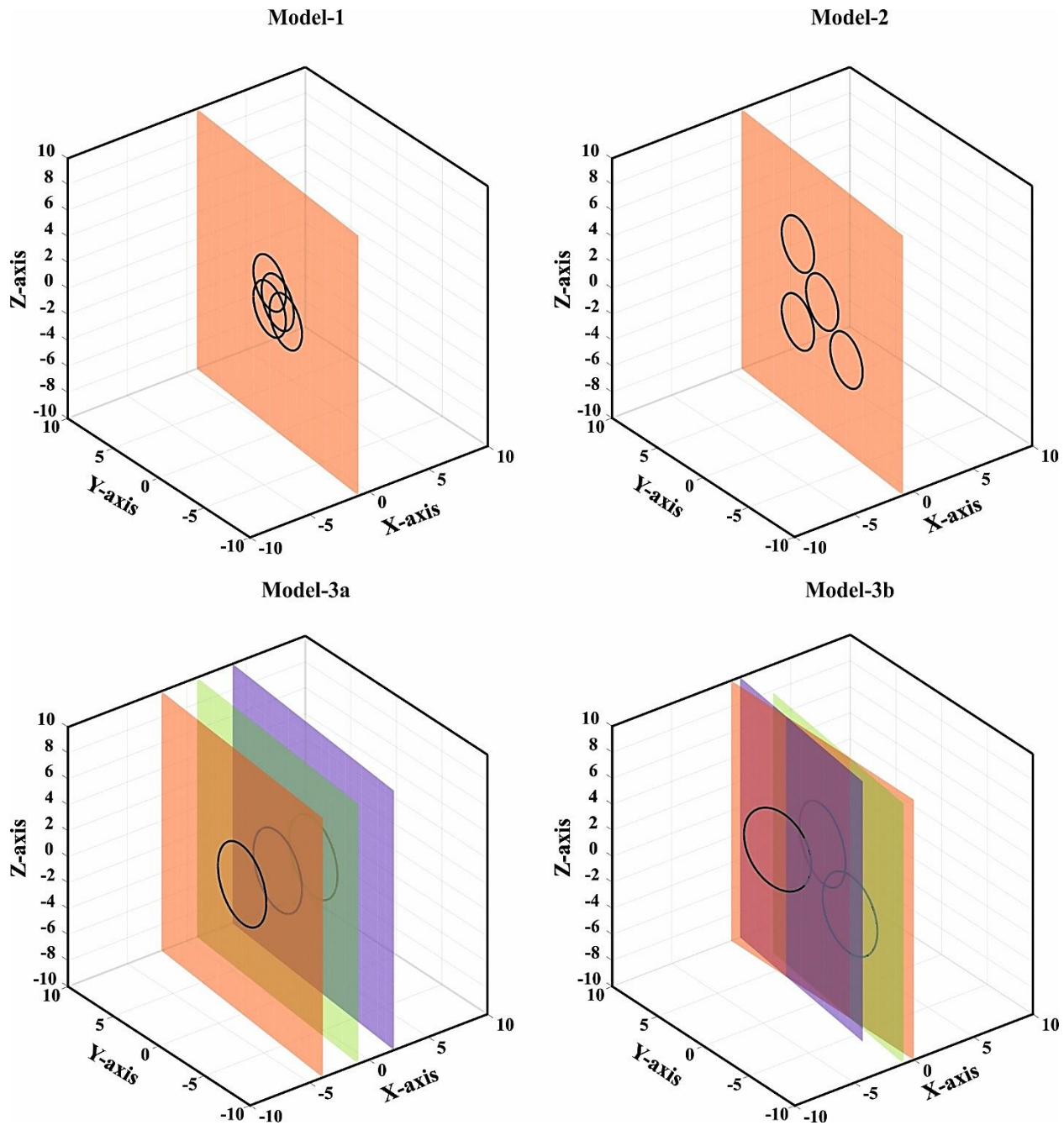
Fig. I.20: The different multiplet fault source models. Model-1 indicates events originating from the same fault patch. Model-2 indicates events originate from different patches along the same fault plane. Model-3 indicates events originate from different faults (3a from parallel fault and 3b from intersected faults).
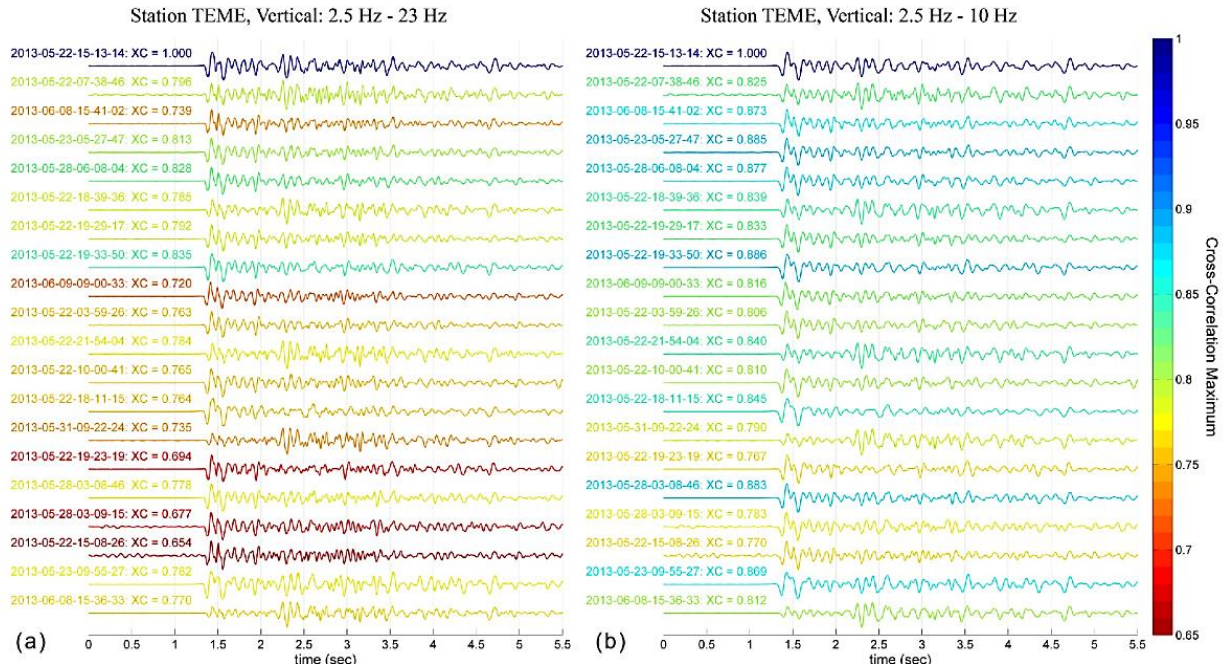
Fig. I.21: Example of multiplet from the 2013 earthquake swarm in Helike, Greece recorded at station TEME, **(a)** filtered between 2.5 and 23 Hz, **(b)** filtered between 2.5 and 10 Hz. Similarity is measured with respect to the first one at the top. Colours refer to the max CC value for the cross-correlation of each waveform with the one at the top of the stack (indicated as XC). After Kapetanidis *et al.* (2015).

I think that the choice of the most appropriate model to explain multiplet may be influenced by the waveform similarity threshold used for event identification. If we categorize the typical cross-correlation (CC) thresholds, which range from 0.7 to 0.99, into three distinct classes:

- $0.7 \leq CC < 0.8$: High similarity
- $0.8 \leq CC < 0.9$: Very high similarity
- $0.9 \leq CC \leq 1$: Extremely high similarity

Events with a CC within the range of [0.7-0.8] are highly similar but still exhibit 20% to 30% dissimilarity. Therefore, these events are less likely to originate from the exact same fault patch as suggested by Model-1. Instead, they are more consistent with Model-3, where parallel or intersecting faults within a complex network could generate such

multiplets. Events with a CC in the range of [0.8-0.9] align well with Model-2, which proposes distinct rupture patches along the same fault plane. Only events with an extremely high similarity, CC values in the range of [0.9-0.99], can be attributed to Model-1, indicating repeated rupture of the exact same fault patch. However, this model may overlap with the definition of repeating earthquakes, which will be discussed further in the next section. It is noteworthy to emphasize that this classification is just an assumption, and it must be verified by simulations.

Another important factor that may help selecting the most appropriate model, is the 3D spatial distribution of the events constituting a multiplet, the horizontal distribution, in addition to an appropriate depth projection, preferably along the assumed fault plane.

I.9.2 Repeating Earthquakes

Repeating earthquakes, or earthquake repeaters, are seismic events that occur on the same fault area, rupturing an identical fault patch multiple time. These earthquakes produce similar waveforms, indicating that the same seismic source is being activated repeatedly. They are typically found in creeping areas of faults, where slow, continuous motion allows stress to accumulate and be released periodically, see **Fig. I.22** (Uchida 2019). While true repeaters should have identical seismic waveforms, small differences in their seismograms can be used to examine subtle changes in source properties or in material properties of the rocks through which the waves propagate. Despite the fact that repeaters are most commonly observed on creeping faults, such as those in subduction zones, they have also been detected within intra-plate regions (Uchida & Bürgmann 2019).
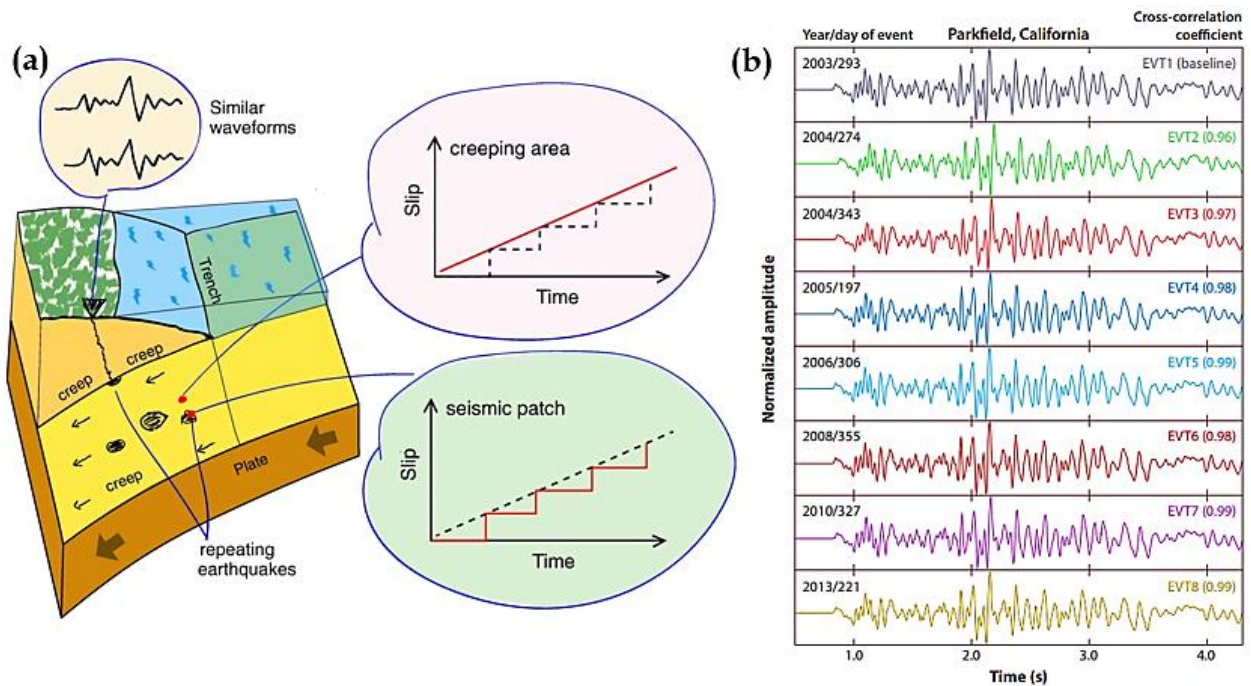
Fig. I.22: Repeating earthquake model and example. **(a)** Schematic model illustrating the environment where repeating earthquakes occur in a subduction zone. These earthquakes take place on a seismic patch (black spots) within the creeping area of the plate boundary. When observed at the same station (top left), they produce similar waveforms because the seismic patch is reloaded by creep in the surrounding area and ruptures repeatedly at the same location. The creeping area (slip shown in red in the top right panel) and the repeating earthquake patch (slip shown in red in the bottom right panel) experience nearly the same long-term cumulative slip, as they are located on adjacent plate boundaries. The dashed line indicates slip in the neighboring area. (After Uchida. 2019). **(b)** Example of repeating earthquakes near Parkfield California (After Kim et al. (2016) and Uchida & Bürgmann. (2019)).

One of the widely known and most studied repeating earthquakes are those that are occurring near Parkfield California, see example in **Fig. I.22b.**

There are three main methods for identifying repeating earthquakes. The first approach is known as the physics-based approach, it is based on the overlap of source areas, which requires precise estimation of interevent distance and source dimensions, necessitating a dense near-source array and high precision relocation of hypocenters to reduce miss-identification. The second, and most common method, called the waveform-

based approach, and it relies on waveform similarity between earthquake pairs, quantified by the cross-correlation coefficient (CC) in the time domain or coherency (Coh) in the frequency domain. As for multiplet earthquakes, The CC threshold for identifying repeaters varies, typically ranging from 0.70 up to 0.99 in areas with sophisticated instrumentation. Nevertheless, the vast majority of researchers do not allow a CC less than 0.95 to identify true repeaters. The third method is a hybrid approach that combines CC with additional criteria, such as examining the time interval between events, the difference in S–P differential times or magnitude differences.

Unlike multiplets, where several fault models are proposed to explain their occurrence, there is a widely accepted model for repeaters. It is generally agreed among researchers that repeaters are events that originate from the exact same fault patch. However, there is no consensus within the seismological community on the best parameters to identify repeaters. Several parameters can be used, but the most important ones include the cross-correlation (CC) threshold, percentage of overlapping source area, magnitude difference, and inter-event distance. Uchida 2019 and Gao *et al*. (2021) compiled lists that exhibit the different parameters used by various authors to identify repeaters, showing a remarkable variety in the selected parameters. This variety raises the question of whether all identified repeaters worldwide are truly repeaters.

For repeaters that are far from plate boundary faults, different source models may be indicated. Some repeaters have been found in areas with little or no resolvable tectonic strain, mostly in the form of burst-type clusters characterized by relatively small recurrence time-interval. These events are known as burst-type repeating earthquakes. Such burst-type repeaters have also been observed in Japan (Igarashi *et al*. 2003) and California (Templeton *et al*. 2008). Interestingly, sequences of high-quality repeaters have been identified in the New Madrid seismic zone in the United States (Bisrat *et al*. 2012) and in the aftershock sequence of the 2000 Western Tottori earthquake (Mw 6.6) (Hayashi & Hiramatsu 2013). It is possible that specific conditions, such as loading by a large mainshock or elevated pore fluid pressure, are necessary to generate repeaters on inland

tectonic faults, which typically experience very low loading rates (Uchida & Bürgmann, 2019).

I.9.3 Ambiguities in Definitions: Distinguishing Multiplets And Repeating Earthquakes

Despite the apparent similarities between multiplet and repeating earthquakes, they represent distinct seismic phenomena. Currently, there is no universally accepted definition for either term within the seismological community. Some researchers, such as Kapetanidis *et al.* (2015), Lengliné *et al.* (2014), Schmittbuhl *et al.* (2016), and Staszek *et al.* (2021), have used the terms interchangeably, without distinguishing between them. In contrast, others, including Gao *et al.* (2021), Uchida 2019, and Uchida & Bürgmann (2019), have exclusively used the term "repeating earthquakes." Massin *et al.* (2013) provided a nuanced distinction by using "multiplet" to describe similar seismic events within a specific group and "repeating earthquakes" for all events belonging to a multiplet within a particular time frame or area. Shaddox *et al.* (2021) introduced another term, "near-repeating earthquakes," to describe similar events that are closely spaced or partially overlapping.

It is crucial to unify the definitions of both multiplet and repeating earthquakes within the seismological community. Without a common definition, ambiguities and uncertainties will persist in the multiplet and repeaters previously identified and those that will be identified in the future. It is important to note that, recently, Gao *et al.* (2023) took the first steps towards unifying the definition of repeating earthquakes by conducting various tests to propose the best possible criteria for identifying these events. They found that a magnitude difference of no more than 0.3 and an inter-event distance that is ≤ 80% of the rupture area of the larger event are the best parameters to identify true repeaters. Nevertheless, they did not discuss the CC/Coh threshold despite its importance. Therefore, their proposed definition may not be well constrained.

I.9.4 Our Used Terminology

In this thesis, we analyze both multiplets and repeating earthquakes. To avoid any potential confusion, we have adopted the following terminology:

1) Multiplet: are clusters of closely spaced events with at least 70% waveform similarity (CC ≥ 0.7) and a minimum average cross-correlation of 0.8. These events originate from the same fault, though not necessarily the exact same fault patch; they may also radiate from parallel or neighboring interconnected faults of the same type (e.g., strike-slip) with approximately similar characteristics (strike, dip, and rake).

2) Repeating earthquakes: are events that repeatedly rupture the exact same fault patch. These events should have a magnitude difference of no more than 0.3 and an inter-event distance that is ≤ 80% of the rupture area of the larger event, as specified by Gao *et al.* (2023). Additionally, we impose a cross-correlation threshold of CC≥ 95%.

I.10 Conclusion

In conclusion, this chapter provides an in-depth exploration of the mechanisms driving fault movement and earthquake generation, combining fundamental concepts with current research debates. By presenting both complex and simplified fault models, we have shown how fault architecture and fault-related fluid flow influence seismicity. The use of focal mechanisms, particularly through moment tensor inversion, allows us to gain insights into fault slip behavior, while the decomposition of moment tensors highlights the significance of non-double couple mechanisms, such as those induced by fluid intrusion. We highlighted the importance of stress tensors and their relationship to faulting. We also delved into seismic rupture dynamics, focusing on fracture expansion modes, cohesive zones, frictional models, and the processes governing rupture nucleation and arrest. This was further related to asperity and barrier models, emphasizing how these factors influence rupture propagation. Additionally, we highlighted the interconnectedness of earthquakes through sequences such as foreshock-mainshock-aftershock patterns and swarms, outlining the potential driving mechanisms discussed in the literature. The chapter also addressed the phenomenon of multiplet and

repeating earthquakes, stressing their role in revealing underlying fault characteristics, despite the ambiguities in distinguishing their definitions. Ultimately, through this chapter, we have presented fundamental yet critical seismological concepts that remain the focus of ongoing scientific debates and research. These important physical backgrounds form the cornerstone of advancing our understanding of earthquake physics.

Chapter II

New Seismotectonic Model
for
Beni-Ilmane Region

Content

II.1 Introduction

In this chapter, we delve into the essential aspects of the BI-2010 earthquake sequence, providing a foundation for the new seismotectonic model proposed in our paper Tikhamarine *et al.* (2024).

Sub-chapter II.1.1 introduces the geological framework of the Beni-Ilmane region, highlighting key tectonic structures that influence seismic activity. **Sub-chapter II.1.2** then examines indicators of fluid accumulation, a key driver in the area's seismicity and aftershock behavior. Finally, **sub-chapter II.1.3** reviews the main scientific literature on the BI-2010 sequence, setting the stage for a critical evaluation of past findings and laying the groundwork for the refined interpretations presented in this chapter. These sections collectively form a comprehensive context, essential to unraveling the complex fault architecture and driving mechanisms at play in the BI-2010 sequence.

II.1.1 Geological Framework of Beni-Ilmane Region

The epicentral region of the BI-2010 earthquake (**Fig. II.1a**) is situated on the southern edge of the Tellian Atlas, within the transitional zone between the Hodna and Bibans mountains (**Fig. II.1b and c**), approximately 200 km from the plate boundary, as noted by Billi *et al.* 2023. Since the late Cretaceous period, the Atlas foreland has experienced deformation due to the N-S to NNW-SSE convergence between the African and Eurasian plates. This convergence initially led to the tectonic inversion of Mesozoic structures (Bracène & Frizon de Lamotte 2002). The structural units, which account for about 30% of the current shortening rate (~5 mm/yr) (Bougrine *et al.* 2019), exhibit low to moderate seismic activity. For an in-depth analysis of the seismicity in the Hodna-Bibans region, refer to Abacha 2015.

A closer examination reveals imbricated thrust sheets (**Fig. II.1c and d**) resulting from the southward progression of the Tell fold-and-thrust belt, accompanied by the formation of a foreland basin system. The study area encompasses the allochthonous

Tellian nappes (sub-Bibanic domain), the parautochthonous Djebel Choukchot (anticline), and the autochthonous Hodna basin (Preatlasic domain) from north to south (**Fig. II.1c**). Within the parautochthonous domain, the Djebel Choukchot anticline contains Miocene rocks of the Ouanouga formation beneath Triassic and Cretaceous formations, displaced by an overthrust reverse fault, indicating recent tectonic activity. NE-SW-trending folds and SE-verging thrusts are prominent in the region (**Fig. II.1d**). This zone has undergone several deformation phases, dating from the Tortonian to early Quaternary (Guiraud 1973), leading to the folding of the Hodna Mountains anticline (e.g., Djebel Choukchot) (**Fig. II.1b**). The eastern section of the Hodna Mountains anticline exhibits more intense fracturing than the western section (Kheidri *et al.* 2007) (**Fig. II.1c**). The Djebel Choukchot and the Hodna Basin are transected by north-south trending faults (René Guiraud 1973). According to (Wildi 1983), pre-existing east-west and NNE-SSW fault networks remain active today.

The epicentral area is highly fractured, reflecting a complex geological history shaped by Mesozoic-Cenozoic tectonic activity and later reactivation during the Pliocene-Quaternary period (Bracène & Frizon de Lamotte 2002). The fault network includes (1) NE-SW to ~E-W trending thrust faults dipping northwest (e.g: TF3 in **Fig. II.1c**), (2) the NNW-SSE Samma strike-slip corridor that crosses Djebel Choukchot (e.g: VF1 in **Fig. II.1c**), (3) E-W dextral strike-slip faults intersecting the Kef El Kherat fold (e.g: VF5 in **Fig. II.1c**), and (4) two conjugate NNE-SSW and NNW-SSE left-lateral strike-slip faults located to the west and east of Beni-Ilmane village, (VF4 and VF2 respectively in **Fig. II.1c**). The main faults are labeled in **Fig. II.1c**, with letters followed by numbers, where "VF" denotes "Vertical Faults" and "TF" denotes "Thrust Faults." Analysis of the map reveals a noteworthy pattern where TF1, TF2, TF3, and TF4 were likely aligned along a unified fault during a particular tectonic phase, which was subsequently offset by vertical faults. By studying shear patterns along thrust faults and the edges of ancient geological formations within the core of Djebel Choukchot, we can infer the nature and kinematics of associated vertical strike-slip faults. Consequently, VF1 and VF2 are NNW-SSE left-

lateral strike-slip faults, VF4 is an NNE-SSW left-lateral strike-slip fault, and VF5 is an E-W right-lateral strike-slip fault.

II.1.2 Indicators of Fluid Accumulation

Frequent surface seeps have been reported in the Sub-Bibanic and Hodna areas, occurring in ENE-WSW to east-west trending zones corresponding to the regional fracture network, indicating an active petroleum system (Kheidri *et al.* 2007). Traps within the Tellian fold belt include anticlines interpreted from reflection seismic profiles (Bracène *et al.* 1998), associated with reverse faults. The underlying Mesozoic-Cenozoic autochthonous sequence in the area contains two potential source rock intervals: Cenomanian-Turonian and Eocene. Reservoir rocks comprise Lower Cretaceous siliciclastics and Upper Cretaceous to Paleogene carbonates. For detailed information on hydrocarbon potential, see Kheidri *et al.* (2007).

The significant influence of strike-slip faults in modifying the thrust system, combined with the assessment of potential fluid reservoirs (oil, gas, or others), prompts an examination of the possible interactions between these structural elements. The release of pressurized fluids following a seismic rupture could act as a driving mechanism, underscoring the importance of re-analyzing the Beni-Ilmane 2010 seismic sequence to gain insights into the complex tectonic processes influencing seismic activity in the area.
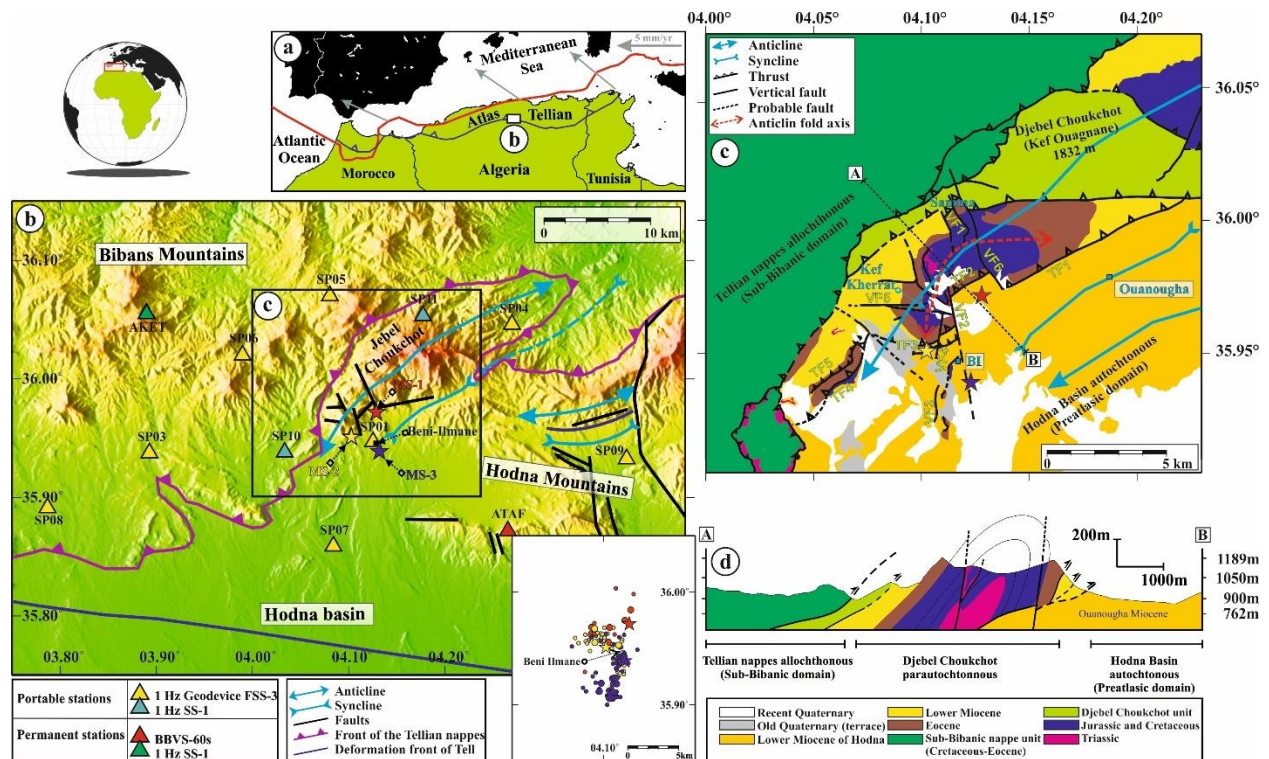
Fig. II.1: geological framework of Beni-Ilmane. **(a)** Geographical representation of the southern region of the Western Mediterranean, outlining the Atlas Tellian System bounded by the South-Atlas Front (dark blue line). The simplified Eurasia-Africa Plate boundary is indicated by the red line (adapted from Bird 2003), with projected velocities along this boundary illustrated by gray arrows (simplified from Nocquet 2012). **(b)** Tectonic illustration of the study area, highlighting key tectonic features, the three mainshocks (MS) marked by red, yellow, and blue stars, respectively, and the locations of seismic stations denoted by triangles. The distribution of all M3+ events is shown in the lower right corner, with colors corresponding to the three mainshocks. **(c)** Structural map zooming in on the epicentral region, presenting the arrangement, orientation, and interconnections of rock layers, faults, and folds (modified from Beldjoudi *et al.* (2016) and Abacha *et al.* (2023a)). **(d)** Geological cross-section [A-B] (modified from Beldjoudi *et al.* (2016) illustrating Ouanougha Miocene rocks thrusting beneath Triassic and Cretaceous formations, while Tellian nappes Overrides Djebel Chakchout formation through NW-verging thrust faults.

II.1.3 Review of Scientific Literature on The BI-2010 Sequence

The Beni-Ilmane earthquake sequence of May 2010 stands out as the most significant seismic event in Algeria over the past two decades, having been the subject of extensive study for more than ten years. This sequence, characterized by three moderate mainshocks (referred to as MS-1, MS-2, and MS-3 in **Fig. II.1b**), resulted in considerable infrastructure damage and triggered a series of aftershocks, causing prolonged fear among the local population. The sequence commenced with MS-1, which had a magnitude of Mw 5.4, on May 14, 2010, at 12:29 GMT. This was followed by two additional mainshocks: MS-2 on May 16, 2010, at 06:52 GMT, with a magnitude of Mw 5.1, and MS-3 on May 23, 2010, at 13:28 GMT, also with a magnitude of Mw 5.1. The sequence produced around 25,000 aftershocks detected by at least one nearby station, underscoring its high aftershock productivity. The epicenters of the mainshocks are located approximately 3 km NNE, 1.5 km WNW, and 1 km SSE of the Beni-Ilmane village, respectively, in the geologically complex southern part of the NE-SW Djebel Choukchot massif, as shown in **Fig. II.1c** and **d**. This massif has experienced substantial deformation since the Upper Cretaceous, leading to the development of a complex network of faults and fractures with varying orientations and types, prompting inquiries into the underlying mechanisms driving this activity and their relationship with pre-existing tectonic structures in the region.

The BI-2010 sequence presents a scientific challenge due to the unusual occurrence of three moderate earthquakes within a single week, coupled with highly energetic aftershock activity, all within the seismotectonic framework of the Algerian foreland. Numerous studies have explored various aspects of this sequence, including seismotectonics (Beldjoudi et al. 2016; Yelles-Chaouche *et al.* 2014), statistical analyses (Hamdache et al. 2018; Rahmani et al. 2023), source parameters (Abacha *et al.* 2019), stress transfer (Beldjoudi 2020), and local earthquake tomography (Abacha *et al.* 2014; Abacha *et al.* 2023a). However, the debate over fault geometry remains unresolved. Yelles-Chaouche et al. (2014) proposed a simplified model involving two faults: an east-west-oriented reverse fault and an NNE-SSW-oriented sinistral strike-slip fault, based on 18

focal mechanisms and the double-difference relocation of two weeks of aftershock activity (comprising 1403 events). In contrast, Beldjoudi *et al.* (2016), using the same dataset as Yelles-Chaouche *et al*. (2014), conducted a comprehensive geological analysis and waveform modeling of the three mainshocks, attributing the fault planes to specific geological faults and developing a three-fault model that did not account for the aftershock distribution. These studies have certain limitations, such as the Yelles-Chaouche *et al.* (2014) model's failure to explain the presence of a strike-slip mechanism within the reversely oriented fault. The location uncertainties, particularly regarding the epicenters of the three mainshocks, pose challenges for Beldjoudi *et al.* (2016) in making definitive fault attributions. Additionally, the investigation into the driving mechanisms, particularly the role of fluids, remains incomplete. Abacha *et al*. (2014) identified a fluid reservoir, and Abacha *et al.* (2023a) utilized additional datasets and 4D Vp/Vs models to image fluid migration from the reservoir to nearby faults, mainly due to MS-3, which likely broke the seal rock. In their hydraulic diffusivity analysis, they divided the seismicity into two clusters (cluster-1 trending E-W and cluster-2 trending NNE-SSW), justifying migration along cluster-2 by pore pressure diffusion but leaving the migration mechanism along cluster-1 unexplained, which they described as ambiguous. Rahmani *et al*. (2023) employed the non-stationary Epidemic Type Aftershock Sequences (ETAS) model to separate background from aftershock activity, interpreting fluids as the driving mechanism following MS-3.

As previously noted, earlier seismotectonic researches have introduced simplified models to account for the seismic activity observed during the BI-2010 sequence. However, considering that the epicentral region is situated within a highly fractured zone and that it is characterized by significant aftershock activity, it raises questions about whether merely two or three faults were responsible for this seismic sequence. We hypothesize that multiple fault segments were likely activated throughout the sequence. In this chapter, our objective is to unravel the complex fault system that was triggered during the BI-2010 seismic sequence. To achieve this, we analyzed the complete seismic activity recorded over four months, from May 14, 2010, to August 31, 2010, encompassing

2827 events—an increase of 100% compared to prior studies—and conducted a thorough data processing. We began by developing a robust new 1D minimum velocity model for the study area, following the methodology outlined by Kissling 1995. Subsequently, we performed a high-precision relocation of seismic events using both HYPODD (Waldhauser 2001) and GrowClust (Trugman & Shearer 2017), leveraging the advantages of each technique. We computed the focal mechanisms for 128 significant events to identify the potentially activated main structures. Utilizing the hierarchical clustering algorithm in GrowClust, we identified 21 multiplet groups, each containing at least five events. By examining these multiplet groups and their corresponding composite focal mechsanisms, we constructed a new seismotectonic model characterized by a complex fault architecture, diverging from the previous simplified models.

II.2 New Minimum 1D Velocity Model for BI Region, And Absolute Locations

The P- and S-wave arrival times of the BI-2010 aftershocks were acquired by merging data from both the permanent stations of the Algerian Digital Seismic Network (ADSN) and a temporary network of 11 portable stations. This resulted in a comprehensive and locatable dataset spanning a period of four months, from May 14 to August 31, 2010. The specific type and technical characteristics of the seismic stations can be found in Yelles-Chaouche et al., (2014).

Locating earthquakes is one of the oldest challenges in seismology (Shearer 1997). Despite the increasing popularity of 3D velocity models, one-dimensional (1D) velocity models continue to be widely used for earthquake location computations in seismological centers or regions with limited high-quality data for constructing 3D models (Husen *et al.* 2011). This highlights the ongoing significance of reliable 1D velocity models in seismology for precise routine earthquake location. One solution lies in addressing the coupled hypocenter-velocity problem (Kissling 1988; Kissling *et al.* 1994).

In our endeavor to construct a robust local P-wave 1D velocity model for the designated study area, we employed the well-established VELEST software, which was developed by Kissling 1995. The primary objective underlying the creation of this

minimum 1D velocity model was to unveil the appropriate distribution of seismic wave velocities within the crust. This model serves as fundamental framework for the initial computation of hypocenter positions. The task of solving the seismic travel-time problem involves nonlinear relationships, entailing the interaction between the seismic velocity model along the ray path and the actual earthquake locations (Kissling *et al.* 1994). The efficacy of the solution provided by the 1D velocity model is contingent upon the accuracy of earthquake location determinations. The discrepancy between the hypocentral parameters and seismic velocity is commonly acknowledged as the 'coupled hypocentre-velocity model problem' (Kissling 1988; Thurber 1992).

Two preceding velocity models, labeled as mod-1 and mod-2, were established for the study area by Yelles-Chaouche et al., (2014) and Abacha et al., (2014), respectively. Mod-1 comprises five layers, characterized by a Vp/Vs ratio of 1.75 and P-velocities distributed at depths of 0, 2, 4, 10, and 30 km. In contrast, mod-2 features four layers with a Vp/Vs ratio of 1.69, and P-velocities positioned at depths of 0, 10, 20, and 30 km. Both models were developed using a trial-and-error approach and were used for absolute location and as inputs for subsequent 3D tomography modeling within the Beni-Ilmane region. The existence of these models furnishes valuable preliminary insights into the distribution of P-wave velocities within the upper crust, thereby aiding in the estimation of an initial starting velocity model.
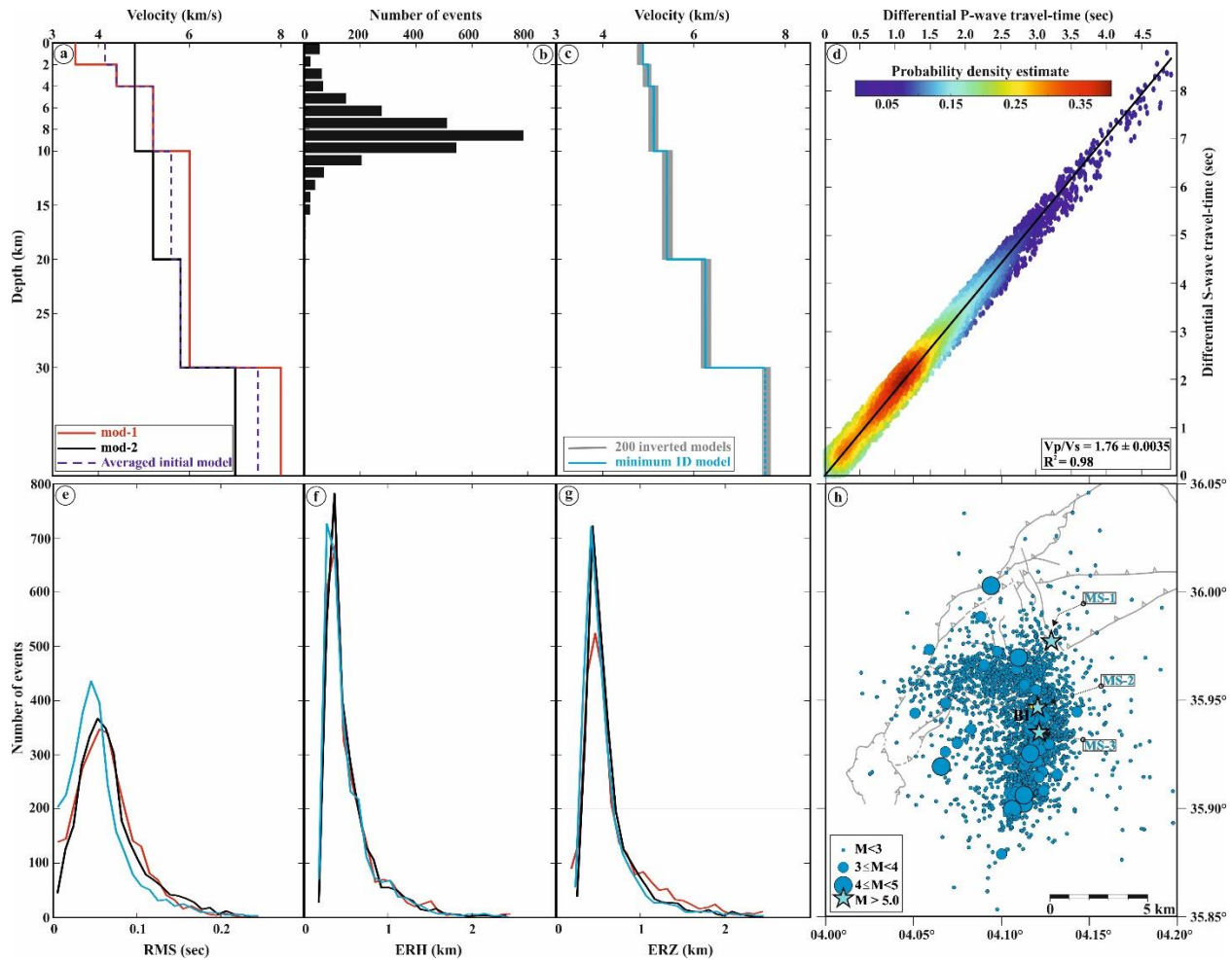
Fig. II.2: Velocity model and absolute location. **(a)** Velocity models: mod-1 (red line), mod-2 (black line), and the averaged initial model (dashed blue line). **(b)** Histogram depicting the distribution of 2827 events within each depth range. **(c)** Illustration of the 200 inverted models (gray solid lines) alongside the best minimum 1-D P-wave velocity model (light blue solid line). **(d)** Modified Wadati diagram for assessing the Vp/Vs ratio. **(e,f, and g)** Distribution of location errors: RMS, ERH, ERZ, respectively, color-coded in accordance with the models in (a) and the newly established minimum model in (c). **(h)** Horizontal distribution of 2827 events located with Hypoinverse2000 using the derived minimum 1D model. The earthquakes are scaled to their magnitudes.

As depicted in **Fig. II.2a,** mod-1 displays clear differentiation within the depth range of 0–10 km and, encompassing four layers. It is noteworthy that a significant proportion of the hypocenters are situated within this depth range, as illustrated in **Fig. II.2b**. Conversely, mod-2 exhibits improved results in terms of location accuracy in

comparison to mod-1. In order to establish an initial velocity model, I computed the average P-wave velocities at common depths between the two models, while retaining the velocity value of one of the models for instances where no common depth was present.

The Vp/Vs ratio emerges as valuable tool to refine the precision of hypocentral depth estimates in location algorithms. In our estimation of the Vp/Vs ratio, we employed a modified Wadati method (Chatelain 1978), originally introduced by (Wadati & Oki, 1933). This method involves plotting the differential S-wave travel time (Ts_i–Ts_j) versus the corresponding P-wave differential travel time (Tp_i–Tp_j) for each event, and for all combinations (i, j) of station pairs. The resultant Wadati diagram, depicted in **Fig. II.2d**, yields a Vp/Vs ratio of 1.7600 ± 0.0035 and an R-squared value of 0.98. We note here that outlier data was removed before performing the regression. Prior to initiating the VELEST inversion process, it is necessary to prepare the main input file (*.cnv file), which contains earthquake data, including hypocenters (longitude, latitude, and depth) and travel times recorded at each station. Since no sub-routine is available to prepare this file, I developed a MATLAB code (prt2cnv.m) that extracts the required information from the *.prt file (the output file of the location program Hypoinverse) and creates the appropriate *.cnv file.

The database was filtered to include only well-located events that meet the following criteria: a minimum of eight P-phase observations, a residual time (RMS) of ≤ 0.2s, a horizontal error (ERH) of ≤ 2 km, a vertical error (ERZ) of ≤ 2 km, and an azimuthal gap of <150°. Due to the insufficient quality and quantity of S-phase observations, our study focused exclusively on determining the P-wave velocity model. Consequently, the S-wave velocity model was inferred from the estimated Vp/Vs ratio. The final dataset comprised 893 events, encompassing 9,612 P-phase observations. In **Fig. II.3**, we illustrate the P-wave ray coverage of the 893 selected events used in the inversion process.
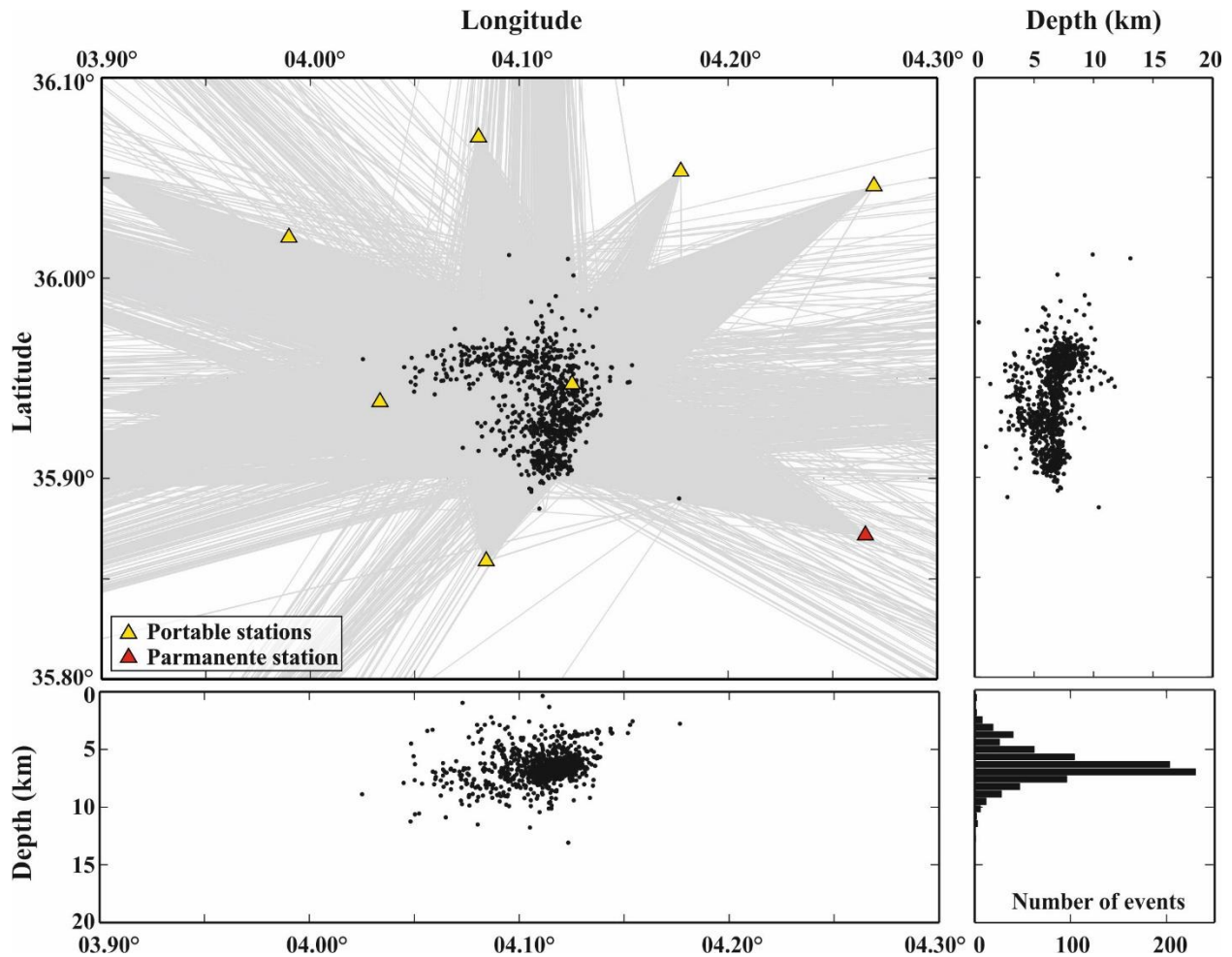
Fig. II.3: Ray coverage map of the 893 selected events used for VELEST inversion. The upper left panel shows the horizontal distribution of the events (black dots). The grey lines represent the ray paths. The upper right panel and the lower left panel, respectively, exhibit the focal depth distribution along latitude and longitude. The lower right panel represents a histogram showing the number of events at each depth range.

The concept of a minimum 1D model pertains the velocity model that yields the lowest location error for a designated set of events (Kissling *et al.* 1994). Nevertheless, the minimum 1D model attained after a single VELEST run, may be influenced by the initial starting model, potentially leading to entrapment in local minima. To address this concern, the generation of multiple VELEST runs using distinct starting models becomes imperative. In our pursuit, we generated 200 trial models by randomly perturbing the established initial model, while maintaining a positive velocity gradient to avoid the introduction of low-velocity layers that could cause inversion instability. The amplitude

of perturbation is generally influenced by the characteristics of the study area and the quality of the seismic data. When the starting model is well-constructed and supported by a substantial amount of data, smaller perturbations are preferred to explore variations without deviating too far from the plausible physical model. These perturbations typically range from 5% to 10% of the starting velocities. Conversely, if the starting model is poorly constrained or if there is a lack of data, larger perturbations are advisable to investigate a broader range of possible models. In such cases, perturbations might range from 20% to 30% of the initial velocities. In our study, we have a good starting model, developed from previously published works, and our study area is characterized by well ray coverage. Therefore, we applied relatively small perturbations of ±0.3 km/s, which is approximately 5% of the starting velocities.

Out of 200 model, the model yielding the lowest RMS value was deemed the best initial model, and its corresponding inverted model emerged as the definitive minimum 1D velocity model Our final iteration of the minimum 1D velocity model encompasses P-velocities of 4.88, 5.0, 5.12, 5.41, 6.25, and 7.55 km/s at depths of 0, 2, 4, 10, 20, and 30 km, respectively, ses **Fig. II.2c**.

We assessed the robustness of our established minimum 1D velocity model using a technique proposed by (Husen *et al.* 1999). This methodology entailed introducing randomness to the final hypocenters derived from the joint inversion process, displacing them randomly in the x, y, and z directions by ±5 km. Subsequently, these perturbed hypocenters were employed as input for VELEST in single-event mode. The principal objective of this test was to ascertain the extent to which initial hypocenter positions influenced the inversion outcome. If the minimum 1D velocity model is indeed robust, any notable variance in hypocenter location should be absent. The results of this assessment are depicted in **Fig. II.4**.
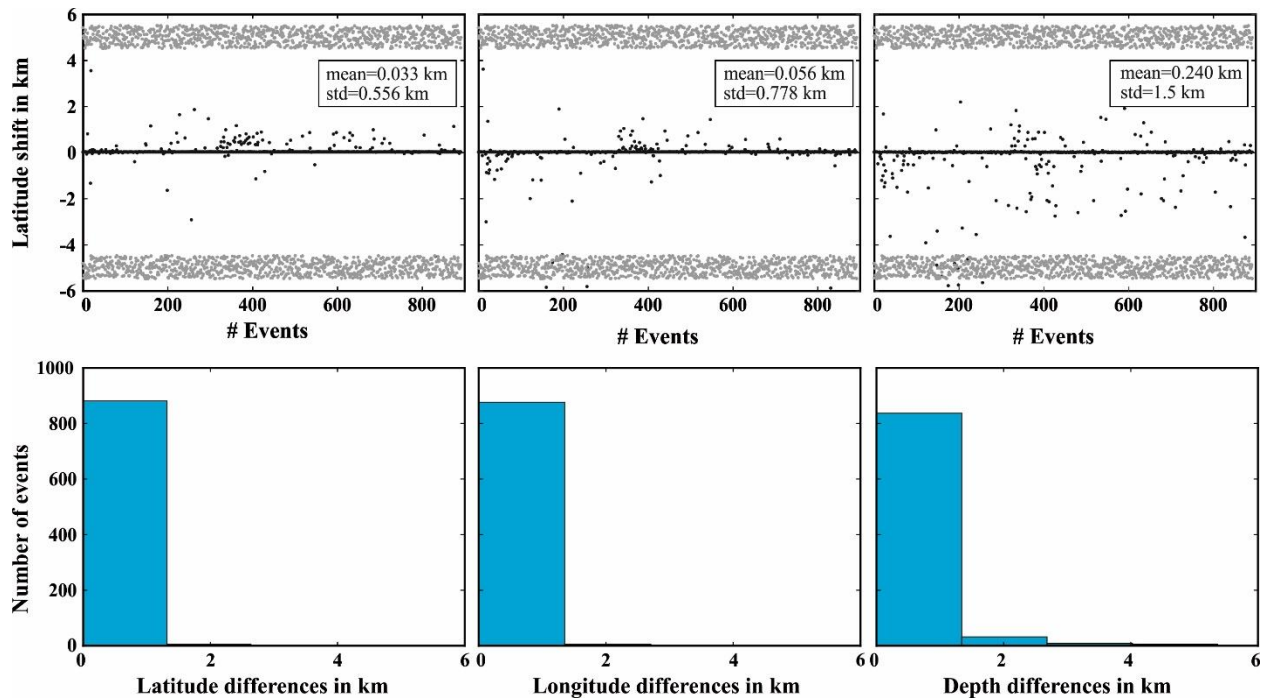
Fig. II.4: VELEST location stability test. The upper three panels demonstrate the model's capability to relocate hypocenters after introducing random perturbations of ±5 km to their initial positions. Grey dots indicate the shifted epicenters (along x, y, and z directions) relative to the original locations. Black dots represent the difference between the relocated hypocenters and their original positions. The lower three panels display histograms illustrating the distribution of deviations in latitude, longitude, and depth.

A scrutiny of the histograms reveals that over 97% of events underwent relocation less than 1 km in both the x and y directions. Approximately 93% of events were shifted by less than 1 km in focal depth. The marginal decline in the percentage of events relocated within 1 km in the Z direction, from 97% to 93%, could be attributed to the insufficiency of S-wave phases in our study.

In order to evaluate the improvements in event localizations, we conducted a comparative analysis of the novel velocity model against mod-1 and mod-2. Using Hypoinverse (Klein 2014), we determined the positions of the 2827 events and subsequently generated plots depicting the location error parameters (RMS (time residuals), ERH (horizontal error), and ERZ(vertical error)) as shown in **Fig. II.2e, II.2f, and II.2g**, respectively. Our investigation reveals a significant reduction in location errors with the implementation of the new model compared to both mod-1 and mod-2,

particularly evident in the substantially reduced RMS values. This indicates that the new 1D model provides a better fit to the observed and computed travel times. Although the new 1D model has horizontal and vertical errors that are somewhat comparable to those of mod-2, it performs better than mod-1.

The evaluation of the goodness of the final location frequently employs the RMS. However, relying solely on the RMS can be unreliable due to its dependence on the number of stations used. In order to provide a more precise assessment of the impact of phase-picking errors on location accuracy, we employed a Monte Carlo procedure as suggested by Billings et al., (1994). To simulate the arrival time picking errors for P- and S-waves, we employed a Gaussian distribution to introduce noise, with a standard deviation of 0.25 seconds for P-waves and 0.5 seconds for S-waves. These values align with the acknowledged error levels for P- and S-waves picking, as noted by Billings et al., (1994). By incorporating Gaussian noise into both P- and S-wave arrivals, we simulated the effect of velocity model errors on both the original and perturbed data. We subsequently used Hypoinverse to determine event locations using the perturbed phases. The process was repeated 500 times. After that we computed the 95% confidence ellipsoids. These ellipsoids allowed us to estimate the location uncertainty, yielding ± 3.7 km in longitude, ± 3.3 km in latitude, and ± 4.0 km in depth, see **Fig. II.5.**
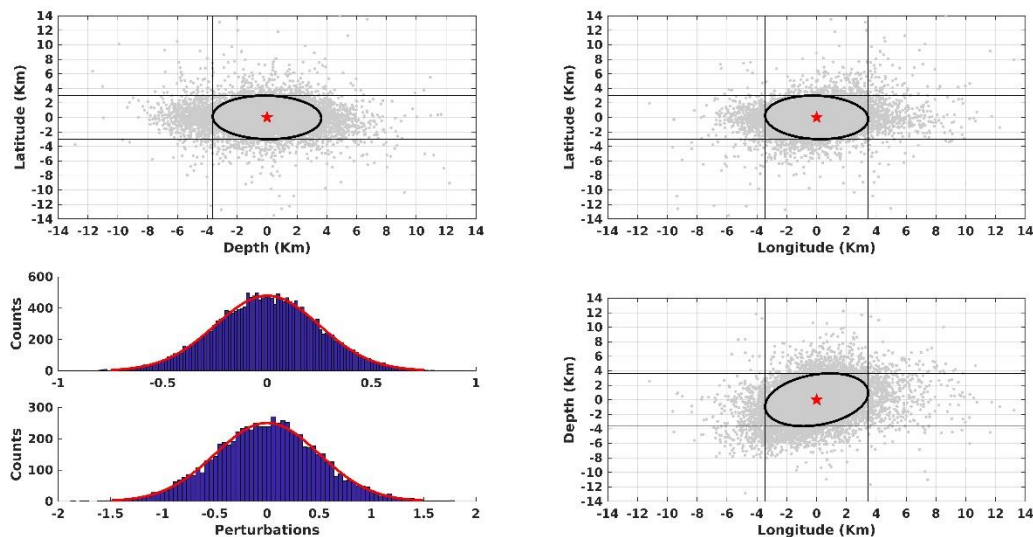
Fig. II.5: Absolute location uncertainty due to phase picking errors. The upper left, upper right, and lower right panels display the distribution of 2827 x 500 events in longitude, latitude, and depth, respectively. The ellipsoid represents 95% confidence region, with the red star indicating the center of the ellipsoid. The lower left panel shows the distribution of normally distributed noise used to perturb P-wave phases (upper curve) and S-wave phases (lower curve).

We used the newly established minimum 1D velocity model to improve the absolute locations within the initial catalog. **Fig. II.2h** visually presents the absolute location of the 2827 events utilizing the updated velocity model. Consistent with prior investigations, the horizontal distribution discloses two prominent clusters: one aligned in an E-W direction (referred to as MainCluster-1 or MC-1), and the other oriented NNE-SSW (termed MainCluster-2 or MC-2). However, it's important to note that due to the substantial number of recorded aftershocks, considerable uncertainties persist concerning the relative positions of the hypocenters. This situation presents challenges in discerning finer details within the sequence, including the identification of potential sub-clusters.

II.3 High Precision Relocation

To attain highly accurate relocated epicenters and to identify groups of events with similar waveforms (multiplets), we employed two relocation approaches, HypoDD and GrowClust, that exploit the distinct advantages of each method. Firstly, the HypoDD algorithm (Waldhauser & Ellsworth 2000) provided a double-difference relocation procedure using differential travel time data from pairs of events with P- and/or S-wave phases, ensuring accurate epicenter locations. Secondly, the GrowClust program (Trugman & Shearer 2017) incorporated a hybrid hierarchical clustering algorithm that excels at grouping events with similar waveforms, allowing for the identification of multiplets in the seismic sequence. The combination of both approaches was essential to meet the dual requirements of accurate relocation and waveform-based clustering. Before initiating the relocation process, it is essential to homogenize the database. The events'

IDs in the catalog must match those in the waveform database; otherwise, the relocation results may be biased.

II.3.1 Hypodd Relocation

The initial approach followed a two-step strategy: First, using ph2dt program, travel time differences were computed between manually selected events in the catalog, considering up to 30 neighbors per event within a maximum separation distance of 6 km. This distance parameter is critical when using HypoDD, and should not be less than the absolute location uncertainty. Each pair required a minimum of 8 observations to be considered strongly linked, since relocation of each pair involves 8 degrees of freedom. setting the minimum observation to a lower value will result in a higher number of selected events; however, the number of weakly linked events will also increase, leading to reduced precision. We also set the maximum number of observations to 50. After this preprocessing, 43,480 strongly linked pairs were identified, consisting of 283,933 P-phases and 95,443 S-phases, and 2,029 selected events out of 2,827. Relocation was then performed using catalog data only, resulting in 1998 relocated events.

Second, waveform similarity and time delay data were generated from the 1998 events. To prepare these data, two methods are commonly used: (1) time-domain cross-correlation, and (2) frequency-domain coherency. In this thesis, I conducted a comparative analysis between the time-domain and frequency-domain approaches to determine the most effective method for preparing waveform similarity and time delay data.

To perform this comparison, I developed two MATLAB codes: *TD_CC.m*, which handles time-domain cross-correlation, and *FD_Coh.m*, which performs frequency-domain coherency. The comparison was conducted as follows: I randomly selected 134 events from the BI-2010 sequence. Then, I performed a pairwise comparison of these events, systematically comparing each event with every other event in the dataset. This involved comparing event 1 with events 2, 3, ..., n; event 2 with events 1, 3, ..., n; and so

forth, until every possible pair of events was analyzed. This exhaustive comparison process allowed us to assess the degree of similarity between each pair of events in both domains, resulting in a total of 17956 operations for each.

a) Time Domain Cross-Correlation (CC)

The time domain cross-correlation of two signals $x_1(t)$ and $x_2(t)$ is given by the integral:

$$R_{x_1 x_2}(\tau) = \int_{-\infty}^{+\infty} x_1^*(t) x_2(t + \tau) dt \qquad (\text{II.1})$$

where * denotes complex conjugation and τ is the time lag between the signals. CC measurements are typically normalized by the values of the autocorrelations at zero lag to bound the estimate between -1 for perfect dissimilarity or polarity inverted and 1 for perfect similarity. Conversely, 0 indicates no linear similarity. The normalized and bounded measure of CC is referred to as the cross-correlation coefficient function, $\rho_{x_1 x_2}(\tau)$, and is giving by:

$$\rho_{x_1 x_2}(\tau) = \frac{R_{x_1 x_2}(\tau)}{\sqrt{R_{x_1 x_1}(0) R_{x_2 x_2}(0)}} \qquad (\text{II.2})$$

The maximum amplitude of the correlation coefficient function indicates the level of similarity between the signals, while its abscissa indicates the time shift between the two seismograms. Only delay times down to the sampling frequency can be calculated.

Before performing cross-correlation, the data are pre-processed as follows:

1) remove mean, also known as baseline correction. The mean value of a seismogram does not carry useful information about the seismic waves. Therefore, removing it centers the data around zero, making it easier to analyze variations that are directly related to seismic events.

2) remove linear trend, also known as detrending. Seismograms can sometimes exhibit a linear trend due to instrumental drift, environmental changes, or other slow, non-seismic

processes. This trend can obscure the true seismic signal. Hence, removing this trend enhance the signal quality. Linear trend is usually observed on Broad-Band stations.

3) apply taper. Tapering data is of utmost importance as it minimizes the edge effects. When analyzing a segment of a seismogram, abrupt changes at the edges of the data window can introduce artificial frequencies (spectral leakage) during Fourier transform or other spectral analysis methods. Tapering smoothly reduces the amplitude of the signal to zero at the edges, minimizing these discontinuities and thus reducing edge effects. Several tapers exist, in our case we applied a 10% Tukey taper.

4) Filtering the data. If the signals have different frequency content, the cross-correlation might not effectively capture the similarity of the seismic events. Filtering ensures that only the relevant frequency bands (where the signals are expected to be similar) are considered, improving the accuracy of the cross-correlation. Additionally, this helps reducing the noise level. Hence, enhancing the Signal-To-Noise ratio (SNR). In this study I used the frequency band of [2.5-23] Hz. A band that is consistent with Kapetanidis & Papadimitriou (2011) where they performed several tests to fix this band for local earthquakes. The 2.5 Hz corner frequency of the high-pass filter effectively removes the long-period trend, which can be prominent in broadband stations, while the low-pass filter at 23 Hz retains sufficient signal complexity in the waveforms.

5) Normalizing the data: Finally, we normalize the data by dividing it by its maximum value, ensuring that the maximum amplitude is unity. This process ensures that only the waveform shape (fluctuations) is taken into account.

I used a variable time window around the P-wave onset. All signals were extracted from vertical components. I conducted the comparison on three distinct stations namely; SP01 (1Hz FSS-3 Short-Period), AKET (SS-1Hz Short-Period) and ATAF (BBVS-60 Broad-Band).

The results on the three stations are depicted on the correlation matrices bellow (**Fig. II.6**)
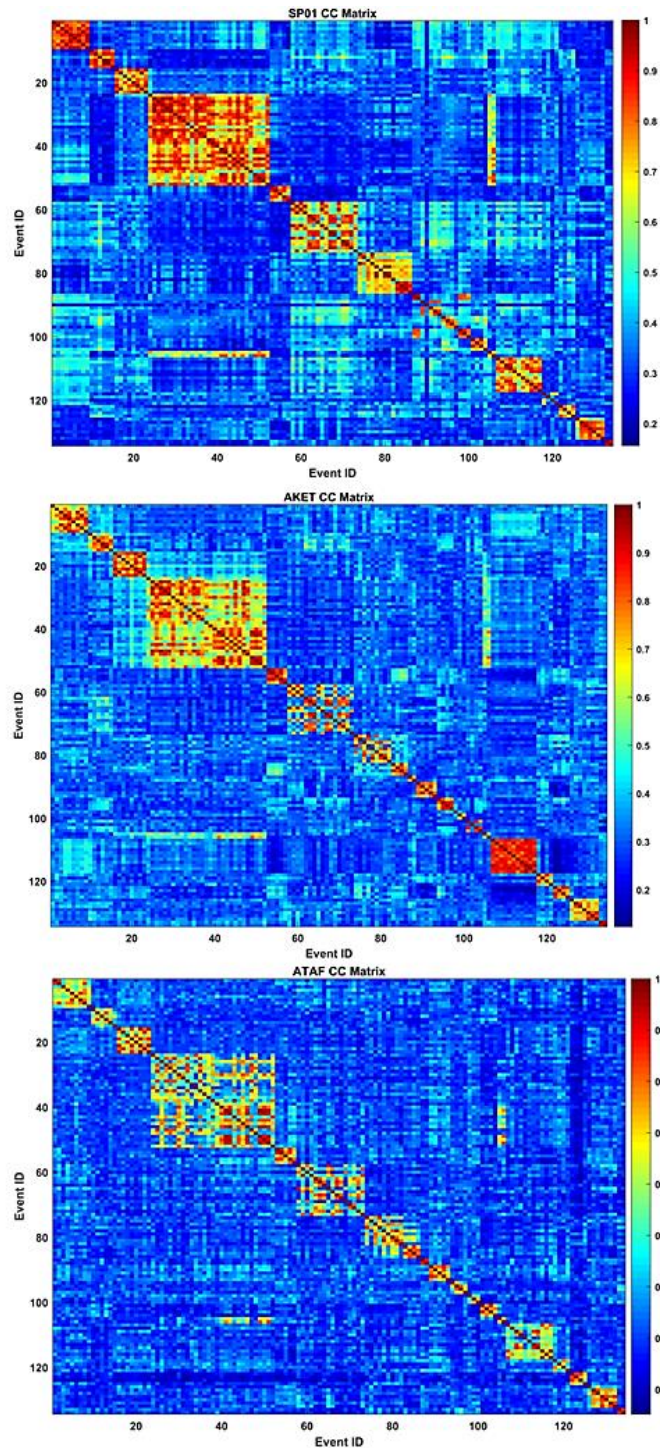
Fig. II.6: Cross-correlation matrices. Results of time domain cross-correlation of the P-wave onset recorded at the vertical component of SP01 (top), AKET (middle) and ATAF (bottom).

b) Frequency Domain Coherency (Coh)

The pre-processing steps from 1-3 were applied to the signals before calculating the coherency. The coherency between two signals $x_1(t)$ and $x_2(t)$ in the frequency domain is giving by:

$$\gamma_{x_1x_2}(f) = \frac{S_{x_1x_2}(f)}{\sqrt{S_{x_1x_1}(f)S_{x_2x_2}(f)}} \qquad (\text{II.3})$$

where $S_{x_1x_2}(f)$ is the cross spectral density and $S_{x_1x_1}(f)$ and $S_{x_2x_2}(f)$ are the auto spectral density functions of $x_1(t)$ and $x_2(t)$ respectively. The coherence function is a complex quantity, and its mean value within a specific frequency range offers a bounded measure of the linear association between two series. It ranges from 0 to 1, where a value of 1 indicates a perfect linear relationship and a value of 0 signifies that the series are uncorrelated. In this study we used a frequency range of [2 - 15] Hz, which is the widely used in many researches (Got *et al.* 1994; Schaff *et al.* 2004)

The Cross spectral density is giving by the multiplication of the spectrum of the first signal, $S_{x1}(f)$, with the complex conjugate of the spectrum of the second signal, $S_2^*(f)$.

$$S_{x_1x_2}(f) = S_{x1}(f) \cdot S_2^*(f) \qquad (\text{II.4})$$

The phase of the cross-spectrum, $\theta_{x_1x_2}(f)$, is a linear function of frequency and is given by:

$$\theta_{x_1x_2}(f) = -\tau 2\pi f \qquad (\text{II.5})$$

The delay τ between the two signals is deduced from the slope of cross-spectrum's phase. It is worth noting that the cross-spectral approach can retrieve delays that are less than the sampling rate, indicating higher precision. The results on the three stations are depicted in the coherency matrices bellow (**Fig. II.7).**
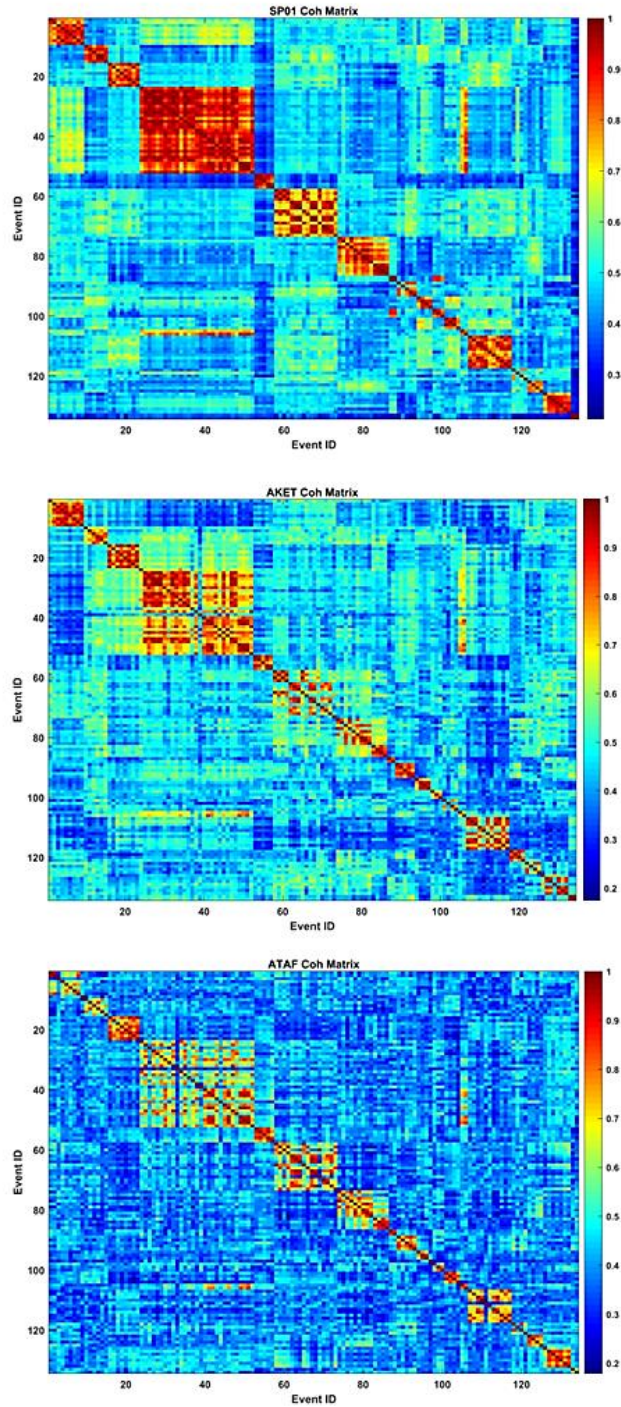
Fig. II.7: Coherency matrices. Results of frequency domain coherency of the P-wave onset recorded at the vertical component of SP01 (top), AKET (middle) and ATAF (bottom).

c) Cross-Correlation V.S Coherency

Upon inspecting the correlation and coherency matrices (**Fig. II.6** and **Fig. II.7**), I observed that the cross-correlation (CC) and coherency (Coh) values differ for the same station and the same set of events. To better visualize the discrepancies between CC and Coh, I cross-plotted 134x134 values of CC versus Coh for the three stations (see **Fig. II.8**). If the two approaches yielded comparable results, one would expect the scatter plot to align with the 1:1 line (red dotted line in the figure). However, the data exhibit different behavior.

From the figure, several intriguing observations can be made:

1) Pairs with a cross-correlation (CC) below 60% tend to have coherency (Coh) values higher than their corresponding cross-correlation values.

2) A linear relationship (nearly consistent with the 1:1 line) is observed between CC and Coh for pairs with CC values above 70%.

3) Some pairs exhibit lower Coh values despite having higher CC values.
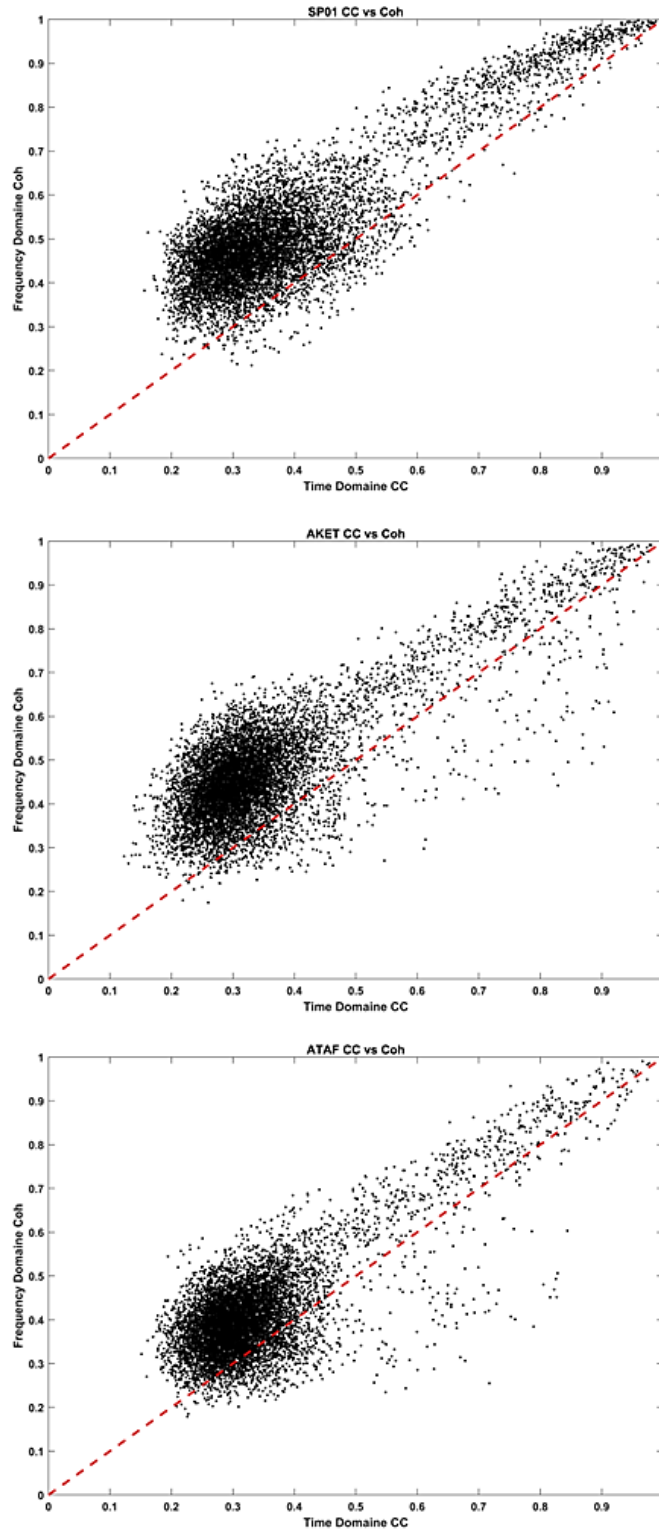
Fig. II.8: Comparison between time domain cross-correlation and frequency domain coherency. SP01 (top), AKET (middle) and ATAF (bottom).

The best way to determine which approach better reflects waveform similarity is to visually assess the degree of similarity. For example, the events on 2010.05.18-23.55.49 and 2010.05.21-10.59.28 exhibited a cross-correlation (CC) value of approximately 0.37, while the coherency (Coh) value was around 0.70. However, when visually examining the signals, it is evident that they do not correlate up to 70% (see **Fig. II.9**). Therefore, a CC value of 0.37 is a more realistic measure of the similarity between these two events. Thousands of pairs exhibited such discrepancy between CC and Coh values.
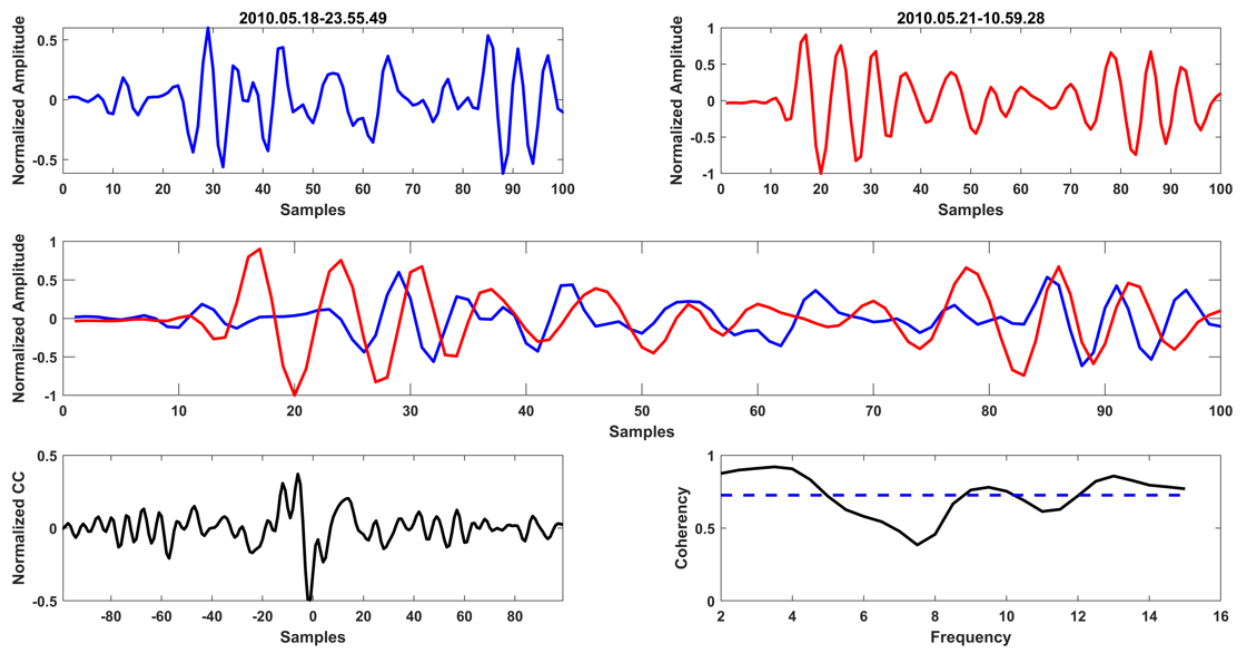
Fig. II.9: Visual comparison between cross-correlation and coherency of two events recorded at SP01 station.

If a similarity of 0.7 is considered, the two events may be relocated closer to each other compared to using a similarity of 0.3. These observations indicate that CC values are better reflecting waveform similarity than Coh values. Additionally, (Kapetanidis *et al.* 2010) also found that Coh values are prone to faster saturation than their corresponding CC values. Moreover, studies by Schaff *et al.* (2004) highlighted that using the time domain CC is often more robust and recovers more observations than the cross-spectral approach. For this reason, I preferred to use time-domain cross-correlation.

In order to prepare cross-correlation data to relocate all the events of the BI-2010 sequence. We used time windows around the P wave onset extracted from vertical components. For seismograms with S-P time > 2.56 sec a fixed 2.56 sec time window was used, with 0.2 sec proceeding the P phase. For seismograms with S-P time ≤ 2.56 sec, we used variable time windows of length equal 0.8*(S-P), with 0.1 sec before the P phase. Due to uncertainties in picking S phases, we estimated the S-P time through a ray-tracing method using our newly retrieved 1D velocity model, and the same Vp/Vs used for earthquake location. The computation was performed on 18 stations within an epicentral distance of less than 100 km, including 11 portable and 7 permanent stations. All our used stations sampled at a frequency of 100 Hz. Pairs with a minimum cross-correlation coefficient (CC) of 0.7 (i.e. 70%) were retained.

After preparing the cross-correlation (CC) data, the relocation process was repeated using both the catalog and cross-correlation data, yielding a refined set of 1998 relocated events, accounting for nearly 71% of the original dataset.

Given the limitations of the LSQR (Least Sequare) approach in reliably indicating true location errors (Waldhauser, 2001), assessing reliable relocation errors is crucial. To accurately evaluate these uncertainties, we used the bootstrapping method (Efron 1979). We generated 1000 samples with replacement from both the residuals vector of travel times and the vector of delays from cross-correlation data. These resampled values were then added with the original catalog and cross-correlation data. For each of the 1000 bootstrapped datasets, we iteratively performed the relocation process, yielding 1000 potential solutions (longitude, latitude, and depth) for each event. The shifts from the original relocation solution were calculated, and the average of these shifts across the 1000 iterations was used as a measure of the relocation uncertainty for each event. To estimate the overall relocation uncertainty across all three dimensions, we used the 95% confidence ellipsoid. See **Fig. II.10**. The estimated uncertainties through the bootstrapping approach are less than 245 m (longitude), 132 m (latitude), and 211 m (depth).
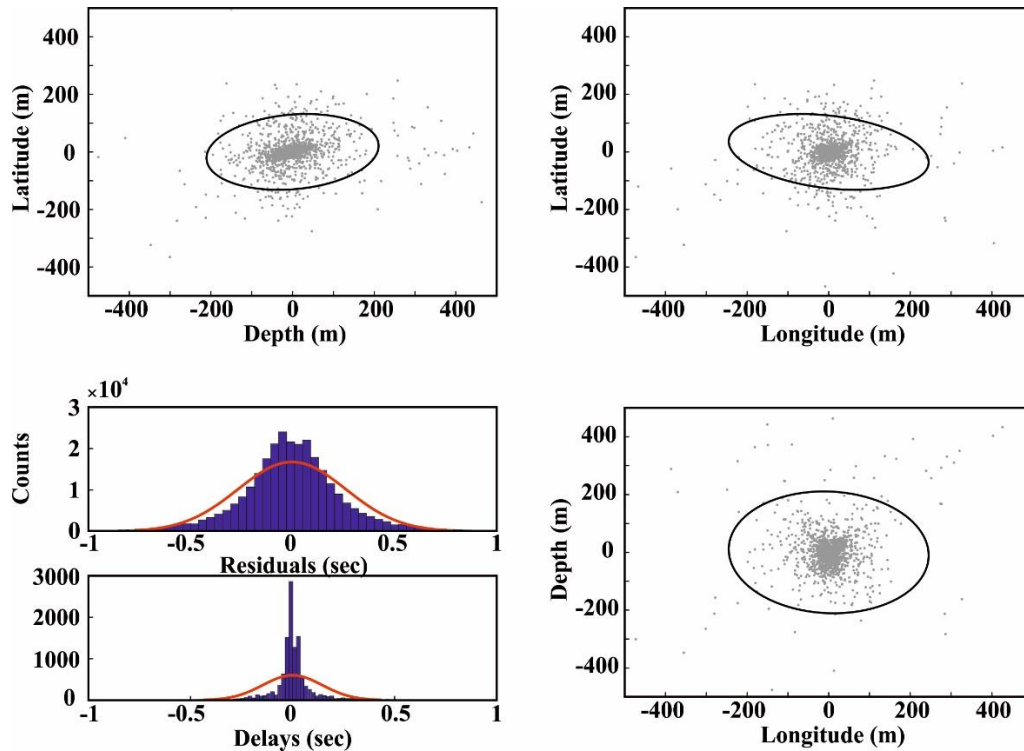
Fig. II.10: Relocation uncertainty estimation. The Upper left and right panels, and the lower right panel display, with grey dots, the estimated errors for each event. The ellipsoid denotes the 95% confidence area. The lower left panel shows the distribution of catalog residuals (upper histogram) and cross-correlation delays (lower histogram).

II.3.2 Growclust Relocation

In the second approach, we used the hypoDD output as the initial input to the GrowClust algorithm. A maximum station distance of 100 km between event pairs was enforced as previously requested, and the CC threshold was set to 0.7. Additionally, minimum average CC of 0.8 over all stations was implemented to further regulate the multiplet clustering procedure. Furthermore, only those pairs with at least five differential times were retained (i.e., at least five stations for each pair). The process relocated 665 out of 1998, while the remaining 1333 events were retained with the initial HypoDD solutions, as they did not meet the selected criteria. In other words, our final catalog of BI-2010 sequence contains 1333 events with HypoDD solution and 665 events with GrowClust solution. The main outcome of the second approach is the robust clustering of events under groups of similar waveforms (doublets and multiplets) based on a hybrid hierarchical clustering algorithm. The GrowClust program includes a

bootstrapping approach that was used to assess the robustness of the relocation for the 665 events. The results showed a significant improvement in the relocation uncertainties, which were reduced to 96 m (longitude), 82 m (latitude), and 120 m (depth).

II.3.3 Why Use Both Hypodd and Growclust?

We acknowledge that the procedure we followed is not common practice for relocation. Therefore, one might argue that using either HypoDD or GrowClust alone would be sufficient, without the need to employ both programs. However, we believe our methodology is both useful and consistent with the objectives we aim to achieve. HypoDD and GrowClust are both designed for earthquake relocation, but they use different approaches, each with its strengths and weaknesses. By combining them, we aim to leverage their strengths while mitigating their limitations.

HypoDD can utilize both catalog and cross-correlation (CC) data for relocation, whereas GrowClust relies solely on CC data. Using only CC data would exclude events that do not meet the CC threshold (70% in our case), including nearly all M3.7+ events from our initial catalog. Therefore, relying solely on GrowClust would result in the loss of 128 key events crucial for understanding faulting mechanisms in our study area (see **sub-chapter II.5**). Therefore, we employed HypoDD to:

1) Enhance initial locations by relocating events using both catalog and CC data.

2) Create a complete relocated catalog that includes all main events and events with good waveform similarity.

One of our primary goals is to identify multiplet groups, a clustering process that depends heavily on accurate relocation. While HypoDD can perform clustering during relocation, GrowClust's hierarchical clustering is more precise and offers several parameters to constrain the clustering process. This precision is why we used GrowClust for clustering. For HypoDD relocation, we used initial event coordinates from absolute locations (Hypoinverse locations). In contrast, for GrowClust, we used initial event

coordinates from the final HypoDD relocation (catalog + CC). This process relocated 665 events, which differed slightly from those relocated by HypoDD, as shown in **Fig. II.11** below. These 665 events consist of doublets, triplets, and multiplets with CC ≥ 0.70 and an average CC ≥ 0.80 (refer to **Table II.2**).
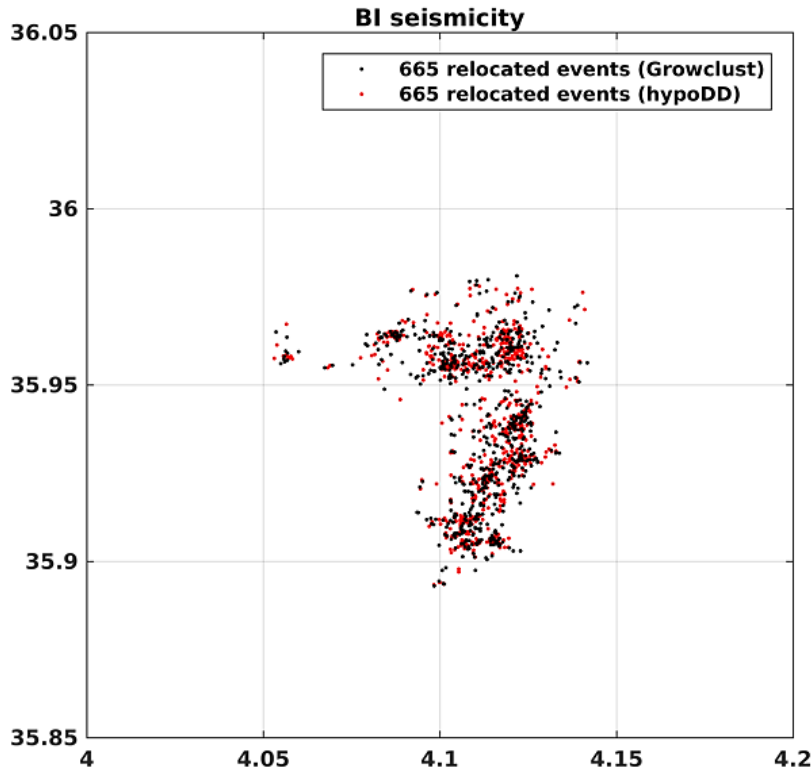
Fig. II.11: Comparison of the relocation results for 665 events using HypoDD (red dots) and GrowClust (black dots).

II.3.4 Results of BI-2010 Seismicty Relocation

In **Fig. II.12a** we depict the horizontal and vertical distribution of the 1998 relocated events compared to their original locations, revealing a notable refinement of the spatial distribution and enabling the identification of a new trend ~ NNW-SSE, positioned between the relocated epicenter of MS-3 to MS-1 (red stars), see the ellipse in the figure. It is noteworthy that the range of seismic activity along MC-1 and MC-2 extends to approximately 7 km and 8 km, respectively. It is remarkable that this range

extends well beyond the rupture size of MS-2 and MS-3 as estimated by Abacha et al. (2019). The spatiotemporal evolution of the seismic events shown in **Fig. II.12b** is difficult to follow due to the large number of events and the limited area affected. There is no overall clear migration of the seismicity after the three mainshocks. Nevertheless, some phases can be identified: the seismic activity started along the northern sector of the Beni-Ilmane village after MS-1. Then a subsequent E-W shift along MC-1 after MS-2. Finally, a notable transition of seismicity mainly along the extension of MC-2 in the first days after MS-3, with some events persisting in the northern part, especially in the last days of activity. Additionally, in **Fig. II.12c**, we present the seismicity rate and magnitude distribution of the relocated events over time. It is observed that the seismicity rate increased after MS-2 compared to MS-1, and similarly, it was higher after MS-3 compared to MS-2. This increase in seismicity rate may suggest the involvement of other forcing mechanisms.
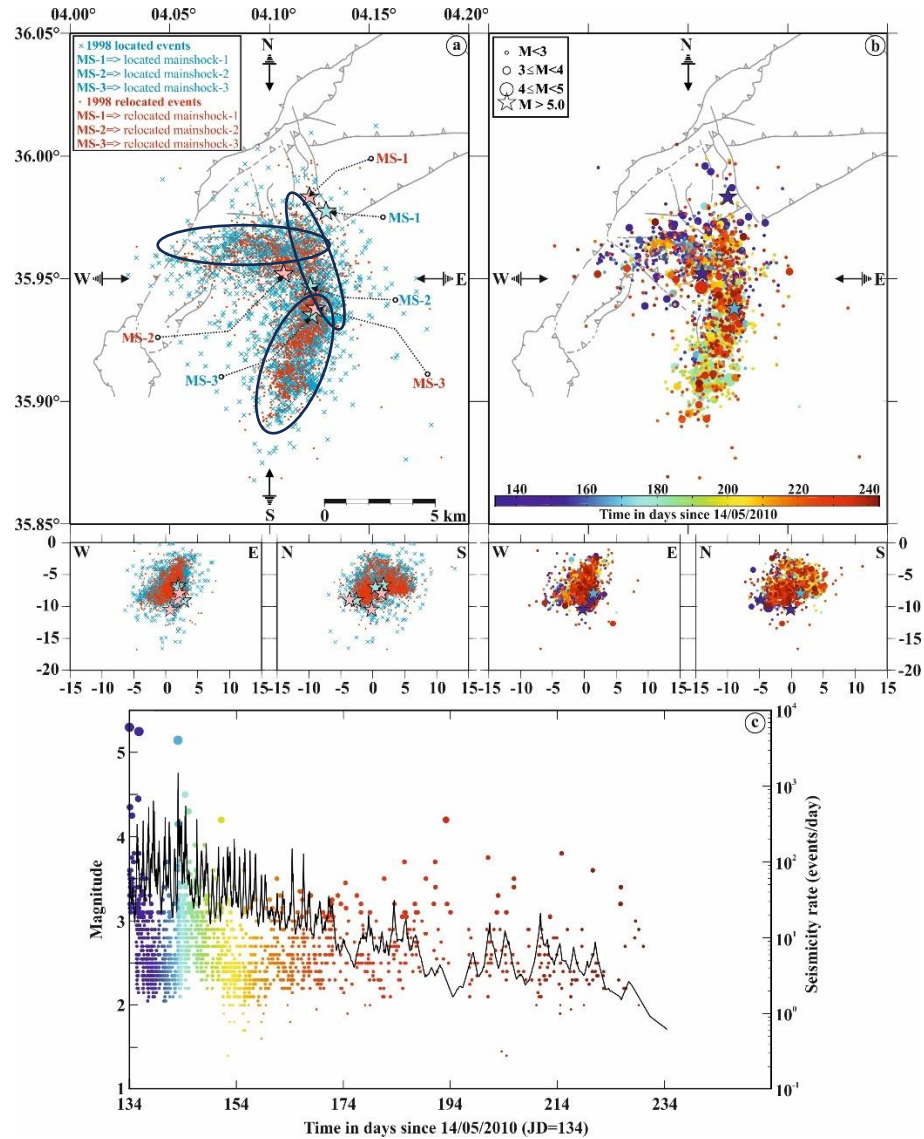
Fig. II.12: Relocation and spatiotemporal evolution. **(a)** Depicts the horizontal and vertical distribution (along E-W and N-S cross-sections) of the 1998 relocated events (red dots), compared with their initial locations (blue x's). **(b)** Shows spatiotemporal distribution of the 1998 relocated events. **(c)** Illustrates the seismicity rate and magnitude distribution as a function of time.

II.4 Moment Tensor Analysis for The Three Mainshocks

Regarding the importance of the three main shocks, we have performed moment tensor analysis for each one. We used the full waveform inversion approach, in this regard we employed the program of Yagi & Nishimura (2011). The approach mitigates the effects of site amplification, isolates the propagation term, and avoids neglecting the

source time function, thus preventing underestimation. To mitigate the effects of low and high frequency noise, the waveforms were filtered using a bandpass range of 0.04–0.08 Hz. The Green's functions were calculated in the newly retrieved minimum 1D model using the "reflectivity method" as proposed by Kohketsu (1985). The inversion process involved a grid search method to determine centroid depths while minimizing the variance between observed and calculated waveforms. The moment tensor inversion results revealed a scalar moment in units of (N.m) and moment magnitude for MS-1, MS-2, and MS-3 to be 1.4120E+17 (Mw5.4), 0.5366E+17 (Mw5.12), and 0.5198E+17 (Mw5.12) respectively. Conversely, the best centroid depths were found to be 5.6 km, 6.8 km, and 7.8 km, respectively, corresponding to variances of 0.14, 0.17, and 0.26, as shown in **Fig. II.13**. The figure also shows the focal mechanisms' solution of the three mainshocks as calculated using the P-wave first motion polarities approach.
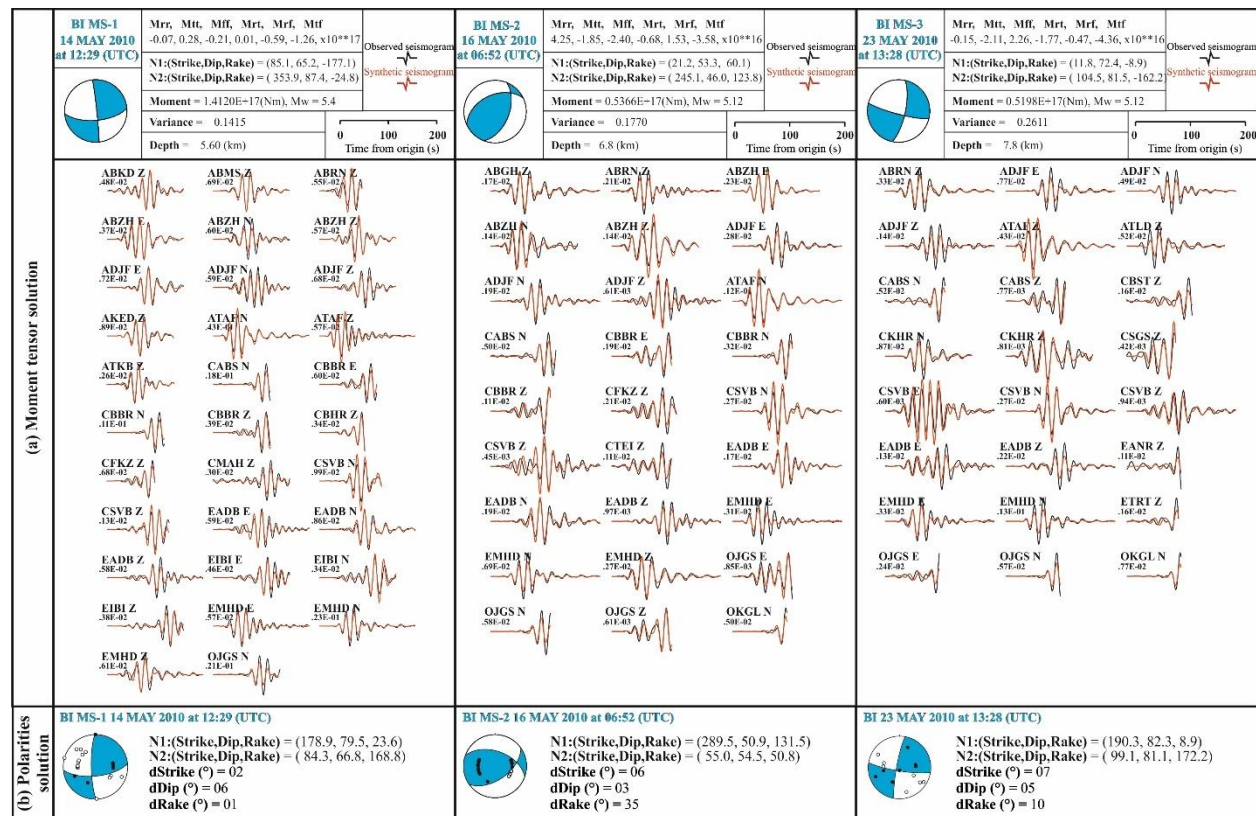
Fig. II.13: Moment tensor analysis. **(a)** Moment tensor solutions for the three mainshocks. MS-1 (left column), MS-2 (middle column), and MS-3 (right column). The tables in the top right of each column provide moment tensor parameters, including best-fit fault-

plane solutions, scalar moment, moment magnitude (Mw), variance, and focal depth. Below the tables, waveform modeling is illustrated with black lines representing instrumentally corrected velocity waveforms and red lines indicating modeled waveforms. Velocity (in cm/sec) is shown below the station code. **(b)** Focal mechanism solutions for MS-1, MS-2, and MS-3 derived from P-wave polarities, along with their corresponding parameters. The lower panels, from left to right, depict MS-1, MS-2, and MS-3, respectively. The parameters dStrike, dDip, and dRake represent the estimated errors (in degrees) in strike, dip, and rake, respectively.

II.5 Focal Mechanism Analysis

The determination of fault plane kinematics was performed using focal mechanism analysis from P-wave first motion polarities. We used azimuths and take-off angles from the positions of the relocated events to ensure better-constrained focal solutions. Focal mechanisms were resolved for 128 key events including the three main shocks, each recorded by at least 12 stations. A prerequisite for each event was the availability of nine unambiguous P-wave polarities. The FPFIT program, developed by Reasenberg & Oppenheimer (1985) was employed to determine the best-fitting mechanisms based on the first-motion polarities in both the vertical up and down directions. This was achieved through a systematic grid search method. The detailed parameters of these 128 key events including uncertainties can be found in the online supplementary material of our paper Tikhamarine *et al.* (2024).

In **Fig. II.14a**, the 128 key events are highlighted and their corresponding FMSs are shown and numbered from 1 to 128 according to their chronological occurrence. Through a meticulous analysis of these FMSs, we identified eight distinct patterns of focal mechanisms (**Fig. II.14b**), based on similarities in fault plane characteristics, horizontal distribution of relocated events, and the geological background. The ellipsoids' sizes (length and width) are set to include all the events associated with each fault pattern.
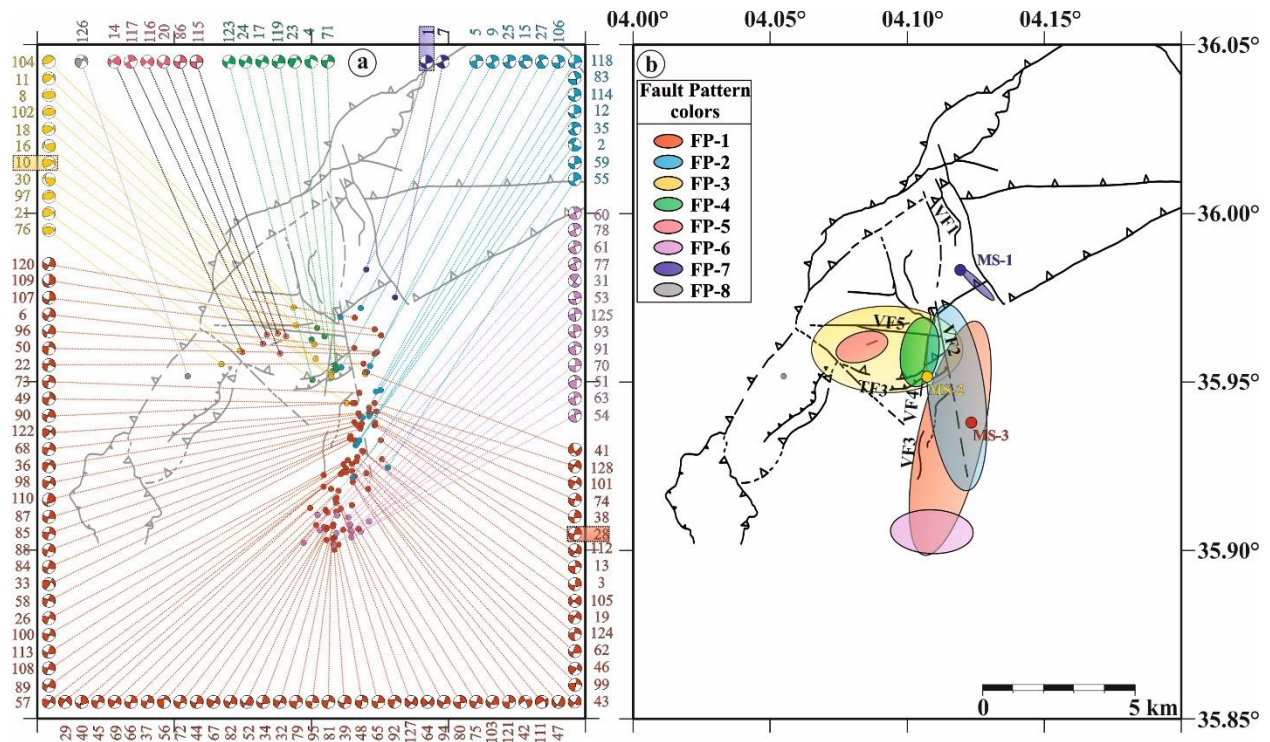
Fig. II.14: Focal mechanisms and faulting patterns. **(a)** Illustrates focal mechanism solutions of 128 key events, sorted chronologically from 1 to 128. **(b)** Shows the ellipsoids that enclose events associated with the 8 fault patterns, categorized based on similarities in fault plane parameters and horizontal distribution. The color code remains consistent across panels **(a) and (b)**: red, light blue, yellow, green, pink, purple, dark blue, and grey correspond to FP-1, FP-2, FP-3, FP-4, FP-5, FP-6, FP-7, and FP-8, respectively.

   Table II.1 summarizes the optimal fault type, orientation, and kinematics attributed to each FP. The proposed optimal focal solutions represent the observed faulting patterns. Despite some differences between each optimal solution and the individual events constituting the faulting pattern, we consider them similar based on Kagan angle analysis (Kagan 1991). We calculated the Kagan angle between each group's optimal solution and its constituent events. All calculated Kagan angles were less than 60°, indicating the optimal solutions' consistency (Pondrelli et al. 2006). In **Fig. II.15** we present the Kagan Angle analysis results.

Table. II.1: Summary of the attributed fault type, orientation, and kinematics for each faulting pattern.

Fault Pattern	Events number	Optimal focal solution and fault plane	The associated geological fault
FP-1	74 (with MS-3)		
FP-2	14		
FP-3	11 (with MS-2)		
FP-4	07		
FP-5	06		
FP-6	13		Blind fault
FP-7	02 (with MS-1)		
FP-8	01		Blind fault
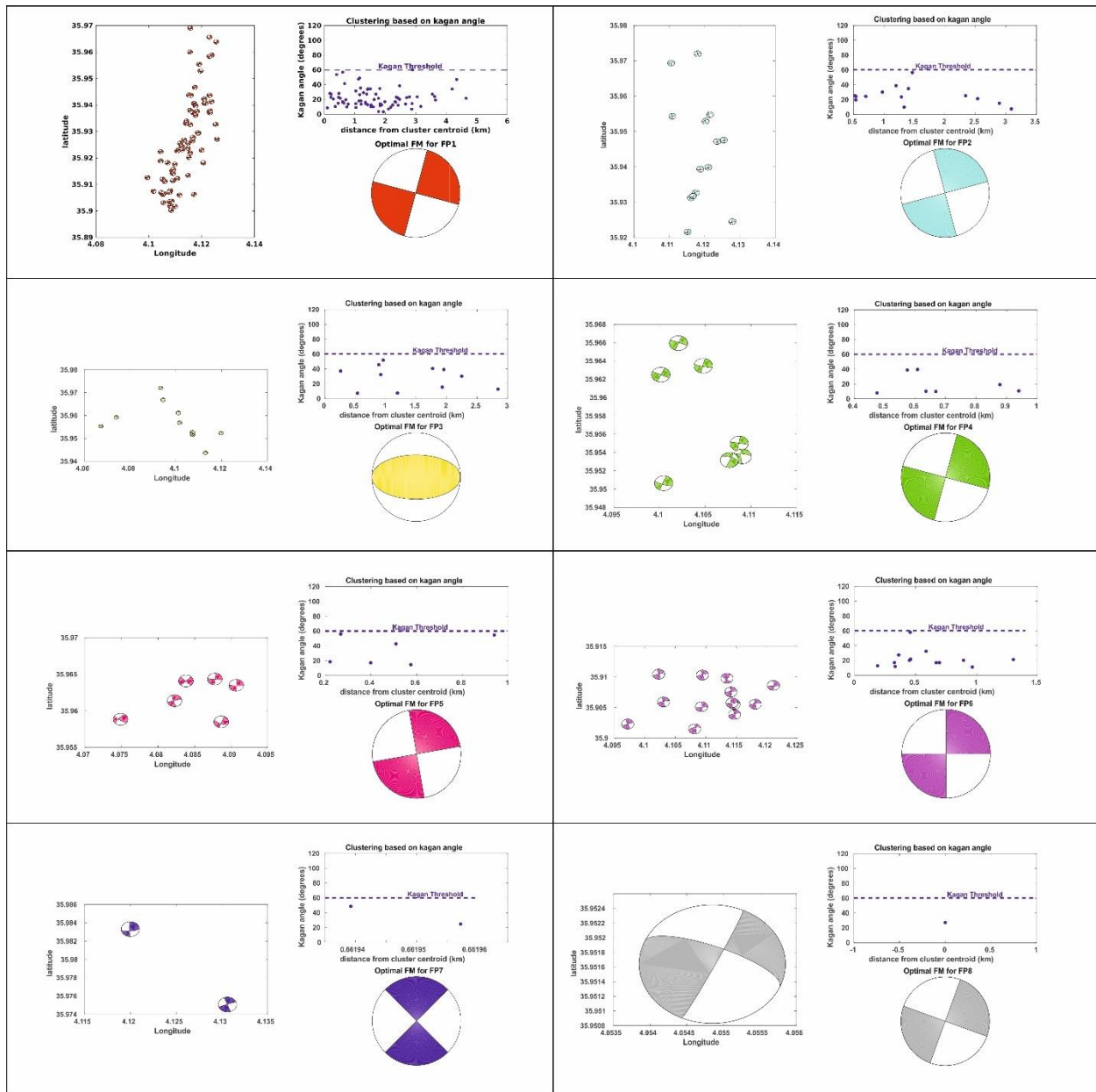
Fig. II.15: Kagan angle analysis indicating the consistency of the chosen optimal focal solution.

However, these global observations (eight faulting patterns) require detailed investigation. For example, upon examining the FP-1 ellipsoid, one can notice that we linked it only to the vertical fault VF3 despite its wide extent. Similarly, we linked the MS-3, to VF3 fault even though it is not on the plumb of the fault. The dispersion of events on sub-vertical faults presents a complex scenario with multiple plausible interpretations.

According to Cattaneo *et al*. (1999), such dispersal could be related to location errors. Alternatively, following Yukutake & Iio (2017), it could indicate that a significant number of aftershocks occur outside the fault damage zone. However, the presence of a highly complex and fractured fault system, coupled with a persistent driving mechanism such as pore pressure, could result in comparable spatial dispersion. Another intriguing observation is that MS-2, at a depth of 6.8 km, lies along the exposed thrust fault TF-3, which we assumed to be the source of MS2. However, such a position suggests that TF-3 is a high-angle reverse fault, yet the calculated dip for MS-2 does not support this possibility (see **Fig. II.13**). This observation raises the question of whether or not TF-3 is the true source of MS-2. Globally, the observed eight fault patterns do indeed indicate the presence of a complex fault system. One of the widely used approaches to highlight active structures within a complex fault system is the detailed analysis of multiplets geometries; this method is useful for characterizing seismically active structures (Carmona et al. 2010; Pacchiani & Lyon-Caen 2010; Rietbrock et al. 1996).

II.6 Multiplet Analysis: Deciphering Complex Fault Structures in BI region

Using GrowClust hybrid hierarchical clustering, we extracted a total of 208 groups of similar waveforms, including doublets, triplets, and multiplets, as presented in **Table II.2**. To ensure the accuracy and reliability of fault plane orientations, we focused on multiplet families containing at least five events, yielding a final selection of 21 distinct groups.

Table. II.2: Categories of the detected multiplets groups.

# event per multiplet	Number of multiplet	Σ of events
>40	1	42
<30 & ≥20	2	45
<20 & ≥10	4	44
<10 & ≥4	31	154
=3	40	120
=2	130	260
Total	208	665

To provide a coherent representation of the fault kinematics, we derived a composite focal mechanism solution for each cluster by superimposing P-wave first-motion polarities data from a minimum of five events. We then used Principal Component Analysis (PCA) to determine the geometry of each group by constructing 95% confidence ellipsoids (Brunton & Kutz 2019), see **Appendix A** for details regarding PCA. These clusters will henceforth be referred to as C, followed by their respective numerical designation. **Fig. II.16** provides a visual illustration of the high waveform similarity (CC ≥ 0.8) for C16, recorded by stations ATAF, SP01, SP03, SP06, and SP10. In addition, **Fig. II.17** provide further examples of high waveform similarity (CC ≥ 0.8) for four other clusters (C01, C04, C10, and C19), all recorded at station SP01.
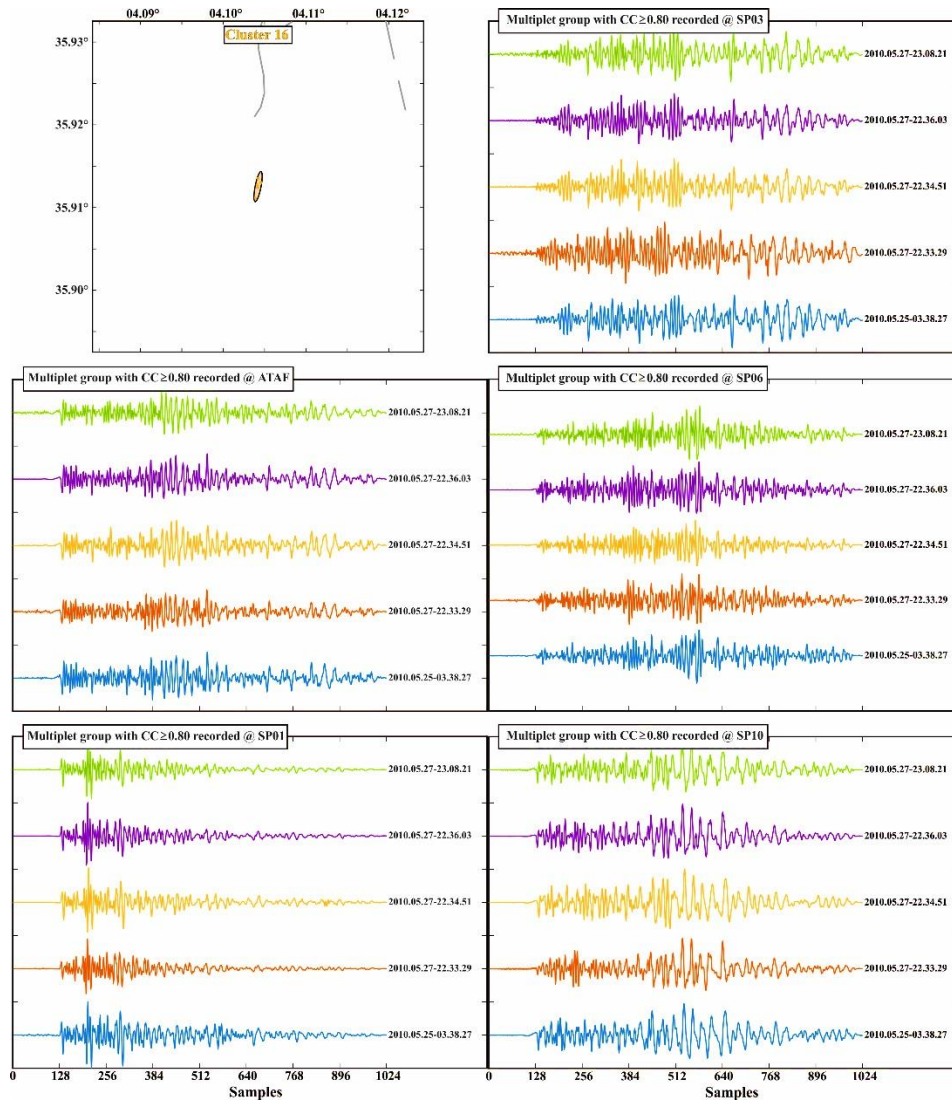
Fig. II.16: Example of waveform similarity (CC ≥ 0.8) within the multiplet group of cluster 16, comprising 5 events. These events were recorded at stations ATAF, SP01, SP03, SP06, and SP10, all operating at a sampling frequency of 100 Hz. Each panel displays 1024 samples (10.24 seconds) with a preceding 128-sample segment (1.28 seconds) prior to the P-wave onset.
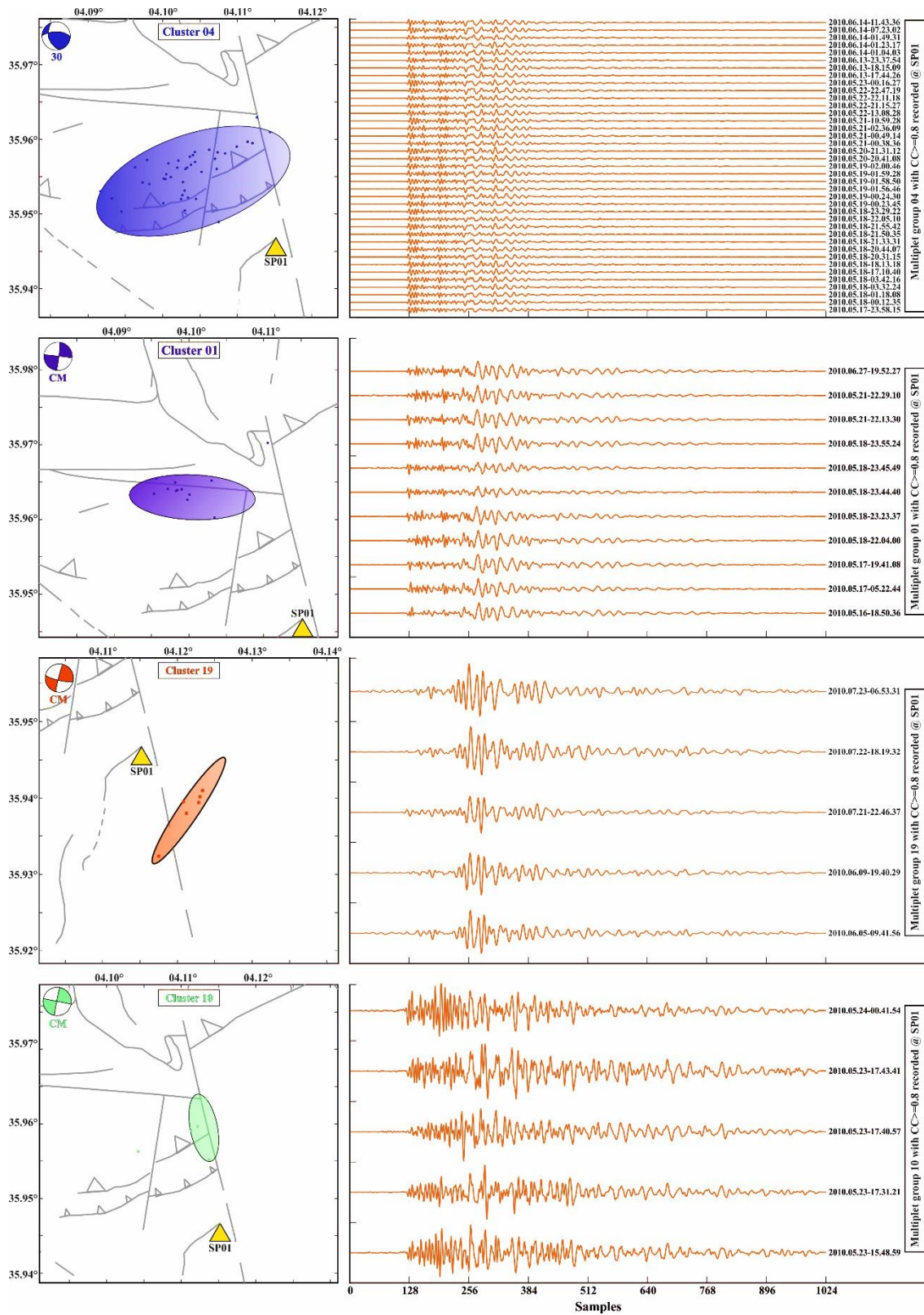
Fig. II.17: Examples of high waveform similarity (CC ≥ 0.8) for four clusters (C01, C04, C10, and C19) recorded at station SP01.

Fig. II.18 encapsulates the spatial distribution of all identified multiplet groups, organized into panels to portray their chronological order of activation from 1 to 21. The upper-left corner of each panel showcases the composite focal mechanism for the corresponding group. Among the 21 multiplet groups analyzed, a consistent alignment was observed between the geometry of each group and one of the nodal planes within the composite mechanisms. In some cases, the mapped structural faults were also aligned with one of the nodal planes, allowing the multiplet geometry to be linked to known faults (see **Fig. II.18**).

However, C02 and C04 revealed inconsistencies between their apparent geometry and the composite focal mechanisms. Cluster C02 comprises 10 seismic events and exhibits a geometry striking NNE-SSW, as determined by PCA (depicted by the black dashed ellipse in **Fig. II.18**). This orientation aligns with the plane of the composite focal mechanism, indicating right-lateral strike-slip motion. However, no visible structures on the available geological maps support this orientation or kinematics. Upon visual inspection of the events constituting cluster C02, a sub-cluster of six events striking NNW-SSE can be observed. The strike of this sub-cluster is consistent with the NNW-SSE left-lateral plane of the composite mechanism and the available mapped faults in the region. We therefore hypothesize that these events originated from the same fault segment, which appears to be nearly parallel to the NNW-SSE left-lateral fault VF2. Conversely, we assume the remaining four events stem from adjacent faults. Nevertheless, it is challenging to trace a probable fault for these events due to their dispersed distribution and lack of alignment with the observed faulting patterns.

Cluster C04 features the highest number of correlated events and its composite focal mechanism suggests strike-slip faulting. Nevertheless, despite the presence of a NNE-SSW strike-slip fault that intersects the nearly E-W curved thrust fault (TF3 in **Fig. II.14b**), the events within C04 are visually aligned along a pre-existing thrust fault. Consequently, the eastern segment of TF3 emerges as a plausible source fault. To corroborate this, we cross-correlated the C04 events (42 events) with those from FP-3 assigned to TF3 (refer to **Fig. II.14b** and **Table II.1**), which are located within or close to

C04. Our analysis revealed that 39 out of the 42 events were effectively correlated (with a coefficient greater than 0.8, at station SP01) with event number 30. We therefore attributed the focal mechanism of event number 30 to C04.
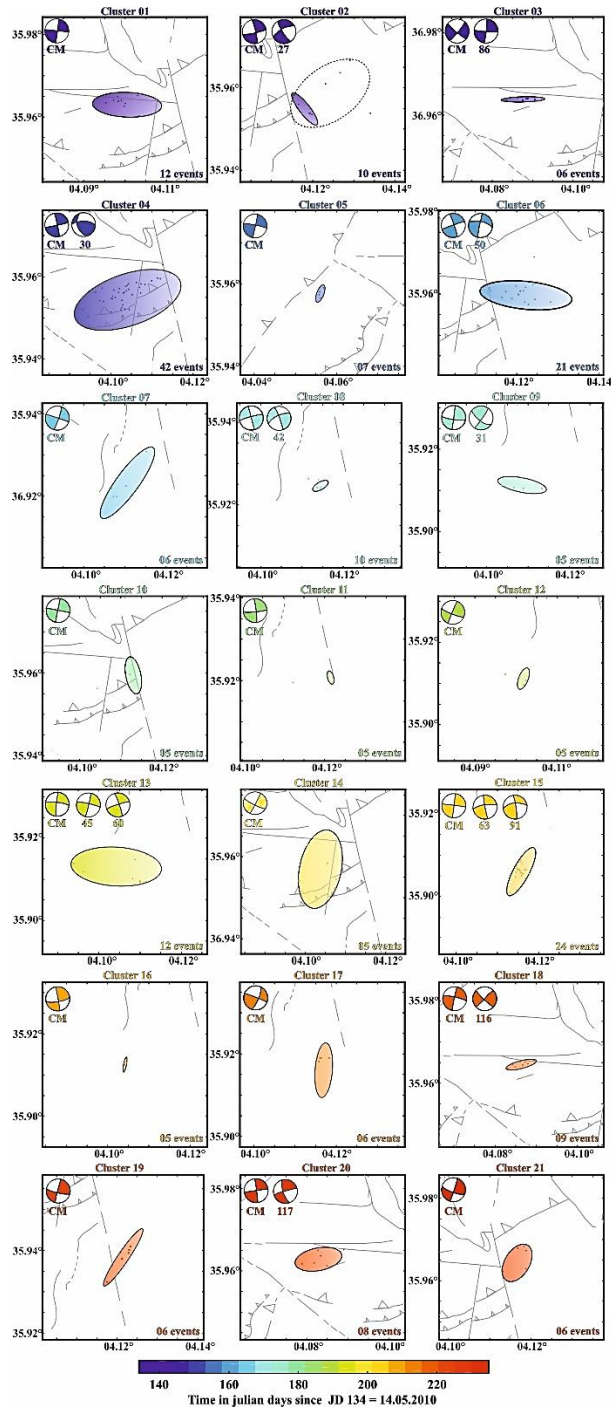
Fig. II.18: Spatial distribution of the retrieved 21 multiplet groups. The panels are sorted chronologically from 1 to 21, with the color bar gradient representing time in Julian days. The upper-left corner of each panel displays the Composite Focal Mechanism (CM) for

the respective group. When available, event(s) from the 128 key events are depicted next to the CM, with their IDs corresponding to those in Fig. 5a. The number of events in each multiplet group is highlighted in the lower right corner. The geometry of each group is represented by a 95% confidence ellipsoid obtained from PCA analysis.

In **Fig. II.19a,** the 21 identified multiplet groups and their corresponding composite focal mechanisms are shown, color-coded chronologically, and juxtaposed with the delineated faults. The first six multiplet groups (from C01 to C06) were activated along MC-1, while C07, C08, and C09 occurred along MC-2. Multiplets C08 and C09 were activated shortly after the nucleation of MS-3. Thereafter, a continuous transition between MC-1 and MC-2 is observed, with 7 out of 12 groups occurring after MS-3. The multiplet groups belonging to the MC-1 are mainly located in the Djebel Choukchot anticline, whereas those belonging to MC-2 are located in the Hodna basin. The spatio-temporal behavior of the 21 multiplets is quite similar to the spatio-temporal behavior of the whole aftershock activity, indicating that these multiplets can be considered as a representative sample of the whole seismic activity in the BI-2010 sequence.
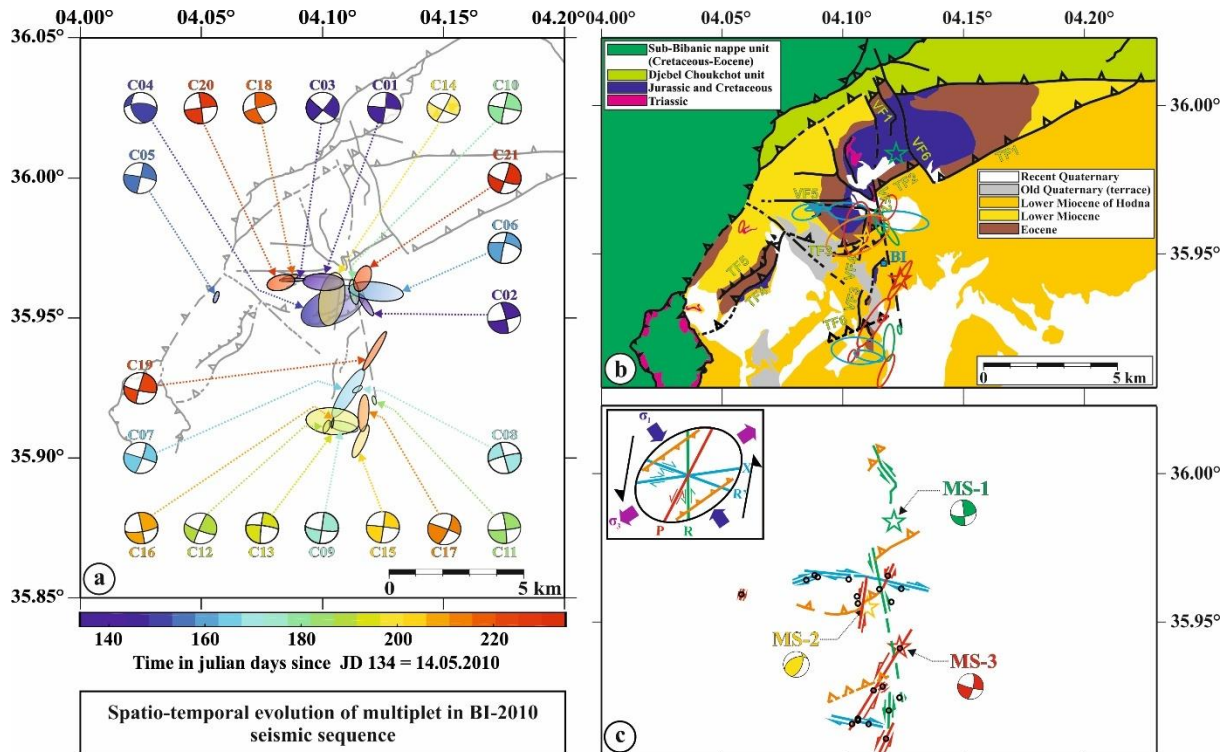
Fig. II.19: New seismotectonic model. **(a)** Depicts the spatiotemporal distribution of the 21 multiplet groups and their corresponding composite focal mechanisms. The gradient color bar indicates their activation time in Julian days. **(b)** Displays an overlay of these multiplet groups onto the structural map (adapted from Beldjoudi et al. 2016 and Abacha et al. 2023a). The kinematics of vertical faults have been deduced in this study from the relative displacements of geological formations in relation to each other and the thrust faults. **(c)** Shows our proposed seismotectonic model responsible for the 2010 Beni-Ilmane sequence, derived from (1) the orientation of multiplet groups, (2) the focal mechanism solutions, and (3) preexisting tectonic structures. The corresponding Riedel shear strain ellipse, depicting R, R', P, and X structures, is also displayed in the upper-left corner.

We have studied the previously highlighted faulting patterns in detail. To refine our newly proposed seismotectonic model, we incorporated the mapped faults and our investigation of focal mechanisms together with the geometries of the 21 identified multiplet groups. In total, we interpreted 14 fault segments, which we classified into four fault classes. We have assigned different colors to each of the four fault classes to facilitate a clearer visualization and analysis of the model's correspondence with the mapped faults (refer to **Fig. II.19b**).

We classified 14 fault segments into four different classes based on their location, focal solutions, and plausible association with pre-existing geological faults. The first fault class consists of five nearly parallel individual faults that exhibit NNE-SSW left-lateral strike-slip movement, represented by the red color (**Fig. II.19b** and **II.19c**). Multiplet groups C12, C16, C07, C08, and C19 (**Fig. II.19a**) are closely associated with a newly identified vertical fault that cuts the southern extent of VF3. This fault is also thought to have hosted the MS-3. VF4 is considered a more likely source for C14. Of note are two recently discovered fault segments, one in the north producing the C21 multiplet cluster and another in the far south producing C15. The small C05 cluster in the westernmost part of the survey area may be related to the reactivation of the fault that hosts the Triassic material. Further geological and geophysical work is required to determine the relationship between the Triassic outcrop and the deep-seated faults that channel it.

The second fault class, consisting of three nearly parallel individual faults with left-lateral strike-slip movement in the NNW-SSE direction, is highlighted in green and is closely associated with the main VF2 structure (**Fig. II.19b** and **II.19c**). The thrust fault system in the study area is segmented not only by the main VF2 structure but also by all parallel structures within the strike-slip corridor. It is inferred that a segment of VF2 contributes to the generation of C02 and C10. The dashed line shown on the map represents the hypothetical southern extension of VF2, which remains hidden beneath unaffected Miocene and Quaternary cover. However, the alignment of the southern end of this dashed line with C11 provides strong evidence for the full extent of VF2. Structures parallel to VF2, are probably responsible for the generation of the C17 multiplet groups located far to the south. The southern continuation of VF1 is likely to have generated the MS-1.

The third fault class, shown in blue, consists of two parallel E-W right-lateral strike-slip faults. VF5, located to the north, is more likely to have hosted multiplet groups C20, C18, C03, C01, and C06 from west to east. The orientation of C06 underlines the eastward extension of VF5 and intersects VF2; however, sediment cover may obscure the surface expression of this fault (**Fig. II.19b** and **II.19c**). The second newly identified fault to the south is associated with the generation of C09 and C13.

The final fault class, highlighted in orange, encompasses thrust faults including TF3 and is characterized by ~E-W to ~ENE-WSW strike. At first glance, TF3 appears to be the source of C04. However, examination of the vertical distribution of events in a N-S cross section and the focal mechanism parameters of event 30 reveals a notable orientation at a dip of 65° (see **Fig. II.20)**. The surface continuity of this dip indicates a shift of about 3 km south of TF3. This suggests that C04 may have been induced by a blind thrust fault located about 3 km south of TF3, here called TF6 (see **Fig. II.19b** and **II.19c).** The same interpretation applies to the events of FP-3, including events 97 and MS-2, which are located on the surface trace and south of TF3, respectively.
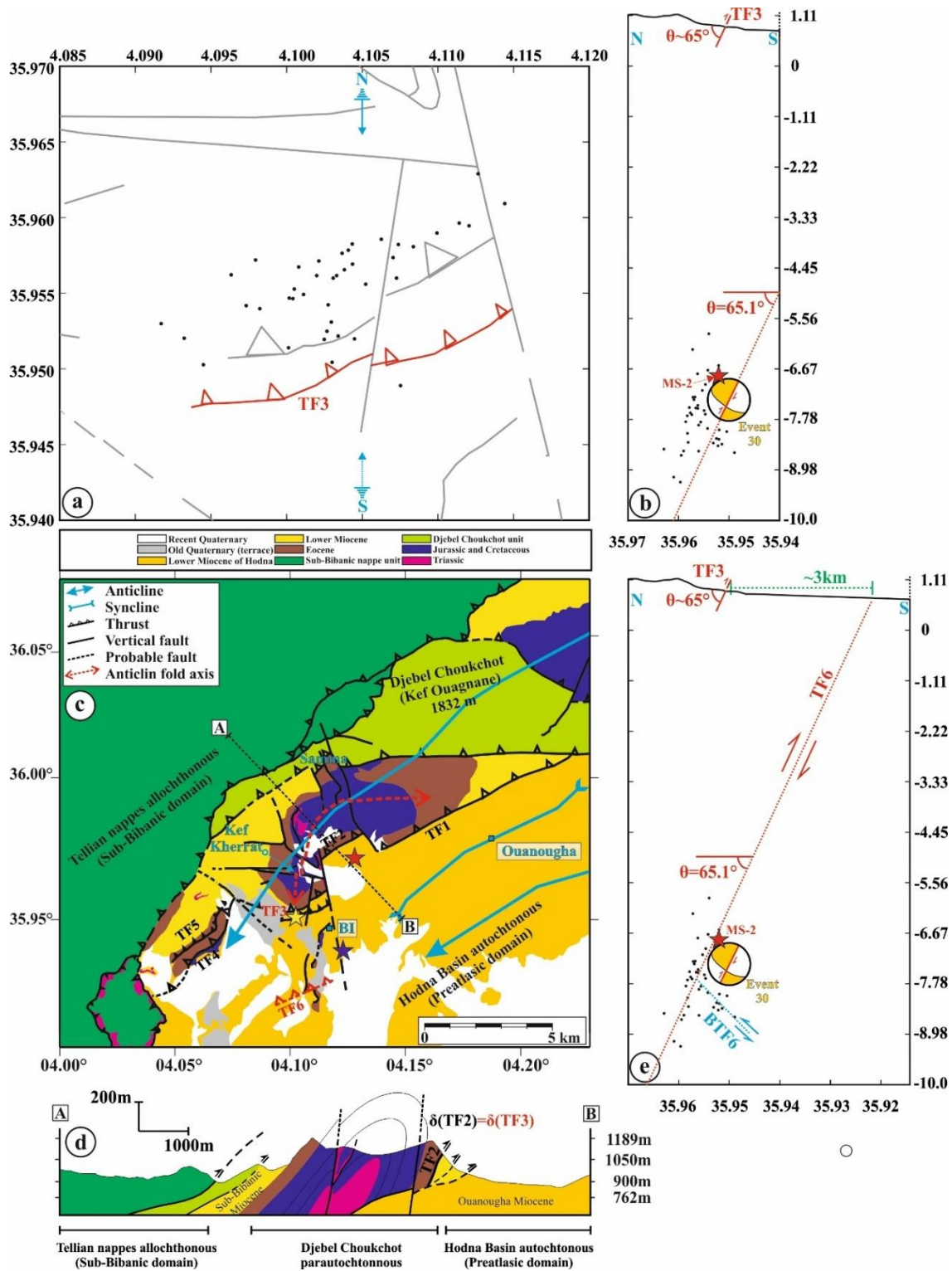
Fig. II.20: Fault source of MS-2, FP-3 and multplet cluster C04. **(a)** Map view of C04 events. **(b)** N-S vertical cross-section of C04 events, showing the sectional view of event 30's focal mechanism (FM) within the C04 events (black dots). The red star indicates the second mainshock, MS-2. **(c)** Geological and tectonic map illustrating major tectonic

structures. **(d)** Geological cross-section (A-B) displaying the dip of TF2 and consequently the dip of TF3. **(e)** Interpretation of the fault TF6, which likely produced C04 and MS-2, with a potential north-dipping back-thrust fault labeled BTF6.

Therefore, the blind thrust fault TF6 is most likely the source fault for cluster C04, fault pattern FP-3, and the second mainshock MS-2. In our seismotectonic model we do not exclude the TF3 fault as we have observed several events aligned along its presumed plane. The cross section also shows a small, distinct, north-dipping event cluster (sub-cluster of C04), suggesting the presence of a potential back-thrust fault called BTF6 (see **Fig. II.20).** Such an observation shows that events from the same multiplet group can originate from neighboring interconnected faults, as we mentioned in our definition of multiplet.

The fault system within the study area adheres to the Riedel shear model, with red faults representing P structures, green faults representing R structures, blue faults corresponding to X or R′ structures, and orange faults representing thrust structures in the deformation ellipsoid (**Fig. II.19c**). The sequence indicates the simultaneous activation of multiple Riedel structures. According to Tchalenko (1970) similarities in structure reflect similarities in formation mechanism. The orientations of the faults suggest that they first developed as parts of Riedel shears due to sinistral movement along a near N-S shear zone under an analogous stress regime. Therefore, the region is controlled by variations in plate tectonic forces through time, allowing the complex fault system to evolve and reactivate mainly following the Riedel shear configuration. It is worth noting that the interplay between strike-slip and thrust belts results in complex geological configurations where fault planes from both the thrust belt and the strike-slip system coexist and interact. Structural variations such as inherited tectonic lineaments and pre-existing obstacles can modify the local stress field, as shown by Morley (2010). This modification often results in asymmetric fault structures, characterized by the predominance of splay faults on one side of the primary fault (in this case VF2, **Fig. II.19b**). Several natural examples illustrate this structural asymmetry (Scholz et al. 2010),

particularly those involving large strike-slip-dominated fault zones interacting with compressional structures (Di Bucci et al. 2006; Fedorik et al. 2019).

II.7: Conceptual Model: Highlighting the Critical Role of Strike-Slip Faults

The complex interplay of tectonic forces and geological structures shapes the Earth's crust, resulting in diverse tectonic settings. In this study, we present a conceptual tectonic model that explores the interactions between thrust sheets and strike-slip faulting, shedding light on the overall tectonic framework of the Beni-Ilman area. The BI-2010 sequence unfolded within a thrust belt intersected by strike-slip faults with the strike-slip faults being predominantly reactivated. This raises the question of the historical role of strike-slip faulting in modifying this thrust system.

Initially, the Hodna Mountains thrust sheets exhibited a large symmetric N040°-N060°E fold, as described by Guiraud 1973 (schematized in **Fig. II.21a**), extending over a few tens of kilometers. These folds, formed during the Atlas phase in the earliest Late Eocene, are also known as the Atlas event. This major compressional event, with a NW-SE shortening direction (N150°-N160°), represents a significant tectonic stage in the evolution of the Maghrebian Alpine Belt (Marmi & Guiraud 2006).
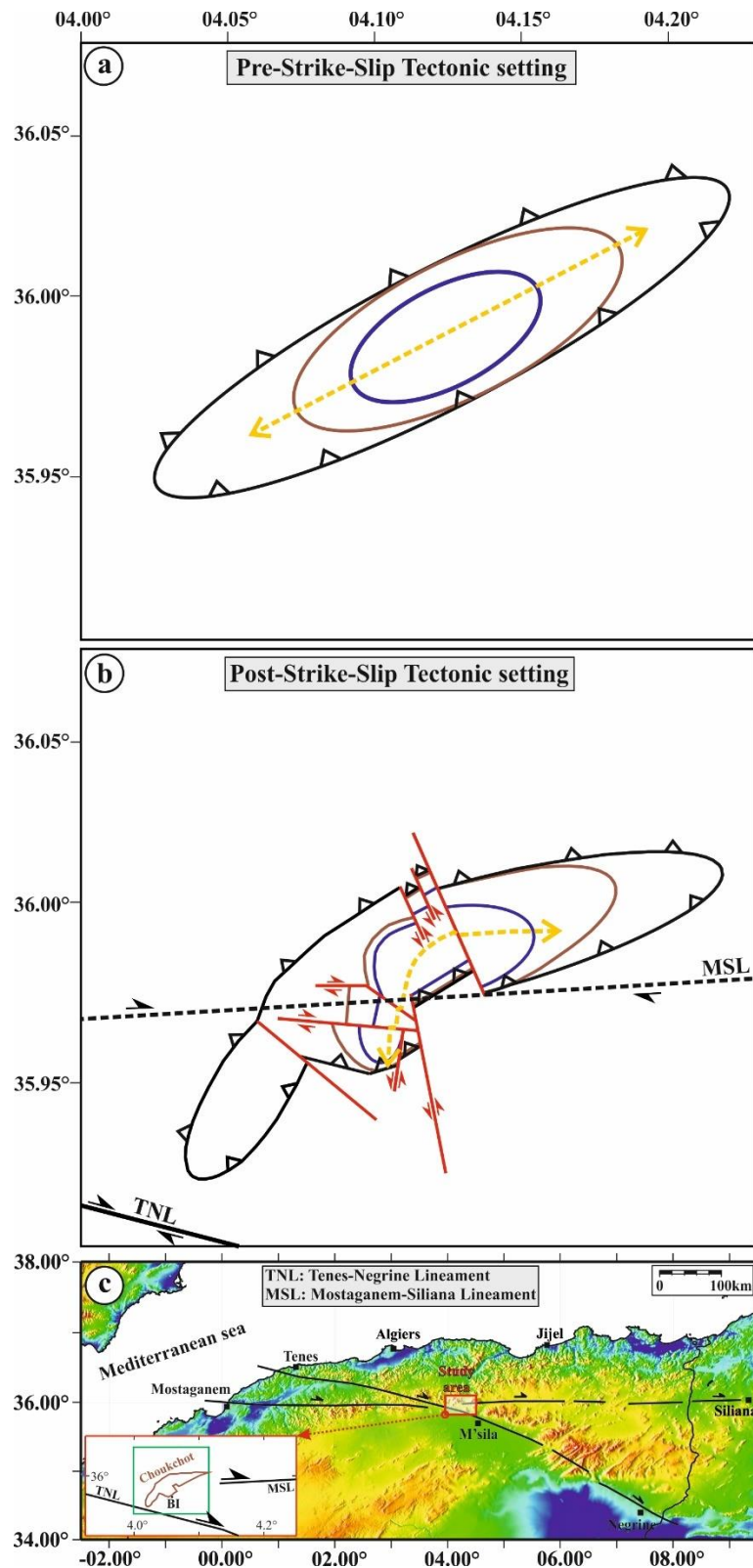
Fig. II.21: Conceptual model of the epicentral area. **(a)** Schematic representation displaying the intact fold-oriented NE-SW, labeled as Pre-Strike-Slip tectonic setting. **(b)** Depicts the highly fractured fold, labeled as Post-Strike-Slip tectonic setting. The

ubiquitous Strike-Slip faults within the thrust fold are indicated in red, and the dashed yellow line represents the reorientation of the fold axis. **(c)** Relief map of Northern Algeria, highlighting two major strike-slip lineaments crossing the study area (after Guemache 2010). The inset figure provides a close-up view of the study region.

It has been identified along the entire North African-Arabian plate margin, including the Algerian Saharan Atlas, the Tunisian Atlas, and the Moroccan High and Middle Atlas (Bumby & Guiraud 2005; Frizon de Lamotte et al. 2000; Guiraud et al. 2005; Mahboubi et al. 2003; Piqué et al. 2002). This tectonic episode resulted in pronounced NE-SW trending folds, referred to as the pre-strike-slip tectonic setting (**Fig. II.21a**). The formation of these folds was synchronized with a conjugate strike-slip fault, with the dextral set oriented NW-SE and the sinistral set oriented NE-SW, as outlined by Marmi & Guiraud (2006). Remarkably, the geometry of the fold remains unchanged despite the associated faults.

The strike-slip tectonics that led to the change in fold coaxiality is referred to as post-strike-slip tectonic setting (**Fig. II.21b**). This tectonic postdates the early Quaternary compressional event (Marmi & Guiraud 2006) and is strongly imprinted in the Pliocene formations. This stress regime has persisted from the beginning of the Quaternary to the present. Similar stress regimes have been observed in the Rif-Tell and Atlas Mountains (Philip & Thomas 1977). Guiraud 1977 extensively documented structural elements including folds, E-W trending reverse faults, N010°-050°W trending dextral strike-slip faults, and N010-20°E trending sinistral strike-slip faults. Marmi (1995) identified sinistral and dextral microfaults oriented at N040°-050°E and N110°-120°E, respectively. These structures resulted from compressional shortening, mainly N-S oriented, and contributed significantly to the present landscape (Guiraud 1977). The activated structures revealed in this study mirror the previously described structures under the current NW-SE oriented stress field (Nocquet 2012; Bougrine et al. 2019).

The counterclockwise reorientation of the SW end of the Djebel Choukchot anticline (**Fig. II.21b**) may be due to the interaction of two major regional lineaments intersecting the study area. The first is the TNL (**Fig. II.21c**), an extensive N110°E to

N120°E dextral shear zone that extends about 700 km from the NW coast of Tenes to the SE region of Negrine. The second lineament, the MSL (**Fig. II.21c**), is an E-W striking dextral fault system extending from Mostaganem (Algeria) to Siliana (Tunisia) (Guemache 2010). Displacements within the anticline were controlled by the activity of strike-slip faults, which split the central-western part in an asymmetric manner. The N-S strike-slip corridor, mainly developed around the VF2 main fault, intersects the thrust belt, resulting in an asymmetric fault structure characterized by the predominance of splay faults on one side of the VF2 main fault, which significantly influenced the configuration of the thrust belt during the post-Pliocene.

II.8 Conclusion

This chapter has provided a comprehensive and in-depth exploration of the seismotectonic dynamics in the Beni-Ilmane region, focusing on the BI-2010 sequence, the most thoroughly studied seismic event in Algeria over the past two decades. By first setting the stage with a detailed introduction to the geological framework of the region, we highlighted the existence of fluid dynamics, suggesting that the region holds a significant fluid potential that may influence its tectonic behavior.

A major contribution of this work is the development of a new minimum 1D velocity model, which has allowed for high-resolution imaging of the aftershock sequences. This model was pivotal in enhancing the precision of our earthquake relocation efforts. Through the high-precision relocation, and rigorous focal mechanism analysis of 128 key seismic events, we identified eight distinct faulting patterns, indicating a more complex seismotectonic framework than previously understood.

To further refine our understanding of this complexity, we employed earthquake multiplet analysis, which led to the identification of 21 distinct multiplet groups, each comprising at least five events. This analysis was crucial in deciphering the complex and overlapping fault systems within the BI region, offering new insights into the intricate tectonic processes at play.

Finally, the chapter culminates in the proposal of a simplified conceptual model that seeks to explain the role of strike-slip faulting in shaping the thrust belt within the study area. This model presents a novel perspective on the interplay between strike-slip and thrust mechanisms, emphasizing their role in the structural evolution of the region. Overall, the findings of this chapter not only shed new light on the seismotectonics of the Beni-Ilmane region but also provide a robust framework for future studies aimed at improving the understanding of complex fault systems and seismic hazards in the region. Through these efforts, we hope to contribute meaningfully to ongoing research and enhance seismic risk mitigation strategies in tectonically active areas.

Chapter III

Dynamic Source Parameters' Analysis

Content

III.1 Introduction

Earthquakes are complex natural phenomena that originate from the sudden release of energy stored within the Earth's crust, leading to the generation of seismic waves that propagate through the Earth's interior and along its surface. The study of earthquakes, particularly their source characteristics, is fundamental to understanding the mechanics of faulting, the behavior of seismic waves, and the assessment of seismic hazards. Central to this understanding are the earthquake dynamic source parameters, which provide critical insights into the nature of the fault rupture, the amount of energy released, and the distribution of this energy over time and space. At the heart of any earthquake is the fault, a fracture in the Earth's crust where blocks of rock have slipped past each other. The fault surface, or rupture plane, is where the seismic slip occurs, and its properties are crucial in defining the earthquake source parameters. These parameters include the seismic moment, stress drop, fault slip, rupture area, and rupture velocity, among others.

In this chapter we analyze source parameters of the most important seismic events in Beni-Ilmane seismic sequence using two different approaches 1) Individual spectra approach and 2) Empirical Green's Function (EGF) approach, with greater focus on the EGF approach. These methods, though distinct in their methodologies, both aim to extract key characteristics of an earthquake's source from the recorded seismic data. The individual spectra approach is a fundamental method in seismology, where the seismic signals generated by an earthquake are analyzed in the frequency domain. By examining the frequency content of the seismic waves, researchers can infer important source parameters that characterize the size, energy release, and dynamic properties of the fault rupture. On the other hand, the EGF approach leverages smaller, nearby earthquakes to enhance the estimation of source parameters for larger events. By using these smaller earthquakes as references, or " Empirical Green's functions," seismologists can more accurately isolate the source characteristics of the larger earthquake. We note that the

results presented in this chapter are part of our forthcoming paper (Tikhamarine et al., in prep).

Understanding earthquake source parameters is not only of academic interest but also has practical implications for earthquake engineering, risk mitigation, and disaster preparedness. As our ability to measure and model these parameters continues to improve, so too will our understanding of the Earth's dynamic behavior and our capacity to protect society from the devastating effects of earthquakes.

III.2 Near and Far Field Displacement

In seismology, the displacement field refers to the spatial distribution of ground displacement caused by seismic waves emanating from a source, such as an earthquake or an explosion. The displacement field is generally divided into near-field and far-field components, each exhibiting distinct characteristics due to their differing proximity to the seismic source.

III.2.1 Near-Field displacement

The near-field displacement occurs in close proximity to the seismic source, typically within a few fault lengths of the rupture area. This region is characterized by complex ground motions that are strongly influenced by the dynamic processes of fault rupture and slip. The near-field displacement is often dominated by the static offset, which is the permanent displacement of the ground that remains after the seismic event has concluded. This static component reflects the direct impact of the fault's motion, making the near-field displacement highly sensitive to the source's geometry, the slip distribution on the fault, and the medium's elastic properties. Additionally, the near-field is where the radiation patterns of seismic waves, including both body waves (P and S waves) and surface waves, are most complex, often displaying significant spatial variability due to the constructive and destructive interference of different wave types, see **Fig. III.1.** Mathematically the near-field decays with $1/r^2$.

III.2.2 Far-Field Displacement

The far-field displacement, on the other hand, occurs at greater distances from the seismic source, typically several fault lengths away or more. In this region, the ground motion is dominated by the radiated seismic waves rather than by static displacement. The far-field displacement primarily reflects the dynamic wave field, where seismic waves have traveled sufficiently far from the source that their amplitude has decreased, and their waveforms have become more coherent and predictable. In the far-field, the displacement field is usually described by simpler models, as the complexities of near-source effects diminish. It is also where the seismic radiation patterns become more pronounced, and the displacement can be used to infer source parameters such as the seismic moment, fault orientation, and the energy released during the rupture. This region is particularly important for seismologists because it is often the displacement observed by distant seismic stations that provides the data used to characterize earthquakes on a global scale, see **Fig. III.1.** Mathematically the far-field decays with $1/r$
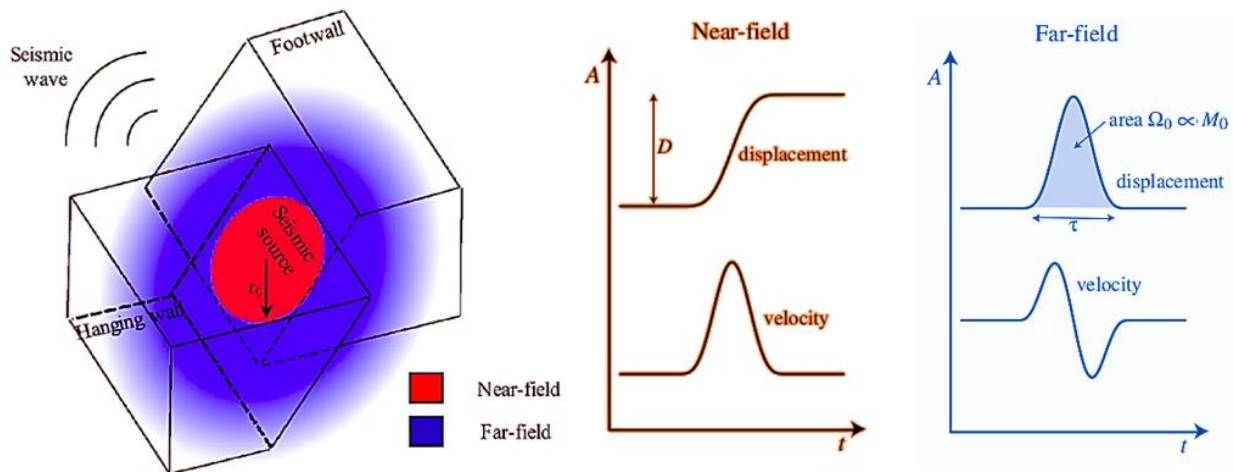
Fig. III.1: Schematized illustration of near and far field approximation, after (Wang *et al.* 2022). On the right, the relationships between near-field displacement, far-field displacement, and velocity for time series are shown, modified from (Shearer 2009)

III.2.3 Limit Between the two fields

The simplified expression of the displacement filed in a spherical medium is giving by:

$$u(r,t) = \frac{\partial \Phi(r,t)}{\partial r} = \underbrace{\left(\frac{1}{r^2}\right) F\left(t - \frac{r}{v_p}\right)}_{\text{Near-field}} + \underbrace{\left(\frac{1}{rv_p}\right) \frac{\partial F\left(t - \frac{r}{v_p}\right)}{\partial \tau}}_{\text{Far-field}} \qquad \text{(III.1)}$$

Where $\tau = \left(t - \frac{r}{v_p}\right)$. is the time delay. Only after τ turned positive (at the time of the arrival of the wave), the surrounding medium is affected. F is the source time function. We observe from III.1 that the near-field term decays with $1/r^2$, while the far-field term decays with $1/r$. As we already mentioned, the near filed is very complex, but the far-field is simpler, and it can be separated into two parts, one that arrives with velocity α, the P waves, and another with velocity β, the S waves (Madariaga 2015):

$$u_{FF}^P(R,t) = \frac{1}{4\pi\rho\alpha^2} \frac{1}{R} \Re^P \dot{M}_0\left(t - \frac{R}{\alpha}\right) \qquad \text{(III.2)}$$

$$u_{FF}^S(R,t) = \frac{1}{4\pi\rho\beta^2} \frac{1}{R} \Re^S \dot{M}_0\left(t - \frac{R}{\beta}\right) \qquad \text{(III.3)}$$

where $\Re^P$ and $\Re^S$ are the radiation patterns of P- and S-waves, respectively, and $\dot{M}_0 = S$ is the moment rate or the source time function.

In seismology, much of the practical analysis is conducted in the far field. The question here is when the recorded seismic waves can be considered as being in the far field? There is no well specified limit to distinguish between near and far field. Nevertheless, it is accepted that the **far-field condition** is typically satisfied when the distance (R) from the seismic source to the observation point is much greater than the wavelength of the seismic waves: $R >> \lambda$ Alternatively, this can be expressed in terms of frequency as: $R/\lambda = Rf/v >> 1$.

λ is the wavelength of a P or S-wave with angular frequency ω, R is the distance from the seismic source to the observation point, v is the wave velocity. f is the frequency.

If we consider a constant distance R, since $\lambda = v/f$, higher frequencies result in shorter wavelengths. Resulting in higher values of the ratio R/λ. Hence, depending on the frequency content of the signal $S(f)$, high-frequency waves will likely be in the far field, while low-frequency components may be in the near field (Madariaga 2015).

III.3 Source Models Commonly Utilized

While several source models exist, two have been widely used in earthquake source seismology: (Haskell 1964, 1966) rectangular source model and (Brune 1970) circular source model. Here, we present both models with a greater focus on Brune's model, as it will be the one used during this thesis. The reasons for preferring this model are mentioned in **sub-chapter III.3.3**.

III.3.1 Haskell's Rectangular Source Model

Haskell (1964) proposed a simple kinematic source model to describe the rupture process of an earthquake. In this model, the fault is represented as a rectangular plane of length L and width W. The rupture propagates along the length (L) with a constant velocity v, while the slip appears instantaneously across the width (W), see **Fig. III.2**.
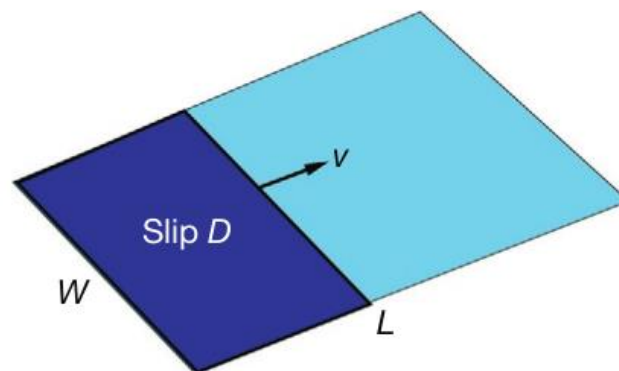
Fig. III.2: Illustration rupture propagation in Haskell's fault model. After (Madariaga 2015)

Although this model technically violates basic principles of continuum mechanics, such as the continuity of matter, it serves as a very useful first approximation for a seismic source. At low frequencies, or when the wavelength is much longer than the fault size, this model provides a reasonable representation of a simple seismic rupture propagating along a strike-slip fault (Madariaga. 2015). In Haskell's model, at time t=0, a dislocation line of width W abruptly forms and then propagates along the fault at a constant rupture velocity, breaking a section of the fault with length L. As the dislocation advances, it leaves behind a zone with a uniform slip D. Assuming the fault lies within a plane defined by the coordinates (x_1, x_2), the slip function can be expressed as:

$$\Delta \dot{u}_1(x_1, x_2, t) = D\dot{s}\left(t - \frac{x_1}{v_r}\right)H(x_1)H(L - x_1)$$

$$for -W/2 < x_2 < W/2$$

(III.4)

where $\dot{s}(t)$ represents the slip rate time function, which, in the simplest version of Haskell's model, remains constant across the fault. Haskell's model is notable for incorporating rupture propagation, represented by a time delay tied to the rupture velocity v_r, which is the speed at which the slip front moves along the fault in the x_1 direction. However, the model has two significant physical limitations: it unrealistically assumes that rupture occurs instantaneously in the x_2 direction, which is not possible in real seismic events, and it allows slip to abruptly drop from the average slip D to zero at the fault's edges, violating matter continuity and invalidating the basic equation of motion near the fault boundaries. Despite these shortcomings, Haskell's model remains a valuable first-order approximation for representing seismic slip and fault finiteness at a finite rupture speed Madariaga (2015). Its simplicity also makes it straightforward to calculate the seismic moment, $M_0 = \mu DLW$, where μ is the shear modulus, D is the constant slip, and LW is the fault area.

III.3.2 Brune's Circular Source Model

The most common model for a circular fault of finite dimensions was proposed by Brune (1970). Brune's model is considered a simple dynamic model, as it involves the sudden application of a shear stress pulse to a circular fault of finite radius. In this model, the stress pulse is applied instantaneously across the entire fault area, meaning there is no fracture propagation. The immediate shear stress drop within the fault generates a plane SH wave that propagates at velocity β perpendicular to the fault plane, which has a radius a, see **Fig. III.3**.
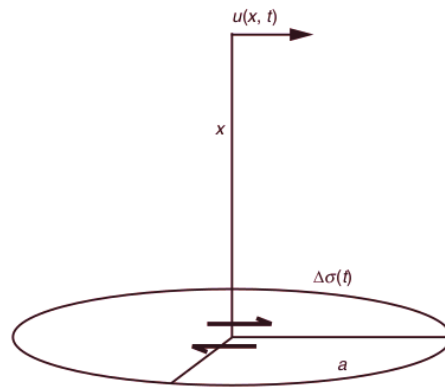
Fig. III.3: Illustration of rupture on circular fault plane, according to Brune's model. After (Udías *et al.* 2014)

Δσ, known as Brune's effective stress, represents the difference between the tectonic stress and the frictional stress. x denotes the distance perpendicular to the fault plane, while u is the shear displacement associated with this stress pulse.

Considering shear stress pulse as a function of time propagating perpendicular to the fault surface with a constant velocity β is given by:

$$\Delta\sigma(x,t) = \Delta\sigma H\left(t - \frac{x}{\beta}\right)$$

(III.5)

Since the stress pulse is the derivative of the shear displacement, and it is given by:

$$\Delta\sigma = \mu\frac{\partial u}{\partial x} \qquad\qquad (\text{III.6})$$

The integration of this stress pulse gives us the shear displacement:

$$u\left(t - \frac{x}{\beta}\right) = \frac{\Delta\sigma}{\mu}\int H\left(t - \frac{x}{\beta}\right)dx = \frac{\Delta\sigma}{\mu}\beta t H\left(t - \frac{x}{\beta}\right) \qquad (\text{III.7})$$

Hence, the displacement on the fault (i,e x=0) is given by:

$$u(t) = \frac{\Delta\sigma}{\mu}\beta t H(t) \qquad\qquad (\text{III.8})$$

Equation (III.8) indicates that, at a point inside the fault, the displacement increases linearly with time until the effects of the boundary (r = a) reach the point and stop the linear increase.

III.3.3 Why Preferring Brune's Model Over Haskell's

Brune's model is often preferred over Haskell's model in certain contexts for several key reasons:

Simplicity and dynamic nature: Brune's model is a simple dynamic model that focuses on the sudden application of a shear stress pulse to a circular fault. This simplicity makes it easier to understand and apply, particularly when analyzing the frequency content of seismic waves.

Realistic representation of stress drop: Brune's model incorporates a more realistic representation of the stress drop within the fault, allowing for a direct calculation of the seismic source spectrum. This is particularly useful for estimating the stress drop, which is a key parameter in understanding the energy release during an earthquake.

Avoidance of unphysical features: Unlike Haskell's model, which has some unphysical features like instantaneous rupture in one direction and discontinuities in slip at the fault edges, Brune's model avoids these issues. The assumption of a radially expanding

rupture is more consistent with observed seismic behavior and does not violate principles of continuum mechanics as severely as Haskell's model.

Better representation of small to moderate earthquakes: Additionally, it has been observed that Brune's model is particularly effective for small crustal earthquakes with magnitudes up to around 6. Earthquakes of this magnitude typically have dimensions of less than 20 km, which is smaller than the total thickness of the seismogenic layer, (Udías *et al.* 2014). This characteristic applies to nearly all earthquakes occurring in Algeria (Yelles-Chaouche *et al.* 2022). In such cases, fractures usually initiate at a point and expand freely in all directions, resulting in an almost circular shape where length equals width (L = W) (**Fig. III.4a**). Conversely, larger earthquakes tend to have a greater length compared to their width (L > W), which is constrained by the thickness of the seismogenic layer. These larger events are better represented by a rectangular fault model (**Fig. III.4b**).
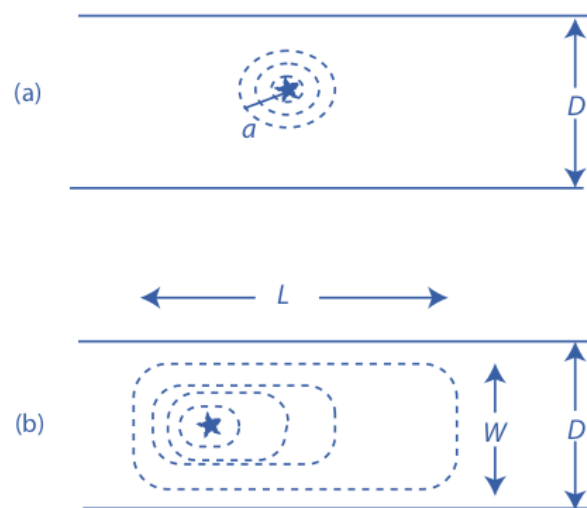
Fig. III.4: Simplified illustration of Brune' s models **(a)**, and Haskell's **(b)**, After (Udías *et al.* 2014)

III.4 The Individual Spectra Approach for Source Parameters Estimation

In practice we usually use velocimeter sensors to record ground motion, these sensors are proportional the ground velocity within their frequency band-width. To estimate source parameters the displacement spectra is used, therefore the velocity

spectra obtained after the removal of the instrument response should be integrated to displacement. The Brune's model predicts the following general form of the spectral amplitude $\Omega(f)$:

$$\Omega(f) = \frac{\Omega_0 e^{-\frac{\pi f t}{Q}}}{\left[1 + \left(\frac{f}{f_c}\right)^{\gamma n}\right]^{\frac{1}{\gamma}}} \tag{III.9}$$

Ω_0 is the long-period (low frequency) level (or asymptote) of the spectrum, f_c is the corner frequency, t is the travel time of the seismic wave of interest (P or S), Q is the frequency-independent whole-path attenuation quality factor, and γ and n are constants that control the shape of the spectrum curvature around the corner frequency and the high frequency fall-off, respectively. If t=0, n=2, and γ=1, **equation (III.9)** corresponds to the spectral shape proposed by Brune (1970). Boatwright (1980) later introduced a modified version of this spectral shape, setting γ=2. This adjustment produces a sharper corner compared to the original Brune model, which Boatwright found provided a better fit for his data, see **Fig. III.5** bellow.
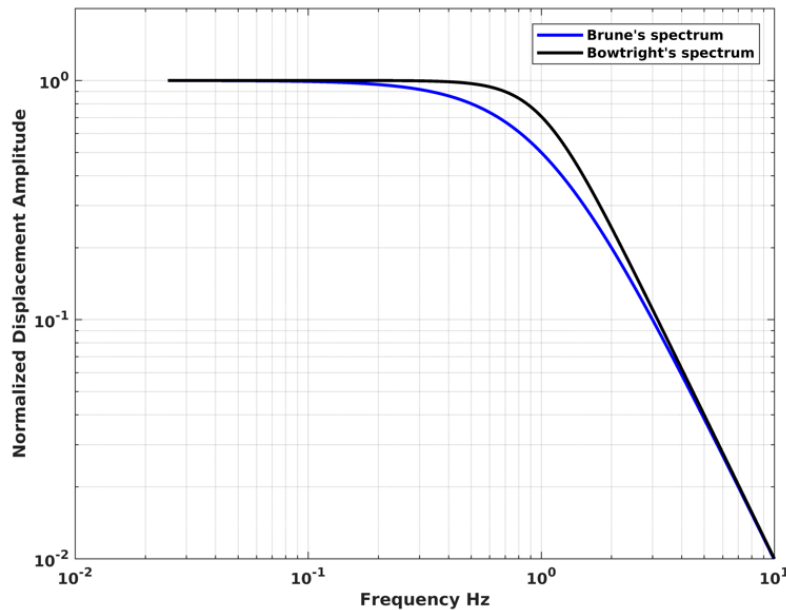
Fig. III.5: A comparison between Brune's and Boatwright's shape of displacement spectrum

Therefore, Brune's displacement spectra is given by:

$$\Omega(f) = \frac{\Omega_0 e^{-\frac{\pi f t}{Q}}}{\left[1 + \left(\frac{f}{f_c}\right)^2\right]} \tag{III.10}$$

and Boatwright's modified spectra is given by:

$$\Omega(f) = \frac{\Omega_0 e^{-\frac{\pi f t}{Q}}}{\left[1 + \left(\frac{f}{f_c}\right)^4\right]^{\frac{1}{2}}} \tag{III.11}$$

knowing that $\Omega_0 = M_0/4\pi\rho v^3$, we can write the Brune's source displacement spectrum as:

$$S(f) = \frac{M_0}{\left[1 + \left(\frac{f}{f_c}\right)^2\right] 4\pi\rho v^3} \tag{III.12}$$

Where M_0 (N.m) is the seismic moment, ρ is the density (kg/m³), v is the velocity (m/s) at the source (P or S-velocity depending on phase) and f_c is the corner frequency.

When we plot the displacement spectra vs frequency in a log-log scale we find that the spectrum is flat at low frequencies, with a level proportional to M_0, whereas at high frequencies, the spectral level decays linearly with a slope of 2. The spectral amplitude at the corner frequency ($f = f_c$) is half that of the flat level.

The **equation (III.11)** gives uncorrected displacement spectrum; corrections of path effects is needed in order to obtain a reliable displacement source spectrum. Geometrical spreading $G(\Delta, h)$ and attenuation will alter the displacement spectrum at the recording station. The observed spectrum may be represented at an epicentral distance (Δ) and a hypocentral depth (h) as:

$$S(f,t) = \frac{M_0 \times 0.6 \times 2.0}{\left[1 + \left(\frac{f}{f_c}\right)^2\right] 4\pi\rho v^3} G(\Delta, H) e^{-\pi f \kappa} e^{\frac{-\pi f t}{Q(f)}} \qquad \text{(III.13)}$$

where t is the travel time (equivalent to using the hypocentral distance divided by the velocity), the factor 0.6 account for average radiation pattern effect, the factor 2.0 is the effect of the free surface, ρ is the density (kg/m³). In practice, the units used are mostly g/cm³ and km/s.

We label the corrected spectra as Dc, and it is used to calculate the observable parameters corner frequency f_c and spectral flat level Ω_0.

$$D_c(f) = \frac{\Omega_0}{\left[1 + \left(\frac{f}{f_c}\right)^2\right]} = \frac{M_0 \times 0.6 \times 2.0}{\left[1 + \left(\frac{f}{f_c}\right)^2\right] 4\pi\rho v^3} G(\Delta, h) \qquad \text{(III.14)}$$

Conversely, the velocity corrected spectrum is given by:

$$V_c(f) = D_c(f) * 2\pi f \qquad \text{(III.15)}$$

And the acceleration corrected spectrum is given by:

$$A_c(f) = V_c(f) * 2\pi f \qquad \text{(III.16)}$$

The corner frequency is the frequency at which the curve representing the Fourier amplitude spectrum of a recorded seismic signal abruptly changes its slope. Therefore, Theoretically, the abscissa of the intersection point of the three curves displacement, velocity and acceleration gives the corner frequency, see, **Fig. III.6**.
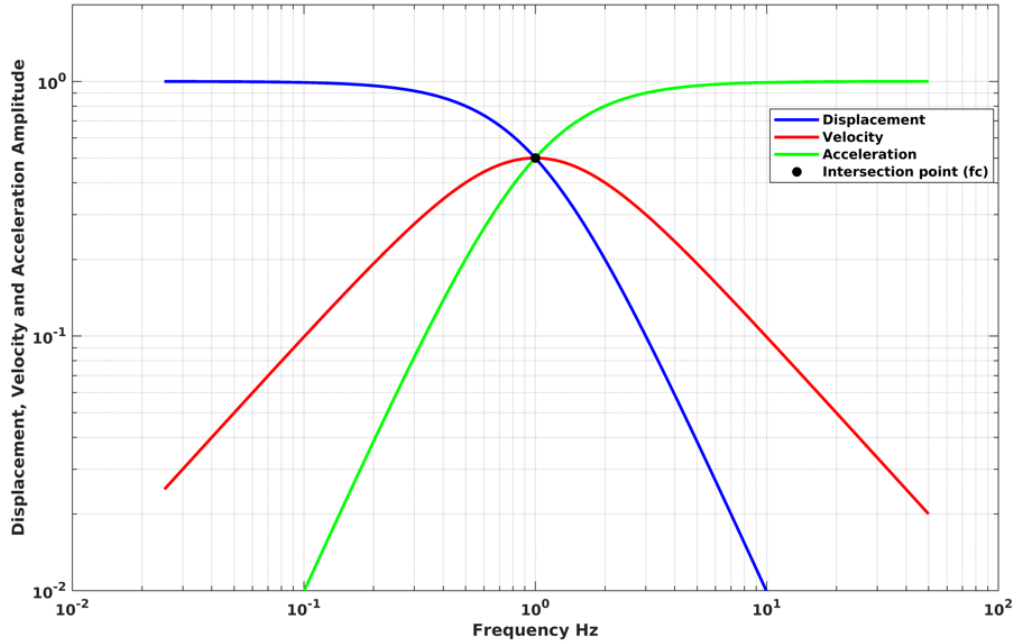
Fig. III.6: Modeled displacement, velocity and acceleration spectra using a normalized spectral amplitude and a corner frequency $f_c = 1$. The intersection of the three spectra at the corner frequency is also observed.

In order to estimate the source parameters, we need to perform an optimization process. In this regard we minimize the difference between the observed and the modeled spectra using the following mis-fit function:

$$\text{res} = \sum |log\Omega_{mod} - log\Omega_{obs}| \tag{III.17}$$

where Ω_{mod} and Ω_{obs} are the modeled and the observed spectra respectively.

The parameters Ω_0 and f_c that yield the minimum residuals with the observed spectra are the best-fit paramaters and they will be used to estimate the remaining parameters as follow:

From the low-frequency level (Ω_0) we estimate the seismic moment using:

$$M_0 = \frac{\Omega_0 4\pi\rho v^3}{0.6 \times 2.0 \times G(\Delta, h)} \tag{III.18}$$

Geometrical spreading for body waves in its simple form is given by $G(\Delta, h) = \frac{1}{r}$ therefore:

$$M_0 = \frac{\Omega_0 4\pi \rho v^3 r}{0.6 \times 2.0} \tag{III.19}$$

From the seismic moment scalar value, the moment magnitude Mw can simply be calculated as:

$$Mw = \frac{2}{3} * \log(M_0) - 6.03 \tag{III.20}$$

where M_0 is in unit of N.m

Using the obtained corner frequency the source radius in Brune's model is given by:

$$r_B = \frac{2.34}{2\pi} \frac{v}{f_c} \tag{III.21}$$

Also, Madariaga (1976), modified this formula to:

$$r_M = \frac{k\beta}{f_c} \tag{III.22}$$

where v is the phase (P or S) velocity, β is the S-wave velocity, k=0.32 and 0.21 for P and S waves respectively.

The average displacement along the fault is given by:

$$U = \frac{M_0}{\mu \pi r^2} \tag{III.23}$$

The stress-drop which is a theoretically well-defined quantity that compares the "before" and "after" stress-strain states of the elastic volume that surrounds the fault, is given by:

$$\Delta\sigma = \frac{7}{16} \frac{M_0}{r^3} \tag{III.24}$$

Fig. III.7 summarizes the methodology for source parameters estimation using individual source spectra.

a

Champ proche $(r_{min} = \lambda_{max})$ Champ lointain

distance source-station (r)

$(r \gg 0)$

$$u(x,t) \propto \frac{1}{r^2(x)} M(t) \quad + \quad \frac{1}{r(x)} \dot{M}(t) \quad \Rightarrow \quad u(x,t) \propto \dot{M}(t)$$

$$u(t) \xrightarrow{FFT} u(f)$$

$$Si: u(f \to 0) \propto \int_{-\infty}^{+\infty} \dot{M}(t)dt = \lim_{t \to \infty} \int_{-\infty}^{t} \dot{M}(t')dt' = M(t \to +\infty)$$

$$\Rightarrow M_0 = M(t \to +\infty) \propto u(f \to 0)$$

$$\Omega_0 \equiv u(f \to 0) \Rightarrow M_0 \propto \Omega_0$$

b

$U(f)$

Ω_0

$\propto f^{-2}$

f_c

f

$$\Delta\sigma = \frac{M_0}{\mu \pi R^2}$$

$$M_0 = \frac{4\pi\rho r v^3 \, \Omega_0}{F \, R_{\theta\varphi}}$$

$$R = \frac{2.34 \, v}{2 \pi \, f_c}$$

$$R \propto f_c$$
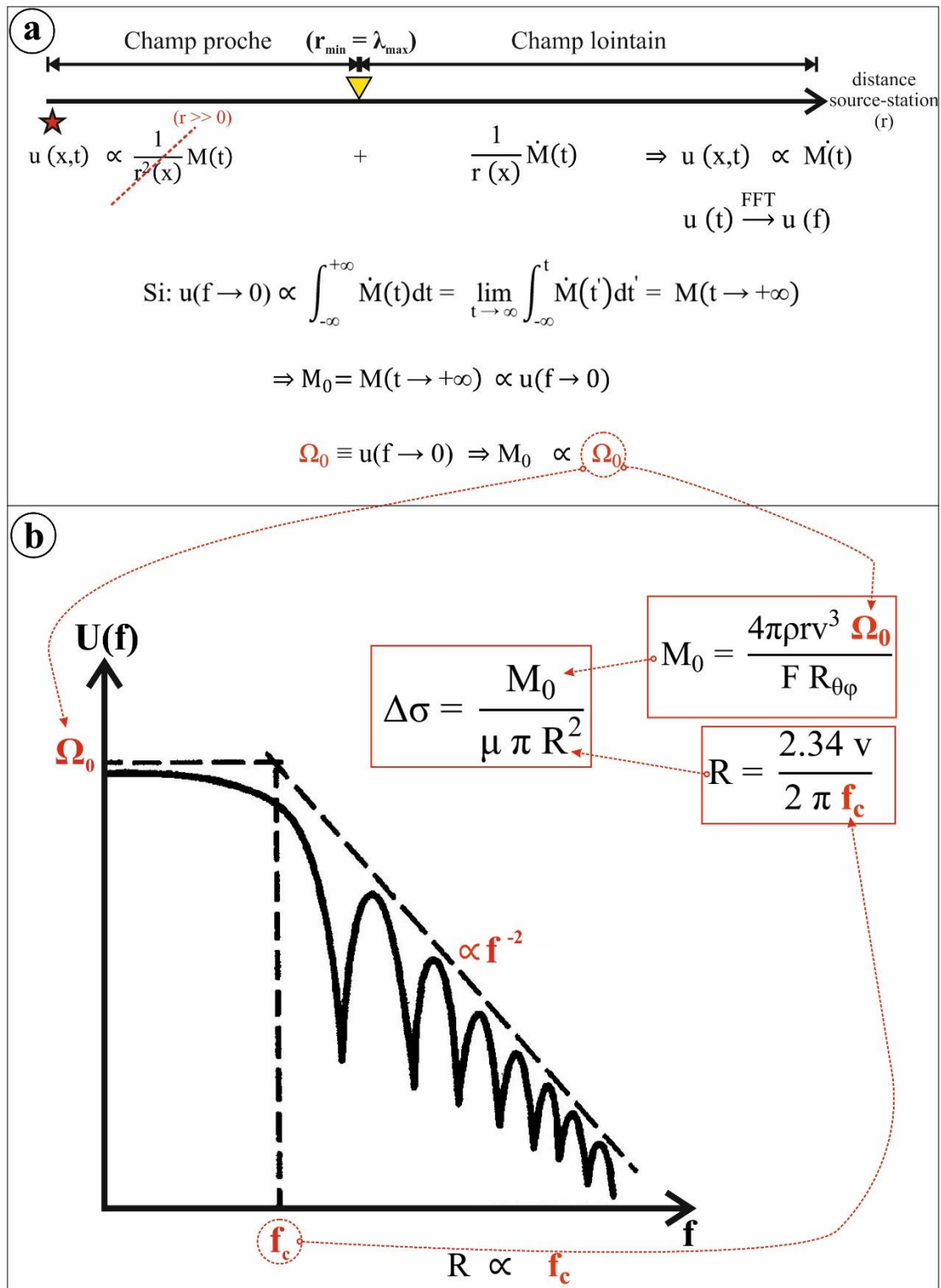
Fig. III.7: Summary of the methodology used in the individual spectra approach for source parameters estimation, after (Boulahia 2022).

III.5 Seismic moment and source time function

The Source Time Function (STF) represents the time dependence of the seismic moment $M_0(t)$. In the far field, the elastic displacements caused by an earthquake are related to the time derivative of the seismic moment, known as the moment rate (see **equation III.2** and **III.3**). This relationship means that instead of modeling the seismic moment directly, it is often more practical to model the moment rate. The moment rate describes how the seismic moment changes over time, and its time-dependent behavior is commonly referred to as the Source Time Function (STF). The simplest form of the STF is, the step function (Udías *et al.* 2014):

$$M_0(t) = M_0 * H(t) \tag{III.25}$$

Where H(t) is Heaviside operator (step function) and is defined by:

$$H(t) = \begin{cases} 0, & if\ t < 0 \\ \dfrac{1}{2}, & if\ t = 0 \\ 1, & if\ t > 0 \end{cases} \tag{III.26}$$

Equation (III.25), suggests that the moment abruptly reaches its maximum value M_0 at the exact moment t=0 and then remains constant. This implies that the fault moves instantaneously and does not return to its original state after the movement. However, this scenario is unrealistic because in real-world seismic events, the fault motion occurs over a finite period, not instantaneously. Moreover, this instantaneous motion leads to a far-field STF in the form of a Dirac delta function (represented by $\dot{M}_0$, the moment rate), see **Fig. III.8**.
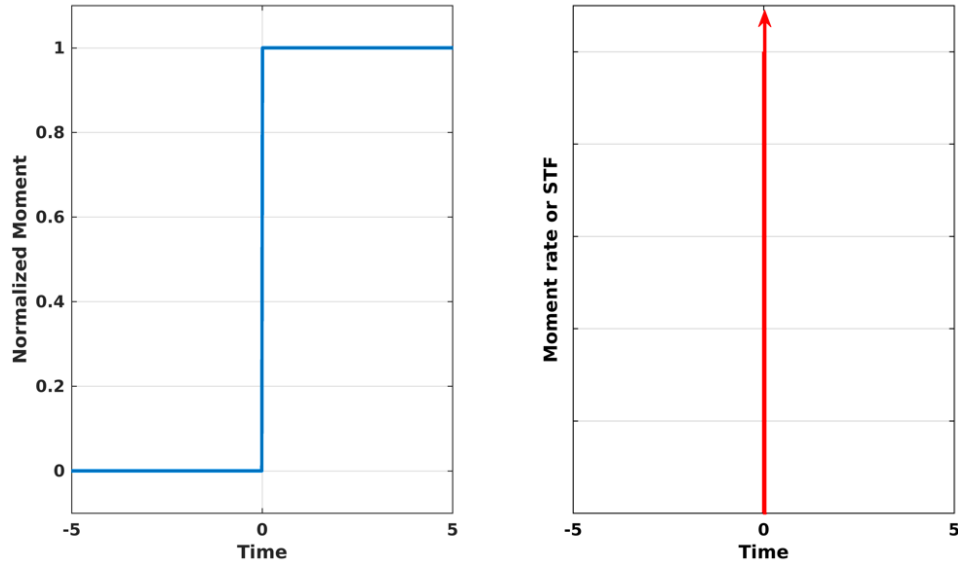
Fig. III.8: Modeled moment and moment rate function. Left: Seismic moment function modeled from **equation (III.25)**. Right: Moment rate function, or source time function (STF), is the derivative from **equation (III.25)**.

To address this, a Source Time Function (STF) is introduced, which includes a rise time τ_r. This rise time represents the period during which the slip gradually increases to its maximum value, rather than occurring instantaneously. Such STF is expressed as:

$$M_0(t) = M_0 \left[\frac{t}{\tau_r} H(t) - \frac{t - \tau_r}{\tau_r} H(t - \tau_r) \right] \tag{III.27}$$

The moment release starts at t=0 and increases linearly until $t = \tau_r$, the time at which it reaches its peak value M_0 (corresponding to the maximum slip (Δu). After this point, it remains constant, see **Fig. III.9**.

In such case the STF is given by

$$\dot{M}_0(t) = \dot{M}_0[H(t) - H(t - \tau_r)] \tag{III.28}$$

In this model, the moment or slip rate suddenly jumps from zero to its peak value $\dot{M}_0$, maintains this level for the duration of τ_r, and then ceases abruptly **Fig. III.9**.

The rectangular source time function, due to its discontinuities at the start and end, causes singularities in the ground velocity field in the far field. Since the radiated energy is proportional to the square of the velocity, these discontinuities lead to an infinite amount of energy in the idealized model. This makes the rectangular STF impractical and physically unrealistic for modeling earthquakes. (Udías *et al.* 2014)
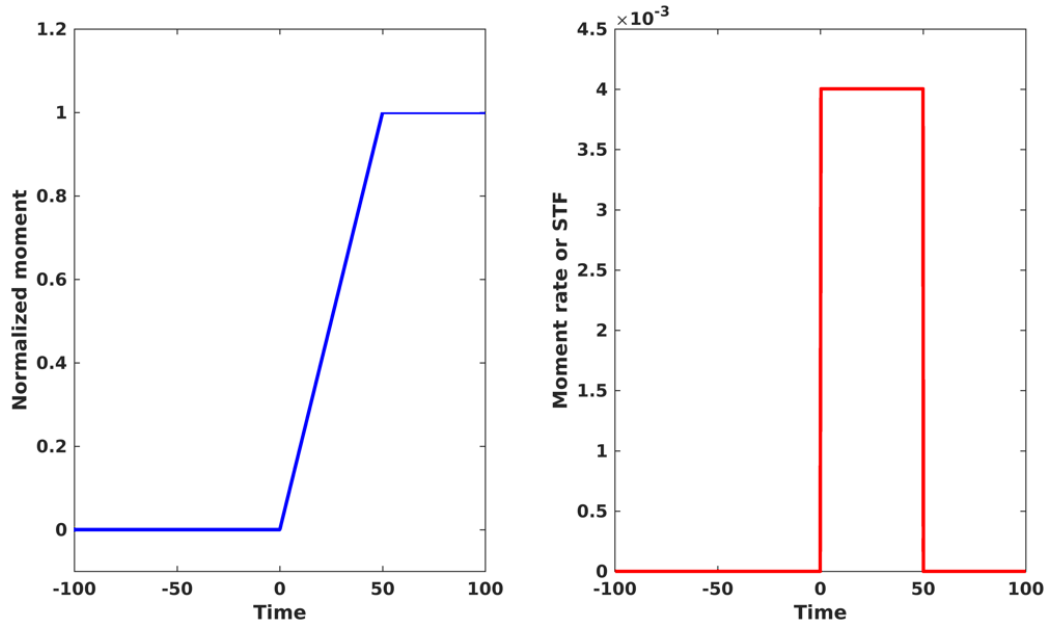
Fig. III.9: Modeled moment and moment rate function (ramp). Left: Seismic moment function (ramp) modeled from **equation (III.27)**, with $\tau_r = 50$. Right: rectangular-shaped source time function, modeled from **equation (III.28)**.

A more realistic source time function (STF) features a continuous moment rate or slip velocity that smoothly increases from zero to a maximum and then decreases back to zero can be produced if we consider a time dependent moment with a continuous increase (segmoid-shaped) see **Fig. III.10**, such moment function is given by:

$$M_0(t) = \begin{cases} M_0 \dfrac{2t^2}{\tau_r^2}, & if\ 0 < t < \tau_r/2 \\[2mm] M_0 \left[\dfrac{2t(2\tau_r - t)}{\tau_r^2} - 1\right], & if\ \tau_r/2 < t < \tau_r \\[2mm] M_0, & if\ \ \ \ \ \ \tau_r < t \end{cases} \tag{III.29}$$

The derivation of this moment function gives us a triangular-shaped STF, (see **Fig. III.10**) where the slip velocity rises and falls linearly, providing a more physically plausible representation of the earthquake's rupture process compared to the idealized rectangular function, such STF is given by:

$$\dot{M}_0(t) = \begin{cases} M_0 \dfrac{4t}{\tau_r^2}, & if \ 0 < t < \tau_r/2 \\[2ex] M_0 \left[\dfrac{4(\tau_r - t)}{\tau_r^2} \right], & if \ \tau_r/2 < t < \tau_r \end{cases} \qquad (III.30)$$
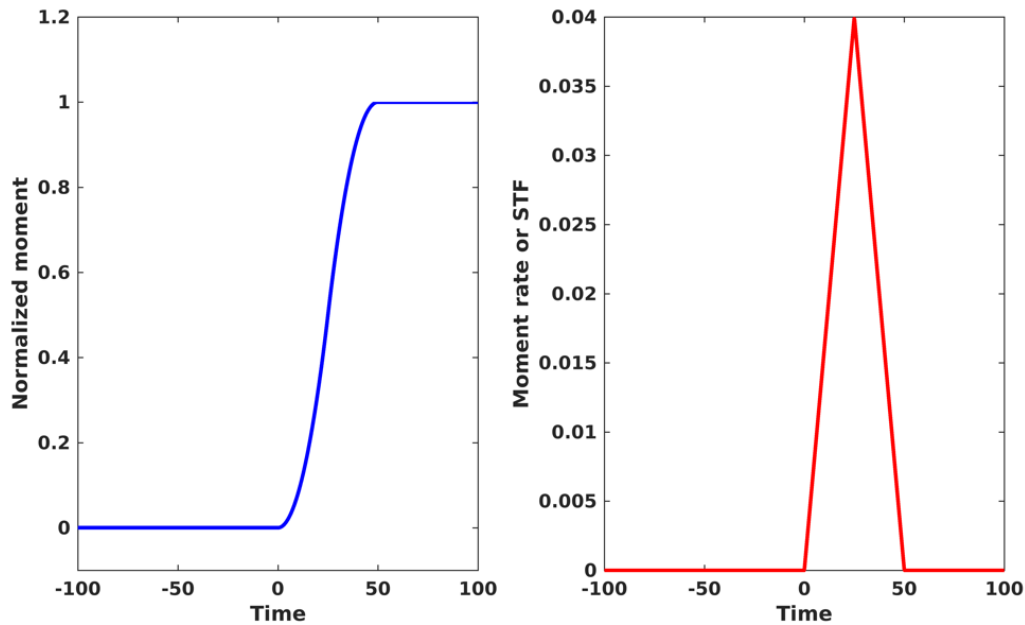
Fig. III.10: Modeled moment and moment rate function (sigmoid). Left: Continuously increasing seismic moment function (sigmoid) modeled from **equation (III.29)**, with $\tau_r = 50$. Right: triangular-shaped source time function, modeled from **equation (III.30)**.

It is important to consider one of the most important source time functions proposed by Brune (1970), which is commonly used to model the seismic radiation from small earthquakes. Unlike some earlier models that may have discontinuities or sharp changes, Brune's model is characterized by the moment being a continuous function of time, see **Fig. III.11**. This continuity makes it more physically realistic and applicable to a wide range of small earthquake scenarios. The time-dependent moment function in this case is given by:

$$M_0(t) = M_0 \left[1 - \left(1 + \frac{t}{\tau_r} \right) e^{\frac{-t}{\tau_r}} \right] H(t) \tag{III.31}$$

The STF for this model is given by:

$$\dot{M}_0(t) = M_0 \frac{t}{\tau_r^2} e^{\frac{t}{\tau_r}} H(t) \tag{III.32}$$

Fig. III.11 exhibits the shape of the STF in this model. In this scenario, the rise time τ_r represents the duration of the source's activity, but after this period, the moment continues to increase gradually, approaching the value M_0 asymptotically.
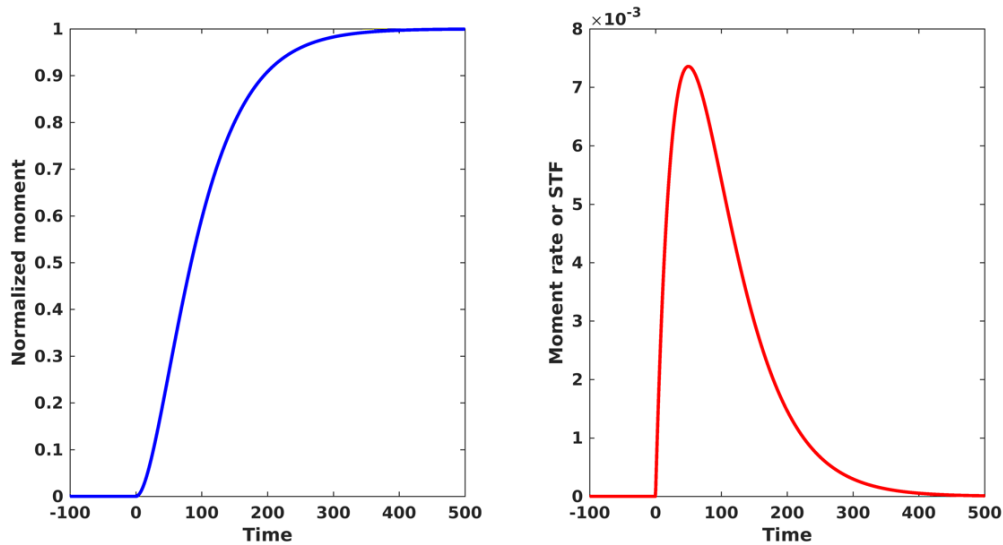
Fig. III.11: Modeled Brune's moment and moment rate function. Left: Brune's seismic moment function modeled from **equation (III.31)**, with $\tau_r = 50$. Right: Brune's source time function, modeled from **equation (III.32)**.

It is quite interesting to investigate the frequency characteristics of source time functions. These characteristics can be observed in Fourier domain. For the two STFs that are realistic, the triangular STF (**equation (III.30)** and **Fig. III.10**) and Brune's signal (**equation (III.32)** and **Fig.III.11**), their Fourier Transforms are respectively:

$$M_0(w) = \frac{M_0}{w} \left[\frac{\tau_r \sin\left(\frac{w\tau_r}{2}\right)}{\frac{w\tau_r}{2}} \right] e^{\left[i\left(\frac{w\tau_r}{2} - \frac{\pi}{2}\right)\right]} \tag{III.33}$$

$$M_0(w) = \frac{M_0}{1 + w^2 \tau_r^2} \tag{III.34}$$

In both cases the amplitude spectrum decays with frequency as w^{-2} (**Fig. III.12** upper and lower right corners). The Fourier spectrum of the STF tend towards M_0 when w tends towards 0 $\left(\lim\limits_{w \to 0} \dot{M}_0(w) = M_0\right)$
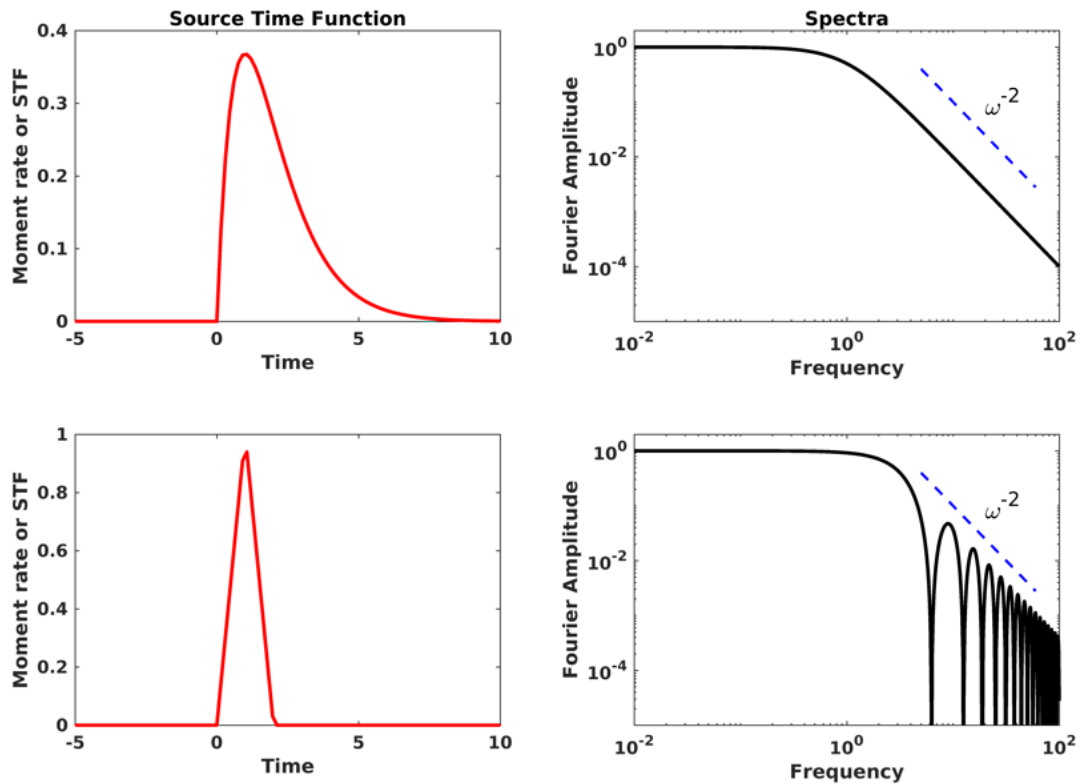
Fig. III.12: Spectral characteristics of STFs; upper and lower left panels are Brune's and triangle STF. Upper and lower right panels are their correspondent Fourier spectra modeled using **equation (III.34)** and **(III.33)**, respectively.

In other words, at low frequencies, the amplitude of the Fourier spectrum closely resembles the time integral of the STF, which corresponds to the earthquake's moment.

This characteristic is evident in the two source time functions given by **equation (III.33)** and **(III.34)**. And **Fig. III.12** (upper and lower right corners).

As the frequency increases, the amplitude begins to decay at the corner frequency $f_c = 1/\tau_r$. This behavior is characteristic of seismic sources with limited duration, where the far-field displacements, having the same time dependence as the moment rate, exhibit a similar frequency decay. This general pattern is observed in many far-field body wave spectra and can be approximated by a constant value at low frequencies and an w^{-2} decay at higher frequencies for point source models with finite rise time τ_r. (Aki 1967; Brune 1970)

III.6 The Empirical Green's Function (EGF) Approach for Source Parameters Estimation

Empirical Green's Function (EGF) is a widely used method in seismology for estimating earthquake source parameters. The technique leverages recordings from smaller, nearby earthquakes (termed "empirical Green's functions") that have similar source, path, and site effects as the larger event of interest. By deconvolving these smaller events from the records of a larger earthquake, we empirically correct the seismogram of the larger events from instrument and whole path effects. Hence, we can better understand the source characteristics of the larger event. To use this method some crucial criteria need to be verified, these criteria are:

1) proximity in space: The EGF event should be located very close to the larger event (horizontally and vertically). This spatial proximity ensures that both events experience similar path effects, such as wave propagation through the Earth's crust, which can otherwise distort the analysis.

2) Similarity in Source Mechanisms: The EGF event should have a source mechanism similar to that of the larger target earthquake. This theoretically imply having similar waveform, to ensure that the radiation patterns of seismic waves are comparable.

3) Magnitude difference: The magnitude difference between the target event and the EGF event should be significant, at least 1 magnitude units. This difference ensures

that the EGF event is small enough to act as a Green's function but still large enough to provide a clear signal for deconvolution.

4) Stationarity of Path Effects: The path effects, such as attenuation and scattering, should be stationary, meaning they do not change significantly between the EGF and target events. This ensures that the path effects can be effectively canceled out during the deconvolution process. This is also called far source condition.

Under the aforementioned conditions, we assume that the seismogram of the smaller earthquake serves as an EGF, which can be utilized to determine the characteristics of the larger shock. The following mathematical development further illustrates this concept.

In seismology it is well known that the seismic record of an earthquake contains information on the earthquake source, the path the seismic waves propagated through, the site response of the geology beneath the recording site, and the response of the instrument that recorded the ground motion. Therefore, an earthquake seismogram, $U(t)$, is the convolution of the radiation from the earthquake source, $S(t)$, with the combined propagation effects, $P(t)$, along the path, and finally the instrument response, $I(t)$.

$$U(t) = S(t) * P(t) * I(t) \qquad \text{(III.35)}$$

If we use the sub-script (M) and (EGF) to refer the main shock and the EGF respectively we can write:

$$U_M(t) = S_M(t) * P_M(t) * I_M(t) \qquad \text{(III.36)}$$

$$U_{EGF}(t) = S_{EGF}(t) * P_{EGF}(t) * I_{EGF}(t) \qquad \text{(III.37)}$$

Passing to the frequency domain where the convolution product becomes a simple multiplication and the deconvolution a simple division, **equation (III.36)** and **(III.37)** can be written respectively as:

$$U_M(f) = S_M(f) \cdot P_M(f) \cdot I_M(f) \qquad \text{(III.38)}$$

$$U_{EGF}(f) = S_{EGF}(f) \cdot P_{EGF}(f) \cdot I_{EGF}(f) \qquad \text{(III.39)}$$

If we look at the propagation effects and the instrument response for both main shock and EGF to be identical, (i,e $P_{EGF}(f) = P_M(f) \; and \; I_{EGF}(f) = I_M(f)$), and we assume that the EGF earthquake source is a point-source in time, and hence, S_{EGF} is a scalar value rather than a function of time. Several studies have confirmed this approximation for EGF events when the main shock is at least one unit of magnitude larger than the EGF event (e.g., Frankel & Kanamori 1983; Hutchings & Wu 1990). Therefore, we can write:

$$U_M(f) = \frac{S_M(f)}{S_{EGF}(f)} \cdot U_{EGF}(f) = RSTF. U_{EGF}(f) \qquad \text{(III.40)}$$

Where RSTF is the relative source time function.

In practice, we calculate the complexes spectra of both target and EGF events, in a window where SNR is good for both events. After that a complex spectral division is performed to obtain a spectral ratio, in this method there is no need to correct the spectra for path and instrument responses as mentioned before.

After that the corner frequencies of the target and the EGF, and the ratio between their seismic moment are estimated by fitting the spectral ratio using the Boatwright, 1980 modified spectral source model of.

$$\Omega_r(f) = \Omega_{0r} \left[\frac{1 + \left(\frac{f}{f_{c2}}\right)^{\gamma n}}{1 + \left(\frac{f}{f_{c1}}\right)^{\gamma n}} \right]^{\frac{1}{\gamma}} \qquad \text{(III.41)}$$

Where $\Omega_r(f)$ is the relative spectral ratio, Ω_{0r} is the ratio between the two seismic moments. f is the frequency, and γ and n are constants ($\gamma = n = 2$ according to boatwright model) that control the shape of the spectrum curvature around the corner frequency and the high frequency falloff, respectively.

The data fitting is done by minimizing the following misfit function:

$$res = \sum_{i=1}^{N} \left(log\Omega_{r\_mod}(f_i) - log\Omega_{r\_obs}(f_i) \right)^2 \qquad (III.42)$$

Where the indices r_mod and r_obs refer to the model and observed spectral ratios respectively, and N is the number of points in the spectral ratio. The values of f_{c1}, f_{c2} and Ω_{0r} that minimize the mis-fit function *(res)* are the best estimates.

Ones the corner frequencies are determined the source parameters (source radius and stress drop) can be calculated using **equation (III.21)** or **(III.22)** for source radius and **(III.24)** for stress drop.

The EGF method only resolve for relative seismic moment, because absolute seismic moment cannot be calculated using this method, (Viegas 2012; Abercrombie 2015) that's why in several studies when it comes to the seismic moment estimation they use individual spectral analysis for seismic moment estimation.

Fig. III.13 illustrates the general concept of the EGF approach.
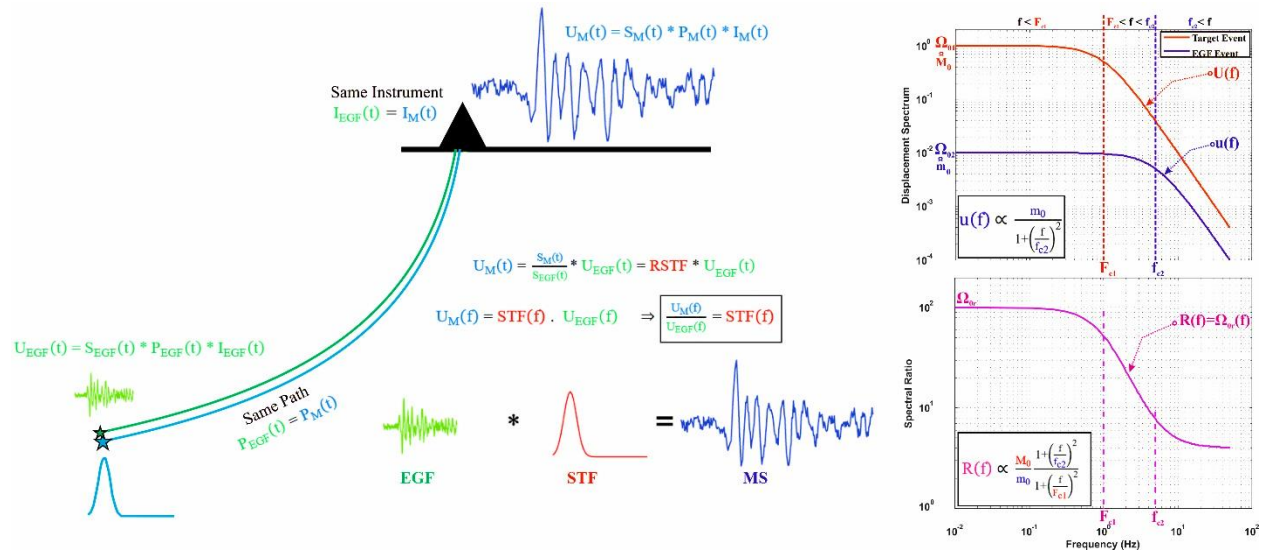
Fig. III.13: Summary of the methodology used in the Empirical Green's Function approach for source parameters estimation. (Modified after Boulahia 2022)

III.7 Scaling relationships

Earthquakes exhibit a vast range in size, from minor events that can only be detected with highly sensitive instruments to large-scale earthquakes that cause catastrophic damage and rupture the ground across hundreds of kilometers. To better understand these events, researchers have developed scaling laws that relate various seismic parameters, allowing some parameters to be expressed in terms of more fundamental ones. The first of these scaling laws was introduced by (Aki 1967). He proposed that different magnitude scales could be unified by assuming that all earthquakes share a seismic wave spectrum characterized by a flat amplitude at low frequencies and a ω^{-2} decay at higher frequencies, akin to the Brune model. By analyzing the spectra of earthquakes of different sizes, Aki discovered that the corner frequency f_c is inversely proportional to the earthquake's size. He further showed that the seismic moment M_0 is proportional to the stress drop $\Delta\sigma$, the cube of the source radius R, and inversely proportional to the cube of the corner frequency:

$$M_0 \approx \Delta\sigma R^3 \approx \Delta\sigma f_c^{-3} \qquad\qquad (\text{III.43})$$

This relationship implies that, within an order of magnitude, the stress drop $\Delta\sigma$ remains fairly consistent across different earthquakes, typically ranging between 0.1 and 100 MPa, as observed by (Kanamori & Anderson 1975; Hanks 1977). These findings are further supported by several compilations of data showing that earthquake moments span 10 orders of magnitude, filling a region bounded by lines corresponding to stress drops of 0.1 to 100 MPa for equivalent circular faults, one of the widely known compilations is that of (Abercrombie & Leary 1993), see **Fig. III.14**. This consistency in stress-drop across diverse seismic events provides key insights into the underlying physics of earthquake rupture processes. Madariaga, 2015.
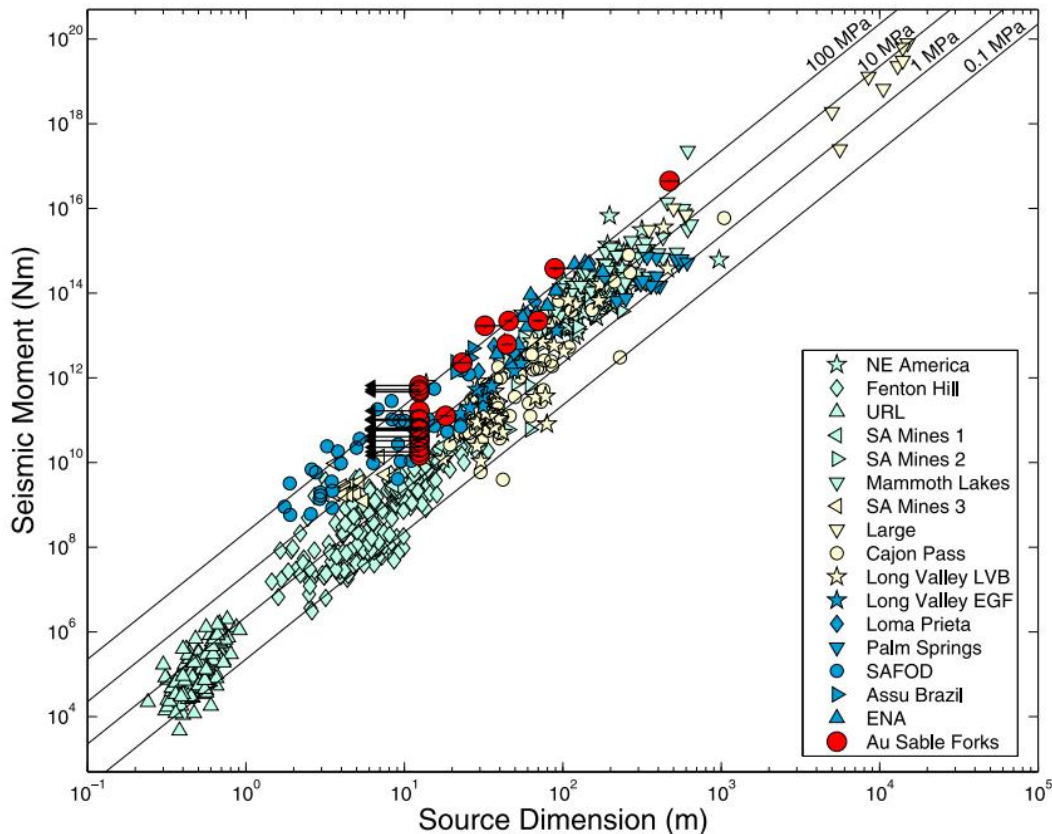
Fig. III.14: Global compilation of seismic moment versus source radius using different methods. After (Viegas *et al.* 2010). Adapted from Abercrombie & Leary (1993).

III.8 Application on BI-2010 seismic sequence

As mentioned in the introduction, understanding earthquake source parameters is essential for unraveling the physics behind earthquake generation and propagation. Key parameters such as seismic moment, stress drop, and source radius provide valuable insights into the energy release, fault dynamics, and scale of seismic events. In the context of the BI-2010 sequence, the only published study in this regard by Abacha *et al.* (2019) analyzed the dynamic source parameters of the 18 largest events (Md ≥ 4) using Brune's (1970) seismic source model. The authors performed both P and S wave analyses and estimated corner frequencies ranging from 0.8 to 2.5 Hz, with $f_c(P) > f_c(S)$, consistent with other studies. They found seismic moments (M_0) ranging from 5.5×10^{14} to 1.6×10^{17} N m, source radii from 735 to 2266 m, and stress drops ($\Delta\sigma$) from 0.2 to 11 MPa. One of their

key findings, through scaling relations, was the identification of linear correlations, indicating constant stress drops for events with $M_0 > 2 \times 10^{16}$ Nm, while smaller events showed decreasing stress drops with decreasing M_0, suggesting a breakdown of self-similarity. This study is of great importance as it represents the first analysis of dynamic source parameters in the BI region. However, our goal is to conduct a more comprehensive analysis, not only of the 18 largest events but of a much larger dataset of 41 events with M3+, utilizing a combined approach that includes both individual and Empirical Green's Function (EGF) methods.

III.8.1 EGF Candidates' Selection

Accurate selection of Empirical Green's Function (EGF) candidates is crucial for reliable seismic source parameter estimation. The EGF method relies on using smaller, simpler earthquakes as proxies to isolate the path and site effects, enabling the extraction of the source characteristics of a larger target earthquake. The effectiveness of this approach hinges on the selection of appropriate EGFs. An accurately chosen EGF ensures that the deconvolution process accurately reflects the source properties of the larger earthquake, minimizing the introduction of artifacts or errors. Conversely, an inappropriate EGF selection can lead to significant misinterpretations of the source parameters, such as incorrect estimates of stress drop, and rupture dimensions. Therefore, careful and precise EGF candidate selection is essential to obtain meaningful and accurate insights into the earthquake source dynamics.

In this regard, I developed a MATLAB code (EGF_candidates.m) to identify all potential M3.0+ events and their best EGF candidates, primarily based on 3D spatial proximity, magnitude differences, and focal mechanism similarities. Since magnitude difference is a critical criterion for selecting suitable EGFs, we used our local magnitude relationship established by Roubeche *et al.* (2024) to calculate the local magnitudes (ML) for the 1998 relocated events when possible. We successfully calculated ML for 1958 of these events.

The EGF_candidates.m program takes the catalog as an input file and, for each event, iteratively verify the following criteria against all the other events in the catalog. The selection procedure adheres to the following conditions:

1. For mainshocks (MS-1, MS-2, or MS-3), the maximum epicentral and hypocentral separations are set to 2 km.

2. For aftershocks, the maximum epicentral and hypocentral separations are set to 1 km.

3. The magnitude difference should be >1 and ≤4 for mainshocks and aftershocks.

Setting a condition on hypocentral separation is crucial because two events might appear close on the horizontal plane but could be distant in depth (see **Fig. III.15-** upper left corner). We assume that events meeting these criteria originate from a common fault source and share the same path to the station (see **Fig. III.15-** upper and lowerright corner).
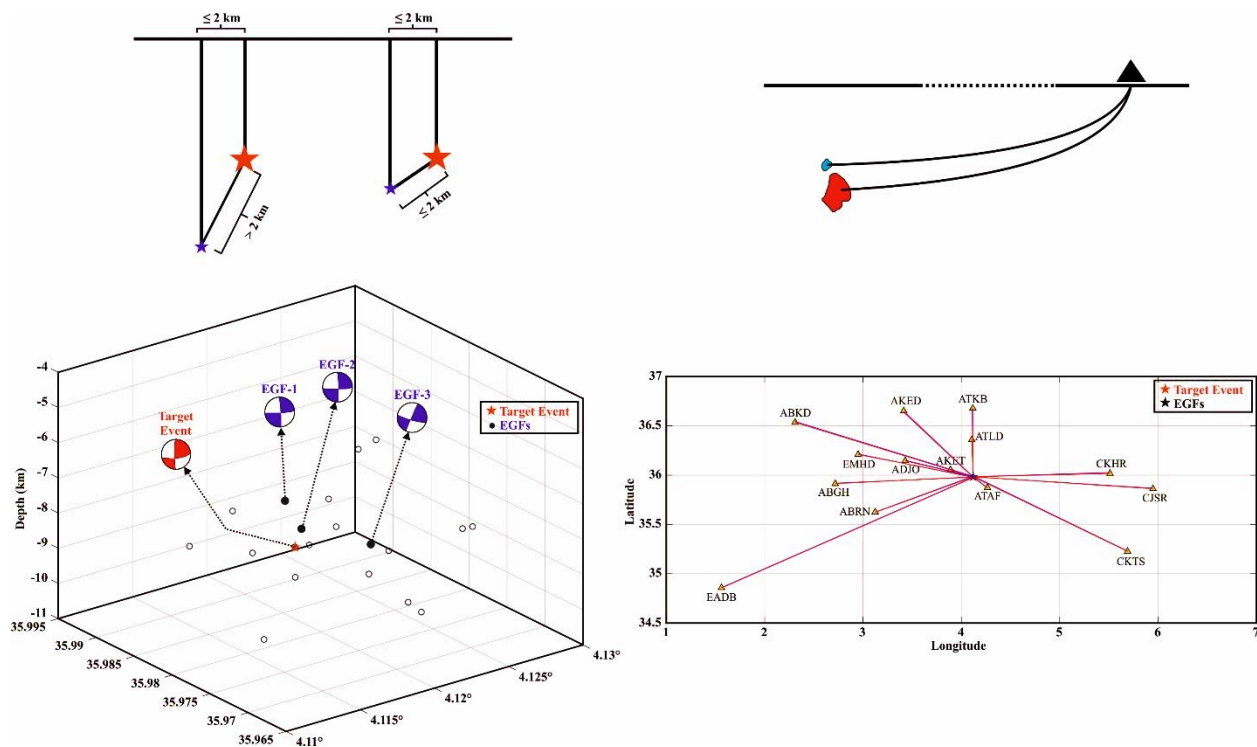
Fig. III.15: EGF candidates' selection; Upper left: the effect of spatial proximity. Upper right: the far source approximation so the target and EGF event travel through approximately the same path. Lower right: horizontal distribution of MS-1 and its best

selected EGFs. Lower left: MS-1 and its best selected EGFs in 3D space, the similarity of faulting mechanism is also depicted.

It is worth noting that some target events may share common EGFs, and some target events may also serve as EGFs for larger ones. However, the fact that multiple EGF candidates exist for each target event (see **Fig. III.15-** lower left corner) does not mean all will be used, as this would be exhaustive. Instead, we select a minimum of 1 and a maximum of the 4 best EGFs for each target event, based on their focal mechanism similarities (see **Fig. III.15-** lower left corner).

Fig. III.16 exhibit the number of EGF candidates for each target events
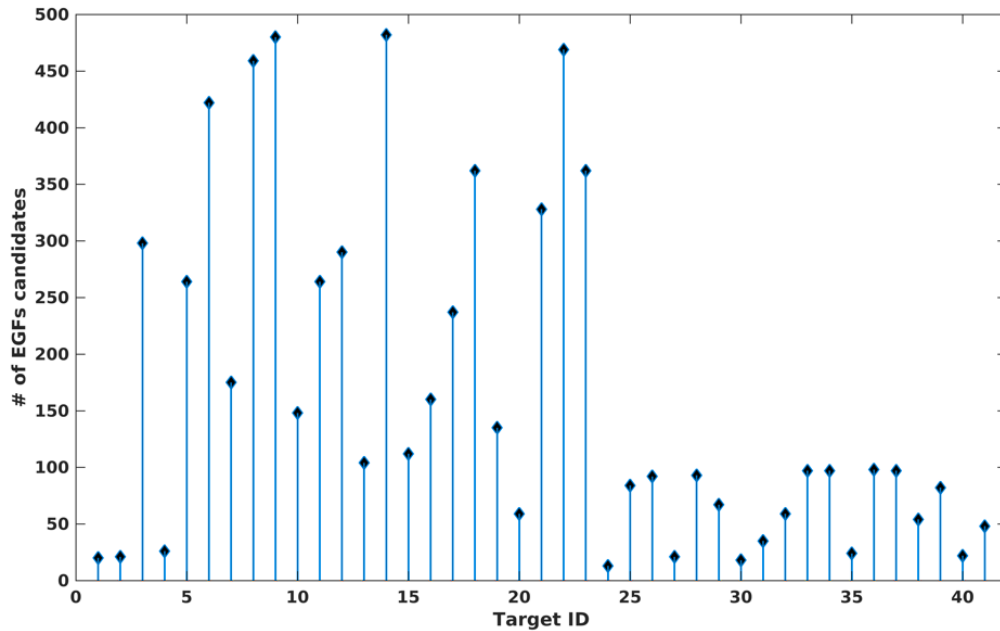
Fig. III.16: number of EGFs candidates per target event.

III.8.2 Source Parameters Estimation (Results)

As we have mentioned before, we estimate source parameters from individual spectra approach and EGF approach simultaneously. In this regard, we used a modified version of codes developed by Boulahia (2022).

a) Individual Spectra Approach

Before initiating the EGF analysis, we estimated the source parameters for each target event using the individual spectra approach, focusing exclusively on the P-wave onset. The analysis was conducted on the vertical component data from 14 stations of the Algerian Digital Seismological Network (ADSN), including stations EADB, ABKD, ABGH, EMHD, ABRN, ADJO, AKED, AKET, ATLD, ATKB, ATAF, CKHR, CJSR, and CKTS. A variable time window of 1 to 5.5 seconds was used for P-waves, depending on the S-P time difference at each station.

We only use data with an SNR>=3. After removing the instrument response, the traces were pre-processed before calculating the Fourier spectra. This pre-processing included baseline correction, removal of linear trends, and the application of a 10% cosine taper. Tapering is a crucial step before transitioning to the Fourier domain to avoid spectral leakage. The resulting amplitude spectra of the velocigrams were then integrated into displacement through a simple division by $2\pi f$.

The displacement spectra from each station were corrected for both geometrical spreading and attenuation. Unlike Abacha et al. (2019), whom corrected their spectra for attenuation using pre-fixed values of Q_0 and $Q\alpha$ and optimized only ω_0 and f_c as free parameters. We employed the Nelder-Mead-Simplex optimization function, and we minimized the misfit function while treating Q_0, $Q\alpha$, ω_0, and f_c as free parameters. The values of f_c, ω_0, and Q that minimize the misfit are considered the best estimates of these parameters. It is important to note that in this study, we will not discuss the obtained attenuation parameters (Q_0 and $Q\alpha$). After obtaining f_c and ω_0, we used the relevant equations to calculate the seismic moment, source radius and stress drop.

Figures (**Fig. III.17, III.18,** and **III.19**) exhibit examples of source parameters estimation of MS-1, MS-2 and MS-3 respectively. All the examples are from ATAF station.
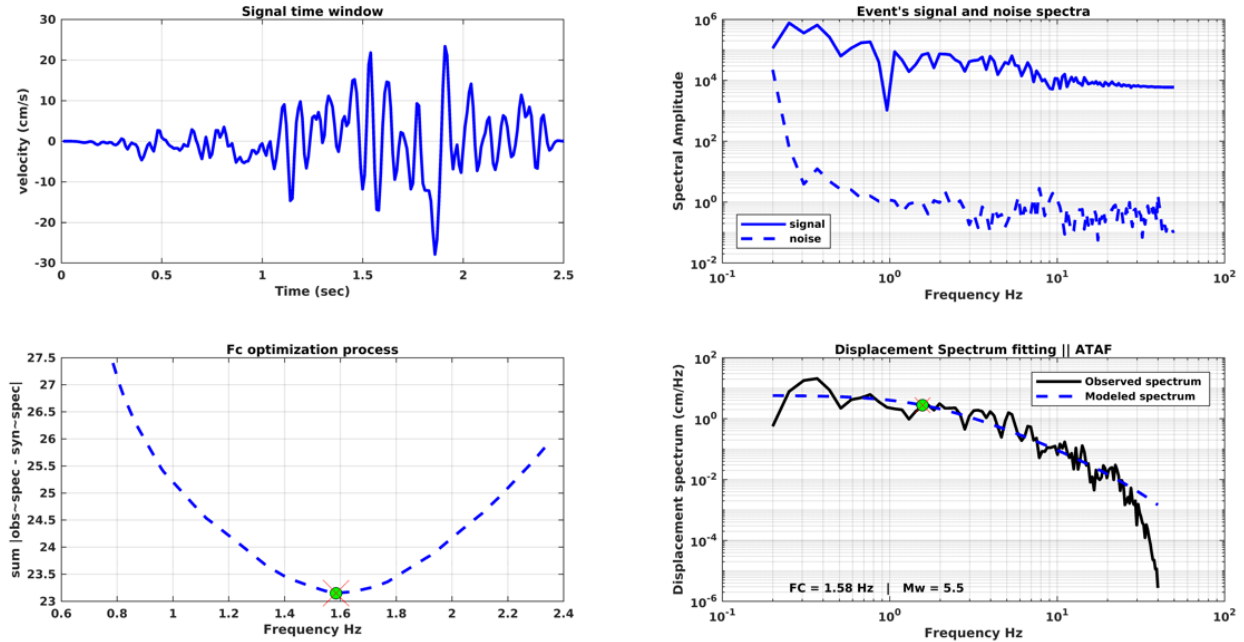
Fig. III.17: Example of source parameters estimation for MS-1 (2010.05.14-12.29.20) using individual spectra approach. Upper left corner: is velocity corrected signal. Upper right corner: signal and noise spectra. Lower left corner: corner frequency optimization process. Lower right corner: black curve is the observed spectrum and the dashed blue line is the modeled spectrum.
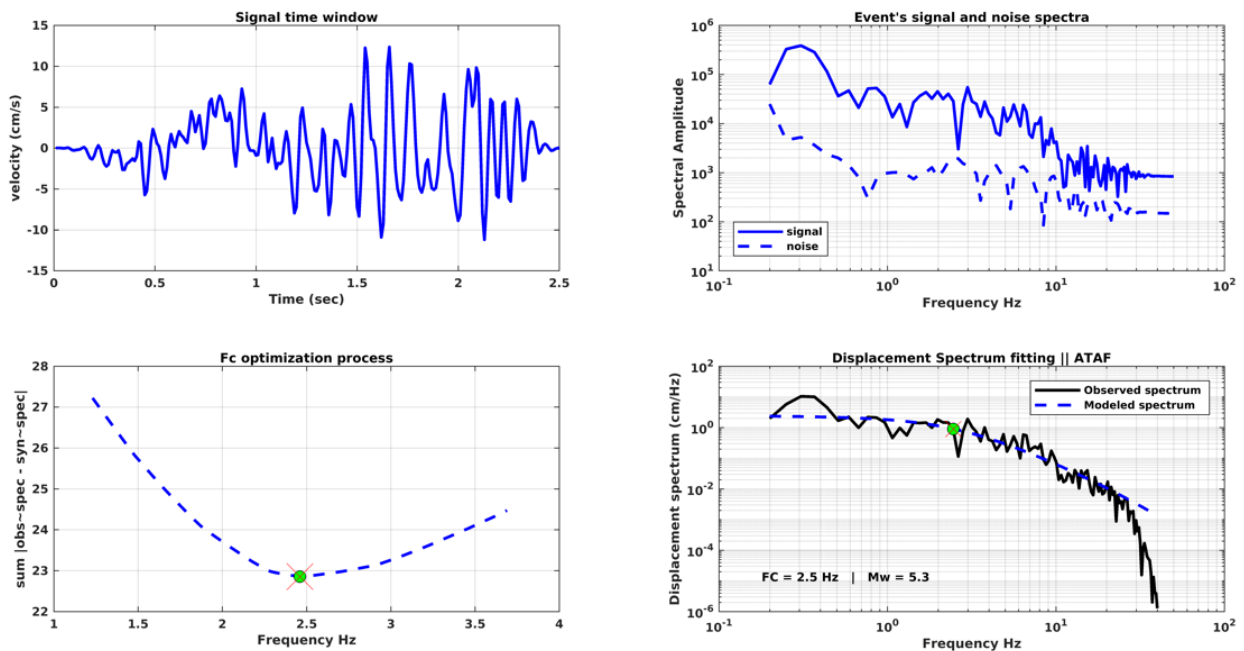
Fig. III.18: The same as fig. III.17, but for MS-2 (2010.05.16-06.52.39).
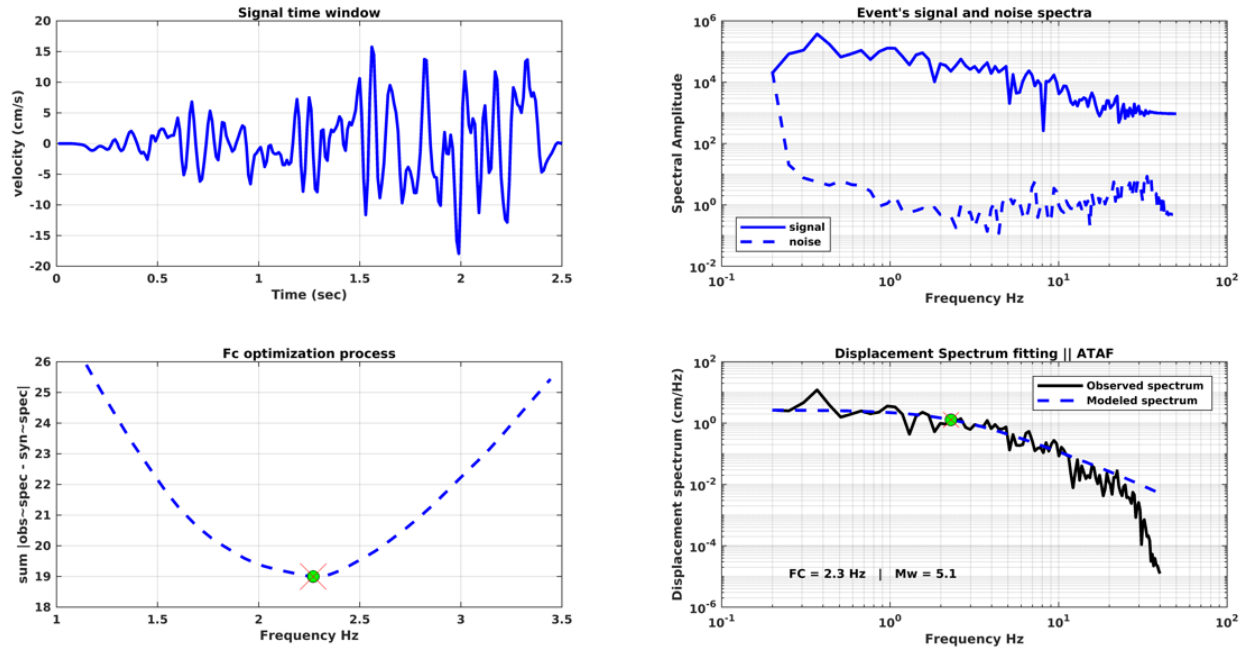
Fig. III.19: The same as Fig. III.17 but for MS-3 (2010.05.23-13.28.16)

The following table (**Table III.1**) presents the results for all 41 target events, with all results averaged using the formulas provided by Archuleta *et al.* (1980).

Table. III.1: Source parameters using individual spectra approach. Columns from left to right: YYYY (year), MM (month), DD (day), HR (hour), MNT (minute), SEC (seconds), M_0 (seismic moment in N.m), M_w (moment magnitude), f_c (corner frequency in Hz), R_B (source radius in meters, using Brune's model), R_M (source radius in meters, using Madariaga's model), $\Delta\sigma_B$ (stress drop in MPa, using Brune's source radius), $\Delta\sigma_M$ (stress drop in MPa, using Madariaga's source radius).

YYYY	MM	DD	HR	MNT	SEC	M_0	M_W	f_c	R_B	R_M	$\Delta\sigma_B$	$\Delta\sigma_M$
2010	5	14	12	29	20	1.28E+17	5.37	0.75	2585.31	1260.22	3.23	27.93
2010	5	16	6	52	40	5.51E+16	5.13	0.79	2454.99	1196.69	1.63	14.07
2010	5	23	13	28	16	6.00E+16	5.15	0.87	2226.07	1085.11	2.38	20.55
2010	5	16	3	51	29	7.73E+15	4.56	1.32	1467.2	715.19	1.07	9.24
2010	5	24	21	0	38	8.88E+15	4.6	1.3	1490.24	726.42	1.17	10.14
2010	5	14	23	43	21	2.91E+15	4.28	1.7	1140.73	556.05	0.86	7.41
2010	5	25	13	5	10	1.42E+15	4.07	2.99	647.74	315.74	2.29	19.79
2010	5	14	15	13	14	4.67E+15	4.41	1.36	1418.86	691.63	0.72	6.18
2010	5	31	16	5	3	4.65E+15	4.41	1.47	1317.66	642.3	0.89	7.67
2010	7	12	16	32	52	1.26E+15	4.04	1.94	998.81	486.87	0.55	4.77
2010	5	26	17	49	44	1.08E+15	3.99	2.11	918.32	447.64	0.61	5.25
2010	5	15	9	12	38	2.96E+14	3.62	3.44	562.96	274.42	0.73	6.27
2010	5	23	23	39	54	9.36E+14	3.95	2.79	695.18	338.87	1.22	10.53
2010	5	28	13	24	44	5.17E+14	3.78	3.13	618.72	301.6	0.95	8.24
2010	7	10	15	33	43	7.54E+13	3.22	5.06	382.73	186.56	0.59	5.08
2010	5	23	13	32	3	5.99E+14	3.82	2.86	677.99	330.49	0.84	7.25
2010	5	26	20	47	39	3.37E+14	3.66	3.21	603.3	294.08	0.67	5.8
2010	7	20	12	55	39	1.86E+14	3.48	3.62	535.05	260.81	0.53	4.59
2010	8	3	8	20	40	2.94E+14	3.62	3.3	586.01	285.65	0.64	5.52

2010	5	16	9	46	2	7.98E+14	3.9	2.74	706.79	344.53	0.99	8.54
2010	5	23	14	9	53	1.91E+14	3.49	3.28	590.43	287.8	0.41	3.51
2010	5	24	23	48	25	2.73E+14	3.59	3.2	604.26	294.55	0.54	4.67
2010	7	4	22	21	29	2.66E+14	3.59	3.45	561.33	273.62	0.66	5.68
2010	7	25	9	3	1	9.05E+13	3.27	4.59	421.92	205.66	0.53	4.55
2010	5	15	0	18	49	6.7E+13	3.19	5.63	343.98	167.67	0.72	6.22
2010	5	25	18	4	26	2.04E+14	3.51	3.55	545.52	265.92	0.55	4.75
2010	5	18	2	47	18	7.19E+13	3.21	4.04	479.36	233.66	0.29	2.47
2010	5	30	4	48	30	7.02E+13	3.2	4.76	406.85	198.32	0.46	3.93
2010	5	25	2	5	0	2.8E+14	3.6	2.9	667.79	325.52	0.41	3.55
2010	5	26	20	49	25	1.53E+14	3.43	3.44	562.96	274.42	0.37	3.24
2010	5	21	12	16	18	5.04E+14	3.77	2.72	711.98	347.06	0.61	5.27
2010	5	15	0	0	41	1.14E+15	4.01	2.29	845.68	412.23	0.82	7.1
2010	5	19	23	59	50	6.94E+14	3.86	2.92	663.22	323.29	1.04	8.99
2010	5	14	16	15	33	2.27E+14	3.54	3.2	604.46	294.64	0.45	3.88
2010	5	25	8	9	5	1.01E+14	3.31	4.2	461.09	224.76	0.45	3.89
2010	5	16	23	2	26	9.07E+13	3.27	4.31	449.33	219.03	0.44	3.78
2010	5	24	13	11	2	2.15E+14	3.52	3.64	532.03	259.34	0.62	5.38
2010	6	23	21	44	59	7.88E+13	3.23	4.73	409.43	199.58	0.5	4.34
2010	8	9	3	40	54	1.67E+14	3.45	3.68	526.25	256.52	0.5	4.33
2010	6	4	22	10	41	1.88E+14	3.49	4.24	456.74	222.64	0.86	7.46
2010	5	17	15	52	29	2.01E+14	3.51	3.54	547.06	266.67	0.54	4.65

b) EGF Approach

As previously mentioned, the EGF method is highly effective in accurately retrieving earthquake source properties, primarily because it empirically corrects for path effects. We used uncorrected raw signals with variable P-wave time windows, depending on the S-P time difference of the EGF event. Additionally, only data with an SNR greater than 3 were used.

To deconvolve the EGF event from the target event, we utilized the code developed by Prieto *et al.* (2009), which automatically calculates the multitapered complex Fourier spectra of the signals from both earthquakes and performs the complex spectral division. Multitapering is an extension of single taper approaches; it involves dividing the data into overlapping subsets, each individually tapered and Fourier transformed. The individual spectral coefficients of each subset are then averaged to reduce variance.

The multitaper technique outperforms standard individual taper methods, such as the Tukey taper method (used in **sub-chapter III.4**), by more effectively preventing spectral leakage and preserving the spectral shape. We used multitapering with a time-bandwidth product of 4 and 7 Slepian tapers, as explained in **Fig. III.20**.
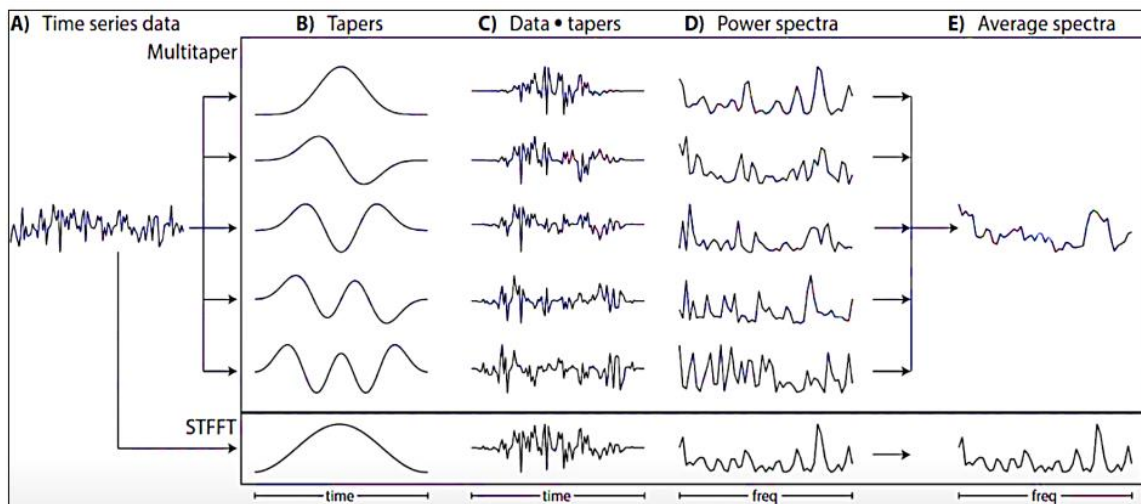
Fig. III.20: illustration of the Single Taper Fast Fourier Transform (STFFT) and the Multi Taper Fast Fourier Transform (MTFFT).

We computed the SNR spectral ratio for noise data using the same window duration on the pre-P portion of the seismogram. Using Boatwright's (1980) modified model (with γ = 2 and n = 2), we modeled the displacement amplitude spectral ratio Ω_r (f) to obtain the corner frequencies of both the target (f_{c1}) and EGF (f_{c2}), as well as the ratio between the two seismic moments $\Omega_{0r}(f)$. The best-fit model was determined by minimizing the objective function (**equation (III.42)**), using the Nelder-Mead-Simplex optimization algorithm. Figures (**Fig. III.21, III.22,** and **III.23**) exhibit examples of source parameters estimation of MS-1, using its three best EGFs; EGF1, EGF2 and EGF3 respectively. All the examples are from ATAF station.
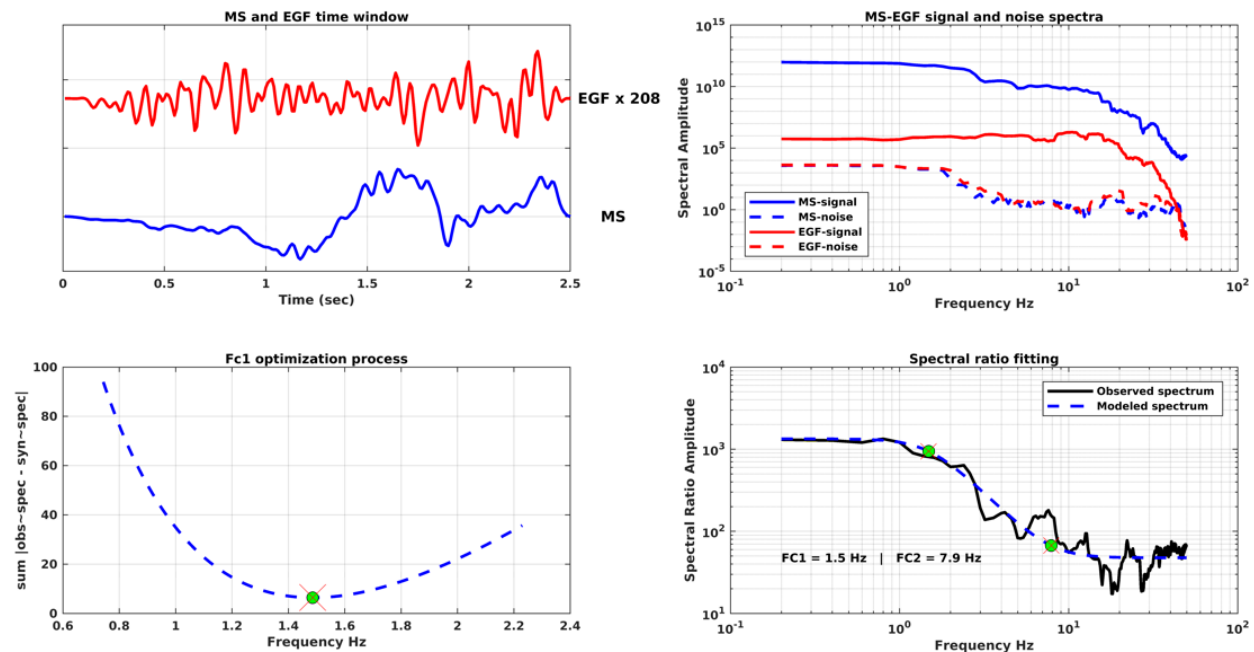
Fig. III.21: Example of source parameters estimation for MS-1 (2010.05.14-12.29.20) using event (2010.05.15-00.18.49) as an EGF. Upper left corner: are the two raw signals MS (blue) and EGF (red). Upper right corner: signal and noise spectra of both MS and EGF. Lower left corner: corner frequency (f_{c1}) optimization process. Lower right corner: black curve is the observed spectral ratio and the dashed blue line is the modeled spectral ratio, the dots indicate corner frequencies.
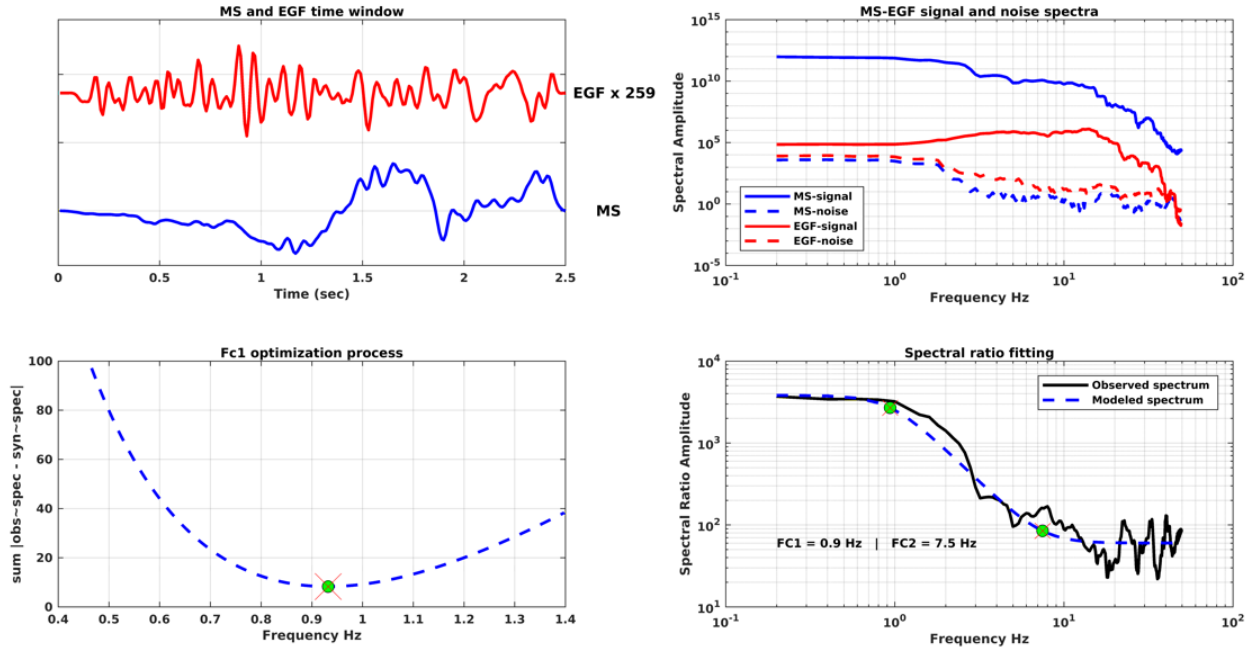
Fig. III.22: The same as fig. III.21, but with event (2010.05.14-16.33.20) as an EGF.
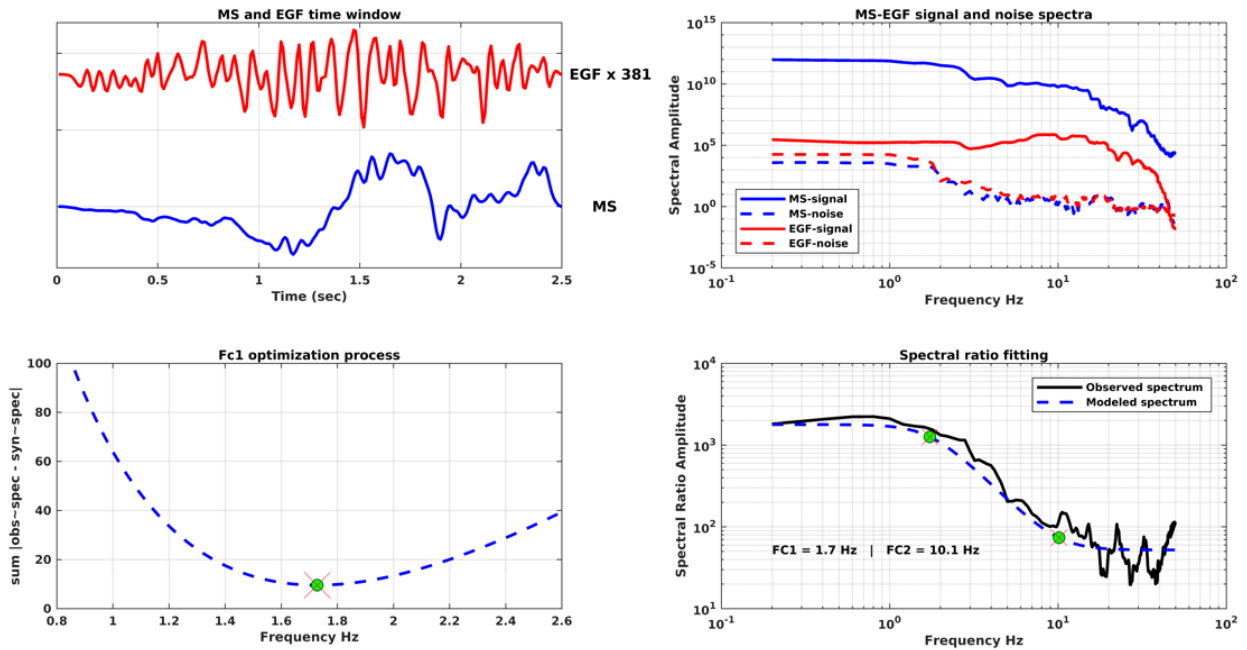
Fig. III.23: The same as fig. III.21, but with event (2010.06.15-21.07.12) as an EGF.

As mentioned earlier, the EGF method does not estimate the seismic moment for either the target or the EGF event directly; instead, it resolves only a relative estimation of the seismic moment of the EGF event. Therefore, we used the estimated seismic moment of the target event from individual source spectra. Then, using the seismic moment ratio (Ω_{0r}), we calculated the seismic moment of the EGF event. According to (Abercrombie & Rice 2005), the moments calculated from spectral ratios are typically within 20% of those calculated from individual spectra. The following table (**Table III.2**) presents the results obtained for the 41 target events using EGF approach. More details are presented in **Appendix B**, where we provide a comprehensive table including all the results from both individual spectra and the EGF method.

Table. III.2: Source parameters using the EGF approach. Columns from left to right: YYYY (year), MM (month), DD (day), HR (hour), MNT (minute), SEC (seconds), M_0 (seismic moment in N.m), M_w (moment magnitude), F_{c1} (corner frequency of the target event in Hz), R_B (source radius in meters, using Brune's model), R_M (source radius in meters, using Madariaga's model), $\Delta\sigma_B$ (stress drop in MPa, using Brune's source radius), $\Delta\sigma_M$ (stress drop in MPa, using Madariaga's source radius).

YYYY	MM	DD	HR	MNT	SEC	M_0	M_w	f_{c1}	R_B	R_M	$\Delta\sigma_B$	$\Delta\sigma_M$
2010	5	14	12	29	20	1.28E+17	5.37	1.12	1731.84	844.19	10.76	92.91
2010	5	16	6	52	40	5.51E+16	5.13	1.36	1421.04	692.69	8.4	72.52
2010	5	23	13	28	16	6.00E+16	5.15	1.35	1439.48	701.68	8.8	76.01
2010	5	16	3	51	29	7.73E+15	4.56	1.85	1045.69	509.73	2.96	25.53
2010	5	24	21	0	38	8.88E+15	4.6	1.81	1072.07	522.59	3.15	27.23
2010	5	14	23	43	21	2.91E+15	4.28	2.76	701.57	341.98	3.69	31.86
2010	5	25	13	5	10	1.42E+15	4.07	5.37	360.88	175.91	13.26	114.45
2010	5	14	15	13	14	4.67E+15	4.41	2.27	853.73	416.15	3.28	28.36
2010	5	31	16	5	3	4.65E+15	4.41	2.33	832.61	405.86	3.52	30.42
2010	7	12	16	32	52	1.26E+15	4.04	2.5	776.09	378.31	1.18	10.17
2010	5	26	17	49	44	1.08E+15	3.99	3.18	609.4	297.05	2.08	17.96
2010	5	15	9	12	38	2.96E+14	3.62	5.51	351.47	171.32	2.99	25.77
2010	5	23	23	39	54	9.36E+14	3.95	4.56	424.9	207.12	5.34	46.11
2010	5	28	13	24	44	5.17E+14	3.78	4.21	460	224.23	2.32	20.05
2010	7	10	15	33	43	7.54E+13	3.22	7.57	255.83	124.7	1.97	17.01
2010	5	23	13	32	3	5.99E+14	3.82	4.27	453.02	220.83	2.82	24.32
2010	5	26	20	47	39	3.37E+14	3.66	5.05	383.48	186.93	2.62	22.58
2010	7	20	12	55	39	1.86E+14	3.48	5.88	329.43	160.58	2.28	19.65
2010	8	3	8	20	40	2.94E+14	3.62	4.64	417.52	203.52	1.77	15.26

2010	5	16	9	46	2	7.98E+14	3.9	4.35	445.19	217.01	3.96	34.16
2010	5	23	14	9	53	1.91E+14	3.49	5.78	335.05	163.32	2.22	19.18
2010	5	24	23	48	25	2.73E+14	3.59	4.98	389.1	189.67	2.03	17.51
2010	7	4	22	21	29	2.66E+14	3.59	4.86	398.48	194.24	1.84	15.89
2010	7	25	9	3	1	9.05E+13	3.27	6.78	285.63	139.23	1.7	14.67
2010	5	15	0	18	49	6.7E+13	3.19	7.87	246.07	119.95	1.97	16.98
2010	5	25	18	4	26	2.04E+14	3.51	5.8	333.9	162.76	2.4	20.72
2010	5	18	2	47	18	7.19E+13	3.21	7.05	274.69	133.9	1.52	13.1
2010	5	30	4	48	30	7.02E+13	3.2	8.76	221.07	107.76	2.84	24.53
2010	5	25	2	5	0	2.8E+14	3.6	4.38	442.15	215.53	1.42	12.22
2010	5	26	20	49	25	1.53E+14	3.43	6.15	314.89	153.5	2.14	18.5
2010	5	21	12	16	18	5.04E+14	3.77	4.3	450.37	219.53	2.41	20.82
2010	5	15	0	0	41	1.14E+15	4.01	3.89	497.84	242.67	4.03	34.81
2010	5	19	23	59	50	6.94E+14	3.86	4.16	465.53	226.92	3.01	26
2010	5	14	16	15	33	2.27E+14	3.54	4.65	416.07	202.81	1.38	11.91
2010	5	25	8	9	5	1.01E+14	3.31	6.87	281.89	137.41	1.97	17.02
2010	5	16	23	2	26	9.07E+13	3.27	6.71	288.61	140.69	1.65	14.25
2010	5	24	13	11	2	2.15E+14	3.52	5.38	359.96	175.46	2.01	17.39
2010	6	23	21	44	59	7.88E+13	3.23	7.97	242.99	118.44	2.4	20.74
2010	8	9	3	40	54	1.67E+14	3.45	6.18	313.37	152.75	2.37	20.49
2010	6	4	22	10	41	1.88E+14	3.49	5.59	346.44	168.87	1.98	17.09
2010	5	17	15	52	29	2.01E+14	3.51	5.73	337.98	164.75	2.28	19.7

III.9 Results Analysis

III.9.1 Does Self-Similarity Really Break Down in Beni-Ilmane?

A significant question in seismology revolves around whether the faulting mechanisms of large and small earthquakes involve fundamentally different physics. Specifically, is a magnitude 9 earthquake simply a scaled-up version of a magnitude 2 earthquake, or does something intrinsically different occur as the scale increases? Aki 1967 introduced the idea of scale invariance in the rupture process, aligning with the observation that many geological processes appear similar across a wide range of scales (Abercrombie 1995). However, ongoing debate exists about whether earthquakes maintain self-similarity across all magnitudes or if systematic deviations from this self-similarity occur as earthquake size increases (Abercrombie, 1995). Self-similarity breakdown is believed to happen when observed scaling relationships no longer hold, often in very large or very small earthquakes.

The study by Abacha et al. (2019) is the only one that estimated dynamic source parameters in Beni-Ilmane. One of their key findings highlights a self-similarity breakdown in Beni-Ilmane for earthquakes with $M_0 < 2 \times 10^{16}$ N.m (Mw~4.8). The authors attributed this observation at low magnitudes to factors such as site effects. However, the magnitude range they refer to ($4 \leq Mw \leq 4.8$) falls within the moderate magnitude range, not small earthquakes. Additionally, Abercrombie (1995) investigated earthquakes from ML = -1 to ML = 5.5 and reported no self-similarity breakdown, raising questions about whether earthquakes in the range of $4 \leq Mw \leq 4.8$ exhibit such phenomena.

Our analysis of 41 target events included the 18 largest events studied by Abacha et al. (2019). We conducted a comparative study between the M_0-R relationship from Abacha et al. (2019) and our M_0-R relationship using the same dataset (18 events). To ensure a meaningful comparison we use Brune's model-based source parameters obtained from individual spectra appraoch. The key difference lies in the method of correcting and fitting the observed spectra. Abacha et al. (2019) used fixed values of Q_0 and $Q\alpha$ to correct for attenuation, while we used optimized values. **Fig. III.24** shows that

our results indicate no breakdown in self-similarity. Abacha et al. (2019) reported $M_0 \propto R^{5.3}$, while our relation indicates $M_0 \propto R^{3.64}$, which is consistent with theoretical expectations ($M_0 \propto R^{3+\alpha}$, with $0 < \alpha < 1$), (Kanamori & Rivera 2004).
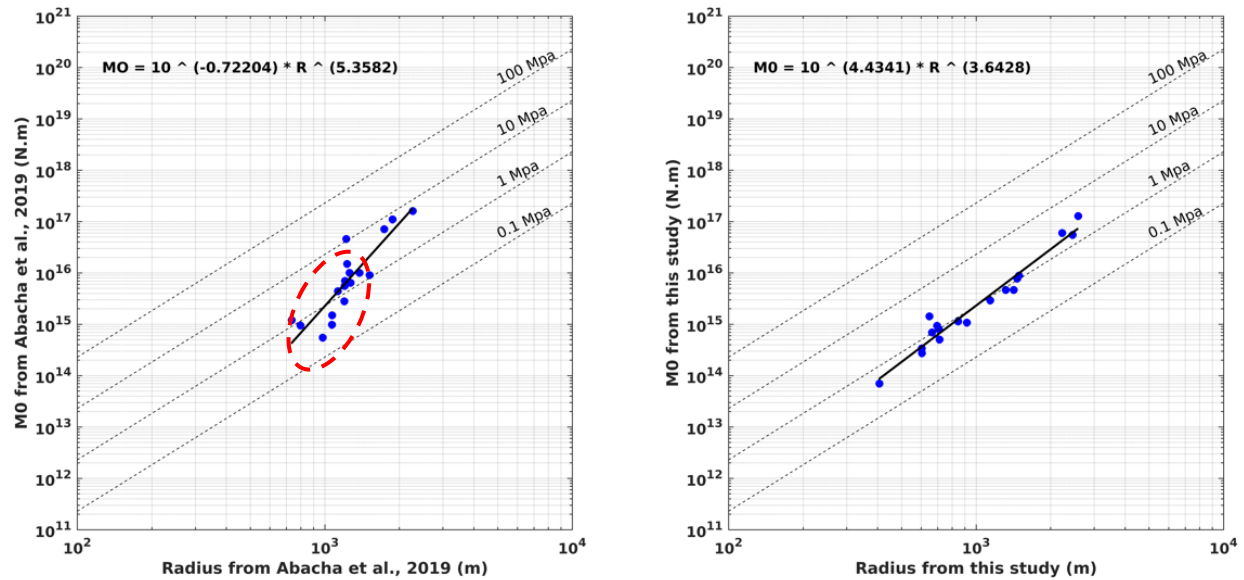
Fig. III.24: M_0-R scaling law comparison between our study (right panel), and Abacha's et al. (2019) (left panel). The parameters enclosed by dashed red ellipse are probably misestimated.

We assume that the deviation from the self-similarity relation observed by Abacha et al. (2019) is likely related to their model for correcting attenuation. It is well-known that attenuation significantly affects the estimation of corner frequency, which in turn impacts the source radius. Additionally, some of their M_0 values may have been underestimated, potentially biasing the M_0-R relationship. In **Fig. III.25**, we present a comparison of the M_0 and f_c values (**Fig. III.25** (left) and **III.25** (right), respectively) between the two studies. We observe that eight values of M_0 and f_c align well with the (1:1) line, indicating consistency between our estimates and Abacha's et al. (2019). Conversely, the remaining ten values exhibit deviation. The corner frequencies and the seismic moments in Abacha's et al. (2019) are under-estimated and over-estimated respectively.
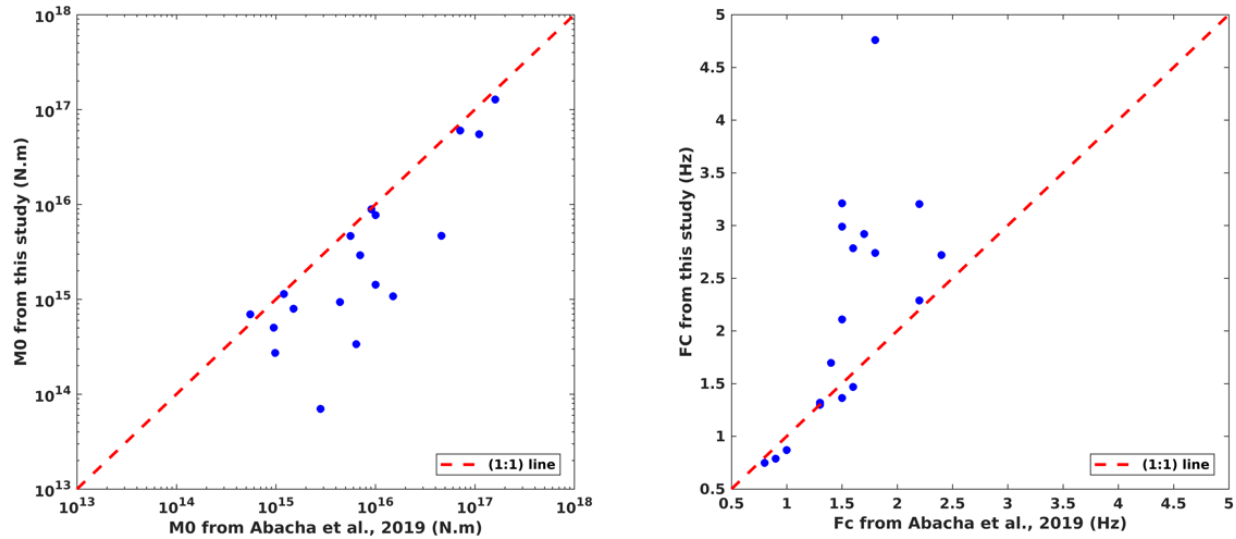
Fig. III.25: Comparison of seismic moments (left panel) and corner frequencies (right panel) between our study and Abacha et al (2019)

III.9.2 Mw-ML Scaling Relationship for Beni-Ilmane Region

In seismology, moment magnitude (Mw) is often preferred over local magnitude (ML) because it provides a more accurate and physically meaningful representation of an earthquake's size and energy release. While ML is based on the amplitude of seismic waves recorded at specific distances, it can saturate at higher magnitudes, failing to distinguish between large earthquakes effectively. In contrast, Mw is derived from the seismic moment, which takes into account the fault area, the average slip on the fault, and the rigidity of the surrounding rocks, offering a direct measure of the total energy released by the earthquake. This makes Mw a more reliable and consistent scale, particularly for comparing the energy of large or distant seismic events across different regions. The scaling relationship between Mw and ML is crucial for converting between these two magnitude scales, especially in regions where ML is commonly used, which is generally the case in Algeria. In this regard we used the moment magnitude of the 41 events (see, **Table III.1**) and their correspondent ML values to retrieve a scaling law between these two important quantities in the Beni-Ilmane region. Our results indicate a linear relation as expected**.** The linear regression resulted in:

$$Mw = ML * 0.800067 + 0.83 \tag{III.44}$$

with an R-squared value of 0.8535, indicating a precision of 85.35%. Additionally, we calculated a standard deviation of 0.211 between the observed Mw values and the calculated ones using the retrieved relationship. Similar works have been conducted by Bellalem *et al.* (2022) and Roubeche et al., (2024), but with regional data from the CRAAG catalogs. They revealed relationships of Mw = 0.762*ML+1.024 and Mw = 0.8046*ML + 1.0203 respectively. Both relations fall within ± 2std of our findings, reflecting consistency between these three studies, see **Fig. III. 26.**
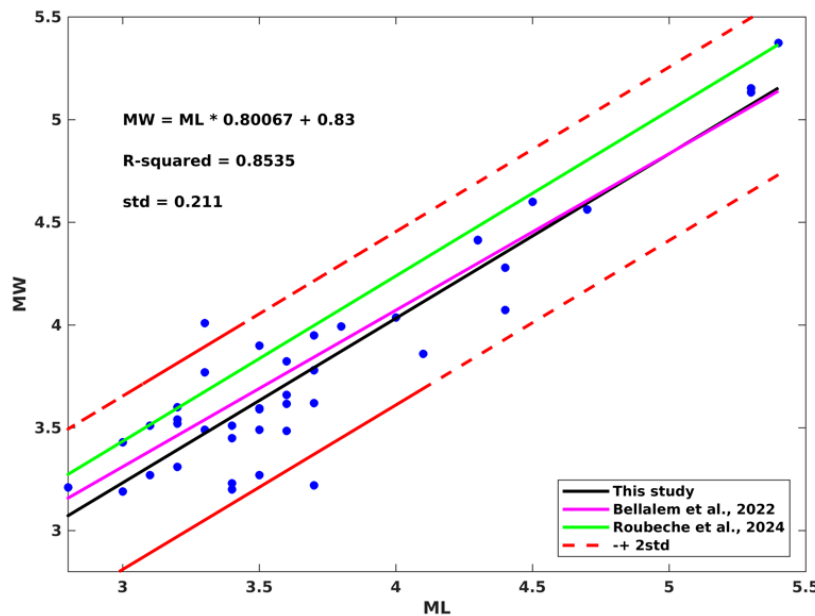
Fig. III.26: Mw-ML conversion relationship, with comparison between the relation retrieved by Bellalem et al., 2021 and Roubeche et al., 2024.

III.9.3 Comparison of EGF and Individual Spectra Source Parameters

Our findings highlight that the EGF method tend to produce higher values of corner frequency and stress drop compared to the individual approach, see **Fig. III.27** and **III.28** respectively. We have calculated an average 1.72 Hz of difference in corner frequency and 2.4 MPa of difference in stress drop. The differences in results between the two methods can be attributed to the trade-offs involved in the analysis. In individual spectral analysis, the observed seismic spectra are affected by various factors, including path effects (e.g., seismic wave attenuation as it travels from the source to the receiver)

and site effects (e.g., local geological conditions at the recording station). These factors can distort the true source characteristics, leading to potential biases in the estimation of corner frequency and stress drop. On the other hand, The EGF method aims to mitigate these issues by using a smaller, nearby earthquake (the "Green's function") as a reference to cancel out the path and site effects. By taking the spectral ratio between the target event and the EGF event, the method reduces the influence of these external factors, isolating the source characteristics more effectively. This leads to a more accurate estimation of the corner frequency and stress drop, which explains why the EGF method tends to yield higher and potentially more reliable values. Similar findings have been highlighted by (Ide *et al.* 2003)
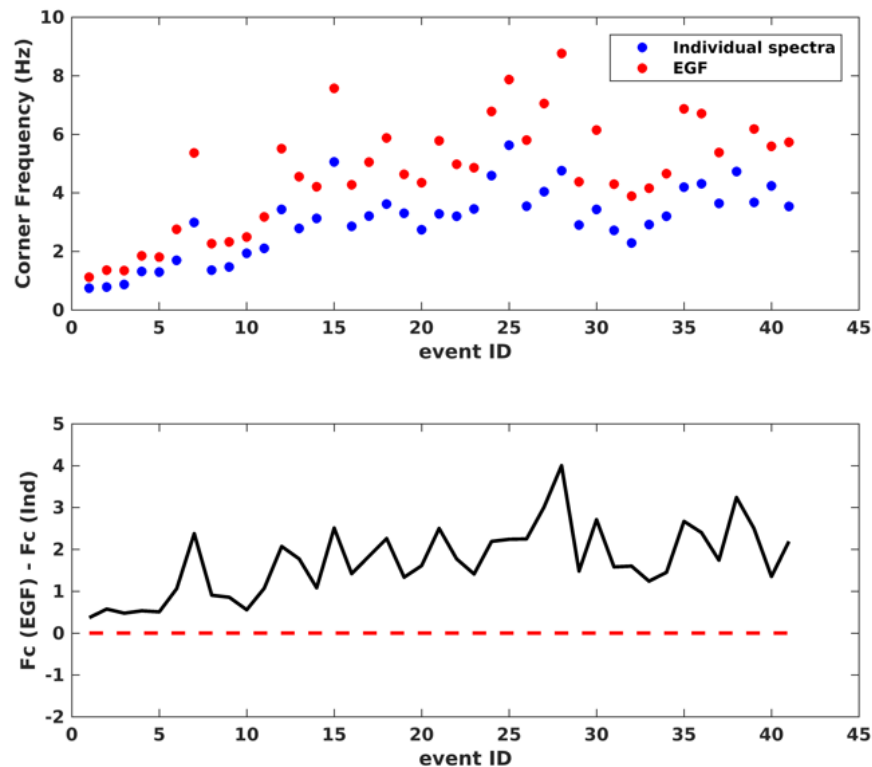
Fig. III.27: upper panel; comparison between corner frequencies from individual spectra approach (blue dots), and corner frequencies from EGF approach (red dots). Lower panel: the difference between the two approaches.
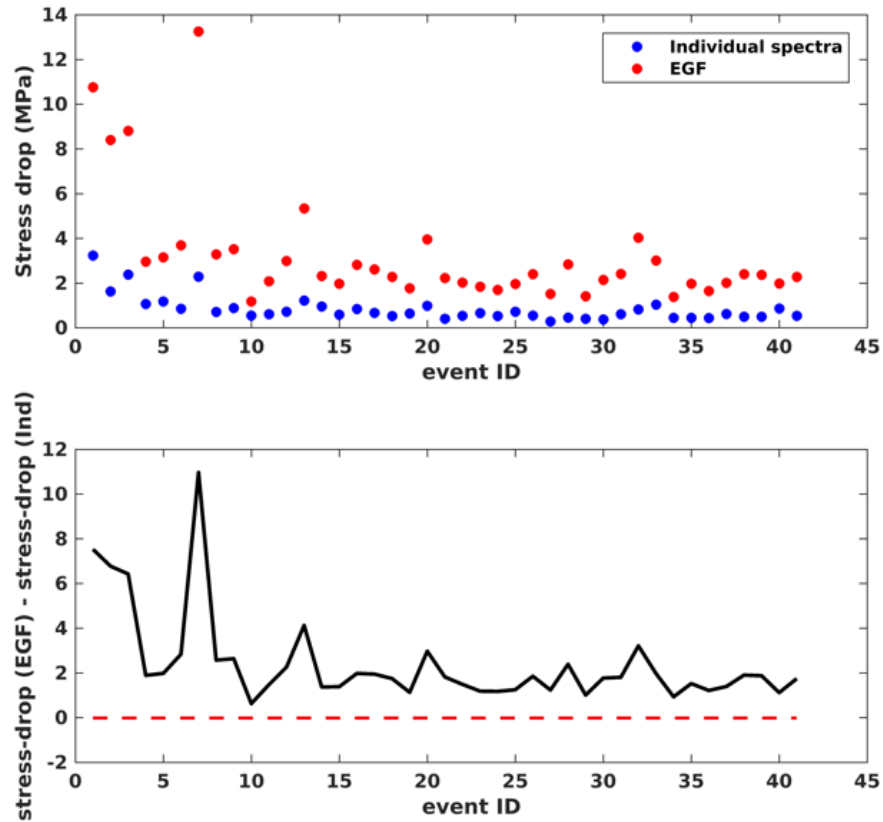
Fig. III.28: The same as Fig. III.27, but with stress drop.

III.9.4 Scaling Relationships from Our Results (M_0-R and M_0-f_c)

In this study, we have determined the source parameters for 41 earthquakes, a number that is sufficient given the comprehensive distribution of these events across a wide magnitude range. This broad distribution ensures that our analysis captures the variability in earthquake behavior, allowing for robust statistical evaluation of scaling relationships. Investigating the relationships between seismic moment (M_0) and source radius (R), as well as between seismic moment (M_0) and corner frequency (f_c), is crucial for understanding the underlying physics of earthquake generation in the study area. These scaling relationships will provide insights into whether the observed seismic events follow expected self-similarity patterns or if deviations occur, which could indicate unique geological or faulting processes at play. Our analysis in this sub-chapter

will include a comparison between individual spectra approach and EGF approach. For each approach we consider two models Brune's model, and Magariaga's modified model. The seismic moment-source radius (M_0-R) and the seismic moment-corner frequency scaling relationships are a fundamental concept in seismology that describes how the seismic moment, a measure of the total energy released by an earthquake, scales with the size of the earthquake's rupture area typically characterized by the source radius (R), and the corner frequency (f_c), which is related to the inverse of the characteristic time of the earthquake's source process. In a self-similar framework, these relationships are often expressed as $M_0 \propto R^3$ and $M_0 \propto f_c^{-3}$ respectively. The M_0-R relation implies that as the rupture area increases, the seismic moment grows cubically. This cubic scaling suggests that larger earthquakes, with greater rupture areas, release significantly more energy than smaller ones. While the M_0-f_c indicates that as the corner frequency decreases, the seismic moment increases significantly. This inverse cubic scaling suggests that larger earthquakes, characterized by lower corner frequencies, have longer source durations (according to the relation $\tau_r = 2*pi/f_c$) and release more energy compared to smaller events with higher corner frequencies.

However, deviations from these scaling relationships can occur due to various factors. In some cases, the observed relationship may differ from the theoretical expectation, indicating the influence of localized geological conditions or the presence of complex fault interactions.

Observing the M_0-R scaling law in both the individual spectra approach (**Fig. III.29** left pane**l**) and the EGF approach (**Fig. III.29** right panel), we find a systematic shift in the radii values when comparing Brune's model to Madariaga's. By calculating the ratio between the two models we find that Brune's source radii are approximately twice (x2) as large as those in Madariaga's model. Other studies suggest a ratio of 1.76 between these radii. Notably, smaller radius values result in larger stress drop values, approximately eight times ($2^3 = 8$) Madariaga's stress-drops are higher than Brune's, see **Table. III.1** and **Table. III.2**. Despite these differences, self-similarity is conserved in both approaches, with M_0 scaling as $R^{3.70}$ in the individual spectra approach and $R^{3.57}$ in the

EGF approach. Both relations align with theoretical expectations and are consistent with the previously analyzed 18 events. While theory traditionally suggests M_0 scales as R^3, studies by Kanamori & Rivera (2004), and others propose that a relation of $M_0 \propto R^{(3+\alpha)}$ is more appropriate, where $0 < \alpha < 1$. This modification is reasonable given observational uncertainties.

The same observations hold true for M_0-f_c scaling law, see **Fig. III.30**. In our analysis both corner frequencies from individual spectra and EGF exhibited similar behavior with $M_0 \propto f_c^{-3.70}$ and $M_0 \propto f_c^{-3.57}$ for individual spectra approach and EGF approach respectively. The exponents are similar to those of the M_0-R relation but with negative sign, which is expected from the same dataset.

We have previously noted that deviations from known self-similarity laws could indicate unique geological or faulting processes. Considering the involvement of fluids as a likely contributing mechanism, as evidenced by the previously mentioned geological and tomographic studies in the Beni-Ilmane region, we stipulate that the minimal observed deviation from $M_0 \propto R^3$ may be influenced by fluid pore pressure in the area.
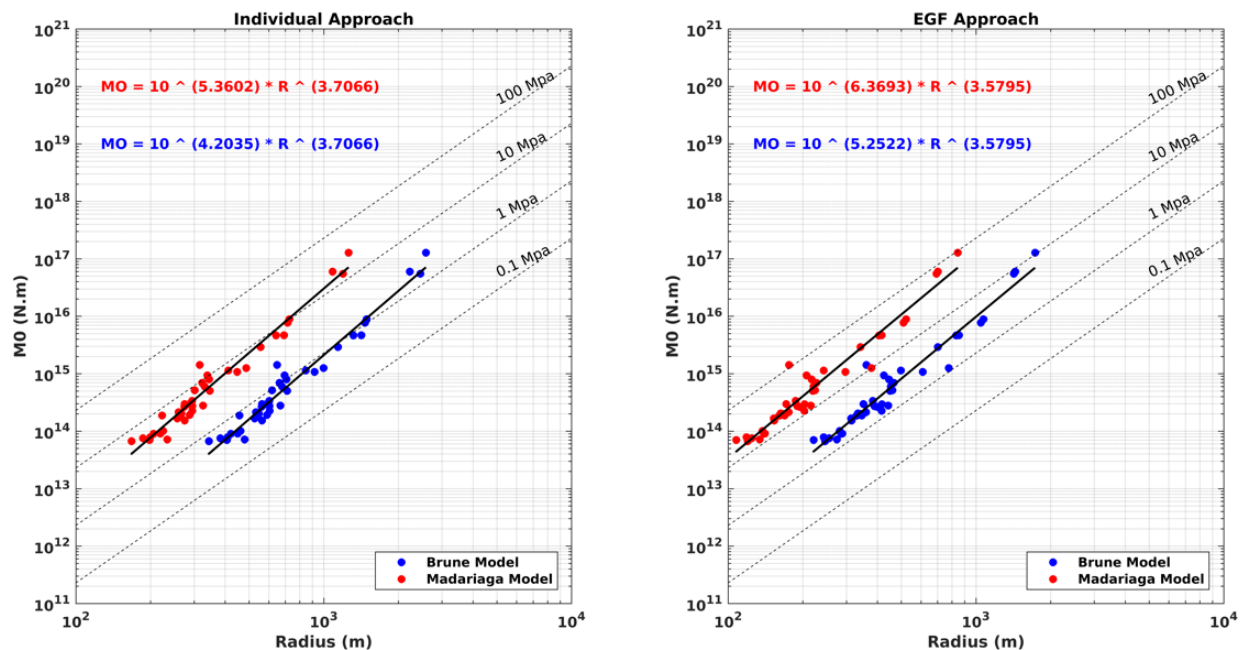
Fig. III.29: M_0-R Scaling relationships. Left panel: from individual spectra approach. Right panel: from EGF approach. In both panels, blue and red dots represent respectively Brune's model and Madariaga's model.
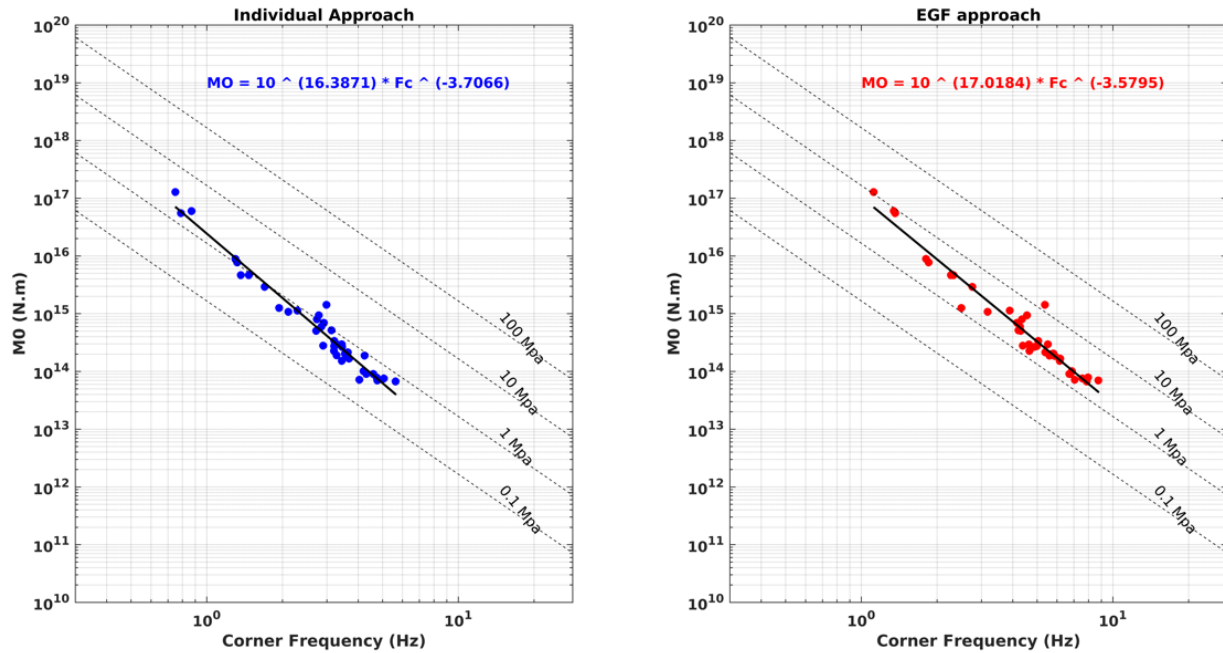
Fig. III.30: The same as fig. III.29, but with M_0-f_c scaling relationships.

III.10 Conclusion

In this chapter, we explored the theoretical foundations of source parameter analysis and applied these concepts to the Beni-Ilmane seismic sequence, analyzing 41 events using both individual spectra and the Empirical Green's Function (EGF) approach. Our analysis contradicts the previously suggested breakdown in self-similarity by previous studies, demonstrating instead that our more accurately resolved parameters indicate a self-similarity consistent with theoretical expectations.

We also derived a new Mw-ML conversion relationship for the Beni-Ilmane region, which aligns well with other established regional data, further validating our methodological approach. Notably, our findings show that source parameters estimated using the EGF method are generally higher than those obtained from individual spectra, emphasizing the importance of method selection in seismic analysis.

Overall, our findings contribute valuable insights into the dynamics of the Beni-Ilmane seismic sequence, offering a refined understanding of source parameters and their variability across different earthquakes' sizes.

Chapter IV

Mechanisms Driving
The BI-2010 Sequence:
An Analysis

Content

IV.1 Introduction

Earthquakes are predominantly generated by tectonic loading, the gradual accumulation of stress along fault lines due to the movement of tectonic plates. This process is the primary driver of seismic activity across the globe, particularly along active plate boundaries where compressional, tensional, or shear forces continuously reshape the Earth's crust. However, while tectonic loading is the main force behind most earthquakes, there are instances where seismic events result from a more intricate interplay between multiple forces, including stress transfer mechanisms (both static and dynamic), fluid-induced seismicity, and aseismic processes.

The movement of tectonic plates acts directly on faults, leading to their loading. This phenomenon is known as "tectonic loading." It is most evident in regions with active plate boundaries, such as the Pacific Ring of Fire, where the Earth's lithosphere is in constant motion, generating frequent and often powerful earthquakes.

In some cases, earthquakes can trigger further seismic events through stress transfer. Static stress transfer occurs when a fault slip causes a redistribution of stress in the surrounding crust, potentially loading nearby faults and bringing them closer to failure. Dynamic stress transfer involves the propagation of seismic waves from one fault to another, which can trigger an immediate response in faults already critically stressed. Both forms of stress transfer can significantly influence the spatial and temporal patterns of aftershock sequences or trigger distant earthquakes.

In addition, earthquakes can be triggered by other factors either in conjunction with or independent of tectonic loading. One such factor is fluid-induced seismicity, which occurs when the movement of fluids within the Earth's crust alters the pressure conditions along fault lines. This can happen naturally, as in hydrothermal systems where the circulation of water deep within the crust can destabilize faults, or it can be anthropogenic, resulting from human activities like fluid injection or extraction.

Another important factor is aseismic afterslip, a process that occurs after a major earthquake. Unlike the sudden rupture of a typical earthquake, aseismic afterslip involves a slow, gradual movement along a fault that can continue for months or even years. While this movement does not generate strong ground shaking, it can redistribute stress within the crust, potentially influencing the timing and location of future earthquakes. In some cases, aseismic afterslip can load nearby faults, bringing them closer to failure and increasing the likelihood of subsequent seismic events.

Thus, while tectonic loading remains the dominant force behind most earthquakes, the occurrence of seismic events can sometimes be the result of a complex interplay between various factors, including stress transfer, fluid-induced seismicity, and aseismic processes. Understanding these mechanisms is essential for accurately assessing seismic hazards and developing strategies to mitigate the risks associated with earthquakes.

IV.2 Tectonic Loading in BI Region

Tectonic loading, the gradual buildup of stress within the Earth's crust due to the movement of tectonic plates, is a fundamental mechanism driving earthquakes. As tectonic plates interact—whether by colliding, diverging, or sliding past each other—stress accumulates along fault lines. When the stress surpasses the rock's strength, it is released suddenly, resulting in an earthquake. This process is particularly pronounced in regions where tectonic plates converge, creating intense compressional forces that can trigger significant seismic activity.

With this in mind, we focus on the African-Eurasian plate boundary in northern Algeria, where tectonic loading is a key driver of the region's seismicity. This boundary is a tectonically active zone characterized by significant seismic events, including the 1980 Mw 7.3 El Asnam (Ouyed *et al.* 1981; Philip & Meghraoui 1983; Yielding *et al.* 1989), the 1985 Ms 6.0 Constantine (Bounif *et al.* 1987), and the 2003 Mw 6.8 Boumerdes earthquakes (Yelles *et al.* 2004; Kherroubi *et al.* 2017). The seismicity in this region is primarily driven

by tectonic loading associated with the convergence between the African and eurasian plates, Bougrine *et al.* (2019).

Current kinematic models indicate a counterclockwise rotation of the African plate relative to the Eurasian plate, leading to a NW-SE convergence that is oblique to the plate boundary. This convergence rate varies from 2–4 mm/yr near Gibraltar to 3–8 mm/yr in the Sicily Strait (Nocquet 2012). In western Algeria, seismic activity is concentrated along the coastal regions within the Tell Atlas, while in the east, it is more widespread, extending from the coastline to the Saharan Atlas (Bahrouni *et al.* 2014). The focal mechanisms of earthquakes in northern Algeria predominantly involve reverse faulting on SW-NE to WSW-ENE-oriented faults, consistent with the regional tectonic stress regime driven by the African-Eurasian plate convergence (Buforn *et al.* 2004; Stich *et al.* 2006). A notable rotation in the shortening direction, from NNW-SSE in the east to NW-SE in the west, suggests a partitioning of the oblique convergence into offshore pure convergence and onshore strike-slip faulting (Stich *et al.* 2010).

The 1980 El Asnam earthquake highlighted the seismic risks associated with foreland faults, while the 2003 Boumerdes earthquake emphasized the significance of the continental margin in the plate boundary deformation system. Recent studies, especially those conducted after the 2003 event, have identified active crustal-scale reverse faults along the Algerian continental margin, indicating that the margin is currently thrusting over the Algerian oceanic basin (Domzig *et al.* 2006; Yelles-Chaouche *et al.* 2009; Mourad *et al.* 2014; Hamai *et al.* 2015; Arab *et al.* 2016; Aïdi *et al.* 2018)

Calculating stress orientation using stress inversion can be a valuable indicator of tectonic loading on faults. By analyzing the orientation of the principal stresses ($\sigma 1$, $\sigma 2$, $\sigma 3$) from earthquake focal mechanisms or fault slip data, stress inversion helps identify the dominant forces acting on the region. When the stress orientations align with regional tectonic forces, such as the direction of plate motion, it suggests that tectonic loading is the primary driver of stress accumulation on the faults. After calculating 128 focal mechanisms (see **Chapter II**), it is useful to invert them to retrieve the local stress field in

Beni-Ilmane region. To assess the current tectonic stress regime in the study area and evaluate how these stresses act on pre-existing structures, we performed a stress inversion on the 128 FMSs using Win-Tensor (Delvaux & Sperner 2003). The stress inversion reveals a sub-vertical orientation for σ_2 (plunge 88°/azimuth N221°E), and sub-horizontal orientations for σ_1 (0°/N325°E) and σ_3 (02°/N55°E). This analysis indicates a strike-slip tectonic regime with R'=1.54 ± 0.37 (see **Fig. IV.1a)**. These results suggest a predominant NW-SE oriented maximum horizontal compression with an average SHmax value of N145°E ± 11.8°, consistent with the regional compressional trend estimated by Bougrine et al. (2019). The local stress tensor calculated in this study shows similarities with the neighboring Ain Azel region (σ_1 striking N325°; Yelles-Chaouche et al. 2022) (see **Fig. IV.1b**). Similarly, on a regional scale, the northwestern (σ_1 striking N325° around the Chellif basin; (Beldjoudi et al. 2012) and eastern (σ_1 striking N325° in the Babors-Bibans zone (Beldjoudi et al. 2009), parts of Algeria exhibit similar orientations. However, a ~N-S reorientation is reported around the Lesser Kabylia Bloc in northeastern Algeria (Abacha et al. 2023b; Bendjama et al. 2021; Boulahia et al. 2021; Yelles-Chaouche et al. 2021) (see **Fig. IV.1b**). This reorientation is attributed to the influence of the major Gharimadou-North-Constantine Fault (GNCF).

We mention that no previous studies conducted local stress inversion using such number of FMs in Beni-Ilmae region. Hence it can be viewed as one of the new outcomes of our study. There is one study be Beldjoudi et al., 2016, where they used four events from their study, 15 events from Yelles-Chaouche et al., 2014, These two studies both are in Beni-Ilmane region, additionally they incorporated 6 events that are ~50km from the Beni-Ilmane region. Their results showed sigma1 at 340 degrees. Therefore, based on the used data our retrieved local stress field is more reliable as we inverted 128 local FMSs.
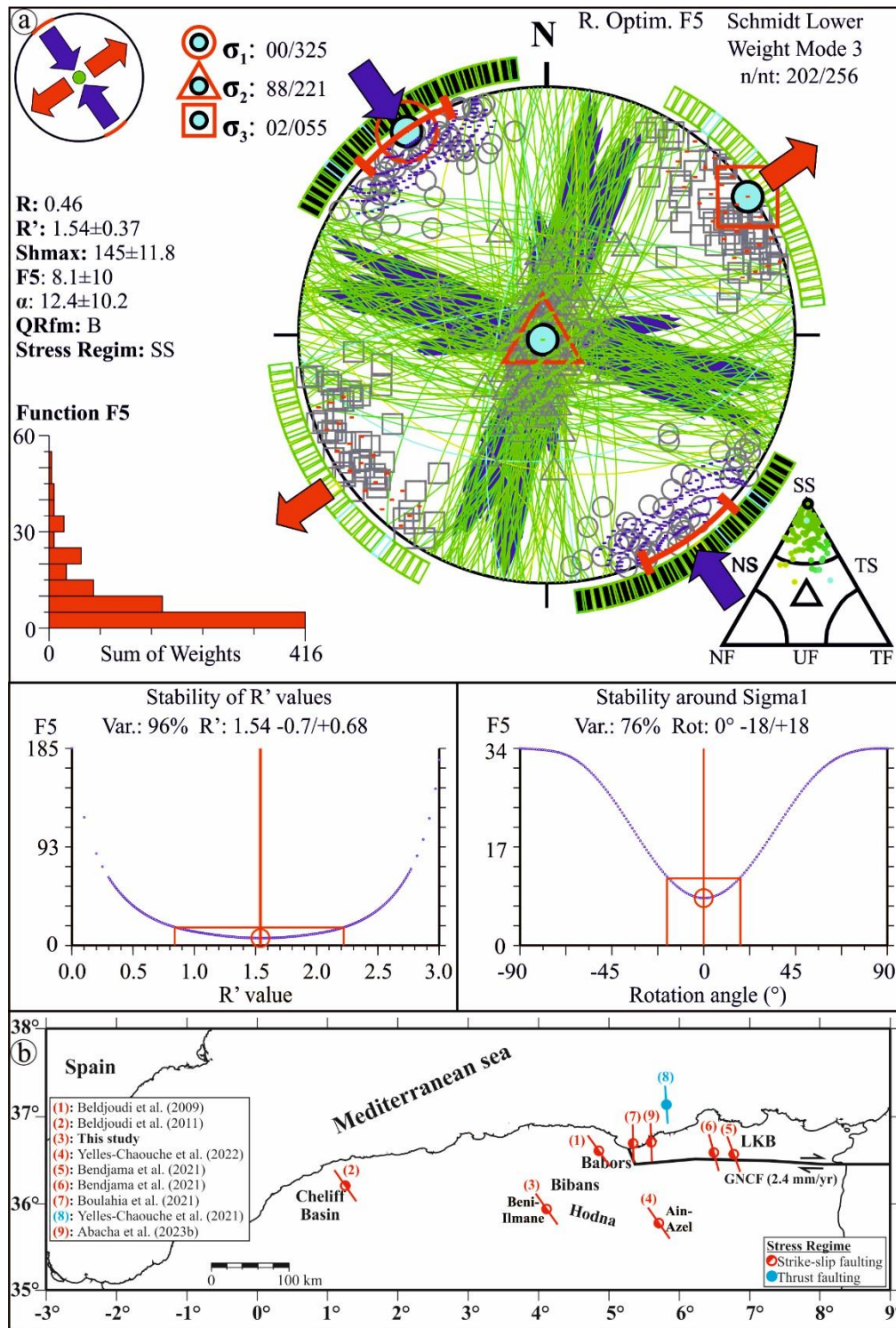
Fig. IV.1: Stress inversion. **(a)** Stress inversion results showing 202 selected focal planes projected (green lines) onto the lower hemisphere (Schmidt stereographic projections), with the three principal stress axes (σ_1: circle, σ_2: triangle, and σ_3: square) and horizontal stress axes (SHmax: purple arrows; SHmin = red arrows). The stress symbols indicate the horizontal stress axes. The histogram shows the distribution of the misfit function F5,

weighted linearly by event magnitude. The F5 function is a misfit minimization method used for rotational optimization, which minimizes the angular misfit between observed and modeled slip on the focal planes, while simultaneously maximizing resolved shear stress and minimizing resolved normal stress. QRfm represents the quality of the inferred SHmax result based on the World Stress Map ranking criteria. α denotes the average deviation between observed and modeled slip lines. The tectonic regime is identified as Strike-Slip (SS). (**b**) Map of SHmax obtained from the inversion of FMs for the main recent seismic events in northern Algeria, including those for our study. GNCF=Gharimadou-North-Constantine Fault, LKB= Lesser Kabylian Block.

IV.3 Can Stress Transfer Alone Explain the Observed Seismicity in The BI-2010 Sequence?

Stress transfer refers to the redistribution of stress in the Earth's crust following a seismic event, where the slip on one fault can alter the stress conditions on surrounding faults. This redistribution occurs in two main forms: static and dynamic stress transfer. Static stress transfer takes place when the permanent deformation from an earthquake alters the stress field around the rupture area, potentially increasing or decreasing stress on neighboring faults. If nearby faults are brought closer to failure due to this change, they may rupture, triggering subsequent earthquakes. Dynamic stress transfer, on the other hand, is driven by seismic waves that radiate outward from the earthquake source. These transient waves can induce stress changes in distant faults that are already close to failure, potentially triggering new seismic events far from the original rupture zone. Both forms of stress transfer are key to understanding earthquake sequences, including aftershocks, as they influence when and where future seismic activity may occur

In this thesis, a detailed investigation of how stress transfer influenced seismicity in the BI region is not a primary objective. However, a study by Beldjoudi et al. (2020) explored this issue, and in this sub-chapter, we aim to discuss their findings in light of one of our main results: the high-precision relocation of seismic events. Static stress transfer, particularly through the Coulomb Failure Function (CFF), is a widely recognized mechanism in seismology, where the redistribution of stress following an earthquake can

either promote or inhibit subsequent seismic activity. However, the application of static stress transfer to explain the complex sequences of aftershocks can be variable. (Hardebeck *et al.* 1998) demonstrated that while stress transfer may account for certain aftershocks, it does not reliably explain all seismic sequences.

In the context of the BI-2010 sequence, which includes three mainshocks (MS-1, MS-2, and MS-3), a plausible hypothesis is that static Coulomb stress transfer from MS-1 triggered MS-2, and both MS-1 and MS-2 contributed to the triggering of MS-3. Beldjoudi. (2020) concluded similarly, suggesting that MS-2 was induced by stress from MS-1, while MS-3 was influenced by stress from both MS-1 and MS-2. However, their study had a critical limitation: the location uncertainties of the mainshocks, estimated to be around 3 km (Beldjoudi et al. 2016). This level of uncertainty raises concerns about the precision of their conclusions.

In contrast, our high-precision relocation, with uncertainties of around one hundred meters, offers a more accurate spatial representation of the events. When we overlay our precisely relocated events onto the Coulomb stress maps from Beldjoudi et al. (2020), we find that MS-2 and several aftershocks are situated within a "stress shadow zone," where the Coulomb stress change is negative. This is problematic because stress shadow zones are generally expected to inhibit seismic activity, making it difficult to attribute the initiation of MS-2 solely to the stress imparted by MS-1. Interestingly, MS-3 is located in a neutral zone, raising further questions about the triggering mechanism, see **Fig. IV.2**.
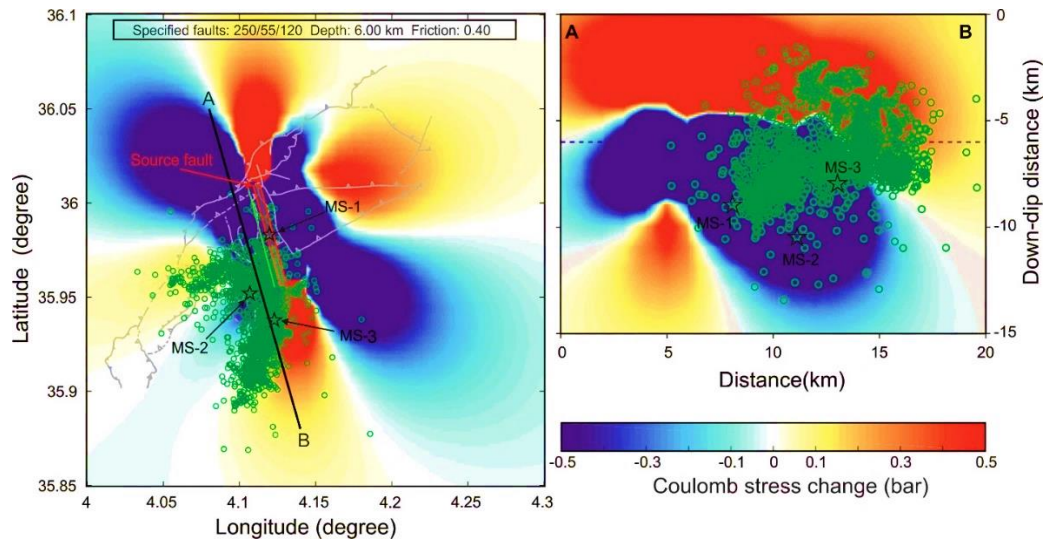
Fig. IV.2: Stress transfer map. Reproduced ΔCFF map from Beldjoudi. (2020), associated with the plane of the first shock (345°/85°/16°) resolved on the plane of the second shock oriented (250°/55°/120°) at a depth of 6 km. **Left panel**: shows the Coulomb stress change in the Beni Ilmane region after MS-1. The green dots are the aftershock's activity, the black stars are the MSs, and the black segment [AB], indicates the cross-section's axe. **Right panel**: exhibits the cross-section [AB] with the distribution in depth of the aftershocks and MSs.

Similar observations have been reported in other seismic studies. (Terakawa *et al.* 2013) found increased seismicity in areas of negative Coulomb stress change following the 2011 Tohoku-Oki earthquake in Japan. They attributed this unexpected behavior to the influence of over-pressured fluids from deep reservoirs. The simplified nature of Coulomb stress modeling, which assumes undrained, homogeneous, and isotropic conditions, does not account for the spatiotemporal changes in pore fluid pressure that can also affect aftershock triggering. In the case of the BI region, fluid reservoirs and high pore pressures have been well documented by Abacha et al. (2014) and Abacha et al. (2023a), suggesting that stress transfer is not the sole driving mechanism.

Furthermore, Segou & Parsons (2014) emphasized that predicting earthquake occurrence within calculated stress shadow zones remains a significant challenge for stress-based earthquake forecasting, as other mechanisms may also contribute to triggering. In line with this perspective, while we acknowledge that static stress transfer

played a role in triggering MS-2, MS-3, and several aftershocks in the BI region, we argue that it is not the sole mechanism. The presence of high pore pressures and other fluid-related processes indicates that static stress transfer alone is insufficient to explain the full range of seismic activity observed. Therefore, while static Coulomb stress transfer provides important insights, a more comprehensive approach that incorporates additional triggering mechanisms is needed to fully understand the seismicity in this region. Further investigation into Coulomb stress triggering falls outside the scope of this thesis.

IV.4 Extra Evidences of Fluid Involvement

As mentioned earlier in **sub-chapter II.1.2**, surface seeps have been identified in the Sub-Bibanic and Hodna regions, following ENE-WSW to east-west oriented zones that align with the regional fracture system. These alignments suggest the presence of an active petroleum system (Kheidri et al., 2007). Abacha et al. (2014) analyzed travel times from 1,406 events in the BI-2010 sequence and performed seismic tomography in the region. Their study of Vp/Vs ratio variations revealed high Vp/Vs values, leading them to assume fluid intrusion during the BI-2010 sequence. Their assumption is supported by the presence of surface seeps and the extensive history of oil and gas exploration in the area. Indeed, oil exploration in this part of Algeria, particularly in the Sidi Aissa region, about 40 km from Beni-Ilmane, began in 1950. The first phase of exploration, from 1950 to 1962, was conducted by Sn Repal (Société Nationale de Recherche et d'Exploitation des Pétroles en Algérie), while the second phase, from 1963 to the present, has been led by SONATRACH (Société Nationale du Transport, de Recherche et de Commercialisation des Hydrocarbures).

In contrast, our more recent study (Abacha et al., 2023a) utilized additional datasets and 4D Vp/Vs models to track fluid migration from reservoirs to nearby faults. One of our key findings was that the increased seismicity rate after MS-3 is likely related to elevated pore pressure caused by MS-3, which may have broken the reservoir seal. Similarly, Rahmani et al. (2023) used a non-stationary Epidemic Type Aftershock

Sequence (ETAS) model to distinguish between background and aftershock contributions, suggesting that fluid migration played a significant role following MS-3.

All these observations and interpretations, derived from various methodologies, suggest that fluid activity played a significant role in driving the BI-2010 seismic sequence. In this section, we introduce two additional lines of evidence that have not yet been explored in the context of the BI-2010 sequence: moment tensor decomposition and variations in stress drop. It is also important to highlight that the presence of multiplets, which we identified in **Chapter II**, further supports fluid involvement. Indeed, Bourouis & Bernard (2007) highlighted that fluid flow creates favorable conditions for the generation of multiplet earthquakes.

IV.4.1 Evidence from Moment tensor decomposition

As we have seen in **Chapter I**, a moment tensor M can be decomposed onto isotropic and deviatoric components ($M = M_{iso} + M_{dev}$). Similarly, the deviatoric component can be decomposed onto a double couple and compensated linear vector dipole ($M_{dev} = M_{DC} + M_{CLVD}$). Moment tensor's scale factors (C_{iso}, C_{CLVD} and C_{DC}) represent the relative contribution of each component and they verify: $|C_{iso}| + |C_{CLVD}| + C_{DC} = 1$

the DC scale factor is always positive ($C_{DC} > 0$), while C_{CLVD} and C_{iso} may have positive or negative scale factors. Hence varying fro -1 to 1.

Despite that in many cases high CLVD percentages (typically higher than 15%) often indicate issues in moment tensor determination from observed data or incorrect assumptions about wave propagation models, in certain instances, higher CLVD's percentage values may indeed, reflects realistic scenarios where the seismic source deviates from pure DC. Several examples exist in this regard, for instance tensile faulting induced by fluid injection in geothermal or volcanic regions has been observed by (Ross et al. 1996; Julian et al. 1997). The general physical properties of the moment tensor decomposition are as follow (Vavryčuk 2015):

- The explosion/implosion is a pure isotropic source, and thus it is characterized by $C_{iso} = \pm 1$ and by $C_{CLVD} = C_{DC} = 0$.

- Shear faulting is represented by the double-couple force and characterized by $C_{DC} = 1$ and $C_{iso} = C_{CLVD} = 0$.

- Pure tensile or compressive faulting is free of shearing and thus characterized by $C_{DC} = 0$. However, the non-DC components contain both C_{iso} and C_{CLVD}. The ISO and CLVD components are of the same sign: they are positive for tensile faulting but negative for compressive faulting (Vavryčuk 2001).

- The shear-tensile (dislocation) source defined as the source which combines both shear and tensile faulting (Vavryčuk 2001), is characterized by non-zero ISO, DC and CLVD components. The positive values of C_{iso} and C_{CLVD} correspond to tensile mechanisms when the fault is opening during rupturing. The negative values of C_{iso} and C_{CLVD} correspond to compressive mechanisms when the fault is closing during rupturing.

- Shear faulting on a non-planar fault is characterized generally by a non-zero C_{DC} and C_{CLVD}. The C_{iso} is zero because no volumetric changes are associated with this type of source.

In **Chapter II** and in our paper (Tikhamarine *et al.* 2024), we calculated moment tensor solutions for the three mainshocks. However, we considered the observed CLVD percentage in the solutions to be potentially influenced by artifacts, and therefore we presented only the pure DC solution. Although our DC solution is reliable, we believe the inclusion of short-period seismometers in the waveform modeling may have biased the actual CLVD component. Short-period seismometers, such as the 1 Hz SS-1 ranger seismometers used in our study, are designed to record high-frequency signals (typically above 1 Hz) but are less sensitive to low-frequency signals. These lower frequencies are essential for accurately resolving seismic moment tensors, as moment tensor inversions

depend significantly on them to capture the full source mechanism—especially for large-scale faulting or events with longer durations.

In **Appendix C**, we demonstrate that short-period sensors are unsuitable for reliable moment tensor solutions when compared to broadband sensors, due to their limited frequency range. Therefore, we aim to revise our previously calculated moment tensor solutions for the mainshocks using two different methods: (1) polarities constrained by spectral amplitudes, and (2) full waveform inversion.

a) Polarity constrained by amplitude information

In order to perform this type of moment tensor inversion, we used HybridMT program, a MATLAB/Shell Environment Package for Seismic Moment Tensor Inversion by Kwiatek *et al.* (2016). The most important parameter in the input file is the *omega* parameter, which represents the area of the first P-wave ground displacement pulse in the time domain. Alternatively, it can be derived from the spectral level of the amplitude spectrum of the P-wave ground displacement. The unit of omega is [m * s] (meter times second). Additionally, the *omega* parameter provides information on the sign of the first P-wave pulse. To calculate this parameter and prepare the input file, I developed a MATLAB code that determines the area under the first P-wave pulse of ground displacement. The code then integrates the take-off angle, azimuth, polarity, and hypocentral distance to create the necessary input file. Since the curve under the first P-wave pulse is irregular, I used the trapezoid method to calculate the area. The area was divided into several trapezoids, and the area of each trapezoid was calculated individually. Finally, all the trapezoid areas were summed together, see **Fig. IV.3.**
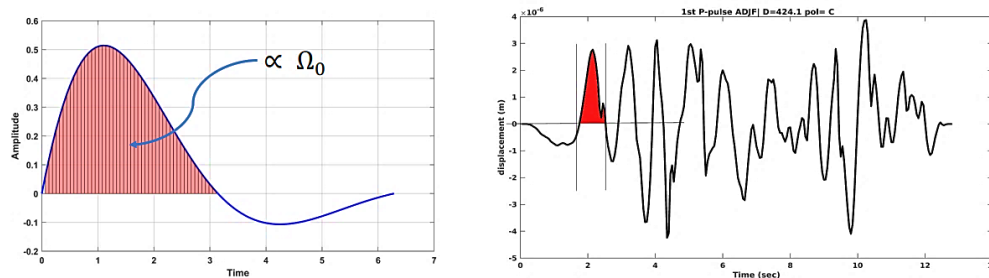
Fig. IV.3: Area under the first P-wave pulse. Left panel: illustration of calculating area under curve using trapezoids method. Right panel: Real example from ADJF station.

Table. IV.1 bellow highlights our obtained results.

Table. IV.1: Results of moment tensor inversion using spectral ratio constrained polarities (HybridMT package)

	DC Solution	Deviatoric Solution
MS-1	$S1° = 175.6$ $S2° = 085.3$ $D1° = 084.4$ $D2° = 087.5$ $R1° = 002.5$ $R2° = 174.4$	$M_{rr} = 1.5347e + 16$ $M_{tt} = 8.2041e + 15$ $M_{ff} = -2.3551e + 16$ $M_{rt} = 1.0530e + 16$ $M_{rf} = -2.1926e + 15$ $M_{tf} = -1.1481e + 17$
MS-2	$S1° = 242.4$ $S2° = 067.8$ $D1° = 034.6$ $D2° = 055.5$ $R1° = 085.6$ $R2° = 093.0$	$M_{rr} = 6.0348e + 16$ $M_{tt} = -4.7974e + 16$ $M_{ff} = -1.2374e + 16$ $M_{rt} = 2.1718e + 16$ $M_{rf} = 6.6382e + 15$ $M_{tf} = -2.1099e + 16$
MS3	$S1° = 242.4$ $S2° = 067.8$ $D1° = 034.6$ $D2° = 055.5$ $R1° = 085.6$ $R2° = 093.0$	$M_{rr} = 7.2723e + 15$ $M_{tt} = -2.0360e + 16$ $M_{ff} = 1.3088e + 16$ $M_{rt} = 5.1420e + 15$ $M_{rf} = -3.7560e + 15$ $M_{tf} = 7.7227e + 16$

b) Full-waveform inversion

To resolve for a reliable moment tensor using full-waveform, we used only three components Broad-Band stations this time. We performed deviatoric moment tensor inversion. We set a minimum distance of 70 Km, and maximum of 1000 Km. All the Green's function were calculated in our newly retrieved minimum 1D model (see **Chapter II**). Additionally, we used a frequency band of [0.04 – 0.08] Hz, and we only considered signals with an SNR>=3. The best centroid depths were found to be 4.8 km, 5.6 km, and 7.0 km, respectively, corresponding to variances of 0.15, 0.21, and 0.26. The following figures (**Fig. IV.4 – IV.11**) displays our results for each mainshock.
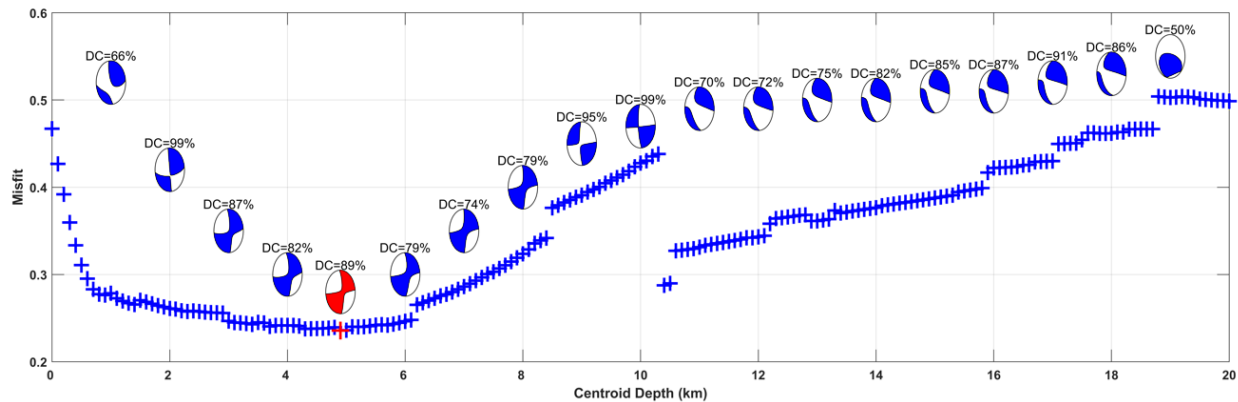
Fig. IV.4: Optimal variance reduction achieved for the moment tensor (MT) inversion process of MS-1.

Beni−Ilmane 14 MAY 2010 at 12:29 (UTC)

Mrr, Mtt, Mff, Mrt, Mrf, Mtf

0.04, 0.17, −0.22, −0.31, −0.08, −1.20, x10**17

(Strike,Dip,Slip) = (355.1, 75.7, −1.6) ; (85.5, 88.4, −165.7)

Moment = 1.2E+17 Nm, Mw = 5.39, Variance = 0.23, Depth = 4.9 km

DC = 88.6 %, CLVD = 11.4 %, ISO = 0.0 %
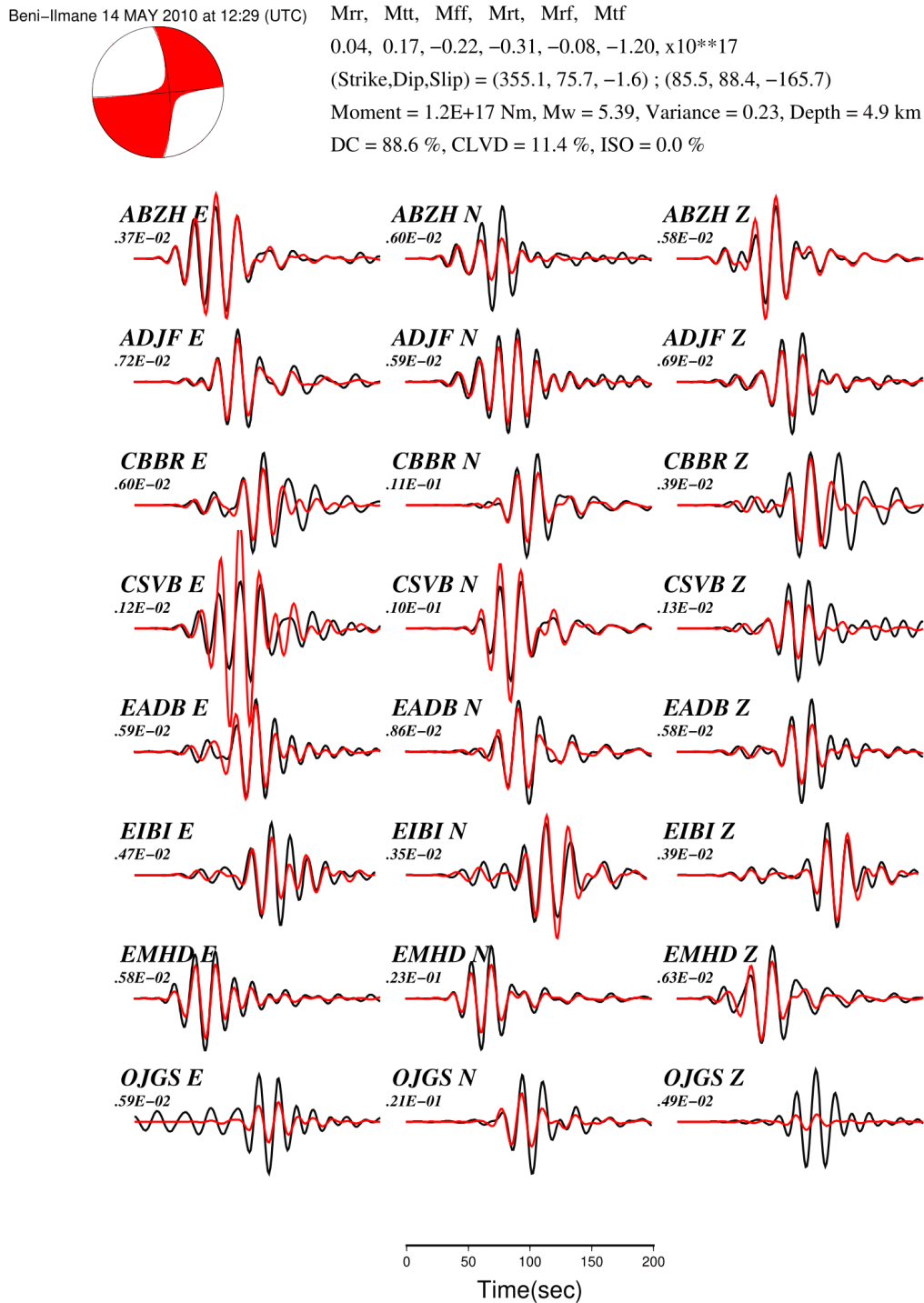
Fig. IV.5: waveform modeling for MS-1. Information in the top provides moment tensor parameters, including best-fit fault-plane solutions, moment tensor components, scalar moment, moment magnitude (Mw), variance, and focal depth. Below the tables, waveform modeling is illustrated with black lines representing instrumentally corrected velocity waveforms and red lines indicating modeled waveforms. Velocity (in cm/sec) is shown below the station code.
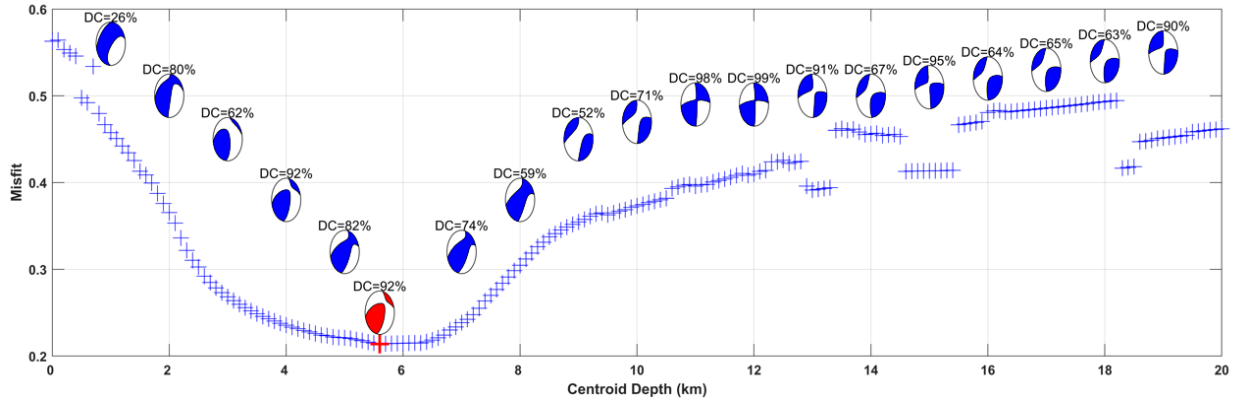
Fig. IV.6: Same as Fig. IV.4 but for MS-2

Beni−Ilmane 16 MAY 2010 at 06:52 (UTC)   Mrr, Mtt, Mff, Mrt, Mrf, Mtf

2.51, −1.23, −1.27, −1.32, 1.95, −3.05, x10**16

(Strike,Dip,Slip) = (257.8, 53.8, 143.1) ; (11.6, 61.0, 42.4)

Moment = 4.4E+16 Nm, Mw = 5.10, Variance = 0.21, Depth = 5.6 km

DC = 92.6 %, CLVD = 7.4 %, ISO = 0.0 %
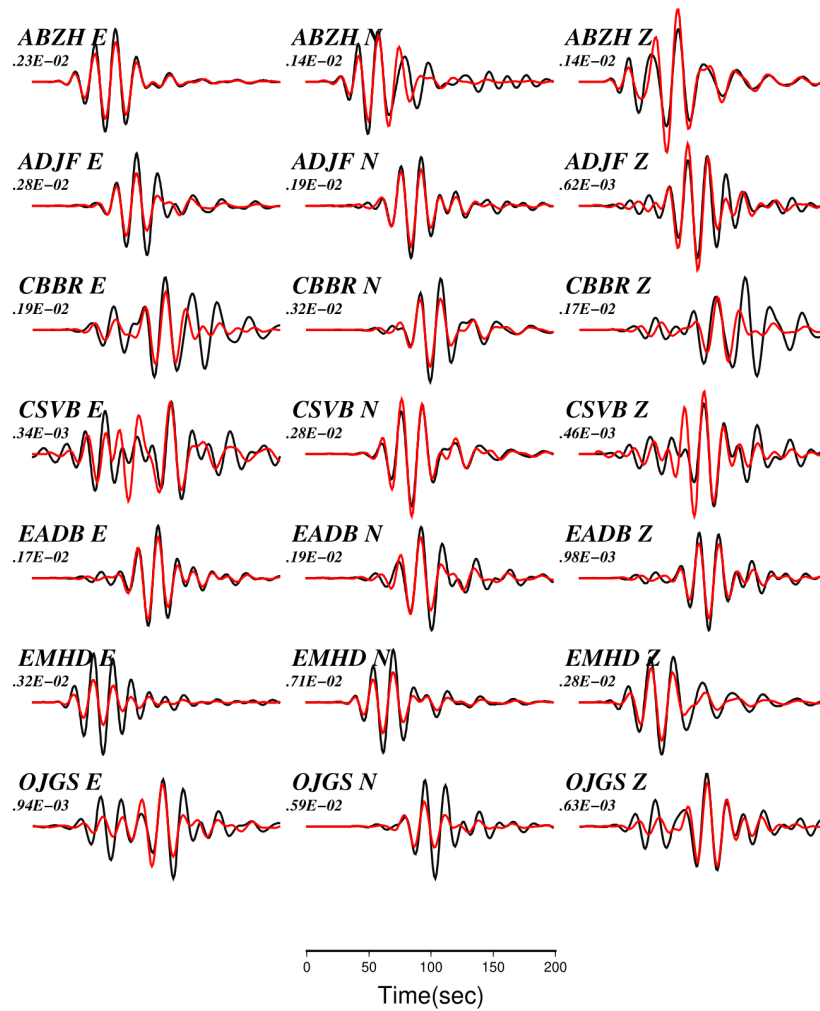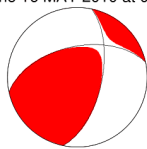
Fig. IV.7: Same as Fig. IV.5, but for MS-2.
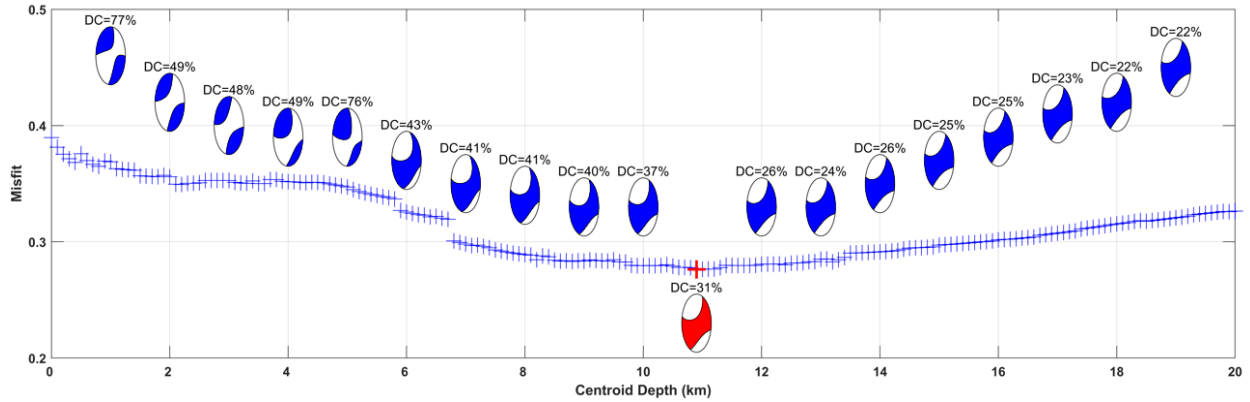
Fig. IV.8: The same as Fig. IV.4, but for MS-3.
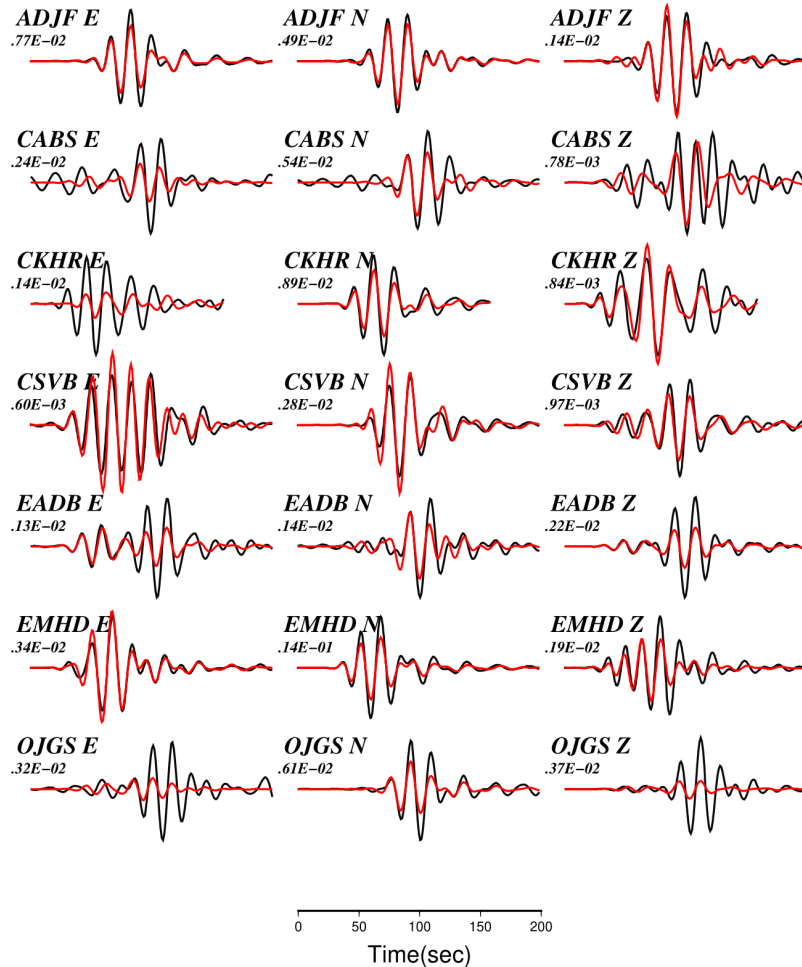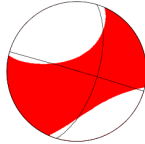
Fig. IV.9: The same as Fig. IV.5, but for MS-3.

c) Results Discussion

We assume that the observed CLVDs in the moment tensor solutions are related to the fluid involvement in the BI-2010, rather than artifacts of inversion processes. The spectral ratio constrained polarity method yielded a CLVD percentages respectively for the three mainshocks (MS-1, MS-2 and MS-3 respectively): 23.60%, 8.37% and 18.57%. These values are not too high, yet they reflect a deviation from a pure DC solution. Conversely, the full-waveform inversion approach yielded percentages for the three mainshocks (MS-1, MS-2 and MS-3 respectively): 11.4%, 7.4% and 69%. For MS-1 and MS-3 we observe a positive CLVD indicative of shear-tensile dislocation, which combines both shear and tensile faulting (Vavryčuk 2001). This shear-tensile faulting suggests that the fault is opening during rupturing. We assume that this opening is related to the fluid intrusion along the fault plane. On the other hand, MS-2 exhibited a negative values CLVD corresponding to compressive mechanisms, indicative of fault closing during rupturing. This fault closure is usually consistent with nature of reverse faults' motion.

The CLVD components for MS-1 and MS-2 are comparable between the two approaches. However, for MS-3, the CLVD obtained from the full waveform inversion is remarkably higher than that from the spectral ratio-constrained polarity method. Despite this elevated value, we believe it is more reliable, given the significantly high seismicity rate following MS-3. This high CLVD for MS-3 may indicate increased pore pressure after the event, resulting in notable fault opening while shearing. Furthermore, the full-waveform inversion approach is considered the most reliable for moment tensor analysis, as it incorporates the full information embedded in the seismogram.

It is noteworthy to mention that GCMT (Global Centroid Moment Tensor) also calculated moment tensor solution with CLVD components for the three mainshocks. Additionally, a work by Beldjoudi et al. (2016) calculated moment tensor solution for the three main shocks, but using pure DC solution. In **Table. IV.2** we exhibit the summary of these solutions.

Table. IV.2: Comparison of moment tensor solution for the three mainshocks from different studies

		MS-1	MS-2	MS-3
This Study	Pure DC	DC = 100%	DC = 100%	DC = 100%
	Deviatoric	CLVD = 28.3%	CLVD = 7.4%	CLVD = 69.1%
GCMT		CLVD = 13.43%	CLVD = 7.99%	CLVD = 15.28%
Beldjoudi et al. (2016)		DC = 100%	DC = 100%	DC = 100%

IV.4.2 Evidence from Stress Drop Variation

One limitation of using magnitude as a measure of an earthquake's impact is that it primarily reflects the overall size or energy release of the earthquake, but it does not capture the dynamics of fault slip during the event. While magnitude provides a single value that quantifies the total energy, it doesn't account for how this energy is distributed across the fault or how quickly the fault slipped. Stress drop ($\Delta\sigma$), on the other hand, offers deeper insight into earthquake dynamics by describing the amount of stress released during the slip, particularly in relation to the fault area and slip rate. Higher stress drop values are associated with more intense, high-frequency energy release,

which occurs when the fault slips rapidly or when the slip is concentrated over a smaller area.

In the BI-2010 sequence, the involvement of fluids as a driving mechanism was initially suspected by Abacha et al. (2014) based on local earthquake tomography. Further investigation in our study by Abacha et al. (2023a) where we used local earthquake tomography and 4D Vp/Vs ratio analysis to track fluid diffusion, observing high Vp/Vs anomalies after the third mainshock (MS-3). These anomalies coincided with a significant increase in aftershock activity, which we attributed to elevated pore pressure following MS-3.

Given that fluids are known to influence accumulated stress, our study analyzed stress-drop variation across 41 events, well-distributed over ~90 days, to seek additional evidence of fluid involvement, particularly after MS-3. Stress drops were calculated using both Brune's and Madariaga's source radius models, employing corner frequencies derived from individual spectra and EGF approaches. Despite the factor of ~8 difference in stress-drop values between the models, whether in individual spectra approach or EGF approach, the temporal variation behavior remained consistent (see Figures. **Fig. IV.10, IV.11**, **IV.12** and **IV.13**). We identified two phases: before and after MS-3. Before MS-3, generally, high stress drops are observed. Additionally, linear relationship between stress-drop and magnitude was observed, with higher magnitudes corresponding to higher stress drops. After MS-3, we observed a noticeable decrease in stress-drop values. Additionally, the previously observed linearity between magnitude and stress-drop was no longer present. Even though some events with relatively high magnitudes occurred during this phase, their stress-drop values remained low. Overall, the second phase is characterized with lower stress drop values.

We assume that the observed low stress drop after MS-3 can be viewed as another evidence of fluid infiltration. Low stress drop values in seismic events are often linked to fluid diffusion and elevated pore pressure within the fault zone. High pore pressure reduces the normal stress on the fault, making it easier for the fault to slip with less shear

stress accumulation. This phenomenon, often associated with the presence of fluids, can result from processes such as fluid injection, natural fluid migration, or hydrothermal activity. Similar results have been observed in other studies, such as (Chen & Shearer 2011), where events with low stress drop were also related to fluid diffusion processes.
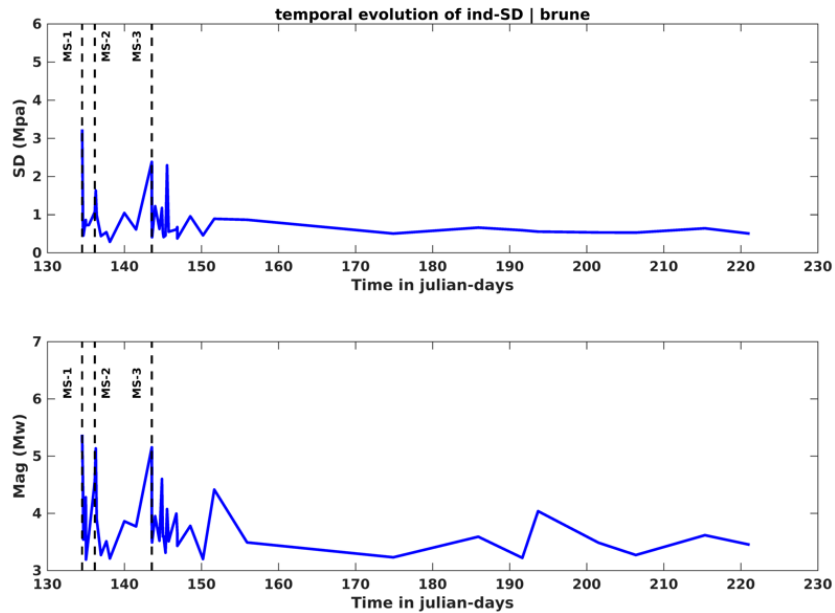
Fig. IV.10: Temporal variation of stress drop and magnitude: Upper panel Brune's model-based stress drop values from individual spectra approach. Lower panel: Temporal evolution of magnitudes. The dashed lines correspond to the ocurrence of the three mainshocks.
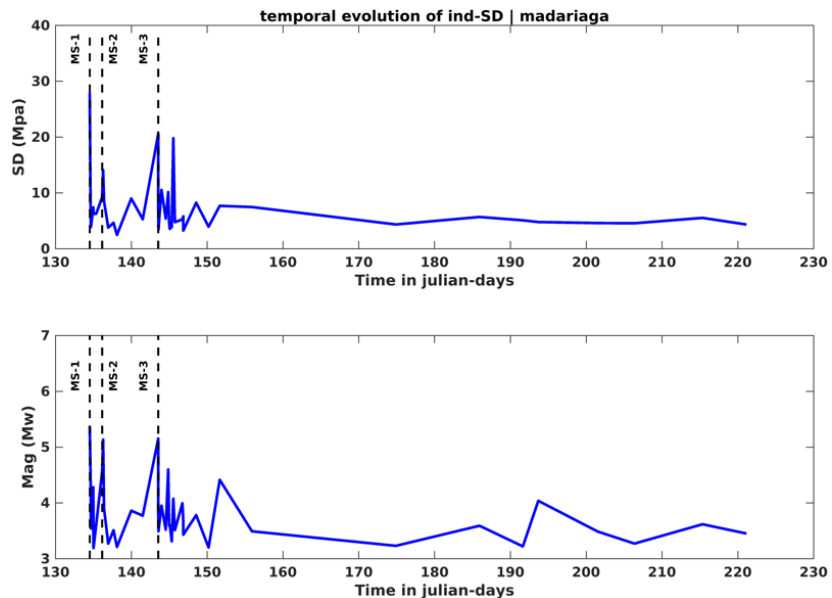
Fig. IV.11: The same as Fig. IV.10, but with Madariaga's model-based stress drop.
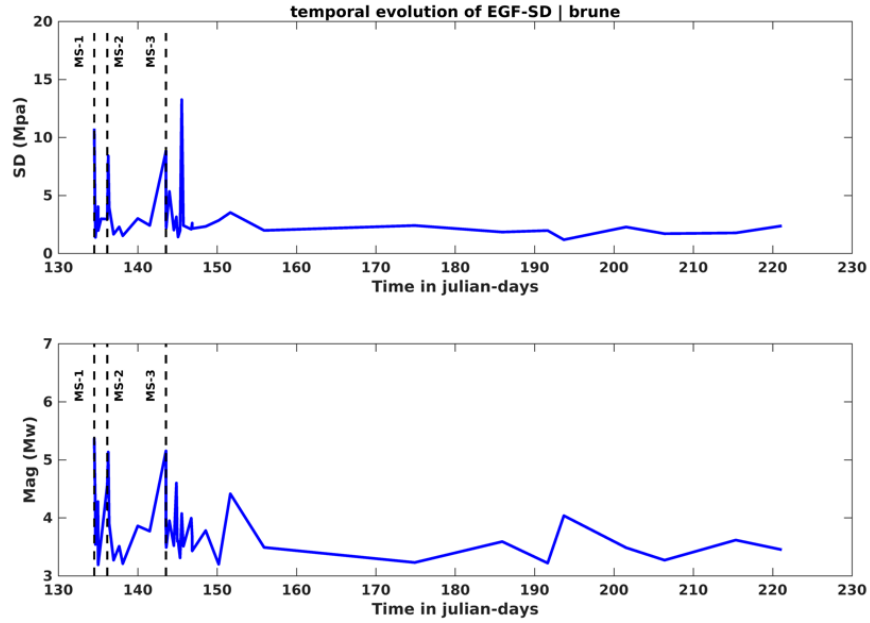
Fig. IV.12: The same as Fig. IV.10, but with EGF approach and Brune's model-based stress drop.
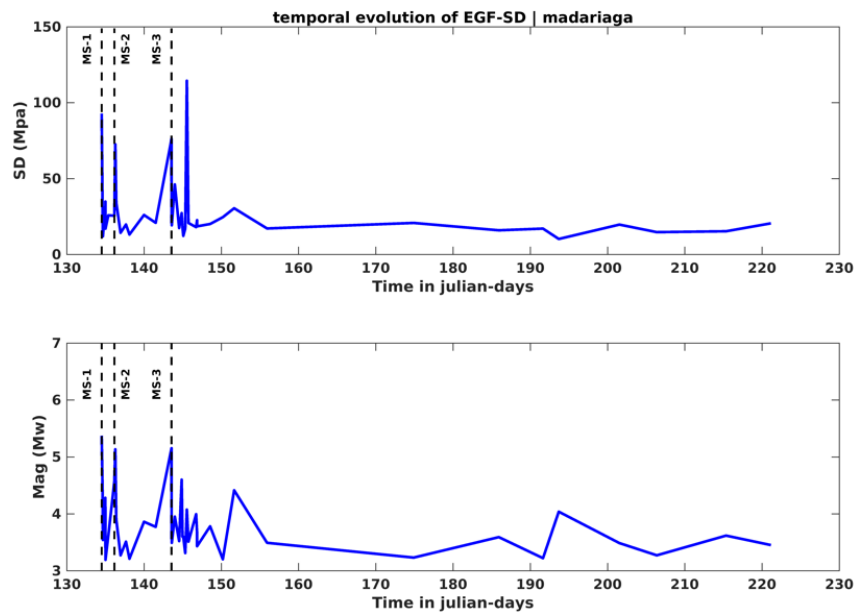
Fig. IV.13: The same as Fig. IV.10, but with EGF approach and Madariaga's model-based stress drop.

IV.5 Insights into Fluid Processes from the Temporal Evolution of Multiplets

An intriguing aspect of the BI-2010 sequence is the contrasting aftershock behavior. While aftershocks typically follow mainshocks, their occurrence in this sequence varies notably. After MS-1 (Mw 5.4), there was a conspicuous lack of aftershock activity, raising questions about the mechanisms controlling aftershock generation. In contrast, the subsequent Mw 5.1 mainshocks were accompanied by a significant increase in aftershock activity. This stark difference warrants further investigation.

We propose two possible explanations:

1. **Stress Triggering on Secondary Faults**: Research suggests that after a large primary rupture, aftershocks can occur on secondary faults parallel to the main fault due to stress redistribution (Perrin *et al.* 2021; Fan *et al.* 2022). In the study area, both the VF1 fault (hosting MS-1) and the parallel VF2 fault exhibit strike-slip, left-lateral faulting mechanisms. After MS-1, aftershock activity shifted to the VF2 fault. This can be observed in the animated movie of seismicity which can be found in the online supplementary materials of our paper Tikhamarine *et al.* (2024), suggesting that static stress transfer probably occurred from VF1 to VF2.

2. **Fluid Dynamics**: According to Miller (2020), the absence of aftershocks may indicate a lack of high-pressure fluid sources at depth, while abundant aftershock activity points to the activation of high-pressure fluid reservoirs. Natural fluids in the Earth's crust can alter the effective normal stress on faults, potentially triggering ruptures. Thus, fluids significantly influence seismicity, including burst-like sequences and swarms (Miller *et al.* (2004), and references therein).
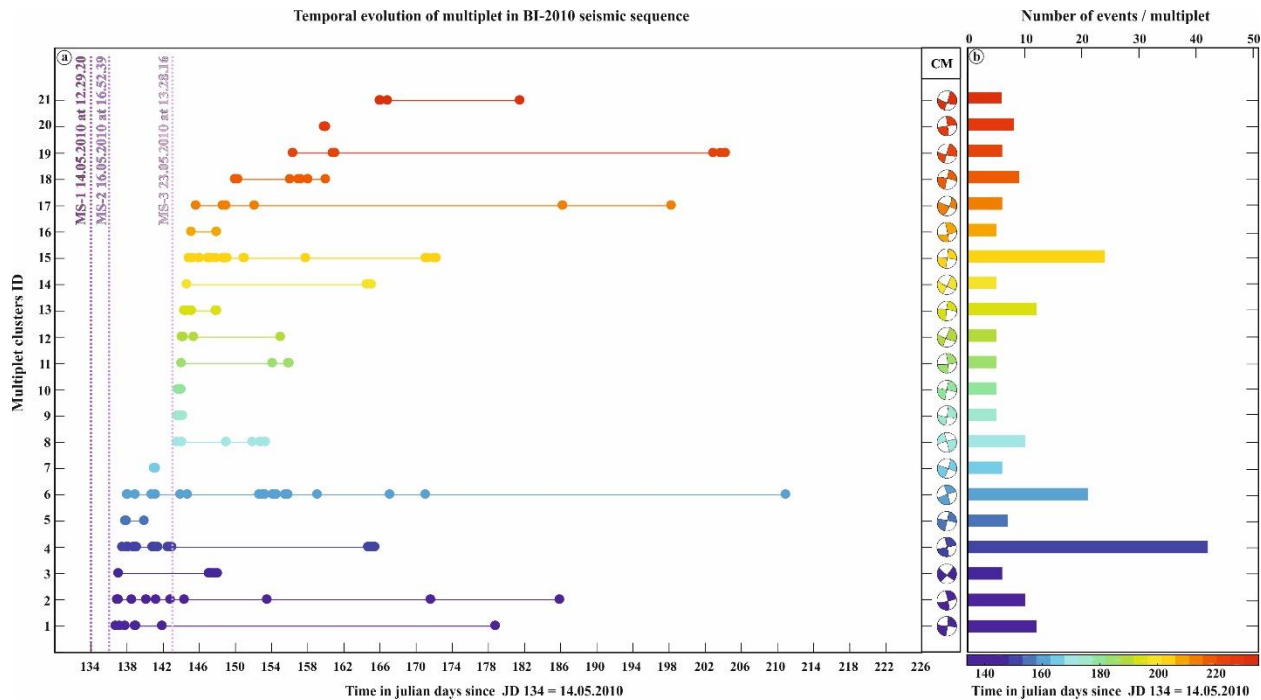
Fig. IV.14: Temporal evolution of multiplet in the BI-2010 seismic sequence. **(a)** presents the activation timeline of the 21 multiplet groups, each consisting of a minimum of 5 events. The vertical purple dotted lines indicate the time occurrences of MS-1, MS-2, and MS-3 mainshocks. The "CM" column represents the composite focal solution for each multiplet group. **(b)** is a bar graph illustrating the number of events per multiplet group.

We propose that fluid movement along pre-existing faults is primarily responsible for generating the multiplet earthquakes observed during the BI-2010 sequence, consistent with findings from Bisrat et al. (2012), Bourouis & Bernard (2007), and Massin et al. (2013).

The temporal evolution of multiplet is of utmost importance, as such analysis can reveal intriguing insights on fluids movements during the BI-2010 sequence. In **Fig. IV.14** we show the activation timeline of the multiplets within the BI-2010 sequence. The temporal pattern of multiplet activity reveals some remarkable aspects: (1) No multiplet group was activated after the appearance of MS-1. (2) Multiplet activity started immediately after MS-2. (3) About two-thirds (2/3) of the multiplet groups were activated after MS-3. In **Fig. IV.15**, we present the temporal history of 78 multiplet

groups, each consisting of at least 3 events. Of these, 54 multiplet groups were activated after MS-3, representing approximately 69% of the total number. (4) The recurrence interval of two consecutive events within each multiplet group is short and irregular. While multiplet C17 with 6 events and an activation duration of ~52.62 days had the longest mean recurrence interval of ~10.52 days, multiplet C20 with 8 events and an activation duration of ~0.22 days had the shortest mean recurrence interval of ~0.027 days, corresponding to ~38.88 minutes.
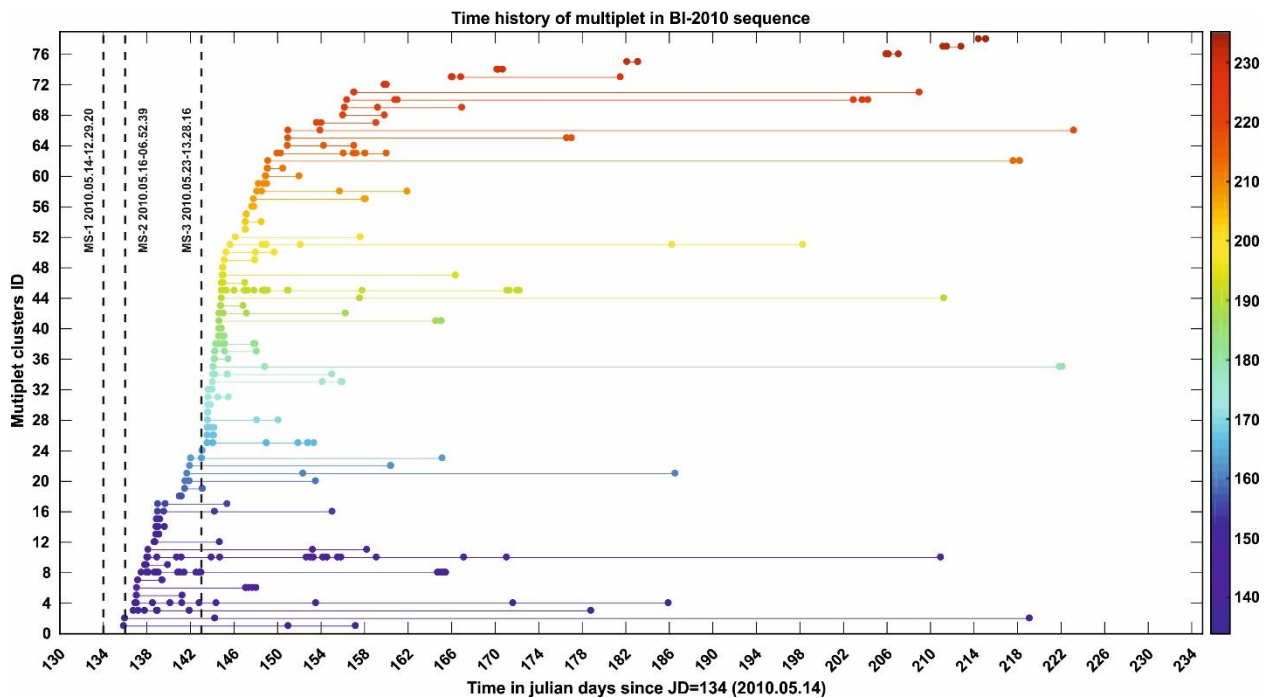
Fig. IV.15: The same as Fig. IV.14, but using 78 multiplet group each with minimum of 3 events.

Considering fluid infiltration is the predominant cause for multiplet generation, supported by Staszek et al. (2021), we interpret the first three aspects previously inferred from **Fig. IV.14** and **IV.15**:

1 Absence of multiplet groups after MS-1: Indicates no fluid intrusion occurred after MS-1.

2 Activation of multiplet groups immediately after MS-2: reflects that fluid infiltration began just after MS-2.

3   Increased rate of multiplet activation after MS-3: suggests that circulating fluid volume had increased, leading to a rise in pore pressure.

In our 4D Vp/Vs model analysis, Abacha et al. (2023a) suggested fluid intrusion may have started before MS-3 due to fractures caused by the seismic activity. However, authors did not specify whether these intrusions started after MS-1 or MS-2. Our multiplet analysis clearly shows that fluid intrusions started immediately after MS-2. Nonetheless, our findings related to increased pore pressure following MS-3 are consistent with those of Abacha et al. (2023a) and Rahmani et al. (2023).

IV.6 Seismicity Migration Analysis: Insights into Aseismic Afterslip

Following our conclusions that fluid intrusion began immediately after MS-2 and that it is the primary forcing mechanism behind multiplet activation, we plotted the R-T diagram using two multiplet dataset: 1) events composing the 21 multiplet groups (218 events) and 2) events composing the 78 multiplet groups (406 events). In both cases with the MS-2 as the point of origin (refer to **Fig. IV.16** upper left and right panels). The distance-time distribution envelopes can be fitted by a diffusion law, $R = \sqrt{(\pi \times D \times T)}$, where D represents the hydraulic diffusiIVty (Shapiro *et al.* 1997). The diffusion coefficient, D, was determined to be 0.36 m²/s and 0.32 m²/s for both datasets respectively. These values are within the range of hydraulic diffusivity values reported by (Do Nascimento et al. 2005) (0.02m²/s < D < 10m²/s). In contrast, Abacha et al. (2023a) considered MS-1 as the origin and analyzed the R-T diagram in the two main clusters MC-1 and MC-2. They showed a migration pattern along MC-2, with a diffusivity of D = 2.4 m²/s, while the migration mechanism along MC-1 was ambiguous (Abacha et al. 2023a). We believe that their choice of MS-1 as the origin and the use of all the sequence events to track the fluid migration introduced a slight bias in their fluid diffusivity results. It is worth noting that not all aftershocks in the BI-2010 sequence are fluid-triggered.
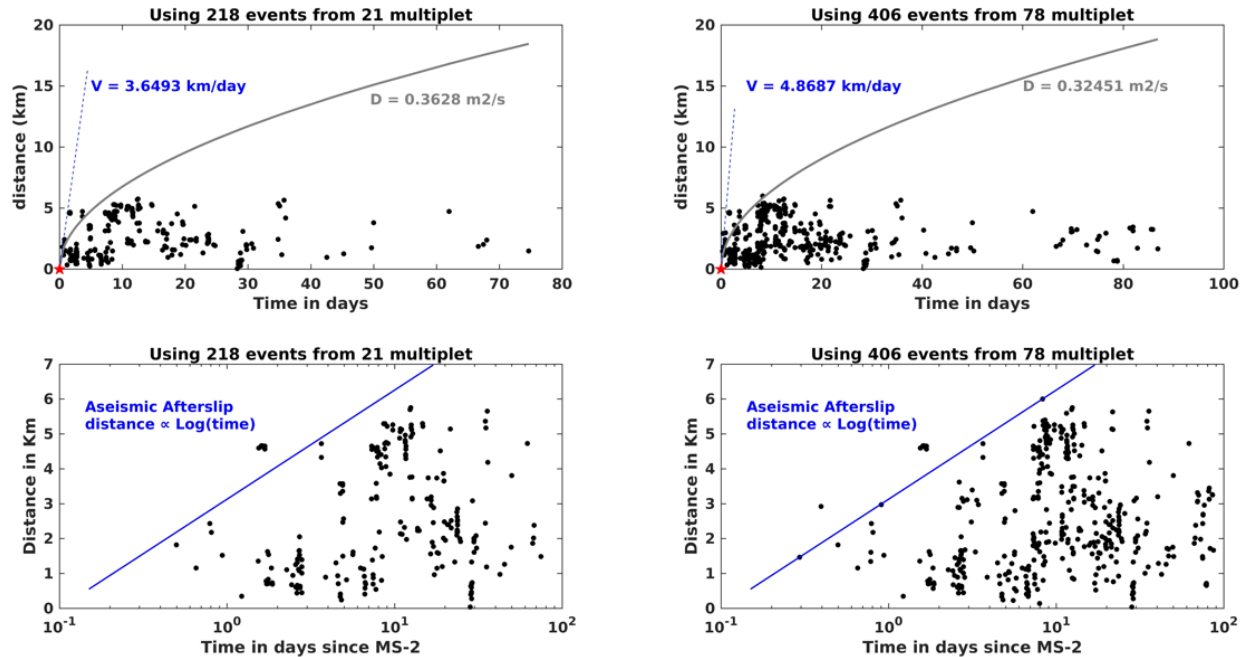
Fig. IV.16: Seismicity Migration Analysis. **Upper left and right)** Linear-time scale (R-T) diagram illustrating events hypocentral distances from MS-2 (Red Star). The dots represent the 218 events comprising the 21 multiplet groups, and the 406 events comprising the 78 multiplet groups, respectively. The curved grey line represents the best-fit solution for a diffusion law (D=0.36 m²/s, D=0.32 m²/s, respectively). The dashed blue line shows a migration velocity of ~3.35 km/day and ~4.86 km/day, respectively, consistent with aseismic afterslip. **Lower left and right)** Expansion of the aftershock area from the rupture edge with the logarithm of time indicative of aseismic afterslip process.

Fig. IV.16 (Lower left and right) show a clear expansion of the aftershock area from the rupture edge as a function of the logarithm of time. This observation suggests that the primary driver of the observed migration is the aseismic afterslip process (Kato 2007). Conversely, a diffusivity coefficients of 0.36 m²/s and 0.32 m²/s suggest the involvement of fluid diffusion. Since aseismic afterslip and fluid diffusion are related mechanisms, we believe that the seismicity migration in BI-2010 is driven by fluid-induced aseismic slip, see **Fig. IV.17**. Similarly, numerous studies have shown that an increase in fluid pressure within a fault triggers aseismic slip in its early stages (Bhattacharya & Viesca 2019; De Barros *et al.* 2020; Danré *et al.* 2022).
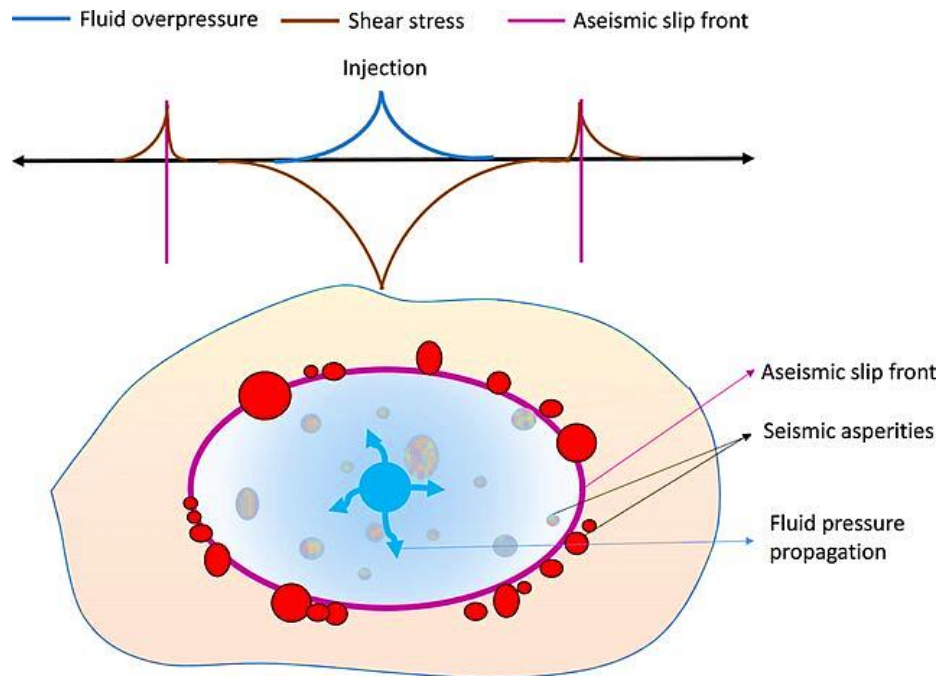
Fig. IV.17: Illustrative model of fluid-induced aseismic slip. Aseismic slip front (purple) propagation leads to shear stress concentration at its tips (brown), triggering seismicity on asperities (red patches), which correspond to the seismicity front. After Danré et al. (2022).

It is crucial to discuss the migration behavior of the BI-2010 sequence. As noted in **sub-chapter II.3.4**, the spatiotemporal evolution shown in **Fig. II.12** lacks a discernible and consistent migration pattern, such as a progressive movement to the south or west. However, this does not imply an absence of seismic migration. The inconsistent migration behavior can be explained by the activation of an intricate fault system. As highlighted in **Chapter II**, the BI-2010 sequence involves the activation of a complex fault system, resulting in more diffuse and less predictable seismic activity. Despite the lack of a clear migration pattern, examining the spatiotemporal evolution of the total aftershock activity (**sub-chapter II.3.4**) and multiplet activation (**sub-chapter II.6**) reveals that seismic activity began along the main cluster MC-1 and transitioned to MC-2 shortly after MS-3. Subsequently, seismicity underwent a continuous transition between MC-1 and MC-2.

IV.7 Repeating Earthquakes: Additional Evidence of Aseismic Slip

The short and irregular recurrence time of co-located earthquakes with highly similar waveforms is a well-known attribute of burst-type repeating earthquakes. Repeaters have been widely used to reveal aseismic slip mechanisms. The fourth aspect observed in **Fig. IV.14** prompted us to investigate the presence of this type of repeating earthquakes within each of the 21 retrieved multiplet groups.

IV.7.1 Detection of Repeating Earthquakes

Burst-type repeating earthquakes are especially observed during swarms or aftershocks associated with large earthquakes (Igarashi et al. 2003). The criterion of overlapping source areas is often crucial for the identification of repeaters. It requires the estimation of source radii for all studied events, either by using estimated corner frequencies from P- or S-wave spectra or by assuming a convenient constant stress (Gao et al. 2021; Mesimeri & Karakostas 2018).

In this study we preferred to use the Empirical Green's Function (EGF) analysis to calculate the equivalent rupture radius (ERR) of each event within each multiplet group, using the P-wave corner frequencies. The ERR commonly represents the rupture area for a circular crack model (Brune 1970; Eshelby 1957). We were able to resolve the source characteristics (corner frequency and ERR) of 14 events out of 218 events that make up all 21 multiplet groups. This limitation in the calculations is mainly due to the magnitude difference condition (the EGF event should be at least one order of magnitude smaller than the target event). It has been observed that multiplet groups tend to have low magnitude variability, see **Fig. IV.18e**. An illustration of the EGF analysis is shown in **Fig. IV.18a-d**, and a summary of the calculated source parameters for the 14 events is given in **Table IV.3.** To estimate the source radius for the remaining 204 events, we performed a linear regression analysis on a log-log scale to establish a scaling relationship between the source radius (ERR) and the seismic moment (M0). Relying on only 14 events for this analysis could lead to biased results due to the narrow seismic moment range. To address this, we incorporated data from 18 additional events reported by Abacha et al. (2019).

Using their corner frequencies, we calculated the source radii with Madariaga's source model (III.22), see **Fig. IV.18f**. Despite that we have resolved a scaling law M_0-R for 41 events in **Chapter III**, we represent here the same results in our paper Tikhamarine et al. (2024). The resulting scaling relationship is:

$$ERR = 10^{-2.39} * M_0^{0.33} \qquad\qquad IV.1$$

This implies $M_0 \propto ERR^{3.03}$, which is consistent with theoretical expectations.
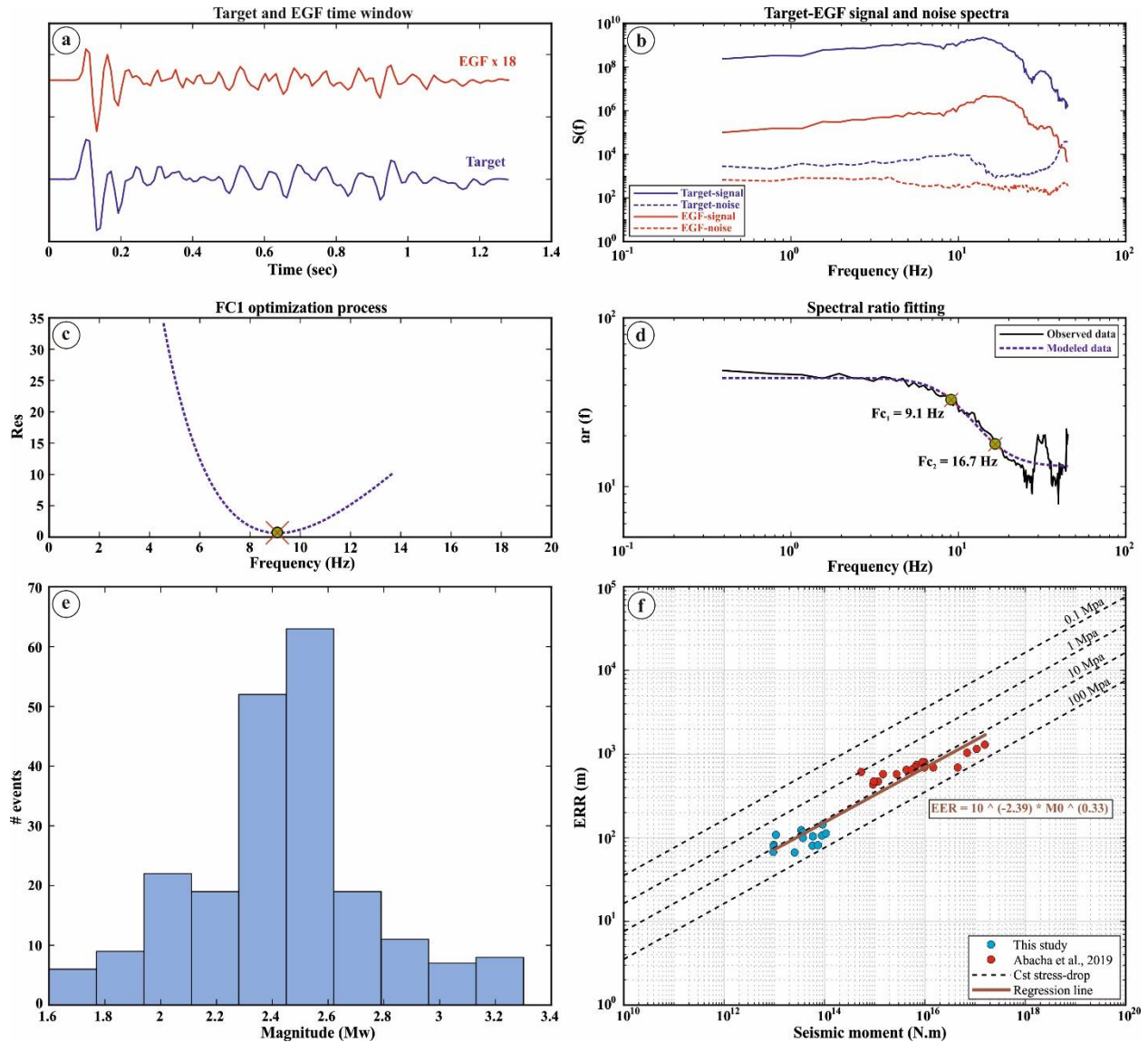
Fig. IV.18: Example of empirical Green's function analysis. **(a)** Displays normalized traces of the target event (2010.05.28–18.51.24 Mw 3.361) and EGF event (2010.05.31–00.44.28 Mw 2.212) shown in blue and red, respectively. **(b)** Shows spectral amplitude of the target

(blue) and EGF (red) signals, with corresponding noise spectra indicated by dashed lines. **(c)** Illustrates the optimization process for fc1. **(d)** Presents spectral ratio fitting, with observed spectral ratio in black, the modelled spectral ratio in blue dashed line and the corner frequencies of the target and EGF events marked by green circles with 'x'. **(e)** Depicts magnitude distribution of 218 events across all 21 multiplet groups. **(f)** Represents scaling relationship between source radius and seismic moment in a log–log scale. The red dots represent the (M0, ERR) values of the 14 events calculated in this study, while the blue dots correspond to the (M0, ERR) values of 18 events from Abacha et al. (2019). The best-fit regression is depicted by the brown solid line.

Table. IV.3: Source parameters of 14 events using EGF.

ID	$M_0(N.m)$	M_W	$F_{C1}(Hz)$	$ERR(m)$
20100521221330	3.5e+13	3.029	8.425	121.53
20100521042648	3.8e+13	3.053	8.984	113.98
20100522200911	9.4e+13	3.315	7.188	142.46
20100516223415	1.0e+13	2.667	12.633	81.05
20100615210712	9.1e+13	3.306	9.758	104.94
20100528185124	1.1e+14	3.361	9.194	111.37
20100524011918	1.0e+13	2.667	13.293	77.03
20100524154200	1.1e+13	2.694	9.565	107.05
20100524084528	5.9e+13	3.180	12.895	79.41
20100523173121	3.8e+13	3.053	10.450	97.98
20100524014532	7.6e+13	3.253	12.712	80.55
20100609003407	2.6e+13	2.943	15.565	65.79
20100517021411	9.8e+12	2.661	15.359	66.66
20100705063911	6.0e+13	3.185	9.991	102.49

We analyzed the source areas overlapping within all multiplet groups on a cross-sectional view along the assumed fault plane. In the absence of specific guidelines or established criteria for identifying events originating from the same fault patch (repeaters) based on minimum overlap areas and a magnitude difference, we adopt the definition proposed by Gao et al. (2023). According to this definition, events are considered to originate from the same fault patch if their inter-event distance does not

exceed 80% of the source radius of the larger event and the events have a magnitude difference less than or equal to 0.3. In addition, we require a waveform similarity of at least 95%. The events meeting these criteria are considered repeating earthquakes.
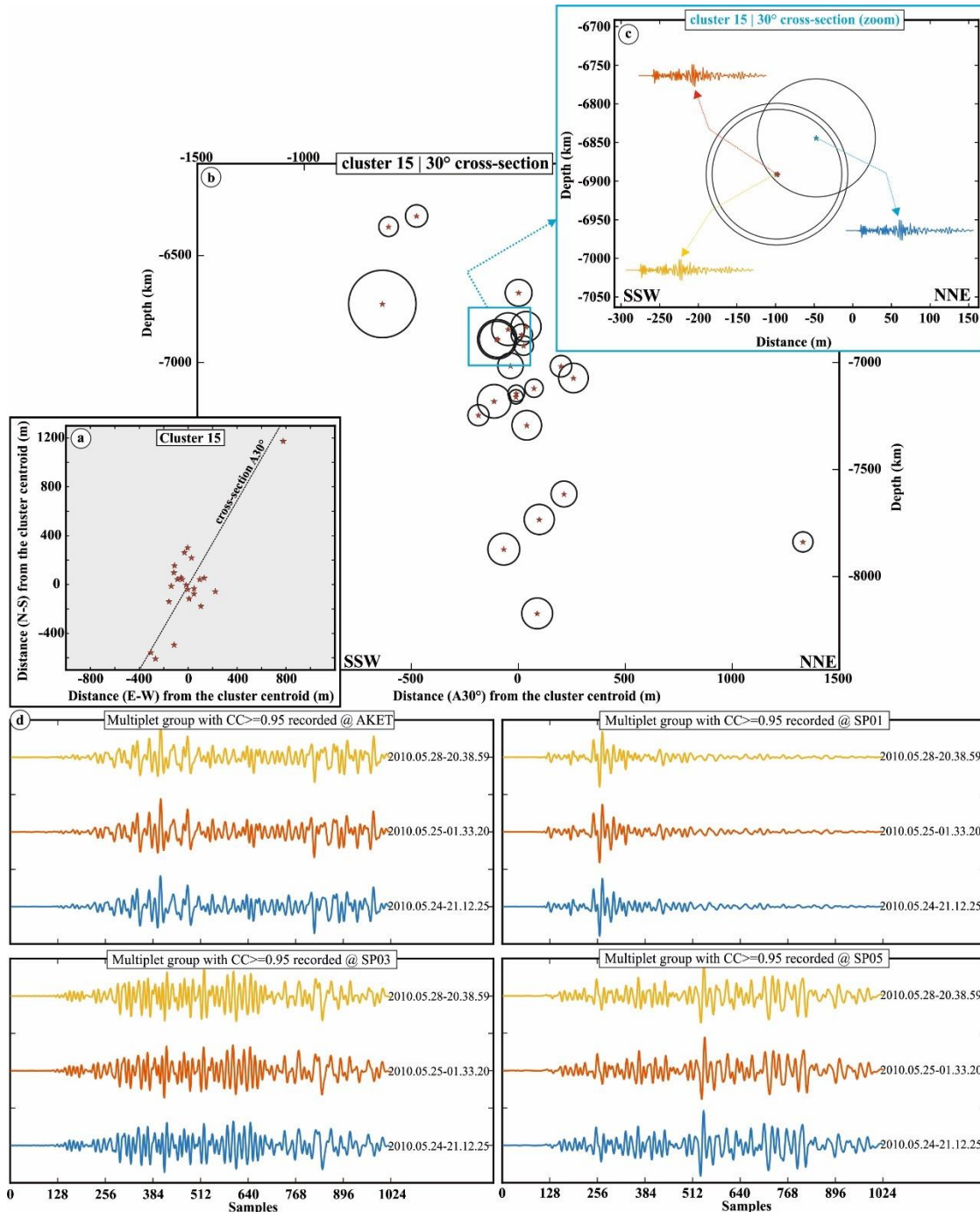
Fig. IV.19: Example of repeating earthquakes from multiplet cluster C15. The events exhibited a CC ≥ 95 per cent at 5 stations. **(a)** shows the horizontal distribution of the events within multiplet cluster C15. **(b)** Shows the cross-sectional view along the

assumed fault plane with projected hypocentres as red stars and rupture areas as circles. **(c)** Zooms in on the cross-section, showing a fault patch with three repeated ruptures; the presented seismograms are recorded at station SP07. **(d)** highlights waveforms recorded at four other stations: AKET, SP01, SP03 and SP05.

In **Fig. IV.19**, we show an example of repeating earthquakes from multiplet group number 15 (cluster C15). The cross section (panel c) indicates the presence of a fault patch that ruptured three times over a period of ~4 days, with two events rupturing at exactly the same location. This short recurrence interval (on the order of days) classifies these repeaters as burst-type and indicates rapid healing and reloading of fault-patches. In total, we identified 12 fault patches with repeated ruptures according to the aforementioned criteria.

IV.7.2 Explanation for Repeating Earthquakes in the BI-2010 Sequence

Repeating earthquakes are a reliable indicator of aseismic slip transients. These events are commonly interpreted as an indicator of fault creep in natural seismicity studies (Uchida & Bürgmann 2019) and have been observed in induced seismicity through fluid injection (Bourouis & Bernard 2007). Near-repeating earthquakes also serve as valuable indicators of aseismic slip transients, as highlighted by Shaddox et al. (2021).

We suggest that periods of high pore pressure during the BI-2010 sequence promoted the initiation of aseismic slip cycles, which in turn triggered the observed repeater groups. The presence of different repeaters during a seismic sequence may indicate the occurrence of cyclic aseismic periods (De Barros *et al.* 2020). The combination of the fast migration rate (3.35 km/day and 4.86 km/day, see **Fig. IV.16**), the expansion of the aftershock area with the logarithm of time and the presence of repeating earthquakes strongly suggests a transient aseismic slip process as a contributing forcing mechanism, at least from MS-2 onward.

IV.8 What Mechanism Drove the BI-2010 Sequence? A Summary

The BI-2010 seismic activity is driven by a nuanced interplay of various factors. Tectonic loading, as evidenced by regional tectonic forces influencing the local stress field, and static stress, as investigated by Beldjoudi (2020), significantly contribute to the seismic behavior. Furthermore, fluid dynamics, as highlighted by Abacha et al. (2014, 2023a) and confirmed by Rahmani *et al.* (2023), Tikhamarine *et al.* (2024) and the present thesis through different methods, played a crucial role. A novel discovery of our research (Tikhamarine *et al.* (2024)) is the significant involvement of aseismic slip transients in shaping the seismic activity.

The combined effects of tectonic forces, static stress transfer, fluid dynamics, and the newly identified aseismic slip transients are responsible for the BI-2010 seismic activity. This multifaceted driving mechanism highlights the imbricated forces at play. Similar observations have been reported by De Barros et al. (2019), Kaviris et al. (2021), Miller (2020), and Ross et al. (2017).

IV.9 Probable Hydromechanical Interpretation of the BI-2010 Sequence

The intricate interplay between complex fault geometry and fluid dynamics, as revealed by this study, is the key to understanding the seismic behavior of the BI-2010 sequence. The activation of small fault segments, emerges as a critical factor that averted the occurrence of a potentially more catastrophic seismic event. In fact, the activation of small fault segments within a complex fault system, reduces the overall stress concentration on any single segment, potentially making it less likely to reach a critical stress point that could trigger a significant earthquake. While fluids can initiate small earthquake ruptures due to high pressure, they can also contribute to the rupture of structures that are already predisposed to failure due to tectonic loading and static stress changes (Micklethwaite & Cox 2006), provoking moderate to large earthquakes. Therefore, it is likely that high fluid pressure was a contributing mechanism in triggering MS-2 and MS-3. Cappa et al. (2009) demonstrated that the presence of two intersecting faults can promote fluid migration along their intersection. This observation is consistent

with our study. The intersected fault geometry, particularly the E-W right-lateral VF5 fault and the NNW-SSE left-lateral VF2 fault (**Fig. II.19b** and **c**), provided a conduit for the upwelling of deep fluids. In addition, the reactivated fault segments formed a conduit network for fluid flow (Sheng et al. 2022). The wider distribution of aftershocks along vertical faults in the Beni-Ilmane region indicates a complex fault zone architecture with multi-core zones and highly fractured damage zones. Such complex fault zone architecture results in a heterogeneous distribution of hydromechanical parameters (Faulkner et al. 2010). The marked differences in hydromechanical properties facilitate fluid accumulation, leading to elevated pressure in certain regions of the damage zone, potentially generating small seismic events (Jeanne et al. 2014). It is highly probable that the periods of high pore pressure during BI-2010 sequence affected the frictional resistance of the faults. As the fluid pressure increases, friction evolves from rate weakening (frictional resistance between fault surfaces decreases as the slip rate increases) to rate strengthening (frictional resistance between fault surfaces increases as the slip rate increases), favoring aseismic slip (Cappa et al. 2019). These hydromechanical correlations with the observed BI-2010 seismicity not only enrich our understanding of seismic phenomena, but also provide useful insights for seismic hazard assessment and risk mitigation strategies.

IV.10 Conclusion

The BI-2010 seismic sequence presents a complex interplay of multiple driving mechanisms. Throughout this chapter, we have demonstrated that tectonic loading—supported by the alignment of stress orientations with the Afrcian-Eurasian plate motion—was a significant force. Additionally, stress transfer between faults likely played a crucial role. Further, we provided compelling evidence of fluid dynamics influencing the sequence, as shown by moment tensor decomposition, stress drop variations, and the presence of multiplet earthquakes. Importantly, for the first time, we identified aseismic afterslip as a key factor, with seismicity migration being driven by an aseismic front. The

existence of repeating earthquakes further substantiates the presence of aseismic slip. Ultimately, we conclude that the BI-2010 sequence was driven by an intricate combination of tectonic loading, stress transfer, fluid intrusions, and aseismic slip. However, the precise contribution of each mechanism remains uncertain, and no single factor can be definitively identified as dominant. Finally, we proposed a probable hydromechanical interpretation, integrating the influence of fluids with fault mechanics in shaping the sequence.

Chapter V

Geometric and Physical Characterization of Active Faults in Northeastern Algeria

Content

V.1 Introduction

The dense deployment of high-quality seismological stations within the Algerian Digital Seismic Network (ADSN) and the installation of several temporary networks following various Algerian earthquakes have enabled CRAAG to compile an exceptional dataset, primarily composed of moderate to weak seismic events. This dataset is invaluable for advancing our understanding of the region's tectonic activity. The detailed analysis of these events, particularly the high-precision relocation of seismic sequences as discussed in **Chapter II**, will allow for the precise identification and classification of active faults. By utilizing techniques such as precise hypocenter relocation, focal mechanisms and source parameters analysis, we can accurately map fault structures and understand their behavior.

Moreover, integrating these findings within the geological framework offers a more comprehensive understanding of the tectonic forces shaping the region. The results from such analyses provide new insights for refining seismic hazard maps in northeastern Algeria, thereby supporting enhanced hazard assessment and risk mitigation efforts in this seismically active area.

Chapters II, III, and **IV** present a comprehensive study of a specific seismic sequence, covering the identification of responsible tectonic structures, characterization of physical properties, and elucidation of underlying mechanisms. Building on this approach, in the current chapter, we aim to determine the geometrical and physical parameters of the various faults responsible for seismic sequences in the northeastern region from 2007 to 2022.

V.2 Algeria's Seismic Hazard Framework

V.2.1 Seismotectonic Features

Seismic activity in northern Algeria is primarily driven by its location along the boundary between the African and Eurasian tectonic plates. The northwest-southeast convergence of these plates results from Africa's counterclockwise rotation relative to

Eurasia, influenced by seafloor spreading at the Atlantic Ridge, occurring at rates of 25 mm/year in the north and 40 mm/year in the south (see the right corner of the **Fig. V.1a**). This tectonic interaction has shaped the region's topography, particularly the Tellian Atlas mountain range (Babors, Hodna, Biban, Chenoua, Dahra, Ouarsenis…). Seismic events are most intense along the Algerian margin and the Tellian Atlas, where major faults are associated with Neogene basins like Mitidja, Chellif, and Mila-Constantine. In contrast, the High Plateaus and Saharan Atlas to the south experience minimal active deformation, with the stable Saharan platform displaying negligible seismic activity (**Fig. V.1a**).

Through the analysis of Algerian seismicity (**Fig. V.1a**), alongside focal mechanisms of significant earthquakes (those with magnitudes exceeding 5.5) and the principal directions of seismic stress depicted as horizontal projections of compression (in red) and tension (in blue) (**Fig. V.1b**), we can identify two distinct zones with relatively consistent tectonic regimes: (1) a broad NE-SW thrust fault zone along the western and central Tell Atlas, where significant earthquakes, such as those in Orleanville (1954), El Asnam (1980), Tipaza (1989), and Boumerdes (2003), have occurred; and (2) a deformation zone characterized by dextral E-W, NW-SE to N-S and sinistral NE-SW strike-slip faults, and some thrust faults mainly in the offshore part, notably in the eastern region, as exemplified by the 1985 Constantine earthquake.
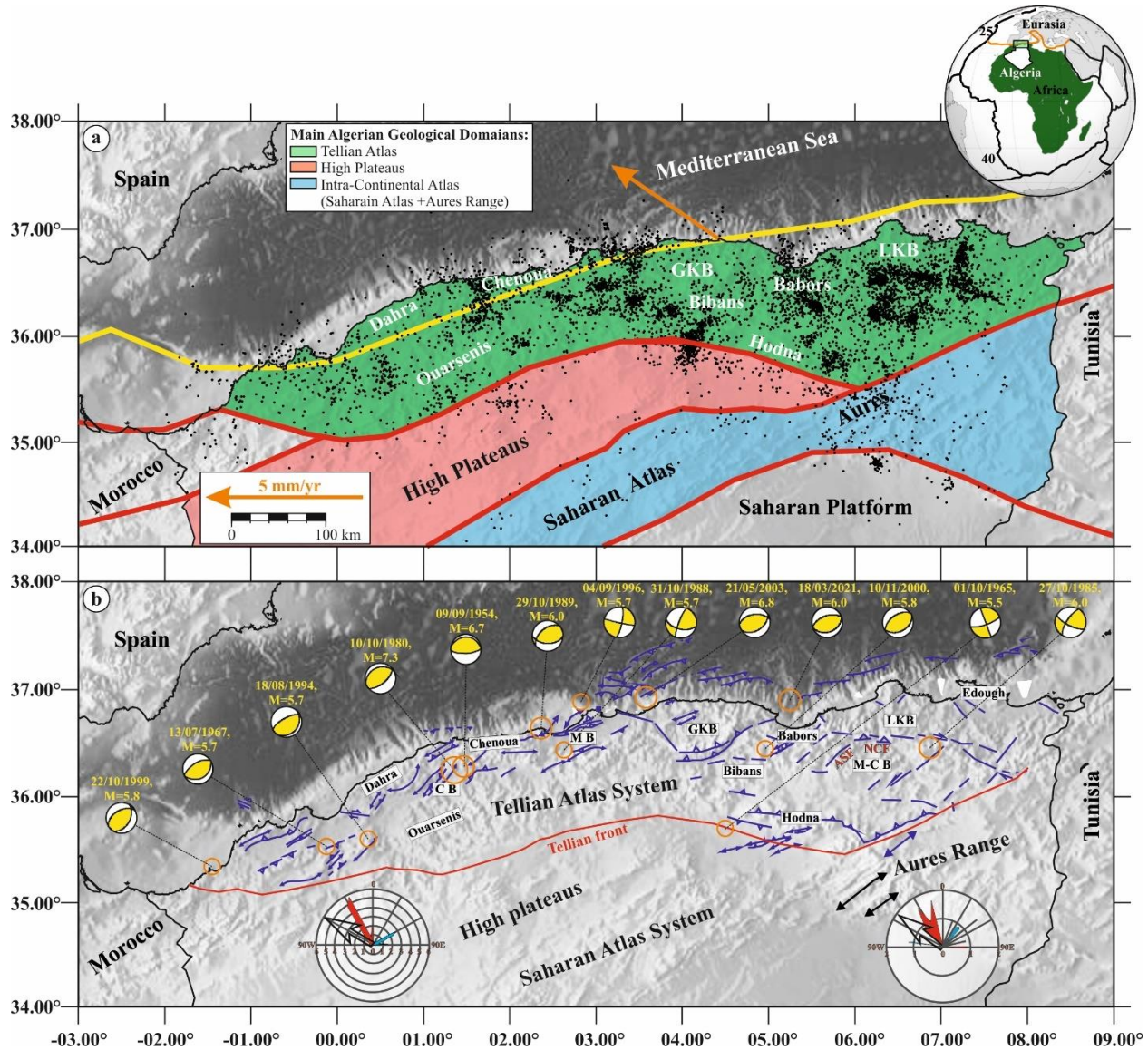
Fig. V.1: Simplified geological framework of Algeria. **(a)** Geological map of Northern Algeria, depicting the main geological units. The yellow line highlights the boundary between the Eurasian and African Plates (simplified from Bird 2003), while the orange arrows indicate the rate and direction of Africa's relative motion toward Eurasia (Bougrine et al., 2019). Seismicity between 2006 and 2021 was also shown. **(b)** Seismotectonic map of northern Algeria, highlighting the main active faults within the Tellian Atlas (adapted from Abacha 2015 and sources therein). The map also shows some significant earthquakes (M ≥ 5.5) with corresponding focal mechanisms. Neogene seismogenic basins (CB: Cheliff Basin, MB: Mitidja Basin, M-CB: Mila-Constantine Basin) and key mountain ranges of the Tellian Atlas are labeled. The Greater and Lesser Kabylia Blocks (GKB and LKB respectively) are identified. Rose diagrams for domains 1 and 2 illustrate the principal P (red) and T (blue) axes orientations, modified from Serpelloni *et al.* (2007).

V.2.2 Seismic Hazards Features

Seismic hazard refers to the probability of earthquake-related natural phenomena, such as ground shaking or fault rupture, occurring in a given area, based solely on geological and seismological factors. In contrast, seismic risk assesses the potential impact of these hazards on people, infrastructure, and economic assets, combining the hazard with factors like population density, building vulnerability, and preparedness. While seismic hazard maps show where earthquakes are likely to occur, seismic risk mitigations inform strategies for reducing potential damage like building codes, emergency preparedness, and land-use planning (Baker *et al.* 2021)

a) **The Most Significant Earthquakes**

Northern Algeria has experienced numerous destructive earthquakes throughout its history. Some of the most significant recent events include the June 24, 1910 earthquake in Aumale (Ms 6.6), the September 9, 1954 earthquake in Orleanville (Ms 6.7), the October 10, 1980 earthquake in El Asnam (Ms 7.3), the October 27, 1985 earthquake in Constantine (Ms 6.0), the October 29, 1989 earthquake in Tipaza (Chenoua Mont) (Mw 6.0), the December 22, 1999 earthquake in Ain Temouchent (Mw 5.7), and the May 21, 2003 earthquake in Boumerdes (Mw 6.8) **(Fig. V.1b)**. These seismic events, which resulted in significant devastation, underscore Algeria's high susceptibility to seismic hazards and risks, especially in the northern region, which is characterized by high population density and industrial activity concentrated in the northern region.

b) **The Maximum Observed Intensity (MOI$_{2014}$)**

Another perspective on seismic risk distribution in Algeria can be depicted through the Maximum Observed Intensities (MOI) maps. Roussel 1973b, using data from 1716 to 1970 constructed the first MOI map, revealing three major regions: Northern Algeria - characterized by high seismic activity, with maximum observed intensities reaching up to degree X. Northern part of the Southern Atlas Flexure - generally exhibits very low seismicity, except for areas around Biskra and Batna, where a few events with

intensities of up to IX have been recorded. The High Plateaus - show low seismic activity, with observed intensities not exceeding degree VI. Bezzeghoud *et al.* (1996) updated this map with data from 1970 to 1990, including major earthquakes like the 1980 El Asnam, the 1985 Constantine, and the 1989 Mont-Chenoua-Tipaza. This updated map identified four major regions with intensity VII: Constantine-Guelma-Souk Ahras, Bibans-Babors-Aures-El Hodna, Algiers-Cherchell-Chellif-Ouarsenis, and Oran-Relizane-Sidi Bel-Abbes. The most recent study by Ayadi & Bezzeghoud (2015) further revised the MOI_{1996} map, incorporating data from 1365 to 2013, including significant events from the last two decades, such as Mascara (1994), Ain Temouchent (1999), Zemmouri (2003), Laalam (2006), and Beni Ilmane (2010) (see MOI_{2015} in **Fig. V.2a**).

The MOI map effectively illustrates the spatial distribution of maximum seismic intensities, helping to identify earthquake-prone areas. Additionally, it serves as a crucial reference for designing structures in seismic zones, ensuring that civil engineering projects incorporate earthquake-resistant features tailored to the specific seismic risks of each region.

c) The Peak Ground Acceleration

The destructive earthquakes in Northern Algeria highlight the critical need for assessing seismic hazards to develop an effective zoning strategy for the region. The first seismic hazard studies in northern Algeria were conducted by Woodward-Clyde Consultants (WCC) in 1984, following the 1980 El Asnam earthquake. More recently, Hamdache has advanced this field by applying probabilistic models in numerous publications, contributing significantly to the understanding and mitigation of seismic risks in the region.
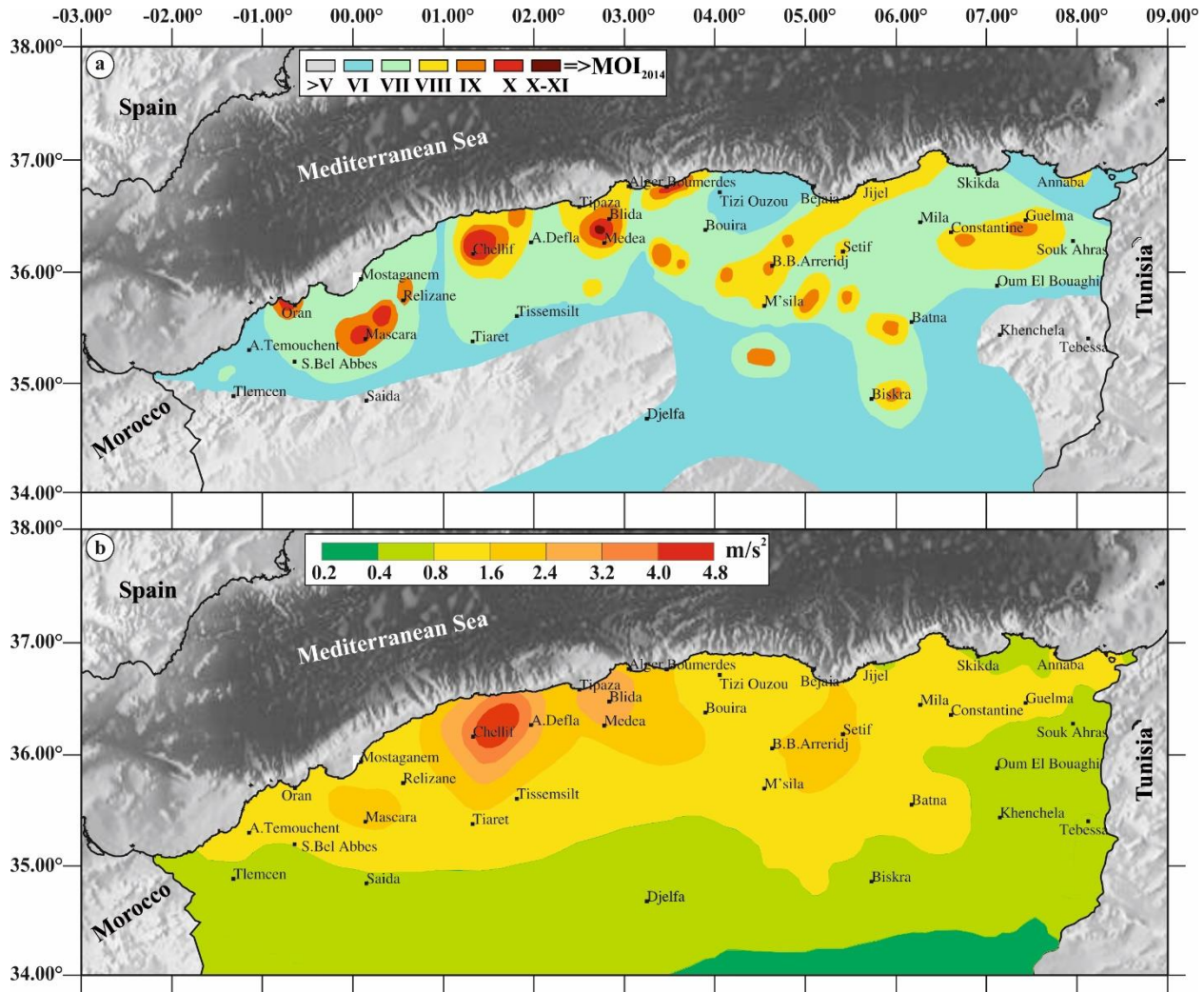
Fig. V.2: PGA and intensity map of Algeria. **(a)** Maximum Observed Intensity (MOI$_{2014}$) map, as determined by Ayadi & Bezzeghoud (2015). **(b)** Mean Peak Ground Acceleration (PGA in g-units) with a 10% probability of exceedance over 50 years, corresponding to a return period of 475 years (based on Peláez *et al.* (2005)).

Fig. V.2b illustrates the seismic hazard map in terms of Peak Ground Acceleration (PGA), reflecting a 10% probability of exceedance within 50 years, corresponding to a return period of 475 years (Peláez *et al.* 2005). The highest seismic hazard values are concentrated in the central Tell Atlas, particularly in the Chellif and Ain Defla regions, where the average PGA exceeds 2.4 m/s² and reaches up to 4.8 m/s² in the area affected by the 1954 and 1980 El Asnam earthquakes. Blida and Algiers also present significant seismic risks, with average PGAs exceeding 2.4 m/s². An area between these zones, including Setif and Mascara, shows a PGA of around 1.6 m/s². The rest of the Tell Atlas

falls within a moderate seismic risk zone with PGA > 0.8 m/s². In contrast, the High Plateaus, Saharan Atlas, and Saharan platform are classified as low-risk zones, with PGAs below 0.8 m/s². This assessment aligns with observed seismicity before 2003. However, following the 2007 installation of the Algerian Digital Seismological Network (ADSN) and the subsequent improvement in detection capabilities, along with numerous recent seismic sequences, an update to this hazard map is warranted.

Additionally, there is a more recent study by Hamidatou *et al.* (2021) that focuses on a relatively small region. Using a seismicity catalog spanning 1365–2018, the study estimates seismic hazard in terms of Peak Ground Acceleration (PGA) and its spatial variation at the surface (**Fig. V.3**). According to the figure, the maximum PGA values are observed in three main areas: (1) in the central part of the M'cid Aïcha Debagh Fault (MADF), reaching 0.27 g near the epicenters of the Ms 6.0 October 27, 1985 Constantine earthquake (C-Eq), the Mw 4.7 El Kantour earthquake (K-Eq) on April 5, 2017, and the Md 3.2 Sidi Dris earthquake (SD-Eq) on April 4, 2017; (2) between the Kherrata Fault (KF) and the Beni-Ilmane Fault Network (BFN), along the Chakchout, Azros, and Nador corridor, near the mb 5.7 Beni-Ourtilane earthquake (BO-Eq) on November 10, 2000, and the Mw 5.4 Beni-Ilmane earthquake (BI-Eq) on May 14, 2010; and (3) in the Babors region, with the occurrence of the Md 5.0 Darguinah earthquake (D-Eq) on June 28, 1974, the Mw 5.2 Lallam earthquake (L-Eq) on March 20, 2006, and the Mw 5.2 Bejaia earthquake (B-Eq) on May 19, 2013. A fourth zone near Oum El Bouaghi is also observed, but it is likely an artifact, as the area lacks significant seismic or tectonic activity. Although this study is considered the most representative of the northeastern region, it needs to be updated to include all significant seismicity that occurred between 2018 and 2022.

Chapter V
          Geometric and Physical Characterization
of Active Faults in Northeastern Algeria
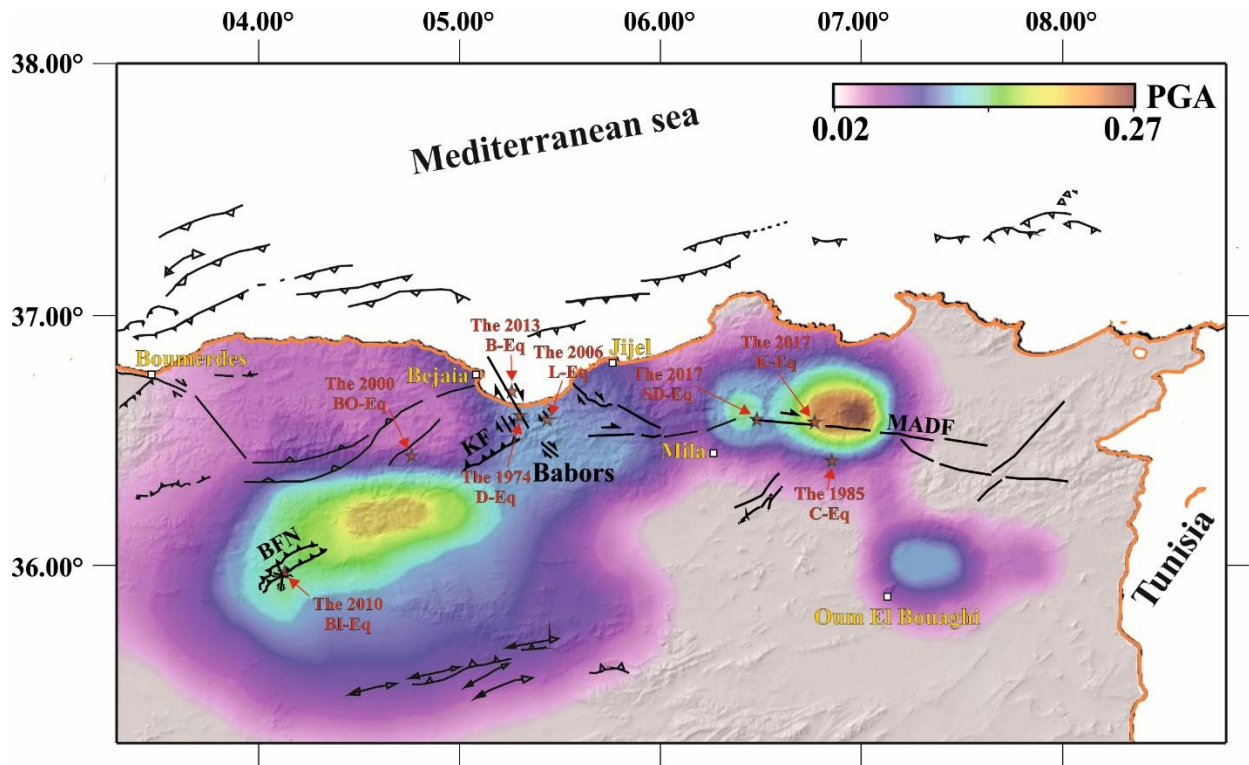
Fig. V.3: PGA values (%g) corresponding to a return period of 475 years (10% probability of exceedance in 50 years) (modified from Hamidatou et al. (2021)). The primary tectonic structures and significant seismic events recorded in the area before 2018 are also presented.

d) Seismic zoning of Algeria

Several studies have focused on seismic zoning in Algeria, each employing different methodologies. Aoudia *et al.* (2000) used deterministic hazard analysis, while (Peláez *et al.* 2003; Peláez *et al.* 2005) employed probabilistic approaches. Harbi. 2001 focused on historical seismicity, Abacha 2015 identified nine seismogenic zones based on seismological data and geological context, and Hamidatou *et al.* (2021) used the Northeastern Algerian catalog. Days before the completion of this thesis, Bellalem *et al.* (2024) made a valuable new contribution to Algerian seismic hazard assessment by incorporating data from 1658 to 2018, using the Parametric-Historic method. However, the exclusion of post-2018 data may make their study less up to date, as northern Algeria has experienced several significant earthquakes since then, including the Mw6.0 Bejaia

earthquake in March 2021. Additionally, the Algerian Seismic Codes (RPA - *Règles Parasismiques Algériennes*) incorporated seismic zoning in its 1999 version, updated in 2003. Most recently, a 2024 revision introduced significant enhancements to seismic risk mitigation strategies.

In contrast to the 2003 RPA, which divided Algeria into five seismic zones, the updated RPA 2024 version introduces a new seismic zoning framework that divides the country into seven distinct zones of increasing seismic hazard (**Fig. V.4**). This revision reflects a better understanding of seismic hazards that takes onto account the recent seismic activity and the major structures. In this zoning, the seismic hazard is quantified by a single parameter, 'A,' which represents the maximum acceleration normalized by the acceleration due to gravity, g. This parameter, known as the zone reference acceleration coefficient, is measured for a Class S1 soil (rock level) for a return period, Tr = 475 years.

Zone	Seismicity	A	Mw	Ts(sec) S1	S2	S3	S4		Category	Description
0	Very low	-	-	-	-	-	-		S1	Rocky
I	Low	0.07	4.5	2.5	3.0	4.0	5.0			
II	Low to moderate	0.10	5.0	3.5	4.0	5.0	6.0	Site	S2	Firm
III	Moderate	0.15	5.5	4.5	5.0	6.5	8.5	→		
IV	Moderate to high	0.20	6.0	6.0	6.5	8.5	11.5	Classification	S3	Moderately Soft
V	High	0.25	6.3	7.0	8.0	10.5	13.5			
VI	High	0.30	6.5	8.5	9.5	12.0	15.0		S4	Soft
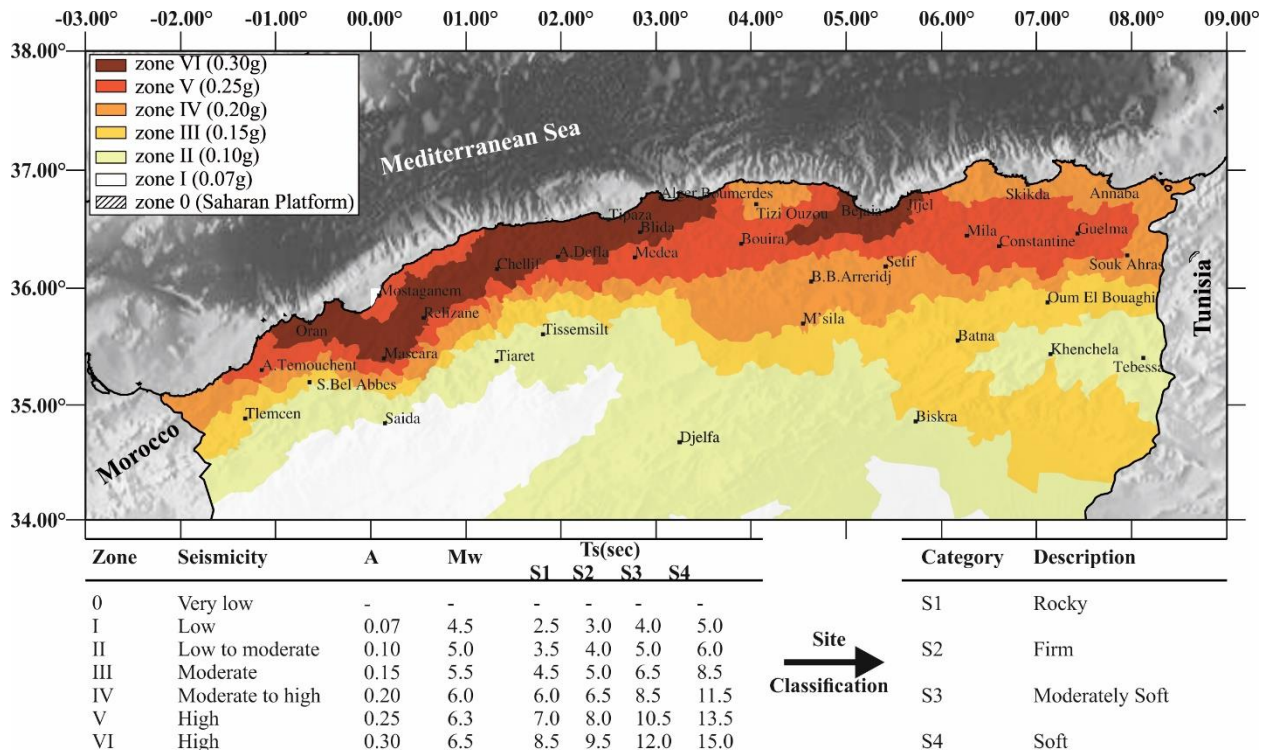
Fig. V.4: RPA 2024 seismic zoning map of northern Algeria, depicting seven zones as defined by the RPA 2024. The figure includes estimated values of magnitude and strong phase duration for the six seismicity zones (I=>VI) and four soil classes (S1=>S4). 'A' represents the acceleration coefficient.

Sites are classified into five categories based on the mechanical properties of the underlying soils. The first four categories, indicated at the bottom of **Fig. V.4**, are determined by the average soil properties over a minimum depth of 30 meters. Additionally, site classification should be based on the average shear wave velocity over the upper 30 meters (V_{s30}), as this parameter is the most reliable for determining site characteristics. The fifth category, considered exceptional, pertains to sites requiring specific investigations (S_S). The categories are defined as follows: *Category S1* (rocky site) is characterized by an average shear wave velocity, $V_s > 800$ m/s. *Category S2* (firm site) has 360 m/s $< V_{s30} \leq 800$ m/s. *Category S3* (moderately soft) is defined by 180 m/s$<Vs30\leq360$ m. *Category S4* (very soft) features $V_{s30}<180$ m/s. *Category S_S* refers to sites that require in-depth investigations and specific studies. **Fig. V.4** also provides the estimated magnitude (Mw) and the strong shaking phase duration (Ts) in the near field for the seven seismicity zones and four site classes. The strong phase, Ts, is critical for earthquake engineering because it exerts the most intense forces on structures, influencing building design requirements and response analysis. Engineers focus on this phase to ensure structures can withstand these peak loads, aiming to prevent collapse and minimize structural and non-structural damage. In the RPA 2024 this phase refers to the stationary phase of the seismic signal, with its start and end defined as the points where 5% and 95% of the signal's energy are reached, respectively. Additional details on the 2024 version of the Algerian Paraseismic Codes (RPA) can be found on this site**:** https://www.gcalgerie.com/regles-parasismiques-algeriennes-rpa-2024/ (*last access: 2024-10-26*)

V.3 Recent Earthquake Activity in Northeastern Algeria

The northeastern region of Algeria, specifically the eastern segment of the Tellian Atlas, has been characterized by a pronounced seismicity, marked by the occurrence of multiple moderate to occasionally strong earthquake sequences. This increased seismicity has led to the concentration of two-thirds of Algeria's total seismic activity in the northeastern region. (Abacha 2015; Yelles-Chaouche *et al.* 2022) (**Fig. V.1a** and **V.5a**).

Recognizing the importance of these seismic events, we have deemed it valuable to extract the geometric and physical characteristics of the seismogenic structures responsible for these earthquakes. These characteristics offer a valuable contribution to seismic hazard and risk mitigation, providing earthquake engineers with essential data to enhance resilient design and construction practices.
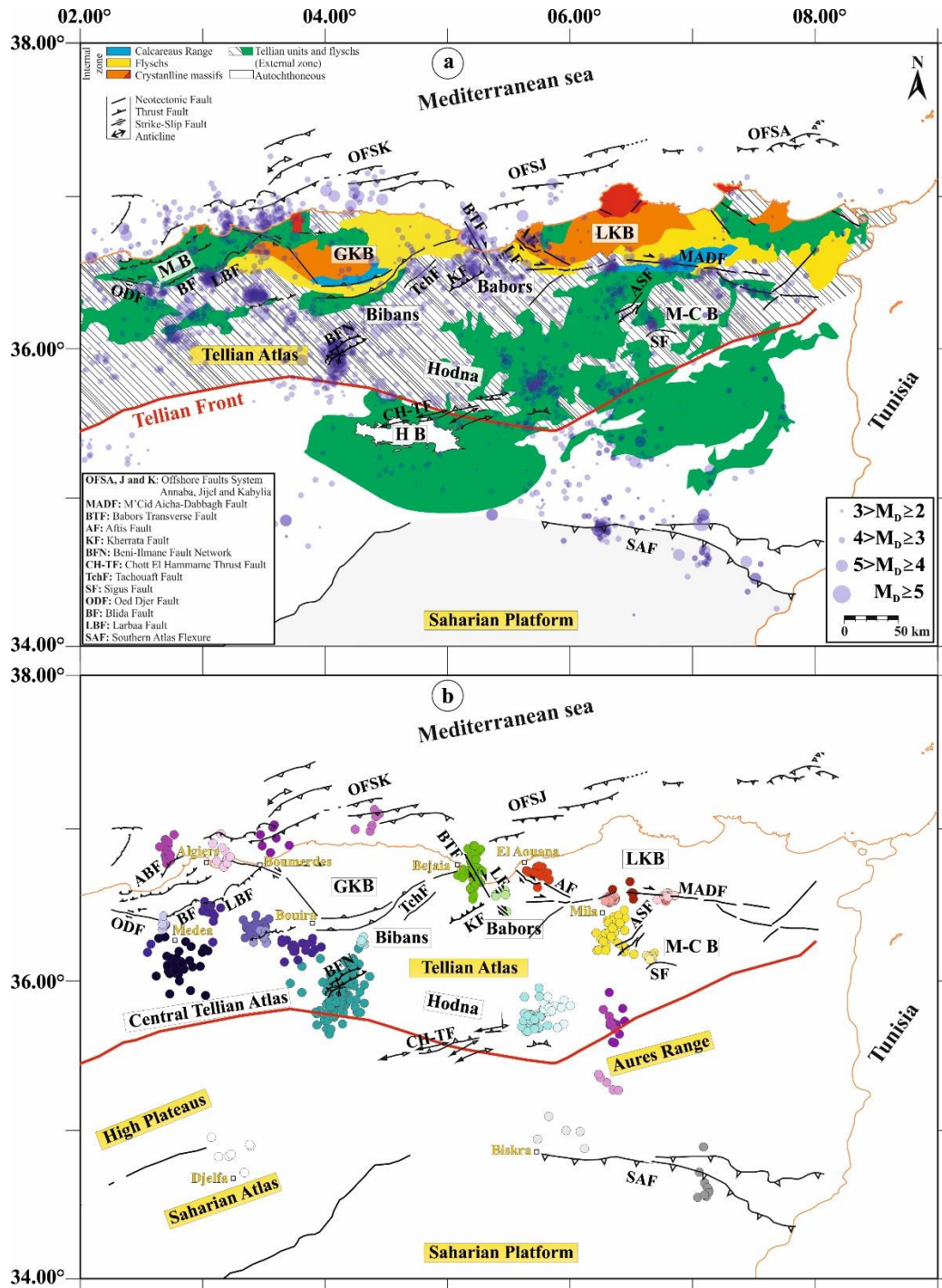
Fig. V.5: Swarms' distribution map. **(a)** Geological map of northeastern Algeria (adapted from Abacha 2015). Circles indicate seismic events from 2006 to 2021, with their sizes proportional to the earthquake magnitudes. **(b)** Spatial distribution of 32 swarm clusters, color-coded according to the 9 identified zones. A gradient scale represents the timing of their occurrence within each zone (Rahamani et al., *in prep*).

V.3.1 Geological Framework and Tectonic Structures of Northeastern Algeria

Geologically, the study area is located in the eastern part of the Tellian Atlas (**Fig. V.5a**). From north to south, the terrains include:

1. **Algerian Submarine Margin**: This area is heavily influenced by deposits related to the Messinian Salinity Crisis (Lofi *et al.* 2011).

2. **Internal Domain (Northern Tell)**: This includes the Kabyle Massifs, comprising the Precambrian and Paleozoic Kabyle basement, which originated from the fragmentation of the AlKaPeCa (Alboran, Kabylies, Peloritain, Calabrais) microcontinent. It also includes the Kabyle Range (Meso-Cenozoic limestone chain), divided into three main units: internal, median, and external (Durand-Delga 1969).

3. **External Domain (Southern Tell)**: Represented by Tellian nappes units (Babors and Bibans), characterized by Mesozoic to Tertiary sedimentation (from the Triassic to the Eocene) of African affinity. This domain is divided into three major units (Vila 1980): Ultra-Tellian units, Tellian units s.s. (sensu-stricto) and Peni-Tellian units.

4. **Between the internal and external domains, there are Flysch nappes**, primarily composed of sandstone-clay alternation, are classified into the Mauretanian Flysch, the Massylian Albo-Aptian Flysch, and the sandstone-micaceous Flysch according to their position relative to the internal or external zone.

5. **Intra-Continental Atlas**: South of the Tell, this domain is separated from the Saharan Platform by the South Atlas Front (or Southern Atlasic Flexure, SAF in **Fig. V5**) and consists of autochthonous units. It is divided into the Saharan Atlas in the center and the Aures region in eastern Algeria.

Several active tectonic structures have been identified in the study area (**Fig. V.5a**), including three major lithospheric faults: the Offshore Fault System (OFS), the Mcid Aicha Debbagh Fault (MADF), and the South Atlas Flexure (SAF). Key tectonic features include:

- **Mcid Aicha Debbagh Fault (MADF):** A right-lateral strike-slip fault over 80 km long, potentially extending to 400 km (Bougrine *et al*. 2019). It separates the internal (Lesser Kabylia Block-LKB) and external (Tellian units) domains of the Tellian Atlas and accommodates 2.4 mm/year of active contraction in northeastern Algeria.

- **Offshore Fault System (OFS):** An ~E-W thrust fault along the Algerian margin, spanning from Bejaia to Annaba, marking the Africa-Eurasia plate boundary and absorbing 1.5 mm/year of convergence. Notable earthquakes, including the 1856 Djidjelli (Jijel) event and the 2021 Gulf of Bejaia earthquake (Mw 6.0), are linked to this system.

- **South Atlas Flexure (SAF):** A major boundary between the Aures Mountains and the Saharan domain, associated with historical and recent seismic events, including the 1869 Biskra and 2016 Biskra earthquakes. It absorbs 1.5 mm/yr of the total Africa–Eurasia plate convergence.

Other significant faults include:

- **Kherrata Fault (KF):** An NE-SW reverse fault in the Babors range of ~40 km length, likely responsible for the 1949 Kherrata earthquake (Md 4.7).

- **Tachouaft Fault (TchF)**: An NE-SW reverse fault in the Soummam Basin, causing the 2000 Beni Ourtilane earthquake (Md 5.3).

- **Chott El Hammam Fault (CH-TF)**: An NE-SW thrust active structure in the Hodna range of 30 km length, linked to the 1965 M'sila earthquake (Md 5.4).

- **Ain Smara Fault (ASF)**: A NE-SW left-lateral strike-slip fault in the Constantine Basin, responsible for several earthquakes, including the 1985 Constantine event (Ms 6.0).

- **Beni-Ilmane Faults Network (BFN):** The Beni-Ilmane complex network contains several significant tectonic structures, including the NE–SW to NNE–SSW thrust faults surrounding Mount Chakchout, the NNW-SSE left-lateral strike-slip Samma corridor, and the ~E-W right-lateral strike-slip fault of Kharret Mountain (see **Chapter II**).

V.3.2 Northeastern Algeria's Seismic Peculiarities

The study area exhibits a distributed deformation pattern characterized by low to moderate-magnitude seismic sequences, primarily associated with various strike-slip faulting mechanisms. Notable among these are NE–SW left-lateral, NW–SE right-lateral, and WNW–ESE right-lateral faults, with the MADF being the most significant (Abacha & Yelles-Chaouche 2019; Bendjama *et al*., 2021; Boulahia *et al*., 2021; Abacha *et al*., 2023b) and also the Beni-Ilmane complex fault networks (Yelles-Chaouche *et al*., 2014; Beldjoudi *et al*., 2016; Abacha *et al*., 2023a; Tikhamarine *et al*., 2024). Additionally, there are instances of approximately E–W thrust faults, particularly in the offshore regions (Yelles-Chaouche *et al*., 2021; 2024). A distinctive characteristic of these seismic sequences is the frequent occurrence of two or more main shocks, accompanied by numerous seismic events that often display spatiotemporal migration (Khelif *et al*. (2018); Abacha & Yelles-Chaouche (2019); Bendjama *et al*. (2021); Boulahia *et al*. (2021); Boulahia 2022; Abacha *et al*. (2022), 2023a; 2023b; Rahamani *et al*. 2024; Tikhamarine *et al*. 2024). Clarifying and categorizing these sequences is crucial for understanding the triggering mechanisms governing this seismicity. This type of seismic activity is known within the seismological community as an earthquake swarm. Abacha's 2015 thesis is a reference in this subject, as it was the first to thoroughly investigate and document this type of sequences in the region.

In our recent study (Rahmani et al., *in prep*), we identified 32 swarms using two statistical methods, some of which consist of sub-clusters. These swarms are part of 13 sequences characterized by multiple mainshock patterns, as well as 19 distinct swarms that lack a clearly identifiable mainshock. To interpret these findings, we categorized the clusters into nine zones based on their geological and tectonic attributes (**Fig. V.5b**). These

seismic swarms exhibit intense temporal and spatial clustering, lasting from days to months and covering distances ranging from a few to several tens of kilometers, occasionally showing migration patterns over several weeks

V.4 Analyzing Earthquake Sequences: Fault Geometry and Seismotectonic Implication

In this section, we aim to investigate all the important seismic sequences that occurred in the study area. All findings presented in this chapter are ours, except for certain sequences where we have incorporated findings from other researches. We highlighting the most important results such as the length, direction, and kinematics of the tectonic faults, as well as key source parameters like seismic moment and stress drop. These characteristics are crucial for updating the seismic hazard assessment. It is worth noting that I was effectively engaged in the analysis of approximately 75% of these sequences, leveraging the experience gained from the BI-2010 seismic sequence analysis (Tikhamarine *et al*. 2024). Some of these studies have already been published, where I was a co-author, others are under revision, while the remaining ones are in preparation as will be detailed later.

To present these results, we divided the study area into four main zones: Hodna Mountain Range, Around LKB, Mila-Constantine Basin and Central Atlas Zone. At the end of the chapter, we present a summary of this lengthy analysis (**Table V.1**), highlighting several parameters, including seismological characteristics, geometric characteristics, physical characteristics and engineering characteristics when available. Additionally, we provide some comments on the lately released revision of the Algerian Seismic Code (RPA 2024) regarding the seismic zoning.

V.4.1 Hodna Mountain Range Zone

This region is characterized by significant N110°-oriented reliefs, forming the Hodna mountains, where a series of anticlines affect recent deposits-oriented NE-SW. These features are similar to other active structures in the Tell and display fold-fault

geometries, such as those observed in the Chott El Hammam Thrust Fault (CH-TF). Between 2010 and 2021, the area experienced four notable seismic events: Beni-Ilmane (2010), Ain Azel (2015 and 2020), El Madher (2010), and Soubella (2021). These sequences highlight the continued high seismic risk in the southern Tellian Atlas adjacent to the High Plateaus, where the topography is relatively flat and seismic activity is lower compared to the Tell region.

The Beni-Ilmane sequence is regarded as one of the most significant recent seismic events due to the large number of aftershocks. This event has been the focus of numerous scientific studies, the most comprehensive of which is presented in this thesis, particularly in the main article (Tikhamarine *et al*. 2024) and the preceding three chapters (**II**, **III**, and **IV**). **Fig. V.6** presents the key findings on the fault geometry that generated the Beni-Ilmane (BI) sequence, as discussed in detail in **Chapter II**. **Fig. V.6b** illustrates our proposed seismotectonic model for the 2010 Beni-Ilmane sequence, based on the orientation of multiplet groups and focal mechanism solutions shown in **Fig. V.6a**. In **Fig. V.6c**, we introduce a simplified model that outlines four major faults, which could represent the true extensions of the segments depicted in **Fig. V.6b**, informed by preexisting tectonic structures. Considering the potential extension of faults beyond the epicentral area ruptured by the mainshock and aftershocks is crucial for accurately assessing seismic hazards.
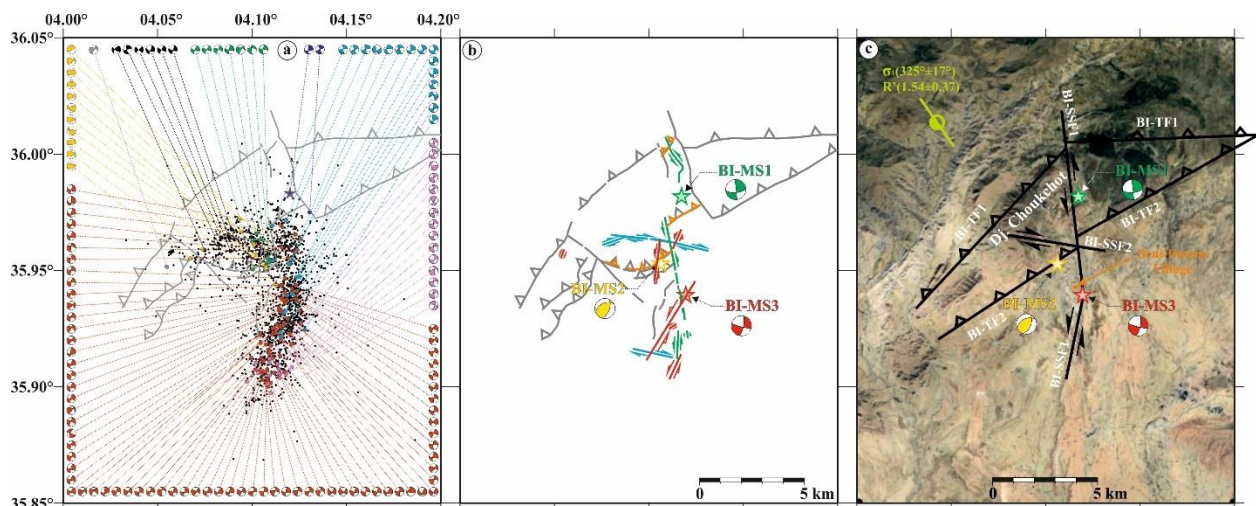
Fig. V.6: Beni-Ilmane region Fault system. **(a)** Focal mechanism solutions of 128 key events, color-coded by their association with different fault patterns and superimposed

on the relocated 1998 events. **(b)** Our detailed proposed seismotectonic model for the Beni-Ilmane sequence. **(c)** A simplified model illustrating four major faults extend beyond the epicentral area, representing possible extensions of the segments depicted in **(b)**.

On February 24, 2021, an Mw 4.7 earthquake struck near the Soubella dam in the Central Hodna Mountain chain, between the BI-2010 and Ain Azel-2015 sequences (see below). Only three events were located—the main shock and two aftershocks—since no portable network was installed to study this sequence. Instead, we relied on data from the ADSN and four accelerometers positioned at the top of the dam. One of the two nodal planes indicated an E-W trending reverse fault, parallel to the major Chott El Hammam Fault Thrust Fault (CH-TF).

In similar situation, where we have a scarcity in the number of recorded aftershocks, it becomes challenging to identify the probable seismogenic structure. Therefore, to overcome this limitation, we relied on the focal mechanism of the mainshock, which revealed a reverse mechanism. Additionally, we considered the geological, topographic, and tectonic characteristics of the study area. Upon the first examination of **Fig. V.7a** we observe that both azimuth and dip of the plane trending NE-SW, are in a good agreement with those of CH-TF. Therefore, it is expected that the dip of CH-TF would be ~58°. In order to verify this expectation, we performed a NW-SE cross-section perpendicular to both CH-TF and the main-shock's focal mechanism see **Fig. V.7a**. We drew the assumed fault plane by connecting the focus of the main-shock to the fault trace on the surface. The intersection of this assumed fault plane with the horizon (earth surface), exhibited a dip angle of 32°, which is quite incompatible with the calculated dip of the focal mechanism.

To address this issue, we turned to the scientific literature dealing with similar cases in a similar tectonic context. Several authors, such as Déverchère *et al.* (2005), Arab *et al.* (2016) and Beldjoudi *et al.* (2016), have described thrust faults in similar context as having three compartments: a first steep dip at depth followed by a low-dipping ramp, and finally a second steep dip near the surface. We applied this configuration to our case

study. Crossing the region from A (NW) to B (SE) see **Fig. V.7a**, we first pass through Jebel Soubbela, where the main-shock is located. Then, we traverse the Soubbela plain, and finally, we reach a small hill called Chebka El Guedah, where the surface trace of the CH-TF is located. This analysis resulted in the construction of the model presented in **Fig. V.7b**. In this model, Jebel Soubbela represents the first steep dip, the Soubbela plain represents the low-dipping ramp, which connects the steep-dipping area at depth to the steep-dipping area at the surface, and finally, the second steep dip is characterized by a surface outcrop revealing the trace of the CH-TF. By using this three-compartment configuration, we were able to explain the inconsistency between the dip of the main-shock focal mechanism and the dip inferred from the line connecting the main-shock's focus to the trace of the CH-TF.

It should be noted that this work has been accepted for publication at the Mediterranean Geosciences Union 2023 (MedGU2023) conference proceeding under the title: " The 2021 Soubella Quake (Mw4.7), NE Algeria: Seismo-tectonic Insights and Source Parameters from Empirical Green Function. Additionally, a broader analysis of this particular event is the subject of a paper by Boulahia et al., *in prep.*

Moreover, we estimated the seismic moment and moment magnitude through waveform inversion, see **Fig. V.7c**. Also, we derived dynamic source parameters (corner frequency, stress drop) using the Empirical Green's Function (EGF) method, see **Fig. V.7d**.
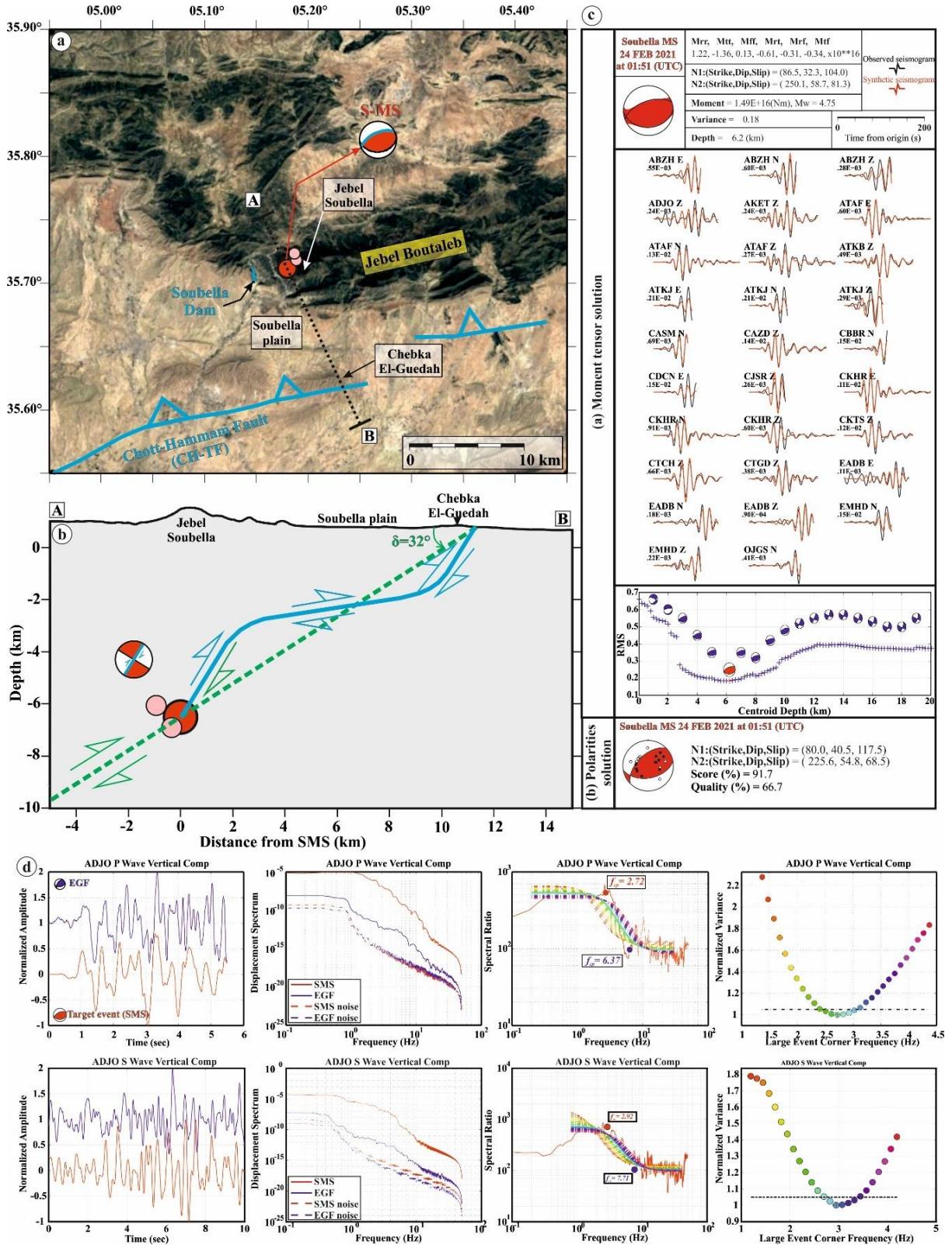
Fig. V.7: Soubella 2021 earthquake analysis. **(a)** Proposed fault configuration. The blue solid line denotes the CH-RF. The solid red circle highlights the Soubella mainshock, with

two solid pink circles indicating key aftershocks (EGF candidates). The focal solution depicts the nodal plane likely to host the earthquake. **(b)** The solid blue line represents the ramp-flat-ramp fault geometry, while the dashed green line illustrates a simplified model with uniform dip. **(c)** Moment tensor solutions and the best-fitted waveforms for the Soubella mainshock (Top). The derived focal sphere solution from the first arrival (P-wave) polarities, along with the corresponding nodal planes parameters for the mainshock (Bottom). **(d)** A composite figure showing several panels organized in columns. These include (1) Normalized time windows of P- and S-waves raw velocity seismograms at station ADJO, associated with corresponding focal solutions. The red trace corresponds to the target event (mainshock), while the blue trace represents the Empirical Green's Function (EGF) . (2) Source spectra of P- and S-waves. The red and blue solid lines show the observed spectra (mainshock and EGF, respectively), while the dashed lines show the noise spectra. (3) The EGF-adjusted spectral ratios match well in the frequency band with a good signal-to-noise ratio. The blue dot denotes f_{c1} and the red dot denotes f_{c2}. (4) The variance has a parabolic shape with a clear minimum (cross). The dashed horizontal line indicates the maximum and minimum 5% error estimates.

The 2015 Ain Azel earthquake sequence (AZ-2015) occurred in the southeastern part of the Hodna Massif,.During this sequence four events (M>4) occurred. Their focal solutions are labeled 1, 2, 3, and 7 **(Fig. V.8a)**. These largest events were recorded over a 6-day period. The first event, of magnitude Mw 4.7, occurred on March 15, 2015, followed by an Mw 4.3 shock on March 17, a Md 4.2 event on March 18, and the largest event, Mw 4.9, on March 21, 2015. Numerous foreshocks and aftershocks accompanied the sequence, starting as early as January 2015 (2.0 ≤ Md ≤ 3.3). Between March 15 and April 30, 2015, a total of 1,008 events were located, with 822 being relocated using the same methods applied to the BI-2010 sequence.

The horizontal distribution of these events reveals a WNW–ESE main cluster aligned with the general direction of the Hodna Massif. A detailed examination of this cluster identifies four sub-clusters (SC1, SC2, SC3, and SC4), ordered according to their time of occurrence. This chronological order of activation can only be depicted through animated seismicity movie. The spatiotemporal evolution shows that SC1 and SC2 occurred almost simultaneously, with SC1 initiating slightly earlier, followed by SC3, and finally SC4 emerging towards the end of the sequence.

The modified Wadati diagram shows a relatively high Vp/Vs ratio of 1.88 (**Fig. V.8b**), compared to other regions in Algeria. One possible explanation for this elevated value is the presence of subsurface fluids. To investigate whether fluid-induced processes were a driving mechanism of the 2015 Ain Azel sequence, we modeled the seismic events using Shapiro's equation, with the results presented as an R-T plot in **Fig. V.8c**. The hyperbolic theoretical curve indicates a diffusivity value of $D = 0.5647$ m²/s, which falls within the range of hydraulic diffusivity proposed by Do Nascimento *et al.* (2005). This suggests a pore-pressure diffusion process. It is important to note that the retrieved diffusivity value may be biased due to the missing of several events at the beginning of the sequence, which is due absence of portable station (gray area in **Fig. 8c**). Nevertheless, we assume that if the missed events were captured, they would probably follow the front curve (Blue curve in **Fig. V.8c**). We do not rely solely on this diffusivity value to infer fluid involvement as a contributing mechanism. Our interpretation is further supported by the presence of several hydrothermal reservoirs in the Ain Azel region. Additionally, a study by Abacha et al. (2022) used statistical analysis suggesting that this seismic sequence may be linked to the circulation of thermal waters.
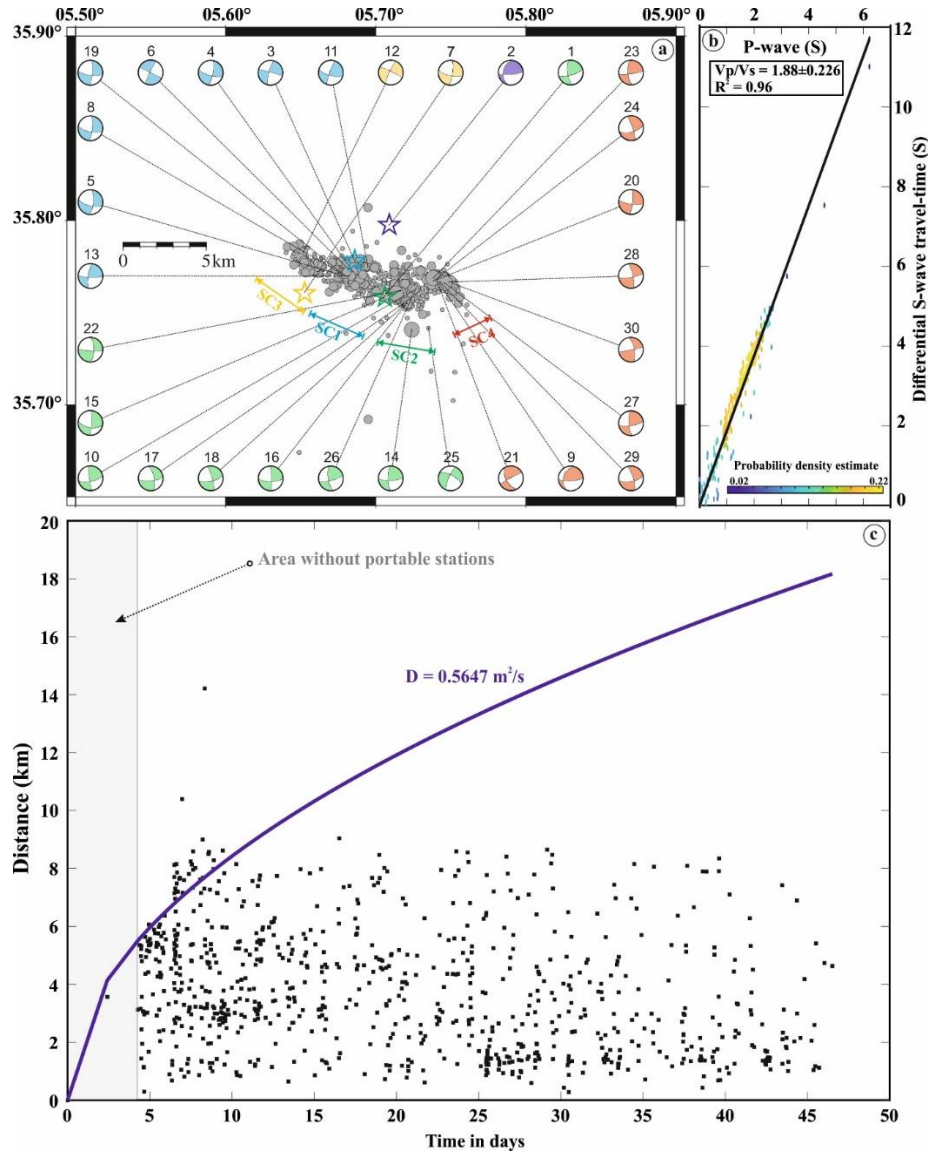
Fig. V.8: AZ-2015 relocation and diffusivity plot. **(a)** Horizontal distribution of the 822 relocated events, including the focal mechanisms of the four largest events and the principal aftershocks. The focal mechanisms are numbered according to their occurrence times and are color-coded to match the four subclusters (SC1, SC2, SC3, and SC4), except for number 2, which is not included in any subcluster. **(b)** Vp/Vs ratio in Ain Azel area via the modified Wadati method (Chatelain 1978). **(c)** R-T plot of the 2015 Ain Azel earthquake sequence, starting from the first largest event on 15 March 2010. Hyperbolic curve represents the seismicity migration front, with a hydraulic diffusivity value of D = 0.5647 m²/s.

Following our approach in Tikhamarine *et al.* (2024), we retrieved 37 cluster including: doublet, triplet and multiplet groups. We used a minimum CC threshold of 0.7, an average CC threshold of 0.8 and a minimum of 2 events per cluster. If the aforementioned criteria are verified on one station or more, the cluster is kept. The 37 clusters include a total of 245 events which we plotted horizontally and vertically in **Fig. V.9a** and **b**, respectively. The separation of the four clusters is better depicted in these figures. In **Fig. V.9a**, we opted to present the spatiotemporal evolution of a smaller subset of events, allowing us to more clearly track the progression compared to using the complete dataset. The figure confirms the previously proposed evolution.

The figure also highlights the three largest events of March 15, 18, and 21, which correspond to SC1, SC2, and SC3, respectively. The March 17 event is not represented, as it was located outside the epicentral area. It is also noteworthy that an Mw 5 earthquake struck the region on March 26, 2020, just 10 km east of the 2015 event (**Fig. V.9a**). Unfortunately, the global COVID-19 pandemic prevented the deployment of a portable network to monitor the aftershock activity. In **Fig. 9c** (top), we superimposed 10 multiple groups, each containing a minimum of five events, onto the 245 events. At the Bottom, we present a waveform similarity example of two groups (02 and 04) recorded at SP01 station.
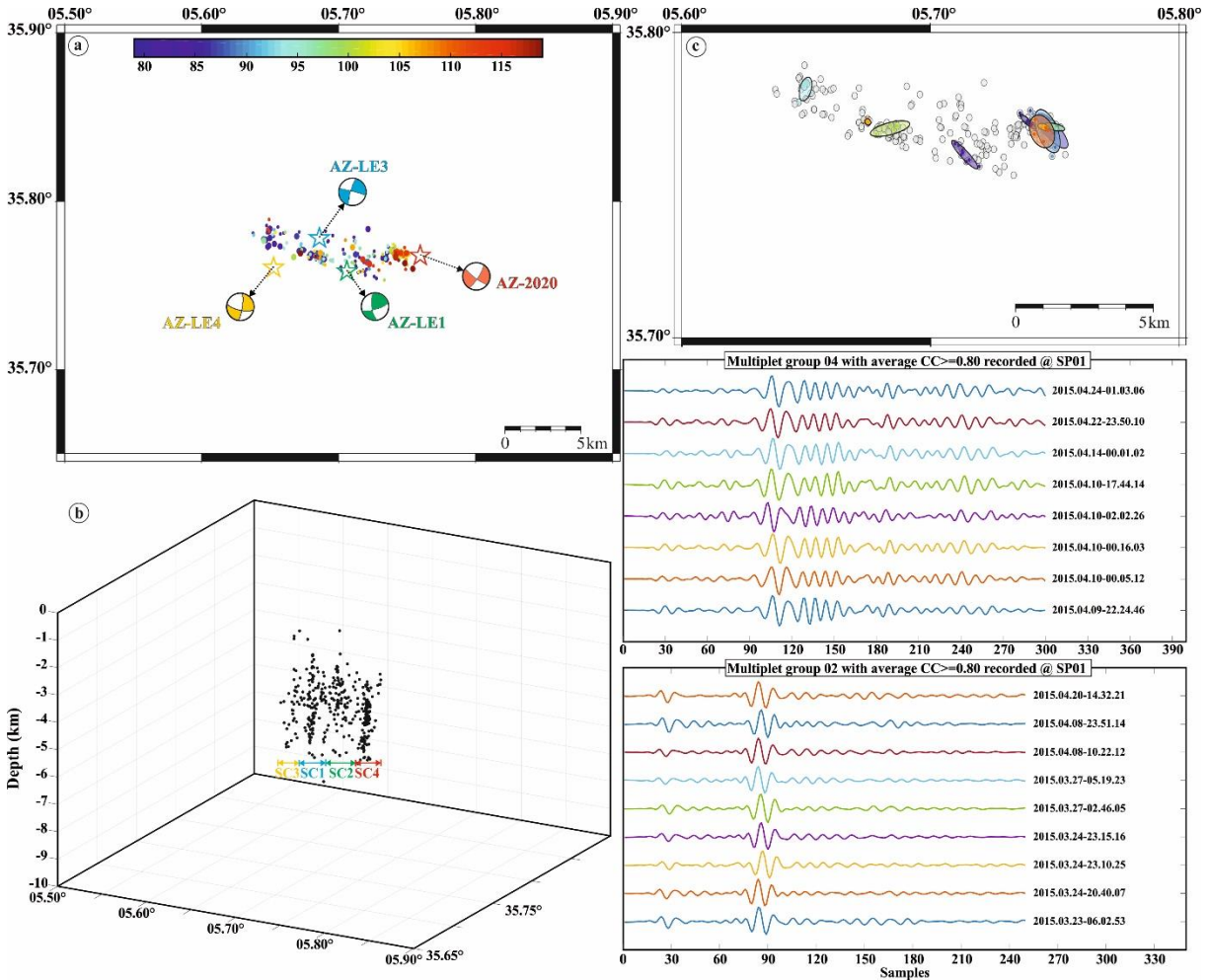
Fig. V.9: AZ-2015 spatio-temporal evolution and multiplet analysis. **(a)** Horizontal distribution of 245 well-relocated events, showing their spatiotemporal evolution. **(b)** Vertical distribution of the same events. **(c)** Top: Overlay of 10 multiplet groups on the 245 relocated events; Bottom: Example of two multiplet groups.

The spatial distribution of the aftershocks, along with the focal mechanism parameters and the 10 multiplet groups, allowed us to propose the seismotectonic model shown in **Fig. V.10**. This model reveals four fault segments: two oriented WNW–ESE, exhibiting right-lateral strike-slip movement, which generated SC1 (blue fault) and SC3 (yellow fault), along with the two associated large events (AZ-LE3 and AZ-LE4). Additionally, two segments oriented ENE–WSW show left-lateral strike-slip kinematics, responsible for SC2 and its large event (AZ-LE1) and SC4 (green and red faults,

respectively). The local stress field in the study area is characterized by pure strike-slip motion. The fault system conforms to the Riedel shear model, where the WNW–ESE right-lateral strike-slip faults correspond to R structures (red fault in the ellipse), and the NNW–SSE left-lateral strike-slip faults correspond to R' structures (green fault in the ellipse).

The superposition of these fault segments onto the geological and tectonic map (**Fig. V.10**) reveals that the area impacted by the sequence is situated in the highly complex region of Fourhal Mount, which is intersected by multiple fractures and faults, primarily oriented ~E-W. These structures are labeled Ain Azel Strike-Slip Faults Network (AZ-SSFN) in **Fig. V.10**. This suggests that the full extent of the faults responsible for the AZ-2015 sequence probably spans the entire surface of the mountain.
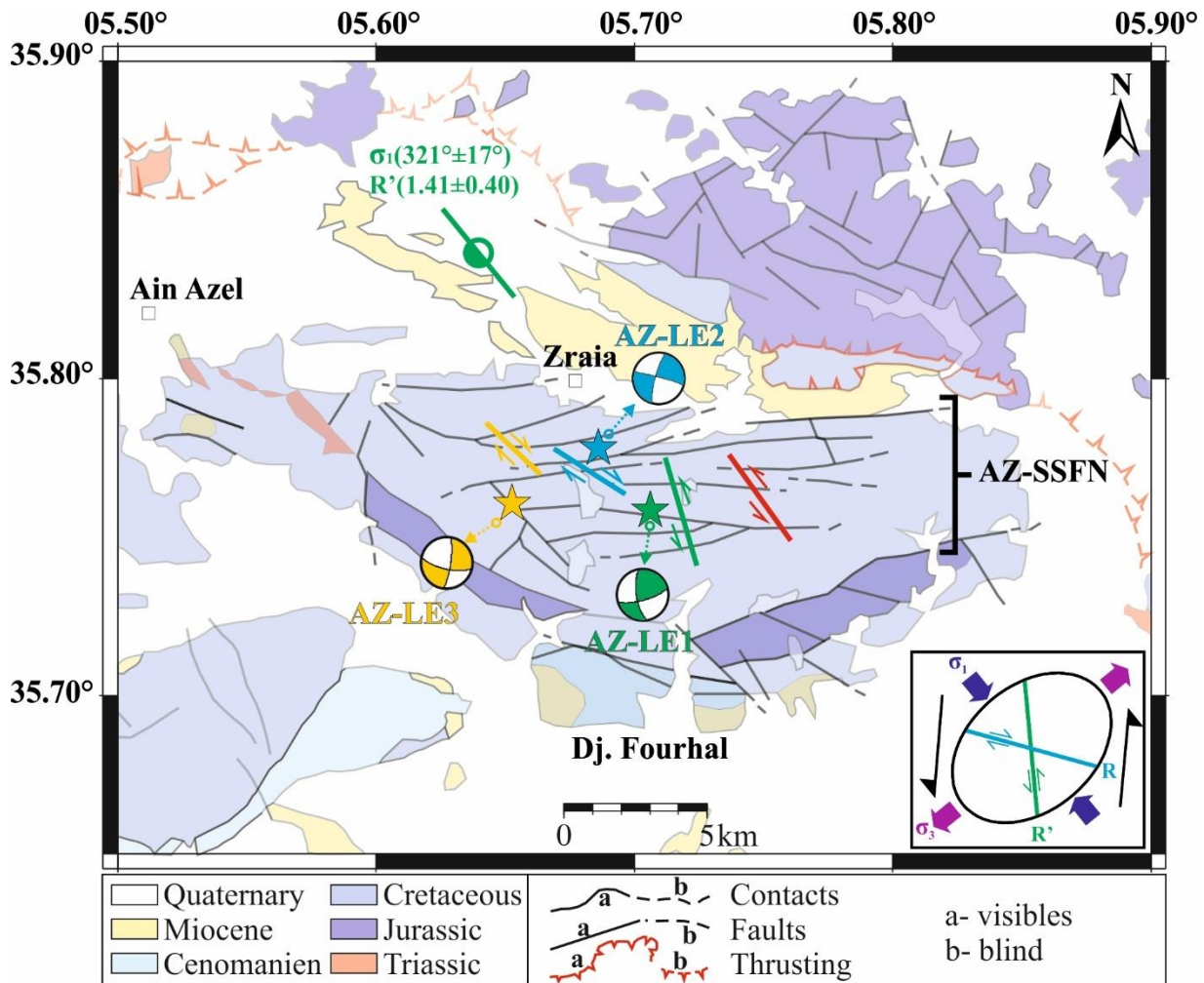
Fig. V.10: Proposed seismotectonic model responsible for AZ-2015 sequence, based on (1) aftershocks distribution, (2) the 10 multiplet groups, and (3) the focal mechanism solutions. The corresponding Riedel shear strain ellipse, showing R and R' structures, is displayed in the lower-right corner. The ellipse is oriented according to the sigma 1 direction of the stress tensor, as shown at the top of the figure. AZ-SSFN: Ain Azel Strike-Slip Faults Network. Modified after a geological map of Ain Beida, SONATRACH 1977.

The last event in this zone was the seismic crisis of April 2010 in El Madher region, which occurred in the geo-suture zone between the Hodna Mountains and the Aures Massif, along the deformation front of the Tellian Atlas, just one month before the BI-2010 sequence. The crisis lasted for three days—April 10, 11, and 12, 2010—producing 22 seismic events, including two with magnitudes greater than 4. These events are shown in **Fig. V.11a**, color-coded in red, blue, and green according to their date of occurrence. The first significant event (EM-LE1), with Mw 4.4 and I0 = V, was recorded at 08:38 UTC on April 10, 2010. The second major event (EM-LE2), with Mw 4.3, occurred at 09:57 UTC on April 11, 2010 **(Fig. V.11b)**. The sequence began with an Mw 3.6 earthquake at 02:08 UTC on April 10, 2010. This seismic crisis was recorded exclusively by the permanent ASDN stations, with the closest station (CTGD) located approximately 20 km from the epicentral area. The spatial distribution of the 22 well-relocated events forms a NE-SW trending cluster about 8 km long, aligning with the region's tectonic structures (folds and faults) (**Fig. V.11b**). One of the fault planes from the focal mechanism solutions for the two largest events matches the orientation of this seismic cluster, indicating a left-lateral strike-slip fault, which we term El Madher Strike-Slip Fault (EM-SSF) well-aligned with the geological preexisting fault F1 (**Fig. V.11b**). Notably, this crisis was preceded by an Mw 4.3 El Madher earthquake on May 20, 1986. We mention that the analysis of this seismic crisis is a subject of a paper that is being prepared by Abacha et al., *in prep.*
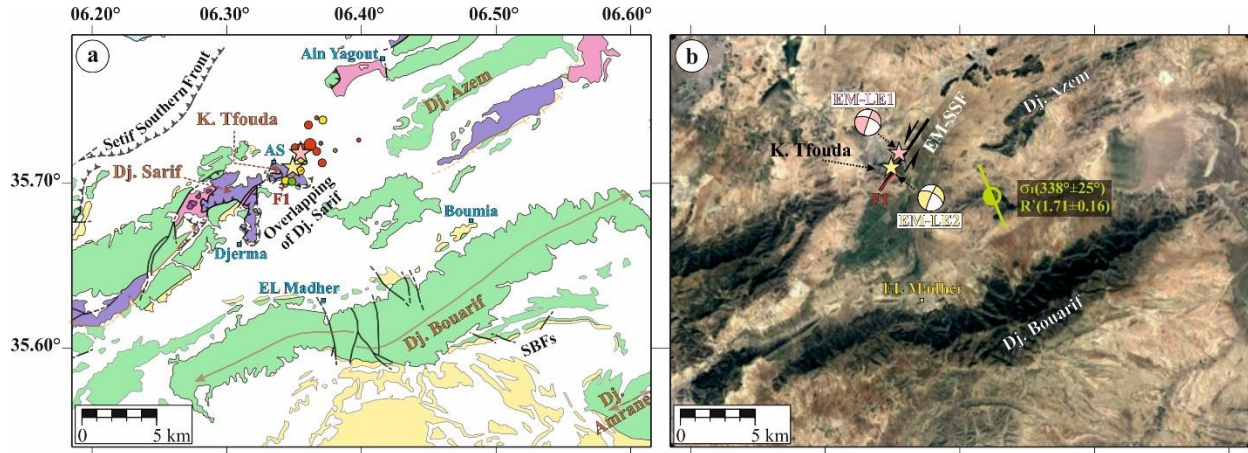
Fig. V.11: The 2010 El Madher seismic crisis. **(a)** Distribution of the 22 well-relocated seismic events overlaid on a geological map, redrawn based on Villa's 1:50,000 map (1977). **(b)** Proposed fault model (EM-SSF) aligned with the preexisting geological fault F1, along with the focal mechanism solutions of the two largest events (EM-LE1 and EM-LE2).

The occurrence of these four recent seismic events—BI-2010, AZ-2015, Soubella 2021, and El Madher 2010—along with significant historical events illustrated in **Fig. V.12**, raises questions about their potential connection through static stress transfer along the Hodna range. The close temporal proximity between BI-2010 and El Madher 2010, separated by only one month, suggests a possible static and/or dynamic relationship. Additionally, considering the high number of casualties in moderate-magnitude events such as the Barhoum1 earthquake, with 277 deaths, and the M'sila1 event, with 33 deaths (Harbi. 2001; Abacha. 2015), it becomes very important to reevaluate seismic risk in this highly active region.
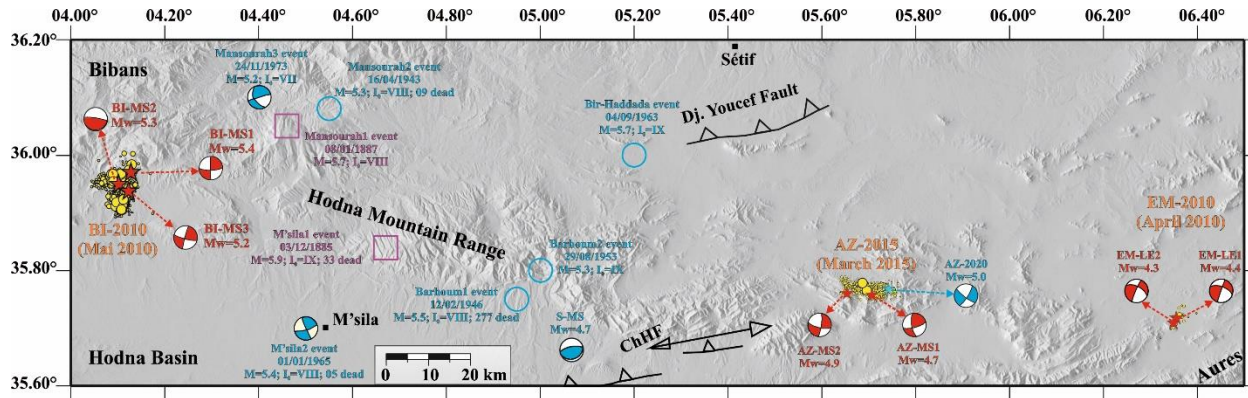
Fig. V.12: Major historical and recent seismic events along the Hodna Mountain Range (Sources: Harbi 2001; Abacha 2015)

V.4.2 Around Lesser Kabylia Block Zone

Now, moving to the northern part of our study area, we encounter the rigid metamorphic block known as the Lesser Kabylia Block (LKB), characterized by low seismicity in contrast to its boundaries, particularly to the west and south, which exhibit significant seismicity, especially in recent times. In the following section, we will examine the seismicity along the western boundary of the LKB, represented by the Babors range and the offshore Bejaia-Jijel junction, as well as along the southern boundary, marked by the M'cid Aïcha-Debbagh Fault (MADF).

a) Babors-Bejaia-Jijel Junction zone

For a long time, the Kherrata Reverse Fault (KF in **Fig. V.5a**) was considered responsible for several seismic events in the Babors range. However, the 1974 Darguinah Earthquake and the 2006 Laalam Earthquake, generated by Laalam Strike-Slip Fault (LA-SSF), provided the first evidence of a new major strike-slip fault perpendicular to the KF. The recent seismic events have since redefined the understanding of seismic and tectonic activity in this region.

A significant advance in the understanding of seismicity began with the 2012–2013 Bejaia-Babors sequences (Boulahia *et al.* 2021), and was followed by the 2019 Jijel Earthquake (Yelles-Chaouche *et al.* 2021), the 2020 El Aouana Earthquake (Abacha, *et al.*

2023b), and most recently, the Bejaia Earthquakes in 2021 and 2022 (Yelles-Chaouche *et
al.* 2024). Independent earthquakes were also recorded between 2012 and 2022. The 2012–
2013 Bejaia-Babors sequences consisted of four main shocks (**Fig. V.13a**), with aftershock
and FMS analyses revealing a main cluster of 252 well-relocated events along a near-
vertical, NW–SE striking right-lateral strike-slip fault. This fault, named the Babors
Transverse Fault (BTF) by Boulahia et *al.* (2021). In this thesis, and to maintain consistent
fault naming conventions, we refer to it as the Bejaia Strike-Slip Fault (BJ-SSF). This fault
extends ~35 km from the Babors mountain range to the Bejaia Gulf. The BJ-SSF is
composed of four segments (S1 to S4), each associated with distinct earthquake clusters
(**Fig. V.13a** and **b**).

Additionally, between 2017 and 2020, a cluster of 11 events ($M_D \geq 3.0$) was
recorded 10 km west of the BJ-SSF along a parallel, NW–SE striking right-lateral strike-
slip fault, named the Tizi N'Berber-Darguinah Fault (TDF in **Fig. V.13b**) (Boulahia *et al.*,
2021).
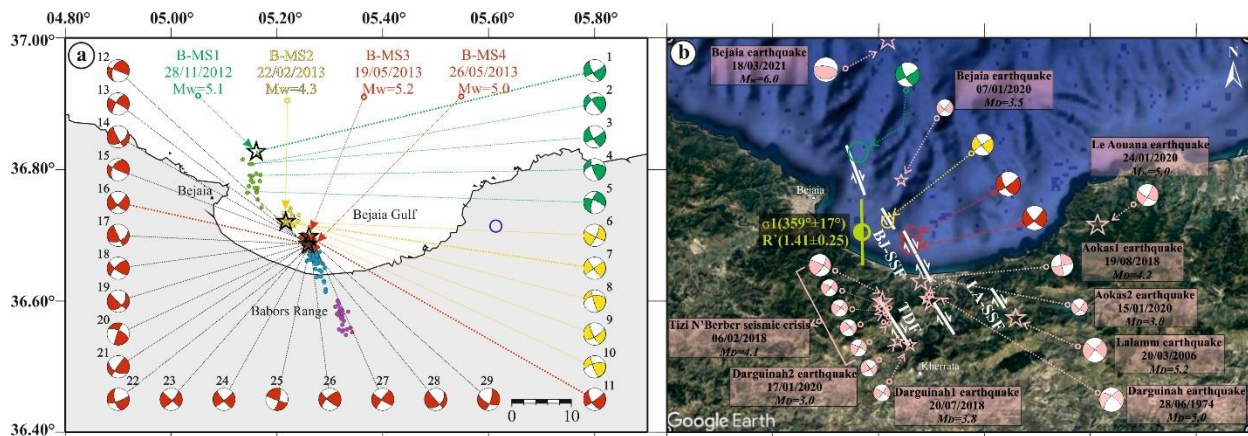
Fig. V.13: Bejaia-Babors sequences (2012-2013) analysis. **(a)** The Bejaia-Babors earthquake
sequences (2012-2013). Horizontal distribution of the 252 relocated events. The first,
second, and third earthquake sequences, with FMSs for events M ≥ 3 (Boulahia *et al.* 2021)
represented by different colors. **(b)** The transfer zone between offshore -thrust- faults
system (OFS) and the MADF consisting of BJ-SSF and TDF. The FMSs of the most recent
significant events between 2014-2021 are shown. The composite solution of the 2006
Lâalam earthquake and the 1974 Darguinah FMS are also reported.

The second event in this zone occurred in the El Aouana region, at the western end of the LKB, on January 24, 2020, with a Mw 5.0. The seismic activity lasted approximately 70 days from the mainshock (EA-MS), during which the largest aftershock (LA) was recorded on February 22, 2020, 28 days after the mainshock. In total, 306 events were located, and 204 were well-relocated (**Fig. V.14a**) (see also our publication Abacha *et al.*, 2023b). This earthquake was associated with the rupture of a NW–SE right-lateral strike-slip fault, 7.6 km long and 2 km wide aftershock cluster, named the El Aouana Strike-Slip Fault (EA-SSF, **Fig. V.14b**), aligned with the preexisting Aftis Fault (AF, **Fig. V.14b**), suggesting that the EA-SSF is part of the AF.

A comprehensive investigation, integrating the analysis of newly identified faults—BJ-SSF and TDF (Boulahia *et al.*, 2021), and EA-SSF (Abacha *et al.*, 2023b)—along with the NNW–SSE offshore active fault to the north and the NNW–SSE right-lateral strike-slip Lalaam Fault to the south, combined with geological, geophysical, and geomorphological data, has revealed the existence of a shear zone termed the Bejaia-Babors Shear Zone (BBSZ) (Abacha *et al.*, 2023b). The BJ-SSF and TDF, along with offshore faults, define the western boundary of the BBSZ, while the EA-SSF, as part of the Aftis Fault (AF), and offshore strike-slip faults form its eastern boundary.
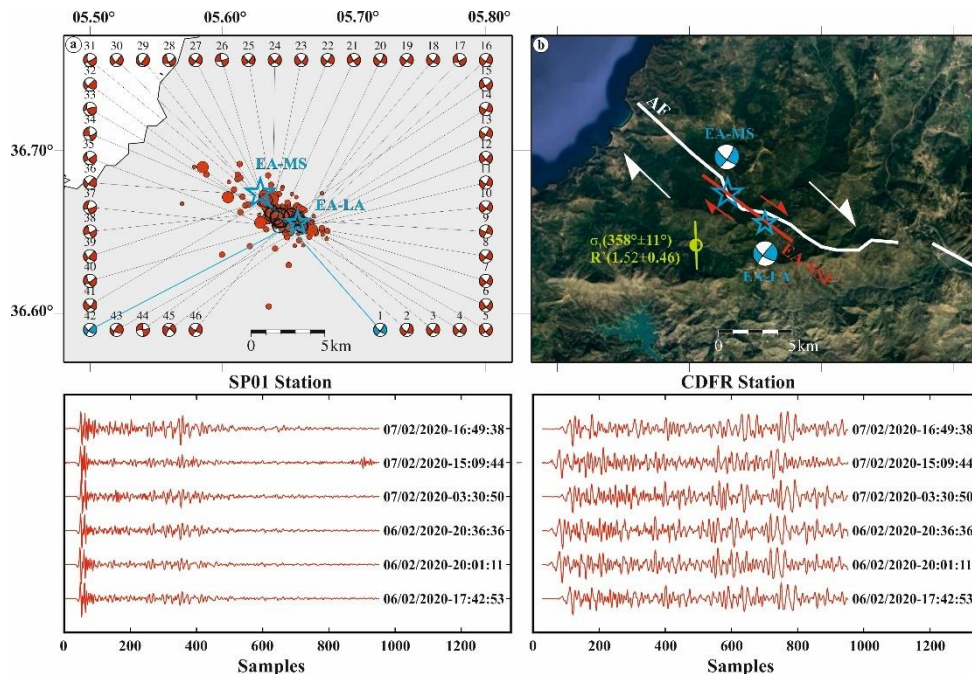
Fig. V.14: El Aouana 2020 sequence analysis. **(a)** Horizontal distribution of the 204 relocated events from the 2020 El Aouana earthquake, showing 44 focal mechanisms of the largest events (Abacha *et al.*, 2023b). **(b)** The El Aouana Strike-Slip Fault (EA-SSF) is the proposed segment determined from the event cluster in (a), which is well aligned with the Aftis Fault (AF). At the bottom, we exhibit an example of waveform similarity recorded on SP01 and CDFR stations.

Seismicity along the Bejaia-Jijel margin has been poorly understood for decades due to a lack of marine investigations and limited seismic network coverage. However, recent marine projects such as MARADJA 1 (2003), MARADJA 2/SAMRA (2005), and SPIRAL (Sismique Profonde de la Région Algérienne, 2009) have mapped key geological structures in this area, including the Offshore Fault System of Jijel (OFSJ), which consists of Eastern, Central, and Western Segments (ES, CS, and WS). This fault system is believed to have caused the destructive earthquakes of August 21–22, 1856 (I0 = X). Another important structure, the Offshore Fault System of Kabylia (OFSK), is located off the coast of Bejaia. Recent seismic events in this margin include the 2014 Ziama, 2019 Jijel, and 2021 and 2022 Bejaia earthquakes.

Seismicity in the Jijel margin remained relatively quiet for over 150 years following the 1856 Djidjelli Earthquake. Two events with an Mw ≥ 4.1 marked the first significant seismic activity in the region. The first event, an Mw 4.1 earthquake, occurred on March 25, 2014, 20 km northwest of Jijel City near Ziama village. The second, an Mw 5.0 earthquake, struck on July 13, 2019, 40 km north of Jijel City (**Fig. V.15a**). Aftershock analysis indicates a cluster of events concentrated within a narrow region along the continental slope of the Jijel margin, spanning 4 km by 10 km, consistent with the E–W thrust fault named Jijel Offshore Thrust Fault Segment (JO-TFS), an extension of the Eastern Segment (ES) (**Fig. V.15b**). The 2014 Ziama event is similarly associated with the rupture of a thrust fault in the Western Segment (WS), referred to as the Ziama Segment (ZS) (Yelles-Chaouche *et al.*, 2021).

Chapter V
        **Geometric and Physical Characterization
of Active Faults in Northeastern Algeria**
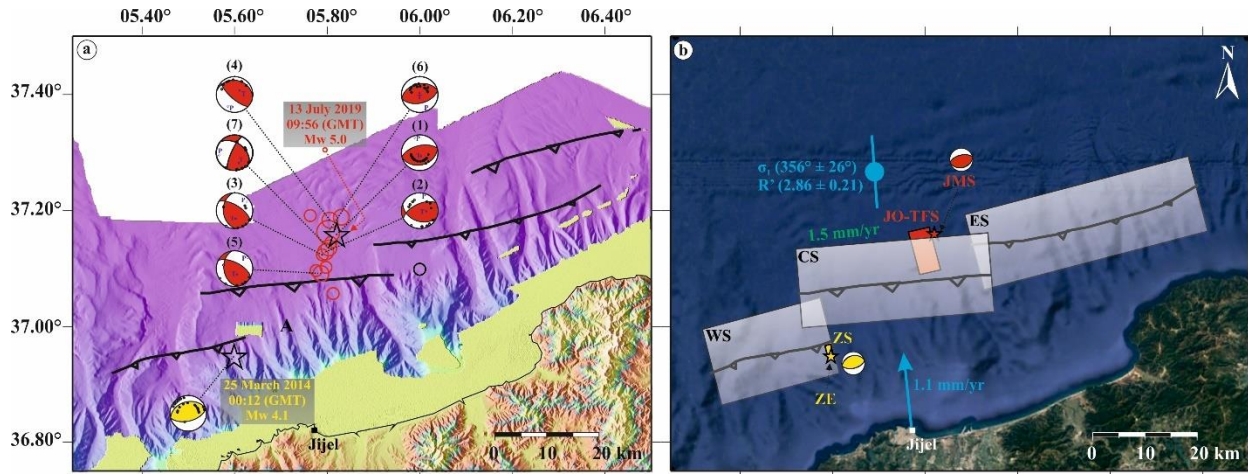
Fig. V.15: Jijel 2014-2019 seismicity analysis. **(a)** Horizontal distribution of the 14 relocated events from the 2019 sequence, including focal mechanisms for the July 13, 2019 Mw 5.0 Jijel mainshock, significant aftershocks, and the March 25, 2014 Mw 4.1 Ziama event. **(b)** Tectonic context of the study area, showing the Jijel Offshore Thrust Faut Segment and Ziama Segments (JO-TFS and ZS) as determined by Yelles-Chaouche *et al.* (2021). Gray rectangles indicate the ES, CS, and WS fault segments, with details provided in Yelles-Chaouche *et al.*, (2009b). Numbers indicate horizontal displacement rates along the offshore faults (mm/yr), and the blue arrow represents GPS velocity (Bougrine *et al.*, 2019).

Recently, a strong earthquake (Mw 6.0) struck 15 km northeast of Cap Carbon in the Bejaia Gulf on March 18, 2021, marking the largest offshore earthquake recorded since the devastating Mw 6.8 Boumerdes earthquake on May 21, 2003. A total of 500 events were detected, of which 420 were located and 334 were well-relocated, following the methods outlined in our article Yelles-Chaouche *et al.* (2024) as well as in the second chapter. From the aftershock distribution and the focal mechanism parameters of 40 key events (**Fig. V.16a**), we propose the fault model illustrated by the green rectangle in **Fig. V.16b**, representing an ENE–WSW thrust fault, dipping SSE, located at the western boundary of the offshore WS thrust segment, referred to as the Bejaia Offshore Thrust Fault Segment (BJO-TFS) in **Fig. V.16b**. Exactly one year later, on March 19, 2022, a moderate earthquake (Mw 5.3) (B2022-MS in **Fig. V.16b**) struck the same epicentral zone, 3 km northwest of the first shock (B2021-MS). Its focal mechanism also revealed an E–W striking reverse fault with a minor strike-slip component.

In summary, **Fig. V.16b** presents all the newly discovered tectonic structures within the NW-SE oriented Bejaia-Babors Shear Zone (BBSZ), situated between the GKB and LKB blocks, as delineated by our work (Abacha *et al.*, 2023b). This shear zone significantly advances our understanding of the region's tectonics. The structural features identified by Boulahia *et al.* (2021) define the western extent of the BBSZ, while those investigated by Abacha *et al.* (2023b) mark its eastern boundary. Additionally, the features outlined by Yelles-Chaouche et al. (2021; 2024) form its northern boundary.
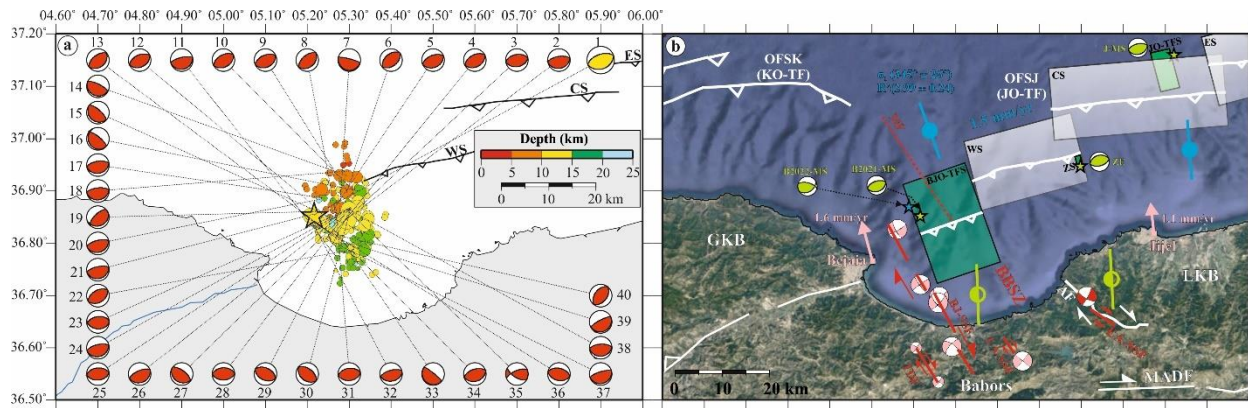
Fig. V.16: Bejaia 2021-2022 seismicity analysis. **(a)** Horizontal distribution of 334 well-relocated events from a total of 420 located events, along with focal mechanisms of the largest aftershocks following the 2021 Mw 6.0 Bejaia earthquake. **(b)** Overview of newly identified fault segments and preexisting geological faults: (1) Offshore fault segments, including the Bejaia Offshore Thrust Fault Segment (BJO-TFS) as reported by our work Yelles-Chaouche *et al.* (2024), and the Jijel Offsore Thrust Fault Segment (JO-TFS) and Ziama Segments (ZS) (Yelles-Chaouche *et al.*, 2021), along with the Eastern (ES), Central (CS), and Western (WS) fault segments. (2) Structural elements of the Bejaia-Babors Shear Zone (BBSZ), including the BJ-SSF, TDF, and LA-SSF (Boulahia *et al.*, 2021), as well as the Aftis Fault (AF) and El Aouana Fault (EA-SSF) as reported by our publication Abacha *et al.*, (2023b). Blue numbers indicate horizontal displacement rates along offshore faults in mm/yr, while the pink arrow represents GPS velocity from Bougrine *et al.* (2019). The main stress tensor parameters are shown in blue for thrust faulting and green for strike-slip faulting.

b) Seismic and Tectonic Features Along the MADF: The Southern Edge of the LKB

Seismicity in this zone is concentrated along the E–W-trending MAD Fault, characterized by intense microseismicity but no significant earthquakes over the past two centuries. Despite its length and high deformation rate, the fault's behavior has been attributed to its composition of small segments (Abacha 2015; Mohammedi 2015). The recent 2017 and 2021 seismic sequences have confirmed this hypothesis. Below, we present the key findings from our analysis of the various seismic sequences, organized by their spatial distribution along the MADF, progressing from west to east from the 2020 Mila sequence to the 2021 Guelma earthquake passing by the 2017 Sidi Dris and 2017-2020 El Kantour sequences.

The 2020 Mila sequence began with an Mw 4.8 earthquake on July 17, 2020, followed by two additional moderate shocks on August 7, 2020, with magnitudes of Mw 5 and Mw 4.5, respectively. This sequence occurred in the northern part of Mila city. We successfully relocated 981 events (**Fig. V.17a**). We identified two swarms: the red swarm, which follows the initial Mw 4.8 shock, and the yellow swarm associated with the Mw 5 and Mw 4.5 shocks. Additionally, we observed a westward migration of seismicity. The first swarm (red) is linked to a NW-SE right-lateral strike-slip fault, labeled Beni Haroun Strike-Slip Fault 1 (BH-SSF1), while the second swarm (yellow) is associated with a NE-SW left-lateral strike-slip fault. labeled Beni Haroun Strike-Slip Fault 2 (BH-SSF2) (**Fig. V.17b**). This is confirmed by the distribution of aftershocks, focal mechanism parameters, and a directivity study conducted by Boulahia 2022.
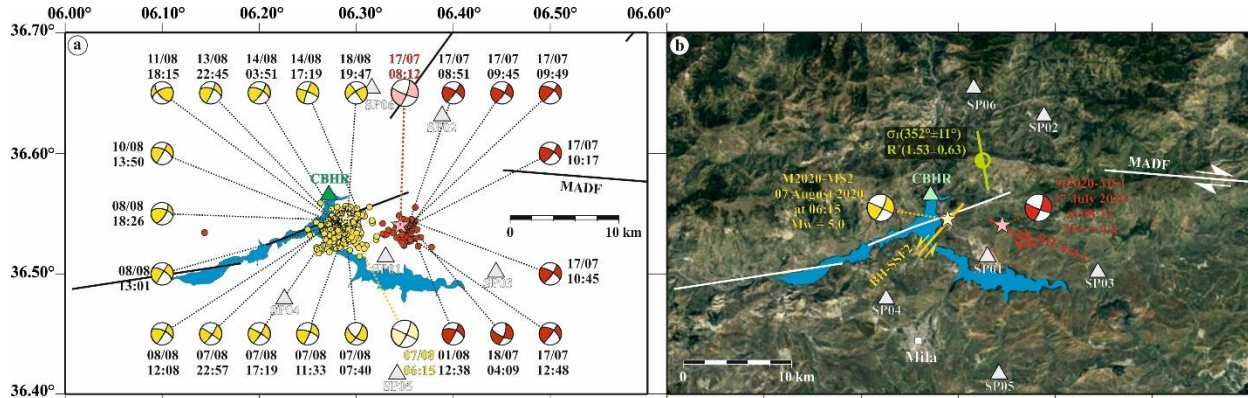
Fig. V.17: Mila 2020 seismic sequence analysis. **(a)** Horizontal distribution of the 981 relocated events from the 2020 Mila seismic sequence, along with the focal mechanisms of the main aftershocks. **(b)** Model of orthogonal conjugate faults revealed after the analysis of this sequence; in red, a NW-SE right-lateral segment (BH-SSF1) associated with the Mw 4.8 shock (M2020-MS1), and in yellow, a NE-SW left-lateral segment (BH-SSF2) associated with the Mw 5 shock (M2020-MS2); the principal local stress σ1 and the deformation regime R' are shown in green.

The analysis of this sequence is the subject of a paper that is being prepared by Boulahia et al., *in prep*.

In the Sidi Driss region, located 20 km east of the 2020 Mila sequence, a seismic crisis consisting of 83 well-located events revealed two parallel seismic clusters oriented NNE-SSW (**Fig. V.18a**) over just two days of recorded data, March 4 and 5, 2017 (Bendjama *et al.* 2021). The first cluster, highlighted in blue, includes the two largest events of the crisis: SD-LE1 with a magnitude of 3.0, and SD-LE2 with a magnitude of 3.1. Based on focal mechanism parameters (**Fig. V.18a**), Bendjama *et al.*, 2021 proposed that these two clusters were generated by two parallel NNE-SSW left-lateral strike-slip faults, one of which aligns perfectly with the pre-existing Sidi Driss Faults (SDF1 and 2 in **Fig. V.18b**).
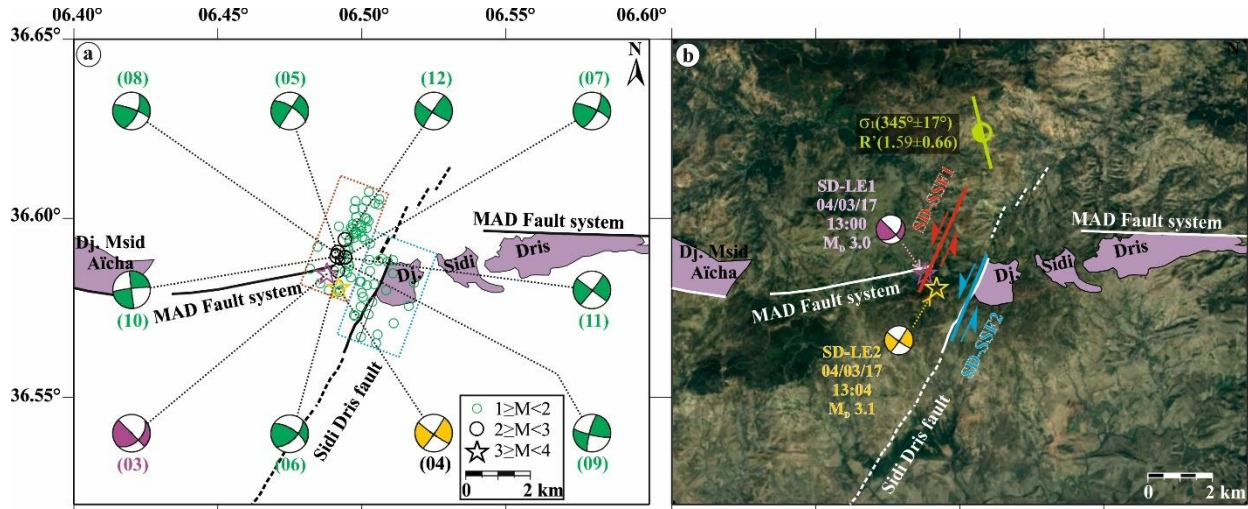
Fig. V.18: Sidi Driss 2017 seismic sequence analysis. **(a)** The distribution of 83 well-located events and the focal mechanism solutions of several key events from the 2017 seismic crisis (modified from Bendjama et al., 2021). **(b)** Our interpretation of the two fault structures that are believed to have triggered this crisis. SD-SSF1 and SD-SSF2 are the two fault segments that have been activated during this swarms. SD-SSF1 hosted the two largest events.

A few kilometers east, in the El Kantour region, a significant earthquake struck on November 22, 2020, at 03:53, registering a mainshock of Mw 5.0. This event stands as the largest recorded earthquake in the region during the instrumental period. Notably, this area also experienced a Mw 4.7 earthquake on March 5, 2017, accompanied by 25 aftershocks, coinciding with the Sidi Dris seismic crisis (Bendjama *et al.* 2021). In total, 595 events were successfully located. Through high-precision relocation we relocated 401 events.

The relocated events (**Fig. V.19a**) reveal an off-fault aftershock distribution, where the main aftershock cluster, oriented approximately east-west, is positioned away from the mainshock location. Off-fault aftershock activity refers to seismic events occurring off the primary rupture plane, within regions of the crust affected by stress redistribution from the mainshock. Interestingly, the timeline of the sequence revealed that the mainshock and most of the largest aftershocks occurred within the first 80 hours, with no initial activity along the ~EW aftershocks' cluster, see **Fig. V.19c.**

As seen in **Fig. V.19a**, the main aftershock cluster (oriented ~EW) predominantly consists of low-magnitude events (M<3). In the cross-sectional view (**Fig. V.19b**), it is evident that events with M < 3 are concentrated in the shallow crust, typically at depths less than 6 km (Zone 1), while events with M ≥ 3 generally occur at depths greater than 6 km (Zone 2). This observation raises intriguing questions: Is there a magnitude-depth variability in El-Kantour region? If such a relationship exists, it could suggest that varying physical characteristics of the crust at different depths influence fault rupture length, and consequently, event magnitude. To address this, a more in-depth analysis is necessary to derive plausible interpretations.

Focal mechanisms solutions for all the M3+ events are shown in **Fig. V.19c.** Additionally, the events assumed to belong to the same fault are enclosed within dashed red ellipsoids.

Based on the aftershock distribution and focal mechanisms, we propose a seismotectonic model (**Fig. V.19d**) illustrating the activation of multiple vertical sub-parallel faults, predominantly oriented N110°. This model confirms the segmented nature of the MAD fault, as previously highlighted by Abacha 2015 and Mohammedi 2015. The analysis of this sequence, including seismotectonics, off-fault aftershocks, stress transfer and more is the focus of a forthcoming paper by Bendjama et al., *in prep.* **Fig. V.19d** also indicates the presence of a dextral WNW-ESE fault labeled K-SSF1, which likely generated the 2017 sequence. Conversely, K-SSF2 is identified as the seismogenic fault responsible for the 2020 sequence.
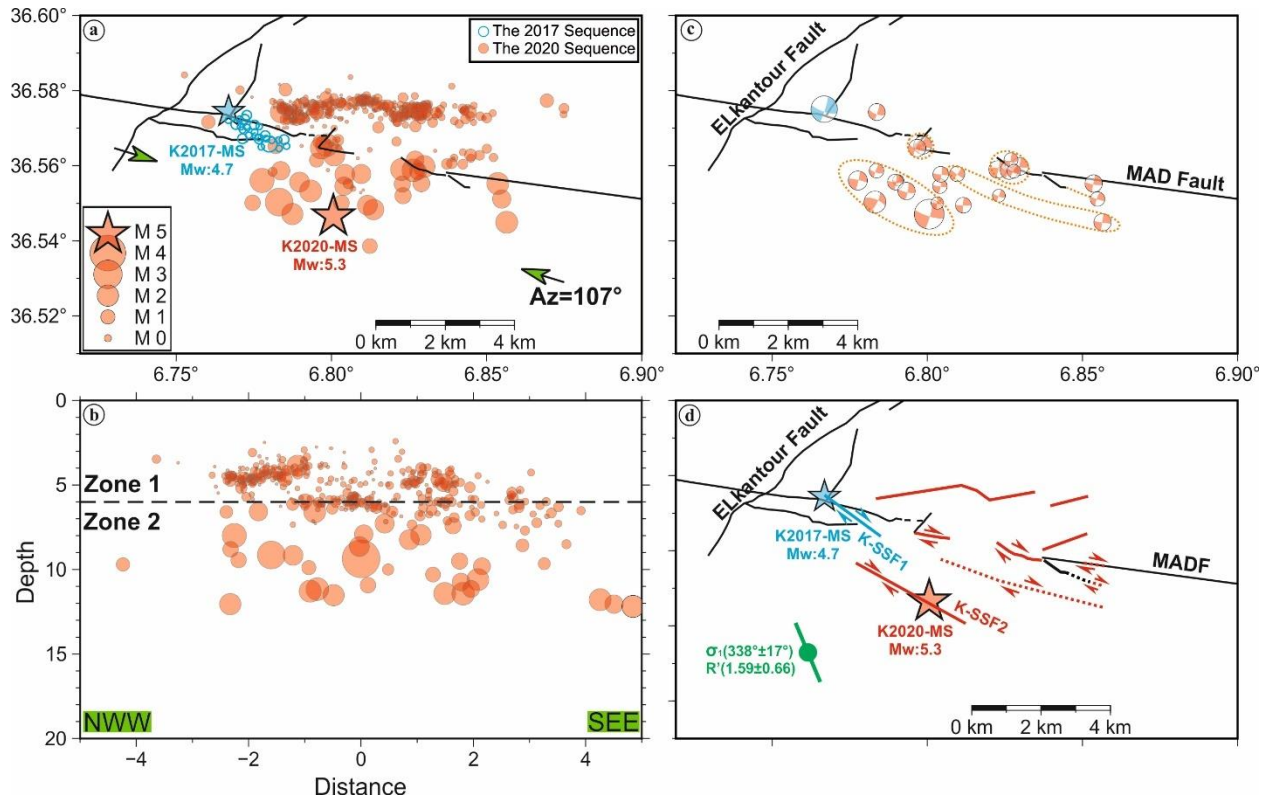
Fig. V.19: El Kantour 2020 seismic sequence analysis. **(a)** The distribution of 25 well-relocated events from the 2017 El Kantour earthquake (Bendjama et al., 2021) alongside 401 well-relocated events from the 2020 El Kantour sequence. **(b)** Cross-section view along N107°. **(c)** Focal mechanism solutions for M3+ events. Dashed red ellipsoids indicate clusters of events that are likely associated with the same source fault. **(d)** Proposed seismotectonic model for El Kantour 2020 sequence.

At the eastern extremity of MADF, south of Dj. Debbagh, lies the Guelma basin, a "pull-apart" structure aligned with a major east-west dextral strike-slip MAD fault (Meghraoui 1988). This basin is highly seismically active, as evidenced by both historical (Abacha 2015) and recent seismic events (Bendjama *et al.*, 2021). The most recent significant event occurred on April 1, 2021, with a magnitude of Mw 4.7 and an intensity of I_0 V. We relocated 98 events (**Fig. V.20a**) using a velocity model derived through the trial-and-error method (**Fig. V.20b**) and a relatively high Vp/Vs ratio of 1.8 (**Fig. V.20c**). Their spatiotemporal distribution suggests a possible migration towards the SE from the main shock (**Fig. V.20a**).

Chapter V
                          Geometric and Physical Characterization
of Active Faults in Northeastern Algeria
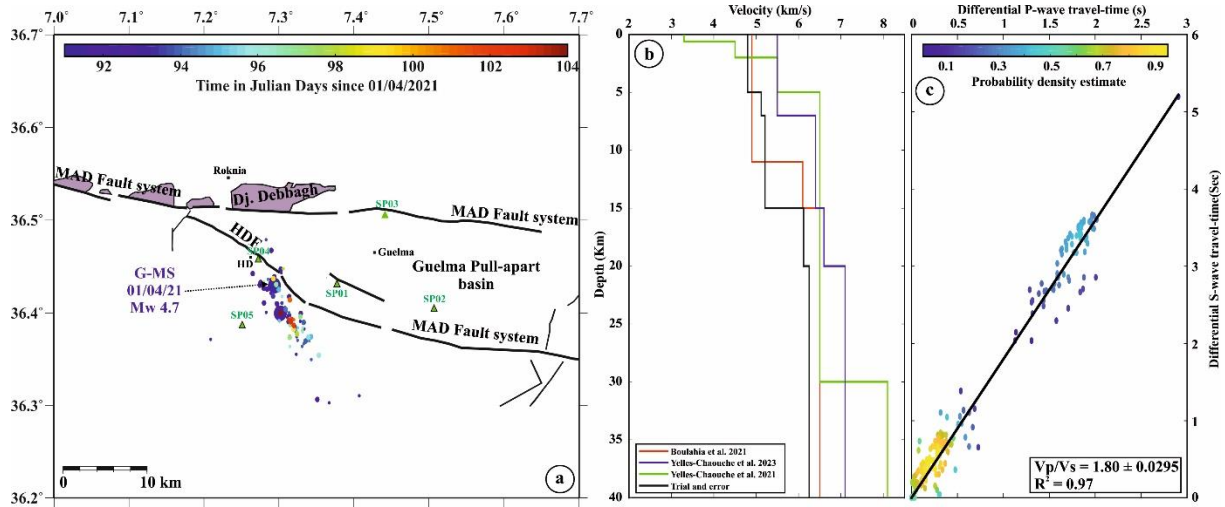
Fig. V.20: Guelma 2021 seismic sequence analysis. **(a)** The spatiotemporal evolution of the 98 relocated events indicates a possible migration towards the SE. **(b)** The obtained 1D velocity model. **(c)** Vp/Vs ratio in the Guelma region.

The spatial distribution of the event cluster, analyzed alongside nine focal mechanisms (**Fig. V.21a** and **c**), reveals the rupture of a near-vertical, dextral NW-SE strike-slip fault approximately 20 km in length, designated as the Guelma Strike-Slip Fault (G-SSF) in this study. This fault lies south of the Hammam Debbagh Fault (HDF) and does not coincide with the western boundary of the Guelma pull-apart basin as outlined by Maghraoui 1988. Conversely, plotting the relocated events on the geological layout of the Guelma Basin, as depicted by Bouaicha 2018, reveals that the western boundary of the basin, as suggested by Maouche *et al.* (2013), was activated during this sequence (see **Fig. V.21b**). The cluster aligns over the southern part of HDF (~7km) and the northern part of F2 faut (~13 km). This likely points to the activation of both faults. The seismicity began on the HDF then migrated towards F2, see Spatio-temporal evolution in **Fig. V.20a**. Furthermore, recent earthquakes identified by Bendjama et al. (2021) align along the HDF segment, with both the HDF and G-SSF forming a "stepover zone" within the pull-apart basin that links parallel segments of the MADF (**Fig. V.21d**). This alignment reinforces the accuracy of Maouche's boundary delimitation.

Seismic activity, previously concentrated along the HDF segment between 2003-2007, shifted to the G-SSF segment in 2021, suggesting a stress transfer between these segments.

Most focal mechanisms reveal a strike-slip faulting solution with a normal component, consistent with the basin's extensional nature and controlled by shear movements along the Principal Deformation Zone (PDZ) and Basement Fault Zone (BFZ) (**Fig. V.21d**). This accommodates the maximum stress oriented NNW-SSE. The presence of thermal springs in the region and the relatively high Vp/Vs ratio further suggests a potential correlation between geothermal activity and the triggering of seismic sequence.

We mention that the analysis of this sequence is the subject of the forthcoming paper by Bouadja et al., *in prep.*
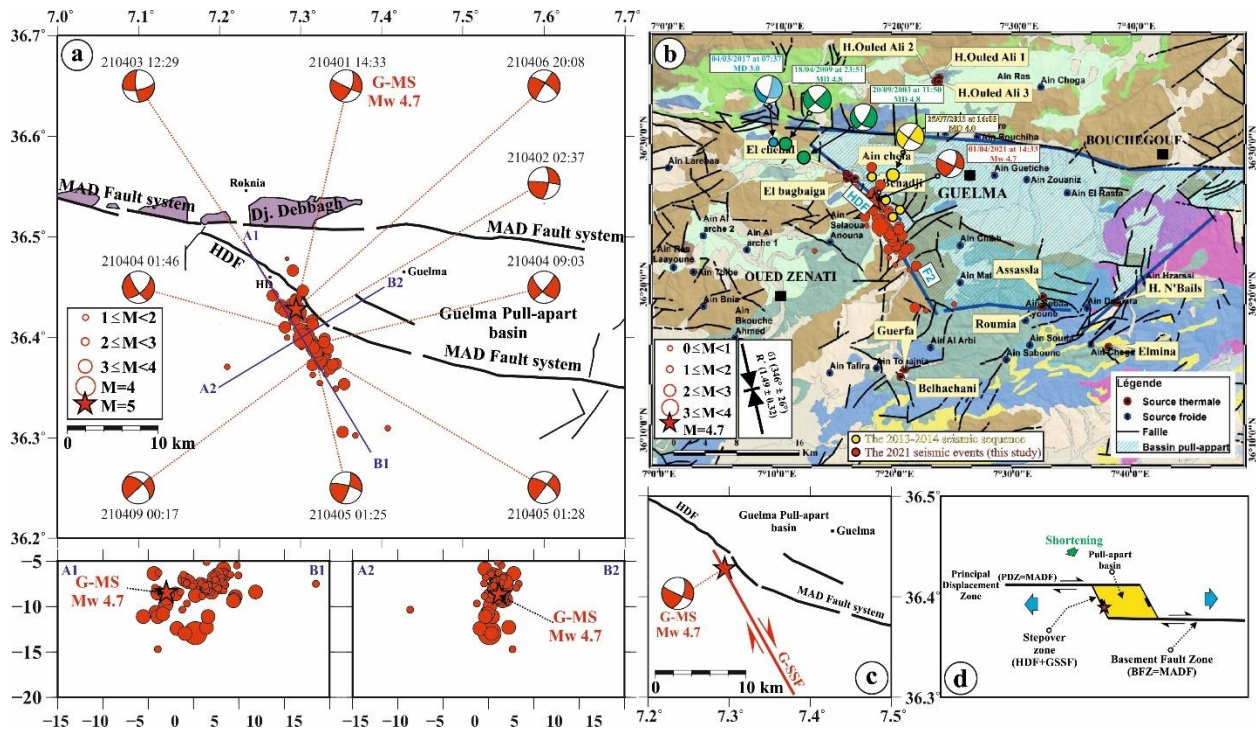
Fig. V.21: Guelma 2021 seismic sequence within the pull-apart basin. **(a)** Spatial distribution of the relocated events along with the 9 focal mechanisms of the main events. **(b)** Superimposition of the relocated events on the geological map of the basin, as established by Bouaicha 2018. In blue, the basin boundaries are marked as per Maouche *et al.* (2013). **(c)** Proposed G-SSF fault model, consistent with the western boundary of the basin as defined by Maouche *et al.* (2013). **(d)** Representation of the pull-apart basin based on the obtained results.

In summary, **Fig. V.22** illustrates the newly identified tectonic structures along the ~E-W right-lateral strike-slip MAD Fault system, which acts as a Principal Deformation Zone (PDZ). The NW-SE oriented red faults correspond to synthetic right-lateral strike-slip faults, known as R Riedel shears, while the NE-SW oriented orange faults represent antithetic left-lateral strike-slip faults, or R' Riedel shears. Notably, the recent seismic activity is concentrated on these subsidiary faults rather than the main fault (MADF). This raises the possibility that a larger section of the E-W trending MADF could rupture, potentially leading to a significant seismic event. Given this scenario, it is crucial to incorporate these findings into a reassessment of seismic hazard for the region.
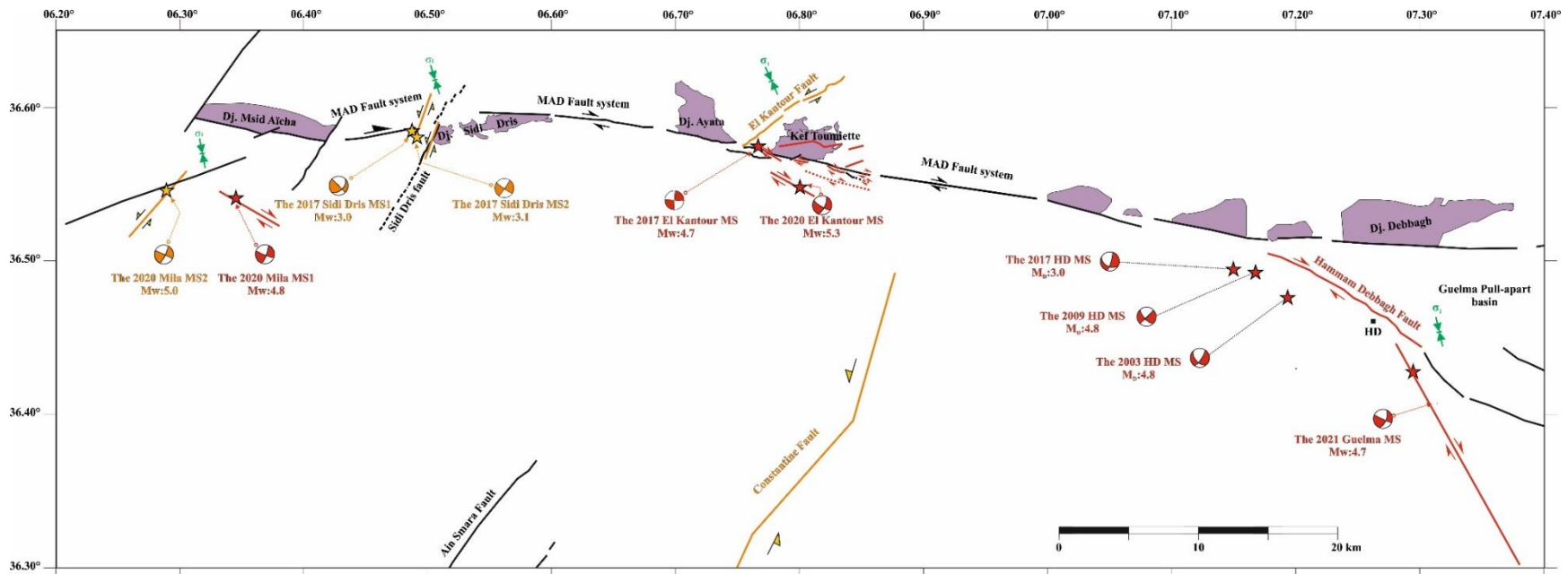
Fig. V.22: MAD fault extent along northeastern Algeria. An approximate model of the faults revealed following the different sequences along a major E-W dextral strike-slip MAD fault that reacted as a Principal Deformation Zone (PDZ). The orange faults represent NE-SW left-lateral strike-slip faulting, while the red faults, trending NW-SE to ~E-W, indicate right-lateral strike-slip faulting. Black lines mark the MAD PDZ as identified in geological studies (Vila 1980; Wildi 1983). Local stress tensors for the different areas are shown in green.

V.4.3 Mila-Constantine Basin Zone

Unlike other intra-mountain basins of the Tellian Atlas, the Constantine basin is situated at a higher altitude. It is bordered to the north by the MADF and is impacted by several neotectonic faults, including the Sigus Fault, which runs E-W and extends nearly 30 km, and the Ain Smara Fault, recognized as active during the Constantine earthquake of October 27, 1985 (Bounif *et al.* 1987). The Ms 6.0 Constantine Earthquake, which struck at 16:34:56 UTC, was the most significant seismic event recorded in the Tellian Atlas since the Ms 7.3 El Asnam Earthquake on October 10, 1980. This earthquake has been extensively studied (Bounif et al., (1987); Deschamps *et al.* (1991); Bounif & Dorbath (1998); Ousadou *et al.* (2012)), highlighting its importance in understanding seismic activity in the region. The spatial distribution of the epicenters (Bounif *et al.*, 1987) reveals a well-defined rupture zone approximately 30 km in length and 2 km in width. A closer examination of this distribution identifies three distinct rupture segments, each with varying orientations relative to the main Constatine Strike-Slip Fault (C-SSF), see **Fig. V.23a** and **b**. Notably, the overall trend of the aftershocks deviates from the expected alignment of the Ain-Smara neotectonic fault, indicating potential complexities in the fault system or the presence of secondary structures influencing the rupture process. A recent study by Ousadou et al. (2012), utilizing fine relocation of aftershocks (**Fig. V.23a**) and analyzing the focal mechanisms of 138 aftershocks (**Fig. V.23b**), has refined our understanding of the rupture process. Their findings identified four activated fault segments rather than the previously assumed three. This detailed analysis underscores the complexity of the fault system and highlights the importance of high-resolution seismic data in accurately mapping rupture dynamics and fault segmentation.
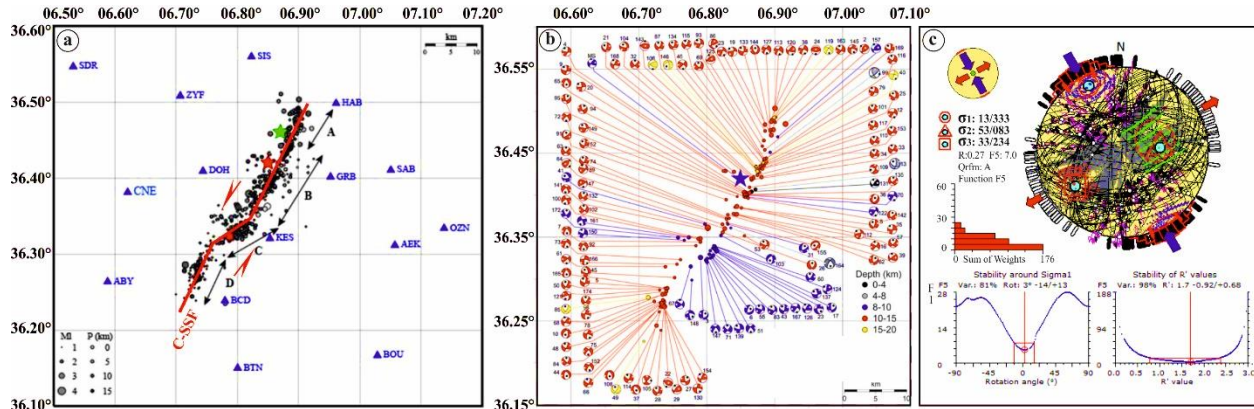
Fig. V.23: Analysis of Constantine 1985 seismic sequence. **(a)** Relocation of the aftershock sequence using tomoDD (modified from Ousadou et al., 2012). **(b)** Focal mechanisms of the aftershock sequence, highlighting the stress distribution and fault-plane orientations. **(c)** Stress inversion analysis results from our inversion of the 108 focal mechanisms mentioned in **(b)**.

The 138 focal mechanisms (FMs) reported by Ousadou *et al.* (2012) were reanalyzed using Win-Tensor to delineate the predominant stress regime and local deformation patterns along the fault system **(Fig. V.23c)**. Ninety-one FMs were inverted during the initial tensor analysis, revealing a dominant stress regime across the entire epicentral region. The resulting focal planes were steeply inclined (60–80°) with NE–SW to NNE–SSW and NW–SE to NWW–SEE orientations. The inversion indicated a pure strike-slip regime (R′ = 1.78 ± 0.23), with a sub-horizontal principal compressive stress (S_{Hmax}) trending NW–SE (N151E ± 10.5). The mean plunge of σ1 was 14°/333°, σ2 was 53°/83°, and σ3 was 33°/234°, corresponding to the mainshock's P-axis (345°) and T-axis (75°). The overall result, with a low $\bar{\alpha}$ of 11.1° and excellent quality (A), confirms a well-defined strike-slip tectonic setting for the region.

In November and December 2007, the Mila region experienced a seismic crisis characterized by hundreds of events, notably without a clear mainshock. Semmane *et al.* (2012) attributed this activity to an anthropogenic induced seismicity, likely caused by water infiltration into the subsurface. This infiltration was facilitated by preexisting fractures, faults, and karst formations, and occurred during the water transfer between the Beni-Haroun dam and the Oued Athemania reservoir. Their study found that only 45% of the transferred water was recovered at the Oued Athemania reservoir, with a

significant amount of pressurized water leaking through defective joints in a tunnel passing through the Akhal mountain.

In this part of the thesis, we reexamined the seismic crisis by reanalyzing data that yielded over 1,000 events, each recorded by at least one station. Of these, 463 events were properly located, and 272 were relocated using catalog and cross-correlation data. The SP04 station was pivotal in both locating and relocating seismic events due to its central position within the epicentral area. Unfortunately, the late installation of this station led to the missed detection of hundreds of events. Moreover, the SP04 station significantly contributed to refining the focal depths of recorded events (see Abacha, 2015; Semmane et al., 2012). **Fig. V.24** shows the spatial distribution of the 272 relocated events and six key focal mechanisms, revealing a primary NNW-SSE oriented cluster associated with a 7.5 km rupture along a left-lateral strike-slip fault. The figure also presents the Vp/Vs ratio in the Mila area, determined using the modified Wadati method. Two velocity models were tested Semmane et al. (2012) and a trial-and-error model. The later yielded slightly better results in term of uncertainties (ERH, ERZ, and RMS).
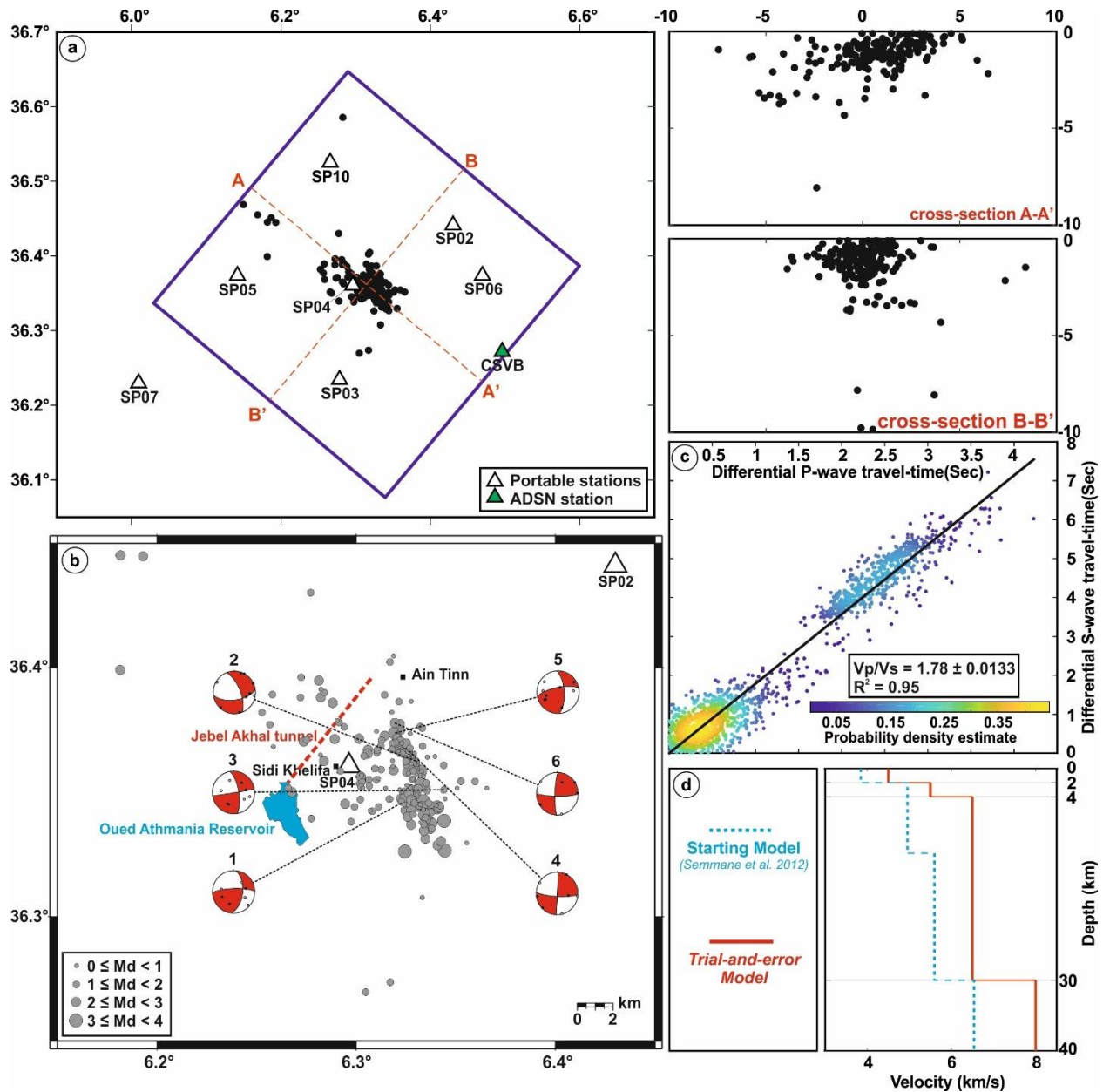
Fig. V.24: Mila 2007 location and relocation. **(a)** Spatial and vertical distribution of 272 relocated events. **(b)** Six key focal mechanisms along the relocated events revealing a primary NNW-SSE oriented cluster, associated with a 7.5 km rupture of a left-lateral strike-slip fault. **(c)** Vp/Vs through modified Wadati diagram. **(d)** The used velocity model, showing the velocity model from Semmane *et al.* 2012 in dashed light blue line, and our trial-and-error approach model used for location and relocation in red solid line.

We extracted nine multiplet groups, each containing at least three events recorded by at least one station with a minimum CC of 0.7 and an average CC threshold of 0.8 (**Fig. V.25**). By superimposing these multiplet groups onto the relocated events, we proposed

the model shown in the lower right corner of the figure. This model suggests that the fault network responsible for this seismic sequence is a small, complex system, where the principal fault is intersected by several segments that may constitute its damage zone. This fault network is labeled Mila Strike-Slip Fault Network (M-SSFN) in **Fig. V.25.**
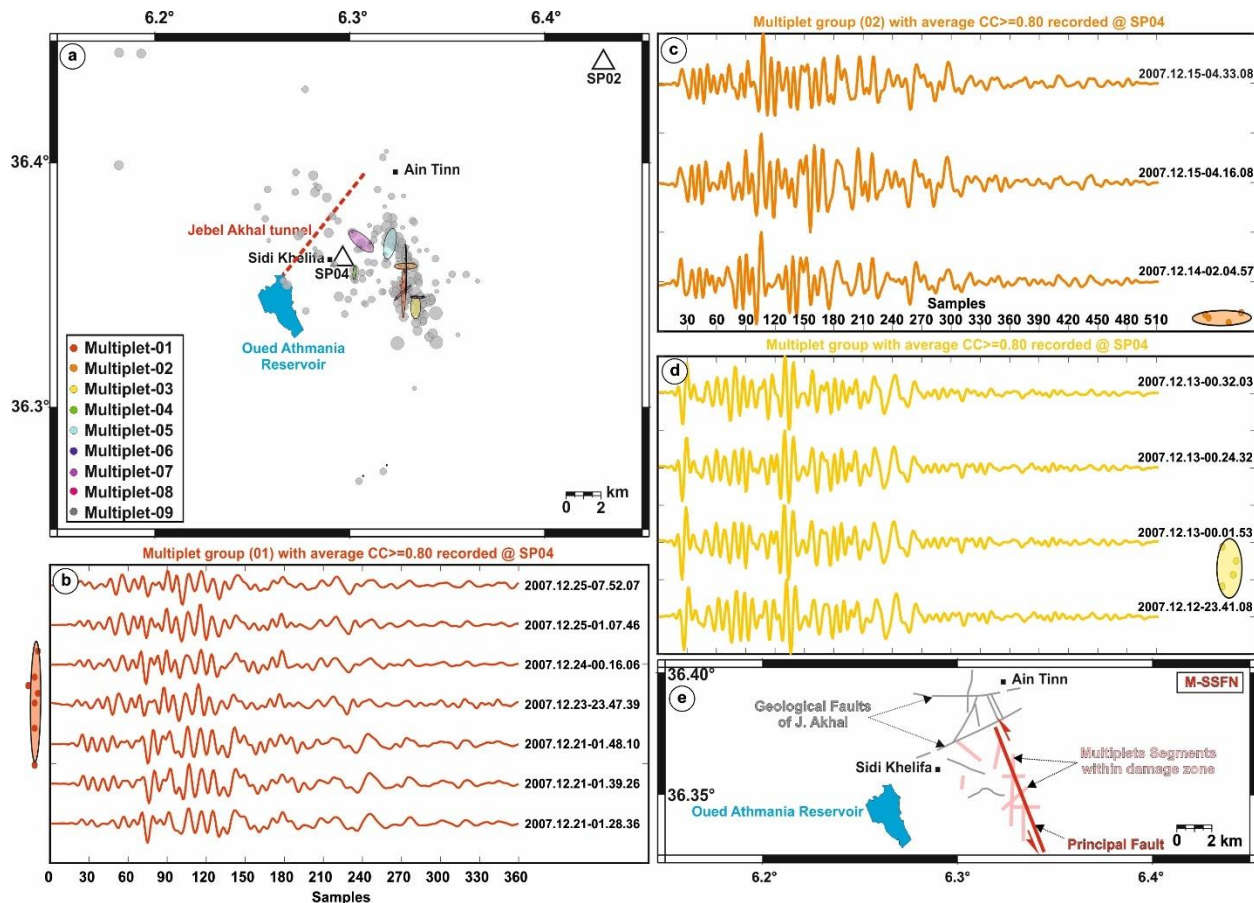
Fig. V.25: Mila 2007 multiplet and proposed fault model. **(a)** Overlay of 9 multiplet groups on relocated events, revealing several hidden sub-clusters. Panels **(b), (c),** and **(d)** show waveform similarities for three multiplet clusters recorded at station SP04. **(e)** Proposed fault model based on multiplet clusters, with the main fault and subsidiary faults shown in red, all forming the Mila Strike-Slip Fault Network (M-SSFN).

In addition to previous results, we analyzed seismicity migration to determine the diffusivity value corresponding to the expansion of aftershock activity. The R-T plot of the 2007 Mila seismic swarm in **Fig. V.26** displays two hyperbolic envelopes: a front and back-front. De Barros *et al.* (2024) observed that this is a systematic phenomenon in natural and anthropogenic earthquake swarms. The first envelope (front) refers to the

leading edge or advance of the seismicity pattern over time, marking the area where new earthquakes are occurring as the swarm progresses. Using Shapiro *et al.* (1997) formula we revealed a hydraulic diffusivity (D_F) of 2.4 m²/s. The second envelope (back-front) describes the trailing edge of seismic activity as the swarm begins to wane in certain areas. The back-front typically lags behind the main front of activity. A back-front has been observed following the cessation of injection activities (Parotidis *et al.* 2004). In our case this represents the cessation of water pumping (t_0 in **Fig. V.26**). We have estimated a back-front diffusivity value of D_{BF} of 0.6 m²/s. Both values fall within the hydraulic diffusivity interval proposed by Do Nascimento *et al.* (2005).

Initially thought to result from fluid diffusion, the seismic front is now better understood as the outcome of aseismic slip induced by fluid propagation. This updated view highlights that rather than direct diffusion, it is the gradual spread of fluid-triggered slip along fault surfaces that drives the seismic front's advancement. This conclusion is supported by several researcher works, (e.g Danré *et al.* (2022); De Barros *et al.* 2024). Hence, we assume that the observed migration pattern in Mila 2007 swarm is related to expansion of fluid-induced aseismic slip. Furthermore, we suggested similar interpretation to explain the observed seismicity migration in BI-2010 sequence, see Tikhamarine *et al.* 2024, and **Fig. IV.17.**
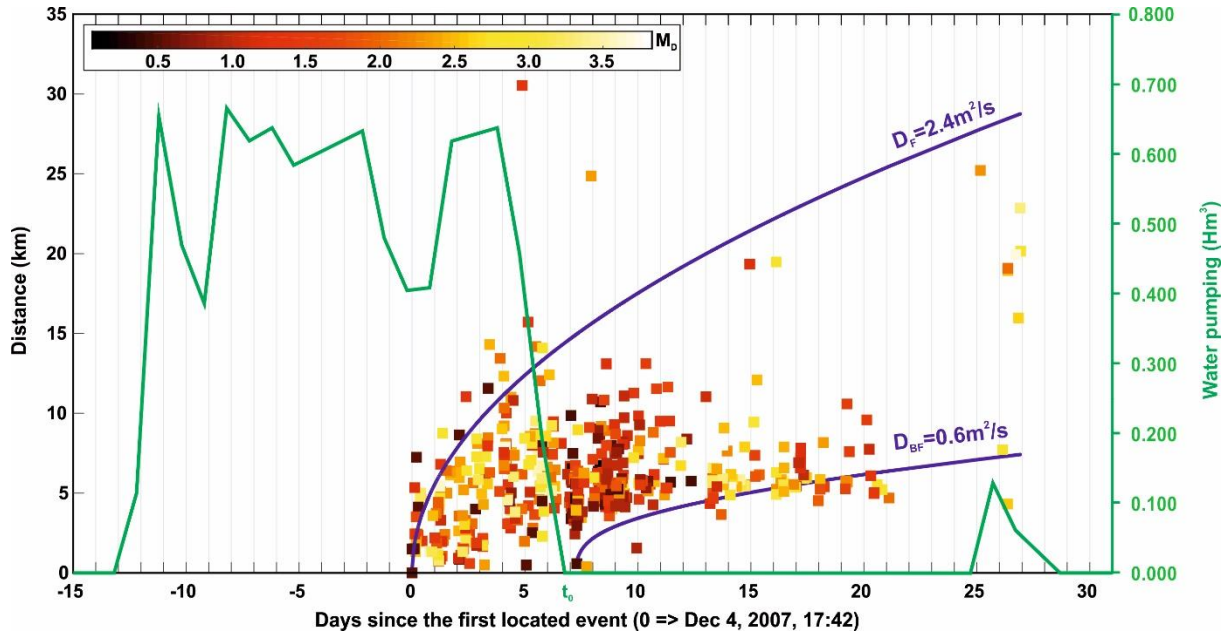
Fig. V.26: R-T plot of the Mila 2007 seismic swarm. Green curve represents the evolution of water pumping from Beni Haroun dam to Oued Athmania reservoir. The blue upper curve (D_F = 2.4 m²/s) represents the seismicity front's hyperbolic envelope, while the lower blue curve (D_{BF} = 0.6 m²/s) shows the back-front.

V.4.4 Central Tellian Atlas Zone

This zone encompasses several Tellian sub-domains, including the Blida Atlas, Tablat Atlas, Bibans Mountains and Algiers area (Mitidja Basin with the offshore part). The Hammam Melouane region, located in the Blida Atlas south of the Mitidja Basin, experienced a notable seismic sequence divided into three sub-sequences during 2013, 2014-2015, and 2016. Three moderate earthquakes marked this sequence: an Mw 5.0 event on July 17, 2013, an Mw 4.9 event on December 23, 2014 and an Mw 4.9 event on February 10th, 2016. The 2013 sequence has been analyzed by Yelles-Chaouche *et al.* (2017), who suggested that the 2014 Hammam Melouane earthquake was likely caused by a right-lateral strike-slip fault adjacent to the fault activated in 2013. On the other hand, Khelif 2019 investigated the entire sequence 2013-2016, highlighting that the Hammam Melouane sequence (2013-2016), like many seismic sequences affecting the Blida Atlas, occurred across multiple faults, each generating a significant number of moderate earthquakes. Khelif 2019 provided three fault model to explain the observed seismicity.

1) A right-lateral strike-slip fault for the 2013 sequence. 2) A reverse fault for the 2014 sequence and another reverse fault for the 2016 sequence.

In this thesis, we re-evaluated the entire sequence from 2013 to 2016. Our data deployment led to a significant increase in detected aftershocks, with 154 events recorded during the 2013 sequence, 304 events in the 2014-2015 sequence, and 94 events in the 2016 sequence, totaling 552 events (**Fig. V.27a**). Using the modified Wadati method we estimated a Vp/Vs = 1.68 (**Fig. V.27c**) slightly different from the one used by Khelif 2019 (Vp/Vs=1.66). Yelles-Chaouche *et al.* (2017) and Khelif 2019 used a velocity model developed from the SPIRAL project Leprêtre *et al.* (2013). Using this model as a starting point, we applied VELEST, following the approach outlined in **Chapter II**, to obtain a velocity model that better fits the recorded data in the study area, see **Fig. V.27b.** Our revised velocity model achieved a mean RMS of 0.1336 seconds, compared to 0.1416 seconds for the initial model, indicating an improvement.
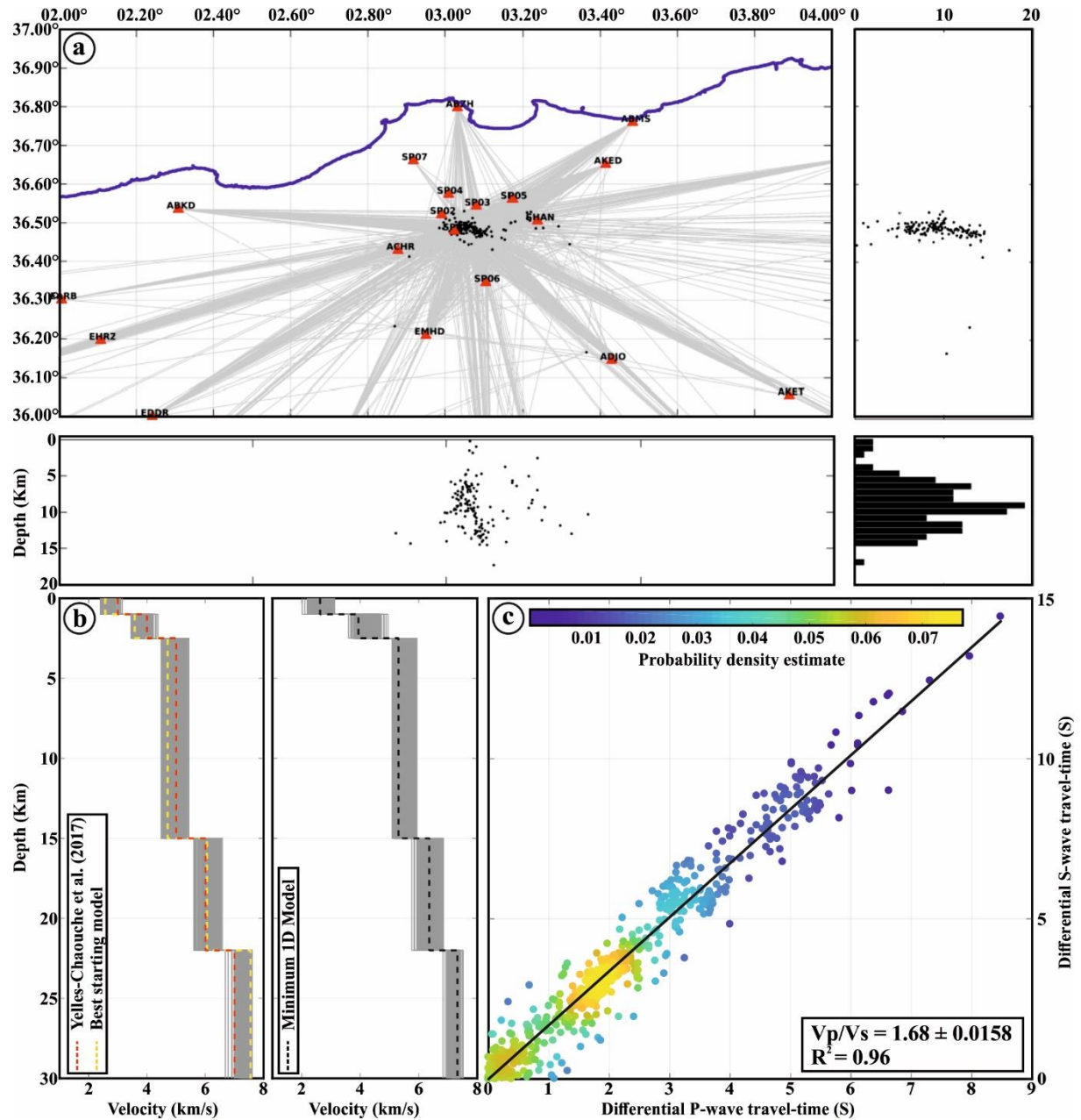
Fig. V.27: Hammam Melouane derived velocity model. **(a)** Ray coverage map of the 552 selected events used in the VELEST inversion. The upper left panel displays the horizontal distribution of events (black dots), with ray paths shown as grey lines. The upper right and lower left panels show focal depth distribution along latitude and longitude, respectively. The lower right panel presents a histogram of event counts across depth ranges. **(b)** The left panel shows the 200 initial models, with red and yellow dashed lines representing the a priori velocity model from Yelles-Chaouche *et al.* (2017) and the best starting model with the lowest residuals. The right panel depicts the 200 inverted models, with the black dashed line representing the minimum 1D model. **(c)** Vp/Vs ratio in the HM area calculated using the modified Wadati metho.

Since all three sequences occurred in the same epicentral area, we chose to relocate the entire 2013–2016 seismicity in a single process, rather than treating each period separately. Our relocation process using both catalog and cross-correlation data resulted in a successful relocation of 334 events as follow: 74 events of the 2013, 192 events of the 2014-2015 sequence and 68 events of the 2016 sequence, see **Fig. V.28.** The spatiotemporal distribution of aftershocks reveals that, following the 2013 sub-sequence (black dots), seismicity gradually migrated northwestward, forming the 2014-2015 sub-sequence (red dots) at approximately the same depth range. Then, it was shifted to the southeastern region for the 2016 sub-sequence (blue dots), occurring at a slightly greater depth than the previous two sequences. This distribution, along with focal mechanism solutions derived from P-wave first-motion polarities, which yield consistent results, suggests that a single NW-SE right-lateral strike-slip fault may have driven the entire three-year sequence. Nevertheless, we do not rule out the activation of nearby reverse faults, as indicated by Khelif 2019. This fault, referred to as Hammam Melouane Strike-Slip Fault (HM-SSF) in this thesis, is situated between two thrust faults: the Laraba Fault (LF) to the east and the Blida Fault (BF) to the west (**Fig. V.28**). These thrust faults define the boundary between the Mitidja basin and the Blida Atlas. A closer examination of both the BF and LF reveals a 15 km right-lateral topographic offset that aligns precisely with the HM-SSF, suggesting that this fault may have a regional extent. This alignment intersects the Mitidja basin, as described by Bonneton & Truillet (1979), extending from the Sahel Central Fault (SCF) in the north to the Blida Atlas Faults in the south (**Fig. V29a**).

Soumaya *et al.* (2018) proposed a seismo-tectonic model for the northeastern and north-central parts of Algeria (**Fig. V.29b**), with our study area highlighted in the yellow frame, clearly indicating the presence of a strike-slip structure. This model, referred to as the Riedel model (**Fig. V.29c**), features an E-W strike-slip corridor alongside NE-SW oriented X-inverse structures and NW-SE oriented R strike-slip faults. The projection of our region into this system (**Fig. V.29d**) shows the Thenia Fault (ThF) to the east and the Oued Djer Fault (ODF) to the west, with the obtained fault model situated in the middle.

This arrangement suggests a continuity toward the north into the central part of the Sahel fault system.
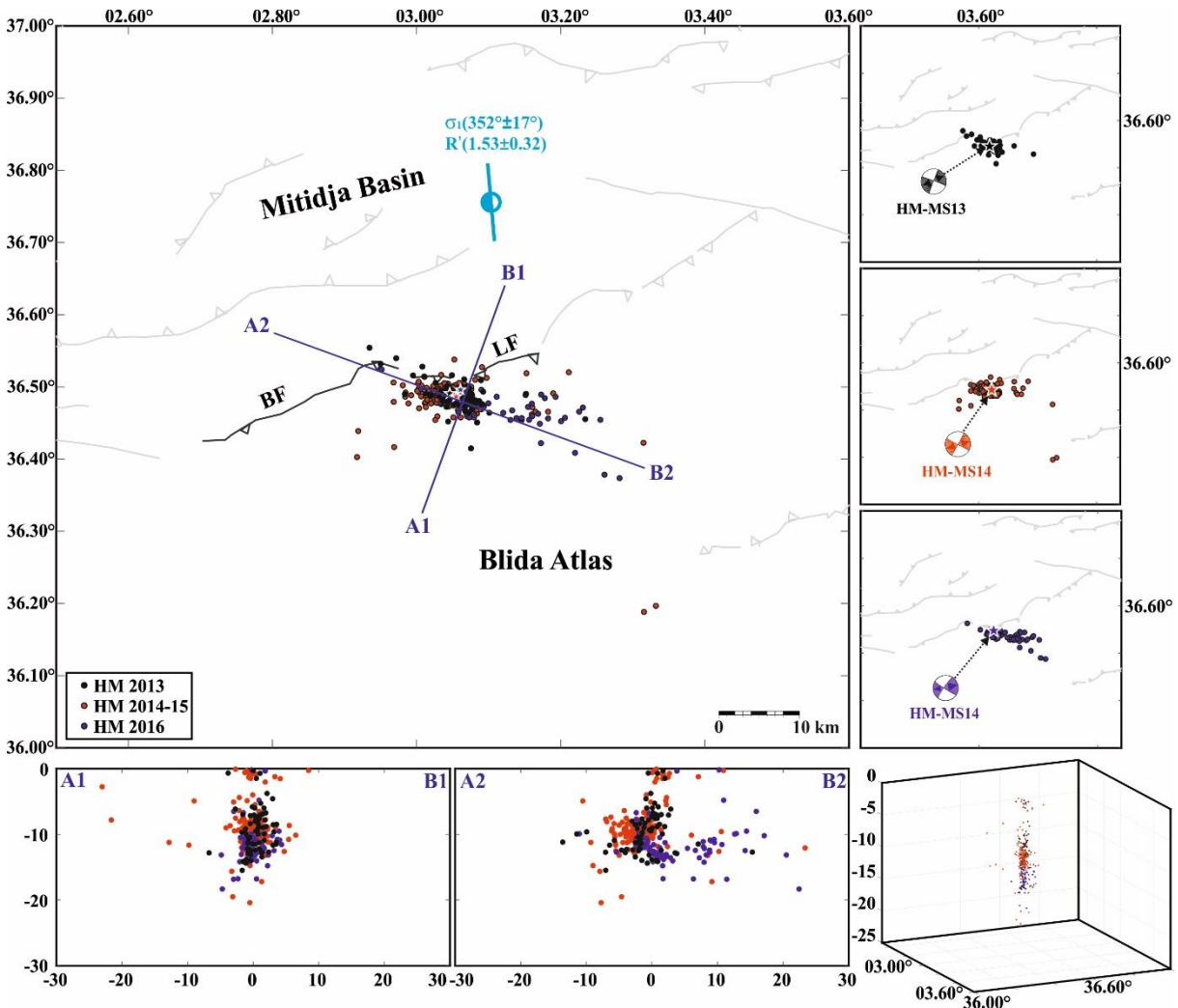
Fig. V.28: Hammam Melouane sequences' horizontal and vertical distribution of 334 relocated events and focal mechanisms of the main shocks from 2013, 2014, and 2016. Events are color-coded according to the three sub-sequences. In the lower right corner, we exhibit a 3D representation of Hammam Melouane relocated seismicity.

The stress tensor indicates a strike-slip regime with a NNW-SSE orientation, representing a reorientation in the positive direction relative to the neighboring stress tensors Yelles-Chaouche *et al.* (2019) in the Algiers region and Khelif *et al.* (2018) in the Mihoub region) (**Fig. V.29.a**). At the same longitude, a similar reorientation of the velocity vector (blue arrow in **Fig. V.29a**) This raises a question that has not yet been addressed: what causes this reorientation along this longitude?

Finally, we should draw attention that this sequence is likely the longest-lasting sequence in Algeria during the instrumental era; typical sequences in Algeria last only days to months, while the Hammam Melouane sequence persisted for nearly three years. The long-lasting aftershock sequences and the migration of seismicity suggest that fluids may have driven this seismic sequence. This is further supported by the presence of geothermal sources in the region, such as the Hammam Meloune source.
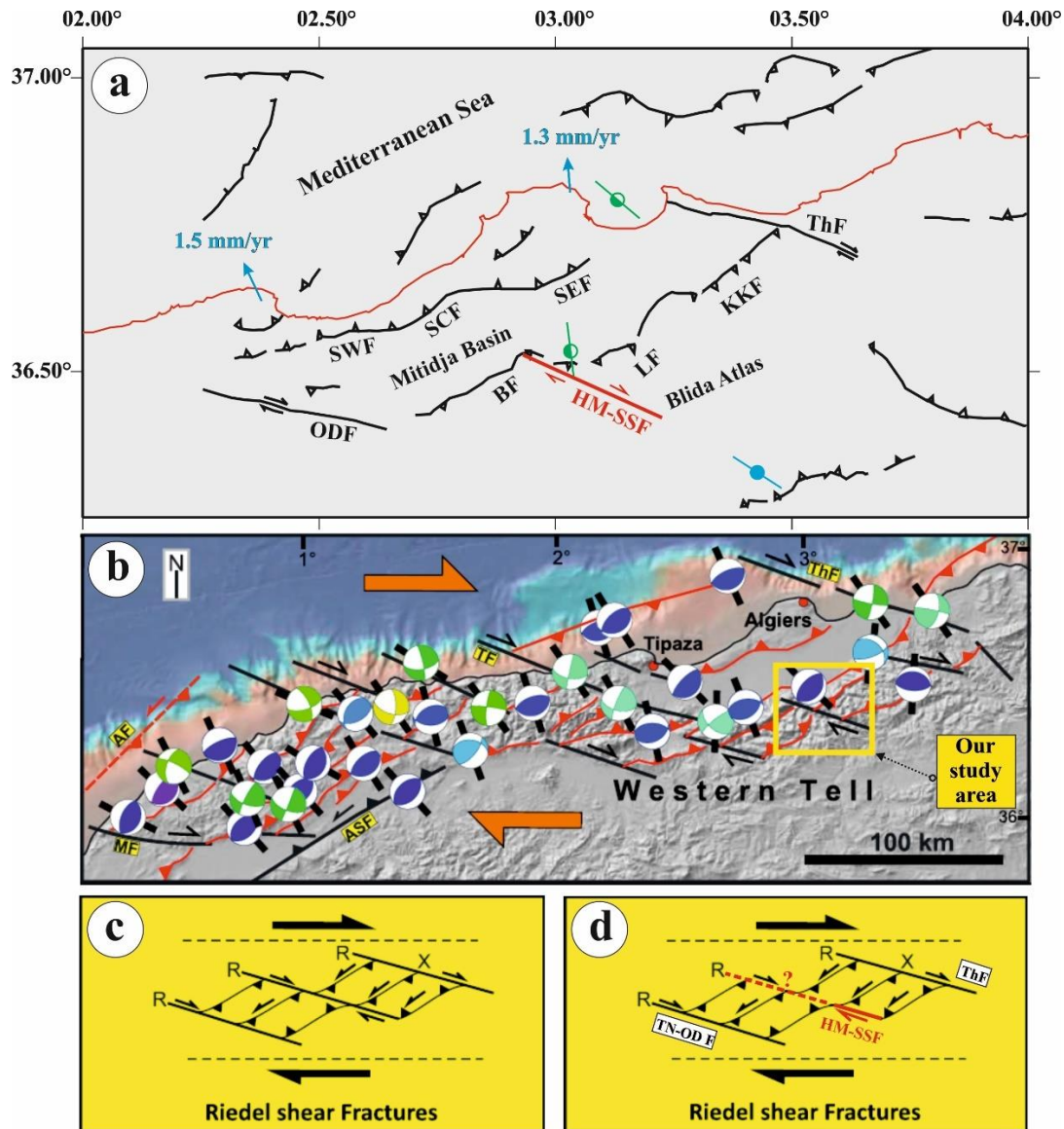
Fig. V.29: Proposed seismotectonic model for Hammam Melouane region. **(a)** Identified fault within the regional seismo-tectonic context. **(b)** North-West and North-Central Algeria seismo-tectonic model proposed by Soumaya *et al.* (2018). **(c)** Riedel model. **(d)** Projection of the obtained fault model onto the Riedel model.

At 30 km southeast of the Hammam Melouane sequence, the Mihoub sequence occurred in the Tablat Atlas in 2016. This sequence included two mainshocks, on April 10 and May 28, 2016, with magnitudes Md 4.9 and Mw 5.4, respectively (**Fig. V.30a** and **b**). Two fault segments are responsible for this sequence: the first is an east-west oriented segment with strike-slip characteristics, where the initial event (Md 4.9, April 10, 2016) was located. The second fault plane, associated with the most significant event of May 28, 2016 (Mw 5.4), is a reverse fault dipping southeastward (Khelif *et al.* 2018) (**Fig. V.30c**). This sequence was not analyzed within this thesis; instead, we rely on the findings of Khelif *et al.* (2018).
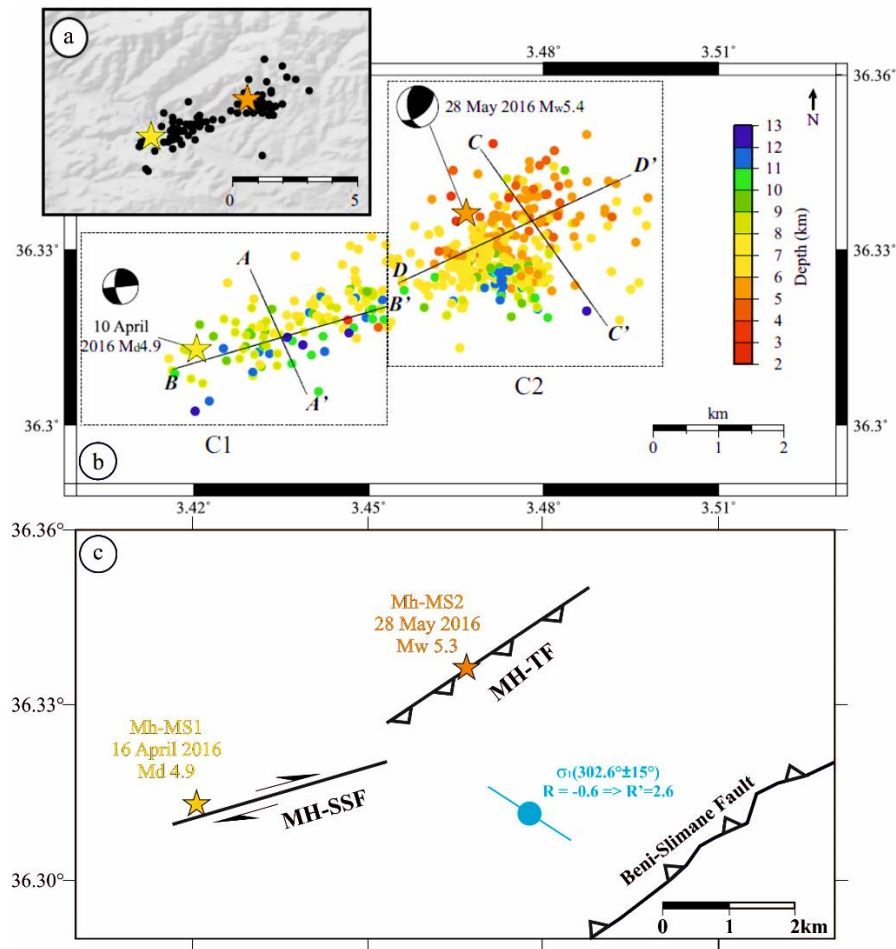
Fig. V.30: Mihoub 2016 sequence analysis. **(a)** and **(b)** Horizontal distribution of the 485 relocated events across the two clusters (after Khelif *et al.* (2018)). The yellow star marks the Md 4.9 event of April 10, 2016, while the orange star represents the Mw 5.4 mainshock of May 28, 2016, with their respective focal mechanisms. **(c)** The two proposed fault segments are determined from the event clusters shown.

Another sequence affected our study region, which we did not analyze directly but instead relied on a previously published study by Yelles-Chaouche *et al.* (2019). This concerns the Algiers seismic sequence, which occurred in the eastern part of Algiers Bay on 01 August 2014. In their analysis of 576 aftershocks recorded in the first month following the mainshock (**Fig. V.31a**), Yelles-Chaouche *et al.* (2019) demonstrate that the earthquake originated from a primary curved NE–SW-striking reverse fault, approximately 4 km in length. This fault strikes N60°E and dips northwestward at an angle of 70° for the first 2 km of depth, transitioning to 55° at greater depths. This fault is labeled Algiers Reverse Fault (Al-RF) in **Fig. V.31b**.

Additionally, a minor strike-slip fault, oriented roughly N–S, intersects the eastern segment of the Al-RF. Stress tensor inversion indicates a main compressional (σ_1) stress axis oriented N310°E. The authors also noted that the 2014 Algiers earthquake occurred along a back-thrust reverse fault associated with the general uplift of the coastline, as the offshore thrust faulting dips northward.
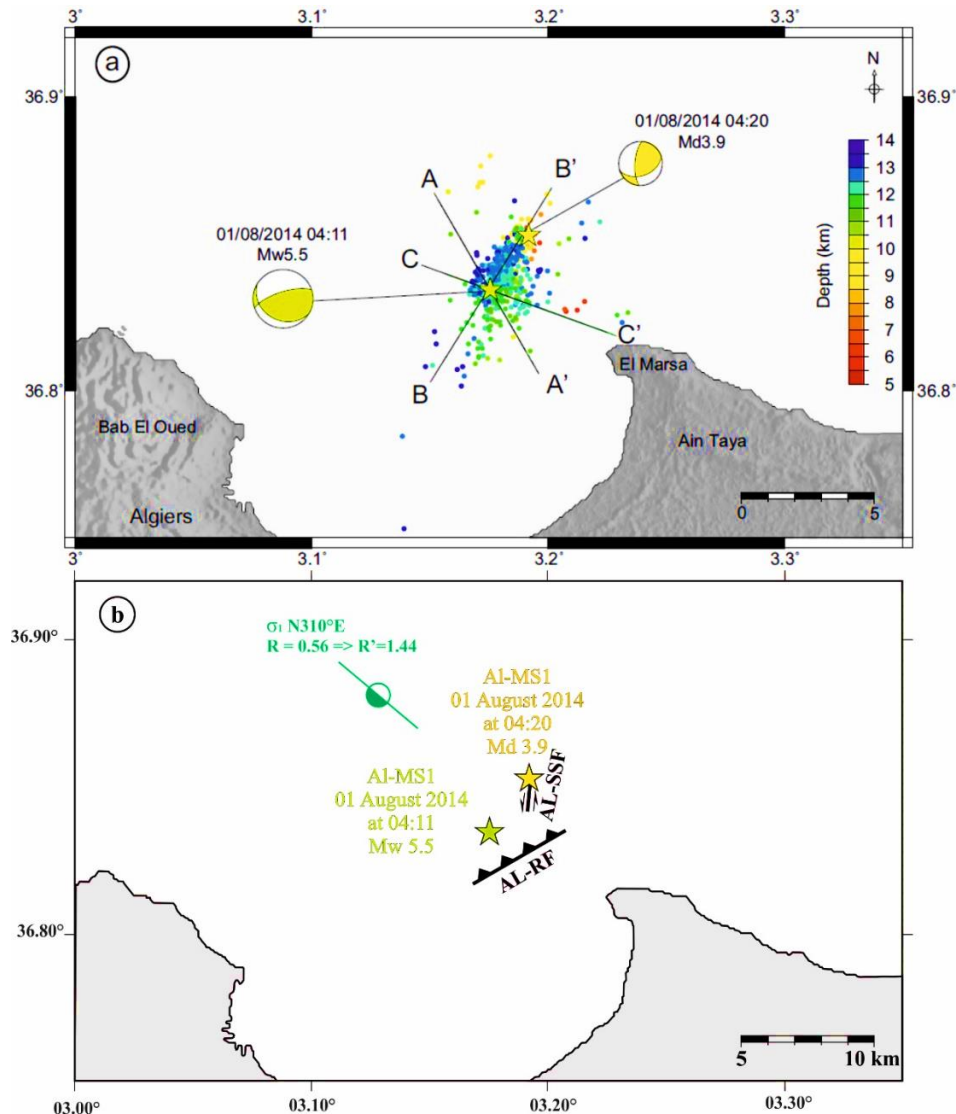
Fig. V.31: Algiers 2014 sequence analysis. **(a)** Horizontal distribution of the 576 relocated events of the 2014 Algiers seismic sequence, color shading corresponds to depth (after Yelles-Chaouche et al. (2018)). The green star marks the Mw 5.5 mainshock of August 01, 2014 at 04:11, while the yellow star represents the Md 3.9 event of August 01, 2014 at 04:20, with their respective focal mechanisms. **(b)** The two proposed fault segments are determined from the event clusters shown in (a).

Approximately 55 km west of the Hammam Meloune epicenter, a moderate earthquake (ML 5.0) struck the Oued Djer region on 2 January 2018, located 10 km southwest of the Mitidja Basin at a depth of 4 km (**Fig. V.32**). Seismological, morphotectonic, and geological analyses by Mohammedi et al. (2020) were conducted to identify the likely seismogenic structure. The focal mechanism of the mainshock, the distribution of 97 aftershocks, and geological investigation of the epicentral area all point

to a north-vergent, south-dipping reverse fault with a length of 3 km. This fault, referred to as Oued Djer Reverse Fault (OD-RF) in this thesis, is identified as part of the Djer River Fault (**Fig. V.32**), along the northeastern edge of the Boumedfaa Basin, as noted in Mohammedi et al. (2020). It has a strike of N80°E, a dip of 65°S, and displays significant right-lateral strike-slip motion (Rake = 112).
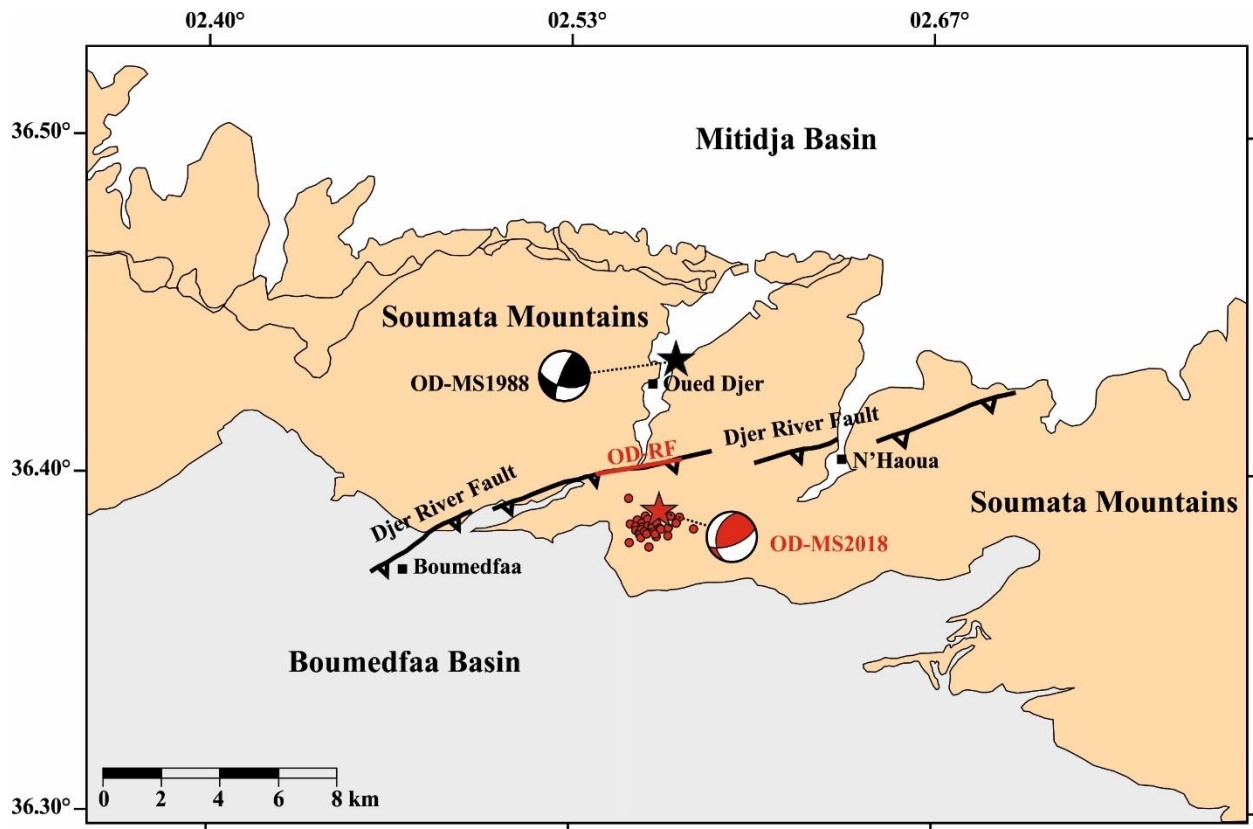
Fig. V.32: Oued Djer 2018 sequence analysis. Simplified morphotectonic map, adapted from Mohammedi et al. (2020), showing the 2018 Oued Djer mainshock (OF-MS2018) and its aftershocks, marked by a red star and red dots, respectively. The focal mechanism of the 1988 Oued Djer earthquake is also displayed. The Oued Djer Reverse Fault (OD-RF), responsible for the 2018 event, is highlighted in red, representing a segment of the larger Djer River Reverse Fault, as proposed by Mohammedi et al. (2020).

The final sequence in this zone is the Medea 2007 sequence, located along the border of the Beni-Slimane basin, between the Blida Atlas and the Bibans Mountains (**Fig. V.33**). This sequence is approximately 40 km southwest of the Hammam Meloune and Oued Djer sequences and about 85 km west of the Mihoub sequence. It began with a moderate Mw 4.4 earthquake on May 8, 2007, followed by two subsequent events on

August 21 and 22, 2007, with magnitudes of Mw 4.1 and Mw 4.6, respectively (Dabouz *et al.* 2021). These events, labeled Medea-Mainshock 1 (MD-MS1), Medea-Mainshock 2 (MD-MS2), and Medea-Mainshock 3 (MD-MS3) in **Fig. V.33**, were part of a seismic swarm consisting of 58 events recorded between August 21 and September 25, 2007; of these, 25 events met the selection criteria based on location error thresholds. According to Dabouz *et al.* (2021), MD-MS1 originated along the N62°E Bouaichoun Strike-Slip Fault (B-SSF), which spans 8 km, while MD-MS2 and MD-MS3 were attributed to the N20°E Rafsah Strike-Slip Fault (R-SSF), measuring 7 km in length. The aftershock distribution indicates that the Rafsah Fault was the primary structure reactivated during this sequence.
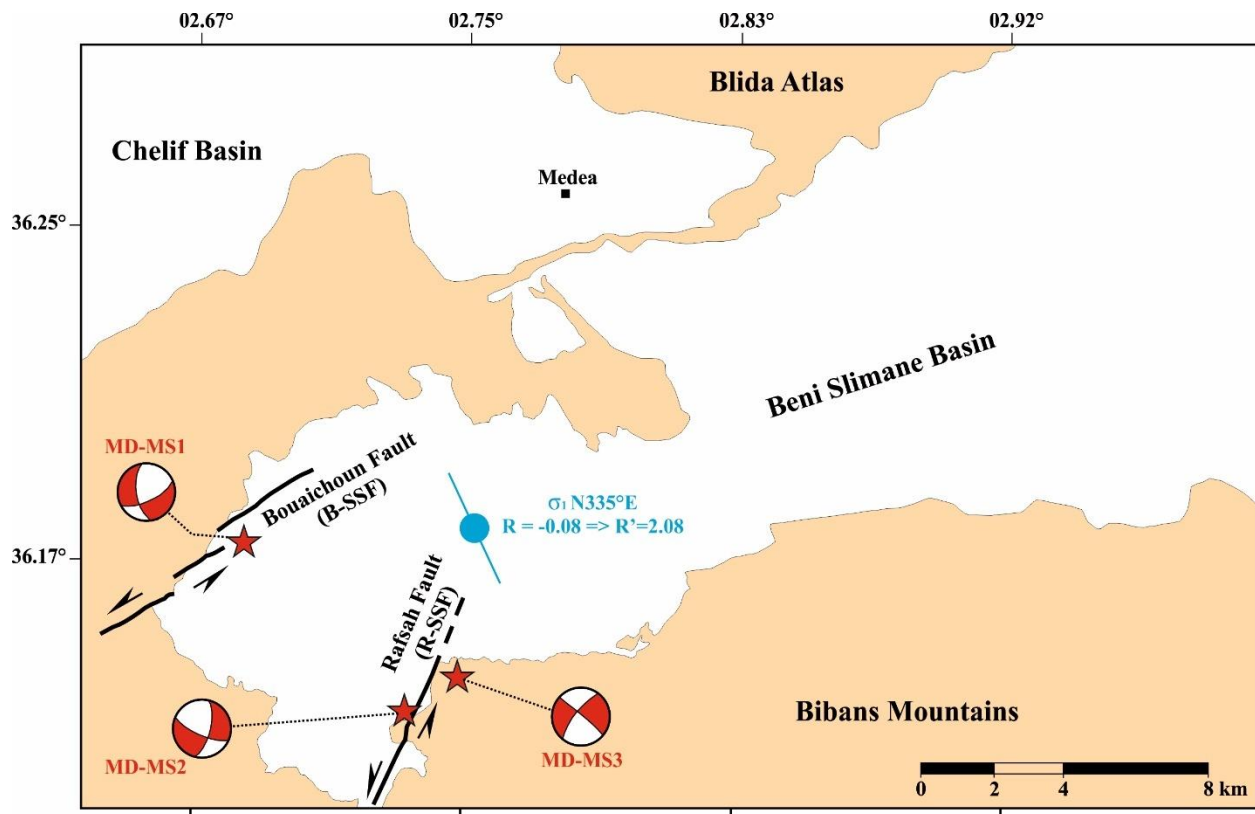
Fig. V.33: Medea 2007 sequence analysis. Simplified morphotectonic map, adapted from Dabouz *et al.* (2021), illustrating the three main shocks of the 2007 Medea earthquake sequence, along with their focal mechanisms and the two faults associated with this sequence. The stress tensor indicates a transpressional regime, with maximum horizontal stress oriented N335°E.

The occurrence of all this recent seismicity (2007-2018), combined with several previous destructive earthquakes, such as the 2003 Boumerdes earthquake (Mw 6.8) and

the 1989 Tipaza earthquake (Ml 6.0), highlights the urgent need for a continuous assessing of seismic risk in Algiers zone and its surroundings. This area includes two strategic cities—Algiers, with a population of approximately 3.5 million, and Blida, with around 1.5 million residents—as well as important industrial and military zones and significant cultural heritage sites, including the Roman city of Cherchell. This context demands highly precise analysis of seismic and tectonic activity in order to improve risk mitigation and preparedness.

NB: The following two pages are in 'A3' paper format.

V.5 A Summary of Geometric and Physical Parameters of the Analyzed Faults

Table. V.1: Recapitulation of Geometric and Physical Characteristics of Significant Seismic Events and Their Seismogenic Source Faults in Northeastern Algeria

Zone	Site	Date dd/mm/yyyy	Longitude (Degrees)	Latitude (Degrees)	Depth (km)	Max Intensity (I_0)	Number Of Aftershocks	Mw	f_c (Hz)	R (km)	$\Delta\sigma$ (MPa)	Fault Label	Total Length (km)	Aftershock Length (km)	Fault kinematics	Strike (Degrees)	Dip (Degrees)	Rake (Degrees)	Number Of Segments	PGA (%g)	PGV (m/s)	Hist Eq	σ_1 Orient	Def Reg R'	Seismic Zone (RPA24)
Hodna Mountain Range Zone	Beni-Ilmane	14/05/2010	4.1199	35.9833	05.60	VII	2885	5.4	0.75	2.58	3.23	BI-SSF2	15	6.5	SSS	178.9	079.5	023.6	2		0.038	1960	325	1.54 (SS)	Z4 (0.2g)
		16/05/2010	4.1071	35.9519	06.80			5.3	0.79	2.45	1.63	BI-TF2	15	7.7	T	289.5	050.3	131.3	2	-	0.023				
		23/05/2010	4.1232	35.9378	07.80			5.2	0.87	2.23	2.38	BI-SSF2	15	6.5	SSS	190.3	082.3	008.9	2		0.026				
	Soubella	24/02/2021	5.1700	35.7100	06.50	-	03	4.7	2.73	0.37	73.2	CH-TF	60	-	T	245.2	058.5	087.7	2	0.27 3km	0.037	1965	-	-	Z3 (0.15g)
	Ain-Azel	15/03/2015	5.7404	35.7780	08.20	VI	1008	4.7	1.08	1.49	1.83	AZ-SSFN	30	3.8	SSS	170.8	069.0	017.3	Faults Network		0.037	-	321	1.41 (SS)	Z3 (0.15g)
		18/03/2015	5.6860	35.7780	05.00			4.5	1.73	1.28	0.77			2.6	DSS	285.4	085.6	-167.9			0.012				
		21/03/2015	5.7028	35.7977	07.90			4.9	0.95	1.67	3.48			3.7	DSS	102.2	070.8	-167.8			0.120				
	Madher	10/04/2010	6.3690	35.7121	09.30	V	22	4.5	-	-	-	EM-SSF	-	8	SSS	199.5	088.0	-030.0	-	-	0.008	1924	338	1.71 (SS)	Z3 (0.15g)
		11/04/2010	6.3600	35.6986	08.10			4.3	-	-	-				SSS	213.0	081.2	-027.7			0.0037				
Babors-Bejaia-Jijel Junction Zone	Bejai-Babors	20/03/2006	5.4343	36.6046	07.70	VII	191	5.2	-	-	-	LA-SSF	05	05	DSS	-	-	-	1		-	1949 1974	359	1.36 (SS)	Z6 (0.30g)
		28/11/2012	5.1600	36.8200	11.30	VI	345	5.1	1.0	1.75	4.3	BJ-SSF	35	35	DSS	152.0	073.0	-170.0	4	-	0.02				
		22/02/2013	5.2100	36.7200	09.80	-		4.3	1.4	1.10	1.1	BJ-SSF	35	35	DSS	144.0	083.0	178.0	4		0.006				
		19/05/2013	5.2600	36.6900	10.20	-		5.2	0.9	1.89	5.9	BJ-SSF	35	35	DSS	149.0	063.0	-170.0	4		0.0084				
		26/05/2013	5.2500	36.6800	09.50	-		5.0	1.2	1.81	2.8	BJ-SSF	35	35	DSS	137.0	073.0	-168.0	4		0.0098				
	Aouana	24/01/2020	5.6320	36.6700	7.0	VI	360	5.0	1.26	1.6	3.96	EA-SSF	26	7.6	DSS	127.8	074.5	-167.9	1	-	0.013	-	358	1.52 (SS)	Z5 (0.25g)
		21/02/2020	5.6610	36.6510	7.6			4.4	1.89	1.1	1.74					126.4	068.8	175.1							
	Jijel Offshore	25/03/2014	5.5900	36.9600	9.8	-	14	4.1	3.36	0.60	6.21	JO-TF	100	-	T	075.4	054.6	090.3	3	-	0.0004	1856	356	2.86 (C)	Z5 (0.25g)
		13/07/2019	5.8100	37.1600	12	VI		5.0	1.72	1.20	7.86		100	4.0	T	075.2	032.3	098.3	3		0.005				
	Bejaia Offshore	18/03/2021	5.2175	36.8543	9.1	VII	500	6.0	0.24	8.66	0.61	BJO-TF	35	14	T	070.7	046.3	076.4	1	-	0.07	1856 1949	345	2.99 (C)	Z6 (0.30g)
		18/03/2021	5.2941	36.8464	8.2			5.1	1.14	1.79	4.00				T	070.3	042.4	076.6			0.014				
		19/03/2022	-	-	10.2			5.2	1.01	2.02	5.91				T	059.6	038.2	055.1			-				

Zone	Name	Date																							
Southern Edge of the Lesser Kabylia Block Zone	Mila	17/07/2020 / 07/08/2020 / 07/08/2020	6.3328		6.4 / 7.9 / 7.6	VII	1126	4.8 / 5.0 / 4.5	0.86 / - / -	1.08 / - / -	6.24 / - / -	BH-SSF1 / BH-SFF1 / -	4.8 / 6.9	4.8 / 6.9	DSS / SSS / SSS				1 / 2 / 2	0.18 / 0.24 / 6km	0.35 / 0.04 / 0.01		352	1.53 (SS)	Z5 (0.25g)
	Sidi Driss	04/03/2017 / 04/03/2017	6.4878 / 6.4919	36.5803 / 36.5803	11.5 / 14.2	IV	83	3.0 / 3.2	- / -	- / -	- / -	SD-SSF1 / SD-SSF1	13 / 13	3.5 / 3.5	SSS / SSS	135.0 / 125.0	089.0 / 025.0	136.0 / -176.0	5	-	-	-	345	1.59 (SS)	Z5 (0.25g)
	El Kanteur	05/03/2017 / 22/11/2020	6.7669 / 6.8006	36.5745 / 36.5471	5.8 / 9.8	V / VI	143 / 595	4.7 / 5.3	1.10 / 1.46	1.46 / 1.31	1.90 / 10.3	K-SSF1 / K-SSF2	05.0 / 3.60	1.8 / 3.60	DSS / DSS	272.0 / 107.8	074.0 / 078.7	-172.0 / -173.4	2 / 1	-	0.006 / 0.03	1985 / 1937	338	1.59 (SS)	Z5 (0.25g)
	Guelma	01/04/2021	7.2943	36.4287	8.5	V	113	4.7	1.68	1.22	2.71	G-SSF	28	27	DSS	115.0	085.5	-150.0	2	-	0.033	1937 / 2003	346	1.49 (SS)	Z5 (0.25g)
Mila-Constantine Basin Zone	Constantine	27/10/1985	6.8700	36.4600	9.0	VIII	1500	5.8	-	-	-	C-SSF	50	50	SSS	217.0	084.0	19.0	4	-	-	1908 / 1947	333	1.78 (SS)	Z5 (0.25g)
	Mila	18/12/2007	6.3196	36.3739	1.1	-	463	3.9	-	-	-	M-SSFN	11	7.5	SSS	267.9	077.2	143.4	Fault Network	-	-	-	-	-	Z5 (0.25g)
Central Tellian Atlas Zone	H. Melouane	17/07/2013 / 23/12/2014 / 10/02/2016	3.0462 / 3.0552 / 3.0611	36.4904 / 36.4862 / 36.4955	11.56 / 10.90 / 11.53	VI	154 / 304 / 94	5.0 / 4.7 / 4.5	1.46 / 1.95 / 1.53	1.41 / 1.05 / 1.34	6.60 / 5.06 / 1.12	HM-SSF	35	35	DSS / DSS / DSS	290.8 / 118.5 / 123.1	084.6 / 087.3 / 082.4	177.6 / -178.8 / 167.0	1	-	0.046 / 0.033 / 0.015	1365 / 1716 / 1989	352	1.53 (SS)	Z6 (0.30g)
	Mihoub	10/04/2016 / 28/05/2016	3.4200 / 3.4660	36.3130 / 36.3360	7.5 / 5.4	VIII	499	4.9 / 5.4	- / -	- / -	- / -	MH-SSF / MH-RF	7.5	3.8 / 3.6	DSS / R	084.0 / 049.7	090.0 / 057.3	155.0 / 131.6	2	-	-	1910	302	2.6 (C)	Z6 (0.30g)
	Algiers	01/08/2014	3.170	36.8360	10.5	VII	576	5.5	-	-	-	AL-RF	8.7	8.7	R	251.0	071.0	070.0	1	-	-	-	310	1.44 (SS)	Z6 (0.30g)
	Oued Djer	02/01/2018	2.5630	36.3830	3.0	-	160	4.9	-	-	-	OD-RF	16	2	R	070.3	063.9	112.6	3	-	0.670	1959 / 1988	-	-	Z6 (0.30g)
	Medea	08/05/2007 / 21/08/2007 / 22/08/2007	2.6800 / 2.7300 / 2.7400	36.1700 / 36.1200 / 36.1300	5.0 / 13.5 / 14.0	-	58	4.4 / 4.1 / 4.6	1.87 / 2.41 / 1.74	0.90 / 0.78 / 1.01	3.82 / 0.90 / 3.83	B-SSF / R-SSF / R-SSF	8.0 / 6.6 / 6.6	8.0 / 6.6 / 6.6	SSS / SSS / SSS	063.0 / 015.0 / 219.0	070.0 / -065.0 / 074.0	-005.0 / -018.0 / -005.0	3 / 3 / 3	-	0.32 / 0.13 / 0.43	-	335	2.08 (C)	Z6 (0.25g)

Table V.1 contains 26 columns. The headers of the first eight (08) columns are self-explanatory. Below, we explain the remaining columns:

- **Physical source parameters column:**

    A) **M_w:** Is the moment magnitude, calculated using **equation (III.20)**. The reader can infer the correspondent seismic moment value in N.m unit using the following equation: $M_0 = 10^{\frac{3}{2}*(M_w+6.03)}$

    B) *f_c:* Is the corner frequency in Hz, obtained by fitting the observed P-wave spectra to the Brune's theoretical spectra. We only considered the individual spectra approach for all the earthquakes (see **sub-chapter III.4**).

    C) *R:* Is the source radius in km. This was inferred using **equation III.21**

    D) *$\Delta\sigma$:* Represents the stress drop in MPa. We estimated it using **equation (III.24)**. Several studies (e.g Holmgren 2020) showed that stress drops can be used as proxies for the stress parameter (Δ_{par}), that is regularly used in the development of ground-motion prediction equations (GMPEs) as an additional tool to describe the high frequency earthquake source characteristics (e.g., Campbell 2003).

- **Geometric parameters column:**

    A) **Fault label:** This is an acronym we used to name faults in a uniform manner. Each fault label is constructed as follows: two or three letters from the epicentral region name, followed by '-' and the fault motion type. The letter 'F' at the end of each label stands for 'Fault.' Fault motion types include: SS for Strike-Slip, T for Thrust, and R for Reverse. In some cases, we added 'N' to indicate the presence of a fault network rather than a single well-defined fault, as in the case of Ain Azel.

B) **Total length:** Is the total mapped length of the fault that we assumed generated the main earthquake or the entire sequence (in km). This length is important because it represents the actual mapped extent of the seismotectonic structure, which could potentially rupture and cause significant earthquakes.

C) **Aftershock length:** Is the portion of the total fault length that was activated during the seismic crisis, measured in kilometers (km).

D) **Fault kinematics:** This indicates the exact motion of the assumed fault plane. SSS stands for Sinistral Strike-Slip, DSS for Dextral Strike-Slip. T for Thrust, and R for Reverse. The distinction between thrust and reverse faults based on dip angle δ is somewhat ambiguous; some geologists classify δ < 30° as thrust and δ > 30° as reverse, while others use δ < 45° for thrust and δ > 45° for reverse. Here, we adopt a threshold angle of 45°, (Brandes & Tanner 2020). We allowed a margin of error of ∓10° due to constraints in the inversion process. Additionally, we consider the seismotectonic context.

E) **Assumed fault plane:** This column is subdivided into three columns: Strike, Dip, and Rake in degrees. These parameters are the ones of the fault plane that we assumed ruptured during the sequence. in most cases based on precise hypocenters relocation and focal mechanism solutions. We basically relied on focal mechanism solutions derived from P-wave first motions and/or waveform inversion to retrieve these geometrical parameters.

F) **Number of segments:** This column indicates whether the fault is segmented. A value of '1' signifies that the fault is unsegmented, while values of more than four segments are labeled as 'Fault Network.

G) **Engineering Parameters:** In this column we provide two of the most critical parameters in earthquake engineering Peak Ground Acceleration (PGA in %g) and Peak Ground Velocity (PGV in m/s). These parameters directly inform the design and assessment of structures to withstand seismic forces. Due to the limited availability of nearby strong ground motion instruments, we were able to retrieve PGA values for only two significant events: (1) the 2021 Soubella Dam event, where we used accelerometers installed by the Agence Nationale des Barrages et Transferts (ANBT) on the dam crest, and (2) the 2020 Mila event near Beni Haroun Dam, for which we utilized the CBHR station of the ADSN. For Peak Ground Velocity (PGV) values, we prioritized data from the closest available three-component stations, where we averaged the PGV on the two horizontal components. If these were unavailable, we used appropriate short-period mono-component stations. The distances at which PGA values were estimated are detailed in **Table V.1**. Bellow in **Table V.2** we highlight the distances at which the PGVs were estimated:

Table. V.2: Station and distances at which the PGVs were estimated.

Site	Events date	Station	Distance
Beni-Ilmane	14/05/2010	ADJO (Short Period)	41.7
	16/05/2010	ADJO (Short Period)	45.2
	23/05/2010	ADJO (Short Period)	46.0
El Madher	10/04/2010	CKHR (Broad Band)	84.0
	11/04/2010	CKHR (Broad Band)	84.0
Ain-Azel	15/03/2015	CKHR (Broad Band)	33.6
	18/05/2015	CKHR (Broad Band)	30.1
	21/05/2015	CKHR (Broad Band)	29.8
Soubella	24/02/2021	CKHR (Broad Band)	46.0
Bejaia-Babors	28/11/2012	CTCH (Short Period)	62.8
	22/02/2013	CTCH (Short Period)	61.0
	19/05/2013	CTCH (Short Period)	58.0

	26/05/2013	CTCH (Short Period)	56.0
El Aouana	24/01/2020	CKHR (Broad Band)	73.0
	21/02/2020		
Jijel Offshore	25/03/2014	CASM (Broad Band)	111.0
	13/07/2019	CASM (Broad Band)	116.0
Bejaia Offshore	18/03/2021	CTCH (Short Period)	69.0
	18/03/2021	CTCH (Short Period)	73.0
Mila 2020	17/07/2020	CBHR (Short Period)	06.0
	07/08/2020	CASM (Broad Band)	32.0
	07/08/2020	CASM (Broad Band)	34.0
El Kantour	05/03/2017	CASM (Broad Band)	41.0
	22/11/2020	CASM (Broad Band)	41.0
Guelma	01/04/2021	CAEH (Broad Band)	56.0
Hammam Melouane	17/07/2013	ABZH (Broad Band)	34.0
	23/12/2014	ABZH (Broad Band)	34.0
	10/02/2016	ABZH (Broad Band)	34.6
Oued Djer	02/01/2018	ABKD (Short Period)	28.0
Medea	08/05/2007	EMHD (Broad Band)	25.0
	21/08/2007	EMHD (Broad Band)	22.0
	22/08/2007	EMHD (Broad Band)	20.0

- **Historical and Regional Context column:**

  A) **Hist Eq:** Used to indicate whether any significant historical earthquake has occurred in the region.

  B) σ_1 **Orientation:** Indicates the orientation of the maximum principal stress aligning with the main compressive force responsible for deformation.

  C) **Def Reg R':** In this column we describe the stress regime, where SS is for Strike-Slip regime and C for Compressional regime.

- **Seismic Zone RPA24:** This column presents the PGA values assigned to each site according to the new Algerian Seismic Code (RPA 2024), expressed in %g.

Table V.3 below lists the scientific resources used to compile **Table V.1.**

Table. V.3: Resources used to compile Table V.1.

Beni-Ilmane 2010 sequence	Tikhamarine *et al*. 2024 Tikhamarine *et al. in prep* This thesis
Soubella 2021 earthquake	Boulahia et al. *in prep*
Ain-Azel 2015 sequence	This thesis Unpublished work
El Madher 2010 sequence	Abacha 2015 This thesis Abacha et al. *in prep*
Bejaia-Babors 2006 sequence **Bejaia-Babors 2012-2013 sequence**	Beldjoudi *et al*. 2009 Abbes *et al*. 2019 Boulahia *et al*. 2021
El Aouana 2020 sequence	Abacha *et al*. 2023b This thesis
Bejaia Offshore 2021-2022 sequence	Yelles-Chaouche *et al*. 2024 This thesis
Jijel 2014-2019 sequence	Yelles-Chaouche *et al*. 2021
Mila 2020 sequence	Boulahia 2022 Boulahia et al. *in prep*
Sidi Dris 2017 sequence	Bendjama *et al*. 2021
El-Kantour 2017-2020	This thesis Bendjama *et al*. 2021 Bendjama *et al. in prep*
Guelma 2021 sequence	This thesis Bouadja et al. *in prep*
Constantine 1985 sequence	Bounif *et al*. 1987 Ousadou *et al*. 2012
Mila 2007 sequence	This thesis Semmane *et al*. 2012 Abacha 2015 Abacha et al. *in prep* Tikhamarine et al. *in prep*
Hammam Melouane 2013-14-16 sequence	This thesis Yelles-Chaouche *et al*. 2017 Unpublished work
Mihoub 2016 sequence	Khelif *et al*. 2018
Algiers 2014 sequence	Yelles-Chaouche *et al*. 2019
Oued Djer 2018 sequence	Mohammedi *et al*. 2020
Medea 2007 sequence	Dabouz *et al*. 2021

V.6 Seismic Hazard in Northern Algeria: Discussions

In this sub-chapter, we aim to discuss the Algerian seismic hazard in the light of findings from our study, the new RPA-2024, and findings from other researchers' studies.

In **Fig. V.34a**, we present all significant events that struck northeastern Algeria, along with their focal mechanisms. We also display the seismotectonic features identified through our seismic data analysis in this thesis, combined with findings from previous studies. These are overlaid on the seismic zoning map from RPA-2024, facilitating constructive discussion and critique. Additionally, **Table V.4** provides further details on these events, including the year of occurrence, event code as shown in **Fig. V.34a**, event location, and moment magnitude.

The first observation is that most of the seismic activity in the northeastern region consists of moderate events, with at least two main shocks generated by a series of small fault segments, each with an average length not exceeding 7 km. However, exceptions include the 1985 Constantine earthquake, the 2000 Beni Ourtilane earthquake, Boumerdes 2003 earthquake and the 2021 Bejaia earthquake, which ruptured relatively larger faults. This suggests that seismic energy is dispersed among multiple smaller segments, reducing the likelihood of a single, large earthquake. While this is reassuring, it does not entirely eliminate the possibility of a larger seismic event.

For example, the MADF raises concerns due to its significant size, despite historical records showing no seismic events exceeding magnitude ~5. The fault is characterized by frequent, low-magnitude seismicity, indicating that it consists of smaller, separate segments that cannot store large amounts of energy. Nevertheless, if multiple segments were to rupture simultaneously, a devastating event could occur, similar to what happened in the 2011 Japan earthquake for example. The 2011 Tohoku-oki earthquake demonstrated the potential for devastating events when multiple fault segments rupture simultaneously. This earthquake ruptured almost all seismic segments along Japan's Pacific coast, revealing an "along-dip double segmentation" pattern previously unrecognized (Koyama *et al.* 2012).
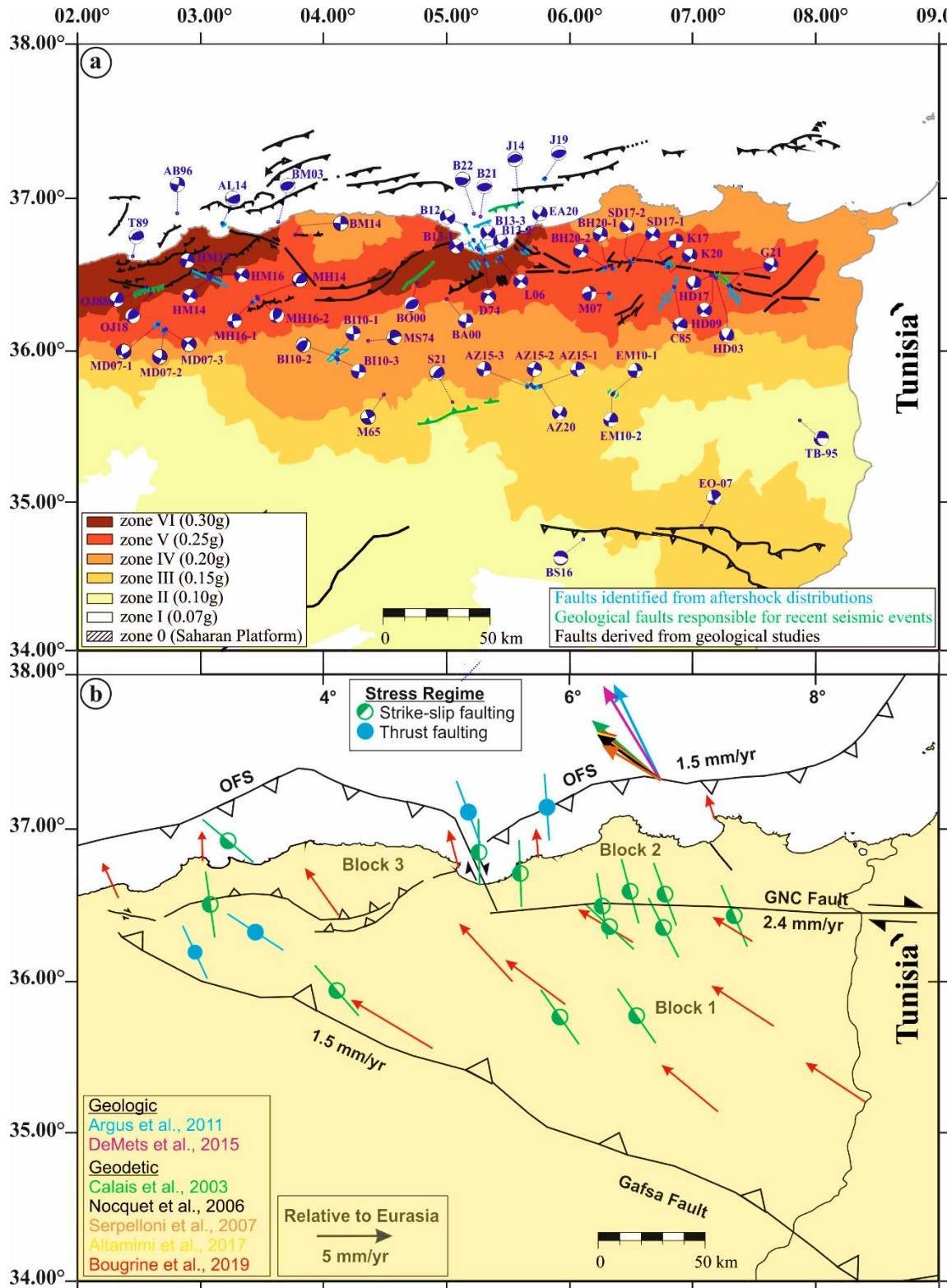
Fig. V.34: A map summarizing the seismic hazard in northeastern Algeria. **(a)** Seismic zoning map of northern Algeria (modified from RPA 2024) showing the main active tectonic structures and the focal mechanism solutions (FMS) of major seismic events.

Solid black lines indicate faults identified through geological studies, while blue lines represent faults determined from aftershock distributions. Green lines depict geological faults believed to have generated recent seismic activity. **(b)** GPS velocity field over northeastern Algeria, with red arrows indicating motion vectors based on Bougrine *et al.* (2019), overlaid on the OFS. The arrows illustrate predicted Africam-Eurasian relative velocities derived from geological and geodetic models. Stress symbols show SHmax (maximum horizontal stress) orientations

Table. V.4: List of the significant events in northeastern Algeria.

Year	Code	Seismic event	Magnitude
1965	M65	The 1965 Msila Eq	ML 5.4
1974	D74	The 1974 Darguinah Eq	ML 5.0
1974	MS74	The 1974 Mansourah Eq	ML 5.2
1985	C85	The 1985 Constantine Eq	Mw 5.8
1988	OJ88	The 1988 Oued Djer Eq	Ms 5.4
1989	T89	The 1989 Tipaza Eq	ML 6.0
1995	TB95	The 1995 Tebessa Eq	ML 5.3
1996	AB96	The 1996 Ain Benian Eq	ML 5.7
2000	BO00	The 2000 Beni-Ouathilane Eq	Mw 5.7
2000	BA00	The 2000 Bouandes Eq	ML 5.2
2003	BM03	The 2003 Boumerdes Eq	Mw 6.8
2003	HD03	The 2003 Hammam Debagh Eq	ML 4.8
2006	L06	The 2006 Lalaam Eq	Mw 5.2
2007	MD07-1	The 2007 Medea Eq sequence	Mw 4.4
	MD07-2		Mw 4.1
	MD07-3		Mw 4.6
2007	M07	The 2007 Mila seismic crisis	Mw 3.9
2007	EO07	The 2007 El Oued Eq	ML 5.2
2009	HD09	The 2009 Hammam Debbagh Eq	ML 4.8
2010	EM10-1	The 2010 El-Madher Eq sequence	Mw 4.5
	EM10-2		Mw 4.3
2010	BI10-1	The 2010 Beni-Ilmane Eq sequence	Mw 5.4
	BI10-2		Mw 5.3
	BI10-3		Mw 5.2
2012-2013	B12	The 2012-2013 Bejaia Eq sequence	Mw 5.1
	B13-1		Mw 4.3
	B13-2		Mw 5.2
	B13-3		Mw 5.0
2013-2016	HM13	The 2013-2016 Hammam Melouane Eq sequence	Mw 5.0
	HM14		Mw 4.7
	HM16		Mw 4.5
2014	J14	The 2014 Jijel Eq	Mw 4.1

2014	AL14	The 2014 Algiers Eq sequence	Mw 5.5
2014	BM14	The 2014 Bordj-Menail earthquake	Mw 4.1
2014	MH14	The 2014 Mihoub earthquake	Mw 4.3
2015	AZ15-1	The 2015 Ain Azel Eq sequence	Mw 4.7
	AZ15-2		Mw 4.5
	AZ15-3		Mw 4.9
2016	BS16	The 2016 Biskra Eq	Mw 5.3
2016	MH16-1	The 2016 Mihoub Eq sequence	Mw 4.9
	MH16-2		Mw 5.4
2017	HD17	The 2017 Hammam Debbagh Eq	ML 3.0
2017	SD17-1	The 2017 Sidi Dris Eq sequence	ML 3.0
	SD17-2		ML 3.2
2017	K17	The 2017 El Kantour Eq	Mw 4.7
2018	OJ18	The 2018 Oued Djer Eq sequence	Mw 4.9
2019	J19	The 2019 Jijel Eq	Mw 5.0
2020	EA20	The 2020 El Aouana Eq sequence	Mw 5.0
2020	AZ20	The 2020 Ain Azel Eq	Mw 5.0
2020	BH20-1	The 2020 Beni-Haroun Eq sequence	Mw 4.8
	BH20-2		Mw 5.0
2020	K20	The 2020 El Kantour Eq sequence	Mw 5.3
2021	S21	The 2021 Soubella Eq	Mw 4.7
2021	B21	The 2021 Bejaia Eq	Mw 6.0
2021	G21	The 2021 Guelma Eq	Mw 4.7
2022	B22	The 2022 Bejaia Eq	Mw 5.2

Unlike the RPA-99-2003, the latest version, RPA-2024, has evaluated a consistent seismic hazard map. For example, this version takes the probable seismic hazard of the MAD fault into serious account. This is clearly illustrated in **Fig. V.34a**, where the entire MADF is enveloped by a zone with a probable Peak Ground Acceleration (PGA) of 0.25g. This value aligns with our measurements in Mila region, see **Table V.1**.

In Mila region, specifically near the Beni Haroun Dam — Algeria's largest dam with a storage capacity of up to one billion cubic meters —, the 2020 earthquake produced an estimated ground acceleration of 0.18 and 0.24g (see **Table V.1**). Despite this relatively low magnitude of the earthquakes, the event triggered substantial landslides in Mila (Hallal *et al.* 2024), attributed to the region's agricultural soil composition (very soft). This highlights that even weak accelerations can lead to significant secondary seismic risks

like landslides. The same applies to the Constantine region, located south of the MADF. This area has historically experienced several major earthquakes, including events in 1908, 1948, and 1985 (Bounif et al., 1987), and remains vulnerable to landslides (Abacha, 2015). According to the RPA-2024, these regions fall within Zone V, reflecting an elevated seismic hazard.

We also note that the map now represents seismic hazards in the Babors region more accurately than previous seismic codes. This area periodically experiences significant earthquakes within the Bejaia-Babors Shear Zone (BBSZ) (Abacha *et al.*, 2023b) and is now classified among the highest-risk zones, with an acceleration value of 0.30g (Zone VI). This classification aligns Babors with regions like Algiers and Chellif, both of which have experienced some of the largest earthquakes in the instrumental seismological era.

On the contrary, we observe that the Hodna Range Zone spans seismic zoning zones III and IV, with a peak ground acceleration (PGA) between 0.15 and 0.20 g (**Fig. 34a**), which does not accurately reflect the significant seismic activity historically and currently recorded in the region, as previously discussed in **sub-chapter V.4.1** Many historical earthquakes have caused considerable loss of life. For instance, we estimated the acceleration from the 2021 Soubella earthquake in central Hodna at 0.27 g (see **Table V.1**), which exceeds the values assigned to zones III and IV according to RPA-2024. Although the largest recorded earthquake in this area has not surpassed magnitude 6, and the high mortality rate is primarily attributed to the fragile construction of buildings, we propose a reassessment of the zoning in this region.

Indeed, the possibility of a chain reaction along the faults running through the Hodna range should not be underestimated. Furthermore, a full rupture of the fault system, rather than isolated segments, could occur. In Beni-Ilmane, for example, the fault responsible for aftershocks was only about 7 km long (based on aftershock distribution), while geological studies and **Fig. V.6** suggest the actual extent of the fault could be as long as 16 km (**Table V.1**). Another point, the Chott El Hammam fault (ChHF), which we assumed to be the source fault of the 2021 Soubella earthquake (Mw 4.7, PGA 0.27 g), has

a total length of about 60 km, and according to Maghraoui 1988, it is capable of generating an earthquake of approximately Mw 7.0. This potential for larger earthquakes necessitates a reconsideration of the seismic zoning to more accurately reflect the seismic hazard in the Hodna Range Zone.

A final important observation regarding the RPA-2024 concerns the Tizi Ouzou basin, now classified as Zone IV with an acceleration value of 0.20g. This region represents a notable seismic gap between two areas previously impacted by major earthquakes: the Mw 6.8 Boumerdes earthquake in 2003 (Delouis *et al.* (2004); Semmane *et al.* (2005)) to the west, and the Mw 6.0 Bejaia earthquake in 2021 (Yelles-Chaouche *et al.*, 2024) to the east—both classified as Zone VI with 0.3g. Aside from a small 2012 swarm of six events near Azzaffoun village in the offshore area (Rahmani et al., *in prep*), there have been no other significant events in this region. It is important to note that this region contains key tectonic structures (see **Fig. V.34**) that accommodate an average deformation rate of 1.5 mm/year, suggesting that this swarm could be a precursor to a larger, potentially destructive earthquake. This assessment aligns with insights from the 2011 Tohoku-Oki earthquake, underscoring that interseismically locked areas are likely sources of future significant earthquakes (Uchida & Bürgmann 2021). A similar observation applies to the region extending from Jijel to Annaba and the northwestern part of the country.

In **Fig. V.34b**, we have compiled several key datasets to enhance our understanding of the region's tectonic activity. These include:

1. The GPS velocity field estimated from various Algerian GPS stations as part of the REGAT Network (REseau GPS de l'ATlas), represented by red arrows (Bougrine *et al.*, 2019).

2. Predicted African-Eurasian (AF-EU) velocities along the OFS (Offshore Fault System), based on geological and geodetic models, illustrated by directional arrows (References are depicted inside the figure).

3. The SHmax orientations derived from this study, as well as from previous analyses of significant seismic events.

This integration of GPS data and stress orientations offers a comprehensive view of the dynamic interactions between tectonic forces in northern Algeria, contributing to a more detailed understanding of the region's seismicity and geodynamics.

From **Fig. V.34b**, we observe that the borders of the LKB (Block 2), located between the MAD Fault zone and the offshore fault systems (OFS), exhibit a distinct clockwise rotation of both the stress and velocity fields compared to the adjacent regions (Blocks 1 and 3), which generally follow the AF-EU orientation. The reorientation of the stress increases as we move northward, reaching a maximum near a N–S orientation in the coastal areas such as Bejaia, El Aouana, and Jijel. This reorientation is also noticeable, though to a lesser degree, along the MAD Fault in regions like Sidi Dris, El Kantour, Hammam Debbagh, and Mila, eventually transitioning to a NW-SE orientation in Block 1, which lies between the Aures Range and the MAD Fault. The N–S-oriented maximum horizontal stress and the velocity field directions in Block 2 reflect two key tectonic influences: (1) The NW–SE oblique convergence of the African and Eurasian plates, which governs the overall stress regime in the region. (2) The E–W strike-slip movement of the MAD Fault, which contributes to the complex stress distribution and rotational patterns observed in the area. These findings have already been discussed in (Bendjama *et al*., 2021; Yelles-Chaouche *et al*., 2021; 2024; Boulahia *et al*., 2021; Abacha *et al*., 2023b).

The N–S orientation and clockwise rotation of SHmax along the E–W strike-slip MAD fault zone is comparable to other major plate boundary strike-slip faults such as the San Andreas Fault (Hickman *et al.* 2004), the Alpine Fault of New Zealand (Rajabi 2016), the Great Sumatra Fault (Mount & Suppe 1992), and the Saharan–Tunisian Atlas domain (Soumaya *et al*., 2018). These similarities may suggest that the MAD fault zone has weak physical properties, as noted in other large-scale strike-slip fault systems (Soumaya *et al*., 2018). This last study also emphasized that the present-day active convergence of northeastern Algeria is primarily accommodated by two active fault systems: (1) The E–W strike-slip MAD fault zone in the Eastern Tell region, and (2) the intra-plate active strike-slip fault system in the Saharan–Tunisian Atlas (South Atlas Flexure-SAF in Algeria **Fig. V.5**). However, despite these broad fault system

identifications, the segmentation of the major structures within these fault zones remains poorly defined, except for a few minor segments that have been mapped. This lack of detailed segmentation presents challenges for fully understanding the seismic hazard posed by these faults.

The NNW–SSE to N–S orientation of maximum stress compression promotes fracturing along transversely oriented faults, resulting in distinct fault movements: **NNE–SSW left-lateral**, **NNW–SSE right-lateral**, and on a smaller scale, **WNW–ESE right-lateral faults**.

Examples of these active structures include:

- The **NE–SW-trending left-lateral strike-slip faults**, such as the **Ain Smara Fault** (in the Mila–Constantine Basin zone), the **Sidi Dris Fault** (in the MAD Fault zone), and the **Beni–Ilmane segment** (in the Hodna Range zone).

- The **NW–SE right-lateral strike-slip faults**, like the **BTF and Lalaam Fault** (in the Babors zone) and the **HDF** (in the MAD Fault zone).

- The **~E–W right-lateral strike-slip faults**, exemplified by the **El Kantour segment** of the **MAD Fault zone,** and the **Beni–Ilmane segment**.

In northwestern Algeria, the SHmax orientation appears more homogeneous compared to eastern Algeria. The active faulting and seismicity are primarily concentrated within a narrow coastal strip (50–100 km wide) that exhibits a compressive stress regime. A NW–SE SHmax orientation, aligned with the African-Eurasian (AF-EU) global convergence, has been calculated in several regions (Beldjoudi *et al.* (2012); Ousadou *et al.* (2014)), with the main compressional stress axis (σ_1) oriented between N325E and N300E. A comparison between the mean SHmax orientation and the relative plate motion direction of the African and Eurasian plates confirms the homogeneous stress distribution in this part of Algeria, as highlighted by Soumaya *et al.* (2018). This suggests that western Algeria's tectonic behavior is more consistently controlled by plate convergence, leading to a more uniform stress regime across the region.

Numerous studies have investigated the regional-scale stress state of the Maghreb region, including works by Buforn *et al.* (2004), Serpelloni *et al.* (2007), Ousadou *et al.*

(2014), and Soumaya *et al*. (2018). These studies have identified a compressive stress regime in western Algeria, while a strike-slip regime is observed in eastern Algeria and the Moroccan Rif. The variation in these stress regimes has been linked to the free-edge effect associated with the Ionian slab subduction in the eastern Maghreb, as well as the tectono-dynamics of the Alboran Sea influencing the western Maghreb region.

V.7 Conclusion

This chapter serves as a basic reference, being the first to compile the most significant seismogenic fault sources in northeastern Algeria and their characteristic parameters, based on a comprehensive analysis of available seismic data. This includes both seismic sequences and isolated events, using a robust methodology based on precise event relocation through cross-correlation techniques. The seismological analysis enabled the determination of essential physical parameters, such as seismic moment, stress drop and corner frequency among others. Additionally, key engineering parameters, including Peak Ground Acceleration and Velocity (PGA and PGV), were assessed.

The seismic sequences were categorized into four zones based on geological and geomorphological compatibility. Our detailed study identified various tectonic models, ranging from simple one- or two-segment structures to complex fault networks, as seen in the BI-2010, AZ-2015, and 2007 Mila sequences, as well as off-fault triggered swarms following the 2020 El-Kantour earthquake. Identifying such complex tectonic networks required an in-depth analysis using earthquake multiplets groups and their geometries— a method applied for the first time to Algerian sequences.

This chapter also addressed seismicity migration, highlighting pore-pressure diffusion as the main triggering mechanism in areas such as the BI-2010, AZ-2015 and 2007 Mila sequences. Lastly, all geometric, physical, and engineering parameters have been compiled into a single table, offering a valuable reference for researchers and engineers studying seismic risk in northeastern Algeria.

Moreover, the chapter integrated valuable information regarding neotectonic faults that, while not producing earthquakes in the instrumental period, remain active according to geological studies. These findings highlight the ongoing tectonic activity and potential risks in the region. The gathered data and analysis were critically compared with the latest Algerian Paraseismic Codes (RPA-2024), providing a meaningful contribution toward refining seismic hazard assessments in this part of the country. We have identified certain areas that we believe are underestimated in the RPA-2024 seismic zoning, such as the Hodna Mountains region, along with two notable seismic gaps in the northern parts of both the Lesser Kabylia Block (LKB) and the Greater Kabylia Block (GKB).

The chapter concludes with a broader discussion of seismic hazard in northern Algeria in light of RPA-2024. Additionally, it integrates an overview of stress and velocity field variations and their reorientation within northern Algeria, linking geodynamical processes to the observed tectonic deformation and seismicity.

This work has been developed to serve as an accessible reference for researchers, engineers, and students involved in seismic hazard assessment in northeastern Algeria.

General Conclusion

This thesis offers a comprehensive analysis of active faults, earthquake source parameters, and the driving mechanisms of recent seismic sequences in northeastern Algeria, with a particular emphasis on the Beni-Ilmane (BI-2010) sequence. By integrating data from diverse sources and employing advanced analyzing techniques, this research contributed to enhance our understanding of seismic hazards in the region. The findings are supported by scientific credibility, as they have been published in peer-reviewed journals (Tikhamarine *et al.*, 2024; Tikhamarine *et al.*, in prep). Additionally, other relevant scientific contributions made during the preparation of this thesis further reinforce the results and conclusions presented (Abacha *et al.*, 2023a; Abacha *et al.*, 2023b; Yelles-Chaouche *et al.*, 2024; Roubeche *et al.*, 2024).

Through this thesis we revealed several key conclusions regarding seismicity analysis and the seismic hazards in northeastern Algeria. Bellow we present our key findings and conclusion:

- **Ambiguities in multiplet and repeating earthquake definitions:** During my researches, I have observed that up to date there is no universally accepted definition for either term (multiplet and repeating earthquakes) within the seismological community. Researchers such as Kapetanidis *et al.* (2015), Lengliné *et al.* (2014), Schmittbuhl *et al.* (2016), and Staszek *et al.* (2021) have used these terms interchangeably, while Gao et al. (2021), Uchida 2019, and Uchida & Bürgmann (2019) have focused exclusively on "repeating earthquakes." Massin et al. (2013) distinguished "multiplets" as groups of similar seismic events and "repeating earthquakes" as events within a multiplet occurring within a specific time or area. Shaddox et al. (2021) introduced "near-repeating earthquakes" for events that are closely spaced or partially overlapping. There is a need for unified definitions to reduce ambiguities and uncertainties. First step towards setting uniform definitions has been initiated by Gao et al. (2023) where they proposed criteria for identifying repeating earthquakes, including a magnitude difference

of no more than 0.3 and an inter-event distance ≤ 80% of the rupture area of the larger event, but did not address the CC/Coh threshold, leaving their definition potentially not well constrained.

- **New minimum 1D velocity model for Beni-Ilmane region:** We have developed a new minimum 1D velocity model for the Beni-Ilmane region using very dense seismic rays from the BI-2010 sequence. This model has been retrieved through comprehensive use of VELEST program. Our retrieved model remarkably minimized the RMS values, indicating that the new 1D model provides a better fit to the observed and computed travel times compared to the previous models in the regions (Yelles-Chaouche et al. 2014 and Abacha et al. 2014). We assume that our model can also be used for the surrounding regions of Beni-Ilmane.

- **The role of location and relocation uncertainties estimation in describing results credibility:** We have assessed location and relocation uncertainties using Monte-Carlo and Bootstrapping approaches. We observed that performing high precision relocation tend to remarkably reduce location uncertainties leading to more precise fault structure determination based on the aftershock distribution.

- **Time domain cross-correlation performs better than frequency domain coherency in determining waveform similarity and time delays:** Our observations indicate that CC values are better reflecting waveform similarity than Coh values. Additionally, Kapetanidis et al. (2010) also found that Coh values are prone to faster saturation than their corresponding CC values. Moreover, studies by Schaff et al. (2004) highlighted that using the time domain CC is often more robust and recovers more observations than the cross-spectral approach. For this reason, we preferred to use time-domain cross-correlation.

- **Earthquake multiplet analysis is a powerful tool to decipher complex fault geometries:** Based on multiplet geometry analysis we revealed a complex fault network that highlighted the activation of fourteen (14) fault segments within an intricate fault system contrary to previously proposed simplified seismotectonic model suggested by (Yelles-Cahouche et al. 2014; Beldjoudi et al., 2016).

General Conclusion

- **Suggestion of conceptual model highlighting the critical role of strike-slip faults in Beni-Ilmane region:** We have constructed a conceptual model that delves into the historical development of the fault system. While this approach extends beyond the immediate results of the study, it is a logical progression grounded in the newfound understanding of the complex fault system, notably the role of the dominant strike-slip faults in reshaping the thrust belt in the region.

- **The importance of convenient EGF candidate selection:** An accurately chosen Empirical Green's Function (EGF) ensures that the deconvolution process reliably reflects the source properties of a larger earthquake, minimizing artifacts or errors. In contrast, an inappropriate EGF can lead to significant misinterpretations, such as incorrect estimates of stress drop or rupture dimensions. Therefore, selecting the right EGF is critical for obtaining accurate insights into earthquake source dynamics. We developed a program that takes the catalog as an input file and, for each event, iteratively verify the following criteria against all the other events in the catalog. The selection procedure adheres to the following conditions: 1) For mainshocks (MS-1, MS-2, or MS-3), the maximum epicentral and hypocentral separations are set to 2 km. 2) For aftershocks, the maximum epicentral and hypocentral separations are set to 1 km. 3) The magnitude difference should be >1 and ≤4 for mainshocks and aftershocks.

- **The EGF approach generally tends to produce higher source parameters estimates compared to the individual spectra approach:** We have calculated an average 1.72 Hz of difference in corner frequency and 2.4 Mpa of difference in stress drop. The differences in results between the two methods can be attributed to the trade-offs involved in the analysis. In individual spectral analysis, the observed seismic spectra are affected by various factors, including path effects (e.g., seismic wave attenuation as it travels from the source to the receiver) and site effects (e.g., local geological conditions at the recording station). Conversely, the EGF approach can mitigate the effect of these factors through empirical

corrections. Our observations here, are consistent with several studies (e.g., Ide *et al.* 2003).

- **No breakdown in self-similarity in Beni-Ilmane region**: Contrary to the findings of Abacha *et al.* (2019), that observed a deviation from the theoretical relationship between seismic moment M_0 and source radius (R) ($M_0 \propto R^3$). Our calculated parameters reveal no breakdown in self-similarity. We assume that the deviation from the self-similarity relation observed by Abacha *et al.* (2019) is likely related to their model for correcting attenuation. It is well-known that attenuation significantly affects the estimation of corner frequency, which in turn impacts the source radius. Additionally, some of their M_0 values may have been underestimated, potentially biasing the M_0-R relationship.

- **Mw-ML conversion relationship in Beni-Ilmane region is consistent with regional conversion relationships:** We have retrieved an Mw-ML conversion relationship as Mw = 0.8*ML+0.83 with an R-squared value of 0.8535, indicating a precision of 85.35%. Additionally, we calculated a standard deviation of 0.211 between the observed Mw values and the calculated ones using the retrieved relationship. Similar works have been conducted by Bellalem *et al.* (2022) and Roubeche *et al.* (2024), but with regional data from the CRAAG catalog. They revealed relationships of Mw = 0.762*ML+1.024 and Mw = 0.8046*ML + 1.0203 respectively. Both relations fall within ± 2std of our findings, reflecting consistency between these three studies.

- **Scaling relationships of M_0-R and M_0-f_c consistent with theoretical expectations:** Using our calculated source parameters whether using EGF approach or individual approach, we found $M_0 \propto R^{(3+\alpha)}$ and $M_0 \propto f_c^{(-3-\alpha)}$ where $0 < |\alpha| < 1$ which falls well withing the theoretical expectation.

- **Tectonic loading effect on Beni-Ilmane region:** Our stress inversion results revealed a sub-vertical orientation for σ_2 (plunge 88°/azimuth N221°E), and sub-horizontal orientations for σ_1 (0°/N325°E) and σ_3 (02°/N55°E). This analysis indicates a strike-slip tectonic regime with R'=1.54 ± 0.37. These results suggest a

predominant NW-SE oriented maximum horizontal compression with an average SHmax value of N145°E ± 11.8°, consistent with the regional compressional trend of NU-EU plate conversion estimated by Bougrine *et al.* (2019).

- **Stress transfer is not sufficient to explain the observed seismicity in the BI-2010 sequence:** We emphasized that stress transfer alone, as mentioned by Beldjoudi *et al.* (2016), cannot fully explain the occurrence of the three mainshocks, nor the aftershock activity, including the presence of earthquake multiplets and repeating earthquakes.

- **Extra evidences of fluid involvement from other methods:** Fluid involvement in Beni-Ilmane region has been initially highlighted by tomographic studies (Abacha *et al.* 2014), then further investigation by Abacha *et al.* 2023a highlighted increased pore pressure after MS-3. Rahmani *et al.* 2023 through statistical analysis confirmed Abacha's *et al.* 2023a findings. In our study we presented additional evidences 1) Moment tensor decomposition revealed relatively high CLVD components especially for MS-3 indicative of shear-tensile faulting probably due to fluid infiltration along the fault plane. 2) Stress drop variation, we observed that relatively low stress drop variation were observed after MS-3, indicative of fluid presence as mentioned by several studies. 3) The existence of several earthquake multiplet groups that have been activated during the sequence, is also a proxy of fluid involvement.

- **Temporal evolution of multiplet activation provide insights on fluid involvement history**: Through our analysis of temporal behavior of multiplet, we observed some intriguing remarks: 1) Absence of multiplet groups after MS-1: Indicates no fluid intrusion occurred after MS-1. 2)Activation of multiplet groups immediately after MS-2: reflects that fluid infiltration began just after MS-2. 3)Increased rate of multiplet activation after MS-3: suggests that circulating fluid volume had increased, leading to a rise in pore pressure. This provide new insights about the origin of fluid infiltrations, which we assume is MS-2, and

confirms the observation of increased seismicity after MS-3 due to an increased pore pressure.

- **Seismicity migration points to aseismic slip:** We observed a clear expansion of the aftershock area from the rupture edge as a function of the logarithm of time. This observation suggests that the primary driver of the observed migration is the aseismic afterslip process (Kato 2007). Conversely, a diffusivity coefficients of 0.36 m²/s and 0.32 m²/s suggest the involvement of fluid diffusion. Since aseismic afterslip and fluid diffusion are related mechanisms, we believe that the seismicity migration in BI-2010 is driven by fluid-induced aseismic slip.

- **Repeating Earthquakes: confirm aseismic slip during BI-2010 sequence:** We have revealed that 12 fault patch experienced repeated ruptures at least two times within relatively short and irregular time interval. This behavior is characteristic of burst-type repeating earthquakes. These repeaters are a good proxy of aseismic slip mechanism.

- **Imbricated driving forces behind BI-2010 seismic sequence:** The BI-2010 seismic activity is driven by a complex interplay of multiple factors. Tectonic loading, influenced by regional forces and static stress transfer (Beldjoudi. 2020), plays a significant role, alongside fluid dynamics (Abacha et al., 2014, 2023a; Rahmani et al. 2023). A key discovery in this research is the significant involvement of aseismic slip transients, which further contribute to the seismic behavior. This multifaceted driving mechanism—comprising tectonic forces, static stress, fluid dynamics, and aseismic slip—reflects the intricate nature of the BI-2010 sequence, aligning with observations from De Barros et al. (2019), Kaviris et al. (2021), Miller (2020), and Ross et al. (2017).

- **The Hodna mountain range is experiencing a continuous seismic activity:** The occurrence of these four recent seismic events—BI-2010, AZ-2015, Soubella 2021, and El Madher 2010—together with significant historical events illustrated in **Fig. V.12**, prompts investigation into their potential interconnection via static stress transfer along the Hodna range.

General Conclusion

- **The Bejaia-Baobors region is characterized by an active shear-zone:** An integrated analysis of newly identified faults (BJ-SSF (BTF), TDF, EA-SSF), along with nearby active faults and geological data, has revealed an active shear zone known as the Bejaia-Babors Shear Zone (BBSZ) (Abacha *et al.*, 2023b).

- **Seismic activity continues along the Mcid Aicha Debbagh Fault:** The El Kantour 2020 seismic sequence provides new evidence of ongoing seismic activity along the MADF, following the unusual activity observed in 2017 (Bendjama *et al.*, 2021).

- **The anthropogenic swarm of Mila 2007 triggrred a complicated fault network:** Earthquake multiplet analysis revealed that this swarm activated a network of intersecting fault segments, rather than a single fault.

- **The Hammam Melouane sequences of 2013, 2014, and 2016 likely resulted from the activation of a single fault (HM-SSF):** The focal mechanisms of the three mainshocks, the spatial distribution of precisely located events, and the proximity of the sequences all suggest repeated activation of the same fault over these three years.

- **Local and regional stress fields in NE Algeria prompt specific fault ruptures:** Faults in northeastern Algeria typically rupture along distinct orientations: NNE–SSW left-lateral faults (e.g., ASF, SD-SSF, BI-SSF1, BH-SSF2), NNW–SSE right-lateral faults (e.g., structures in the BBSZ, HDF, G-SSF, BH-SSF1, HM-SSF), WNW–ESE right-lateral faults (e.g., K-SSF1, K-SSF2), and approximately E–W thrust faults (e.g., BI-TF1, OJ-RF, BJO-TF, JO-TF). These fault orientations align with the Riedel shear model, highlighting a well-organized faulting pattern that reflects the underlying stress regime in the region.

- **The rupture of smaller fault segments in NE Algeria may reduce the overall seismic hazard in the region:** While large faults like the MAD Fault exist in northeastern Algeria, much of the region's seismicity is driven by earthquake sequences and swarms involving multiple moderate mainshocks, typically generated by smaller fault segments or complex fault networks. This unique seismic behavior contributes to a relatively lower overall seismic hazard in the

eastern region, making it less prone to large event ruptures compared to the western region of Algeria, which is characterized by a more homogeneous and potentially more hazardous tectonic domain.

- **The recently released Algerian seismic code (RPA 2024) shows significant improvement in seismic zoning compared to previous versions:** Unlike the RPA-99-2003, the latest version, RPA-2024, presents a more consistent seismic hazard map. For instance, this updated code gives serious consideration to the seismic hazard posed by the MAD fault. As clearly illustrated in **Fig. V.31a**, the entire MAD Fault is encompassed by a zone with a probable Peak Ground Acceleration (PGA) of 0.25g, a value that aligns with our measurements in the Mila region.

- **Contributions to improved seismic hazard assessment in NE Algeria:** This thesis provides a comprehensive summary of the geometric, physical, and engineering characteristics of significant seismic events in a single table (**Table V.1**). It also includes a map (**Fig. V.34**) that outlines the seismic zoning of northeastern Algeria (from RPA 2024), highlighting key active tectonic structures, focal mechanism solutions (FMS) of major seismic events, recent seismic activity, the GPS velocity field, and SHmax orientations. This compilation serves as an important and easily accessible reference for researchers, engineers, and students engaged in seismic hazard assessment in the region.

- **Constructive Criticism of RPA2024:** The data and findings presented in this work were critically compared with the latest Algerian seismic code (RPA2024), highlighting specific areas where the current seismic zoning may be underestimated. By identifying these discrepancies, this study provides valuable insights for refining seismic hazard assessments in the region, ultimately improving the accuracy and effectiveness of future seismic risk management strategies in Algeria. Additionally, it is essential to consider areas that may be prone to future devastating earthquakes, rather than focusing solely on regions with past seismic activity. Adopting this proactive approach will better assess and

General Conclusion

mitigate seismic risks in areas that, while not yet affected by significant earthquakes, remain vulnerable due to their seismotectonic context.

The outcomes of this thesis represent a well-grounded contribution to enhancing seismic hazard assessment strategies in northeastern Algeria. By providing a detailed analysis of active fault structures, earthquake source parameters, and the driving mechanisms behind recent seismic sequences. This research offers valuable insights into the region's seismic behavior. The integration of high-resolution imaging, advanced analytical techniques, and the identification of key factors such as aseismic slip and fluid dynamics enriches the understanding of seismic hazards in the area. These findings can be utilized to refine seismic hazard models, improve risk mitigations, and inform the development of more effective mitigation strategies, ultimately contributing to the protection of communities and infrastructure in this seismically active region.

References

References

Abacha, I., 2015. *Étude de la sismicité de la région nord-est de l'Algérie*.

Abacha, I., Bendjama, H., Boulahia, O., Yelles-Chaouche, A., Roubeche, K., Rahmani, S.T.-E., Melaim, M.A., *et al.*, 2023. Fluid-driven processes triggering the 2010 Beni-Ilmane earthquake sequence (Algeria): evidence from local earthquake tomography and 4D Vp/Vs models. *Journal of Seismology*, **27**, 77–94. doi:10.1007/s10950-022-10130-8

Abacha, I., Boulahia, O., Yelles-Chaouche, A., Bendjama, H., Fossen, H., Chabou, M.C., Roubeche, K., *et al.*, 2023. The 24 January 2020 Mw 5.0 El Aouana Earthquake, Northeastern Algeria: Insights into a New NW–SE Right-Lateral Bejaia-Babors Shear Zone. *Pure and Applied Geophysics*, **180**, 1945–1971. doi:10.1007/s00024-023-03265-3

Abacha, I., Boulahia, O., Yelles-Chaouche, A., Semmane, F., Beldjoudi, H. & Bendjama, H., 2019. The 2010 Beni-Ilmane, Algeria, earthquake sequence: statistical analysis, source parameters, and scaling relationships. *Journal of Seismology*, **23**, 181–193. doi:10.1007/s10950-018-9800-7

Abacha, I., Koulakov, I., Semmane, F. & Yelles-Chaouche, A.K., 2014. Seismic tomography of the area of the 2010 Beni-Ilmane earthquake sequence, north-central Algeria. *SpringerPlus*, **3**, 650. doi:10.1186/2193-1801-3-650

Abacha, I. & Yelles-Chaouche, A., 2019. Overview of Recent Seismic Activity in Northeastern Algeria: Trends and Applications in Science and Engineering, pp. 203–206. doi:10.1007/978-3-030-01656-2_46

Abacha, I., Yelles-Chaouche, A. & Boulahia, O., 2022. Statistical Study of Earthquake Swarms in Northeastern Algeria with Special Reference to the Ain Azel Swarm; Hodna Chain, 2015, pp. 145–148. doi:10.1007/978-3-030-73026-0_34

Abbes, K., Dorbath, C., Dorbath, L., Bouhadad, Y., Ousadou, F. & Bezzeghoud, M., 2019. Revisiting the Laalam (Eastern Algeria) March 20, 2006 (Mw 5.1) Earthquake and its Seismotectonic Implication. *Pure and Applied Geophysics*, **176**, 4213–4222. doi:10.1007/s00024-019-02206-3

Abercrombie, R. & Leary, P., 1993. Source parameters of small earthquakes recorded at 2.5 km depth, Cajon Pass, southern California: Implications for earthquake scaling. *Geophysical Research Letters*, **20**, 1511–1514, John Wiley & Sons, Ltd. doi:10.1029/93GL00367

Abercrombie, R.E., 1995. Earthquake source scaling relationships from −1 to 5 ML using seismograms recorded at 2.5-km depth. *Journal of Geophysical Research: Solid Earth*, **100**, 24015–24036, John Wiley & Sons, Ltd. doi:10.1029/95JB02397

Abercrombie, R.E., 2015. Investigating uncertainties in empirical Green's function analysis of earthquake source parameters. *Journal of Geophysical Research: Solid Earth*, **120**, 4263–4277, John Wiley & Sons, Ltd. doi:10.1002/2015JB011984

Abercrombie, R.E. & Rice, J.R., 2005. Can observations of earthquake scaling constrain slip weakening? *Geophysical Journal International*, **162**, 406–424. doi:10.1111/j.1365-246X.2005.02579.x

Aïdi, C., Beslier, M.-O., Yelles-Chaouche, A.K., Klingelhoefer, F., Bracene, R., Galve, A., Bounif, A., *et al.*, 2018. Deep structure of the continental margin and basin off Greater Kabylia, Algeria – New insights from wide-angle seismic data modeling and multichannel seismic interpretation. *Tectonophysics*, **728–729**, 1–22. doi:10.1016/j.tecto.2018.01.007

Akande, W., Gan, Q., Cornwell, D. & De Siena, L., 2021. Thermo-Hydro-Mechanical Model and Caprock Deformation Explain the Onset of an Ongoing Seismo-Volcanic Unrest. *Journal of Geophysical Research: Solid Earth*, **126**. doi:10.1029/2020JB020449

Aki, K., 1967. Scaling law of seismic spectrum. *Journal of Geophysical Research (1896-1977)*, **72**, 1217–1231, John Wiley & Sons, Ltd. doi:10.1029/JZ072i004p01217

References

Aki, K., 1984. Asperities, barriers, characteristic earthquakes and strong motion prediction. *Journal of Geophysical Research: Solid Earth*, **89**, 5867–5872, John Wiley & Sons, Ltd. doi:10.1029/JB089iB07p05867

Aki, K. & Richards, P.G., 1980. Quantitative Seismology: Theory and Methods. Retrieved from https://api.semanticscholar.org/CorpusID:58794764

Aoudia, A., Vaccari, F. & Suhadolc, P., 2000. Seismogenic potential and earthquake hazard assessment in the Tell Atlas of Algeria. *Journal of Seismology*, **4**, 79–98. doi:10.1023/A:1009848714019

Arab, M., Rabineau, M., Déverchère, J., Bracene, R., Belhai, D., Roure, F., Marok, A., *et al.*, 2016. Tectonostratigraphic evolution of the eastern Algerian margin and basin from seismic data and onshore-offshore correlation. *Marine and Petroleum Geology*, **77**, 1355–1375. doi:10.1016/j.marpetgeo.2016.08.021

Archuleta, R.J., Cranswick, E., Mueller, C. & Spudich, P., 1982. Source parameters of the 1980 Mammoth Lakes, California, earthquake sequence. *Journal of Geophysical Research: Solid Earth*, **87**, 4595–4607, John Wiley & Sons, Ltd. doi:10.1029/JB087iB06p04595

Ayadi, A. & Bezzeghoud, M., 2015. Seismicity of Algeria from 1365 to 2013: Maximum Observed Intensity Map (MOI2014). *Seismological Research Letters*, **86**, 236–244. doi:10.1785/0220140075

B. Efron, 1979. Bootstrap Methods: Another Look at the Jackknife. *The Annals of Statistics*, **7**, 1–26. doi:10.1214/aos/1176344552

Bahrouni, N., Bouaziz, S., Soumaya, A., Ben Ayed, N., Attafi, K., Houla, Y., El Ghali, A., *et al.*, 2014. Neotectonic and seismotectonic investigation of seismically active regions in Tunisia: A multidisciplinary approach. *Journal of Seismology*, **18**. doi:10.1007/s10950-013-9395-y

Baker, J., Bradley, B. & Stafford, P., 2021. *Seismic Hazard and Risk Analysis*, Cambridge University Press. doi:10.1017/9781108425056

Barenblatt, G.I., 1962. The Mathematical Theory of Equilibrium Cracks in Brittle Fracture. in *Advances in Applied Mechanics*, Vol. 7, pp. 55–129, eds. Dryden, H.L., Kármán, Th. von, Kuerti, G., Dungen, F.H. van den & Howarth, L., Elsevier. doi:10.1016/S0065-2156(08)70121-2

Beldjoudi, H., Delouis, B., Djellit, H., Yelles-Chaouche, A., Gharbi, S. & Abacha, I., 2016. The Beni-Ilmane (Algeria) seismic sequence of May 2010: Seismic sources and stress tensor calculations. *Tectonophysics*, **670**, 101–114. doi:10.1016/j.tecto.2015.12.021

Beldjoudi, H., Delouis, B., Heddar, A., Nouar, O.B. & Yelles-Chaouche, A., 2012. The Tadjena Earthquake (Mw = 5.0) of December 16, 2006 in the Cheliff Region (Northern Algeria): Waveform Modelling, Regional Stresses, and Relation with the Boukadir Fault. *Pure and Applied Geophysics*, **169**, 677–691. doi:10.1007/s00024-011-0337-8

Beldjoudi, H., Guemache, M.A., Kherroubi, A., Semmane, F., Yelles-Chaouche, A.K., Djellit, H., Amrani, A., *et al.*, 2009. The Lâalam (Béjaïa, North-East Algeria) Moderate Earthquake (Mw = 5.2) on March 20, 2006. *Pure and Applied Geophysics*, **166**, 623–640. doi:10.1007/s00024-009-0462-9

Beldjoudi, Hamoud, 2020. Fault interaction for the Beni-Ilmane (east of Algeria) seismic sequence on May 2010. *Arabian Journal of Geosciences*, **13**, 959. doi:10.1007/s12517-020-05968-6

Bellalem, F., Pavlenko, V., Molina, S., Maouche, S., Sawires, R., Bezzeghoud, M., Talbi, A., *et al.*, 2024. Probabilistic seismic hazard analysis in Northern Algeria using the Parametric-Historic method. *Natural Hazards*, 1–32. doi:10.1007/s11069-024-06978-3

Bellalem, F., Talbi, A. & Maouche, S., 2022. A unified MW parametric earthquake catalog for Algeria and adjacent regions (PECAAR). *Mediterranean Geoscience Reviews*, **4**. doi:10.1007/s42990-022-00085-w

Bendjama, H., Yelles-Chaouche, A., Boulahia, O., Abacha, I., Mohammedi, Y., Beldjoudi, H., Rahmani, S.T.-E., *et al.*, 2021. The March 2017 earthquake sequence along the E-W-trending Mcid Aïcha-Debbagh Fault, northeast Algeria. *Geosciences Journal*, **25**, 697–713. doi:10.1007/s12303-020-0059-y

References

Bense, V.F., Gleeson, T., Loveless, S.E., Bour, O. & Scibek, J., 2013. Fault zone hydrogeology. *Earth-Science Reviews*, **127**, 171–192. doi:10.1016/j.earscirev.2013.09.008

Bezzeghoud, M., Ayadi, A., Sebai, A., Ait Messaoud, A., Mokrane, A. & Benhallou, H., 1996. Seismicity of Algeria between 1365 and 1989: Map of Maximum observed intensities (MOI). *Avances en Geofisica y Geodesia*, 107–114.

Bhattacharya, P. & Viesca, R.C., 2019. Fluid-induced aseismic fault slip outpaces pore-fluid migration. *Science*, **364**, 464–468, American Association for the Advancement of Science. doi:10.1126/science.aaw7354

Billi, A., Cuffaro, M., Orecchio, B., Palano, M., Presti, D. & Totaro, C., 2023. Retracing the Africa–Eurasia nascent convergent boundary in the western Mediterranean based on earthquake and GNSS data. *Earth and Planetary Science Letters*, **601**, 117906. doi:10.1016/j.epsl.2022.117906

Billings, S.D., Sambridge, M.S. & Kennett, B.L.N., 1994. Errors in hypocenter location: Picking, model, and magnitude dependence. *Bulletin of the Seismological Society of America*, **84**, 1978–1990. doi:10.1785/BSSA0840061978

Bird, P., 2003. An updated digital model of plate boundaries. *Geochemistry, Geophysics, Geosystems*, **4**, John Wiley & Sons, Ltd. doi:10.1029/2001GC000252

Bisrat, S., Deshon, H. & Rowe, C., 2012. Microseismic Swarm Activity in the New Madrid Seismic Zone. *The Bulletin of the Seismological Society of America*, **102**, 1167–1178. doi:10.1785/0120100315

Boatwright, J., 1980. A spectral theory for circular seismic sources; simple estimates of source dimension, dynamic stress drop, and radiated seismic energy. *Bulletin of the Seismological Society of America*, **70**, 1–27. doi:10.1785/BSSA0700010001

Bonneton & Truillet, 1979. Mise en évidence, dans la plaine de la Mitidja, d'accidents profonds. Conséquences hydrologiques et pédologiques (Algérie septentrionale). *C R Som. Soc. Géol. Fr*, 23–25.

Bouaicha, F., 2018. *Le Geothermalisme De La Region De Guelma*.

Bouchon, M., Durand, V., Marsan, D., Karabulut, H. & Schmittbuhl, J., 2013. The long precursory phase of most large interplate earthquakes. *Nature Geoscience*, **6**, 299–302. doi:10.1038/ngeo1770

Bougrine, A., Yelles-Chaouche, A.K. & Calais, E., 2019. Active deformation in Algeria from continuous GPS measurements. *Geophysical Journal International*, **217**, 572–588. doi:10.1093/gji/ggz035

Boulahia, O., 2022. *Identification, caractérisation et interaction des sources sismiques : Implication sur des séquences d'évènements sismiques de la période 2010-2021 dans le Nord-Est Algérien*.

Boulahia, O., Abacha, I., Yelles-Chaouche, A., Bendjama, H., Kherroubi, A., Mohammedi, Y., Aidi, C., *et al.*, 2021. Recent Seismic Activity in the Bejaia–Babors Region (Northeastern Algeria): The Case of the 2012–2013 Bejaia Earthquake Sequences. *Pure and Applied Geophysics*, **178**, 1253–1279. doi:10.1007/s00024-021-02711-4

Bounif, A. & Dorbath, C., 1998. Three dimensional velocity structure and relocated aftershocks for the 1985 Constantine, Algeria (MS = 5.9) earthquake. *Annali di Geofisica*, **41**. doi:10.4401/ag-3792

Bounif, A., Haessler, H. & Meghraoui, M., 1987. The Constantine (northeast Algeria) earthquake of October 27, 1985: surface ruptures and aftershock study. *Earth and Planetary Science Letters*, **85**, 451–460. doi:10.1016/0012-821X(87)90140-3

Bourouis, S., 2004. *Sismicité induite et comportement mécanique d' un massif granitique fracturé par injection d'eau : application au site géothermique de Soultz -sous-Forêt*.

Bourouis, S. & Bernard, P., 2007. Evidence for coupled seismic and aseismic fault slip during water injection in the geothermal site of Soultz (France), and implications for seismogenic transients. *Geophysical Journal International*, **169**, 723–732. doi:10.1111/j.1365-246X.2006.03325.x

References

Bracène R., Bellahcène A., Bekkouche D., Mercier E., & de Lamotte D. Frizon, 1998. The thin-skinned style of the South Atlas Front in Central Algeria. *Geological Society, London, Special Publications*, **132**, 395–404, The Geological Society of London. doi:10.1144/GSL.SP.1998.132.01.22

Bracène, R. & Frizon de Lamotte, D., 2002. The origin of intraplate deformation in the Atlas system of western and central Algeria: from Jurassic rifting to Cenozoic–Quaternary inversion. *Tectonophysics*, **357**, 207–226. doi:10.1016/S0040-1951(02)00369-4

Brandes, C. & Tanner, D.C., 2020. Chapter 2 - Fault mechanics and earthquakes. in *Understanding Faults*, pp. 11–80, eds. Tanner, D. & Brandes, C., Elsevier. doi:10.1016/B978-0-12-815985-9.00002-3

Brune, J.N., 1970. Tectonic stress and the spectra of seismic shear waves from earthquakes. *Journal of Geophysical Research (1896-1977)*, **75**, 4997–5009, John Wiley & Sons, Ltd. doi:10.1029/JB075i026p04997

Brunton, S.L. & Kutz, J.N. (Eds.), 2019. Singular Value Decomposition (SVD). in *Data-Driven Science and Engineering: Machine Learning, Dynamical Systems, and Control*, pp. 3–46, Cambridge University Press. doi:10.1017/9781108380690.002

Buforn, E., Bezzeghoud, M., UdÍas, A. & Pro, C., 2004. Seismic Sources on the Iberia-African Plate Boundary and their Tectonic Implications. *pure and applied geophysics*, **161**, 623–646. doi:10.1007/s00024-003-2466-1

Bumby, A.J. & Guiraud, R., 2005. The geodynamic setting of the Phanerozoic basins of Africa. *Journal of African Earth Sciences*, **43**, 1–12. doi:10.1016/j.jafrearsci.2005.07.016

Burridge, R. & Knopoff, L., 1967. Model and theoretical seismicity. *Bulletin of the Seismological Society of America*, **57**, 341–371. doi:10.1785/BSSA0570030341

Caine, J., Evans, J. & Forster, C., 1996. Fault zone architecture and permeability structure. *Geology*, **24**, 1025–1028. doi:10.1130/0091-7613(1996)024<1025:FZAAPS>2.3.CO;2

Campbell, K.W., 2003. Prediction of Strong Ground Motion Using the Hybrid Empirical Method and Its Use in the Development of Ground-Motion (Attenuation) Relations in Eastern North America. *Bulletin of the Seismological Society of America*, **93**, 1012–1033. doi:10.1785/0120020002

Cappa, F. & Rutqvist, J., 2011. Impact of CO_2 geological sequestration on the nucleation of earthquakes. *Geophysical Research Letters*, **38**, John Wiley & Sons, Ltd. doi:10.1029/2011GL048487

Cappa, F., Rutqvist, J. & Yamamoto, K., 2009. Modeling crustal deformation and rupture processes related to upwelling of deep CO_2-rich fluids during the 1965–1967 Matsushiro earthquake swarm in Japan. *Journal of Geophysical Research: Solid Earth*, **114**, John Wiley & Sons, Ltd. doi:10.1029/2009JB006398

Cappa, F., Scuderi, M.M., Collettini, C., Guglielmi, Y. & Avouac, J.-P., 2019. Stabilization of fault slip by fluid injection in the laboratory and in situ. *Science Advances*, **5**, eaau4065, American Association for the Advancement of Science. doi:10.1126/sciadv.aau4065

Carmona, E., Almendros, J., Peña, J.A. & Ibáñez, J.M., 2010. Characterization of fracture systems using precise array locations of earthquake multiplets: An example at Deception Island volcano, Antarctica. *Journal of Geophysical Research: Solid Earth*, **115**, John Wiley & Sons, Ltd. doi:10.1029/2009JB006865

Cattaneo, M., Augliera, P., Spallarossa, D. & Lanza, V., 1999. A Waveform Similarity Approach to Investigate Seismicity Patterns. *Natural Hazards*, **19**, 123–138. doi:10.1023/A:1008099705858

Chatelain, J.-L., 1978. *Etude fine de la sismicité en zone de collision continentale au moyen d'un réseau de stations portables: la région Hindu-Kush Pamir*.

Chen, X. & Shearer, P.M., 2011. Comprehensive analysis of earthquake source spectra and swarms in the Salton Trough, California. *Journal of Geophysical Research: Solid Earth*, **116**, John Wiley & Sons, Ltd. doi:10.1029/2011JB008263

References

Dabouz, G., Beldjoudi, H., Delouis, B., Boulahia, O., Mohammedi, Y. & Yelles-Chaouche, A., 2021. The 2007 Medea Seismic Sequence, North-Central Algeria: Source Parameters, Stress Tensor, and Static Stress Changes. *Pure and Applied Geophysics*, **178**, 3313–3337. doi:10.1007/s00024-021-02827-7

Danré, P., De Barros, L., Cappa, F. & Ampuero, J.-P., 2022. Prevalence of Aseismic Slip Linking Fluid Injection to Natural and Anthropogenic Seismic Swarms. *Journal of Geophysical Research: Solid Earth*, **127**, e2022JB025571, John Wiley & Sons, Ltd. doi:10.1029/2022JB025571

Das, S. & Aki, K., 1977. Fault plane with barriers: A versatile earthquake model. *Journal of Geophysical Research (1896-1977)*, **82**, 5658–5670, John Wiley & Sons, Ltd. doi:10.1029/JB082i036p05658

Das, S. & Scholz, C.H., 1981. Off-fault aftershock clusters caused by shear stress increase? *Bulletin of the Seismological Society of America*, **71**, 1669–1675. doi:10.1785/BSSA0710051669

De Barros, L., Baques, M., Godano, M., Helmstetter, A., Deschamps, A., Larroque, C. & Courboulex, F., 2019. Fluid-Induced Swarms and Coseismic Stress Transfer: A Dual Process Highlighted in the Aftershock Sequence of the 7 April 2014 Earthquake (Ml 4.8, Ubaye, France). *Journal of Geophysical Research: Solid Earth*, **124**, 3918–3932, John Wiley & Sons, Ltd. doi:10.1029/2018JB017226

De Barros, L., Cappa, F., Deschamps, A. & Dublanchet, P., 2020. Imbricated Aseismic Slip and Fluid Diffusion Drive a Seismic Swarm in the Corinth Gulf, Greece. *Geophysical Research Letters*, **47**, e2020GL087142, John Wiley & Sons, Ltd. doi:10.1029/2020GL087142

De Barros, L., Danré, P., Garagash, D., Cappa, F. & Lengliné, O., 2024. Systematic observation of a seismic back-front during fluid injection in both natural and anthropogenic earthquake swarms. *Earth and Planetary Science Letters*, **641**, 118849. doi:10.1016/j.epsl.2024.118849

Delouis, B., Vallée, M., Meghraoui, M., Calais, E., Maouche, S., Lammali, K., Mahsas, A., *et al.*, 2004. Slip distribution of the 2003 Boumerdes-Zemmouri earthquake, Algeria, from teleseismic, GPS, and coastal uplift data. *Geophysical Research Letters*, **31**, John Wiley & Sons, Ltd. doi:10.1029/2004GL020687

Delvaux, D. & Sperner, B., 2003. New aspects of tectonic stress inversion with reference to the TENSOR program. *Geological Society, London, Special Publications*, **212**, 75–100. doi:10.1144/GSL.SP.2003.212.01.06

Deschamps, A., Bezzeghoud, M. & Bounif, A., 1991. Seismological study of the Constantine (Algeria) earthquake (27 October 1985), **8**, 163–173.

Déverchère, J., Yelles, K., Domzig, A., Mercier de Lépinay, B., Bouillin, J.-P., Gaullier, V., Bracène, R., *et al.*, 2005. Active thrust faulting offshore Boumerdes, Algeria, and its relations to the 2003 Mw 6.9 earthquake. *Geophysical Research Letters*, **32**, John Wiley & Sons, Ltd. doi:10.1029/2004GL021646

Di Bucci, D., Ravaglia, A., Seno, S., Toscani, G., Fracassi, U. & Valensise, G., 2006. Seismotectonics of the southern Apennines and Adriatic foreland: Insights on active regional E-W shear zones from analogue modeling. *Tectonics*, **25**, John Wiley & Sons, Ltd. doi:10.1029/2005TC001898

Ding, H., Zhou, Y., Ge, Z., Taymaz, T., Ghosh, A., Xu, H., Irmak, T.S., *et al.*, 2023. High-resolution seismicity imaging and early aftershock migration of the 2023 Kahramanmaraş (SE Türkiye) MW7.9 & 7.8 earthquake doublet. *Earthquake Science*, **36**, 417–432. doi:10.1016/j.eqs.2023.06.002

Dogan, D.D., 2023. A study on the effects of fault architecture on fluid circulation in the Gediz Graben by the finite volume method. *Solid Earth Sciences*, **8**, 146–159. doi:10.1016/j.sesci.2023.05.001

Domzig, A., Yelles, K., Le Roy, C., Déverchère, J., Bouillin, J.-P., Bracène, R., Mercier de Lépinay, B., *et al.*, 2006. Searching for the Africa–Eurasia Miocene boundary offshore western Algeria (MARADJA'03 cruise). *Comptes Rendus Geoscience*, **338**, 80–91. doi:10.1016/j.crte.2005.11.009

Durand, D., 1969. *Mise au point sur la structure du Nord-Est de la Berbérie*.

Earle, S., BCcampus, Panchuk, K. & Projectditor, B.O.T., 2019. *Physical Geology*, BCcampus, BC Open Textbook Project. Retrieved from https://books.google.dz/books?id=lSwwywEACAAJ

References

Ellsworth, W.L. & Beroza, G.C., 1995. Seismic Evidence for an Earthquake Nucleation Phase. *Science*, **268**, 851–855, American Association for the Advancement of Science. doi:10.1126/science.268.5212.851

Eshelby, J.D., 1957. The Determination of the Elastic Field of an Ellipsoidal Inclusion, and Related Problems. *Proceedings of the Royal Society of London. Series A, Mathematical and Physical Sciences*, **241**, 376–396, The Royal Society.

Fan, X., Zhang, G., Zhao, D., Xie, C., Huang, C. & Shan, X., 2022. Fault geometry and kinematics of the 2021 Mw 7.3 Maduo earthquake from aftershocks and InSAR observations. *Frontiers in Earth Science*, **10**. doi:10.3389/feart.2022.993984

Faulkner, D.R., Jackson, C.A.L., Lunn, R.J., Schlische, R.W., Shipton, Z.K., Wibberley, C.A.J. & Withjack, M.O., 2010. A review of recent developments concerning the structure, mechanics and fluid flow properties of fault zones. *Journal of Structural Geology*, **32**, 1557–1575. doi:10.1016/j.jsg.2010.06.009

Fedorik, J., Zwaan, F., Schreurs, G., Toscani, G., Bonini, L. & Seno, S., 2019. The interaction between strike-slip dominated fault zones and thrust belt structures: Insights from 4D analogue models. *Journal of Structural Geology*, **122**, 89–105. doi:10.1016/j.jsg.2019.02.010

Fossen, H., 2020. Chapter 8 - Fault classification, fault growth and displacement. in *Regional Geology and Tectonics (Second Edition)*, pp. 119–147, eds. Scarselli, N., Adam, J., Chiarella, D., Roberts, D.G. & Bally, A.W., Elsevier. doi:10.1016/B978-0-444-64134-2.00007-9

Frankel, A. & Kanamori, H., 1983. Determination of rupture duration and stress drop for earthquakes in southern California. *Bulletin of the Seismological Society of America*, **73**, 1527–1551. doi:10.1785/BSSA07306A1527

Fréchet, J.F., 1985. *Sismogénèse et doublets sismiques*. Retrieved from https://books.google.dz/books?id=MpqAtgAACAAJ

Frizon de Lamotte, D., Saint Bezar, B., Bracène, R. & Mercier, E., 2000. The two main steps of the Atlas building and geodynamics of the western Mediterranean. *Tectonics*, **19**, 740–761, John Wiley & Sons, Ltd. doi:10.1029/2000TC900003

Frohlich, C., 2006. *Deep Earthquakes*, Cambridge University Press. doi:10.1017/CBO9781107297562

Gabrielsen, R., Foerseth, R.B., Steel, R., Idil, S. & Klovjan, O.S., 1990. Architectural styles of basin fill in the northern Viking Graben. *Tectonic evolution of the North Sea rifts*, 158–179.

Gan, Q. & Elsworth, D., 2014. Analysis of fluid injection-induced fault reactivation and seismic slip in geothermal reservoirs. *Journal of Geophysical Research: Solid Earth*, **119**, 3340–3353, John Wiley & Sons, Ltd. doi:10.1002/2013JB010679

Gao, D., Kao, H. & Liu, J., 2023. Identification of Repeating Earthquakes: Controversy and Rectification. *Seismological Research Letters*, **94**, 2655–2665. doi:10.1785/0220230124

Gao, D., Kao, H. & Wang, B., 2021. Misconception of Waveform Similarity in the Identification of Repeating Earthquakes. *Geophysical Research Letters*, **48**, e2021GL092815, John Wiley & Sons, Ltd. doi:10.1029/2021GL092815

Got, J.-L., Fréchet, J. & Klein, F.W., 1994. Deep fault plane geometry inferred from multiplet relative relocation beneath the south flank of Kilauea. *Journal of Geophysical Research: Solid Earth*, **99**, 15375–15386, John Wiley & Sons, Ltd. doi:10.1029/94JB00577

Guemache, M.A., 2010. *Evolution géodynamique des bassins sismogènes de l\'Algérois (Algérie) [ressource textuelle, sauf manuscrits] : approche pluridisciplinaire (méthodes géologiques et géophysiques)*.

Guiraud, R., Bosworth, W., Thierry, J. & Delplanque, A., 2005. Phanerozoic geological evolution of Northern and Central Africa: An overview. *Journal of African Earth Sciences*, **43**, 83–143. doi:10.1016/j.jafrearsci.2005.07.017

References

Guiraud, R., 1977. Sur la neotectonique des regions ouest-constantinoises. *Bulletin de la Société Géologique de France*, **S7-XIX**, 645–650. doi:10.2113/gssgfbull.S7-XIX.3.645

Guiraud, René, 1973. *Evolution post-triasique de l'avant-pays de la chaîne alpine en Algérie*, PhD Thesis, Toulouse.

Hallal, N., Hamidatou, M., Hamai, L., Aguemoune, S. & Lamali, A., 2024. Landslides triggered by the August 2020 Mw 5.0 Mila, Algeria, earthquake: spatial distribution and susceptibility mapping. *Euro-Mediterranean Journal for Environmental Integration*, **9**, 1063–1085. doi:10.1007/s41207-024-00471-w

Hamai, L., Petit, C., Abtout, A., Yelles-Chaouche, A. & Déverchère, J., 2015. Flexural behaviour of the north Algerian margin and tectonic implications. *Geophysical Journal International*, **201**, 1426–1436. doi:10.1093/gji/ggv098

Hamdache, M., Peláez, J.A., Gospodinov, D. & Henares, J., 2018. Statistical Features of the 2010 Beni-Ilmane, Algeria, Aftershock Sequence. *Pure and Applied Geophysics*, **175**, 773–792. doi:10.1007/s00024-017-1708-6

Hamidatou, M., Yahia, M., Yelles-Chaouche, A., Thallak, I., Stromeyer, D., Lebdioui, S., Cotton, F., *et al.*, 2021. Seismic Hazard Analysis of Surface Level, Using Topographic Condition in the Northeast of Algeria. *Pure and Applied Geophysics*, **178**. doi:10.1007/s00024-019-02310-4

Hanks, T.C., 1977. Earthquake stress drops, ambient tectonic stresses and stresses that drive plate motions. *pure and applied geophysics*, **115**, 441–458. doi:10.1007/BF01637120

Harbi, I., 2001. *Analyse de la sismicité et mise en évidence d'accidents Actifs dans le Nord-Est Algerien.*

Hardebeck, J.L., Nazareth, J.J. & Hauksson, E., 1998. The static stress change triggering model: Constraints from two southern California aftershock sequences. *Journal of Geophysical Research: Solid Earth*, **103**, 24427–24437, John Wiley & Sons, Ltd. doi:10.1029/98JB00573

Haskell, N.A., 1964. Total energy and energy spectral density of elastic wave radiation from propagating faults. *Bulletin of the Seismological Society of America*, **54**, 1811–1841. doi:10.1785/BSSA05406A1811

Haskell, N.A., 1966. Total energy and energy spectral density of elastic wave radiation from propagating faults. Part II. A statistical source model. *Bulletin of the Seismological Society of America*, **56**, 125–140. doi:10.1785/BSSA0560010125

Havskov, J. & Ottemoller, L., 2010. *Routine Data Processing in Earthquake Seismology*. *Routine Data Processing in Earthquake Seismology, by Jens Havskov and Lars Ottemoller. Berlin: Springer, 2010. ISBN: 978-90-481-8696-9*. doi:10.1007/978-90-481-8697-6

Hayashi, M. & Hiramatsu, Y., 2013. Spatial distribution of similar aftershocks of a large inland earthquake, the 2000 Western Tottori earthquake, in Japan. *Earth, Planets and Space*, **65**, 1587–1592. doi:10.5047/eps.2013.09.002

Heidbach, O., Rajabi, M., Cui, X., Fuchs, K., Müller, B., Reinecker, J., Reiter, K., *et al.*, 2018. The World Stress Map database release 2016: Crustal stress pattern across scales. *Tectonophysics*, **744**, 484–498. doi:10.1016/j.tecto.2018.07.007

Hickman, S., Zoback, M. & Ellsworth, W., 2004. Introduction to special section: Preparing for the San Andreas Fault Observatory at Depth. *Geophysical Research Letters*, **31**, John Wiley & Sons, Ltd. doi:10.1029/2004GL020688

Holmgren, J., 2020. *Source Parameters of Induced Seismicity in North America*.

Husen, S., Kissling, E., Flueh, E. & Asch, G., 1999. Accurate hypocentre determination in the seismogenic zone of the subducting Nazca Plate in northern Chile using a combined on-/offshore network. *Geophysical Journal International*, **138**, 687–701. doi:10.1046/j.1365-246x.1999.00893.x

References

Husen, Stephan, Kissling, E. & Clinton, J.F., 2011. Local and regional minimum 1D models for earthquake location and data quality assessment in complex tectonic regions: application to Switzerland. *Swiss Journal of Geosciences*, **104**, 455–469. doi:10.1007/s00015-011-0071-3

Hutchings, L. & Wu, F., 1990. Empirical Green's Functions from small earthquakes: A waveform study of locally recorded aftershocks of the 1971 San Fernando Earthquake. *Journal of Geophysical Research: Solid Earth*, **95**, 1187–1214, John Wiley & Sons, Ltd. doi:10.1029/JB095iB02p01187

Ida, Y., 1973. Stress concentration and unsteady propagation of longitudinal shear cracks. *Journal of Geophysical Research (1896-1977)*, **78**, 3418–3429, John Wiley & Sons, Ltd. doi:10.1029/JB078i017p03418

Ide, S., Beroza, G.C., Prejean, S.G. & Ellsworth, W.L., 2003. Apparent break in earthquake scaling due to path and site effects on deep borehole recordings. *Journal of Geophysical Research: Solid Earth*, **108**, John Wiley & Sons, Ltd. doi:10.1029/2001JB001617

Igarashi, T., Matsuzawa, T. & Hasegawa, A., 2003. Repeating earthquakes and interplate aseismic slip in the northeastern Japan subduction zone. *Journal of Geophysical Research: Solid Earth*, **108**, John Wiley & Sons, Ltd. doi:10.1029/2002JB001920

Improta, L. & Bruno, P.P., 2007. Combining seismic reflection with multifold wide-aperture profiling: An effective strategy for high-resolution shallow imaging of active faults. *Geophysical Research Letters*, **34**, John Wiley & Sons, Ltd. doi:10.1029/2007GL031893

Irwin, G.R., 1957. Analysis of stresses and strains near the end of a crack traversing a plate, American Society of Mechanical Engineers.

Ishiyama, T., Sato, H., Abe, S., Kawasaki, S. & Kato, N., 2016. High-resolution 3D seismic reflection imaging across active faults and its impact on seismic hazard estimation in the Tokyo metropolitan area. *Tectonophysics*, **689**, 79–88. doi:10.1016/j.tecto.2016.01.042

Jeanne, P., Guglielmi, Y., Cappa, F., Rinaldi, A.P. & Rutqvist, J., 2014. The effects of lateral property variations on fault-zone reactivation by fluid pressurization: Application to CO2 pressurization effects within major and undetected fault zones. *Journal of Structural Geology*, **62**, 97–108. doi:10.1016/j.jsg.2014.01.017

Jeffreys, H. & Bullen, K., 1958. Seismological tables//Brit. Assoc. for the advancement of Sci. *London: Gray-Milne Trust*, **65**.

Jones, L.M. & Molnar, P., 1979. Some characteristics of foreshocks and their possible relationship to earthquake prediction and premonitory slip on faults. *Journal of Geophysical Research: Solid Earth*, **84**, 3596–3608, John Wiley & Sons, Ltd. doi:10.1029/JB084iB07p03596

Jost, M.L. & Herrmann, R.B., 1989. A Student's Guide to and Review of Moment Tensors. *Seismological Research Letters*, **60**, 37–57. doi:10.1785/gssrl.60.2.37

Julian, B.R., Miller, A.D. & Foulger, G.R., 1997. Non-double-couple earthquake mechanisms at the Hengill-Grensdalur Volcanic Complex, Southwest Iceland. *Geophysical Research Letters*, **24**, 743–746, John Wiley & Sons, Ltd. doi:10.1029/97GL00499

Kagan, Y.Y., 1991. 3-D rotation of double-couple earthquake sources. *Geophysical Journal International*, **106**, 709–716. doi:10.1111/j.1365-246X.1991.tb06343.x

Kaiser, A.E., Green, A.G., Campbell, F.M., Horstmeyer, H., Manukyan, E., Langridge, R.M., McClymont, A.F., *et al.*, 2009. Ultrahigh-resolution seismic reflection imaging of the Alpine Fault, New Zealand. *Journal of Geophysical Research: Solid Earth*, **114**, John Wiley & Sons, Ltd. doi:10.1029/2009JB006338

Kanamori, H. & Anderson, D.L., 1975. Theoretical basis of some empirical relations in seismology. *Bulletin of the Seismological Society of America*, **65**, 1073–1095. doi:10.1785/BSSA0650051073

References

Kanamori, H. & Given, J.W., 1981. Use of long-period surface waves for rapid determination of earthquake-source parameters. *Physics of the Earth and Planetary Interiors*, **27**, 8–31. doi:10.1016/0031-9201(81)90083-2

Kanamori, H. & Rivera, L., 2004. Static and Dynamic Scaling Relations for Earthquakes and Their Implications for Rupture Speed and Stress Drop. *Bulletin of the Seismological Society of America*, **94**, 314–319. doi:10.1785/0120030159

Kanamori, H. & Stewart, G.S., 1978. Seismological aspects of the Guatemala Earthquake of February 4, 1976. *Journal of Geophysical Research: Solid Earth*, **83**, 3427–3434, John Wiley & Sons, Ltd. doi:10.1029/JB083iB07p03427

Kapetanidis, V., Deschamps, A., Papadimitriou, P., Matrullo, E., Karakonstantis, A., Bozionelos, G., Kaviris, G., *et al.*, 2015. The 2013 earthquake swarm in Helike, Greece: seismic activity at the root of old normal faults. *Geophysical Journal International*, **202**, 2044–2073. doi:10.1093/gji/ggv249

Kapetanidis, V. & Papadimitriou, P., 2011. Estimation of arrival-times in intense seismic sequences using a Master-Events methodology based on waveform similarity. *Geophysical Journal International*, **187**, 889–917. doi:10.1111/j.1365-246X.2011.05178.x

Kapetanidis, Vasilis, P., P. & Makropoulos, K., 2010. *A cross-correlation technique for relocation of seismicity in the western Corinth rift*.

Kato, N., 2007. Expansion of aftershock areas caused by propagating post-seismic sliding. *Geophysical Journal International*, **168**, 797–808. doi:10.1111/j.1365-246X.2006.03255.x

Kaviris, G., Elias, P., Kapetanidis, V., Serpetsidaki, A., Karakonstantis, A., Plicka, V., De Barros, L., *et al.*, 2021. The Western Gulf of Corinth (Greece) 2020–2021 Seismic Crisis and Cascading Events: First Results from the Corinth Rift Laboratory Network. *The Seismic Record*, **1**, 85–95. doi:10.1785/0320210021

Kawasaki, I. & Tanimoto, T., 1981. Radiation patterns of body waves due to the seismic dislocation occurring in an anisotropic source medium. *Bulletin of the Seismological Society of America*, **71**, 37–50. doi:10.1785/BSSA0710010037

Kheidri, H.L., Zazoun, R.S. & Sabaou, N., 2007. Neogene Tectonic History Of The Sub-Bibanic And M'sila Basins, Northern Algeria: Implications For Hydrocarbon Potential. *Journal of Petroleum Geology*, **30**, 159–174, John Wiley & Sons, Ltd. doi:10.1111/j.1747-5457.2007.00159.x

Khelif, M.F., Yelles-Chaouche, A., Benaissa, Z., Semmane, F., Beldjoudi, H., Haned, A., Issaadi, A., *et al.*, 2018. The 2016 Mihoub (north-central Algeria) earthquake sequence: Seismological and tectonic aspects. *Tectonophysics*, **736**, 62–74. doi:10.1016/j.tecto.2018.03.015

Khelif, M.F.-A., 2019. *La sismicité récente de la région algéroise*.

Kherroubi, A., Yelles-Chaouche, A., Koulakov, I., Déverchère, J., Beldjoudi, H., Haned, A., Semmane, F., *et al.*, 2017. Full Aftershock Sequence of the Mw 6.9 2003 Boumerdes Earthquake, Algeria: Space–Time Distribution, Local Tomography and Seismotectonic Implications. *Pure and Applied Geophysics*, **174**, 2495–2521. doi:10.1007/s00024-017-1571-5

Kim, A., Dreger, D.S., Taira, T. & Nadeau, R.M., 2016. Changes in repeating earthquake slip behavior following the 2004 Parkfield main shock from waveform empirical Green's functions finite-source inversion. *Journal of Geophysical Research: Solid Earth*, **121**, 1910–1926, John Wiley & Sons, Ltd. doi:10.1002/2015JB012562

Kissling, E., Ellsworth, W.L., Eberhart-Phillips, D. & Kradolfer, U., 1994. Initial reference models in local earthquake tomography. *Journal of Geophysical Research: Solid Earth*, **99**, 19635–19646, John Wiley & Sons, Ltd. doi:10.1029/93JB03138

Kissling, Edi, 1988. Geotomography with local earthquake data. *Reviews of Geophysics*, **26**, 659–698, John Wiley & Sons, Ltd. doi:10.1029/RG026i004p00659

References

Kissling, Edi, 1995. Velest User's Guide. *Int. Inst. Geophys.*, 1–26.

Kisslinger, C., 1975. Processes during the Matsushiro, Japan, Earthquake Swarm as Revealed by Leveling, Gravity, and Spring-Flow Observations. *Geology*, **3**, 57–62. doi:10.1130/0091-7613(1975)3<57:PDTMJE>2.0.CO;2

Klein, F., 2014. *User's Guide to HYPOINVERSE-2000, a Fortran Program to Solve for Earthquake Locations and Magnitudes, Version 1.40, June 2014.* doi:10.13140/2.1.4859.3602

Knopoff, L. & Randall, M.J., 1970. The compensated linear-vector dipole: A possible mechanism for deep earthquakes. *Journal of Geophysical Research (1896-1977)*, **75**, 4957–4963, John Wiley & Sons, Ltd. doi:10.1029/JB075i026p04957

Kohketsu, K., 1985. The Extended Reflectivity Method For Synthetic Near-Field Seismogram. *Journal of Physics of the Earth*, **33**, 121–131. doi:10.4294/jpe1952.33.121

Kostrov, B.V. & Das, S., 1988. *Principles of Earthquake Source Mechanics*. Cambridge Monographs on Mechanics, Cambridge University Press. Retrieved from https://books.google.dz/books?id=aXADpiXRH5QC

Koyama, J., Yoshizawa, K., Yomogida, K. & Tsuzuki, M., 2012. Variability of megathrust earthquakes in the world revealed by the 2011 Tohoku-oki Earthquake. *Earth, Planets and Space*, **64**, 1189–1198. doi:10.5047/eps.2012.04.011

Kwiatek, G., Martínez-Garzón, P. & Bohnhoff, M., 2016. HybridMT: A MATLAB/Shell Environment package for seismic moment tensor inversion and refinement. *Seismological Research Letters*, **87**, 964–976. doi:10.1785/0220150251

Lay, T. & Kanamori, H., 1981. An Asperity Model of Large Earthquake Sequences. in *Earthquake Prediction* Maurice Ewing Series, pp. 579–592. doi:10.1029/ME004p0579

Lay, T. & Wallace, T., 1995. Modern Global Seimology, Vol. 58.

Lengliné, O., Lamourette, L., Vivin, L., Cuenot, N. & Schmittbuhl, J., 2014. Fluid-induced earthquakes with variable stress drop. *Journal of Geophysical Research: Solid Earth*, **119**, 8900–8913, John Wiley & Sons, Ltd. doi:10.1002/2014JB011282

Leprêtre, A., Klingelhoefer, F., Graindorge, D., Schnurle, P., Beslier, M.O., Yelles, K., Déverchère, J., *et al.*, 2013. Multiphased tectonic evolution of the Central Algerian margin from combined wide-angle and reflection seismic data off Tipaza, Algeria. *Journal of Geophysical Research: Solid Earth*, **118**, 3899–3916, John Wiley & Sons, Ltd. doi:10.1002/jgrb.50318

Lofi, J., Déverchère, J., Gaullier, V., Gillet, H., Gorini, C., Guennoc, P., Loncke, L., *et al.*, 2011. *Seismic Atlas of the Messinian Salinity Crisis markers in the Mediterranean and Black Seas*. (C. for the G. M. of the World, Ed.)Mémoires de la Société Géologique de France, Vol. t. 179, Société Géologique de France. Retrieved from https://brgm.hal.science/hal-00593502

Loveless, S., Pluymaekers, M., Lagrou, D., De Boever, E., Doornenbal, H. & Laenen, B., 2014. Mapping the Geothermal Potential of Fault Zones in the Belgium-Netherlands Border Region. *Energy Procedia*, **59**, 351–358. doi:10.1016/j.egypro.2014.10.388

Madariaga, Raul, 1976. Dynamics of an expanding circular fault. *Bulletin of the Seismological Society of America*, **66**, 639–666. doi:10.1785/BSSA0660030639

Madariaga, Raúl, 2015. Seismic Source Theory. in *Treatise on Geophysics: Second Edition*, pp. 51–71. doi:10.1016/B978-0-444-53802-4.00070-1

Madariaga, Raúl & Ruiz, S., 2016. Earthquake dynamics on circular faults: a review 1970–2015. *Journal of Seismology*, **20**. doi:10.1007/s10950-016-9590-8

References

Mahboubi, M., Tabuce, R., Mebrouk, F., Coiffait, B., Coiffait, P.-E. & Jaeger, J.-J., 2003. L Eocene Continental A Vertebres De La Bordure Sud Des Monts Des Nementcha (Atlas Saharien Oriental, Algerie) - Précisions Stratigraphiques Et Implications Paléobiogéographiques -. *Bulletin du Service Géologique de l'Algérie*, **14**, 27–35.

Maouche, S., Abtout, A., Merabet, N.-E., Aïfa, T., Lamali, A., Bouyahiaoui, B., Bougchiche, S., *et al.*, 2013. Tectonic and Hydrothermal Activities in Debagh, Guelma Basin (Algeria). *Journal of Geological Research*, **2013**, 409475, John Wiley & Sons, Ltd. doi:10.1155/2013/409475

Marmi, R, 1995. *Les bassins continentaux de l'avant-pays de la chaîne alpine d'Algérie nord orientale. Etudes stratigraphiques, sédimentaires, structurales et géochimiques*, PhD Thesis, Thèse Doct Univ. Henri Poincaré, Nancy1, 283.

Marmi, Ramdane & Guiraud, R., 2006. End Cretaceous to recent polyphased compressive tectonics along the "Môle Constantinois" and foreland (NE Algeria). *Journal of African Earth Sciences*, **45**, 123–136. doi:10.1016/j.jafrearsci.2006.01.009

Massin, F., Farrell, J. & Smith, R., 2013. Repeating earthquakes in the Yellowstone volcanic field: Implications for rupture dynamics, ground deformation, and migration in earthquake swarms. *Journal of Volcanology and Geothermal Research*, **257**, 159–173. doi:10.1016/j.jvolgeores.2013.03.022

McGuire, J.J., Boettcher, M.S. & Jordan, T.H., 2005. Foreshock sequences and short-term earthquake predictability on East Pacific Rise transform faults. *Nature*, **434**, 457–461. doi:10.1038/nature03377

Meghraoui, M., 1988. *Géologie des zones sismiques du Nord de l'Algérie : paléosismologie, tectonique active et synthèse sismotectonique*.

Mesimeri, M. & Karakostas, V., 2018. Repeating earthquakes in western Corinth Gulf (Greece): implications for aseismic slip near locked faults. *Geophysical Journal International*, **215**, 659–676. doi:10.1093/gji/ggy301

Micklethwaite, S. & Cox, S.F., 2006. Progressive fault triggering and fluid flow in aftershock domains: Examples from mineralized Archaean fault systems. *Earth and Planetary Science Letters*, **250**, 318–330. doi:10.1016/j.epsl.2006.07.050

Miller, S.A., 2020. Aftershocks are fluid-driven and decay rates controlled by permeability dynamics. *Nature Communications*, **11**, 5787. doi:10.1038/s41467-020-19590-3

Miller, S.A., Collettini, C., Chiaraluce, L., Cocco, M., Barchi, M. & Kaus, B.J.P., 2004. Aftershocks driven by a high-pressure CO2 source at depth. *Nature*, **427**, 724–727. doi:10.1038/nature02251

Mohammedi, Y., 2015. *Etude sismotectonique de bassin néogène sismogène de Constantine/Grarem-Gouga*.

Mohammedi, Y., Yelles-Chaouche, A., Chami, A., Khelif, M.F., Aidi, C., Hamidatou, M. & Hallal, N., 2020. The 02 January 2018 ML 5.0 Oued Djer Earthquake in the Seismotectonic Context of the Southwestern Mitidja Basin Area, North-Central Algeria. *Pure and Applied Geophysics*, **177**, 681–702. doi:10.1007/s00024-019-02350-w

Morley, C.K., 2010. Stress re-orientation along zones of weak fabrics in rifts: An explanation for pure extension in 'oblique' rift segments? *Earth and Planetary Science Letters*, **297**, 667–673. doi:10.1016/j.epsl.2010.07.022

Mount, V.S. & Suppe, J., 1992. Present-day stress orientations adjacent to active strike-slip faults: California and Sumatra. *Journal of Geophysical Research: Solid Earth*, **97**, 11995–12013, John Wiley & Sons, Ltd. doi:10.1029/92JB00130

Mourad, M., Déverchère, J., Graindorge, D., Bracène, R., Badji, R., Ouabadi, A., Yelles-Chaouche, A., *et al.*, 2014. The transition from Alboran to Algerian basins (Western Mediterranean Sea): Chronostratigraphy, deep crustal structure and tectonic evolution at the rear of a narrow slab rollback system. *Journal of Geodynamics*, **77**. doi:10.1016/j.jog.2014.01.003

References

Do Nascimento, A.F, Lunn, R.J. & Cowie, P.A., 2005. Numerical modelling of pore-pressure diffusion in a reservoir-induced seismicity site in northeast Brazil. *Geophysical Journal International*, **160**, 249–262. doi:10.1111/j.1365-246X.2005.02473.x

Nocquet, J.-M., 2012. Present-day kinematics of the Mediterranean: A comprehensive overview of GPS results. *Tectonophysics*, **579**, 220–242. doi:10.1016/j.tecto.2012.03.037

Nur, A., 1974. Matsushiro, Japan, Earthquake Swarm: Confirmation of the Dilatancy-Fluid Diffusion Model. *Geology*, **2**, 217–221. doi:10.1130/0091-7613(1974)2<217:MJESCO>2.0.CO;2

Ohnaka, M., 2000. A Physical Scaling Relation Between the Size of an Earthquake and its Nucleation Zone Size. *pure and applied geophysics*, **157**, 2259–2282. doi:10.1007/PL00001084

Ohnaka, Mitiyasu, 2010. The Physics of Rock Failure and Earthquakes. *The Physics of Rock Failure and Earthquakes*, 1–270. doi:10.1017/CBO9781139342865

Ohnaka, Mitiyasu, 2013. *The Physics of Rock Failure and Earthquakes*, Cambridge University Press. doi:10.1017/CBO9781139342865

Ousadou, F., Dorbath, L., Ayadi, A., Dorbath, C. & Sofiane, G., 2014. Stress field variations along the Maghreb region derived from inversion of major seismic crisis fault plan solutions. *Tectonophysics*, **632**. doi:10.1016/j.tecto.2014.06.017

Ousadou, F., Dorbath, L., Dorbath, C., Bounif, M. & Benhallou, H., 2012. The Constantine (Algeria) seismic sequence of 27 October 1985: A new rupture model from aftershock relocation, focal mechanisms, and stress tensors. *Journal of Seismology*, **17**. doi:10.1007/s10950-012-9320-9

Ouyed, M., Meghraoui, M., Cisternas, A., Deschamps, A., Dorel, J., Frechet, J., Gaulon, R., *et al.*, 1981. Seismotectonics of the El Asnam earthquake. *Nature*, **292**, 26–31. doi:10.1038/292026a0

Pacchiani, F. & Lyon-Caen, H., 2010. Geometry and spatio-temporal evolution of the 2001 Agios Ioanis earthquake swarm (Corinth Rift, Greece). *Geophysical Journal International*, **180**, 59–72. doi:10.1111/j.1365-246X.2009.04409.x

Palmer, A. & Rice, J., 1973. The Growth of Slip Surfaces in the Progressive Failure of Over-Consolidated Clay. *Royal Society of London Proceedings Series A*, **332**, 527–548. doi:10.1098/rspa.1973.0040

Parotidis, M., Shapiro, S.A. & Rothert, E., 2004. Back front of seismicity induced after termination of borehole fluid injection. *Geophysical Research Letters*, **31**, John Wiley & Sons, Ltd. doi:10.1029/2003GL018987

Peláez, J., Mohamed, H. & Casado, C., 2005. Updating the Probabilistic Seismic Hazard Values of Northern Algeria with the 21 May 2003 M 6.8 Algiers Earthquake Included. *Pure and Applied Geophysics*, **162**, 2163–2177. doi:10.1007/s00024-005-2708-5

Peláez Montilla, J.A., Hamdache, M. & López Casado, C., 2003. Seismic hazard in Northern Algeria using spatially smoothed seismicity. Results for peak ground acceleration. *Tectonophysics*, **372**, 105–119. doi:10.1016/S0040-1951(03)00234-8

Perrin, C., Waldhauser, F. & Scholz, C.H., 2021. The Shear Deformation Zone and the Smoothing of Faults With Displacement. *Journal of Geophysical Research: Solid Earth*, **126**, e2020JB020447, John Wiley & Sons, Ltd. doi:10.1029/2020JB020447

Philip, H. & Meghraoui, M., 1983. Structural analysis and interpretation of the surface deformations of the El Asnam Earthquake of October 10, 1980. *Tectonics*, **2**, 17–49, John Wiley & Sons, Ltd. doi:10.1029/TC002i001p00017

Philip, H. & Thomas, G., 1977. Détermination de la direction de raccourcissement de la phase de compression quaternaire en Oranie (Algérie). *Revue de géographie physique et de géologie dynamique*, **19**, 315–324.

References

Piqué, A., Tricart, P., Guiraud, R., Laville, E., Bouaziz, S., Amrhar, M. & Ouali, R.A., 2002. The Mesozoic-Cenozoic Atlas belt (North Africa): an overview. *Geodinamica Acta*, **15**, 185–208, Taylor & Francis. doi:10.1080/09853111.2002.10510752

Pondrelli, S., Salimbeni, S., Ekström, G., Morelli, A., Gasperini, P. & Vannucci, G., 2006. The Italian CMT dataset from 1977 to the present. *Physics of the Earth and Planetary Interiors*, **159**, 286–303. doi:10.1016/j.pepi.2006.07.008

Poupinet, G., Ratdomopurbo, A. & Coutant, O., 1996. On the use of earthquake multiplets to study fractures and the temporal evolution of an active volcano. *Annali di Geofisica*, **39**, 253–264. doi:10.4401/ag-3968

Prieto, G.A., Parker, R.L. & Vernon III, F.L., 2009. A Fortran 90 library for multitaper spectrum analysis. *Computers & Geosciences*, **35**, 1701–1710. doi:10.1016/j.cageo.2008.06.007

Qian, R. & Liu, L., 2020. Imaging the active faults with ambient noise passive seismics and its application to characterize the Huangzhuang-Gaoliying fault in Beijing Area, northern China. *Engineering Geology*, **268**, 105520. doi:10.1016/j.enggeo.2020.105520

Rahmani, S.T.-E., Abacha, I., Boulahia, O., Yelles-Chaouche, A., Crespo-Martín, C. & Roubeche, K., 2023. Time-dependent and spatiotemporal statistical analysis of seismicity: Application on the complete data set of the 2010 Beni-Ilmane earthquake sequence. *Geophysical Journal International*, ggad483. doi:10.1093/gji/ggad483

Rajabi, M., 2016. *Present-day crustal stress pattern across spatial scales: analysis and interpretation from plate-wide to local-scales*.

Reasenberg, P.A. & Oppenheimer, D., 1985. FPFIT, FPPLOT and FPPAGE; Fortran computer programs for calculating and displaying earthquake fault-plane solutions. Retrieved from https://api.semanticscholar.org/CorpusID:59200668

Rietbrock, A., Tiberi, C., Scherbaum, F. & Lyon-Caen, H., 1996. Seismic slip on a low angle normal fault in the Gulf of Corinth: Evidence from high-resolution cluster analysis of microearthquakes. *Geophysical Research Letters*, **23**, 1817–1820, John Wiley & Sons, Ltd. doi:10.1029/96GL01257

Roche, V., Sternai, P., Guillou-Frottier, L., Menant, A., Jolivet, L., Bouchot, V. & Gerya, T., 2018. Emplacement of metamorphic core complexes and associated geothermal systems controlled by slab dynamics. *Earth and Planetary Science Letters*, **498**, 322–333. doi:10.1016/j.epsl.2018.06.043

Ross, A., Foulger, G.R. & Julian, B.R., 1996. Non-double-couple earthquake mechanisms at the Geysers Geothermal Area, California. *Geophysical Research Letters*, **23**, 877–880, John Wiley & Sons, Ltd. doi:10.1029/96GL00590

Ross, Z.E., Rollins, C., Cochran, E.S., Hauksson, E., Avouac, J.-P. & Ben-Zion, Y., 2017. Aftershocks driven by afterslip and fluid pressure sweeping through a fault-fracture mesh. *Geophysical Research Letters*, **44**, 8260–8267, John Wiley & Sons, Ltd. doi:10.1002/2017GL074634

Roubeche, K., Semmane, F., Abacha, I., Boulahia, O., Rahmani, S.T.-E. & Tikhamarine, E.-M., 2024. A local magnitude scale (ML) for Northern Algeria. *Tectonophysics*, **886**, 230435. doi:10.1016/j.tecto.2024.230435

Roussel, J., 1973. Les zones actives et la fréquence des séismes en Algérie (1716-1970). *Bulletin de la Société d'Histoire naturelle de l'Afrique du nord*, 211–228.

Rudajev, V. & Šílený, J., 1985. Seismic events with non-shear component: II. Rock bursts with implosive source component. *Pure and Applied Geophysics*, **123**, 17–25. doi:10.1007/BF00877046

Schaff, D.P., Bokelmann, G.H.R., Ellsworth, W.L., Zanzerkia, E., Waldhauser, F. & Beroza, G.C., 2004. Optimizing correlation techniques for improved earthquake location. *Bulletin of the Seismological Society of America*, **94**, 705–721. doi:10.1785/0120020238

References

Schmittbuhl, J., Karabulut, H., Lengliné, O. & Bouchon, M., 2016. Long-lasting seismic repeaters in the Central Basin of the Main Marmara Fault. *Geophysical Research Letters*, **43**, 9527–9534, John Wiley & Sons, Ltd. doi:10.1002/2016GL070505

Scholz, C.H., 2019. *The Mechanics of Earthquakes and Faulting*, 3rd ed., Cambridge University Press. doi:10.1017/9781316681473

Scholz, C.H., Ando, R. & Shaw, B.E., 2010. The mechanics of first order splay faulting: The strike-slip case. *Journal of Structural Geology*, **32**, 118–126. doi:10.1016/j.jsg.2009.10.007

Segou, M. & Parsons, T., 2014. The stress shadow problem in physics-based aftershock forecasting: Does incorporation of secondary stress changes help? *Geophysical Research Letters*, **41**, 3810–3817, John Wiley & Sons, Ltd. doi:10.1002/2013GL058744

Semmane, F., Abacha, I., Yelles-Chaouche, A., Haned, A., Beldjoudi, H. & Amrani, A., 2012. The earthquake swarm of December 2007 in the Mila region of northeastern Algeria. *Natural Hazards*, **64**. doi:10.1007/s11069-012-0338-7

Semmane, F., Campillo, M. & Cotton, F., 2005. Fault location and source process of the Boumerdes, Algeria, earthquake inferred from geodetic and strong motion data. *Geophysical Research Letters*, **32**, John Wiley & Sons, Ltd. doi:10.1029/2004GL021268

Serpelloni, E., Vannucci, G., Pondrelli, S., Argnani, A., Casula, G., Anzidei, M., Baldi, P., *et al.*, 2007. Kinematics of the Western Africa-Eurasia plate boundary from focal mechanisms and GPS data. *Geophysical Journal International*, **169**, 1180–1200. doi:10.1111/j.1365-246X.2007.03367.x

Shaddox, H., Schwartz, S. & Bartlow, N., 2021. Afterslip and Spontaneous Aseismic Slip on the Anza Segment of the San Jacinto Fault Zone, Southern California. *Journal of Geophysical Research: Solid Earth*, **126**. doi:10.1029/2020JB020460

Shapiro, S.A., Huenges, E. & Borm, G., 1997. Estimating the crust permeability from fluid-injection-induced seismic emission at the KTB site. *Geophysical Journal International*, **131**, F15–F18. doi:10.1111/j.1365-246X.1997.tb01215.x

Shearer, P.M., 1997. Improving local earthquake locations using the L1 norm and waveform cross correlation: Application to the Whittier Narrows, California, aftershock sequence. *Journal of Geophysical Research: Solid Earth*, **102**, 8269–8283, John Wiley & Sons, Ltd. doi:10.1029/96JB03228

Shearer, P.M., 2009. *Introduction to Seismology*, 2nd ed., Cambridge University Press. doi:10.1017/CBO9780511841552

Sheng, M., Chu, R., Peng, Z., Wei, Z., Zeng, X., Wang, Q. & Wang, Y., 2022. Earthquakes Triggered by Fluid Diffusion and Boosted by Fault Reactivation in Weiyuan, China Due to Hydraulic Fracturing. *Journal of Geophysical Research: Solid Earth*, **127**, e2021JB022963, John Wiley & Sons, Ltd. doi:10.1029/2021JB022963

Šílený, J. & Milev, A., 2008. Source mechanism of mining induced seismic events — Resolution of double couple and non double couple models. *Tectonophysics*, **456**, 3–15. doi:10.1016/j.tecto.2006.09.021

Sipkin, S.A., 1986. Interpretation of non-double-couple earthquake mechanisms derived from moment tensor inversion. *Journal of Geophysical Research: Solid Earth*, **91**, 531–547, John Wiley & Sons, Ltd. doi:10.1029/JB091iB01p00531

Soumaya, A., Ben Ayed, N., Rajabi, M., Meghraoui, M., Delvaux, D., Kadri, A., Ziegler, M., *et al.*, 2018. Active Faulting Geometry and Stress Pattern Near Complex Strike-Slip Systems Along the Maghreb Region: Constraints on Active Convergence in the Western Mediterranean. *Tectonics*, **37**, 3148–3173, John Wiley & Sons, Ltd. doi:10.1029/2018TC004983

Staszek, M., Rudziński, Ł. & Kwiatek, G., 2021. Spatial and temporal multiplet analysis for identification of dominant fluid migration path at The Geysers geothermal field, California. *Scientific Reports*, **11**, 23908. doi:10.1038/s41598-021-03267-y

References

Stein, S. & Wysession, M., 2009. *An Introduction to Seismology, Earthquakes, and Earth Structure*, Wiley. Retrieved from https://books.google.dz/books?id=-z80yrwFsqoC

Stich, D., Martín, R. & Morales, J., 2010. Moment tensor inversion for Iberia–Maghreb earthquakes 2005–2008. *Tectonophysics*, **483**, 390–398. doi:10.1016/j.tecto.2009.11.006

Stich, D., Serpelloni, E., Lis Mancilla, F. de & Morales, J., 2006. Kinematics of the Iberia–Maghreb plate contact from seismic moment tensors and GPS observations. *Tectonophysics*, **426**, 295–317. doi:10.1016/j.tecto.2006.08.004

Sykes, L.R., 1970. Earthquake swarms and sea-floor spreading. *Journal of Geophysical Research (1896-1977)*, **75**, 6598–6611, John Wiley & Sons, Ltd. doi:10.1029/JB075i032p06598

Tchalenko, J.S., 1970. Similarities between Shear Zones of Different Magnitudes. *GSA Bulletin*, **81**, 1625–1640. doi:10.1130/0016-7606(1970)81[1625:SBSZOD]2.0.CO;2

Templeton, D., Nadeau, R. & Burgmann, R., 2008. Behavior of Repeating Earthquake Sequences in Central California and the Implications for Subsurface Fault Creep. *Bulletin of The Seismological Society of America - BULL SEISMOL SOC AMER*, **98**, 52–65. doi:10.1785/0120070026

Terakawa, T., Hashimoto, C. & Matsu'ura, M., 2013. Changes in seismic activity following the 2011 Tohoku-oki earthquake: Effects of pore fluid pressure. *Earth and Planetary Science Letters*, **365**, 17–24. doi:10.1016/j.epsl.2013.01.017

Thurber, C.H., 1992. Hypocenter-velocity structure coupling in local earthquake tomography. *Physics of the Earth and Planetary Interiors*, **75**, 55–62. doi:10.1016/0031-9201(92)90117-E

Tikhamarine, E.-M., Abacha, I., Boulahia, O., Bendjama, H., Roubeche, K. & Rahmani, S.T.-E., 2024. Unveiling complex fault geometry and driving mechanisms: insights from a refined data processing and multiplet analysis of the 2010 Beni-Ilmane seismic sequence (NE Algeria). *Geophysical Journal International*, ggae327. doi:10.1093/gji/ggae327

Torabi, A., Johannessen, M.U. & Ellingsen, T.S.S., 2019. Fault Core Thickness: Insights from Siliciclastic and Carbonate Rocks. *Geofluids*, **2019**, 2918673, John Wiley & Sons, Ltd. doi:10.1155/2019/2918673

Trugman, D.T. & Shearer, P.M., 2017. GrowClust: A Hierarchical Clustering Algorithm for Relative Earthquake Relocation, with Application to the Spanish Springs and Sheldon, Nevada, Earthquake Sequences. *Seismological Research Letters*, **88**, 379–391. doi:10.1785/0220160188

Uchida, N. & Bürgmann, R., 2021. A Decade of Lessons Learned from the 2011 Tohoku-Oki Earthquake. *Reviews of Geophysics*, **59**, e2020RG000713, John Wiley & Sons, Ltd. doi:10.1029/2020RG000713

Uchida, Naoki, 2019. Detection of repeating earthquakes and their application in characterizing slow fault slip. *Progress in Earth and Planetary Science*, **6**, 40. doi:10.1186/s40645-019-0284-z

Uchida, Naoki & Bürgmann, R., 2019. Repeating Earthquakes. *Annu. Rev. Earth Planet. Sci.*, **47**, 305–332, Annual Reviews. doi:10.1146/annurev-earth-053018-060119

Udías, A., Madariaga, R. & Buforn, E., 2014. *Source Mechanisms of Earthquakes: Theory and Practice*, Cambridge University Press. doi:10.1017/CBO9781139628792

Utsu, T., 1971. Aftershocks and Earthquake Statistics(2) : Further Investigation of Aftershocks and Other Earthquake Sequences Based on a New Classification of Earthquake Sequences. *Journal of the Faculty of Science, Hokkaido University. Series 7, Geophysics*, **3**, 197–266, Hokkaido University.

Utsu, T., 1972. Aftershocks and Earthquake Statistics (3) : Analyses of the Distribution of Earthquakes in Magnitude, Time and Space with Special Consideration to Clustering Characteristics of Earthquake Occurrence(1). *Journal of the Faculty of Science, Hokkaido University. Series 7, Geophysics*, **3**, 379–441, Hokkaido University.

References

Vavryčuk, V., 2001. Inversion for parameters of tensile earthquakes. *Journal of Geophysical Research: Solid Earth*, **106**, 16339–16355, John Wiley & Sons, Ltd. doi:10.1029/2001JB000372

Vavryčuk, V., 2005. Focal mechanisms in anisotropic media. *Geophysical Journal International*, **161**, 334–346. doi:10.1111/j.1365-246X.2005.02585.x

Vavryčuk, V., 2015. Moment tensor decompositions revisited. *Journal of Seismology*, **19**, 231–252. doi:10.1007/s10950-014-9463-y

Viegas, G., 2012. Source Parameters of the 16 July 2010 Mw 3.4 Germantown, Maryland, Earthquake. *Seismological Research Letters*, **83**, 933–944. doi:10.1785/0220110056

Viegas, G., Abercrombie, R.E. & Kim, W.-Y., 2010. The 2002 M5 Au Sable Forks, NY, earthquake sequence: Source scaling relationships and energy budget. *Journal of Geophysical Research: Solid Earth*, **115**, John Wiley & Sons, Ltd. doi:10.1029/2009JB006799

Vila, J.-M., 1980. *La chaîne alpine d'Algérie orientale et des confins algéro-tunisiens*, [s.n.], [S.l.]. Retrieved from WorldCat.

Wadati, K. & Oki, S., 1933. On the Travel Time of Earthquake Waves. (Part II). *Journal of the Meteorological Society of Japan. Ser. II*, **11**, 14–28. doi:10.2151/jmsj1923.11.1_14

Waldhauser, F., 2001. hypoDD – A Program to Compute Double-Difference Hypocenter Locations. Retrieved from https://api.semanticscholar.org/CorpusID:15914772

Waldhauser, F. & Ellsworth, W.L., 2000. A Double-Difference Earthquake Location Algorithm: Method and Application to the Northern Hayward Fault, California. *Bulletin of the Seismological Society of America*, **90**, 1353–1368. doi:10.1785/0120000006

Wang, C., Si, G., Zhang, C., Cao, A. & Canbulat, I., 2022. Ground motion characteristics and their cumulative impacts to burst risks in underground coal mines. *Geomechanics and Geophysics for Geo-Energy and Geo-Resources*, **8**. doi:10.1007/s40948-022-00340-2

Wibberley, C., Yielding, G. & DiToro, G., 2008. Recent advances in the understanding of fault zone internal structure: A review. *Geological Society London Special Publications*, **299**, 5–33. doi:10.1144/SP299.2

Wildi, W., 1983. La chaîne tello-rifaine (Algérie, Maroc, Tunisie): structure, stratigraphie et évolution du Trias au Miocène, **24**, 201–297.

Yagi, Y. & Nishimura, N., 2011. Moment tensor inversion of near source seismograms. *Bulletin of the International Institute of Seismology and Earthquake Engineering*, **45**, 133–138.

Yamashita, T. & Ohnaka, M., 1991. Nucleation process of unstable rupture in the brittle regime: A theoretical approach based on experimentally inferred relations. *Journal of Geophysical Research: Solid Earth*, **96**, 8351–8367, John Wiley & Sons, Ltd. doi:10.1029/91JB00106

Yelles, K., Lammali, K., Mahsas, A., Calais, E. & Briole, P., 2004. Coseismic deformation of the May 21st, 2003, M = 6.8 Boumerdes earthquake, Algeria, from GPS measurements. *Geophysical Research Letters*, **31**, John Wiley & Sons, Ltd. doi:10.1029/2004GL019884

Yelles-Chaouche, A., Khelif, M.F., Haned, A., Chami, A., Aidi, C., Beldjoudi, H., Kherroubi, A., *et al.*, 2019. The Algiers (north central Algeria) earthquake of August 1st, 2014 Mw 5.5 in the Algiers Bay tectonic context. *Journal of Seismology*, **23**, 287–302. doi:10.1007/s10950-018-9806-1

Yelles-Chaouche, AbdelKarim, Abacha, I., Boulahia, O., Aidi, C., Chami, A., Belheouane, A., Rahmani, S.T.-E., *et al.*, 2021. The 13 July 2019 Mw 5.0 Jijel Earthquake, northern Algeria: An indicator of active deformation along the eastern Algerian margin. *Journal of African Earth Sciences*, **177**, 104149. doi:10.1016/j.jafrearsci.2021.104149

Yelles-Chaouche, Abdelkarim, Abacha, I., Boulahia, O., Beldjoudi, H., Aidi, C., Bendjama, H., Tikhamarine, E.-M., *et al.*, 2024. The 2021–2022 Mw 6.0 Bejaia Bay, NE Algeria, earthquake sequence:

References

tectonic implications at the Algerian margin between lesser and greater Kabylian blocks. *Acta Geophysica*, **72**, 529–551. doi:10.1007/s11600-023-01171-9

Yelles-Chaouche, AbdelKarim, Aidi, C., Beldjoudi, H., Abacha, I., Chami, A., Boulahia, O., Mohammedi, Y., *et al.*, 2022. The recent seismicity of northern Algeria: the 2006–2020 catalogue. *Mediterranean Geoscience Reviews*, **4**, 407–426. doi:10.1007/s42990-022-00092-x

Yelles-Chaouche, Abdelkarim, Roger, J., Déverchère, J., Bracène, R., Domzig, A., Hébert, H. & Kherroubi, A., 2009. The 1856 Tsunami of Djidjelli (Eastern Algeria): Seismotectonics, Modelling and Hazard Implications for the Algerian Coast. *Pure and Applied Geophysics*, **166**, 283–300. doi:10.1007/s00024-008-0433-6

Yelles-Chaouche, A.K., Abacha, I., Semmane, F., Beldjoudi, H. & Djellit, H., 2014. The Beni-Ilmane (North-Central Algeria) Earthquake Sequence of May 2010. *Pure and Applied Geophysics*, **171**, 1283–1298. doi:10.1007/s00024-013-0709-3

Yelles-Chaouche, A.K., Haned, A., Aidi, C., Beldjoudi, H., Kherroubi, A., Semmane, F., Benabdeloued, B.Y.N., *et al.*, 2017. The Mw 5.0 Hammam Melouane Earthquake (North Central Algeria) of 17 July 2013 in the Context of the Tellian Atlas Seismicity. *Pure and Applied Geophysics*, **174**, 1601–1614. doi:10.1007/s00024-017-1492-3

Yielding, G., Ouyed, M., King, G.C.P. & Hatzfeld, D., 1989. Active tectonics of the Algerian Atlas Mountains—evidence from aftershocks of the 1980 El Asnam earthquake. *Geophysical Journal International*, 99, 761–788. doi:10.1111/j.1365-246X.1989.tb02057.x

Yukutake, Y. & Iio, Y., 2017. Why do aftershocks occur? Relationship between mainshock rupture and aftershock sequence based on highly resolved hypocenter and focal mechanism distributions. *Earth, Planets and Space*, 69, 68. doi:10.1186/s40623-017-0650-2

Appendices

Appendix A: Principal Component Analysis (PCA) for Constructing 95% Confidence Ellipsoids to Determine Multiplet Group Geometry.

PCA is usually explained via an eigen-decomposition of the covariance matrix. However, it can also be performed via Singular Value Decomposition (SVD) of the data matrix. Briefly we used the SVD approach. The details bellow explains the relationship between PCA and SVD:

NB: the following analysis was performed for each multiplets cluster separately.

Let the real values data matrix **X** be of $n \times p$ size, where n is the number of samples (in our case we have two samples which are longitudes and latitudes of the events forming each multiplets cluster). and p is the number of variables (in our case the different events in each multiplets group).

For each multiplet group we have the following data matrix X:

$$X = \begin{bmatrix} \text{lon1 lon2 lon3 lon4 } \dots \dots \text{lon(n)} \\ \text{lat1 lat2 lat3 lat4 } \dots \dots \dots \text{lat(n)} \end{bmatrix} \tag{1}$$

We construct the mean-substructed data matrix by substracting the row-wise mean.

$$B = X - \bar{X} \tag{2}$$

covariance matrix C is given by:

$$C = \frac{B^T B}{n - 1} \tag{3}$$

The eigen-decomposition of C is given by:

$$C = V \Lambda V \tag{4}$$

where V is a matrix of eigenvectors (each column is an eigenvector) and Λ is a diagonal matrix with eigenvalues λi in the decreasing order on the diagonal.

The eigenvectors (columns of V) are the principal axes, also called priciple directions in the feature space along which the data varies the most. The eigenvalues in

Λ represent the variance explained by each principal direction. Projections of the data on the principal directions are called *principal components*, also known as *PC scores*; these can be seen as new, transformed, variables. The *j*-th principal component is given by *j*-th column of BV. The coordinates of the *i*-th data point in the new PC space are given by the *i*-th row of BV.

If we now perform singular value decomposition of B, we obtain:

$$B = U\Sigma V^T \tag{5}$$

where U is a unitary matrix (with columns called left singular vectors), Σ is the diagonal matrix of singular values *si* and V columns are called right singular vectors. From here one can easily see that

$$C = \frac{(V\Sigma U^T)(U\Sigma V^T)}{n-1} = V\frac{\Sigma^2}{n-1}V^T \tag{6}$$

comparing (4) and (6), one can notice that right singular vectors V are principal directions (eigenvectors) and that singular values are related to the eigenvalues of covariance matrix via $\lambda i = si^2/(n-1)$. Principal components are given by $BV = U\Sigma V^T V = U\Sigma$

For more detailed explanations and examples with applications in MATLAB and Python, see the book *Data-Driven Science & Engineering: Machine Learning, Dynamical Systems, and Control* by Steven L. Brunton and J. Nathan Kutz.

Appendix B: Table presenting all the calculated source parameters for 41 events from the BI-2010 seismic sequence, determined using both individual spectra and Empirical Green's Function approaches.

NB: The following two pages are in 'A3' paper format.

The table below details the averaged parameters from **Table III.1** and **Table III.2**. Each event was analyzed using at least one EGF across a minimum of three common stations, with some events utilizing up to four (4) EGFs. Subscripts are defined as follows: **ind**: indicates parameters from the individual spectra approach; **T**: denotes target event parameters; **EGF**: refers to Empirical Green's Function event parameters; **B**: and **M** correspond to parameters obtained using Brune's and Madariaga's models, respectively. Abbreviations include: **ML** (local magnitude), M_w (moment magnitude), M_0 (seismic moment, N·m), f_c (corner frequency, Hz), **R** (source radius, m), and **Δσ** (stress drop, MPa).

Target Event		EGF Event		Target Event Source Parameters												EGF Event Source Parameters						
				Using Individual Approach							Using EGF Approach											
Date & Time	ML_T	Date & Time	ML_{EGF}	$M_{0\text{-}T}$	$M_{w\text{-}T}$	$f_{c\text{-}ind}$	$R_{B\text{-}ind}$	$R_{M\text{-}ind}$	$\Delta\sigma_{B\text{-}ind}$	$\Delta\sigma_{M\text{-}ind}$	$f_{c\text{-}T}$	$R_{T\text{-}B}$	$R_{T\text{-}M}$	$\Delta\sigma_{TB}$	$\Delta\sigma_{T\text{-}M}$	$M_{0\text{-}EGF}$	$M_{w\text{-}EGF}$	$f_{c\text{-}EGF}$	$R_{EGF\text{-}B}$	$R_{EGF\text{-}M}$	$\Delta\sigma_{EGF\text{-}B}$	$\Delta\sigma_{EGF\text{-}M}$
2010.05.14-12.29.20	5.40	2010.05.15-00.18.49	3.00	1.40E+17	5.40	0.74	2617.02	1275.68	3.42	29.53	1.08	1793.15	874.07	10.63	91.79	1.04E+14	3.32	4.56	424.69	207.02	0.60	5.15
2010.05.14-12.29.20	5.40	2010.05.14-16.33.20	2.70	1.26E+17	5.37	0.71	2727.60	1329.58	2.72	23.51	1.21	1600.49	780.17	13.48	116.36	2.29E+13	2.88	7.02	275.87	134.47	0.48	4.12
2010.05.14-12.29.20	5.40	2010.06.15-21.07.12	2.60	1.18E+17	5.35	0.80	2420.75	1180.00	3.63	31.38	1.07	1809.90	882.24	8.70	75.09	2.89E+13	2.94	7.96	243.29	118.59	0.88	7.57
2010.05.16-06.52.39	5.30	2010.07.12-16.32.51	4.00	6.95E+16	5.20	0.75	2582.13	1258.67	1.77	15.26	1.31	1478.32	720.61	9.42	81.30	7.73E+14	3.90	2.6	744.85	363.08	0.82	7.07
2010.05.16-06.52.39	5.30	2010.05.25-18.04.26	3.10	4.89E+16	5.10	0.85	2278.35	1110.59	1.81	15.61	1.39	1393.24	679.14	7.91	68.26	1.10E+14	3.33	4.69	412.92	201.28	0.68	5.91
2010.05.16-06.52.39	5.30	2010.05.18-02.47.18	2.80	4.92E+16	5.10	0.77	2515.06	1225.97	1.35	11.68	1.39	1393.24	679.14	7.96	68.73	6.76E+13	3.19	4.98	388.87	189.56	0.50	4.34
2010.05.23-13.28.16	5.30	2010.08.03-08.20.39	3.60	7.57E+16	5.22	0.86	2251.86	1097.67	2.90	25.04	1.32	1467.12	715.15	10.49	90.53	4.59E+14	3.74	3.83	505.64	246.48	1.55	13.42
2010.05.23-13.28.16	5.30	2010.07.04-22.21.29	3.50	6.80E+16	5.19	0.88	2200.68	1072.73	2.79	24.11	1.29	1501.24	731.78	8.80	75.96	3.11E+14	3.63	4.15	466.65	227.47	1.34	11.54
2010.05.23-13.28.16	5.30	2010.05.30-04.48.30	3.40	4.20E+16	5.05	0.87	2225.97	1085.06	1.67	14.38	1.43	1354.26	660.14	7.40	63.86	1.12E+14	3.34	5.24	369.58	180.15	0.97	8.40
2010.05.16-03.51.29	4.70	2010.06.02-09.02.49	2.80	6.86E+15	4.53	1.33	1456.09	709.77	0.97	8.39	1.95	993.13	484.10	3.06	26.46	1.63E+13	2.78	8.23	235.31	114.70	0.55	4.71
2010.05.16-03.51.29	4.70	2010.06.26-19.12.56	2.70	1.01E+16	4.64	1.33	1456.09	709.77	1.43	12.35	1.78	1087.98	530.34	3.43	29.60	2.34E+13	2.88	7.16	270.47	131.84	0.52	4.46
2010.05.16-03.51.29	4.70	2010.05.16-07.35.15	2.60	6.67E+15	4.52	1.30	1489.69	726.15	0.88	7.62	1.83	1058.25	515.85	2.46	21.25	9.55E+12	2.62	9.7	199.65	97.32	0.52	4.53
2010.05.24-21.00.38	4.50	2010.05.23-14.09.53	3.50	8.01E+15	4.57	1.27	1524.88	743.31	0.99	8.54	1.85	1046.81	510.27	3.06	26.39	3.04E+14	3.63	3.53	548.61	267.42	0.81	6.96
2010.05.24-21.00.38	4.50	2010.05.25-02.05.00	3.20	8.58E+15	4.59	1.28	1512.97	737.50	1.08	9.36	1.78	1087.98	530.34	2.92	25.18	1.33E+14	3.39	2.98	649.86	316.78	0.21	1.84
2010.05.24-21.00.38	4.50	2010.05.26-20.49.25	3.00	1.02E+16	4.64	1.35	1434.52	699.26	1.51	13.03	1.79	1081.90	527.37	3.52	30.37	1.05E+14	3.32	4.45	435.19	212.13	0.56	4.81
2010.05.14-23.43.21	4.40	2010.05.14-16.15.33	3.10	3.14E+15	4.30	1.58	1225.69	597.47	0.75	6.44	2.38	813.70	396.64	2.55	22.02	9.75E+13	3.30	5.03	385.01	187.67	0.75	6.46
2010.05.14-23.43.21	4.40	2010.05.25-18.04.26	3.10	2.31E+15	4.21	1.96	988.06	481.63	1.05	9.03	3.09	626.73	305.50	4.10	35.39	1.00E+14	3.30	6.5	297.94	145.23	1.66	14.34
2010.05.14-23.43.21	4.40	2010.05.21-20.47.26	2.90	3.41E+15	4.33	1.58	1225.69	597.47	0.81	6.99	2.86	677.13	330.07	4.81	41.49	4.13E+13	3.05	6.91	280.26	136.61	0.82	7.08
2010.05.25-13.05.10	4.40	2010.05.24-19.32.30	3.00	1.51E+15	4.09	3.04	637.04	310.53	2.56	22.08	5.23	370.29	180.50	13.02	112.41	3.39E+13	2.99	12.04	160.85	78.41	3.56	30.74
2010.05.25-13.05.10	4.40	2010.05.28-18.51.24	2.90	1.37E+15	4.06	2.96	654.26	318.92	2.13	18.43	5.76	336.21	163.89	15.73	135.78	2.39E+13	2.89	11.22	172.60	84.14	2.03	17.52
2010.05.25-13.05.10	4.40	2010.07.17-07.08.56	2.90	1.40E+15	4.07	2.97	652.05	317.85	2.21	19.06	5.13	377.50	184.02	11.38	98.21	1.25E+12	2.03	22.9	84.57	41.22	0.90	7.78
2010.05.14-15.13.13	4.30	2010.05.25-08.09.05	3.20	4.32E+15	4.39	1.36	1423.97	694.12	0.65	5.65	2.03	953.99	465.02	2.17	18.78	1.63E+14	3.44	5.42	357.31	174.17	1.56	13.46
2010.05.14-15.13.13	4.30	2010.05.16-23.02.26	3.10	4.97E+15	4.43	1.34	1445.22	704.48	0.72	6.22	2.41	803.57	391.70	4.19	36.18	2.32E+14	3.55	5.35	361.98	176.45	2.14	18.47
2010.05.14-15.13.13	4.30	2010.06.02-23.19.15	3.00	5.40E+15	4.46	1.38	1403.33	684.06	0.86	7.38	2.05	944.68	460.49	2.80	24.20	9.26E+13	3.28	5.55	348.94	170.09	0.95	8.23
2010.05.14-15.13.13	4.30	2010.07.10-15.33.43	3.70	4.11E+15	4.38	1.38	1403.33	684.06	0.65	5.62	2.64	733.56	357.58	4.56	39.34	1.31E+14	3.38	5.42	357.31	174.17	1.26	10.84
2010.05.31-16.05.03	4.30	2010.07.25-09.15.06	3.30	4.25E+15	4.39	1.49	1299.73	633.56	0.85	7.31	2.29	845.68	412.23	3.07	26.53	1.11E+14	3.33	5.09	380.47	185.46	0.88	7.63
2010.05.31-16.05.03	4.30	2010.05.16-23.02.26	3.10	4.48E+15	4.40	1.49	1299.73	633.56	0.89	7.71	2.41	803.57	391.70	3.78	32.62	2.54E+14	3.57	4.68	413.80	201.71	1.57	13.56
2010.05.31-16.05.03	4.30	2010.05.24-20.25.36	2.70	5.28E+15	4.45	1.43	1354.26	660.14	0.93	8.02	2.28	849.38	414.04	3.77	32.53	5.11E+13	3.11	6.47	299.32	145.90	0.83	7.20
2010.07.12-16.32.51	4.00	2010.05.23-20.54.11	2.90	1.28E+15	4.04	1.87	1035.61	504.81	0.50	4.34	2.3	842.00	410.43	0.93	8.07	5.08E+13	3.11	5.1	379.72	185.10	0.41	3.50
2010.07.12-16.32.51	4.00	2010.05.23-13.54.16	2.60	1.18E+15	4.02	2.13	909.20	443.19	0.69	5.93	2.78	696.62	339.57	1.53	13.19	1.96E+13	2.83	6.34	305.46	148.90	0.30	2.60
2010.07.12-16.32.51	4.00	2010.05.29-01.05.46	2.20	1.33E+15	4.05	1.83	1058.25	515.85	0.49	4.23	2.43	796.95	388.48	1.15	9.90	6.38E+12	2.51	8.1	239.09	116.54	0.20	1.76
2010.05.26-17.49.44	3.80	2010.05.24-06.57.48	2.70	1.26E+15	4.04	2.02	958.71	467.33	0.62	5.39	3.59	539.44	262.95	3.50	30.24	7.21E+13	3.21	5.8	333.90	162.76	0.85	7.31
2010.05.26-17.49.44	3.80	2010.05.24-20.25.36	2.70	8.995E+14	3.94	2.12	913.49	445.28	0.52	4.46	3.01	643.39	313.62	1.48	12.76	3.19E+13	2.97	6.01	322.23	157.07	0.42	3.60
2010.05.26-17.49.44	3.80	2010.05.23-21.27.48	2.40	1.10E+15	4.00	2.19	884.29	431.05	0.70	6.02	2.97	652.05	317.85	1.74	15.02	2.23E+13	2.87	5.93	326.58	159.19	0.28	2.42
2010.05.15-09.12.38	3.70	2010.06.15-21.07.12	2.60	2.962E+14	3.62	3.44	562.96	274.42	0.73	6.27	5.51	351.47	171.32	2.99	25.77	8.70E+12	2.60	11.66	166.09	80.96	0.83	7.18

2010.05.23-23.39.54	3.70	2010.05.24-20.25.36	2.70	7.349E+14	3.88	2.74	706.79	344.53	0.91	7.86	4.12	470.05	229.13	3.10	26.73	3.06E+13	2.96	6.17	313.87	153.00	0.43	3.74
2010.05.23-23.39.54	3.70	2010.05.25-18.34.33	2.70	1.24E+15	4.03	3.00	645.53	314.67	2.01	17.39	4.69	412.92	201.28	7.70	66.45	3.08E+13	2.96	6.28	308.38	150.32	0.46	3.97
2010.05.23-23.39.54	3.70	2010.05.25-01.51.18	2.40	9.017E+14	3.94	2.63	736.35	358.94	0.99	8.53	4.9	395.22	192.65	6.39	55.17	1.88E+13	2.82	11.25	172.14	83.91	1.61	13.89
2010.05.28-13.24.44	3.70	2010.05.28-15.09.04	2.50	5.166E+14	3.78	3.13	618.72	301.60	0.95	8.24	4.21	460.00	224.23	2.32	20.05	1.46E+13	2.75	9.39	206.24	100.53	0.73	6.29
2010.07.10-15.33.43	3.70	2010.07.22-18.19.32	2.10	7.539E+13	3.22	5.06	382.73	186.56	0.59	5.08	7.57	255.83	124.70	1.97	17.01	9.07E+11	1.94	23	84.20	41.04	0.67	5.74
2010.05.23-13.32.03	3.60	2010.05.28-20.20.45	2.40	6.327E+14	3.84	2.85	679.51	331.23	0.88	7.62	4.92	393.62	191.87	4.54	39.19	8.34E+12	2.58	9.95	194.63	94.87	0.49	4.27
2010.05.23-13.32.03	3.60	2010.05.26-02.03.39	2.20	6.412E+14	3.84	2.91	665.50	324.40	0.95	8.22	4.03	480.55	234.24	2.53	21.83	9.38E+12	2.62	9.82	197.21	96.13	0.53	4.62
2010.05.23-13.32.03	3.60	2010.05.24-21.25.58	2.00	5.285E+14	3.79	2.81	689.18	335.94	0.71	6.10	3.94	491.52	239.59	1.95	16.81	4.71E+12	2.42	9.64	200.89	97.93	0.25	2.20
2010.05.26-20.47.40	3.60	2010.05.23-15.18.48	2.40	3.371E+14	3.66	3.21	603.30	294.08	0.67	5.80	5.05	383.48	186.93	2.62	22.58	9.26E+12	2.61	10.68	181.33	88.39	0.68	5.86
2010.07.20-12.55.39	3.60	2010.05.27-01.54.49	2.50	1.889E+14	3.49	3.56	543.99	265.17	0.51	4.43	6.01	322.23	157.07	2.47	21.32	5.92E+12	2.49	11.53	167.96	81.87	0.55	4.72
2010.07.20-12.55.39	3.60	2010.06.04-05.16.31	2.30	1.831E+14	3.48	3.68	526.25	256.52	0.55	4.75	5.75	336.80	164.17	2.10	18.10	3.25E+12	2.31	12.37	156.56	76.31	0.37	3.19
2010.08.03-08.20.39	3.60	2010.05.17-12.32.28	2.60	2.857E+14	3.61	3.59	539.44	262.95	0.80	6.88	4.94	392.02	191.09	2.07	17.92	2.62E+13	2.92	7.87	246.07	119.95	0.77	6.64
2010.08.03-08.20.39	3.60	2010.05.22-20.09.11	2.50	3.083E+14	3.63	3.01	643.39	313.62	0.51	4.37	4	484.15	236.00	1.19	10.26	3.96E+13	3.04	6.92	279.86	136.42	0.79	6.82
2010.08.03-08.20.39	3.60	2010.05.28-00.17.17	2.10	2.885E+14	3.61	3.34	579.82	282.63	0.65	5.59	5.05	383.48	186.93	2.24	19.32	3.39E+12	2.32	14.08	137.54	67.05	0.57	4.92
2010.05.16-09.46.02	3.50	2010.05.16-01.46.22	2.40	7.981E+14	3.90	2.74	706.79	344.53	0.99	8.54	4.35	445.19	217.01	3.96	34.16	2.60E+13	2.91	7.82	247.65	120.72	0.75	6.47
2010.05.23-14.09.53	3.50	2010.05.23-21.27.48	2.40	1.91E+14	3.49	3.28	590.43	287.80	0.41	3.51	5.78	335.05	163.32	2.22	19.18	5.54E+12	2.47	11.36	170.48	83.10	0.49	4.23
2010.05.24-23.48.25	3.50	2010.05.25-11.54.02	2.50	3.012E+14	3.62	3.18	608.99	296.86	0.58	5.04	4.81	402.62	196.26	2.02	17.43	1.18E+13	2.68	9.32	207.79	101.29	0.57	4.96
2010.05.24-23.48.25	3.50	2010.05.28-22.14.02	2.50	2.475E+14	3.57	3.23	599.57	292.26	0.50	4.34	5.15	376.04	183.30	2.04	17.58	1.05E+13	2.65	10.17	190.42	92.82	0.67	5.77
2010.07.04-22.21.29	3.50	2010.05.27-01.54.49	2.50	2.661E+14	3.59	3.45	561.33	273.62	0.66	5.68	4.86	398.48	194.24	1.84	15.89	6.95E+12	2.53	10.98	176.37	85.97	0.55	4.79
2010.07.25-09.03.00	3.50	2010.05.19-22.36.18	2.20	9.053E+13	3.27	4.59	421.92	205.66	0.53	4.55	6.78	285.63	139.23	1.70	14.67	3.01E+12	2.29	17.16	112.86	55.01	0.92	7.91
2010.05.15-00.18.49	3.00	2010.06.15-00.34.33	1.70	6.698E+13	3.19	5.63	343.98	167.67	0.72	6.22	7.87	246.07	119.95	1.97	16.98	4.64E+11	1.75	25.09	77.19	37.62	0.44	3.81
2010.05.25-18.04.26	3.10	2010.06.15-21.07.12	2.60	2.042E+14	3.51	3.55	545.52	265.92	0.55	4.75	5.8	333.90	162.76	2.40	20.72	9.67E+12	2.63	10.47	184.97	90.16	0.67	5.77
2010.05.18-02.47.18	2.80	2010.05.21-10.59.28	2.00	7.19E+13	3.21	4.04	479.36	233.66	0.29	2.47	7.05	274.69	133.90	1.52	13.10	5.51E+12	2.46	10.48	184.79	90.08	0.38	3.30
2010.05.30-04.48.30	3.40	2010.05.28-00.17.17	2.10	7.015E+13	3.20	4.76	406.85	198.32	0.46	3.93	8.76	221.07	107.76	2.84	24.53	1.43E+12	2.07	16.94	114.32	55.73	0.42	3.61
2010.05.25-02.05.00	3.20	2010.05.23-14.08.52	2.80	2.797E+14	3.60	2.90	667.79	325.52	0.41	3.55	4.38	442.15	215.53	1.42	12.22	5.32E+13	3.12	6.94	279.05	136.02	1.07	9.24
2010.05.26-20.49.25	3.00	2010.05.26-23.55.36	2.40	1.529E+14	3.43	3.44	562.96	274.42	0.37	3.24	6.15	314.89	153.50	2.14	18.50	4.65E+12	2.41	10.47	184.97	90.16	0.32	2.78
2010.05.21-12.16.18	3.30	2010.06.15-21.07.12	2.60	5.036E+14	3.77	2.72	711.98	347.06	0.61	5.27	4.3	450.37	219.53	2.41	20.82	3.19E+13	2.97	9.26	209.14	101.94	1.53	13.19
2010.05.15-00.00.41	3.30	2010.06.15-21.07.12	2.60	1.14E+15	4.01	2.29	845.68	412.23	0.82	7.10	3.89	497.84	242.67	4.03	34.81	7.25E+13	3.21	7.95	243.60	118.74	2.19	18.94
2010.05.19-23.59.50	4.10	2010.05.18-02.47.18	2.80	6.943E+14	3.86	2.92	663.22	323.29	1.04	8.99	4.16	465.53	226.92	3.01	26.00	5.53E+13	3.13	7.46	259.60	126.54	1.38	11.93
2010.05.14-16.15.33	3.20	2010.06.15-21.07.12	2.60	2.097E+14	3.52	3.12	620.70	302.56	0.38	3.31	4.72	410.30	200.00	1.33	11.47	4.52E+13	3.07	7.34	263.84	128.61	1.08	9.29
2010.05.14-16.15.33	3.20	2010.05.22-20.09.11	2.50	2.459E+14	3.56	3.29	588.63	286.93	0.53	4.55	4.59	421.92	205.66	1.43	12.36	3.74E+13	3.02	7.28	266.02	129.67	0.87	7.51
2010.05.25-08.09.05	3.20	2010.05.25-16.27.09	2.40	1.009E+14	3.31	4.20	461.09	224.76	0.45	3.89	6.87	281.89	137.41	1.97	17.02	3.45E+12	2.33	11.32	171.08	83.39	0.30	2.60
2010.05.16-23.02.26	3.10	2010.05.25-16.27.09	2.40	9.067E+13	3.27	4.31	449.33	219.03	0.44	3.78	6.71	288.61	140.69	1.65	14.25	5.16E+12	2.44	9.12	212.35	103.51	0.24	2.03
2010.05.24-13.11.02	3.20	2010.05.25-11.54.02	2.50	2.147E+14	3.52	3.64	532.03	259.34	0.62	5.38	5.38	359.96	175.46	2.01	17.39	1.37E+13	2.73	8.97	215.90	105.24	0.60	5.16
2010.06.23-21.44.59	3.40	2010.06.24-00.31.16	2.50	7.879E+13	3.23	4.73	409.43	199.58	0.50	4.34	7.97	242.99	118.44	2.40	20.74	5.51E+12	2.46	12.7	152.49	74.33	0.68	5.87
2010.08.09-03.40.54	3.40	2010.08.09-18.24.25	1.80	1.669E+14	3.45	3.68	526.25	256.52	0.50	4.33	6.18	313.37	152.75	2.37	20.49	1.85E+12	2.15	14.33	135.14	65.88	0.33	2.83
2010.06.04-22.10.41	3.30	2010.06.24-00.31.16	2.50	1.882E+14	3.49	4.24	456.74	222.64	0.86	7.46	5.59	346.44	168.87	1.98	17.09	1.48E+13	2.75	10.19	190.05	92.64	0.94	8.15
2010.05.17-15.52.29	3.40	2010.05.17-17.26.43	2.20	2.014E+14	3.51	3.54	547.06	266.67	0.54	4.65	5.73	337.98	164.75	2.28	19.70	8.57E+12	2.59	10.77	179.81	87.65	0.64	5.57

Appendix C: Inadequacy of Short-Period seismometers for moment tensor inversion using full-waveform inversion

Various types of seismometers exist, each tailored to capture specific frequency ranges of ground motion. Among the widely used models are the Short-period (SP) SS-1 seismometer and the Broad-band (BB) STS-2 seismometer. The SS-1 is optimized for high-frequency signals, responding linearly to ground shaking for frequencies above 1 Hz, making it suitable for studying local earthquakes and high-frequency seismic waves. In contrast, the STS-2 is designed to capture a broader spectrum of seismic signals, with a linear response extending down to very low frequencies (f > 1/120 Hz or 120 s period), enabling it to record global seismic events and long-period ground motions effectively.

Fig. C.1 illustrates the amplitude response spectra of the three types of instruments generally used by CRAAG: SS-1 Short-Period seismometer, STS-2 Broad-Band both of Kinemetrcis and BBVS-60s of GeoDevice.
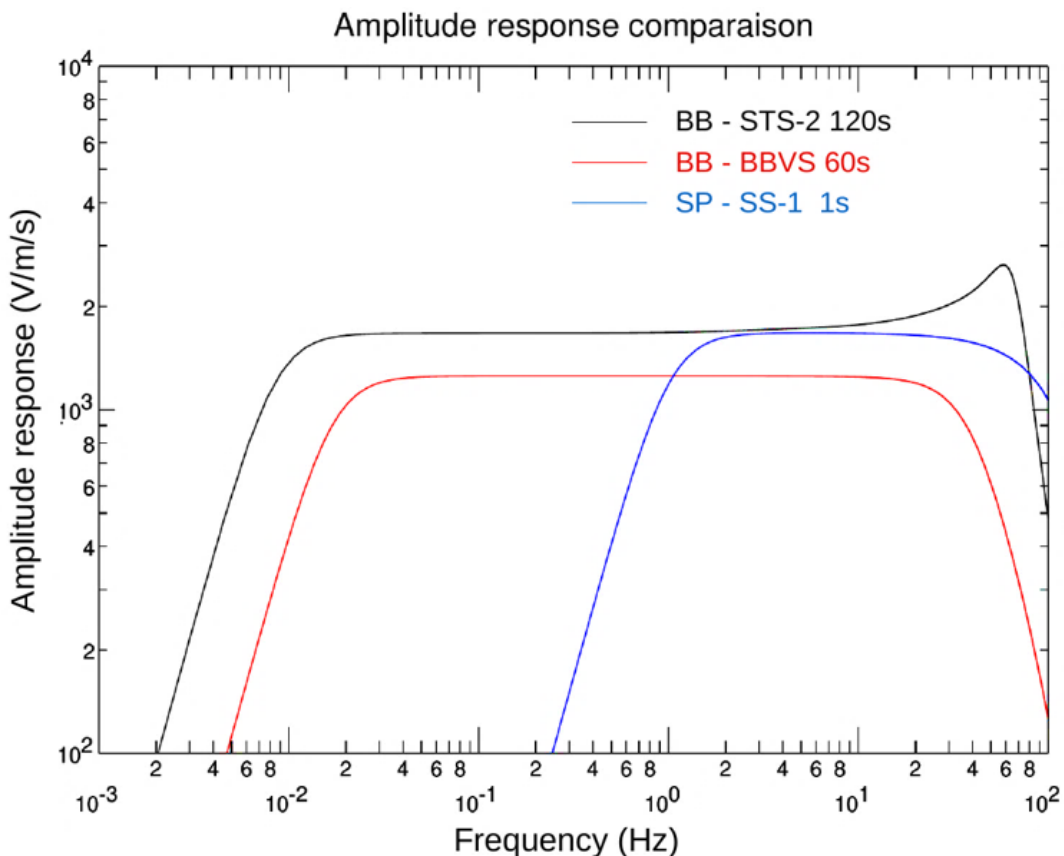

Fig. C.1: ADSN seismometers' response functions. These curves have been plotted using SAC (Seismic Analysis Code) program. These curves represent the impulse response of the seismometers, illustrating how they react to a unit input of ground motion across different frequencies.

For full waveform inversion in moment tensor solutions, seismologists focus on low-frequency signals, typically in the range of 0.01–0.1 Hz. From **Fig. C.1**, it is evident that the SS-1 attenuates amplitudes below 1 Hz, whereas broad-band sensors such as the STS-2 or BBVS maintain a linear response at frequencies as low as 0.0083 Hz and 0.016 Hz, respectively.

To evaluate the performance of these instruments, CRAAG researchers Boulahia Oualid and Semmane Fethi conducted comparative tests. They installed an SS-1 sensor adjacent to an STS-2 sensor and operated them simultaneously over several months. During this period, some earthquakes occurred. Here we consider the event of April 1st, 2018, at 16:42:30. The recordings from this event were used to compare the SP and BB sensors across different frequency bands: [0.05–0.5] Hz (below the effective band for SS-1), [0.5–1] Hz (near the effective band of SS-1), and [1–5] Hz (well within the SS-1 effective band). After deconvolving the instrument responses and applying the relevant filters, the results (**Fig. C.2**, **Fig. C.3** and **Fig. C.4**) show that at low frequencies (<1 Hz), SS-1 records are significantly attenuated compared to BB records. Conversely, for frequencies above 1 Hz, both Broad-Band and Short-Period records exhibit similar amplitudes after removing their instrument responses.

These findings indicate that Short-Period sensors, such as the SS-1, are inadequate for frequencies below 1 Hz. Consequently, their use in waveform inversion is not recommended for such low-frequency analyses.
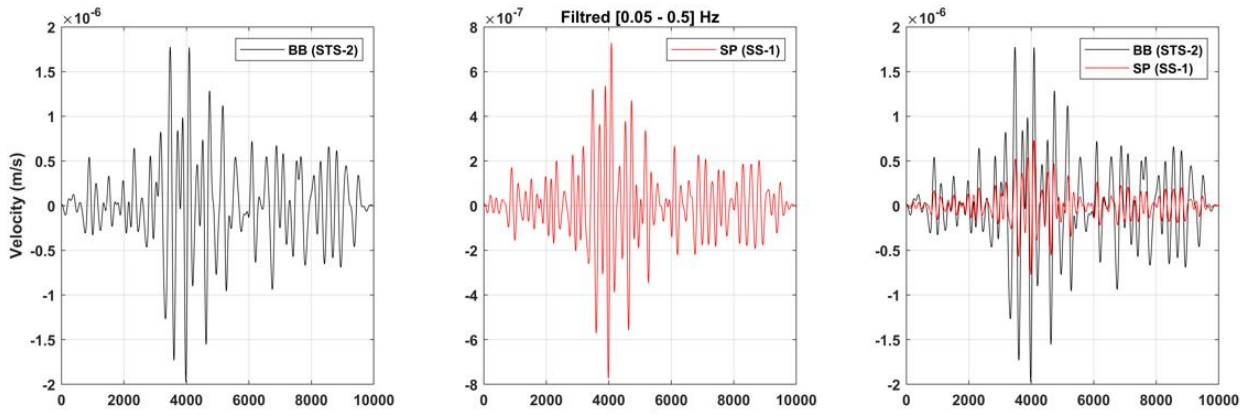
Fig. C.2: Comparison of the recorded velocity amplitudes from Broad-Band and Short-Period stations in the [0.05–0.5] Hz frequency range, showing significant attenuation in the Short-Period station compared to the Broad-Band station.
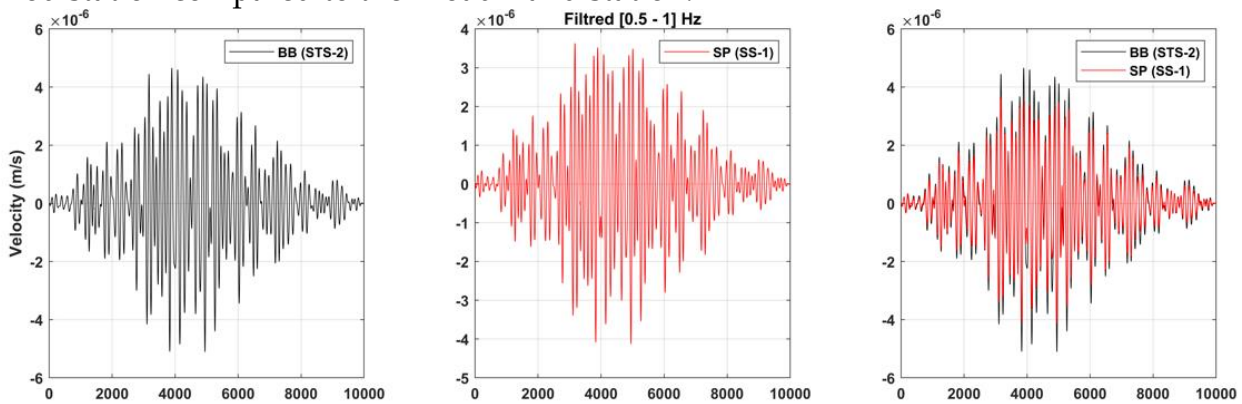

Fig. C.3: Similar to Fig. C.2, but for the [0.5–1] Hz frequency range, showing less attenuation in the Short-Period station as we approach its effective frequency band.
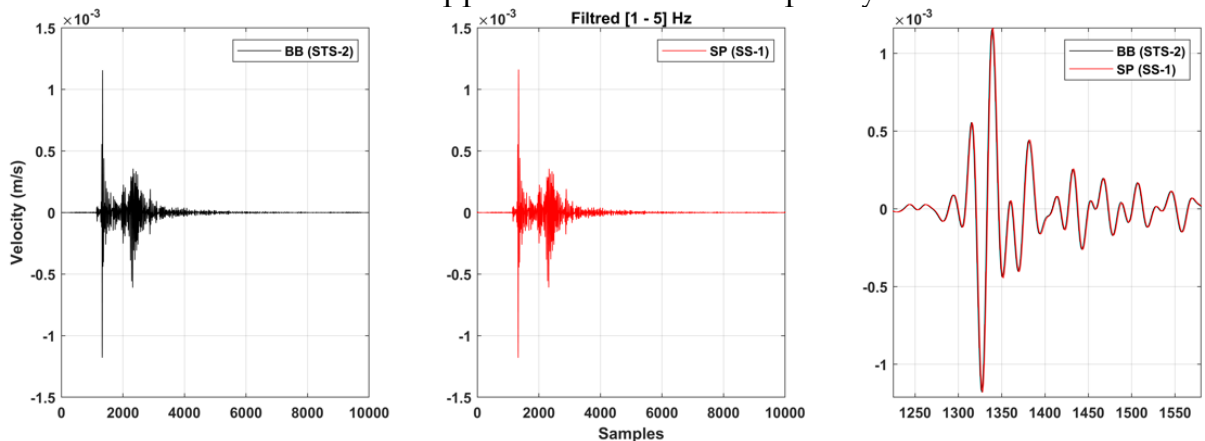

Fig. C.4: The same as Fig. C.2 and Fig. C.3 but at [1-5] Hz showing a similar amplitude between Short-Period and Broad-Band at the effective frequency band of Short-Period sensors.

Appendix D: Scientific publications in peer-reviewed journals

Geophysical Journal International

Unveiling complex fault geometry and driving mechanisms: insights from a refined data processing and multiplet analysis of the 2010 Beni-Ilmane seismic sequence (NE Algeria)

El-Mahdi Tikhamarine [1], Issam Abacha,[2] Oualid Boulahia,[2] Hichem Bendjama,[2] Khaled Roubeche[1,2] and Sofiane Taki-Eddine Rahmani[1,2]

[1]*Department of Physics, Faculty of Sciences, University Ferhat Abbas of Setif (UFAS-*1*), Campus El Bez, Algiers Road, Setif* 19137*, Algeria. E-mail:*
elmahdi_tm@outlook.com
[2]*Center of Research in Astronomy, Astrophysics, and Geophysics, CRAAG, Route de l'Observatoire BP 63 Bouzaréah, Algiers* 16340*, Algeria*

SUMMARY

This paper offers a comprehensive re-analysis of the Beni-Ilmane 2010 seismic sequence, using a data set that is 100 per cent larger than previous studies. This unprecedented sequence in Algeria features three main shocks with magnitudes M_w 5.4, 5.1 and 5.1. Our approach involves high-precision relocation, which includes the development of a new 1-D minimum velocity model, followed by a double-difference (DD) procedure and hierarchical clustering. We determined the focal mechanisms (FMs) for 128 key events and identified 21 multiplet groups using an average cross-correlation threshold of 0.8. Our analysis offers new insights into fault geometry and addresses ongoing debates, by proposing a seismotectonic model that reveals the activation of 14 fault segments during the sequence, in contrast to previous oversimplified models that suggested two or three faults. The computed stress field from the inversion of 128 FMs aligns with a tectonic loading force due to the convergence of the African and Eurasian plates. These findings highlight the complexity of the fault network in the study area and shed light on the role of strike-slip faults in shaping the thrust belt. We found a strong link between multiplet groups and fluid movement along the fault network. Analysis of the temporal history of these multiplet groups provides new insights into fluid dynamics timescales, with an estimated hydraulic diffusivity (*D*) of 0.36 $m^2\,s^{-1}$ suggesting a fluid pressure diffusion process. The observed expansion of the aftershock area with the logarithm of time and the existence of repeating earthquakes indicates, for the first time, an aseismic slip mechanism that adds an additional layer to the driven processes. In conclusion, our results suggest that the underlying mechanisms governing the BI-2010 seismic sequence involve a complex interplay of tectonic loading, coseismic stress transfer, fluid dynamics and aseismic slip transients. We attempt to correlate our findings with various studies linking the structure, mechanics and fluid flow properties of fault zones and fault systems. The activation of smaller fault segments potentially averted a larger quake, resulting in three moderate main shocks and numerous aftershocks. This work not only enrich our understanding of seismic phenomena but also provides useful insights for seismic hazard assessment and risk mitigation strategies.

Key words: Fracture and flow; Earthquake dynamics; Induced seismicity; Dynamics and mechanics of faulting.

1 INTRODUCTION

The Beni-Ilmane earthquake sequence of May 2010, hereafter referred to as BI-2010, has been extensively studied for more than a decade. This sequence occurred on the southern front of the Tellian Atlas (Fig. 1a), within the transition zone between the Hodna and Bibans mountains (Figs 1b and c), about 200 km from the plate boundary, as reported by Billi *et al.* (2023). The sequence, marked by three moderate main shocks (MS-1, MS-2 and MS-3 in Fig. 1b), caused damage to infrastructure and triggered subsequent aftershocks, inducing fear among the population for weeks. It began with MS-1, measuring M_w 5.4, on 14 May 2010, at 12:29 (GMT),

Paper's link: https://academic.oup.com/gji/article/239/2/1170/7754191

RESEARCH ARTICLE - SOLID EARTH SCIENCES

The 2021–2022 Mw 6.0 Bejaia Bay, NE Algeria, earthquake sequence: tectonic implications at the Algerian margin between lesser and greater Kabylian blocks

Abdelkarim Yelles-Chaouche[1] · Issam Abacha[1] · Oualid Boulahia[1] · Hamoud Beldjoudi[1] · Chafik Aidi[1] · Hichem Bendjama[1] · El-Mahdi Tikhamarine[2] · Yahia Mohammedi[1] · Adel Chami[1] · Redouane Chimouni[1] · Abdelaziz Kherroubi[1]

Abstract

On March 18, 2021, at 00:04 UTC, a strong earthquake (Mw 6.0) hit Bejaia city, 200 km east of Algiers. Its epicenter was 15 km northeast of Cap Carbon in Bejaia Bay, making it the largest earthquake recorded offshore since the devastating earthquake (Mw 6.8) in Boumerdes on May 21, 2003. The earthquake had a maximum intensity of VII (EMS 98), triggering hundreds of aftershocks and damaging 2000 houses and social infrastructures, as well as causing several rock falls along the rocky coastline, but no human casualties were reported. The waveform inversion and spectral analysis of the mainshock and its largest aftershocks indicate an alignment along an E-W thrust fault plane offshore, dipping southward, the mainshock seismic moment of $M_0 = 9.7e + 17$ N.m. corresponding to a magnitude Mw = 6.0. The aftershocks illuminated a surface 22 km long (N–S) and 12 km wide; their statistical parameters were assessed by Guttenberg–Richter relationship, Omori decay, and temporal clustering. The b-value is estimated at 0.83, the p value at 0.95, and the n-value at 0.75 (i.e., 75% triggered events), which follows classical patterns of aftershock sequences and suggests the sequence tectonic genesis. Furthermore, previous studies showed that the epicentral area was positively charged by coseismic static stresses transferred from recent events in the Bejaia–Jijel margin. Exactly one year later, on March 19, 2022, a moderate earthquake struck the same epicentral zone, 3 km NW of the first shock, generating a moment $M_0 = 8.5e + 16$ N.m. corresponding to a magnitude Mw = 5.3; its focal mechanism also revealed an E–W striking reverse fault with a small strike-slip component. The present-day local stress field is characterized by a contractional tectonic regime ($R' = 2.99 \pm 0.24$) and σ1 orientation (N345°E) consistent with the maximum regional compressive stress direction (NNW–SSE). The 2021–2022 Bejaia Bay seismic sequence underlined the active tectonics linking the major E–W offshore thrust fault system and the NW–SE strike-slip Babors Transverse Fault system. This sequence, along with a number of other earthquakes that occurred around the Lesser Kabylia Block (LKB) over the last decade, likely highlights the ongoing incipient subduction process between Africa and Eurasia along the northern Algerian margin.

Introduction

In the last decade, there has been intense seismic activity in eastern Algeria around the Lesser Kabylian Block (LKB) (Yelles-Chaouche et al. 2022), one of the two main blocks representing the internal domain of the Maghrebides Chain (Fig. 1a). The active structures fringing the LKB are: The E-W Offshore Thrust Fault System (OFS) in the north, the NW–SE Babors Transverse Fault (BTF) system in the west, the major E–W Mcid Aïcha-Debbagh (MAD) fault in the

Edited by Prof. Ramon Zuñiga (CO-EDITOR-IN-CHIEF).

✉ Issam Abacha
  abacha.issam@yahoo.fr

[1] Research Center in Astronomy, Astrophysics, and Geophysics, 16340 Algiers, Algeria

[2] University Ferhat Abbas of Setif, Setif, Algeria

 Springer

Paper's link: https://link.springer.com/article/10.1007/s11600-023-01171-9

Pure and Applied Geophysics

The 24 January 2020 Mw 5.0 El Aouana Earthquake, Northeastern Algeria: Insights into a New NW–SE Right-Lateral Bejaia-Babors Shear Zone

Issam Abacha,[1] Oualid Boulahia,[1] Abdelkarim Yelles-Chaouche,[1] Hichem Bendjama,[1] Haakon Fossen,[2] Moulley Charaf Chabou,[3] Khaled Roubeche,[1] Sofiane Taki-Eddine Rahmani,[1] El-Mahdi Tikhamarine,[4] Yahia Mohammedi,[1] and Chafik Aidi[1]

Abstract—On January 24, 2020, a Mw 5.0 earthquake occurred in the El Aouana region, northeastern Algeria. This region is located at the western end of the Lesser Kabylian Block (LKB), a rigid body that was weakly deformed during the late Cenozoic tectonic phase, and it is characterized by a lower seismic activity than that in its bounding regions. The mainshock focal mechanism was estimated via both the P-wave first motion and waveform modeling methods. The earthquake was associated with the rupture of a NW–SE-oriented right-lateral strike-slip fault, as revealed by a 6 km long and 2 km wide aftershock cluster. The seismic moment estimated through waveform modeling was 3.6×10^{16} Nm, while spectral analysis yielded a value of 3.9×10^{16} Nm corresponding to a magnitude of Mw 5.0, a source radius of 1.6 km, and a stress drop of 4 MPa. The spatiotemporal evolution of the aftershock sequence, as modeled using a restricted epidemic-type aftershock sequence (RETAS) stochastic model, yielded a slope p = 1, indicating that the earthquake was generated by tectonic forces and that the aftershock sequence included many subsequences. The calculated stress tensor suggested N–S compression, rotated clockwise relative to NW–SE Eurasia–Africa convergence. Finally, the recent seismic activity (2012–2021) and geological observations in the area led to the suggestion of a new NW–SE right-lateral shear zone, namely, the Bejaia-Babors shear zone, which was incorporated into a seismotectonic growth model involving slip along inherited E–W structures. The pattern of stepover structures throughout this wide shear zone was enhanced during the recent seismic evolution.

Keywords: El Aouana, RETAS, source parameters, stress tensor, shear zone, stepovers.

[1] Center of Research in Astronomy, Astrophysics, and Geophysics, CRAAG, Route de l'Observatoire BP 63 Bouzaréah, Algiers, Algeria. E-mail: abacha.issam@yahoo.fr

[2] Museum of Natural History, University of Bergen, Allégaten 41, 5007 Bergen, Norway.

[3] Emerging Materials Research Unit, Department of Earth Sciences, Institute of Architecture and Earth Sciences, Ferhat Abbas University Setif 1, Setif, Algeria.

[4] Departement of Physics, Ferhat Abbas University Setif 1, Setif, Algeria.

Birkhäuser

1. Introduction

Northeastern Algeria is subjected to substantial, moderate, and shallow seismic activity due to its location along the African–Eurasian plate boundary (blue line in Fig. 1a). One of the main statistical characteristics of Algerian seismicity is its concentration in the country's eastern part, where nearly two-thirds of the recorded seismic events have occurred (Abacha, 2015; Yelles-Chaouche et al., 2006). In this territory, numerous seismic sequences took place over the past decade (2012–2021), particularly around the Lesser Kabylian Block (LKB) (Fig. 1b). These include the 2017 seismic sequences along the Mcid Aïcha-Debbagh Fault (MADF) in the south (Bendjama et al., 2021), the 2014 Ziama and 2019 Jijel earthquakes in the north (Yelles-Chaouche et al., 2021), and the 2012–2013 Bejaia-Babors sequences in the west (Boulahia et al., 2021).

On January 24, 2020, at 07 h 24 m 20 s, the region of Jijel was shaken once more by a shallow earthquake of magnitude Mw 5.0, namely, the El Aouana earthquake at the western boundary of the LKB, 20 km southwest of Jijel (Fig. 1c). The western transverse fault system of Bejaia-Babors constitutes a NW–SE-trending structure associated with right-lateral strike-slip earthquake focal mechanisms. Recent advances in understanding the fault geometry mechanism in this region have been obtained by Boulahia et al. (2021), who identified the majority of the currently known en echelon fault segments that define the western boundary of the transverse fault system. The El Aouana 2020 earthquake exhibits a focal mechanism with one of the planes subparallel to the eastern boundary of the transverse fault system.

Paper's link: https://link.springer.com/article/10.1007/s00024-023-03265-3

Contents lists available at ScienceDirect

Tectonophysics

journal homepage: www.elsevier.com/locate/tecto

ELSEVIER

A local magnitude scale (M_L) for Northern Algeria

Khaled Roubeche [a,b,*], Fethi Semmane [a], Issam Abacha [a], Oualid Boulahia [a],
Sofiane Taki-Eddine Rahmani [a,b], El-Mahdi Tikhamarine [b]

[a] *Center of Research in Astronomy, Astrophysics and Geophysics (CRAAG), BP 63, Bouzareah, Algiers, Algeria*
[b] *University Ferhat Abbas, Department of Physics, Setif, Algeria*

A B S T R A C T

This study presents a local magnitude scale (M_L) based on the original Richter definition and designed for use within the Algerian Digital Seismic Network (ADSN). The magnitude scale is derived from the analysis of 17,377 zero-peak maximum amplitude traces extracted from the vertical component, simulated as Wood-Anderson seismograms. These traces are taken from a dataset of 1901 earthquakes recorded between January 1, 2010, and June 1, 2022, at a minimum of five stations in the ADSN network. To better account for the attenuation of direct and refracted waves in northern Algeria, amplitude decay analysis reveals the presence of two transition distances at 90 and 190 km, resulting in three segments. A distance correction term, $-\log_{10}(A0)$, is introduced and described by the following trilinear function:

$$-log(A0) = \begin{cases} 0.6747*\log_{10}(R) + 0.0002*R + 1.6306 & R \leq 90 \\ 1.7736*\log_{10}(R) + 0.0002*R - 0.5169 & 90 < R \leq 190 \\ 2.4580*\log_{10}(R) + 0.0002*R - 2.0765 & R > 190 \end{cases}$$

R represents the hypocentral distance in kilometers. The derived distance correction formula provides a well-constrained M_L relationship for northern Algeria that is valid over a distance range of 5 to 600 km. Compared to other local magnitude relationships, the methodology proposed in this study consistently gives M_L values slightly higher than those calculated by the Southern California relationship over all distances, with an average difference of 0.2 units. We computed corrections for 72 stations by minimizing the M_L residuals. These corrections range from −0.50 to 0.54, highlighting the influence of local site effects on the amplitude of the seismic signal. The magnitude residuals using our magnitude relationship and incorporating the station corrections, show that the standard deviation has improved significantly, from 0.34 to 0.24. An M_L relationship specific to the northern Algerian region provides a valuable tool for seismic monitoring, hazard assessment, and earthquake research in the region.

1. Introduction

The magnitude is a fundamental seismological parameter that is closely linked to both earthquake shaking and seismic hazard. It is an integral part of numerous scientific activities, such as the creation of earthquake catalogs used, among other things, for the statistical analysis of earthquakes. These studies are essential for seismic hazard assessment and the calculation of parameters such as the Gutenberg-Richter b value (Wiemer and Wyss, 2002; Wyss, 2004; Ghosh et al., 2008). Since 1935 (Richter, 1935), a variety of magnitude scales have been developed.

Richter magnitude (also known as Local Magnitude, M_L) continues to be widely used as a significant reference point due to its simplicity and global reach, particularly in the media. M_L quantifies energy released by local earthquakes and evaluates seismic activity in specific regions (e.g., Richter, 1958; Kanamori and Jennings, 1978; Hutton and Boore, 1987; Boore, 1989). The local magnitude scale was originally created by measuring the highest horizontal amplitude, specifically from the zero to the peak of ground displacement on a Wood-Anderson seismogram. The Wood-Anderson seismometer is a horizontal torsion design with a natural period of 0.8 s, a magnification of 2800, and a damping constant

Paper's link: https://www.sciencedirect.com/science/article/abs/pii/S0040195124002373?via%3Dihub

ORIGINAL ARTICLE

Fluid-driven processes triggering the 2010 Beni-Ilmane earthquake sequence (Algeria): evidence from local earthquake tomography and 4D Vp/Vs models

Issam Abacha · Hichem Bendjama · Oualid Boulahia · AbdelKarim Yelles-Chaouche · Khaled Roubeche · Sofiane Taki-Eddine Rahmani · Mohamed Anis Melaim · El-Mahdi Tikhamarine

Abstract The 2010 Beni-Ilmane earthquake sequence, with 3 Mw ≥ 5.2 mainshocks, occurred in the southern Tellian Atlas approximately 200 km southeast of the Algiers. We offer updated 3D Vp and Vs models, and we outline the space and time variations in the Vp/Vs ratio of the Beni-Ilmane crust based on 2297 well-located aftershocks representing the complete aftershock sequence. Two main P-wave low-velocity patterns correspond to fault alignments determined from geological studies: the NE–SW thrust fault located at the foot of Djebel Choukchot and the NNW–SSE oriented Samma strike-slip corridor. The former crosscuts the two P-wave high-velocity anomalies of the Kef Ouagnane and Kef Kherrat summits of the Choukchot Mountains. The third high-velocity anomaly represents the Jebel Affroun Mountain in the sub-Bibanic domain. Two high-Vp/Vs ratio patterns were revealed in the central aftershock part and along the NE–SW Ouanougha syncline, which constitutes a fluid reservoir and a fluid-saturated fault zone filled after aftershock activity. The 4D Vp/Vs models monitored fluid migration, and the modeled pore-pressure diffusion revealed that earthquake rupture along an ~N–S blind strike-slip fault fractured the closed reservoir and released high-pressure fluids, provoking a notable and long-lasting aftershock sequence. Our study underlines that local earthquake tomography (LET) can provide useful insights into the upward migration of fluids from a compartmentalized hydrocarbon reservoir.

Highlights
• This updated investigation used twice the number of events from a previous study.
• A high-Vp/Vs anomaly coincided with hydrocarbon reservoirs and fluid-saturated faults.
• The migration of high-pressure fluids released from a ruptured reservoir caused aftershock activity.

I. Abacha (✉) · H. Bendjama · O. Boulahia · A. Yelles-Chaouche · K. Roubeche · S. T.-E. Rahmani
Center of Research in Astronomy, Astrophysics, and Geophysics, CRAAG, Route de L'Observatoire BP 63 Bouzaréah, Algiers, Algeria
e-mail: abacha.issam@yahoo.fr

M. A. Melaim · E.-M. Tikhamarine
University Ferhat Abbas of Setif, Setif, Algeria

1 Introduction

In May 2010, the Beni-Ilmane region (north-central Algeria, Fig. 1a) was struck by a never-before-seen seismic sequence, as this was the first time in Algeria that a sequence was observed with three mainshocks of a Mw ≥ 5.2 magnitude, recorded on May 14, 16,

Ⓢ Springer

Paper's link: https://link.springer.com/article/10.1007/s10950-022-10130-8
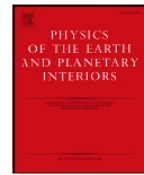
Exploring the structural components of the Bejaia-Babors shear zone (BBSZ) in NE Algeria: Evidence from local earthquake tomography using recent seismic events (2012–2022)

Issam Abacha [a,*], Khaled Roubeche [a], Hichem Bendjama [a], El-Mahdi Tikhamarine [b],
Oualid Boulahia [a], Radia Kherchouche [a], Sofiane Taki-Eddine Rahmani [a], Hamoud Beldjoudi [a]

[a] *Center of Research in Astronomy, Astrophysics, and Geophysics, CRAAG, Route de l'Observatoire BP 63 Bouzaréah, Algiers, Algeria*
[b] *University Ferhat Abbas of Setif, Algeria*

ABSTRACT

In recent years, the Algerian region of Bejaia-Babors (BB) has experienced significant seismic activity, including the Bejaia-Babors seismic sequence in 2012–2013, the Jijel earthquake in 2019, the El Aouana earthquake in 2020, and Bejaia subsequent earthquakes in 2021 and 2022. These seismic events have not only brought to light the existence of the Bejaia-Babors Shear Zone (BBSZ) but have also emphasized the importance of discerning its structural components, depth, and extent. Our study focuses on the analysis of seismological data from 2012 to 2022, with a particular emphasis on elucidating the intricacies of this geological structure. Using the LOTOS (local tomography software) algorithm, we conducted three iterations of tomographic inversion, successfully obtaining horizontal and vertical sections that facilitated the identification and characterization of subsurface anomalies. The resulting 3D velocity models unveiled key tectonic structures within the BBSZ, including the Offshore Faults System of Jijel (OFSJ), South Greater Kabylia Fault (SGKF), Transversal Fault 1 (TF1), and the collision between the Lesser Kabylia Block (LKB) and the Babors (THF-1). Futhermore, brittle-ductile shears were identified along the Aftis Fault (AF) in the east and brittle shears along the Babors Transverse Fault (BTF) in the west. P-wave velocity analysis indicated the presence of rigid blocks. The observed high Vp/Vs ratio near segment 3 of the BTF fault suggests the presence of a fluid reservoir, likely involved in the Bejaia-Babors seismic sequence (2012–2013), as previously documented. These findings provide valuable insights into the tectonic framework of the BBSZ, highlighting major fault systems and the interaction between different tectonic blocks. The presence of brittle-ductile shears along the AF suggests complex deformation processes in this region. Overall, by identifying key fault systems, characterizing subsurface anomalies, and unveiling the presence of fluid reservoirs, our research not only contributes significantly to geodynamic knowledge but also holds immense significance for seismic hazard assessment, resource exploration, and future research in this field.

1. Introduction

Over the past decade and since the establishment of the large digital network known as ADSN in 2007, the Bejaia-Babors region, hereafter referred to as BB, located in northeastern Algeria, has witnessed a notable increase in seismic activity characterized by events of small to moderate magnitudes. From a geological perspective, this region lies between two distinct blocks of Kabylia: The Greater Kabylia Block (GKB) to the west and the Lesser Kabylia Block (LKB) to the east. These two blocks emerged following the fragmentation of the AlKaPeCa

microplate, as evidenced by the presence of red surfaces in Fig. 1a. During the Oligocene-Lower Miocene period, the GKB and LKB blocks, constituting the internal domains, underwent a phase of collision and over-thrusting against the African margin, particularly in the Babors range, a component of the Tellian Atlas formation (specifically detailed by Durand-Delga (1969) (refer to Fig. 1b). The BB zone occupies an intermediate position, marked by the yellow box in Fig. 1b, considered as a transition area between two contrasting deformation regimes: (1) a broad belt characterized by folds and thrusts, represented by the red rectangle in Fig. 1b, prevalent in the western and central regions of

Paper's link: https://www.sciencedirect.com/science/article/abs/pii/S0031920125000123?via%3Dihub

République Algérienne Démocratique et Populaire
Ministère de l'Intérieur, des Collectivités Locales et de l'Aménagement du Territoire
Centre de Recherche en Astronomie, Astrophysique et Géophysique

Projet :
Imagerie Haute Résolution des Failles Actives Dans L'est Algérien. Réévaluation de L'aléa Sismique

Chef de projet : Issam Abacha
Equipe : Sismologie
Division : Etudes sismologiques
Référence : ES-04-2020

Résumé

Le déploiement dense de stations sismologiques de haute qualité du réseau numérique permanent (ADSN), et l'installation de plusieurs réseaux temporaires suite aux différents séismes algériens, ont permis au CRAAG de construire un jeu de données unique contenant principalement des évènements sismiques modérés. L'étude détaillée de ces évènements et notamment la relocalisation de toutes les séquences par des techniques de haute résolution permettrait l'identification fine et la classification des failles actives. Leurs caractérisations se fait en calculant les paramètres de la source sismique et l'établissement des lois d'échelle. La réévaluation des cartes de l'aléa sismique se fera en tenant en compte de tous ces résultats et des autres études récentes dans la région.

Affiliation institutionnelle et adresse de correspondance *(Equipe, Division, e-mail)*

(CRAAG/Sismologie, Des études sismologiques, i.abacha@craag.dz)

Noms des chercheurs impliqués *(diplômes, grades, institutions : internes et externes, y compris doctorants)*

Yelles-Chaouche AbdelKarim (PhD, DR, CRAAG)
Boulahia Oualid (MAG, AR, CRAAG)
Bendjama Hichem (MAG, AR, CRAAG)
Semmane Fethi (DN, DR, CRAAG)
Radi Zohir (DS + HDR et MR A)
Rahmani Sofiane Taki-Eddine (MSc, Ingénieur, CRAAG)
Roubeche Khaled (MSc, Ingénieur, CRAAG)
Tikhamarine El-Mahdi (MSc, Doctorant, UFAS1)
Melaime Mohamed Anis (MSc, Doctorant, UFAS1)
Boudraa Nadjoua (Licence, Etudiante en MSc, UFAS1)

République Algérienne Démocratique et Populaire
Ministère de l'Intérieur, des Collectivités Locales et de l'Aménagement du Territoire
Centre de Recherche en Astronomie, Astrophysique et Géophysique

Projet :
Amélioration de l'évaluation de l'aléa sismique en Algérie : Modélisation du mouvement du sol post-séisme majeur et projection des répliques « forecasting »

Chef de projet : Issam Abacha
Equipe : Sismologie
Division : Etudes sismologiques
Référence : ES-01-2024

Résumé

Le projet ES-04-2020 a permis une caractérisation approfondie des failles sismiques, comprenant la relocalisation des séismes, l'analyse spatio-temporelle, l'estimation des paramètres de source, et l'identification des mécanismes des séquences sismiques. Une base de données des failles actives a été développée pour réévaluer l'aléa sismique. En continuité, le projet ES-01-2024 explore deux axes principaux : la simulation des mouvements forts du sol et l'anticipation de l'évolution des répliques sismiques. La simulation vise à estimer l'accélération des secousses lors de séismes majeurs, en intégrant la magnitude, la rupture, la distance à la source et les conditions géologiques locales, tout en utilisant de petits séismes pour modéliser de plus grands. L'anticipation des répliques concerne leur distribution spatio-temporelle et leur magnitude maximale. Ces résultats renforcent l'évaluation de l'aléa sismique et contribuent à une révision continue du code parasismique (RPA).

Affiliation institutionnelle et adresse de correspondance *(Equipe, Division, e-mail)*

(CRAAG/Sismologie, Des études sismologiques, i.abacha@craag.dz)

Noms des chercheurs impliqués *(diplômes, grades, institutions : internes et externes, y compris doctorants)*

Boulahia Oualid (DS, MR B, CRAAG)
Bendjama Hichem (DS, MR B, CRAAG)
Rahmani Sofiane Taki-Eddine (MSc, Ingénieur, CRAAG)
Tikhamarine El-Mahdi (MSc, Doctorant, UFAS1)
Beldjoudi Hamoud (DS, DR, CRAAG)
Kherroubi Abdelaziz (DS, DR, CRAAG)
Roubeche Khaled (MSc, Ingénieur, CRAAG)
Mohammedi Yahia (MAG, Attaché de Recherche, CRAAG)
Dilmi Takieddine (MSc, Ingénieur, CRAAG)
Guettouche Salim (MAG, Chargé de Recherche, CRAAG)
Bouadja Foued (MAG, MA, Université de Constantine)
Radi Zohir (DS, DR, CRAAG)

Abstract

Seismology has experienced significant advancements since its establishment in the mid-20th century, driven by the increasing need to comprehend and mitigate the impacts of earthquakes. Earthquakes, often sudden and violent, have long been a source of fear and terror due to their devastating effects on both infrastructure and human lives. As the understanding of plate tectonics and seismic activity evolved, modern seismology emerged as a powerful tool to investigate the underlying causes of these natural phenomena. The present thesis, titled "High-Resolution Aftershock-Based Imaging of Active Faults, Source Parameters, and Earthquake Driving Mechanisms: A Contribution to Seismic Hazard Assessment in Northeastern Algeria" builds upon these developments. The main aim is to contribute valuable insights to the assessment of seismic hazards in the northeastern region of Algeria. The thesis is structured around three core components. First, it focuses on high-resolution aftershock-based imaging, providing detailed depictions of fault systems to improve the understanding of fault geometries and potential earthquake nucleation zones. Utilizing advanced techniques such as double-difference relocation and hierarchical clustering of earthquake multiplet, this work identifies previously unmapped fault segments. Second, it involves the analysis of earthquake source parameters, including seismic moment, fault geometry, stress drop, and source radius. These parameters provide crucial insights into earthquake mechanics and the characteristics of faults in the study area. Third, the research investigates earthquake driving mechanisms, including tectonic loading, stress transfer, fluid intrusion, and aseismic slip, to unravel the complex factors contributing to earthquake occurrence in this tectonically active region. Our research began with a detailed analysis of the Beni-Ilmane sequence 2010, serving as a foundation for generalizing our methodology to seismic sequences that occurred between 2007 and 2022 across northeastern Algeria. By analyzing seismic sequences from 2007 to 2022, this research compiles a comprehensive database of active faults, seismic parameters, and earthquake mechanisms. The Findings serves as a critical resource for evaluating seismic hazard and developing risk mitigation strategies. This work highlights the importance of integrating seismic data, fault imaging, and earthquake modeling to enhance the resilience of infrastructures in northeastern Algeria against future seismic events.

Key words: High precision relocation. Aftershocks-based imaging. Focal mechanism analysis. Moment tensor analysis. Earthquake mutiplet. Repeating earthquakes. Driving mechanisms. Earthquake source parameters. Active faults. Northeastern Algeria. Beni-Ilmane. Seismic hazards.

الملخص

شهد علم الزلازل تطورات كبيرة منذ نشأته في منتصف القرن العشرين، مدفوعًا بالحاجة المتزايدة لفهم وتخفيف آثار الزلازل. كانت الزلازل، التي غالبًا ما تكون مفاجئة وعنيفة، مصدرًا للرعب والاهتمام نظرًا لتأثيراتها المدمرة على البنية التحتية والحياة البشرية. مع تطور فهم الصفائح التكتونية والنشاط الزلزالي، برز علم الزلازل الحديث كأداة قوية للتحقيق في الأسباب الكامنة وراء هذه الظواهر الطبيعية. تبني الأطروحة الحالية، بعنوان "التصوير عالي الدقة للفوالق النشطة من خلال الهزات الارتدادية، خصائص المصدر الزلزالي، وآليات حدوث الزلازل: مساهمة في تقييم المخاطر الزلزالية في شمال شرق الجزائر"، على هذه التطورات. الهدف الرئيسي هو تقديم رؤى قيمة للمساهمة في تقليل المخاطر الزلزالية في منطقة شمال شرق الجزائر. تُبنى الأطروحة حول ثلاثة ركائز أساسية. أولاً، تركز على التصوير عالي الدقة للفوالق النشطة اعتمادا على توزع الهزات الارتدادية، حيث تقدم تصورات دقيقة لأنظمة الفوالق لتحسين فهم هندسة الفوالق ومناطق نشوء الزلازل المحتملة. باستخدام تقنيات متقدمة مثل إعادة تحديد المواقع باستخدام طريقة الفرق المزدوج وتصنيف مجموعات الزلازل المتعددة بطريقة هرمية، تُحدد هذه الدراسة قطاعات فوالق غير معروفة سابقًا. ثانيًا، تتناول الأطروحة تحليل خصائص المصدر الزلزالي، بما في ذلك العزم الزلزالي، وفرق الإجهاد، ونصف قطر المصدر. تقدم هذه المعلومات رؤى أساسية حول ميكانيكا الزلازل وخصائص الفوالق في منطقة الدراسة. ثالثًا، تدرس الأطروحة الآليات المحركة للزلازل، بما في ذلك التحميل التكتوني، وانتقال الإجهاد، وتأثير السوائل، والانزلاق الزلزالي، لفهم العوامل المعقدة التي تساهم في حدوث الزلازل في هذه المنطقة النشطة تكتونيًا. بدأت دراستنا بتحليل مفصل لسلسلة زلازل بني يلمان 2010، والذي شكل الأساس لتعميم منهجيتنا على التسلسلات الزلزالية التي حدثت بين عامي 2007 و2022 عبر شمال شرق الجزائر. من خلال تحليل التسلسلات الزلزالية من 2007 إلى 2022، تجمع هذه الدراسة قاعدة بيانات شاملة للفوالق النشطة، وخصائصها الزلزالية، وآليات حدوث الزلازل. تُعد نتائج هذه الاطروحة هذه موردًا هامًا لتقييم المخاطر الزلزالية وتطوير استراتيجيات التخفيف من المخاطر. كما وتسلط هذه الدراسة الضوء على أهمية دمج البيانات الزلزالية وتصوير الفوالق ونمذجة الزلازل لتعزيز جاهزية البنى التحتية في شمال شرق الجزائر أمام الأحداث الزلزالية التي قد تحدث.

كلمات مفتاحية

إعادة تحديد المواقع بدقة عالية. تصوير الفوالق بالستعمال الهزات الارتدادية. تحليل الآليات البؤرية. تحليل العزم الزلزالي. زلازل متعددة. الزلازل المتكررة. الآليات المحرضة للزلازل. خصائص المصدر الزلزالي. الفوالق النشطة. شمال شرق الجزائر. بني يلمان. المخاطر الزلزالية.

Résumé

La sismologie a connu des avancées significatives depuis sa création au milieu du XXe siècle, en réponse à un besoin croissant de comprendre et d'atténuer les effets des tremblements de terre. Ces derniers, souvent soudains et violents, suscitent à la fois crainte et terreur en raison de leurs conséquences dévastatrices sur les infrastructures et les vies humaines. Avec l'évolution des connaissances sur la tectonique des plaques et l'activité sismique, la sismologie moderne est devenue un outil puissant pour explorer les causes profondes de ces phénomènes naturels. La présente thèse, intitulée « Imagerie haute résolution des failles actives à partir des répliques, paramètres de source et mécanismes déclencheurs des séismes : une contribution à l'évaluation de l'aléa sismique dans le nord-est de l'Algérie. », s'appuie sur ces avancées. L'objectif principal est d'apporter des contributions importantes pour l'évaluation de l'aléa sismique dans la région nord-est de l'Algérie. La thèse est structurée autour de trois composantes principales. Tout d'abord, elle se concentre sur l'imagerie haute résolution basée sur les répliques, fournissant des représentations détaillées des systèmes de failles pour améliorer la compréhension de la géométrie des failles et des zones potentielles de nucléation des séismes. Grâce à des techniques avancées telles que la relocalisation par double différence et le regroupement hiérarchique des multiplets sismiques, ce travail identifie des segments de failles non cartographiés précédemment. Ensuite, elle analyse les paramètres des sources sismiques, tels que le moment sismique, la géométrie des failles, la chute de contrainte et le rayon de la source. Ces paramètres fournissent des informations cruciales sur la mécanique des tremblements de terre et les caractéristiques des failles dans la zone étudiée. Enfin, cette recherche explore les mécanismes forçants des tremblements de terre, notamment le chargement tectonique, le transfert de contraintes, l'intrusion de fluides et le glissement asismique, afin de comprendre les facteurs complexes qui contribuent à l'occurrence des séismes dans cette région tectoniquement active. Notre recherche a débuté par une analyse détaillée de la séquence de Beni-Ilmane 2010, servant de base pour généraliser notre méthodologie aux séquences sismiques ayant eu lieu entre 2007 et 2022 dans le nord-est de l'Algérie. En analysant les séquences sismiques de 2007 à 2022, cette recherche compile une base de données exhaustive sur les failles actives, les paramètres sismiques et les mécanismes de déclenchement des tremblements de terre. Cette base de données constitue une ressource essentielle pour évaluer l'aléa sismique et élaborer des stratégies de réduction des risques. Ce travail souligne l'importance d'intégrer les données sismiques, l'imagerie des failles et la modélisation des séismes afin de renforcer la résilience des infrastructures du nord-est de l'Algérie face aux futurs événements sismiques.

Mots-clés : Relocalisation de haute précision. Imagerie des failles à partir les répliques. Analyse des mécanismes focaux. Analyse du tenseur de moment. Multiplets sismiques. Séismes récurrents. Mécanismes forçant. Paramètres de la source sismique. Failles actives. Nord-est de l'Algérie. Beni-Ilmane. Aléa sismique.